

UNCLASSIFIED

AD NUMBER	
AD516032	
CLASSIFICATION CHANGES	
TO:	unclassified
FROM:	confidential
LIMITATION CHANGES	
TO:	Approved for public release, distribution unlimited
FROM:	Distribution authorized to U.S. Gov't. agencies and their contractors; Administrative/Operational Use; Mar 1971. Other requests shall be referred to Air Force Flight Dynamics Lab., Wright-Patterson AFB, OH 45433.
AUTHORITY	
31 Mar 1977, GDS, DoD 5200.1-r; AFFDL ltr, 28 Nov 1979	

THIS PAGE IS UNCLASSIFIED

THIS REPORT HAS BEEN DELIMITED
AND CLEARED FOR PUBLIC RELEASE
UNDER EOD DIRECTIVE 5200.20 AND
NO RESTRICTIONS ARE IMPOSED UPON
ITS USE AND DISCLOSURE.

DISTRIBUTION STATEMENT A

APPROVED FOR PUBLIC RELEASE;
DISTRIBUTION UNLIMITED.

GENERAL DECLASSIFICATION SCHEDULE

**IN ACCORDANCE WITH
DOD 5200.1-R & EXECUTIVE ORDER 11652**

SECURITY MARKING

The classified or limited status of this report applies to each page, unless otherwise marked.

Separate page printouts MUST be marked accordingly.

THIS DOCUMENT CONTAINS INFORMATION AFFECTING THE NATIONAL DEFENSE OF THE UNITED STATES WITHIN THE MEANING OF THE ESPIONAGE LAWS, TITLE 18, U.S.C., SECTIONS 793 AND 794. THE TRANSMISSION OR THE REVELATION OF ITS CONTENTS IN ANY MANNER TO AN UNAUTHORIZED PERSON IS PROHIBITED BY LAW.

NOTICE: When government or other drawings, specifications or other data are used for any purpose other than in connection with a definitely related government procurement operation, the U.S. Government thereby incurs no responsibility, nor any obligation whatsoever; and the fact that the Government may have formulated, furnished, or in any way supplied the said drawings, specifications, or other data is not to be regarded by implication or otherwise as in any manner licensing the holder or any other person or corporation, or conveying any rights or permission to manufacture, use or sell any patented invention that may in any way be related thereto.

CONFIDENTIAL

AFFDL-TR-71-34

AN EXPERIMENTAL STUDY OF PLUME EFFECTS ON LIFTING REENTRY VEHICLES (u)

CONVAIR AEROSPACE DIVISION OF GENERAL DYNAMICS

MARCH 1971

TECHNICAL REPORT AFFDL-TR-71-34

This material contains information affecting the national defense of the United States within the meaning of the Espionage Laws (Title 18, U.S.C., sections 793 and 794) the transmission or revelation of which in any manner to an unauthorized person is prohibited by law.

In addition to security requirements which must be met, this document is subject to special export controls and each transmittal to foreign governments or foreign nationals may be made only with prior approval of Air Force Flight Dynamics Laboratory (FDMG), Wright-Patterson AFB, Ohio 45433.

GROUP 4

Downgraded at 3 year intervals;

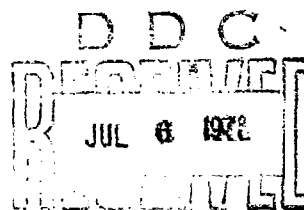
Declassified after 12 years.

DOD DIR 5200.10

**AIR FORCE FLIGHT DYNAMICS LABORATORY
AIR FORCE SYSTEMS COMMAND
WRIGHT-PATTERSON AIR FORCE BASE, OHIO**

CONFIDENTIAL

AD516032



UNCLASSIFIED

NOTICE

When Government drawings, specifications, or other data are used for any purpose other than in connection with a definitely related Government procurement operation, the United States Government thereby incurs no responsibility nor any obligation whatsoever; and the fact that the government may have formulated, furnished, or in any way supplied the said drawings, specifications, or other data, is not to be regarded by implication or otherwise as in any manner licensing the holder or any other person or corporation, or conveying any rights or permission to manufacture, use, or sell any patented invention that may in any way be related thereto.

Copies of this report should not be returned unless return is required by security considerations, contractual obligations, or notice on a specific document.

UNCLASSIFIED

CONFIDENTIAL

AN EXPERIMENTAL STUDY OF PLUME EFFECTS ON LIFTING REENTRY VEHICLES (u)

John R. Rausch

This material contains information affecting the national defense of the United States within the meaning of the Espionage Laws (Title 18, U.S.C., sections 793 and 794) the transmission or revelation of which in any manner to an unauthorized person is prohibited by law.

In addition to security requirements which must be met, this document is subject to special export controls and each transmittal to foreign governments or foreign nationals may be made only with prior approval of Air Force Flight Dynamics Laboratory (FDMG), Wright-Patterson AFB, Ohio 45433.

RECORDED
JUL 6 1951
INDEXED

CONFIDENTIAL

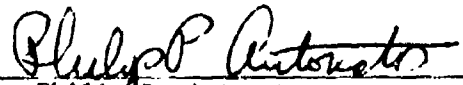
UNCLASSIFIED

FOREWORD

This is the final report of the work accomplished under Air Force Contract F33615-70-C-1048 and provides the results of work performed during the period from 15 September 1969 to 15 March 1971. The work was administered under the direction of the Air Force Flight Dynamics Laboratory, Wright Patterson Air Force Base, by Mr. Richard Smith to whom appreciation is given for his guidance and assistance.

The model design was performed by Messers J. Beard and W. K. Alexander of the Convair Model Design Group and models were fabricated by H & N Minicraft. The tests were conducted at AEDC and special appreciation must be given to W. T. Strike the test conductor for his interest and assistance in the program. Miss E. B. Hearn assisted in the data compilation, correlation, and analysis tasks and Mrs. D. Hall assisted in final report preparation.

This technical report has been reviewed and is approved.



Philip P. Antonatos
Chief, Flight Mechanics Division
Air Force Flight Dynamics Laboratory

UNCLASSIFIED

UNCLASSIFIED

CONFIDENTIAL

UNCLASSIFIED ABSTRACT

Tests were conducted at Mach numbers of 6, 8, and 10 on a representative lifting body entry vehicle and a Mach number of 10 on a flat plate using heated air and other gases to simulate rocket exhaust plumes. Extensive flow separation resulting from the plumes was observed on both configurations during the test program and the most powerful parameters which affected plume induced separation included:

1. model shape
2. angle of attack
3. Reynolds number
4. nozzle expansion ratio
5. nozzle total pressure
6. nozzle gas temperature and specific heat.

The flat plate model showed much less flow separation than the delta planform at similar test conditions, however, serious problems in control effectiveness were indicated on both models for the aft mounted elevon. The data did not correlate well with existing semi-empirical correlations developed for control surface induced separation and plume shape. New semi-empirical correlations were developed for predicting plume shape in a region of plume induced separation and for predicting the pressure and the extent of the separated region.

UNCLASSIFIED

UNCLASSIFIED

TABLE OF CONTENTS

<u>Section</u>	<u>Page</u>
1. Introduction	1
2. Test Facilities	3
2.1 Test Facilities	3
2.1.1 Auxiliary Air Supply	4
2.2 Model Description	4
2.2.1 Delta Planform Configuration	5
2.2.2 Flat Plate Configuration	6
2.2.3 Exhaust Nozzles and Extensions	6
2.2.4 Instrumentation	8
2.2.5 Flow Survey Pake	10
2.3 Test Summary.	13
2.3.1 Pressure Tests Summary	13
2.3.2 Oil Flow Summary	14
2.3.3 Flow Field Surveys	20
2.4 Data Accuracy	20
3. Test Results	22
3.1 Flat Plate Data	22
3.1.1 Flat Plate Centerline Data	22
3.1.2 Flat Plate Spanwise Pressure Distribution	24
3.1.3 Summary of Flat Plate Test Results	26
3.2 Test Results on Delta Bottom Centerline	27
3.2.1 Bottom Centerline Data at a Mach Number of 10	27
3.2.2 Delta Bottom Centerline Data at Mach 8	29
3.2.3 Bottom Centerline Data at a Mach Number of 6	30
3.3 Delta Bottom Spanwise Distribution.	31
3.3.1 Spanwise Distribution at Mach 10	32
3.3.2 Bottom Pressure Distributions at Mach 8	32
3.3.3 Bottom Pressure Distributions at Mach 6	32

UNCLASSIFIED

<u>Section</u>	<u>Page</u>
3.4 Upper Surface Pressure Distribution	33
3.4.1 Upper Surface Pressures at Mach 10	33
3.4.2 Upper Surface Pressures at Mach 8	34
3.4.3 Upper Surface Pressures at Mach 6	35
3.5 Base Pressure Data	36
3.6 Summary of Delta Configuration Pressure Results	36
3.7 Oil Flow Data	37
3.8 Schlieren Data	37
3.9 Flow Survey Data	38
3.9.1 Flow Surveys with Disc	39
4. Data Analysis	41
4.1 Plume Shape	41
4.1.1 Initial Turning Angle	41
4.1.2 Plume Initial Radius	42
4.2 Separation Length Analysis	47
4.2.1 Upstream Interaction Length at Zero Angle of . . .	47
Attack	
4.2.2 Upstream Interaction Length at Positive Angle. . .	51
of Attack	
4.2.3 Upstream Interaction Length on Leeward Surface . .	51
4.2.4 Free Interaction Length	52
4.3 Plateau Pressure Analysis	53
4.3.1 Plateau Pressure at Zero Angle of Attack	53
4.3.2 Plateau Pressure on Windward Surfaces	55
4.3.3 Plateau Pressure on Leeward Surfaces	55
4.4 Recommended Method.	55
4.4.1 Windward Surfaces	56
4.4.2 Leeward Surfaces or Surfaces not Exposed to. . . .	57
Stream	
4.4.3 Methods to Minimize Plume Induced Separation . . .	57
5. Conclusions and Recommendations	58
6. References	59

UNCLASSIFIED

<u>Section</u>		<u>Page</u>
	Appendices	
I	Test Conditions.	291
II	Flat Plate and Bottom Centerline Data	298
III	Upper Surface Data	305
IV	Plume Data	307

UNCLASSIFIED

LIST OF ILLUSTRATIONS

<u>Figure No.</u>		<u>Page</u>
1	Delta Planform Configuration.....	61
2	Vertical Fin Modification.....	62
3	Delta Model Installed in Tunnel C.....	63
4	Delta Model Mounted in Inverted Position for Tests in Tunnel C.....	64
5	Rear View of Delta Model Mounted on Sting.....	65
6	Flat Plate Model Assembly.....	66
7	Flat Plate Installed in Tunnel C.....	67
8	Nozzle Exit Locations.....	68
9	Nozzle in Basic Position on Flat Plate Model.....	69
10	Instrumentation on the Flat Plate Surface.....	70
11	Delta Planform Bottom Surface Instrumentation.....	71
12	Upper Surface Pressure Tap Circumferential Locations.....	72
13	Upper Surface Instrumentation.....	73
14	Base Pressure Instrumentation Locations.....	74
15	Flow Field Survey Rake.....	75
16	Effect of Angle of Attack on Flat Plate Centerline Pressure at Mach 10 and $R_e = .51 \times 10^{-6}$ / ft.....	76
17	Effect of Reynolds Number on the Flat Plate Centerline Pressure at a Mach Number of 10 and $P_j/P_\infty = 0$	77
18	Effect of Jet Pressure Ratio on Flat Plate Center- line Pressure at Zero Angle of Attack for Nozzle 6.	78
19	Flat Plate Oil Flow Visualization of the Effect of Jet Pressure Ratio.....	79
20	Effect of Jet Pressure Ratio on Flat Plate Centerline Pressure at 5° Angle of Attack for Nozzle 6.....	80
21	Effect of Jet Pressure Ratios on Flat Plate Center- line Pressure at 10° Angle of Attack for Nozzle 6..	81
22	Effect of Jet Pressure Ratio on Flat Plate Center- line Pressure at 15° Angle of Attack for Nozzle 6..	82

UNCLASSIFIED

LIST OF ILLUSTRATIONS (continued)

<u>Figure No.</u>		<u>Page</u>
23	Effect of Jet Pressure Ratio on Flat Plate Centerline Pressure at an Angle of Attack of -5° for Nozzle 6.....	83
24	Effect of Jet Pressure Ratio on Flat Plate Centerline Pressure at an Angle of Attack of -10° for Nozzle 6.....	84
25	Effect of Jet Pressure Ratio on Flat Plate Centerline Pressure at Zero Angle of Attack for Nozzle 2.....	85
26	Flat Plate Oil Flow Visualization of the Effect of Nozzle Expansion Ratio.....	86
27	Effect of Jet Pressure Ratio on Flat Plate Centerline Pressure at Zero Angle of Attack for Nozzle 3.....	87
28	A Comparison of Nozzle Expansion Ratio Effects on Flat Plate Centerline Pressure for Nozzles 2 and 3 at a Chamber Pressure of 1500 psi.....	88
29	Effect of Nozzle Size on Flat Plate Centerline Pressure at Zero Angle of Attack.....	89
30	A Comparison of Nozzle Exit Angle Effects on Flat Plate Centerline Pressure at Zero Angle of Attack.....	90
31	Effect of Nozzle Position on Flat Plate Centerline Pressure for Nozzle 6.....	91
32	A Comparison of Exhaust Gas Effects on Flat Plate Centerline Pressure at Zero Angle of Attack.....	92
33	Effect of Reynolds Number on Flat Plate Centerline Pressure at Zero Angle of Attack and a Jet Pressure Ratio of 8500 for Nozzle 6.....	93
34	Effect of Elevon Extensions on Flat Plate Centerline Pressure at Zero Angle of Attack and a Jet Pressure Ratio of 8000 for Nozzle 6.....	94
35	Flat Plate Oil Flow Visualization of the Effect of Elevon.....	95
36	Effect of a Control Deflection of -15° on Flat Plate Centerline Pressure at Zero Angle of Attack and a Jet Pressure Ratio of 17000 for Nozzle 6.....	96
37	Effect of Plume Combined with $+20^{\circ}$ Control Deflection on Flat Plate Centerline Pressure.....	97

UNCLASSIFIED

LIST OF ILLUSTRATIONS (continued)

<u>Figure No.</u>		<u>Page</u>
38	Flat Plate Spanwise Pressure Distribution for $P_j/P_\infty = 2157$	98
39	Flat Plate Spanwise Pressure Distribution for $P_j/P_\infty = 4342$	99
40	Flat Plate Spanwise Pressure Distribution for $P_j/P_\infty = 8398$	100
41	Flat Plate Spanwise Distribution for $P_j/P_\infty = 17471$	101
42	Flat Plate Spanwise Distribution for $P_j/P_\infty = 34086$	102
43	Flat Plate Spanwise Pressure Distribution for $P_j/P_\infty = 68663$	103
44	Flat Plate Spanwise Pressure Distribution for $P_j/P_\infty = 89290$	104
45	Flat Plate Pressure Distribution at $\alpha = -10^\circ$ and $P_j/P_\infty = 4399$	105
46	Flat Plate Spanwise Distribution for Nozzle 2 and $P_j/P_\infty = 4264$	106
47	Spanwise Pressure Distribution for Nozzle 2 and $P_j/P_\infty = 8628$	107
48	Flat Plate Spanwise Pressure Distribution for Nozzle 3 and $P_j/P_\infty = 1241$	108
49	Flat Plate Spanwise Distribution with Extension Installed.....	109
50	Effect of Control Surface Deflection on the Flat Plate Spanwise Pressure Distribution.....	110
51	Flat Plate Spanwise Pressure Distribution with Control Deflection and Plume.....	111
52	Delta Bottom Centerline Pressure Without a Plume at a Mach Number of 10.....	112
53	Effect of -15 Degree Control Deflection on Delta Planform Bottom Centerline Pressure at Mach 10.....	113
54	Effect of a +20 Degree Control Deflection on Delta Planform Bottom Centerline Pressure at a Mach Number of 10 and $P_j/P_\infty = 0$	114
55	Effect of Reynolds Number on the Delta Planform Bottom Centerline Pressure at a Mach Number of 10 and $P_j/P_\infty = 0$	115

UNCLASSIFIED

LIST OF ILLUSTRATIONS (continued)

<u>Figure No.</u>		<u>Page</u>
56	A Comparison of Centerline Pressure on the Bottom Centerline of the Flat Plate and Delta Configuration at $M = 10$ and $R_e = .5 \times 10^{-6}/ft$	116
57	Effect of Jet Pressure Ratio on Bottom Centerline Pressure on the Delta Planform at a Mach Number of 10 and Zero Angle of Attack for Nozzle 6.....	117
58	Oil Flow Visualization of the Effect of Jet Pressure Ratio on the Delta Configuration.....	118
59	Effect of Jet Pressure Ratio on Bottom Centerline Pressure on the Delta Planform at a Mach Number of 10 and 2.5° Angle of Attack for Nozzle 6.....	119
60	Effect of Jet Pressure Ratio on Bottom Centerline Pressure on the Delta Planform at Mach 10 and 5° Angle of Attack.....	120
61	Effect of Jet Pressure Ratio on Bottom Centerline Pressure on the Delta Planform at Mach 10 and 7.5° Angle of Attack.....	121
62	Effect of Jet Pressure Ratio on Delta Bottom Centerline Pressure at Mach 10 and 10° Angle of Attack....	122
63	Effect of Jet Pressure Ratio in Delta Bottom Centerline Pressure at Mach 10 and 15° Angle of Attack....	123
64	Effect of Jet Pressure Ratio on Delta Bottom Centerline Pressure at Mach 10 and 20° Angle of Attack....	124
65	Angle of Attack Effect on Separation Location at Mach 10.....	125
66	Flow Visualization of the Effect of Angle of Attack on Plume-induced Separation.....	126
67	Effect of Jet Pressure Ratio on Bottom Centerline Pressure on the Delta Planform at a Mach Number of 10 and Zero Angle of Attack for Nozzle 2.....	127
68	Flow Visualization of the Effect of Nozzle Expansion Ratio on Plume-Induced Separation.....	128
69	Effect of Nozzle Expansion Ratio on Bottom Centerline.....	129
70	Effect of Nozzle Size on Bottom Centerline Pressure on the Delta Planform at a Mach Number of 10 and Zero Angle of Attack.....	130
71	Effect of Nozzle Size on Bottom Centerline Pressure on the Delta Planform at a Mach Number of 10 and Zero Angle of Attack.....	131

UNCLASSIFIED

LIST OF ILLUSTRATIONS (continued)

<u>Figure No.</u>		<u>Page</u>
72	Effect of Nozzle Exit Angle on Bottom Centerline Pressure on the Delta Planform at a Mach Number of 10 and Zero Angle of Attack.....	132
73	Effect of Nozzle Position on Bottom Centerline Pressure on the Delta Planform at a Mach Number of 10 and Zero Angle of Attack.....	133
74	Oil Flow Visualization of the Effect of Nozzle Axial Location on Separation on the Delta Configuration.....	134
75	Oil Flow Visualization of the Effect of Nozzle Vertical Position on the Separation of the Delta Configuration...	135
76	Effect of Exhaust Gas on Bottom Centerline Pressure on the Delta Planform at a Mach Number of 10 and Zero angle of Attack.....	136
77	Effect of Exhaust Gas on Bottom Centerline Pressure on the Delta Planform at a Mach Number of 10 and Zero Angle of Attack.....	137
78	Effect of Gas Supply Temperature on Plume Induced Separation at Mach 10 for $P_j/P_\infty = 88500$	138
79	Effect of Gas Supply Temperature on Plume Induced Separation at Mach 10.....	139
80	Effect of a -15° Control Deflection on Bottom Centerline Pressure on the Delta Planform at Mach 10 and Zero Angle of Attack.....	140
81	Effect of a $+20^\circ$ Control Deflection on Bottom Centerline Pressure Mach 10.....	141
82	Flow Visualization of the Effect of Plume with Control Deflection at Zero Angle of Attack.....	142
83	Flow Visualization of the Effect of Plume with Control Deflection at 10 Degree Angle of Attack.....	143
84	Effect of Angle of Attack on Bottom Centerline Pressure on the Delta Planform and a Mach Number of 7.9, $P_j/P_\infty = 0$	144
85	Effect of Reynolds Number on the Delta Planform Bottom Centerline Pressure at a Mach Number of 7.9.....	145
86	Effect of Jet Pressure Ratio on Plume Induced Separation at Mach 7.9 with Nozzle 6 at Zero Angle of Attack..	146
87	Effect of Jet Pressure Ratio on Plume Induced Separation at Mach 7.9 and 5° Angle of Attack.....	147

UNCLASSIFIED

LIST OF ILLUSTRATIONS (continued)

<u>Figure No.</u>		<u>Page</u>
88	Effect of Jet Pressure Ratio on Plume Induced Separation at Mach 7.9 and 10° Angle of Attack.....	148
89	A Comparison of Sonic Nozzle Data with That of of an Expansion Ratio of 2.25 at Mach 7.9.....	149
90	Effect of Nozzle Exit Angle at Mach 7.9 and Zero Angle of Attack.....	150
91	Effect of Nozzle Size on Plume Induced Separation at Mach 7.9.....	151
92	Effect of Nozzle Position on Plume Induced Separation at Mach 7.9.....	152
93	Effect of Exhaust Gas on Plume Induced Separation at Mach 7.9 and $P_j/P_\infty = 8000$	153
94	Effect of Exhaust Gas on Plume Induced Separation at Mach 7.9 and $P_j/P_\infty = 15700$	154
95	Effect of Free Stream Reynolds Number on Plume Induced Separation at Mach 7.9 and $P_j/P_\infty = 4000$	155
96	Effect of Free Stream Reynolds Number on Plume Induced Separation at Mach 7.9 and $P_j/P_\infty = 8000$	156
97	Effect of a -15° Elevon Deflection on Plume Induced Separation at Mach 7.9.....	157
98	Effect of a $+20^\circ$ Control Deflection on Plume Induced Separation at Mach 7.9.....	158
99	Effect of Angle of Attack on Bottom Centerline Pressure on the Delta Planform at a Mach Number of 5.9, $P_j/P_\infty = 0$	159
100	Effect of Control Deflection on Bottom Centerline Pressure on the Delta Planform at $M = 5.96$, $P_j/P_\infty = 0$	160
101	Effect of Jet Pressure Ratio on Bottom Centerline Pressure at Mach 5.96.....	161
102	Effect of Jet Pressure Ratio on Bottom Centerline ...	162
103	A Comparison of Sonic Orifice Nozzle Data With an Expansion Ratio 2.25 Nozzle at Mach 5.96....	163
104	Effect of Nozzle Exit Angle on Bottom Centerline Pressure: at Mach 5.96.....	164
105	Effect of Nozzle Size on Bottom Centerline Pressure at Mach 5.96.....	165
106	Effect of Nozzle Location on Plume Induced Separation at Mach 5.96.....	166

UNCLASSIFIED

LIST OF ILLUSTRATIONS (continued)

<u>Figure No.</u>		<u>Page</u>
107	Effect of a -15° Elevon Deflection with Plume on Bottom Centerline Pressure at Mach 5.96.....	167
108	Effect of a $+20^\circ$ Elevon and Plume on Bottom Centerline Pressure. at Mach 5.96.....	168
109	Effect of Mach Number on Separation Location.....	169
110	Mach Number Effect on Plateau Pressure Ratio.....	170
111	Mach Number Effect on Plateau Pressure Coefficient.....	171
112	Delta Bottom Pressures at Mach = 10.08.....	172
113	Bottom Pressure Distribution at Mach = 10.08 and $P_j/P_\infty = 2200$	173
114	Bottom Pressure Distribution at Mach = 10.08 and $P_j/P_\infty = 4000$	174
115	Bottom Pressure Distribution at Mach = 10.08 and $P_j/P_\infty = 8500$	175
116	Bottom Pressure Distribution at Mach = 10.08 and $P_j/P_\infty = 17400$	176
117	Bottom Pressure Distribution at Mach = 10.08 and $P_j/P_\infty = 22600$	177
118	Bottom Pressure Distribution at Mach = 10.08 and $P_j/P_\infty = 68500$	178
119	Bottom Pressure Distribution at Mach = 10.08 and $P_j/P_\infty = 88500$	179
120	Bottom Pressure Distribution at Mach 7.9.....	180
121	Bottom Pressures at Mach = 7.9 and $P_j/P_\infty = 1000$	180
122	Bottom Pressures at Mach = 7.9 and $P_j/P_\infty = 4000$	181
123	Bottom Pressures at Mach = 7.9 and $P_j/P_\infty = 15900$	181
124	Bottom Pressures at Mach = 7.9 and $P_j/P_\infty = 31500$	182
125	Bottom Pressures at Mach = 5.96.....	183
126	Bottom Pressures at Mach = 5.96 and $P_j/P_\infty = 2100$	183
127	Bottom Pressures at Mach = 5.96 and $P_j/P_\infty = 3500$	184
128	Bottom Pressures at Mach = 5.96 and $P_j/P_\infty = 7100$	184

UNCLASSIFIED

LIST OF ILLUSTRATIONS (continued)

Figure No.		Page
129	Bottom Pressures at Mach = 5.96 and $P_j/P_\infty = 14800$	185
130	Bottom Pressures at Mach = 5.96 and $P_j/P_\infty = 32200$	185
131	A Comparison of Separation Locations on the Bottom of the Delta Configuration.....	186
132	Sweep Angle of Spanwise Separation Location.....	187
133	Upper Surface Pressures without Plume at M = 10.08..	188
134	Effect of Reynolds Number on Upper Surface Pressure at M = 10.08.....	189
135a	Effect of Jet Pressure Ratio on Upper Surface Pressures at $\alpha = 0^\circ$ and M = 10.08.....	190
135b	Effect of Jet Pressure Ratio on Upper Surface Pressures at $\alpha = 0^\circ$ and M = 10.08.....	191
136a	Delta Oil Flow Visualization, Effect of Jet Pressure Ratio (top view).....	192
136b	Delta Oil Flow Visualization, Effect of Jet Pressure Ratio (side view).....	193
137	Effect of Jet Pressure Ratio on Upper Surface Pressures at $\alpha = 2.5^\circ$ and M = 10.08.....	194
138	Effect of Jet Pressure Ratio on Upper Surface Pressures at $\alpha = 5^\circ$ and M = 10.08.....	195
139	Effect of Jet Pressure Ratio on Upper Surface Pressure at $\alpha = 10^\circ$ and M = 10.08.....	196
140	Effect of Jet Pressure Ratio on Upper Surface Pressures at $\alpha = 15^\circ$ and M = 10.08.....	197
141	Effect of Jet Pressure Ratio on Upper Surface Pressures at $\alpha = 20^\circ$ and M = 10.08.....	198
142	Angle of Attack Effect on Separation Location at M = 10.....	199
143	Angle of Attack Effect on Upper Surface Plateau at M = 10.....	200
144	Upper Surface Pressures at M = 7.9.....	201
145	Effect of Reynolds Number on Upper Surface Pressures at M = 7.9.....	202
146	Effect of Jet Pressure Ratio on Upper Surface Pressures at $\alpha = 0^\circ$ and M = 7.9.....	203
147	Effect of Jet Pressure Ratio on Upper Surface Pressures at $\alpha = 5^\circ$ and M = 7.9.....	204

UNCLASSIFIED

LIST OF ILLUSTRATIONS (continued)

<u>Figure No.</u>		<u>Page</u>
148	Effect of Jet Pressure Ratio on Upper Surface Pressures at $\alpha = 10^\circ$ and $M = 7.9$	205
149	Effect of Jet Pressure Ratio on Upper Surface Pressures at $\alpha = 15^\circ$ and $M = 7.9$	206
150	Upper Surface Pressures at $M = 5.96$	207
151	Effect of Jet Pressure Ratio on Upper Surface Pressures at $\alpha = 0^\circ$ and $M = 5.96$	208
152	Effect of Jet Pressure Ratio on Upper Surface Pressure at $\alpha = 10^\circ$ and $M = 5.96$	209
153	Effect of Jet Pressure Ratios on Upper Surface Pressures at $\alpha = 15^\circ$ and $M = 5.96$	210
154	A Comparison of Upper and Lower Surface Plateau Pressures.....	211
155	A comparison of Upper and Lower Surface Separation Locations at $\alpha = 0^\circ$	212
156	Angle of Attack Affects on Upper Surface Plateau Pressure.....	213
157	Angle of Attack Effect on Upper Surface Separation Location.....	214
158	Effect of Jet Pressure Ratio on Base Pressure at $M = 10.08$	215
159	A Comparison of Base Pressure and Lower Surface Plateau Pressure at $M = 10.08$	216
160	Angle of Attack Effect on Base Pressure at $M=10.08$..	217
161	A Comparison of Oil Flow Versus Pressure Results on Separation Point Flat Plate Centerline.....	218
162	A Comparison of Separation Points from Oil Flow and Pressure Data on Delta Configuration Centerline.	219
163	Delta Configuration Spanwise Separation Line Sweep Angle Comparison.....	220
164	Schematic of Plume Interaction Measurements.....	221
165	Effect of Jet Pressure Ratio on Plume at $M = 10.08$ and $\alpha = 0^\circ$	222
166	Effect of Angle of Attack on Plume at $M = 10.08$	223
167	A Comparison of Plumes at Mach 6, 8, and Mach 10....	224
168	Effect of Nozzle Size on the Plume at $M = 5.96$	225
169	A Comparison of Exhaust Gas on the Plume at $M = 5.96$.	226

UNCLASSIFIED

LIST OF ILLUSTRATIONS (Continued)

<u>Figure No.</u>		<u>Page</u>
170	A Comparison of Exit Angle Effects at $M = 5.96$	227
171	Effect of Nozzle Location on Plume at $M = 5.96$	228
172	Measured Plume Initial Radius as a Function of Jet Pressure Ratio	229
173	Measured Flow Separation Angle as a Function of Jet Pressure Ratio.....	230
174	Flow Surveys at Mach 10 without a Plume.....	231
175	Flow Survey at Mach 10 with $P_j/P_\infty = 17200$	234
176	Flow Surveys at Mach 10 and $P_j/P_\infty = 8500$	241
177	Effect of the Nozzle 2 Plume at 5 Axial Locations on Bottom Surface of Delta Planform.....	242
178	Expansion Ratio Effect on Flow Surveys at $M = 10$...	243
179	A Comparison of Flow Separation Caused by a Disk Representing a Plume.....	246
180	A Comparison of Flow Surveys with a Disc Representing a Plume	247
181	Centerline Pressure Distribution Using Large Disc for Plume Simulation	248
182	Centerline Pressure Distribution Using Small Disc for Plume Simulation	249
183	Plume Initial Turning Angle for the Sonic Nozzles..	250
184	Plume Initial Turning Angle for the $A/A_* = 2.25$ Nozzles	251
185	A Comparison of Plume Initial Radii by Mach Number.	252
186	Plume Radius Comparison Based on Jet Pressure Ratioed to Ambient Pressure.....	253
187	Plume Comparisons Using Plateau Pressure.....	254
188	Plume Comparison Based on Modified Model.....	255
189	Plume Comparison with Total Temperature Ratio Correction.....	261
190	A Comparison of Plume Shapes with Ambient Temperature Ratio Correction.....	263
191	A Comparison of Plume Shape with Expansion Ratio and Mach Corrections.....	264

UNCLASSIFIED

LIST OF ILLUSTRATIONS (Continued)

<u>Figure No.</u>		<u>Page</u>
192	Definition of Interaction Parameters for Separated Flow.....	265
193	Upstream Interaction Length as a Function of Nozzle Total Pressure Ratio.....	267
194	A Comparison of Upstream Interaction Length with Laminar Control Separation Correlations.....	268
195	A Comparison of Upstream Interaction Length with a Turbulent Control Separation Correlation.....	269
196	A Correlation of Upstream Interaction Length Based on a Laminar Boundary Layer.....	270
197	Upstream Interaction Length at $\alpha = 0$ and $R_e = 0.5 \times 10^6/\text{ft}$	271
198	Upstream Interaction Length Correlations with Reynolds Number.....	272
199	Flat Plate Upstream Interaction Length at $\alpha = 0$	273
200	Upstream Interaction Length Correlation at Positive Angle of Attack.....	274
201	Flat Plate Upstream Interaction Length Correlation at Mach 10.....	275
202	Upper Surface Interaction Location Comparison.....	276
203	A Comparison of Flat Plate Interaction Points at Negative Incidence.....	277
204	Free Interaction Length Correlation Based on a Laminar Boundary Layer.....	278
205	Free Interaction Length Correlation Based on a Turbulent Boundary Layer Thickness.....	279
206	Free Interaction Length Correlation Against Plateau Pressure Coefficient.....	280
207	Base Pressure Correlated with Plume Initial Turning Angle.....	281
208	Base Pressure Correlated by Reynolds Number at the Interaction Point.....	282
209	Plateau Pressure Correlation Based on a Laminar Boundary Layer.....	283
210	Plateau Pressure Correlation Based on a Turbulent Boundary Layer Assumption.....	284

UNCLASSIFIED

LIST OF ILLUSTRATIONS (Continued)

<u>Figure No.</u>		<u>Page</u>
211	Plateau Pressure Correlated with Jet Pressure Ratio.....	285
212	Plateau Pressure Correlated with Reynolds Number at Interaction Point.....	286
213	Flat Plate Pressure Correlation at a Mach Number of 10.....	287
214	Plateau Pressure Correlation at $\alpha = 0^\circ$	288
215	Plateau Pressure Correlated with Reynolds Number Based on Local Condition	289
216	Plateau Pressure at Positive Angles of Attack.....	290

UNCLASSIFIED

LIST OF TABLES

<u>Table</u>		<u>Page</u>
I	Nozzle Characteristics	7
II	Instrumentation Allocation	8
III	Flat Plate Pressure Locations	9
IV	Delta Configuration Pressure Tap Locations	11
V	Flat Plate Parameters Tested at Mach 10	15
VI	Delta Configuration Pressure Test Parameters at Mach 10 . .	16
VII	Delta Configuration Pressure Test Parameters at Mach 8 . . .	17
VIII	Delta Configuration Parameters Tested at Mach 6	18
IX	Oil Flow Visualization at Mach 10	19
X	Flow Field Survey Data Obtained at Mach 10	20
XI	Estimated Computed Data Accuracy	21
XII	Estimated Reduced Data Accuracy	21

UNCLASSIFIED

SYMBOLS

A	=	area ft ²
A	=	constant in ft ² curve fit Equations 8 and 9
A	=	$C_{P_P} (R_{e_\alpha})^{.25} (M_\alpha^2 - 1)$ in Equation 31
A _*	=	throat area
A/A _*	=	nozzle expansion ratio
b	=	base span of model ~ ft
B	=	constant in curve fit Equations 8 and 9
C	=	constant in curve fit Equation 9
C _P	=	pressure coefficient = $\frac{P_b - P_\infty}{.7 P_\infty M_\infty^2}$
C _{P_b}	=	base pressure coefficient = $\frac{P_b - P_\infty}{.7 P_\infty M_\infty^2}$
C _{P_P}	=	plateau pressure coefficient = $\frac{P_P - P_\infty}{.7 P_\infty M_\infty^2}$
D	=	constant in curve fit Equation 8
D _{max}	=	maximum plume diameter ~ ft
d ₁	=	upstream interaction length — see Figure 192 ~ ft
d ₂	=	downstream interaction distance to peak pressure — see Figure 192 ~ ft
d ₃	=	downstream interaction distance to pressure rise — see Figure 192 ~ ft
d ₄	=	free interaction length — see Figure 192 ~ ft
d _j	=	nozzle exit diameter — Table I ~ inches
d _t	=	nozzle throat diameter — Table I ~ inches
f ₁	=	plume shape parameter see Equations 1 and 15

xx

UNCLASSIFIED

UNCLASSIFIED

SYMBOLS

f_2	=	plume shape parameter — see Equations 1 and 15
K	=	constant in curve fit Equation 8
L	=	model length = 1.667 ft
l_N	=	nozzle length in Table I ~ inches
l_S	=	separation length — see Figure 192 ~ ft
M	=	Mach number
M_∞	=	free stream Mach number
M_α	=	local Mach number at a point on surface accounting for local pressure — see Equation 23
MWL	=	model water line measured up from rear lower surface ~ inches
MBL	=	model butt line measured from model axis of symmetry ~ inches
P	=	pressure ~ PSF
P_∞	=	ambient pressure ~ PSF
P_α	=	pressure at a local point accounting for angle of attack ~ PSF
P_{oi}	=	pressure at interaction point — see Figure 192 ~ PSF
P_o	=	measured freestream total pressure by flow survey probe ~ PSF
P_{oj}	=	nozzle exit total pressure ~ PSF
P_j	=	nozzle exit static pressure ~ PSF
P_b	=	base pressure ~ PSF
P_E	=	pressure at end of body in Equation 29 ~ PSF
P_p	=	plateau pressure in separated region — see Figure 192 ~ PSF
$P_{p'}$	=	plateau pressure accounting for local slope in Equation 28 ~ PSF
P_W	=	pressure at a local point accounting for angle of attack and nose blunting ~ PSF
P_Z	=	measured local total pressure from flow survey probe ~ PSF
R	=	plume initial radius in Section 4.1
R_e	=	Reynolds Number

UNCLASSIFIED

SYMBOLS

$R_{e/X}$	=	unit Reynolds Number $\sim \text{ft}^{-1}$
$R_{e\alpha}$	=	Reynolds at a point on body accounting for local flow properties
$R_{e\alpha/X}$	=	unit Reynolds Number at point on body accounting for local flow properties $\sim \text{ft}^{-1}$
R_e^*	=	Reynolds number based on reference conditions — see Equation 20
$R_{e\alpha}^*$	=	Reference condition Reynolds number at a point on body accounting for local flow properties
R_{e_o}	=	Reynolds Number at interaction point based on free stream conditions
r_o	=	local plume radius measured from centerline $\sim \text{ft}$
r_e	=	nozzle exit radius $\sim \text{ft}$
r_{\max}	=	maximum plume radius measured from centerline $\sim \text{ft}$
T	=	temperature $\sim ^\circ\text{R}$
T^*	=	reference temperature — see Equation 21 $\sim ^\circ\text{R}$
T_∞	=	ambient temperature $\sim ^\circ\text{R}$
T_o	=	free stream total temperature $\sim ^\circ\text{R}$
T_{oj}	=	nozzle exit total temperature $\sim ^\circ\text{R}$
T_j	=	nozzle exit ambient temperature $\sim ^\circ\text{R}$
T_α	=	local temperature at a point on body accounting for local conditions $\sim ^\circ\text{R}$
T_{aw}	=	adiabatic wall temperature — see Equation 21 $\sim ^\circ\text{R}$
T_w	=	wall temperature — see Equation 21 $\sim ^\circ\text{R}$
T_Z	=	local corrected total temperature by flow survey probe $\sim ^\circ\text{R}$
U	=	velocity $\sim \text{ft/sec}$
U_∞	=	freestream velocity $\sim \text{ft/sec}$
X	=	location along body measured from L.E. or nose $\sim \text{ft}$
X_o	=	upstream interaction point measured from nose $\sim \text{ft}$

UNCLASSIFIED

SYMBOLS

X	=	distance on plume centerline measured from nozzle exit ~ ft
X_{\max}	=	location of plume maximum radius measured from nozzle ~ ft
X_r	=	axial location of separated flow reattachment to plume measured from end of body ~ inches
Y	=	spanwise distance on body measured from centerline ~ ft
Y_r	=	vertical location of separated flow reattachment to plume measured from bottom of body ~ inches
z_n	=	vertical distance from centerline of nozzle to edge of body ~ ft
α	=	angle of attack ~ DEG
γ	=	specific heat ratio
γ_∞	=	free stream specific heat ratio
γ_j	=	nozzle gas specific heat ratio
δ_F	=	flap deflection angle in Figure 192 ~ DEG
δ_L	=	laminar boundary layer displacement thickness — see Equation 19 ~ ft
δ_T	=	turbulent boundary layer displacement and thickness — see Equation 24 ~ ft
δ_e	=	lower control surface deflection ~ deg
ρ	=	density ~ slug/ft
ρ_∞	=	free stream density ~ slugs/ft
θ_N	=	nozzle exit angle ~ deg

Subscripts

α	local conditions at a point
o	interaction point
j	nozzle exit
∞	free stream

UNCLASSIFIED

SECTION I INTRODUCTION

- (U) High altitude flight experience, which has been obtained to the present time, has generally been limited to non-recoverable launch vehicles and to the X-15 aircraft which used rocket engines to propel them out of the atmosphere with a minimum of aerodynamic maneuvering. Flight test observation particularly on the Saturn 5 (reference 1) and limited wind tunnel tests (references 2 through 7) have indicated that the rocket plume can cause extensive flow separation on the body surface which can have significant effects on the aerodynamic characteristics of a vehicle. This has been of small interest in the past since the primary concern was to keep the vehicle stable primarily with reaction or thrust vector control, during ascent out of the atmosphere. However, vehicles which must be capable of sustained flight at high altitude are now being investigated and some are at various stages of pre-design. The vehicles include:
- a) lifting re-entry vehicles
 - b) recoverable launch vehicles
 - c) hypersonic cruise vehicles.
- (U) A lifting re-entry vehicle may undertake high altitude aerodynamic maneuvers to achieve orbital plane changes (synergetic maneuvering), to reach a desired landing site (cross-range maneuvering), or to achieve a safe re-entry from sub-orbital or orbital abort. The use of thrust is necessary to de-orbit and re-orbit the vehicle after a synergetic plane change. Studies have indicated (reference 8) that the aerocruise maneuver which uses thrust throughout the aerodynamic turn is the best type of synergetic maneuver. Re-entry cross-range can be extended by use of an aerocruise maneuver. Recoverable launch vehicles may perform aerocruise maneuvers during abort to jettison the remaining fuel by burning with the engines or may be required to reach a safe landing site. Thrust may also be used on abort to correct unfavorable re-entry conditions and to avoid re-entry heating or load constraints. Recoverable launch vehicles must have similar re-entry and abort capability as that described for lifting re-entry vehicles and thus must have aerocruise capability. The problems of plume effects on stability during launch are more severe for these vehicles because of the very large weight penalties for small errors in these vehicles. Hypersonic cruise is only feasible at high altitude with an accompanying large plume.
- (U) Thus plume-induced disturbances can no longer be ignored for vehicles which are intended to maneuver at high altitude. The altered aerodynamic pressure distribution which results from plume-induced flow separation could result in significant losses in aerodynamic lift, stability, and control. Loss of lift could seriously reduce the performance potential of aerocruise maneuvers while reductions in aerodynamic stability and control could have serious effects on vehicle design necessary to perform these maneuvers or to insure safe abort capability.

UNCLASSIFIED

- (U) This report documents the work accomplished under Air Force Contract F33615-70-C-1048 "Experimental Study of Exhaust Plume Effects". The basic objectives of this program were to obtain test data of rocket exhaust plume effects on a typical lifting re-entry vehicle shape and on a flat plate, to identify the most significant parameters, and to develop correlation techniques for plume effects.
- (U) The lifting body which was used in this study was the FDL-6 shape hypersonic ($L/D > 2.5$) lift to drag vehicles developed by the Air Force Flight Dynamics Laboratory and the data obtained from it should be representative for this class of vehicle. The flat plate data was obtained to help assess the three-dimensional effects. Little data exists for the problem of plume effects on lifting body shapes. Therefore, this test and that of reference 9 on a flat plate, represent exploratory tests to determine the magnitude of the plume induced separation on lifting body shapes.
- (U) The primary tests were performed at nominal Mach number of 10 with Mach effects tests at Mach numbers of 6 and 8. The test was performed primarily at a unit Reynolds number of $0.6 \times 10^6/\text{ft}$ with limited variations in Reynolds number to assess Reynold number effects. Plume simulation was accomplished using heated auxiliary tunnel air as a "cold gas" simulation through a rocket nozzle. The purpose of the heater is to avoid problems of air liquification, to provide better plume simulation. Carbon dioxide and argon were also used as test gases to determine the effect of exhaust gas specific heat on plume induced separation.
- (U) Nozzle effects were tested using three different expansion ratios, three different exit angles, and two different nozzle sizes for a total of six different nozzles. Nozzle location was a test parameter also with two vertical and three axial positions tested. A limited amount of testing was also accomplished with control deflection of a lower surface elevon on both the flat plate and lifting body (delta planform).
- (U) The data obtained consisted primarily of flat plate and delta planform lifting body surface pressure measurements. A limited number of flow field surveys were obtained above and behind the delta planform and limited oil-flow photographs were obtained on both the flat plate and the delta planform.
- (U) Reference 10 documents the analytic study which preceded this experimental program and on which the test plans were based while reference 11 presents the AEDC test report of the experimental phase of this study. Reference 15 presents a very interesting analyses of plume induced separation based on the data of reference 9 and the data presented in this report and the author recommends it to the reader for further insight into plume induced separation.

UNCLASSIFIED

UNCLASSIFIED

SECTION 2 TEST FACILITIES

2.1 TEST FACILITIES

- (U) The experimental testing of this program was accomplished in tunnels B and C of the von Karman Facility at AEDC. These tunnels are closed circuit hypersonic tunnels which have axisymmetric contoured nozzles with 50 inch diameter test sections. Tunnel B has Mach 6 and 8 nozzles while tunnel C has Mach 10 and 12 nozzles.
- (U) Tunnel B operates over a stagnation pressure range of 20 to 300 psia at Mach 6 and 50 to 900 psia at Mach 8 with stagnation temperatures up to 1350 R. Tunnel C operates over a stagnation pressure range of 200 to 2000 psia with a stagnation temperature up to 1900°R at Mach 10. Stagnation temperatures sufficient to avoid liquefaction in the test section are obtained through the use of a natural-gas-force combustion heater in combination with the compressor heat of compression at Mach 6 and 8 and in combination with electric resistance heaters at Mach 10 and 12. Each entire tunnel (throat, nozzle, test section, and diffuser) is cooled by integral, external water jackets. Both tunnels have identical test sections equipped with model injection systems.
- (U) Directly below each test section is a test section tank into which the model and its support can be retracted. When the model and support are retracted, the test section can be sealed from its tank so that the tunnel can remain running while the tank is vented to atmospheric pressure in order that personnel may enter the tank to make modifications to the model or its support system. After the desired modifications are made and the tank entrance door is closed, the tank is vented to the test section pressure, the doors between the tank and test section are opened, and the model is injected into the air stream to obtain the desired data. Upon completion of the data acquisition, the model is retracted and the cycle completed. The injection system is also used for transient heat-transfer tests in which the model is cooled in the retracted position, set at the desired attitude, and injected into the air stream to obtain the time history of the temperatures at various locations on the model. The minimum injection time is about two seconds and the maximum acceleration or deceleration is about one g.
- (U) Each test section is equipped with six fused quartz windows. The two on either side are used for the shadowgraph or schlieren system and the two on top are used for other photographic purposes. The viewing area of each window is about 17.25 in. in diameter.
- (U) 128 pressures can be measured on a model in tunnel B, 112 in tunnel C, with available transducers and pressure switching valves.

UNCLASSIFIED

- (U) Each pair of side windows of each tunnel is equipped with a conventional single-pass schlieren system or parallel-beam refocused shadowgraph system. Still pictures are photographed on 70-mm film using a spark light source of about one-microsecond duration.
- (U) Reference 12 presents a more complete description of these facilities.
- (U) 2.1.1 AUXILIARY AIR SUPPLY. A high-pressure air supply system is provided near the test section of each tunnel with a maximum pressure of 4000 psia. This supply was throttled to approximately 1500 psia and was then passed through an electric heater constructed for this test. The heater was capable of heating a 1 pound/sec mass flow to 1100°R. Supply pressure could be increased to 2000 psia by bypassing the heater but the gas temperature decreased to 500°R.
- (U) The mass flow through the heater was controlled remotely from the tunnel control room by manually adjusting a valve to maintain a pre-selected value of nozzle plenum pressure within the model. Because of the manual operation nozzle plenum pressure varied as much as 5% on a few runs. The temperature control on the heater was operated manually also but no precise control was attempted on supply gas temperature.
- (U) Both Argon and Carbon dioxide were also used as test gases during the test. These gases were supplied from a number of small tanks which were manifolded together and the tanks were immersed in a tank of heated water. The pre-heating of the test gas was used to prevent liquefaction of the gas in the electric heater and to maintain the desired supply pressure into the heater. The capacity of this system was small and only limited tests were accomplished with the smallest nozzle to minimize mass flow.

2.2 MODEL DESCRIPTION

- (U) The two basic configurations which were tested included a flat plate model and a delta planform lifting body configuration which is similar in shape to the FDL6 configuration. The model was designed and fabricated so that the flat plate could be mounted in place of the lower surface of the delta planform and thus could use a common support fixture, auxiliary air supply line, and nozzle mounting assembly. The support fixture was fabricated as the upper surface of the Delta planform by extending and thickening the vertical fin to serve as blade sting adapter as is shown in Figure 1 which presents an assembly drawing of the delta planform configuration.
- (U) The model consisted of three major parts:
 - a) delta planform upper surface sting assembly
 - b) delta planform lower surface
 - c) flat plate assembly

and a number of smaller parts including:

4

UNCLASSIFIED

UNCLASSIFIED

- a) exhaust nozzles and extensions
- b) elevons and brackets

all parts were fabricated from 17-4 PH stainless steel.

- (U) 2.2.1 DELTA PLANFORM CONFIGURATION. The delta planform shown in Figure 1 was derived from a lines drawing supplied by AFFDL, modified to agree with an aluminum model which was used as a contour pattern for the upper surface. The original fin was modified as shown in Figure 2 to give it the necessary strength to act as a blade sting (Figure 3) and the necessary internal volume to carry the pressure instrumentation tubing and thermocouple instrumentation leads from the model into the sting adapter. There was not sufficient volume to carry the auxiliary air line of desired diameter inside the fin so that a 3/4 inch line was carried on the right side of the fin (viewed from the rear with the model right side up) as is shown in Figure 4. All of the pressure measurements were taken on the left side (viewed from back, right side up) to avoid interference effects from the gas supply. The radius of the leading edge of the delta varied from 0.125 inches at the nose of the model to 0.1 inches at the base.
- (U) The delta configuration was instrumented with a total of 97 pressure taps and 9 thermocouples including those in the nozzle plenum, in the base region, and on the lower surface elevon. Section 2.2.4 will detail the instrumentation locations.
- (U) The nozzle plenum assembly was machined as an integral part of the upper surface assembly and had two holes drilled and tapped to receive nozzles or extensions as is shown in Figure 5. The upper surface contained all of the base pressure instrumentation as well as nozzle plenum instrumentation which was used on both delta planform and flat plate tests. In addition this assembly contained all upper surface pressure and thermocouple instrumentation aft of model station 2.9 and above model water line 0.79 (split line) which were disconnected at the sting adapter and not used during the flat plate tests. The flat plate assembly and delta bottom were attached to the upper assembly by nine cap screws and the mounting holes were plastered over as is visible in Figures 3 and 4.
- (U) The delta configuration has both upper and lower surface elevons as shown in Figures 1 and 5. These elevons were fabricated out of stainless steel and were mounted to the body by means of brackets. Brackets were then fabricated to obtain the desired deflection angle.

The upper surface elevons were not instrumented and were mounted at zero deflection only for this series of tests because of the relatively low importance of these surfaces for hypersonic trim and because there were too many other variables to test, however, a few pressure runs were made with these elevons removed.

- (U) The lower surface elevon is shown as a split surface on the original drawing

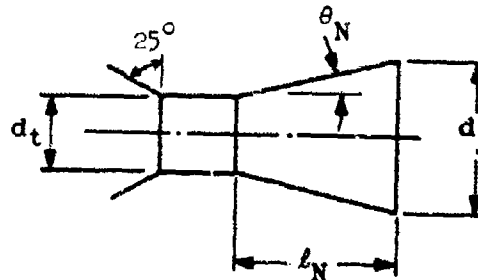
UNCLASSIFIED

for use as a roll control. For this test it was built as a one piece elevon so that no roll control deflections could be tested. Brackets were built so that this control surface could be set at zero (0) deflection, at 20 degrees trailing edge down into the stream ($+20^\circ$), or at -15 degrees trailing up out of the stream. The nozzle interfered with the -15° control deflection and had to be located in its most elevated position in order to obtain this deflection angle. Both the flat plate and delta tests were conducted with the lower elevon at zero control deflection. A limited number of tests of the configurations were made at both $+20^\circ$ and -15° elevon.

- (U) The elevon contained seven (7) pressure taps and one thermocouple as instrumentation for this test.
- (U) 2.2.2 FLAT PLATE CONFIGURATION. The flat plate bottom was 20 inches long and 15 inches wide and has provisions at the trailing edge for mounting the lower surface elevon and elevon extensions as is shown in Figure 6. The leading edge radius chosen in the same radius as on the swept leading edge of the delta bottom (0.125 inches). The flat plate had a thickness of 0.79 inches and had a 15° wedge angle on the side of the plate from the leading edge radius to this thickness on the side of the plate which mated to the delta-upper surface support assembly. The flat plate was machined on the mating surface to provide the volume necessary for the pressure tubing, and this machined area was closed by a cover plate. This allowed pressure taps to be located with few restrictions while no cut-outs of any kind other than elevon bracket pads were made in the instrumented surface as is shown in Figure 7.
- (U) The purpose of the elevon extensions was to make the plate appear longer without an elevon. This was done because the elevon could not be detached from the model without disconnecting the pressure tubes and thermocouple which was not desirable during the test. These extensions contained no instrumentation.
- (U) The flat plate model contained a total of 82 pressure taps and 6 thermocouples including those in nozzle plenum, base region, and elevon during this test series and changes from the flat plate to the delta bottom assembly called for a new tunnel installation to lead the tubing through the tunnel support.
- (U) 2.2.3 EXHAUST NOZZLES AND EXTENSIONS. A set of six nozzles were fabricated for this test with expansion ratios (A/A_t) ranging from 1.0 to 20 with a basic throat diameter (d_t) of 0.2245 inches. However, early in the first test series (flat plate test at Mach 10) it was decided that larger plumes were needed and so the basic throat diameter was increased to 0.316 inches with one sonic nozzle kept at 0.2245 inches. Thus, the geometric characteristics of the nozzles which were tested are listed in table I below:

UNCLASSIFIED

TABLE I
NOZZLE CHARACTERISTICS



Nozzle	d_t , in.	d_j , in.	θ_N , deg	l_N , in.	A/A^*
1	0.2245	0.225	0	1.250	1.0
2	0.316	0.478	15	1.449	2.25
3		1.000	15	0.468	10.00
4		0.477	7.5	0.217	2.25
5		0.476	30.0	0.952	2.25
6		0.316	0	0.316	1.0

- (U) The sonic orifices were used because of the ease of obtaining large plumes with relatively low supply pressure and because of the limit on gas supply pressure (1500 psia at heater).
- (U) The small sonic orifice (nozzle 1) was retained to test the effects of nozzle size and to minimize the Argon and Carbon dioxide mass flow requirements. Nozzles 2 to 5 are conical nozzles with a cylindrical throat section of length approximately equal to throat diameter. Nozzle 6 became the basic nozzle with which most tests were made for effects of parameters other than specific nozzle parameters. Nozzle area ratio or exit Mach number effects were tested by comparing data with nozzles 6, 2, and 3; nozzle exit angle using data with nozzles 2, 4, and 5; nozzle size from nozzles 1 and 6, and exhaust gas using nozzle 1.
- (U) The nozzle plenum was drilled to receive nozzles in two vertical positions and in addition two cylindrical adapters were made so that three longitudinal positions could be tested. Thus there were 6 potential positions to locate the nozzle to test the effect of nozzle location of which 4 were utilized as shown in Figure 8. All nozzles were made with a 0.5 inch diameter

7
UNCLASSIFIED

UNCLASSIFIED

passage connecting it to the plenum of sufficient length so that they shared a common exit plane when mounted directly to the plenum or on either extension. The shorter extension was 0.625 inches long because this was the minimum length needed to accommodate the threaded joint and the longer extension was chosen as twice the length of the shorter. Figure 9 shows nozzle 1 mounted in the basic position on the flat plate model.

- (U) 2.2.4 INSTRUMENTATION. Table II presents the allocation of instrumentation for the various components of this model and Figures 10 to 13 present sketches of the locations of the surface pressure taps together with the associated thermocouples.

TABLE II
INSTRUMENTATION ALLOCATION

Location	Pressure	Thermocouple
Nozzle Plenum	2	2
Elevon	7	1
Base	4	0
Fin	6	1
Flat Plate	69	3
Delta Lower Surface	51	3
Delta Upper Surface	28	2

- (U) Figure 10 and Table III show that two-thirds of the flat plate instrumentation has been concentrated aft of 75% of the plate length with the rest essentially equally spaced over the remaining plate length. This division was based on the assumption of the collapse of the separated area with increasing angle of attack when the surface is a windward surface. Instrumentation was located near the leading edge because it was expected that the entire plate would be affected when it was a leeward surface. All taps (except 3) were concentrated on the left side of the model to obtain more detailed data based on symmetry of the model.

- (U) Figure 11 presents the locations of the pressure taps on the bottom surface of the delta planform. 85 percent of the pressure taps were located aft of the ramp and in the same basic pattern as on the flat plate.

UNCLASSIFIED

TABLE III
FLAT PLATE PRESSURE LOCATIONS

<u>TAP</u>	<u>X/L</u>	<u>Y/L</u>	<u>TAP</u>	<u>X/L</u>	<u>Y/L</u>
1	.0305	0	40	.9572	.1
2	.15	0	41	1.025	.1
3	.30	0	42	1.05	.1
4	.45	0	43	.9675	.125
5	.60	0	44	.60	.15
6	.675	0	45	.675	.15
7	.75	0	46	.75	.15
8	.80	0	47	.80	.15
9	.85	0	48	.85	.15
10	.90	0	49	.90	.15
11	.925	0	50	.925	.15
12	.95	0	51	.95	.15
13	.9675	0	52	.9675	.15
14	1.025	0	53	.9675	.175
15	1.05	0	54	.0305	.20
16	1.075	0	55	.15	.20
17	.60	.05	56	.30	.20
18	.675	.05	57	.45	.20
19	.75	.05	58	.60	.20
20	.80	.05	59	.675	.20
21	.85	.05	60	.75	.20
22	.90	.05	61	.80	.20
23	.925	.05	62	.85	.20
24	.95	.05	63	.90	.20
25	.9675	.05	64	.925	.20
26	1.025	.05	65	.95	.20
27	1.05	.05	66	.9675	.20
28	.0305	.1	67	.9675	.225
29	.15	.1	68	.9675	.250
30	.30	.1	69	.0305	-.1
31	.45	.1	70	.45	-.1
32	.60	.1	71	.9675	-.1
33	.675	.1	72	.70	0
34	.75	.1	73	.725	0
35	.80	.1	74	.775	0
36	.85	.1	75	.825	0
37	.90	.1	76	.875	0
38	.925	.1	93	Base	
39	.95	.1	94	Base	
			95	Base	
			96	Nozzle	
			98	Plenum	
			99	Plenum	

UNCLASSIFIED

- (U) The test results indicate that more taps should have been located on the ramp centerline and surface.
- (U) The upper surface pressures were measured at twelve stations along the body and the taps were located as is shown in Figure 12. The triangular section had a tap on the top centerline, 45° off top centerline, and two on the side with one located at model water line 0.665 and one located at the center of the top radius. Aft of the expansion corner (Figure 12b) the taps were located at model water line 2.62, model water line 0.665, and at a point half the width of the rear deck. The taps along water line 0.665 become leading edge taps aft of model station 17. Figure 13 shows the tap locations and code numbers for upper surface and fin taps and thermocouples while table IV gives the pressure tap locations for all taps on the delta planform.
- (U) Four (4) pressure taps were located in the base region of the configuration as shown in Figure 14 and were used for base pressure measurements on both the delta and flat plate tests.
- (U) Two pressure taps were mounted in the nozzle plenum chamber in order to measure the total pressure supplied to the nozzles. These taps were calibrated by surveying the nozzle exit with a total head survey probe during nozzle calibration runs performed prior to the first tunnel run and before the nozzle expansion ratios were reduced.
- (U) Two thermocouples were also installed in the plenum to measure gas temperature but were found to be unreliable because they could not be completely shielded from the model. Thus the gas temperature used for the data was the gas temperature measured downstream of the heater.
- (U) All pressure tubes in the model were type 321 stainless steel with .03 inch O.D. This tubing was spliced to 0.093-inch O.D. by 0.014-inch wall stainless steel tubing approximately 18-ft long which connected to the pressure measuring system. The thermocouples were installed near the selected pressure orifices by drilling small holes through the model and 30 gauge chromel-alumel thermocouples were threaded through to the external surface where the junction was made.
- (U) 2.2.5 FLOW SURVEY RAKE. Figure 15 presents a sketch of the probe flow survey rake which was furnished by AEDC. The rake consisted of four pitot probes and two total-temperature probes. As shown in Figure 15, three of the pitot probes were inclined 20° toward the fourth pitot probe. An installation photograph of the survey rake supported above the delta model is shown in Figure 4. The grid wire shown on the tunnel windows was used as a scaling reference for the schlieren data. The rake drive system was digitized to indicate a displacement in each of the three coordinate directions x, y, and z. In the streamwise direction, the rake could be positioned to within ± 0.01 in. The probe height above the model surface was obtained by

UNCLASSIFIED

TABLE IV
DELTA CONFIGURATION PRESSURE TAP LOCATIONS

<u>Tap Number</u>	<u>X/L</u>	<u>Y/L</u>		<u>X/L</u>	<u>Y/L</u>
1	.0305	0	41	1.025	.1
2	.1515	0	42	1.05	.1
3	.273	0	43	.0305	.0125
4	.454	0	44	.1515	.035
5	.606	0	45	.273	.0505
6	.65	0	46	.394	.070
7	.75	0	47	.4545	.085
8	.80	0	48	.576	.1075
9	.85	0	49	.6365	.118
10	.90	0	50	.697	.129
11	.925	0	51	.7575	.140
12	.95	0	52	.818	.149
13	.9685	0	53	.879	.16
14	1.025	0	54	.9395	.17
15	1.05	0	55	.273	-.0505
16	1.075	0	56	.6365	-.118
17	.606	.05	57	0	0
18	.65	.05	58	.0305	0
19	.75	.05	59	.1515	.035
20	.576	0	60	.1515	.015
21	.85	.05	61	.1515	0
22	.364	0	62	.273	.0505
23	.454	.05	63	.273	.0251
24	.85	.05	64	.273	0
25	.9685	.05	65	.394	.070
26	1.025	.05	66	.394	.034
27	1.05	.05	67	.394	0
28	.65	-.05	68	.4545	.085
29	.85	-.05	69	.4545	.0425
30	.75	.1275	70	.4545	0
31	.85	.135	71	.576	.1075
32	.606	.1	72	.576	.051
33	.65	.1	73	.576	0
34	.75	.1	74	.6365	.118
35	.95	.1425	75	.6365	.052
36	.85	.1	76	.6375	0
37	.576	0	77	.697	.1175
38	.70	0	78	.697	.054
39	.95	.1	79	.7575	.115
40	.9685	.1	80	.7575	.047

UNCLASSIFIED

TABLE IV
DELTA CONFIGURATION PRESSURE TAP LOCATIONS (cont'd)

<u>Tap Number</u>	<u>X/L</u>	<u>Y/L</u>
81	.7575	0
82	.818	.115
83	.818	.04
84	.818	.02
85	.879	.112
86	.879	.035
87	.879	.02
88	.9395	.11
89	.9395	.03
90	.9395	.02
91	1.00	.02
92	1.055	.02
93	Base	
94	Base	
95	Base	
96	Nozzle	
97	Plenum	
98	Plenum	

UNCLASSIFIED

monitoring the change in height from a position where the lower pitot probe made electrical contact with the model. It is estimated that the electrically determined pitot probe contact point was known to within ± 0.001 in. The incremental change in position of the probes above the model surface were known to within ± 0.001 in., and the lateral or y displacement was known to within ± 0.025 in.

- (U) The flow-field surveys were made normal to either the nozzle axis in the jet plume region or normal to the aft portion of the model surface in the region upstream of the model trailing edge.

2.3 TEST SUMMARY

- (U) A total of 200 hours of tunnel occupancy in tunnels B and C were used to perform this test program during which the following data were obtained:

- a) 360 surface pressure distributions
- b) 5 nozzle calibration runs
- c) 19 flow field surveys
- d) 53 oil flow runs
- e) 104 Schlieren runs
- f) 5 Holograph runs

- (U) Schlieren data was taken with each pressure distribution and the 104 Schlieren runs were separate runs made at the end of the test in combination with the oil flow runs to obtain data missed earlier in the program because of a different sting adapter on some runs and to try to obtain better visualization on other runs. The holograph runs made on a low priority basis as to see whether flow field density data could be derived for the separated flow region. This holographic data is not presented in this report.

- (U) Fifty seven (57) pressure runs were obtained at a nominal Mach number of 6; sixty six (66) pressure runs were obtained at a nominal Mach number of 8; and all the rest of the data was obtained at a nominal Mach number of 10. The primary geometry variations were between the delta planform which was tested at all conditions and the flat plate model which was tested only at a Mach number of 10.

- (U) 2.3.1 PRESSURE TESTS SUMMARY. Ninety one (91) pressure runs were made on the flat plate configuration at a nominal Mach number of 10 and are summarized in table V, where nozzle code is given in table I and nozzle position code is defined in Figure 8. The flat plate tests were conducted primarily at a unit Reynolds number of $0.5 \times 10^6/\text{ft}$ with Reynolds number perturbations from $0.25 \times 10^6/\text{ft}$ to $0.89 \times 10^6/\text{ft}$. The angle of attack ranged from -10° to $+15^\circ$ but the majority of runs were made at 0 and 10° . Tables VI to VIII summarize the delta configuration tests at Mach 10, 8, and 6 respectively. The values of unit Reynolds number and jet static pressure ratio (P_j/P_∞) listed in these tables are nominal values used to illustrate the variation of parameters achieved in the test.

UNCLASSIFIED

- (U) Early test runs were made at angles of attack from 0° to 26.5° but the sting adapter was later changed and the angle of attack range was changed to -2° to $+15^\circ$. This change was made to improve Schlieren viewing of the model at low angles and because most tests were performed at angles of attack of 0° and 10° . Mach 8 and 6 tests were essentially similar to the Mach 10 tests except that the highest unit Reynolds number tested ($2.4 \times 10^6/\text{ft}$) was performed at Mach 8 and that the desired test condition at Mach 6 was missed so that most Mach 6 data were obtained at a unit Reynolds number of $0.6 \times 10^6/\text{ft}$. Only one Reynolds number variation was tested at Mach 6. Angle of attack at both Mach 6 and 8 varied from 0° to 15° with most data obtained at 0° and 10° .
- (U) The jet pressure ratios tested far exceed any that would be attained with an actual rocket engine but were used to obtain large plumes to generalize the results since it was believed that the separation data should be related with plume size rather than engine parameters.
- (U) During the flow survey tests, two sets of centerline pressures were obtained using disks to represent a plume.
- (U) 2.3.2 OIL FLOW SUMMARY. Zlygo oil was used for a limited set of flow visualization runs which are summarized in table 9. One special oil flow run was made using dual nozzles instead of one to determine the effect on the separation pattern.

UNCLASSIFIED

TABLE V
FLAT PLATE PARAMETERS TESTED AT MACH 10

NOZZLE	NOZZLE POSITION	δ_c	$R_c \times 10^{-6}/ft$	P_j/P_∞	α	GAS	OTHER
	-	0°	.89	0	0°→15°	air	
	-	0	.22	0	0 & 10	air	
	-	0	.5	0	-10→+15		
	-	+20	.5	0	0 & +10		
1	1	0	.89	1000	-10→+15	air	
1	1	0	.22	4000	0 → 10	air	
1	1	0	.50	16000	0 → 10	air	
1	1	0	.5	8000	0 → 10	CO ₂	
1	1	0	.5	16000	0	CO ₂	
1	1	0	.5	8000	0 & 10	Argon	
2	1	0	.5	4000	0 & 10	air	
2	1	0	.5	8000	0 → 10	air	
2	1	0	.5	12000	0 & 10	air	
3	1	0	.5	1000	0 & 10	air	
3	1	0	.5	1200	0 & 10	air	
4	1	0	.5	4000	0 & 10	air	
4	1	0	.5	8000	0 & 10	air	
5	1	0	.5	8000	0 & 10	air	
6	1	0	.89	4000	0	air	
6	1	0	.89	1000	0	air	
6	1	0	.89	8000	0 & 10	air	
6	1	0	.22	8000	0 & 10	air	
6	1	0	.5	2000	-10→5	air	
6	1	0	.5	4000	-10→10	air	
6	1	0	.5	8000	-10→15	air	
6	1	0	.5	16000	-10→15	air	
6	1	0	.5	34000	0	air	
6	1	0	.5	69000	0	air	
6	1	0	.5	89000	0	air	
6	1	0	.5	8000	0 & 10	air	Extensions on
6	1	0	.5	16000	0 & 10	air	Extensions on
6	1	+20	.5	16000	0	air	
6	2	0	.5	16000	0 & 10	air	
6	3	0	.5	16000	0 & 10	air	
6	4	0	.5	16000	0 & 10	air	
6	4	-15	.5	16000	0 & 10	air	

UNCLASSIFIED

TABLE VI
DELTA CONFIGURATION PRESSURE TEST PARAMETERS AT MACH 10

NOZZLE	POSITION	δ_e	$R_e \times 10^{-6}/ft$	P_j/P_∞	α	GAS	OTHER
-	-	0°	.39	0	0 → 10°		
-	-	0	.22	0	0 → 20		
-	-	0	.5	0	0 → 26.5		
-	-	-15°	.5	0	0 → 15		
-	-	+20°	.5	0	0 → 20		
1	1	0	.5	16000	0 → 15	air	
1	1	0	.5	68000	0 → 15	air	
1	1	0	.5	8000	0 → 5	CO ₂	
1	1	0	.5	16000	0 → 5	CO ₂	
1	1	0	.5	8000	0 → 2.5	Argon	
1	1	0	.39	4000	0 → 10	air	
1	1	0	.22	4000	0 → 10	air	
1	1	0	.5	1000	0 → 10	air	
1	1	0	.5	4000	0 → 15	air	
1	1	0	.5	8000	0 → 15	air	
1	1	0	.5	13000	0 & 10	air	
1	1	0	.5	1000	0 → 10	air	
1	1	0	.5	4000	0 → 10	air	
1	1	0	.5	8000	0 → 10	air	
1	1	0	.5	4000	0 → 15	air	
1	1	0	.5	8000	0 → 10	air	
1	1	0	.22	8000	0 → 10	air	
6	2	0	.22	16000	0 → 10	air	
6	4	0	.22	16000	0 → 10	air	
6	1	0	.89	8000	0 → 15	air	
6	1	0	.89	16000	0 → 10	air	
6	1	0	.5	2000	0 → 15	air	
6	1	0	.5	4000	0 → 15	air	
6	1	0	.5	8000	0 → 15	air	
6	1	0	.5	16000	-2 → 26.5	air	
6	1	0	.5	22000	0	air	
6	1	0	.5	34000	0	air	
6	1	0	.5	68000	0 → 20	air	
6	1	0	.5	89000	0	cold	
6	1	0	.5	89000	0 → 20	air	
6	2	0	.5	16000	0 → 10	air	
6	3	0	.5	16000	0 → 10	air	
6	4	0	.5	16000	0 → 10	air	
6	4	-15°	.5	16000	0 → 20	air	
6	1	+20	.5	16000	0 → 10	air	
6	1	0	.5	16000	0 → 10	air	upper elevons off

UNCLASSIFIED

TABLE VII

DELTA CONFIGURATION PRESSURE TEST PARAMETERS AT MACH 8.

NOZZLE	POSITION	δ_e	$R_e \times 10^{-6}/ft$	P_c/P_∞	α	GAS	OTHER
-	-	0°	.55	0	0° → 15°		
-	-	-15	.55	0	0 & 10		
-	-	+20	.55	0	0 & 5		
-	-	0	.25	0	0 & 5		
-	-	0	2.4	0	0 & 10		
-	-	0	.55	8000	0 & 5	air	
1	1	0	.55	16000	0	air	
1	1	0	.55	8000	0 → 5	CO ₂	
1	1	0	.55	16000	5	CO ₂	
1	1	0	.55	8000	0 & 2.5	Argon	
1	1	0	.55	4000	0 & 10	air	
2	1	0	.55	4000	0 & 10	air	
4	1	0	.55	4000	0 & 10	air	
5	1	0	.55	1000	0	air	
6	1	0	.55	4000	0 → 15	air	
6	1	0	.25	4000	0 & 5	air	
6	1	0	2.4	4000	0 → 10	air	
6	1	0	.55	7000	0 & 10	air	
6	1	0	.55	8000	0 → 15	air	
6	1	0	.25	8000	0 & 5	air	
6	1	0	2.4	8000	0 & 10	air	
6	1	0	.55	16000	0 & 10	air	
6	1	0	.55	32000	0 → 15	air	
6	1	0	.55	8000	0 & 10	air	
6	2	0	.55	8000	0 & 10	air	
6	3	0	.55	8000	0 → 10	air	
6	4	0	.55	8000	0 & 10	air	
6	4	-15	.55	8000	0 & 5	air	
6	1	+20	.55	8000	0 & 5	air	

UNCLASSIFIED

TABLE VIII

DELTA CONFIGURATION PARAMETERS TESTED AT MACH 6

NOZZLE	POSITION	δ_e	$R_e \times 10^{-6}/ft$	P_j/P_∞	α	GAS	OTHER
-	-	0°	.66	0	0° → 15°		
-	-	0	.37	0	0 & 5		
-	-	-15	.66	0	0 & 10		
-	-	+20	.66	0	0 & 5		
1	1	0	.66	7000	0 → 15	Air	
1	1	0	.66	15000	0	CO ₂	
1	1	0	.66	7000	0	CO ₂	
1	1	0	.66	7000	0	Argon	
1	1	0	.66	3800	0	Argon	
1	1	0	.66	3800	0 & 10	Air	
2	1	0	.66	3800	0 & 10	Air	
4	1	0	.66	3800	0 & 10	Air	
5	1	0	.66	2000	0 & 5	Air	
6	1	0	.66	3500	0 & 5	Air	
6	1	0	.37	3500	0	Air	
6	1	0	.66	7000	0 → 15	Air	
6	1	0	.37	7000	0 & 5	Air	
6	1	0	.66	8000	0	Air	
6	1	0	.66	7000	0 → 15	Air	
6	1	0	.37	7000	0 & 5	Air	
6	1	0	.66	8000	0	Air	
6	1	0	.66	15000	0 → 10	Air	
6	1	0	.66	32000	0 → 15	Air	
6	2	0	.66	7000	0 & 10	Air	
6	3	0	.66	7000	0 & 10	Air	
6	4	0	.66	7000	0 → 10	Air	
6	4	-15	.66	7000	0 & 10	Air	
6	1	+20	.66	7000	0 & 5	Air	

UNCLASSIFIED

TABLE IX
OIL FLOW VISUALIZATION AT MACH 10

CONFIGURATION	NOZZLE	POSITION	δ_e	$R_e \times 10^{-6}/ft$	P_j/P_∞	α	GAS	OTHER
flat plate	6	1	0°	.5	8500	0°	air	
" "	6	1	0	.5	17000	0 & 5	air	
" "	6	1	0	.5	34000	0	air	
" "	6	1	0	.5	68000	0	air	
" "	6	1	0	.5	17000	0	air	Extensions on
" "	1	1	0	.5	17000	0	air	
" "	5	1	0	.5	8500	0	air	
Delta	-	-	+20	.5	0	0 → 15		
"	1	1	0	.5	17000	0 & 10	air	
"	2	1	0	.5	1000	0	air	
"	2	1	0	.5	4500	0 & 10	air	
"	2	1	0	.5	8500	0 & 10	air	
"	2	1	0	.5	13000	0 & 10	air	
"	2	1	0	.5	4500	5	air	
"	2	1	0	.5	8500	0	air	
"	6	1	0	.5	2000	0 & 2.5	air	
"	6	1	0	.5	4500	0	air	
"	6	1	0	.5	8500	0	air	
"	6	1	0	.5	1700	0 → 15	air	
"	6	1	0	.5	34000	0	air	
"	6	1	0	.5	89000	0	air	
"	6	1	0	.89	8500	0 & 5	air	
"	6	1	0	.89	17000	0 & 5	air	
"	6	2	0	.5	17000	0	air	
"	6	3	0	.5	17000	0	air	
"	6	4	-15	.5	17000	0 → 15	air	
"	6	1	+20	.5	17000	0 → 10	air	
"	-	-	0	.5	0	0	large disk	

UNCLASSIFIED

- (U) 2.3.3 FLOW FIELD SURVEYS. Flow field surveys were made on four configurations as shown in table 10. The disks were sized to be as large as the point where the separated flow attached itself to the plume for the $P_j/P_\infty = 8500$ case with nozzle 6 and the surveys were made to compare the separation region which resulted from the plume.

2.4 DATA ACCURACY

- (U) Table XI presents an estimate of data accuracy for these tests taken from reference 11 and which appears to be correct for this basic data as recorded and computed.

TABLE X

FLOW FIELD SURVEY DATA OBTAINED AT MACH 10

NOZZLE	LOCATION	δ_c	$R_\delta \times 10^{-6}/ft$	P_j/P_∞	GAS	SURVEY LOCATION X FROM NOSE INCHES
-	-	0°	.5	0	-	15.29
-	-	0	.5	0	-	18.49
-	-	0	.5	0	-	21.69
6	1	0	.5	8500	air	12.09
6	1	0	.5	8500	air	15.29
6	1	0	.5	8500	air	21.69
6	1	0	.5	8500	air	22.0
6	1	0	.5	17000	air	8.89
6	1	0	.5	17000	air	12.09
6	1	0	.5	17000	air	15.29
6	1	0	.5	17000	air	21.69
6	1	0	.5	17000	air	22.0
6	1	0	.5	17000	air	22.32
6	1	0	.5	17000	air	22.94
2	1	0	.5	3500	air	12.09
2	1	0	.5	8500	air	18.49
2	1	0	.5	8500	air	21.69
2	1	0	.5	8500	air	22.0
2	1	0	.5	8500	air	22.94
Small Disk		0	.5	-	-	15.29
		0	.5	-	-	18.49
Large Disk		0	.5	-	-	15.29
"	"	0	.5	-	-	18.49

UNCLASSIFIED

TABLE XI
ESTIMATED COMPUTED DATA
ACCURACY

<u>Parameter *</u>	<u>Estimated Uncertainty, percent</u>
Mach number, M_∞	± 0.5
Reynolds number per foot, Re/ft	± 2.35
Model surface pressure ratio, p/p_∞	± 3.8
Nozzle chamber pressure ratio, p_{0j}/p_∞	± 3.8
Pitot probe pressure ratio, $p_z/p_{0'}$	± 1.4
Velocity ratio, U/U_∞	± 0.9 to 1.7
Density ratio, ρ/ρ_∞	± 2.1

* (from reference 11)

- (U) The pressure data was used to obtain two basic separation parameters for which the error depends on the spacing of the pressure points and consequently have a greater error. The Schlieren data was reduced to obtain various plume parameters and because of the small scale of the pictures and the relatively poor contrast of the separated region the error is fairly large. Thus table 12 presents estimates of the uncertainty of these parameters.

TABLE XII
ESTIMATED REDUCED
DATA ACCURACY

	<u>Uncertainty Percent</u>
Separation location x/L	± 2.5
Free interaction length d_4/L	± 2.5
Plateau pressure P/P_∞	± 4
Plume initial radius R/L	± 5
All measured angles from pictures	$\pm 2^\circ$

UNCLASSIFIED

SECTION 3 TEST RESULTS

3.1 FLAT PLATE DATA

- (U) The flat plate was tested only at a nominal Mach number of 10 in AEDC tunnel C and was the first configuration tested in the chronology of this series of tests. The test results will be presented basically using the centerline pressure distribution to illustrate the effects of the major test parameters and then the spanwise distributions will be discussed. All of the pressure data which will be shown will be plotted as the ratio of local pressure to tunnel ambient pressure (P/P_∞). The plume data shown on the plots will be presented as jet exit static pressure ratioed to tunnel ambient pressure (P_j/P_∞) and the Reynolds number as the unit Reynolds number $\times 10^{-6}/ft$. The axial location (X/L), where the plume induced pressure disturbance starts, is arbitrarily called the separation point in the discussion which follows for convenience. The author realizes that the actual flow separation occurs aft of this point.
- (U) 3.1.1 FLAT PLATE CENTERLINE PRESSURE DATA. Figure 16 presents the centerline pressure distribution on the flat plate model as a function of angle of attack with no exhaust plume. This figure shows a strong decay in pressure from the leading edge which results in the zero angle of attack data never reaching ambient pressure even at the trailing edge of the elevon. The leading edge diameter number is 0.25 inches ($d/L = .0125$) and this strong pressure gradient was not expected to persist so far downstream. The pressure gradient is evident at all angles of attack shown on this plot. Figure 17 shows little effect of Reynolds numbers tested on the basic pressure distribution at zero angle of attack.
- (U) The effect of increasing jet pressure ratio at zero angle of attack for the largest sonic orifice (nozzle 6) located in the basic position (position 1 on Figure 8) is shown in Figure 18. The pressure rise caused by the plume starts on the elevon and moves forward onto the plate as jet pressure ratio is increased. A plateau in the plume induced pressure rise appears when the separation point moves forward to about 90% of body length while at the same time a pressure peak appears in the elevon. Increasing pressure ratio beyond this causes the separation point to move forward and both the plateau and peak pressures to increase. The pressure peak is probably due to plume flow recirculating into the separated region and onto the plate. Figure 19 presents oil flow visualizations of increasing pressure ratio at zero angle of attack which shows a clean spot on the elevon and the flow forward and outward from this region of peak pressure. The separation point moves forward near the edges of the plate due to edge effects. Figures 20 to 22 show the effect of positive angle of attack on the plume induced separation. Positive angle of attack exposes the flat plate as a windward surface and this causes the separation to move aft very rapidly, however, separation still occurs on the elevon at 10 degrees angle of attack (Figure 21) and at

UNCLASSIFIED

15° (Figure 22). Negative angles of attack are shown in Figures 23 and 24 which show much the same trends as the zero angle of attack data with the appearance of a plateau and a pressure peak on the elevon. The plateau occurs at a more lower jet pressure ratio at -5° (Figure 23) than at 0° (Figure 18) but the plateau pressure rise appears to be much smaller. The plateau pressure at a -10° is slightly above ambient pressure and extends not much further forward than that of -5°. These data trends indicate that the effect on leeward surfaces should diminish with increasing angle of attack.

- (U) Figure 25 shows the effect of increasing jet pressure ratio of the 2.25 expansion ratio nozzle (nozzle 2, position 1) indicating more separation than that of the sonic orifice of Figure 18, when compared at the same jet exit static pressure ratio (P_j/P_∞). This is confirmed by the comparison of oil flows of Figure 26. The plateau pressures on Figure 25 appear to be close to those of Figure 18 for data with the same separation point, implying that separation plateau pressure is more related to separation point than to nozzle jet pressure ratio.
- (U) Nozzle 3 data ($A/A^* = 10$), shown in Figure 27 for position 1, further indicates that increasing expansion ratio increases separation when compared on a jet exit pressure ratio basis because the separation shown here is nearly that of nozzle 2 at a pressure ratio of 4000 (Figure 25). It takes a much higher total pressure to achieve the same jet exit pressure ratio with nozzle 3 because of the higher expansion ratio compared to the other nozzles and an exit jet pressure ratio of 1200 was the maximum attainable with this nozzle. Figure 28 shows that if nozzles 2 and 3 are compared on the basis of nozzle total pressure ratio (P_{01}/P_∞) that the higher expansion ratio nozzle shows much less separation. Thus the effect of expansion ratio depends on which pressure ratio is chosen as the basis for comparison.
- (U) The effect of nozzle size is shown by Figure 29 showing a comparison of the data from nozzles 1 and 6 which are sonic orifices and nozzle 6 has twice the throat area of nozzle 1. Nozzle 1 shows less separation, partly due to the jet pressure ratio difference of the test condition and corresponds roughly to the separation caused by the larger nozzle with a jet pressure ratio of 8000 (Figure 18). Thus it appears that exit area or radius is an important plume separation parameter.
- (U) The effect of nozzle exit angle on flat plate centerline pressures for the nozzles with an expansion ratio of 2.25 is shown on Figure 30. The separation point moves forward with increasing nozzle exit angle in almost a linear manner and the separation location for the 30° nozzle is almost at the same point for the 15° nozzle with a jet pressure ratio of 13000 (Figure 25). The plateau pressure rises as the separation point moves forward but again the plateau pressure corresponds very well with that of both nozzle 6 (Figure 18) and nozzle 2 (Figure 25) considering comparable separation points, reinforcing the opinion that plateau pressure is more related to separation point than to nozzle parameters.

UNCLASSIFIED

- (U) The effect of nozzle position is shown in Figure 31 where data for three axial positions and two vertical positions is presented. The axial position shift increments are not large (.031L) but there is a significant rearward movement of the separation point for the most aft case (.062L). The separation point corresponds to that for this nozzle in the basic position with a jet pressure ratio of about 8000. The effect is non-linear since the data with the nozzle at the midpoint of axial travel shows very little difference with the basic position. A vertical shift of .072L appears to cause little change in the separation point also. Thus small shifts in nozzle location do not appear to exert much change on plume induced separation at least for the limited case tested on the flat plate model.
- (U) Figure 32 presents the effect of exhaust gas specific heat variation on plume induced separation by presenting data obtained when carbon dioxide ($\gamma = 1.29$) and Argon ($\gamma = 1.66$) were used as test gases. This data shows a large difference in the separation point caused by the different gases and the carbon dioxide data corresponds very well with that for air from the same nozzle (nozzle 1) at a jet pressure ratio of 15000 as shown in Figure 29. The plateau pressure for this CO₂ run corresponds very well with the plateau pressure of other figures with the same separation point further confirming that plateau pressure depends on separation point and not on nozzle parameters.
- (U) Figure 33 presents a comparison of data at three Reynolds numbers for the flat plate at zero angle of attack with nozzle 6 and a jet pressure ratio of 8500. These data show very little difference between the data of the low and intermediate Reynolds numbers but a reduction of the separation area at the highest Reynolds number. Figure 34 presents data with the elevon extensions on and off. No effect on centerline pressure is evident and the oil flows of Figure 35 show that there is very little effect anywhere on the plate.
- (U) The effect of control deflection is shown in Figures 36 and 37 where Figure 36 shows the control deflected 15° out of the stream (-15°) and Figure 37 shows the control deflected 20° into the stream. Figure 36 shows that the plume induced separation is not affected by the negative control deflection since the elevon has the same plateau pressure acting on it as it did at zero deflection.
- (U) The elevon controls are usually deflected up out of the stream to increase angle of attack but the figure shows that this cannot be done in the presence of plume induced separation and this could be a serious problem if similar results are obtained on the delta configuration. Figure 37 shows just the opposite for the compression corner case in that control induced separation predominates and that the plume effects are negligible.
- (U) 3.1.2 FLAT PLATE SPANWISE PRESSURE DISTRIBUTION. The oil flow visualizations shown in Figures 26 and 35 indicated the separation location is the same across the span of the model except in the regions of edge effect and we will now examine the pressure data to see if it agrees with this observation.

UNCLASSIFIED

- (U) Figures 38 through 44 present pressure distributions on one half the flat plate for the largest sonic nozzle (nozzle 6) in nozzle position 1 in order of increasing jet pressure ratio. Figure 38 shows the plate centerline is the X/L axis and that the plate is $.75 L$ wide. The area of the plate shown is concentrated where the main sets of pressure taps were located on the plate and elevon. The pressure data were slotted and connected by straight line segments along lines of constant spanwise location (Y/L) and the data for the non-blowing case is presented also to help define the spanwise effects. Three spanwise lines have also been faired through the data, the dashed line ($X/L = .968$) is the last set of taps on the aft end of the flat plate, while the other two lines are pressure taps located on the elevon at $X/L = 1.032$ and $X/L = 1.05$. Figure 38 shows that at low jet pressure ratio the pressure disturbance is confined to the elevon surface; the separation point appears to be near the leading edge of the elevon across the surface but the pressure disturbance decays fairly rapidly in the spanwise direction. The jet pressure ratio has been increased to 4300 for Figure 39 and the separation point appears to have moved onto the plate ahead of the elevon but no effect is seen outboard of the elevon. The pressures on the elevon still show a strong spanwise effect but no effect is noted on the body. Figure 40 shows that separation has started all the way across the plate as the jet pressure was increased to 8400. The separation line moves aft outboard of the elevon but appears to be at the same location ahead of the elevon. The spanwise pressure variation is diminishing on the elevon but a spanwise variation is seen at $X/L = 0.968$. Figure 41 marks the beginning of a plateau in the centerline pressure and this apparently causes the separation line to straighten out across the plate and the spanwise pressure gradient to become much smaller. Figure 42 shows that all pressure gradients have disappeared at a jet pressure ratio of 34000 while Figure 43 and 44 show that the high pressure peak begins to spread across the elevon as jet pressure ratio is increased further. Figure 45 shows that the results are similar at negative angles of attack.
- (U) Figures 46 and 47 present spanwise data for nozzle 2 at two pressure ratios which when compared on a common separation location basis with the nozzle 6 data show excellent correlation of the spanwise pressures. Figure 46 compares very well with Figure 40 while Figure 47 compares very well with Figure 41. Figure 48 shows nozzle 3 data which compares very well with Figure 39 thus it removes any doubt that spanwise distribution is related only to centerline separation and not to other nozzle parameters.
- (U) Figure 49 presents the spanwise pressure distribution with the elevon extensions installed for the case where separation is just starting on the plate when the extensions are off. This data is exactly the same as that with the extensions off, shown in Figure 40, showing that the elevon does not affect the data and the spanwise distribution must depend only on the separation at the centerline. Figure 50 shows the flow separation in the compression corner caused by a $+20^\circ$ control deflection and that it is not carried into the plate outboard of the elevon. Figure 51 shows that the plume does induce separation outboard of the elevon and this feeds into the control separation area to raise the pressure slightly on the plate ahead of the control but not on the control surface itself.

CONFIDENTIAL

(This page is Unclassified)

(U) 3.1.3 SUMMARY OF FLAT PLATE TEST RESULTS. In summary plume induced separation up to a maximum of 50% of the plate length were observed on the flat plate model. This separation was strongly dependent on:

- a) nozzle jet pressure ratio
- b) nozzle expansion ratio
- c) nozzle exit angle
- d) nozzle size
- e) exhaust gas
- f) positive angle of attack (windward surface)
- g) positive control deflection

and only weakly dependent on:

- a) nozzle position
- b) elevon width
- c) negative angle of attack (leeward surface)
- d) negative control deflection
- e) small changes in unit Reynold number.

- (U) The plateau pressure and spanwise pressure distribution appeared to depend solely on the centerline separation point and not on nozzle characteristics thus, data for different nozzles compared very well when separation points matched. The effect of nozzle expansion ratio depends on the jet pressure parameter used to correlate the effects but increasing expansion ratio at constant total pressure reduces the plume induced separation.
- (U) Negative control deflection of a lower surface elevon to achieve a nose up moment appears to be ineffective in the presence of plume induced separation.
- (U) The effect of angle of attack is to reduce plume induced separation on a windward surface and to cause some increases in pressure on a leeward surface.
- (U) Carbon dioxide plumes caused significantly more separation than air or Argon plumes. Argon plumes caused the least separation.

CONFIDENTIAL

3.2 TEST RESULTS ON THE DELTA BOTTOM CENTERLINE

- (C) The description of the test results from the delta configuration will be divided into three sections based on geometry:

- a) bottom centerline data
- b) bottom distribution data
- c) upper surface pressure data

and these sections will be further subdivided by test Mach number to best describe the data in an orderly manner.

- (C) 3.2.1 BOTTOM CENTERLINE DATA AT A MACH NUMBER OF 10. Figures 52 through 54 present the bottom centerline data of the delta planform as a function of angle of attack for the three lower surface elevon deflections tested during this study. These figures show some nose bluntness effect near the front end of the ramp and the expansion corner effect aft of the juncture of the front ramp and flat surface (.606L). Figure 53 shows the control deflected -15° and the expansion corner effects at the aft end of the body. Figure 54 shows the compression corner effect which results from a $+20^\circ$ control deflection. The control induced separation moves aft but never disappears with increasing angle of attack. Figure 55 shows that increasing unit Reynolds number decreased the local pressure but the pressure distribution remained essentially the same along the centerline. A comparison of flat plate and delta centerline pressures without a plume is shown in Figure 56 which shows that the nose bluntness effects were much more severe on the flat plate and so the delta planform pressures tend to be lower than those of the flat plate at low angles of attack.
- (C) The effect of jet pressure ratio on the delta configuration centerline at angles of attack from 0° to 20° are shown in Figures 57 through 66. Figure 57 shows that separation of almost the complete vehicle was obtained at the highest pressure ratio tested with this nozzle and comparing this with the flat plate data of Figure 18 shows that separation occurs at a lower jet pressure ratio and much more separation occurs on the delta configuration than the flat plate at the same nozzle exit pressure ratio. The flat plate data also showed a more level plateau pressure than is evident on the delta configuration data however, the plateau pressures are fairly close if compared on the basis of a common separation point. Figure 58 presents the oil flow visualization of the effect of jet pressure ratio at zero angle of attack. The separation is strongly affected by angle of attack as seen in Figures 59 through 64 so that by 20° angle of attack very little separation occurs ahead of the elevon even at the highest jet pressure ratio. Figure 65

CONFIDENTIAL

shows that the angle of attack effect is strongest at low angles of attack and diminishes as angle of attack increases at constant jet pressure ratio while Figure 66 presents the oil flow visualization which shows very graphically the reduction in separated area with increasing angle of attack.

- (C) Figure 67 presents the effect of increasing jet pressure ratio with nozzle 2 ($A/A_* = 2.25$) which shows much more separation than the sonic nozzle data of Figure 57 when compared at the same jet pressure ratio. The pressure rise in the separated region is very similar for both nozzles when the data is compared for a common separation point which is similar to the flat plate plateau pressures. Figure 68 provides a comparison of flow visualizations of the effect of nozzle expansion ratio at zero angle of attack for the same exit jet pressure ratios which shows a similar result to that of the pressure data. Figure 69 presents a comparison of nozzles 2 ($A/A_* = 2.25$) and 3 ($A/A_* = 10$) at jet pressure ratio of 1050 and which again shows that the higher expansion ratio causes more separation when compared on jet exit pressure ratio. The nozzle 3 data of this plot would appear to correspond to that of a jet pressure ratio of about 4000 for nozzle 2 and this same correspondence was noted on the flat plate data.
- (C) Nozzle size comparisons are shown on Figures 70 and 71 between the sonic nozzles 6 and 1. There is a small difference in Figure 70 but no difference in Figure 71 at the higher jet pressure ratio. This result is not the same as the flat plate result obtained at a much shorter separation length. The implication of this is that nozzle size effects disappear as the plumes become larger and separation increases.
- (C) The effect of nozzle exit angle on separation caused by an $A/A_* = 2.25$ nozzle is shown in Figure 72 which shows that increasing nozzle exit angle increases separation in much the same manner as for the flat plate (Figure 30). Figures 73 to 75 present pressure data and oil flow visualizations obtained on the effect of nozzle position. Figure 73 apparently shows that moving the nozzle aft results in more separation which was not expected and does not agree with the flat plate results (Figure 31). However, this is not believed to be a nozzle position effect so much as a small angle of attack difference recalling the sensitivity of separation point to angle of attack in Figure 65 and the oil flows of Figure 74 show no appreciable moving forward of the separation point. The effect of vertical position change (Figures 72 and 75) is more pronounced on the delta model than on the flat plate (Figure 31).
- (C) The variations in plume induced separation by changing plume gases is shown in Figures 76 and 77. These figures show that using CO_2 as the test gas results in much more separation than air or Argon and exhaust gas specific heat is a sensitive parameter as was also shown in the flat plate data.

CONFIDENTIAL

CONFIDENTIAL

- (C) Figures 78 and 79 shows the differences which were observed caused by using cold air ($\sim 550^{\circ}\text{R}$) instead of heated air as the test gas. The cooler air had little effect at lower jet pressure ratios but became increasing important at higher pressure ratios and the difference was sufficient to cause the flow over the entire vehicle to be separated at the highest jet pressure ratio tested. Thus it appears that not only gas specific heat but also supply temperature are important parameters to be considered.
- (C) The effect of control deflection on pressures is shown in Figures 80 and 81 for -15° and $+20^{\circ}$ control deflections respectively. Figure 80 confirms the flat plate result that negative control deflection in the presence of plume induced separation is ineffective; however, Figure 81 shows that the $+20^{\circ}$ control deflection is ineffective also which is a different result than that of the flat plate (Figure 37). In both cases (Figures 80 and 81) the plume induced separation is directly comparable to the zero deflection case and so for this test condition the lower surface elevon appears to be completely ineffective. Figures 82 and 83 present oil flow visualization of the $+20^{\circ}$ degree control deflection case which shows how the plume separation predominates at zero angle of attack but also how the compression corner separation predominates at 10 degrees angle of attack.
- (C) 3.2.2 DELTA BOTTOM CENTERLINE DATA AT MACH 8. A short series of tests were conducted at both a Mach number of 8 and 6 primarily to determine Mach number effects on plume induced separation. Figure 84 presents the bottom centerline pressure data as a function of angle of attack without a plume which when compared to Figure 52 shows much less pressure variation across the front ramp than at Mach 10. The Reynolds number range tested at Mach 8 was larger than at either Mach 10 or Mach 6 and Figure 85 shows that this Reynolds number variation primarily changes the pressure level and the expansion onto the flat surface at the lowest Reynolds number only.
- (C) The effect of jet pressure ratio with the sonic nozzle is shown on Figure 86, which, when compared to similar data at Mach 10 in Figure 57 shows that the separation points are close. If there is a Mach effect, it is small and causes the separation point to be slightly further forward on the Mach 8 data. The plateau pressures are very definitely lower at Mach 8 compared to Mach 10, as, also are the pressure peaks on the elevon at higher pressure ratios. The effects of angle of attack (Figures 87 and 88) are comparable at both Mach numbers.
- (C) Expansion ratio effects, similar to that at Mach 10, are shown by the data of Figure 89 where again the nozzle 2 data exhibits slightly more separation and lower plateau pressure than that of Figure 67 at Mach 10. Figure 90 shows that increasing nozzle exit angle moves the separation point forward as was also

CONFIDENTIAL

seen at Mach 10. The nozzle size comparison shown in Figure 91 shows that the larger nozzle causes more separation but not by a factor on the order of the difference of mass flows of the two nozzles.

- (C) The effect of nozzle position is shown in Figure 92 which shows the same results as that of Figure 73 for Mach 10. The data for axial location, shows that the most aft position moves the separation forward while that of the other positions show no difference. The forward movement of separation by aft nozzle position is rejected again being caused by a slight negative angle of attack during the data run.
- (C) The effect of other exhaust gases is shown in Figures 93 and 94 which show that Argon causes the least separation and carbon dioxide the most indicating that decreasing exhaust gas specific heat (γ) causes more separation but also show this effect decreases with increasing jet pressure ratio. A parametric variation of free stream unit Reynolds number is shown in Figures 95 and 96 which show a strong trend toward decreasing separation with increasing Reynolds number. The higher Reynolds number pressure data lacks the plateau which occurs at lower Reynolds numbers and this difference is attributed to the boundary layer being turbulent at separation for the higher Reynolds number case whereas the other cases are probably laminar boundary layer separations. There is much more data scatter in the undisturbed pressure regions on Figures 95 and 96 than was evident in Figure 85 without a plume but this was assumed to be normal data scatter.
- (C) Figures 97 and 98 present pressure data with plume and control deflection at two angles of attack. Figure 97 shows that the control deflected at -15° is completely within the separated area at zero angle of attack and comparing this to 0° deflection with plume data of Figure 86 shows no change in the plume induced separation. The data at 10° angle of attack shows that the separation has moved back onto the elevator and raises the pressure only slightly thus the elevator still has some control effectiveness left at negative deflections at this angle of attack. The $+20^\circ$ deflection data of Figure 98 shows that the plume induced separation completely dominates at zero angle of attack while the control induced separation completely dominates at an angle of attack of 5° which is similar to the results obtained at Mach 10 (Figures 81 and 82).
- (C) 3.2.3 BOTTOM CENTERLINE DATA AT A MACH NUMBER OF 6. Figures 99 and 100 present the basic bottom centerline data without a plume as a function of angle of attack (Figure 99) and with lower elevator deflection (Figure 100). This data corresponds well with the data obtained at Mach 10 (Figures 52 to 54) and at Mach 8 (Figure 84).

CONFIDENTIAL

CONFIDENTIAL

- (C) The effect of jet pressure ratio for the sonic nozzle is shown in Figure 101 at zero angle of attack and in Figure 102 at an angle of attack of 5° . Figure 109 compares the separation locations for Mach 6, 8, and 10 and shows that there is no consistent Mach effect. The slightly higher Reynolds number of the Mach 6 data is believed to account for the lower separation for some of that data. Figures 110 and 111 compare plateau pressure ratio and plateau pressure coefficient at the three Mach numbers. The differences noted previously in plateau pressure ratio are seen in Figure 110 but reducing the data to pressure coefficient form (Figure 111) removes this Mach effect. Thus it would appear that the data is independent of Mach over the range of Mach numbers tested in this program.
- (C) Figures 103 to 105 presents the effects of nozzle expansion ratio, nozzle exit angle, and nozzle size at Mach 6 which are consistent with the trends established at the higher Mach numbers. The data at various nozzle axial locations shown in Figure 106 shows that moving the nozzle aft causes a slight reduction in separation at both aft locations. This data has been inconsistent at the other Mach numbers and the apparent differences caused by axial location shifts is small enough to be masked by the normal variation in other test parameters between tunnel runs. All the data on vertical position has been consistent and shows that moving the nozzle vertically away from a surface results in reducing the separation region. Figure 107 and 108 show the same effects on elevon deflection in the presence of plume induced separation as was shown at Mach 10 and 8.

3.3 DELTA BOTTOM SPANWISE DISTRIBUTION

- (C) The need for upper surface instrumentation resulted in many fewer pressure taps in the bottom surface of the delta (42) compared to that of the flat plate model (77). Figure 11 shows that pressure taps were principally arrayed along the bottom centerline ($Y/L = 0$) with a few located on two other chordwise lines 1" off the centerline ($Y/L = .05$) and 2" off the centerline ($Y/L = .1$) with most of the taps on the rear surface ($X/L > .6$) or on the elevon. Thus the spanwise distributions are less detailed than those of the flat plate. The half-span of the bottom surface excluding compression sharing sides is 2.22 inches wide ($Y/L = .111$) and thus the two off center lines cover the half-span of the bottom.
- (C) This data presentation will be limited to the nozzle 6 data at zero angle of attack since this data covers the range of separation locations seen during the test. The data was connected by point to point straight lines by computer plotting so that the curves are not smoothed as in the preceding section.

CONFIDENTIAL

- (c) 3.3.1 SPANWISE DISTRIBUTION AT MACH 10. Figure 112 presents the basic pressure distribution on the bottom of the delta planform along three spanwise lines. The data shows some scatter but no spanwise variation in pressure distribution at this condition. The effect of increasing jet pressure ratio on bottom pressures is shown in Figures 113 through 119. These figures all show that the centerline has the most separation but that the separated region spreads rapidly on the surface and the edge is separated less than 10% aft of the centerline. These figures also show little spanwise variation in plateau pressure and the pressure peak, which occurs on the end of the elevon on the centerline, never spreads to the other spanwise locations. Figure 58 presents oil flow pictures of the bottom surface separation which is directly comparable to Figures 114, 116, and 119.
- (c) 3.3.2 BOTTOM PRESSURE DISTRIBUTIONS AT MACH 8. Figures 120 through 124 present typical bottom pressure results obtained at Mach 8 and zero angle of attack with increasing plume jet pressure ratio. The results are similar to those obtained at Mach 10.
- (c) 3.3.3 BOTTOM PRESSURE DISTRIBUTIONS AT MACH 6. Figures 125 through 130 show typical results at Mach 6 with increasing jet pressure ratio which are very much like the results at the other Mach numbers. Figure 131 presents a comparison of centerline separation with that at the $Y/L = .1$ location. This data shows that there is no Mach number effect in the spanwise variation and since the data was taken for a number of different jet pressure ratios there appears to be no plume size effect other than that which determines centerline separation location. The flat plate data indicated that the spanwise pressure distribution caused by plume induced separation depended only on the centerline distribution and it appears that a similar result has been shown for the bottom of the delta configuration. The curve faired through the data has been extrapolated to the nose and to the end of the vehicle.
- (c) Figure 132 presents an attempt to approximate the spanwise variation in separation location as a straight line which is swept at some angle to the stream and Figure 132 plots sweep angle as a function of centerline separation location and free-stream Mach number. This straight line representation was chosen based on the oil flow data (Figures 58, 66, 68, 74 and 75) and the data shown on Figure 132 was computed from the spanwise data of Figure 131. The curve shown on Figure 132 was computed based on the faired curve on Figure 131 and can be used as a first approximation prediction method for the spanwise variation of separation on other configurations if the separation on the centerline is known.

CONFIDENTIAL

CONFIDENTIAL

3.4 UPPER SURFACE PRESSURE DISTRIBUTION

- (C) Fifty pressure taps were located in the upper surface of the delta configuration and in the fin as shown in Figure 13. These taps were divided along four lengthwise lines on the body and one lengthwise line on the fin. Figure 12 shows that one set of taps was located on the top centerline of the body up to the base of the vertical fin. One set of taps was located at 45° off the top centerline through model station 12.73, which is the location of the maximum cross section of the vehicle and aft of this point the vehicle narrows down into a vertical fin section and sloping upper deck. This set of taps was located at a constant height (MWL 2.62) after station 12.73 in this expansion surface region. The third set of taps was located on the side of the vehicle along the centerline of the top radius (90° off top centerline) through model station 12.73 and aft of this station this line of taps was continued at the mid-point of the rear expansion deck. The fourth line of taps was located on the side of the vehicle at a constant height above the base (MWL .665). This set of taps carried onto the aft expansion surface until the leading edge radius of the compression sharing surface reached waterline .665 and the last two taps are on this leading edge. The fin tap set includes one leading edge tap and five side taps located in a line at constant height above the base of the model (model water line 4.08). The division of pressure taps is that 29 were located ahead of the upper surface expansion corner and 15 aft of the expansion corner. None were located on the upper surface elevons.
- (C) 3.4.1. UPPER SURFACE PRESSURES AT MACH 10. Figure 133 presents the upper surface and fin pressure distributions as a function of angle of attack without a plume. The end of the top centerline taps ($X/L = .636$) is the location of the maximum thickness and the start of the expansion corner. The leading edge tap of the fin is located at an X/L of .757. This set of data shows that although the entire front surface is shielded from the flow at angles of attack greater than 10 degrees that positive pressures persist at higher angles and that the lower the location on the upper surface the higher this pressure tends to be. Aft of the expansion corner the pressures are at or below ambient ($P/P_\infty = 1$) above 10° angle of attack except near the edge of the lower surface (MWL = .66). The modified fin is fairly blunt and shows the effect of nose bluntness at low angles of attack but is completely separated at angles of attack above 10° . Figure 134 shows that the Reynolds number variation tested at Mach 10 caused little variation in upper surface pressures except near the nose of the model. The effect of increasing jet pressure ratio at zero angle of attack is shown in Figure 135a and 135b. These data show that the plume does cause separation but this separation never progresses very far ahead of the expansion corner. Thus the lower surface (Figures 57 and 119) is experiencing much more separation than the

CONFIDENTIAL

CONFIDENTIAL

upper surface and which is probably due to the larger angle that this surface (approximately 80°) presents to the airstream than that for the front ramp (30°) of the lower surface. Figures 136a and 136b present a top view and a side view of oil flow visualizations of the delta for conditions similar to Figure 135 to show the extent of the separated region. These photographs indicate that the separation region is limited to the expansion surface of the model. There is a streak on the side of the model at the higher jet pressure ratios which has been interpreted (reference 11) as a small separated region which extends far forward of the expansion corner but this is not confirmed by the pressure data and is not believed to be any separation. The effect of increasing angle of attack in plume induced separation is shown in Figures 137 through 141 at angles of attack from 2.5 degrees through 20 degrees. Increasing angle of attack causes the separation point to move forward on the upper surface with the top centerline showing the most separation and the taps closest to the bottom edge the least separation. Figure 142 shows that it still takes a large plume (high P_j/P_∞) to affect the surface pressures ahead of the expansion corner even at 20 degrees angle of attack. While Figures 59 through 64 show the rapid collapse of the separated area on the lower surface Figure 142 shows that the area affected by the plume grows larger on the upper surface at high jet pressure ratios. The plateau pressure in the affected area is constant on all rays and on the fin and appears to decrease with increasing angle of attack for the lower jet pressure ratios as is shown in Figure 143. The higher jet pressure ratio curves show an increase in plateau pressure at the higher angle of attack. Only one data point was taken at the 26.5 degree angle of attack and this point was at too low a pressure ratio to confirm this trend of increasing plateau pressure.

- (c) 3.4.2 UPPER SURFACE PRESSURES AT MACH 8. Figures 144 and 145 show the effect of angle of attack and Reynolds number respectively on the upper surface pressures at Mach 8 without an exhaust plume. These effects are much the same as those seen at Mach 10 in Figures 133 and 134.
- (c) The effect of jet pressure ratios to 32000 at angles of attack from 0 to 15 degrees are shown in Figures 146 through 149. The jet pressure ratio was limited in this test series by supply pressure limitations and the higher ambient pressure of the tunnel. The angle of attack was limited to 15° to use a sting installation to give good Schlieren coverage of the plume. Very little separation was achieved ahead of the expansion corner and neither angle of attack or jet pressure ratio were high enough to verify the hock in the plateau pressure curve seen at Mach 10 (Figure 143).

CONFIDENTIAL

CONFIDENTIAL

- (c) 3.4.3 UPPER SURFACE PRESSURES AT MACH 6. Figures 150 through 153 present typical results of upper surface pressures with and without plumes at angles of attack from 0 to 15°. The same limitations were imposed here as at Mach 8 and essentially the same results are seen.
- (c) Figure 154 presents a comparison of upper and lower surface plateau pressure coefficients at zero angle of attack and this curve shows that there appears to be a linear relationship between the upper and lower plateau pressures where the upper plateau pressure tends to be slightly higher than the lower. There also appears to be no Mach number effect in this data. Figure 155 shows how the upper surface separation never moves ahead of the expansion corner while the lower surface separation moves ahead on the model at zero angle of attack. The effect of angle of attack on plateau pressure was indicated in Figure 143 at Mach 10 and Figure 156 presents data for all three Mach numbers in terms of the plateau pressure coefficient at that angle of attack ratioed to the plateau pressure coefficient at zero angle of attack. There is a fair amount of scatter but no significant Mach number effect and the trend is consistent of reducing plateau pressure with increasing angle of attack except for the one value obtained at 20 degrees for the highest jet pressure ratio at Mach 10, which showed an increase in plateau pressure. Figure 157 shows that while no consistent trend could be found in the upper surface separation location as a function of angle of attack or Mach; it appears that a jet pressure ratio of about 20000 for nozzle 6 was sufficient to move the separation location ahead of the expansion corner and at higher angles of attack, essentially all of the upper surface saw plume effects when this pressure ratio was exceeded.

CONFIDENTIAL

3.5 BASE PRESSURE DATA

- (C) Four pressure taps were located in the base of the model as shown in Figure 14. Figure 158 presents average base pressure results at zero angle of attack, as a function of jet pressure ratio for nozzle 6, which shows that the base pressure initially shows a large increase with increasing jet pressure ratio but the base pressure becomes much less sensitive to pressure ratio as it continues to increase. Figure 159 shows a linear relationship between plateau pressure and base pressure for all nozzles at zero angle of attack implying that one depends on the other. Figure 160 shows the effect of angle of attack on base pressures at three jet pressure ratios for nozzle 6 at Mach 10. The base pressures apparently decline with increasing angle of attack but then appear to rise again, which is similar to the type of behavior seen in the upper surface plateau pressure. The base pressure may be related to upper surface plateau pressure at higher angles of attack.

3.6 SUMMARY OF DELTA CONFIGURATION PRESSURE RESULTS

- (C) The delta configuration showed that it had much more separation than the flat plate for a given nozzle, nozzle flow parameters, and tunnel condition. This plume induced separation on the bottom surface was very sensitive to:

- a) angle of attack
- b) exhaust jet pressure ratio
- c) nozzle expansion ratio
- d) nozzle exit angle
- e) plume gas
- f) plume gas temperature
- g) Reynolds number

The plume induced separation was relatively insensitive to:

- a) Mach number
- b) nozzle longitudinal position
- c) control deflection at low angles of attack

- (C) Plateau pressure coefficients appear to be independent of test Mach number and correlate very well when compared by common separation location regardless of the nozzle causing the separation suggesting a result similar to that of compression corner separation where plateau pressure is related only to conditions at the separation point.
- (C) The upper surface expansion corner strongly affected the separation of the upper surface and fixed the separation point except at high angles of attack and high jet pressure ratios where most of the surface was affected. The

CONFIDENTIAL

upper surface plateau pressure at zero angle of attack was slightly higher than but definitely related to lower surface plateau pressure. Upper surface plateau pressure decreased with angle of attack except at high angle of attack and high jet pressure ratio where it tended to return to the zero angle of attack value.

3.7 OIL FLOW DATA

- (C) Fifty-eight (58) oil flow runs were made with the flat plate model or the delta model at Mach 10. These runs were made primarily for flow visualization on the bottom surface of both configurations although a few photographs were obtained of upper surface flow on the delta configuration. The technique used consisted of spraying the model with zygo penetrating oil and lighting the model with ultra-violet lights after injecting it into the tunnel. The zygo oil glows under the ultra-violet light which allows the surface flow pattern to be observed and photographed. Representative oil flow visualization photographs have been presented with the flat plate and delta planform pressure data and will not be repeated here. This data was reduced to obtain flow separation location and Figures 161 and 162 present comparisons of centerline separation location as measured from the oil flow to that obtained from the pressure data. The point used in the pressure data was at the start of the pressure disturbance and these figures show that this point is about 5% of the vehicle length ahead of separation point measured on the oil flow pictures for the flat plate, and about 10% for the delta configuration. Figure 163 presents a comparison of the sweep angle of the spanwise separation line from the oil-flows with that taken from the pressure data of Figure 132. The data is displaced from the curve by the difference shown in Figure 162, but the trend appears to be much the same except for the scatter for the cases of least separation.

3.8 SCHLIEREN DATA

- (C) Schlieren photographs were taken during each pressure test run and a number of runs were repeated at the end of the test in order to try to get better flow visualization of the plume boundary and separated region. Schlieren photographs were the only means available for obtaining plume geometry and Figure 164 presents a schematic of the plume and separation region, and the measurements which were made on the Schlieren photographs. It was extremely difficult to see the plume and separation region in most photographs and the net result was a large amount of scatter in the data obtained. This figure shows the model in an inverted position since that is the way the test program was run and the way the typical test results are presented.
- (C) Figure 165 presents a set of Schlieren photographs which show the relative

CONFIDENTIAL

size of the plume to the model base at Mach 10 and show how the plume increases in size with increasing exit jet pressure ratio for the sonic nozzle. It appears that the plume boundary may strike the rear edge of the lower surface elevon at the higher exit pressure ratios. The effect of positive angle of attack in reducing the plume size on the windward side of the vehicle is shown in Figure 166. The shock wave due to separation is barely visible at low angles of attack and the boundary layer becomes more visible as angle of attack increases. Figure 167 shows a comparison of plumes at Mach 6, 8, and 10 for a common nozzle flow condition which shows very little Mach number effect on plume size or shape.

- (c) The effect of nozzle size is shown in Figure 168 for zero angle of attack at Mach 5.96. Nozzle 1 has half the mass flow of nozzle 6 and this is reflected in the smaller plume for that nozzle. Figure 169 presents a comparison of plumes for the three different gases used in this study. The carbon dioxide plume is noticeably larger than that of air while the Argon plume is the smallest. The effect of nozzle exit angle is shown in Figure 170 which shows that increasing exit angle increases plume size close to the model. Figure 171 shows that moving the nozzle aft does not change plume size appreciably but moving the nozzle vertically away from the surface (position 4) does reduce the plume size which is visible to that surface considerably.
- (c) Figures 172 and 173 show representative data for plume initial radius and flow separation angle which were derived from the film data. The scatter in the data is appreciable, partly the result of scaling the data from the film but also in large measure due to the poor definition of the separated flow on the film. These data show no Mach number effect and the sensitivity to jet pressure ratio as a parameter is low. The data was mostly taken at zero angle of attack and was read for the bottom surface of the configuration.

3.9 FLOW SURVEY DATA

- (c) The six probe pitot rake which was used to perform these flow surveys is shown on Figure 15. This probe was used to obtain 24 flow surveys of the flow on the bottom surface of the delta configuration at Mach 10 and zero angle of attack with and without an exhaust plume and also behind the delta configuration with a plume. The probe data was reduced at AEDC and reference 11 presents more details of the data reduction procedure used to convert the probe output into velocity, temperature, and pressure profiles. The main assumption in the data reduction is the use of static pressure measured on the model surface as the static pressure throughout the survey. The probe

CONFIDENTIAL

CONFIDENTIAL

was moved normal to the surface and the velocity and total temperature profile data which will be presented is plotted as a function of distance from the surface.

- (C) Figure 174a to 174c presents the velocity and temperature profiles at three stations on the centerline of the vehicle at zero angle of attack without an exhaust plume. These three stations are located aft of the lower surface expansion corner and the last station ($X/L = 1.084$) is at the trailing edge of the lower surface elevon or right at the end of the body and at the exit plane of the nozzle in position 1. This data shows a boundary layer approximately 1.1 inches thick over this rear surface. Figure 175 a through 175 g show the flow field on and behind the body with an exhaust plume. Two stations ahead of the expansion corner are shown in Figures 175 a and 175 b and these stations show no separation region although Figure 57 shows the plume induced pressure rise to start at an $X/L = .42$. The plateau pressure region on Figure 57 is reached at about .7 of the length back and Figure 175 c shows a separated region forming. The separated region appears to be 1.25 inches deep at the end of the body (Figure 175 d). Aft of the body (Figures 175 e through 175 g) the zero value of z still corresponds to model water line zero so that these surveys are limited to the portion of the plume seen by the lower surface. The Schlieren data indicated that the separated boundary layer intersected the plume at an X/L of 1.12 so that Figures 175 e and 175 f should contain separated flow region data outside the plume. This is believed to be shown on Figure 175 e by the hook in the curve at about 1.25 inches but is not seen in Figures 175f and 175g. Figures 175f and 175g are surveys aft of flow reattachment to the plume.
- (C) Figure 176 presents the velocity ratio data for the same nozzle at one-half the jet pressure ratio of that in Figure 175 and which shows the same trends as indicated in Figure 175 except that the separated layer is slightly thinner in Figure 176. Figure 177 presents the velocity profiles at 5 stations (3 on the vehicle and 2 aft) with the expansion ratio 2.25 nozzle used to create the plume. Comparing this data to the sonic nozzle data of Figure 176, Figure 178 shows that the separation has occurred earlier for nozzle 2 (Figure 178 a) but that the separated layer is thinner at the rear of the vehicle (Figure 178 b). Both nozzles were supplied with gas at the same supply temperature and because of the higher expansion the ambient temperature at the nozzle exit for nozzle 2 is much colder than for nozzle 1 (on the order of half) and this colder data can be seen in the data at all stations. The velocity in the plume (Figure 178 c) is lower because of this temperature difference.
- (C) 3.9.1 FLOW SURVEYS WITH DISC. An attempt was made during the flow field survey runs to size a solid plate disc to represent the plume and to gather

CONFIDENTIAL

CONFIDENTIAL

flow field survey and centerline pressure data to compare with the plume data to see how well this disc could represent a plume. Two discs were sized and located based on measurements made on Schlieren photographs. The discs were circular in shape and the smaller was 3.7 inches in diameter located at model station 22.32 while the larger was 5.3 inches in diameter and was located at model station 22.94. Figure 179 presents an oil flow comparison between the larger disc and a nozzle 1 plume with a jet pressure ratio of 17000 which shows the separation shapes to be similar although the disc appears to induce slightly more separation. Figure 180 shows that smaller disc appears to cause a slightly deeper separated area than the larger disc but not quite as deep as the plume induced separation case. However, when we compare centerline pressure distributions for the disc with that of plume induced separation we see that the data for the larger disc correlates well with the nozzle 6 data at a jet pressure ratio of 17000 (Figure 181) while the smaller disc (Figure 182) shows very little separation and would correlate with a plume of jet pressure ratio less than 4000. The discs were sized for the jet pressure ratio of 17000 cases where the smaller disc was sized by the diameter of the plume where the boundary layer intersected the plume and the larger by the separation shock intersection. Evidently if that point could be predicted a disc could possibly be used to represent the plume.

CONFIDENTIAL

CONFIDENTIAL

SECTION 4 DATA ANALYSIS

- (C) The general approach (reference 10), which has usually been taken for the problem of predicting plume induced separation, has been to assume that the control induced separation data defining the relationship between separation point and plateau pressure is valid for the plume problem. Thus a separation point is assumed, a plateau pressure coefficient is computed and is used to define the plume boundary. A criteria for defining re-attachment of the separated flow on the plume is established and then the problem can be iterated assuming separation points and finding reattachment points until the separation wedge geometry is satisfied.
- (C) Figure 57 presents typical pressure profiles through the plume induced separated region showing pressure profiles which are similar to those observed for control induced separation although the pressure continues to rise throughout the separated region and can have a peak on the end of the surface. The shape of the distribution tends to be similar to that expected for a turbulent type compression corner separation rather than that for the laminar case.
- (C) The approach which has been utilized in the analysis of this data was to try first to determine the parameters necessary to correlate plume shape and based on this to try to define the relationship of the separation parameters to the plume shape. Thus the analysis section will be divided into the following subsections:
 - 4.1 Plume Shape Analysis
 - 4.2 Separation Point Analysis
 - 4.3 Plateau and Base Pressures Analysis
 - 4.4 Recommended Method

4.1 PLUME SHAPE

- (C) Two pieces of information were available and read from the Schlieren photographs which are related to plume shape. They are initial turning angle of the plume and plume initial radius. These are the only data which can be used to define plume shape in the photographs since the region of flow reattachment to the plume completely changes the shape thereafter. Assuming Latvala's model (reference 13) these are sufficient to define the plume contour close to the body.
- (C) 4.1.1 INITIAL TURNING ANGLE. Figure 183 presents the data for the plume initial turning angle for the sonic nozzles (nozzles 1 and 6) compared to the Prandtl-Meyer turning angle for the pressure ratio at the exit. The ratio of exit pressure to measured base pressure was used because the base pressure is

CONFIDENTIAL

the most representative external pressure at the nozzle exit. The data shows a fair amount of scatter indicating the difficulty of making the measurement, however, there is no apparent Mach number effect and no angles over 90 degrees were measured although the jet pressure ratios should cause flow into the base at angles greater than 90° according to the Prandtl-Meyer turning angle limit. The data available on the 3 nozzles with an expansion ratio of 2.25 and different exit angles is much more sparse but is presented in Figure 184. The initial expansion angle was measured with respect to the nozzle centerline and so the exit angle of the nozzle must be added to the Prandtl-Meyer turning angle. The data for the 7.5° and 15° nozzles is fairly close to the predicted turning angle, however, the 30° data is within the scatter of the other two nozzles. Considering the scatter of the data and the poor comparison with the predicted turning angle of Figures 183 and 184 this data does not appear useful in developing improved plume boundary predictions. The data did show, however, no turning angles greater than 90° and this fact was used in the radius computation.

- (c) 4.1.2 PLUME INITIAL RADIUS. The initial radius of a plume is dependent only on jet exit Mach number in the Latvala model and it is the initial turning angle which depends on jet pressure ratio. The plume size as seen in the Schlieren photographs strongly depended on jet pressure ratio and with no consistent trend seen in the initial turning angle, the Latvala model initial radius did not agree with the test results. The Lockheed 5 point method (reference 10) was then used to define the plume boundary which was fitted with a hyperbolic curve so that the initial radius could be computed. The curve fit was then used to evaluate the plume diameter at two points close to the nozzle (arbitrary chosen as one and two nozzle exit radii away from the nozzle) and the radius of the curve which fit through these three points ($x = 0$, $x = r_e$, $x = 2r_e$) was computed as the initial plume radius.

The Lockheed 5 point model is given as:

$$f_1 = \frac{A}{A_*} \frac{P_\infty}{P_{0j}} (1 + \gamma_\infty M_\infty^2)^{1/4} (1 - \sin \theta_N)^{-1} \quad (1)$$

$$\frac{x_{\max}}{r_e} = 1.076 f_1^{-.563} \quad (2)$$

$$f_2 = \frac{x_{\max}}{r_e} \left[\left(\frac{A}{A_*} \right)^{1/4} (1 + \gamma_\infty M_\infty^2)^{1/8} (1 - \sin \theta_N) \right]^{-1} \quad (3)$$

CONFIDENTIAL

CONFIDENTIAL

$$\frac{r_{\max}}{r_e} = 0.65 f_2^{.91} \quad (4)$$

$$\text{at } x = 1/4 \quad x_{\max} \quad \frac{r}{r_e} = 0.686 \left(\frac{r_{\max}}{r_e} \right)^{0.963} \quad (5)$$

$$\text{at } x = 1/2 \quad x_{\max} \quad \frac{r}{r_e} = 0.871 \left(\frac{r_{\max}}{r_e} \right)^{0.992} \quad (6)$$

$$\text{at } x = 3/4 \quad x_{\max} \quad \frac{r}{r_e} = 0.969 \frac{r_{\max}}{r_e} \quad (7)$$

where

- $\frac{A}{A_*}$ = nozzle expansion ratio
- θ_N = nozzle exit angle
- P_{0j} = nozzle chamber pressure
- P_∞ = ambient pressure at exit
- M_∞ = free stream Mach number
- γ_∞ = specific heat ratio

(C) This method was derived in reference 10 for an exhaust gas specific heat ratio of 1.38 and zero angle of attack.

(C) The hyperbolic curve fit (KABD) which was fitted through four points ($x = 0$ nozzle exit, $x = 1/4 x_{\max}$, $x = 1/2 x_{\max}$, $x = 3/4 x_{\max}$) is given by the equation

$$r = \frac{K}{x-A} + B + Dx \quad (8)$$

where K, A, B, and D were determined by the four points. This curve has no maximum or minimum values nor does it have any points of inflection in the range where it is fitted thus the local slope at the nozzle exit can never exceed 90° at the nozzle exit but then Figures 183 and 184 indicate that it never does. A number of the plume contours were also fitted with a curve of the form (parabolic)

$$r = Ax^2 + Bx + C \quad (9)$$

CONFIDENTIAL

and the initial radius computed from this fit was found to agree with the KARD fit. Higher order curves were not tried because it was felt that the maximum curvature was between the nozzle and the first plume contour point and without additional points to fit in this area nothing could be gained by higher order fits.

- (C) Figures 185 and 186 presents a comparison of initial radius as measured from the Schlieren pictures compared with the initial radius using equations 1 through 8 with the data presented by Mach and nozzle.
- (C) The data shows that there is a considerable amount of scatter in the measured radius but no radius exceeded 10 inches while the computed radius based on P_{0j}/P_{∞} exceeded 30 inches for the sonic orifice (nozzle 6) at the higher jet total pressures. The scatter in the data is apparently caused by the large radius resulting from increasing jet total pressure ratio. All Mach numbers are included in this comparison but this is not the prime cause of the scatter. Since we are interested in the contour in the region of plume induced separation in which pressures are higher than ambient it was expected that this computation would result in large scatter and that a better representation of plume shape would be obtained if the pressure in the separated region were used in the jet pressure ratio term of equation 1. Analytic methods have generally assumed that plateau pressure in the separation region determined the base pressure and is a function of Mach and Reynolds number at separation so that it is reasonable to assume that the pressure ratio should be jet total pressure divided by plateau pressure. Figure 187 presents the comparison of radii based on plateau pressure, which shows a large reduction in computed initial radius compared to Figure 186 but the computed radii at the higher total pressures still indicate that the pressure ratio term or some other parameter related to pressure ratio is too strong in the prediction equation. The expansion ratio 2.25 and 10 data shows too large a computed radius but this was attributed to the relatively large values of total pressure ratio tested with these nozzles. It appears that the problem is that the pressure ratio term in equation 1 is too strong and a pressure ratio factor can be derived to reduce this effect. Equation 1 was modified to become:

$$r_1 = \frac{A}{A_*} \left(\frac{P_p}{P_{0j}} \right)^{\frac{\gamma+1}{2\gamma}} (1 + \gamma_{\infty} M_{\infty}^2)^{1/4} (1 - \sin \theta_N)^{-1} \quad (10)$$

and the constant (1.076) in equation 2 was increased to 1.6 and the effect of exhaust gas specific heat has been introduced through the factor on jet pressure ratio. Figure 188a presents the results of these changes. The constant of equation 2 was changed based on an unpublished check of equations 1-7 made at General Dynamics on plume data obtained in flight test. Figure 188a

CONFIDENTIAL

shows that the data is now grouped around the correlating line although there is still a large amount of scatter. Figures 188b and c show that this remaining scatter has no apparent Mach number or Reynolds number trends. Figures 188d through f also show no consistent trends for exhaust gas, model geometry, or nozzle location.

- (C) The data was checked to try and reduce reading error and also for any further parameters which showed large variation and which had not been taken into account by the plume model. It was found that although the gas supply temperature had been controlled there was significant variation in supply temperature between data runs. A temperature correction was incorporated into equation 10 based on the ratio of nozzle total temperature to free-stream total temperature:

$$f_1 = \frac{A}{A_*} \left(\frac{P_P}{P_{Oj}} \right)^{\frac{\gamma_j+1}{2\gamma_j}} \left(\frac{T_{O\infty}}{T_{Oj}} \right)^{-5} (1 + \gamma_\infty M_\infty^2)^{1/4} (1 - \sin \theta_N)^{-1} \quad (11)$$

and the results are shown in Figure 189. Comparing Figure 189a to Figure 188a shows that a reduction in the scatter had been achieved but not the desired amount and Figure 189b shows that this reduction in scatter occurred mostly in the Mach 8 and 10 data. A number of other temperature relationships were tried without results until it was decided that the pressure and temperature should be to the same power and that nozzle exit static temperature ratioed to ambient should be the best temperature ratio and equation (1) was modified to:

$$f_1 = \frac{A}{A_*} \frac{P_P}{P_{Oj}} \frac{T_j}{T_\infty} (1 + \gamma_\infty M_\infty^2)^{1/4} (1 - \sin \theta_N)^{-1} \quad (12)$$

- (C) Figure 190 showed that this relationship causes the sonic nozzle computed ratios to be too small compared to the measured values, which can be adjusted in the constants of equations 2 or 4, and makes the scatter in the sonic data appear to be fairly small primarily due to the small values of computed radius. The data exhibits a strong trend based on expansion ratio which was not seen previously and which was caused by temperature effects masking the expansion ratio effect.
- (C) Both equations 1 and 3 contain expansion ratio as a factor, however they act in opposite ways; expansion ratio in equation 1 acts to reduce x_{\max} and hence r_{\max} while that in equation 3 acts to increase r_{\max} . The desired effect is to reduce r_{\max} and necessarily x_{\max} to keep the initial turning angle large thus equation 12 was modified by multiplying by expansion ratio. Because temper-

CONFIDENTIAL

ature is a linear factor it is expected that the exhaust gas specific heat belongs in the equations with the temperature ratio. These changes did not eliminate the differences caused by freestream Mach number, which is a weak term in equations 1 and 3, but apparently is causing a difference in the computed radius that is not seen in the measured radius or any other separation terms. Therefore the Mach dependent terms were eliminated in equations 12 and 3 and equation 12 becomes:

$$f_1 = \frac{P_p}{P_{oj}} \frac{\gamma_j T_j}{\gamma_\infty T_\infty} (1 - \sin \theta_N)^{-1} \left(\frac{A}{A_*} \right)^2 \quad (13)$$

while equation 3 becomes:

$$f_2 = \frac{X_{max}}{r_e} \left[\left(\frac{A}{A_*} \right)^{1/4} (1 - \sin \theta_N) \right]^{-1} \quad (14)$$

- (C) The constants of equations 3 and 4 were modified to account for these changes and the results are shown in Figure 191. The scatter is still large but is much improved over the original comparison of Figure 187. The remaining scatter is due in large part to the reading error in measuring plume radius from Schlieren photographs, however, it is also partly due to the scatter in the measured plateau pressure which is used in the plume computation. The KABD curve fitting technique and method of computing initial radius for the plume computation also must add some scatter and the initial turning angles computed from the curve fit tended to be about 10 degrees low compared to the test data. Selection of another equation to fit the data which results in closer agreement on initial turning angle may improve the correlation, however, it is believed that the major parameters have been identified and accounted for through the techniques described in this section.

- (C) In summary, the Lockheed 5 point plume model has been modified to predict a Pseudo plume shape which provides a better measure of plume induced separation interactions. The revised parts of model are:

$$f_1 = \frac{P_p}{P_{oj}} \frac{\gamma_j T_j}{\gamma_\infty T_\infty} (1 - \sin \theta_N)^{-1} \left(\frac{A}{A_*} \right)^2 \quad (15)$$

$$\frac{X_{max}}{r_e} = .758 f_1^{-.563} \quad (16)$$

CONFIDENTIAL

$$f_2 = \frac{x_{\max}}{r_e} \left[\left(\frac{A}{A^*} \right)^{1/4} (1 - \sin \theta_N) \right]^1 \quad (17)$$

$$\frac{r_{\max}}{r_e} = .65 f_2^{.91} \quad (18)$$

and equations 5 to 7 remain unchanged.

- (C) This model cannot be expected to match plume contours far from the nozzle nor for plumes where no plume induced separation has occurred and much work needs to be done to obtain plume contour data in regions of plume induced separation so that better models can be generated.

4.2 SEPARATION LENGTH ANALYSIS

- (C) Figure 192a presents a sketch, from reference 14, of compression corner induced separation and the various parameters used to define it. Laminar flow compression corner induced separation is generally characterized by a pressure rise to a plateau on the surface ahead of the corner which is carried onto the flap, where in the course of the flow re-attaching to the surface, the pressure rises to another plateau on the flap. The distance from the leading edge of the surface to the start of the pressure rise is defined interaction distance (X_i) and this point measured forward from the hinge line has been called up-stream interaction length (d_i). The distance from the start of interaction to the plateau pressure has been defined as free-interaction length (d_f). These along with plateau pressure are the separation parameters which we will deal with in this analysis, Figure 192b. The reference point for measuring upstream interaction length has been defined as the plane of the nozzle exit. The down stream parameters are dependent on the plume and cannot be measured directly except that the re-attachement point was scaled from the Schlieren pictures.
- (C) 4.2.1 UPSTREAM INTERACTION LENGTH AT ZERO ANGLE OF ATTACK. Figure 193 presents a compilation of upstream interaction length data, for the delta configuration at zero angle of attack, plotted against jet total pressure ratio. Total pressure ratio is used since it was found to be a better parameter than exit static pressure and since total pressure is the parameter used in the plume computation equation 15. This curve briefly shows that there is a distinct effect of nozzle size, nozzle expansion ratio, and nozzle exit angle. The data for Mach 6, 8, and 10 are presented in this plot and this causes some scatter in the nozzle 6 data but free stream Mach appears to be a very weak parameter which was also shown in Figure 103. Plume induced separation appears to be very similar in general characteristics to that of

CONFIDENTIAL

of control induced separation so that some comparisons with control induced separation parameters are in order. Thus Figure 194 presents a comparison of the parameter $\left\{ \frac{d_1}{\delta_L} \right\}$ for the delta configuration versus plateau pressure

ratio with curves from reference 14. The parameter (d_1/δ_L) is the upstream interaction length ratioed by the laminar boundary layer thickness at the interaction point which was defined from reference 14 as:

$$\delta_L = \frac{5.2 x}{\sqrt{\frac{P_w}{P_\alpha} Re_\alpha^*}} \quad (19)$$

where

$$\frac{Re_\alpha^*}{x} \approx \frac{Re_\alpha}{x} \left(\frac{T_\alpha}{T^*} \right)^{1.76} \quad (20)$$

and

$$\frac{T^*}{T_\alpha} = .28 + .5 \frac{T_w}{T_\alpha} + .22 \frac{T_{aw}}{T_\alpha} \quad (21)$$

$$\frac{(Re/X)_\alpha}{(Re/X)_\infty} = \frac{P_\alpha}{P_\infty} \left[\frac{1 + 0.2 M_\alpha^2}{1 + 0.2 M_\infty^2} \right]^2 \frac{M_\alpha}{M_\infty} \left[\frac{\frac{T_\infty (1 + 0.2 M_\infty^2)}{1 + 0.2 M_\alpha^2} + 198.6}{T_\infty + 198.6} \right] \quad (22)$$

$$M_\alpha = \left[\frac{M_\infty^2 \left(6 \frac{P_\alpha}{P_\infty} + 1 \right) - 5 \left(\left(\frac{P_\alpha}{P_\infty} \right)^2 - 1 \right)}{\frac{P_\alpha}{P_\infty} \left(\frac{P_\alpha}{P_\infty} + 6 \right)} \right]^{\frac{1}{2}} \quad (23)$$

Subscript α defines local conditions at a point on the body accounting for angle of attack effects.

CONFIDENTIAL

CONFIDENTIAL

- (C) The data on Figure 194 shows a large spread by Mach number which is primarily caused by the use of the plateau pressure ratio. Figure 104 showed the differences in plateau pressure ratio which were accounted for by using plateau pressure coefficient (Figure 105). The control induced is perhaps more similar to turbulent control separation since it does not show the long plateau of pressure as the laminar case, thus turbulent boundary layer thickness was defined (reference 14)

$$\delta_r = \frac{0.154 x}{\left[(Re_{\alpha x}) \left(\frac{T_\alpha}{T^*} \right) \left(\frac{\mu_\alpha}{\mu^*} \right) \right]^{1/7}} = \frac{0.154 x}{\left[(Re_{\alpha x}) \left(\frac{T_\alpha}{T^*} \right)^{1.67} \right]^{1/7}} \quad (24)$$

and the turbulent separation correlation (reference 14) was attempted as shown in Figure 195. The data shows a smaller spread from Mach number effects because the ordinate contains local Mach however, neither figures 194 or 195 show much agreement between the plume induced separation and control separation it is presumed because the plume represents a curved mixing boundary which injects mass into the separation region.

- (C) Figure 193 showed that the primary parameters acting on upstream interaction length were:
- a) exhaust pressure ratio
 - b) nozzle size
 - c) nozzle expansion ratio
 - d) nozzle exit angle.
- (C) These parameters are all accounted for in the plume shape equations and since it would be very desirable to be able to correlate upstream interaction length with plume size; correlations were made with a number of plume parameters such as exposed plume height, plume initial radius, plume maximum radius and plume initial turning angle.
- (C) Figure 196 presents a correlation of upstream interaction length ratioed by laminar boundary layer thickness at separation from equation 19 plotted as a function of plume maximum diameter from equations 15 to 18. The scatter is due in part to the magnifying of separation location error involved by ratioing to boundary layer thickness and also to the scatter in plateau pressure being incorporated into the plume diameter computation. A tentative line has been faired through the data and its equation is

CONFIDENTIAL

CONFIDENTIAL

$$\frac{d_1}{\delta_L} = 75 \left(\frac{D_{max}}{b} - \frac{2Z_n}{b} \right)^{1.8} \quad (25)$$

where

- d_1 = upstream interaction length
- δ_L = laminar boundary layer thickness at d_1
- D_{max} = Pseudo plume maximum diameter
- b = span
- Z_n = distance from nozzle centerline to surface

- (C) The term Z_n has been included because the data indicates that there is no separation where the plume is not visible to the flow along the surface. The upstream interaction length is measured forward from the plane of the nozzle exit so that nozzle axial location is accounted for in this manner.
- (C) Figure 197 presents another correlation of upstream interaction length which shows as good a correlation as the preceding figure. This figure presents interaction length directly as a function of plume maximum diameter for a unit Reynolds number of $.5 \times 10^6/\text{ft}$. The data at other Reynolds number (Figure 198) indicates that there is a Reynolds number effect which decreases interaction length with increasing unit Reynolds number. A curve has been fitted through this data and is given by the equation:

$$\frac{d_1}{L} = .656 \times 10^3 \left(\frac{D_{max}}{b} - \frac{2Z_n}{b} \right)^{.6} (R_e/X)^{-.5} \quad (26)$$

L = vehicle length

R_e/X = unit Reynolds number $(\text{ft})^{-1}$

where the definition of other terms is the same as equation 25. The plume diameter is non-dimensionalized in both equations 25 and 26 by vehicle span at the base since it was believed that this is a better parameter to use rather than vehicle length for finite span vehicles.

- (C) Vehicle length was used as the parameter for the flat plate data shown in

CONFIDENTIAL

Figure 199 where the data indicates nearly a straight line trend and where a curve

$$\frac{d_1}{L} = 1071 \frac{(r_{\max} - z_n)}{L}^{.78} (R_e/X)^{-.5} \quad (27)$$

has been fitted.

- (c) 4.2.2 UPSTREAM INTERACTION LENGTH AT POSITIVE ANGLE OF ATTACK. Control separation analysis treats positive angle of attack by considering that the pressure at the interaction point is solely determined by the local slope of the surface relative to the stream. Thus, knowing the pressure, the other conditions are determined and solved by extending the zero angle of attack solution. The plateau pressure data of Section 4.4 shows that this is true and thus the correlations were tried in which the plateau pressure term of equation 15 was corrected by

$$P'_P = P_P + P_\alpha \quad (28)$$

P_P = Plateau pressure

P_α = pressure due to local slope

and Figures 200 and 201 show that approximation works fairly well because it causes the plume to become much smaller as angle of attack increases which agrees with the Schlieren results. There is a region of scatter due to the data where no plateau exists because the upstream interaction length is less than the free interaction length. In this case it is recommended that the plateau pressure used be defined by

$$P_E = P'_P \frac{d_1}{d_h} \quad (29)$$

where plateau pressure will be defined in Section 4.4.

- (c) 4.2.3 UPSTREAM INTERACTION LENGTH ON LEEWARD SURFACES. The data up to this point has been all data from the bottom surface of the delta principally because it is a flat surface without the geometric complications of the upper surface. The preceding section shows very well why the flow never proceeded past the expansion corner at zero angle of attack. This is because the local slope of the front faces of the body are at about 8 degrees to the stream. The upper surface separation remains essentially at the expansion corner until the forward faces of upper surface disappears from the flow. The base pressure and upper surface plateau pressure were controlled

CONFIDENTIAL

by lower surface separation (Figure 154). When no part of the upper surface is at a positive local slope the plume is shielded by a considerable amount of surface from being exposed to the flow and Figure 202 presents a comparison of upper surface interaction data with equation 27, using an estimated height to expose the plume to the flow. The correlation is not very good for the case with large separation, however, the interaction location is not very precise either because of the sparseness of pressure taps near the front end of the vehicle. It would appear that using a exposure height as a function of angle of attack body thickness, and length would be a first approximation for estimating upper surface separation location.

- (c) Very little data was obtained on the flat plate at negative incidence and as shown in Figure 203 the data shows the separation moves forward slightly with increasing negative angle of attack. The nose bluntness induced pressures apparently keep it from spreading much further forward on the plate. The only criteria which might be tried is to assume zero angle of attack, compute the flat plate pressures without a plume, and find the plateau pressure resulting from this condition. Determine where the pressure at negative incidence is equal to that at a zero incidence and use that as the interaction point along with the zero angle of attack plateau pressure.
- (c) 4.2.4 FREE INTERACTION LENGTH. The first part of the pressure profile, from the interaction point to the start of the plateau pressure region, has been called the ~~free~~ interaction length because it is generally assumed that this region is dependent only on the local flow conditions in this region, and on the plateau pressure and not on the mechanism which is causing the separation to occur. The data was compared, therefore, to the free interaction length correlations of reference 14 which were derived from control induced separation and the results assuming a laminar boundary layer (equation 19) are shown in Figure 204 and assuming a turbulent boundary layer (equation 24) in Figure 205. In both cases the data indicates a scatter, primarily based on Mach number, which is due to using the plateau pressure ratio rather than plateau pressure coefficient as the ordinate. In neither case is the agreement very good with the correlating line derived from the control data and it is assumed the difference occurs because plume gases are mixed into the separation region. It is reasonable to expect that the flow should be laminar for most of the cases analyzed here so the data from Figure 204 was recorrelated using plateau pressure coefficient as the correlating parameter and the results are shown in Figure 206. The scatter seen in Figure 204 has largely disappeared through the use of plateau pressure coefficient as the ordinate; the data at the lower end of the curve tends to have more scatter because many of these points are taken in the region where the plateau region on the vehicle was very short and measured values of plateau pressure and free interaction length both become more doubtful. A correlating line was faired through the data and

CONFIDENTIAL

CONFIDENTIAL

equation is:

$$\frac{d_4}{\delta_L} = 2.33 \times 10^4 (C_{P_P})^{2.53} \quad (30)$$

where d_4 = free interaction length

δ_L = laminar boundary layer thickness at interaction point

C_{P_P} = plateau pressure coefficient

4.3 PLATEAU PRESSURE ANALYSIS

- (C) Plateau pressure is the most important parameter to be correlated for plume induced separation because it must be predicted before the plume shape can be predicted (equation 15), which must be known to predict interaction location (equation 25), and plateau pressure is needed to predict free interaction length (equation 30). Thus, the whole definition of the problem depends on starting with a plateau pressure prediction. Figure 159 showed that the plateau pressure and the base pressure were definitely related and the data was examined to determine whether base pressure determined plateau pressure or if the reverse were true. Figure 207 presents base pressure as a function of the initial turning angle of the flow from the nozzle computed using Prandtl-Meyer relationships and accounting for the nozzle exit angle. The spread of the data indicates that base pressure for a given nozzle depends on some other parameter but not on initial turning angle. In contrast, Figure 208 presents base pressure as a function of Reynolds number at the interaction point and the data shows a consistent trend for all nozzles. Thus, these figures indicate rather strongly that the plateau pressure determines base pressure and not the reverse and as a consequence of this it would be expected that the plateau pressure relationships should depend more on the parameters which influence control induced separation rather than nozzle exit parameters.

4.3.1 PLATEAU PRESSURE AT ZERO ANGLE OF ATTACK

- (C) Figures 209 and 210 present comparisons of the plateau pressure data to the laminar and turbulent boundary layer plateau pressures correlations of reference 14. The data shows closer agreement with the laminar relationship (Figure 209) even though the general shape of the pressures in the separated region tend to be more like that of a turbulent boundary layer control separation. The primary cause of the spread in the data appears to be Mach number

CONFIDENTIAL

and the trend in the data at a given Mach number does not appear to agree with the correlating line.

- (C) Figure 211 presents a correlation of plateau pressure from reference 10 in which the relationship of Figure 209 was corrected by jet pressure ratio. The data has the same general trend as the correlating curve of reference 10 but has a very large scatter induced primarily by the different nozzles. A better curve fitted through this data would be

$$A = .271 (P_j/P_\infty)^{.245} \quad (31)$$

but would probably be valid only for sonic nozzles or low expansion nozzles.

- (C) The base pressure data of Figure 208 indicated a strong relationship with the Reynolds number at separation and the same is seen in Figure 212. The scatter is less in this figure than in the other correlations (Figures 209 and 211) and it appears that the same relationships holds for the flat plate data shown in Figure 213. Both Figure 212 and 213 compare well with each other and the Reynolds number used for comparison in each is the free-stream Reynolds number. The data are presented together in Figure 214 which contains data at all 3 Mach numbers and all Reynolds numbers tested. An approximate curve has been fitted through the data and its equation is:

$$C_{P_P} = 20.4 R_{e_o}^{-.5} \quad (32)$$

where

C_{P_P} = plateau pressure coefficient

R_{e_o} = Reynolds number at the upstream interaction point
based on free stream conditions

- (C) Figure 215 presents the data correlated using the Reynolds based on local conditions at the interaction point based on equations 20 to 23. The data shows the same trend as the previous figure with an increase rather than a reduction scatter. An approximate curve has been fitted through this data and is given as:

$$C_{P_P} = 19.8 R_{e_\alpha}^{-.6} \quad (33)$$

- (C) No other parameters were found to reduce the scatter in Figures 214 or 215, however, because of the shape of the pressure curve in the separated region did not have a true flat plateau most of the remaining scatter is believed to be reading error.

CONFIDENTIAL

- (C) 4.3.2 PLATEAU PRESSURE ON WINDWARD SURFACES. The rapid collapse of the separated region with increasing angle of attack left few cases where the upstream interaction region was longer than the free interaction region and so few values of plateau pressure were available to correlate. Figure 216 presents the data as plateau pressure coefficient defined as

$$C_{P_P} = \frac{P_P - P_\alpha}{.7P_\infty M^2} \quad (34)$$

where P_α = pressure on surface due to local slope to stream ~ PSI

C_{P_P} = plateau pressure coefficient

P_P = plateau pressure ~ PSI

$.7P_\infty M^2$ = dynamic pressure ~ PSI

- (C) These data compare fairly well with the data of Figure 214 and so this is the recommended approach to use and is the basis of equation 28. When upstream interaction length is shorter than free interaction length no plateau occurs and it appears that the pressure at the end of the vehicle can be approximated by computing a plateau pressure and ratioing it down by the ratio of these lengths

$$C_{P_E} = C_{P_P} \left(\frac{d_1}{d_4} \right) \quad (35)$$

- (C) 4.3.3 PLATEAU PRESSURE ON LEEWARD SURFACES. Figure 154 demonstrated that the plateau pressure aft of the expansion corner at zero angle of attack was essentially that of the lower surface plateau pressure. As long as the vehicle upper surface shields the plume (Figure 202), Figure 143 shows that the plateau pressure declines with increasing angle of attack, however, when the plume becomes large enough to be exposed to the flow the plateau pressure increases returning to near the zero angle of attack values. A first approximation of angle of attack effects would be to use the lower surface pressure from equations 34 or 35 to define the upper surface pressure coefficient so long as the plume is hidden by the body and the zero angle of attack value if the plume is not hidden by the body.

4.4 RECOMMENDED METHOD

- (C) Sections 4.1 to 4.3 give the basis of a model for plume induced separation which can be used to predict magnitude of the plateau pressure and the extent

CONFIDENTIAL

of the surface of a vehicle which is affected by it. This model however requires iteration to converge to a solution and thus precludes drawing general design charts which would be applicable to a number of configurations over a range of flight conditions. The model is in the form of equations which could be implemented into a computer program to provide the iterating mechanism to allow rapid solutions of this problem. The basic elements of the plume induced separation model are outlined below:

1. given
 - a) vehicle geometry
 - b) nozzle geometry
 - c) nozzle chamber and exit conditions
 - d) flight conditions
2. compute plume maximum diameter using Lockheed 5 point model (equations 1 to 4) and flight conditions
3. If plume is not exposed to air stream there is no separation.

(c) 4.4.1 WINDWARD SURFACES.

1. If plume is exposed to air stream separation may have occurred and iteration is necessary on each surface of the vehicle.
2. On a given surface exposed to the stream assume a separation location and compute pressure based on local slope and Reynolds number based on free stream conditions.
3. Compute plateau pressure from equations 32 and 34.
4. Compute pseudo plume maximum diameter from equations 15 to 18.
5. Compute upstream interaction length from equation 26 for a 3 dimensional configuration or equation 27 for a 2 dimensional configuration and interaction point from nozzle location.
6. Compute up stream interaction length from equation 30.
7. Compute new local pressure and Reynolds number for interaction point.
8. Compute new plateau pressure as in step 3.

CONFIDENTIAL

CONFIDENTIAL

9. Correct plateau pressure by equation 35 if free interaction length is longer than up stream interaction length.
 10. Repeat steps 4-9 as necessary to converge.
 11. Predict spanwise distribution using Figure 132
- (C) 4.4.2 LEEWARD SURFACES OR SURFACES NOT EXPOSED TO STREAM.
1. Leeward surfaces require a prediction of the plume size necessary to expose plume from vehicle geometry and angle of attack.
 2. If plume is not exposed use plateau pressure coefficient of exposed surface as plateau coefficient of surface.
 3. If plume is exposed to flow and assume a separation point use zero local slope and proceed through steps 3 to 10 in Section 4.4.1.
 4. Extent of separation region for the case outlined in step 2 is to be determined by point where surface pressure is greater than ambient pressure.
- (C) 4.4.3 METHODS TO MINIMIZE PLUME INDUCED SEPARATION. The data indicates that certain things can be done to minimize plume induced separation and these include:
1. use the largest expansion ratio nozzle feasible for the design
 2. use a contoured nozzle to minimize exit angle
 3. mount the nozzle as far from the important surface as possible
 4. increase local body slopes near base of body
 5. select propellants that result in a large specific heat ratio.

UNCLASSIFIED

SECTION 5

CONCLUSIONS AND RECOMMENDATIONS

- (U) Tests were conducted at Mach numbers of 6, 8, and 10 on a representative lifting body entry vehicle and a Mach number of 10 on a flat plate using heated air and other gases to simulate rocket exhaust plumes. Extensive flow separation resulting from the plumes was observed on both configurations during the test program and the most powerful parameters which affected plume induced separation included:
1. model shape
 2. angle of attack
 3. Reynolds number
 4. nozzle expansion ratio
 5. nozzle total pressure
 6. nozzle gas temperature and specific heat.
- (U) The least important parameter was free-stream Mach number. The flat plate model showed much less flow separation than the delta planform at similar test conditions, however, serious problems in control effectiveness were indicated on both models for the aft mounted elevon.
- (U) The data did not correlate well with existing semi-empirical correlations developed for control surface induced separation and plume shape. New semi-empirical correlations were developed for predicting plume shape in a region of plume induced separation and for predicting the pressure in and the extent of the separated region. Much work, however, needs to be done on leeward surface separation and to extend and refine these models for plume shape and separation. It is therefore recommended that any future study of plume induced separation be primarily experimental in nature and include the following test parameters:
- a) additional Reynolds number variation
 - b) multiple nozzle plumes
 - c) wide range of shapes particularly upper surface
 - d) effects of nose bluntness
 - e) surface temperature control
 - f) forced boundary layer transition

UNCLASSIFIED

SECTION 6

REFERENCES

1. Wilkinson, C. L., "Aerodynamic and Heat Transfer Effects of Saturn V Plume-Induced Flow Separation", Proceedings of the 8th U. S. Navy Symposium on Aeroballistics, Corona, California, 6-8 May, 1969.
2. Salmi, Reino, J., "Effects of Jet Billowing on Stability of Missile-Type Bodies at Mach 3.85", NASA TN D-284, June 1960.
3. Falanga, R. A., Hinson, W. F. and Crawford, D. H., "Exploratory Tests of the Effects of Jet Plumes on the Flow Over Cone-Cylinder-Flare Bodies", NASA TN D-1000, February 1962.
4. Hinson, W. F. and Falanga, R. A., "Effects of Jet Plumbing on the Static Stability of Cone-Cylinder-Flare Configuration at a Mach Number of 9.65", NASA TN D-1352, September 1962.
5. Alpinieri, L. J., and Adams, R. H., "Flow Separation Due to Jet Plumbing", AIAA Journal, pp. 1865-1866, October, 1966.
6. McGhee, Robert J., "Some Effects of Jet Plumbing on the Static Stability of Ballistic Bodies at a Mach Number of 6.00," NASA TN D-3698, November 1966.
7. Hinson, William F., and Robert J. McGhee, "Effects of Jet Plumbing on the Static Stability of Five Rocket Models at Mach Numbers of 4, 5, 6 and Static Pressure Ratios up to 26,000", NASA TN D-4064, August 1967
8. Linneman, E. R., "Reentry Maneuver Optimization with Heating Restraints", Lockheed California Company Report LR 21223, December 1967.
9. Strike, W. T., "Jet Plume Simulation at Mach Number 10", AEDC Technical Report AEDC-TR-70-118, August 1970.
10. Fong, M. C., Ehrlich, C. F., Jr., "Propulsion Effects on Aerodynamic characteristics of Lifting Reentry Vehicles", Air Force Flight Dynamics Laboratory Technical Report AFFDL-TR-70-12, March 1970.
11. Strike, W. T. Jr., "Simulated Rocket Plume Effects on a Delta Wing Reentry Body at Mach Numbers of 6, 8, and 10 (U)," AEDC Technical Report AEDC-TR-70-258, November 1970, Confidential.
12. Anon: "Test Facilities Handbook (Eighth Edition). Von Karman Gas Dynamics Facility, Vol. 4." Arnold Engineering Development Center, December 1969 (AD863646).

UNCLASSIFIED

13. Pindzola, M., "Jet Simulation in Ground Test Facilities", AGARDograph 79, Nov. 1963.
14. Popinski, Z., Ehrlich, C. F., "Development Design Methods for Predicting Hypersonic Aerodynamic Control Characteristics", Air Force Flight Dynamics Laboratory Technical Report AFFDL-TR-66-85, Sept. 1966.
15. Strike, W. T., Flaherty, J., "Plume Induced Separation Effects in an External Stream", JANNAF 6th Plume Technology Meeting, Feb. 1971, Confidential.

UNCLASSIFIED

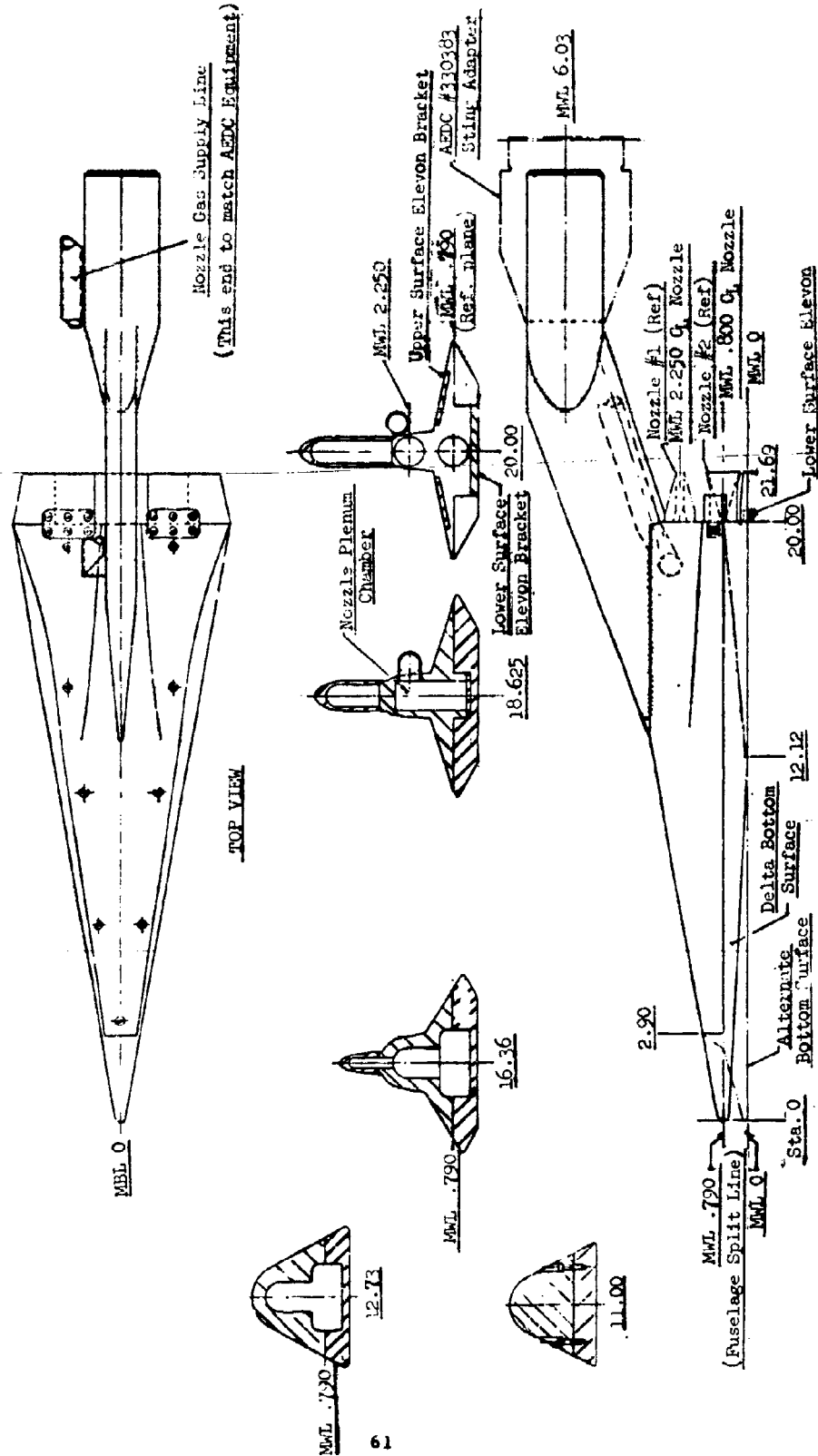
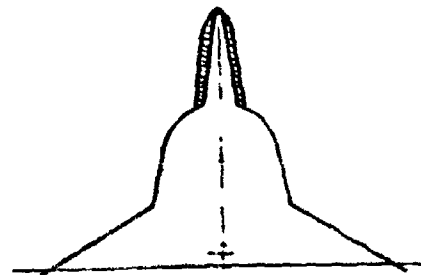


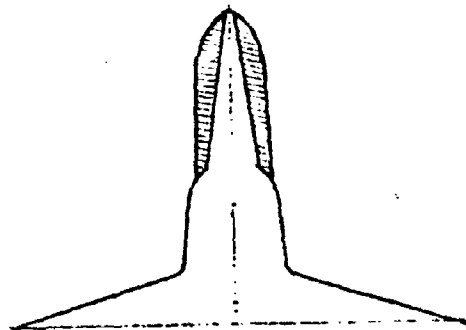
Figure 1. Delta Planform Configuration

UNCLASSIFIED

UNCLASSIFIED



Sta. 16.35



Sta. 18.76

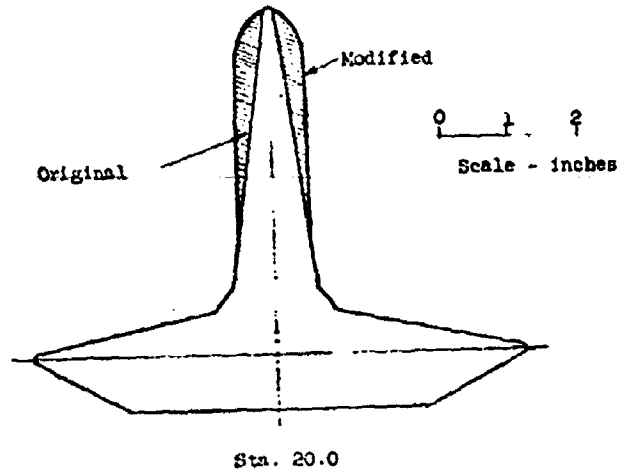


Figure 2. Vertical Fin Modification

62

UNCLASSIFIED

UNCLASSIFIED



Figure 3. Delta Model Installed in Tunnel C

UNCLASSIFIED

UNCLASSIFIED

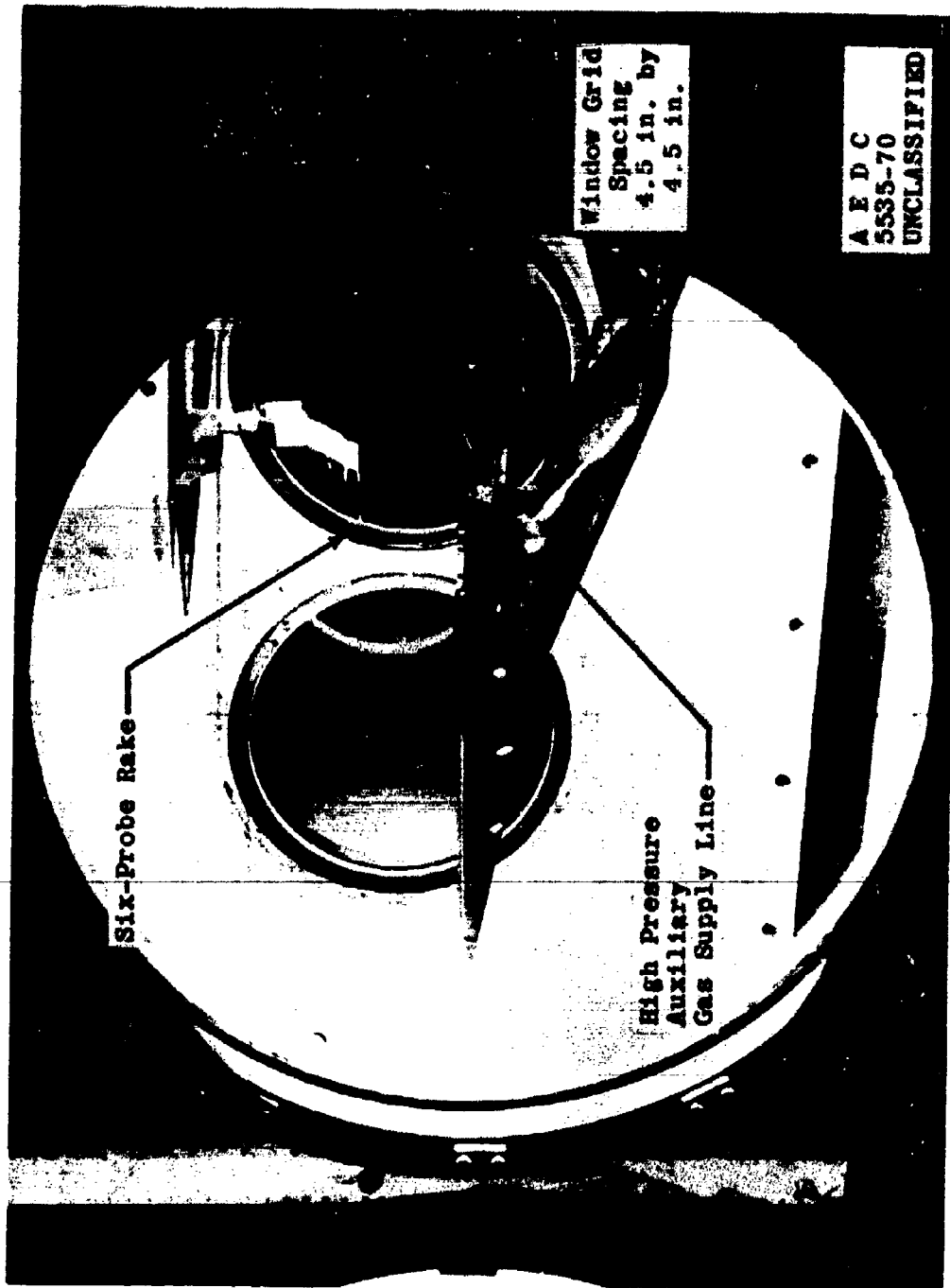


Figure 4. Delta Model Mounted in Inverted Position for Tests in Tunnel C

64
UNCLASSIFIED

UNCLASSIFIED

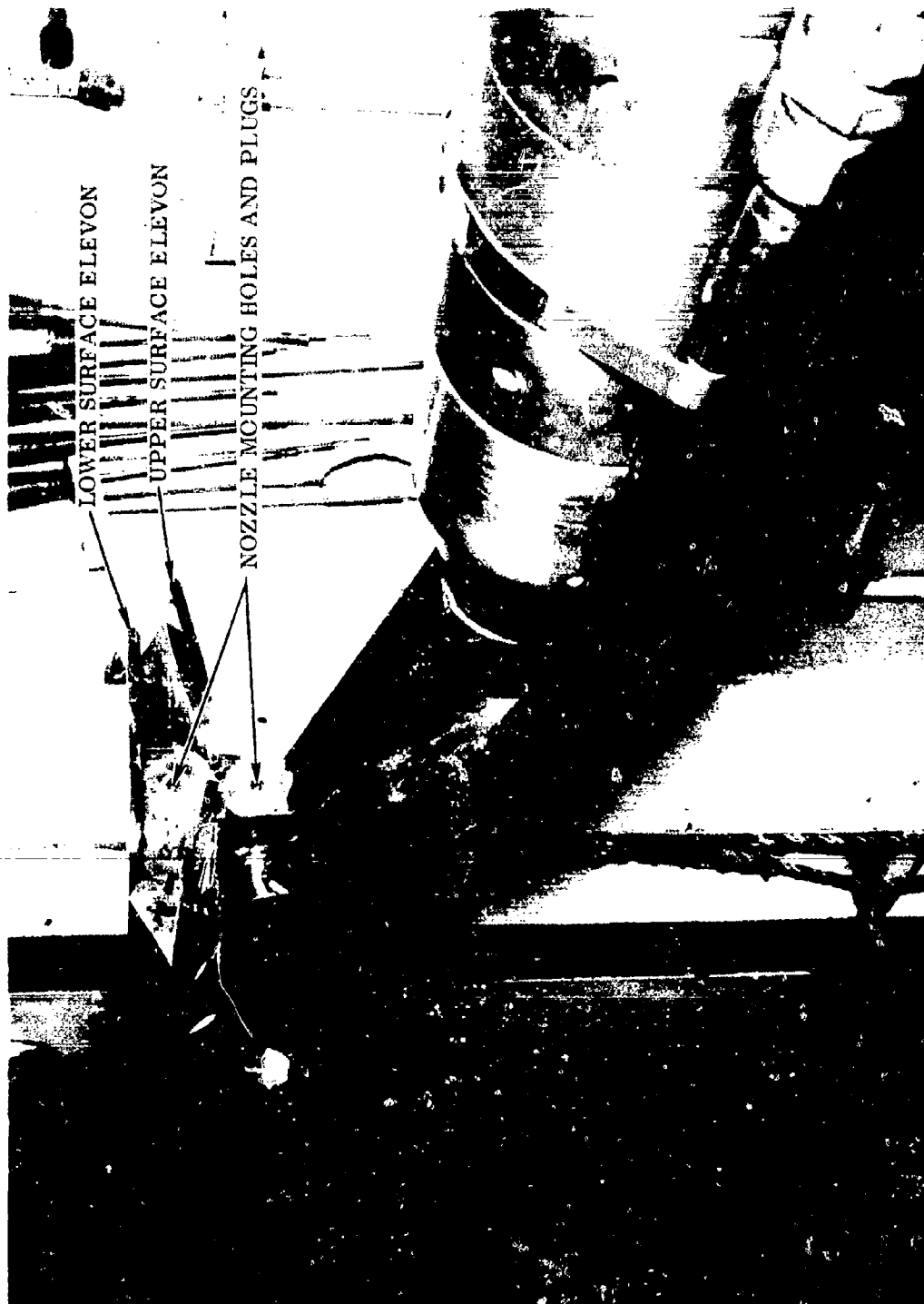


Figure 5. Rear View of Delta Model Mounted on Sting

65
UNCLASSIFIED

UNCLASSIFIED

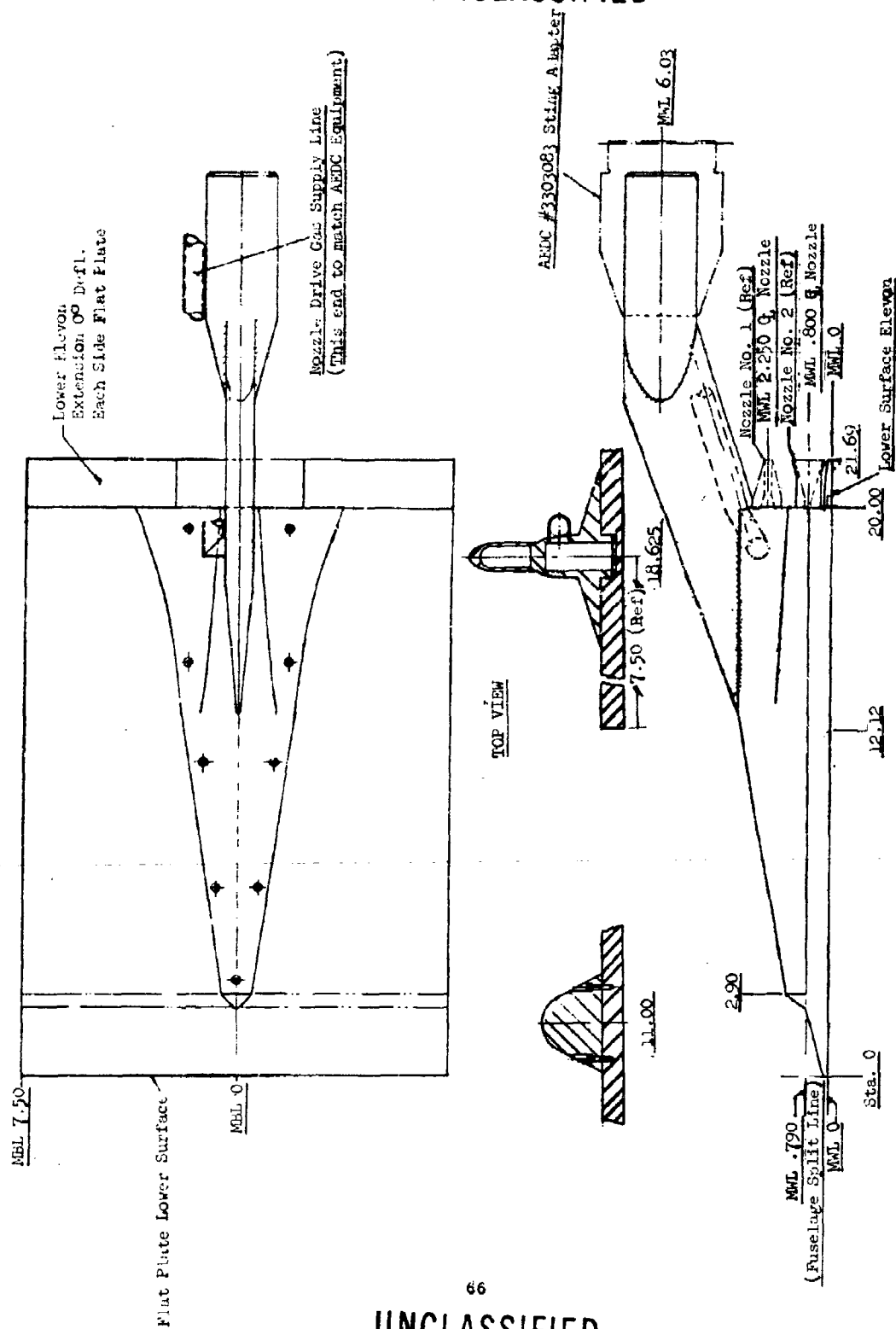


Figure 6. Flat Plate Model Assembly

UNCLASSIFIED

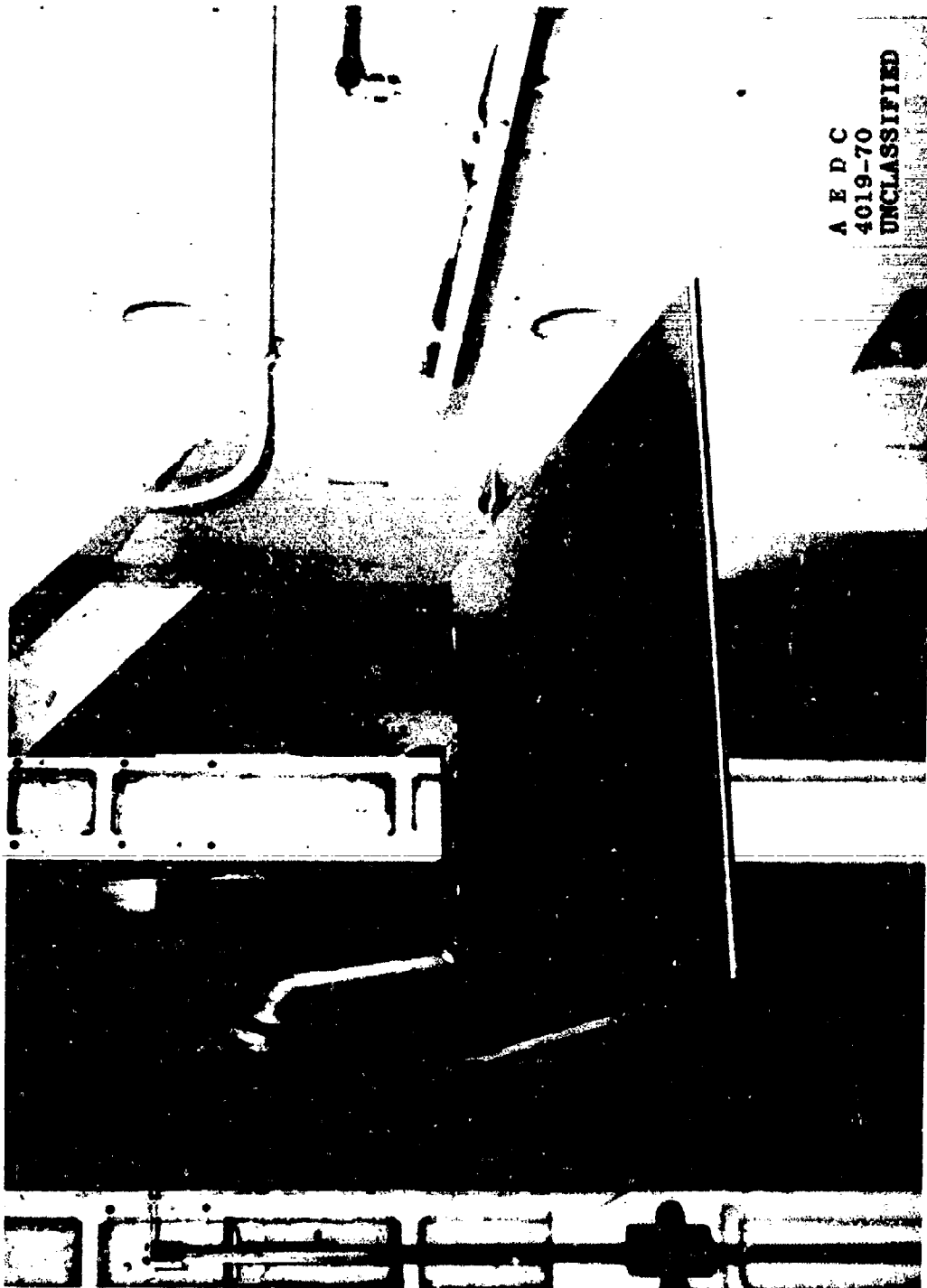


Figure 7. Flat Plate Installed In Tunnel C

⁶⁷
UNCLASSIFIED

UNCLASSIFIED

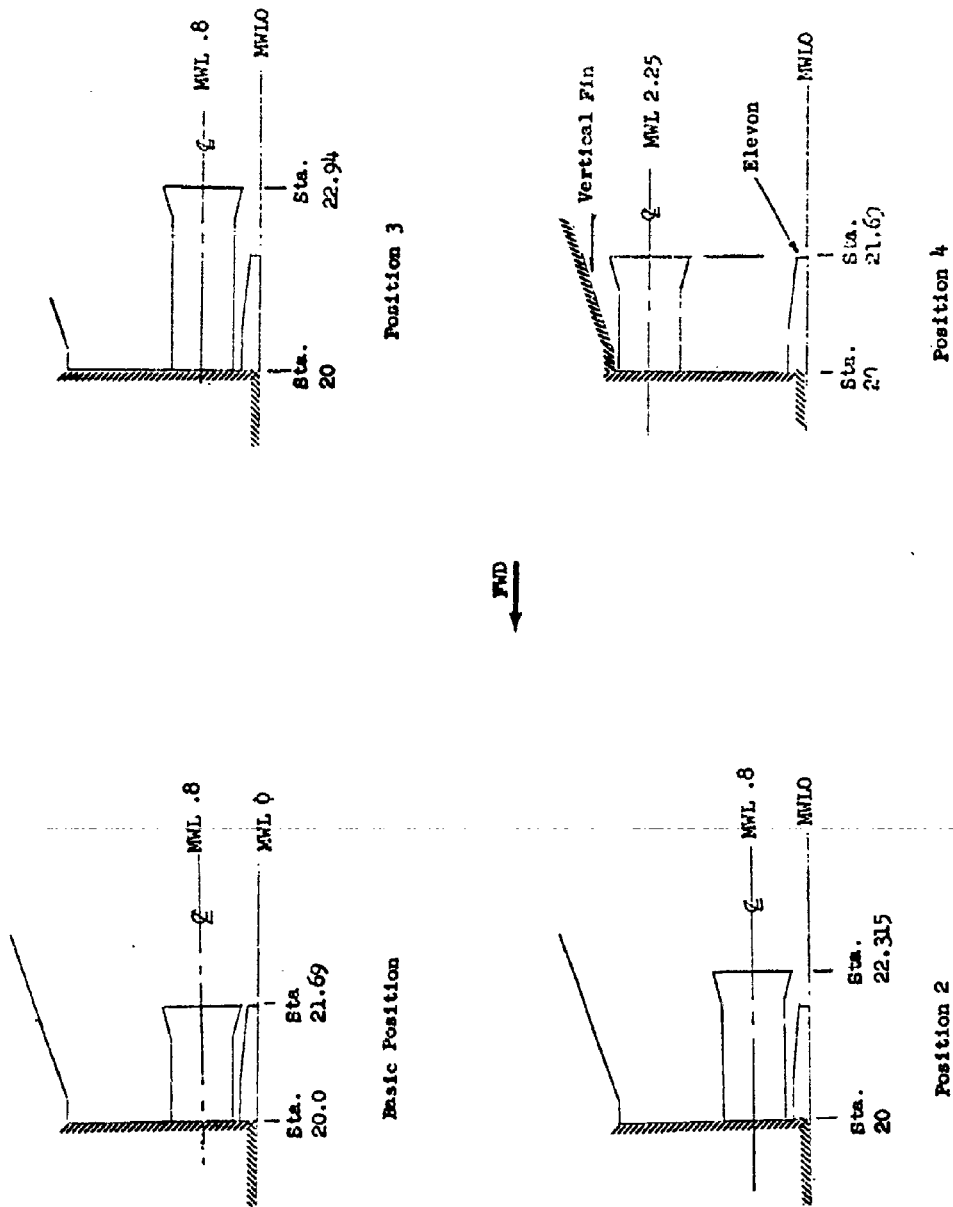


Figure 8. Nozzle Exit Locations

68
UNCLASSIFIED

UNCLASSIFIED

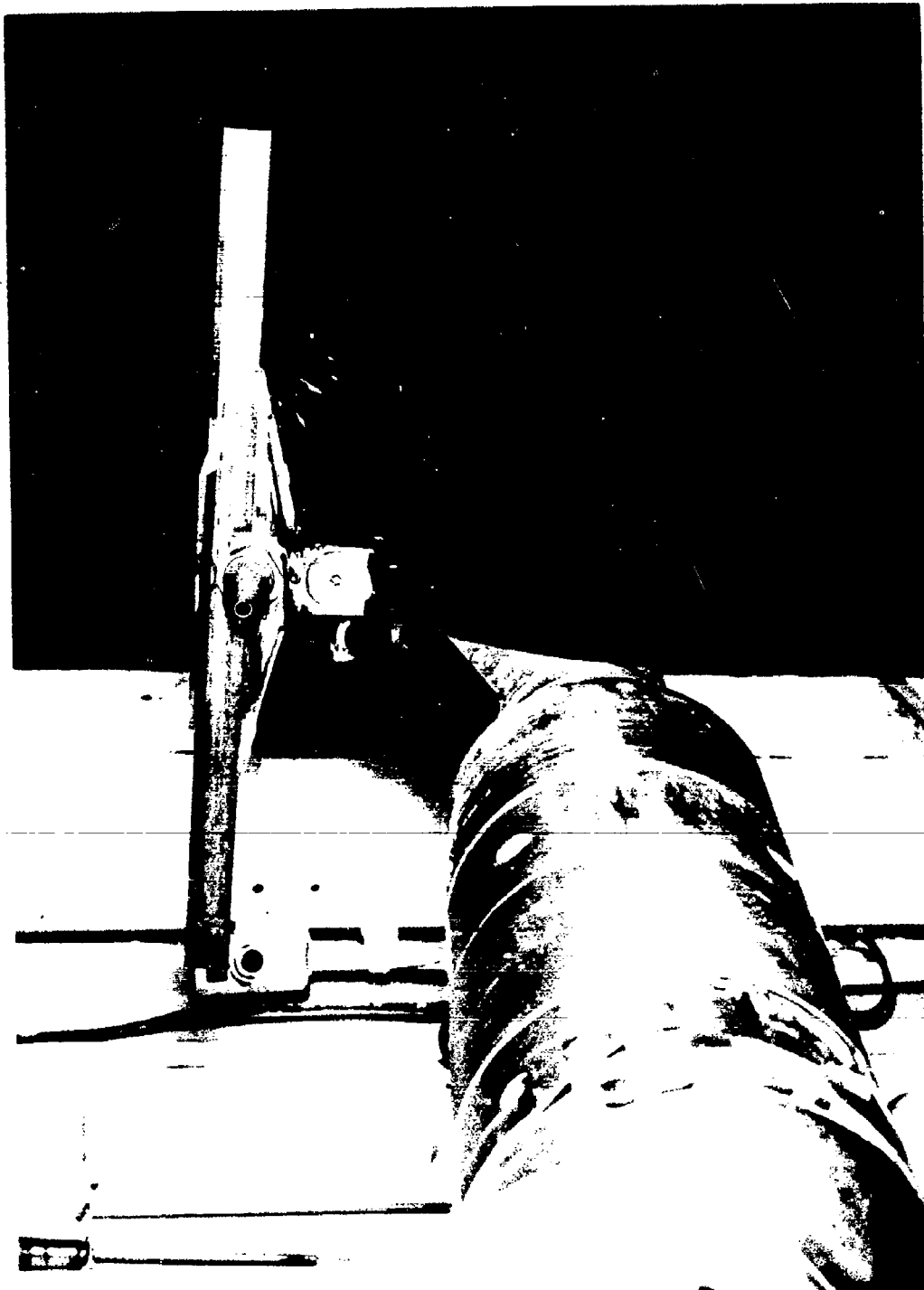
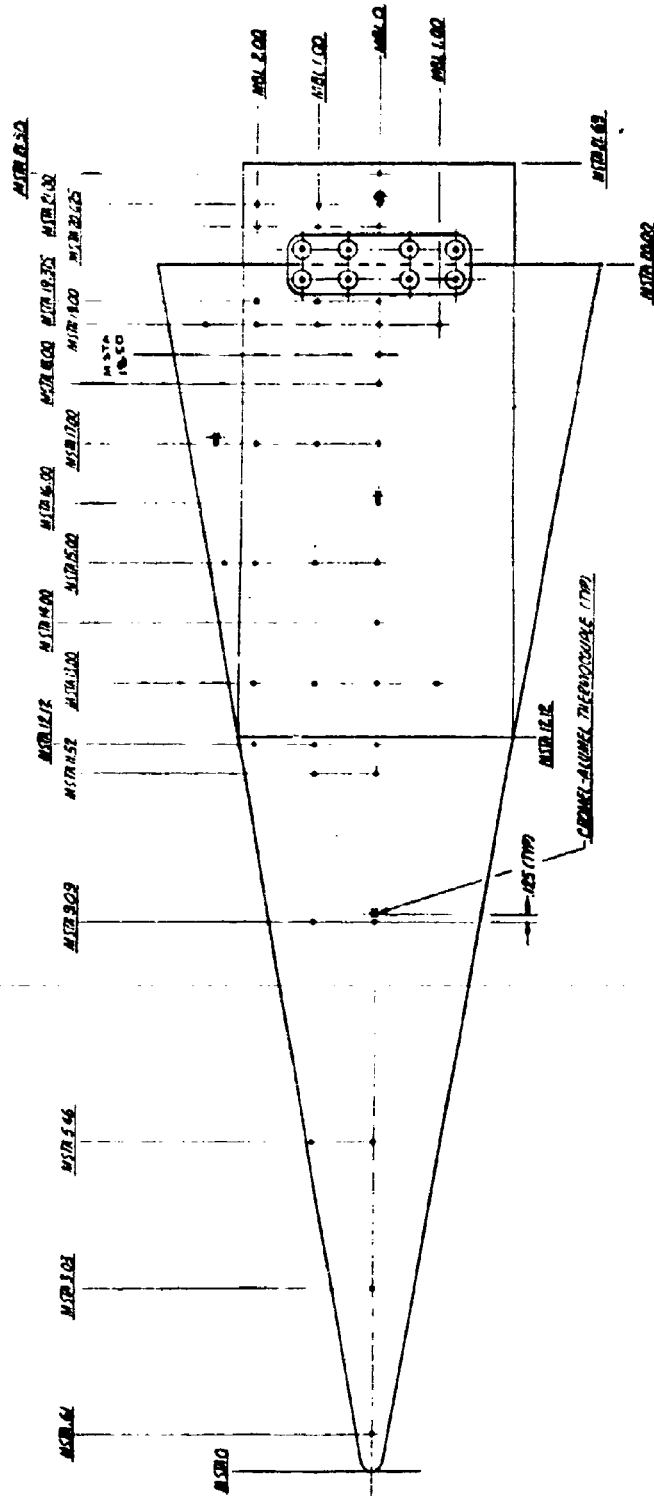


Figure 9. Nozzle in Basic Position on Flat Plate Model

UNCLASSIFIED⁶⁹

UNCLASSIFIED



BOTTOM VIEW "DELTA" CONFIGURATION

Figure 11. Delta Platform Bottom Surface Instrumentation

UNCLASSIFIED

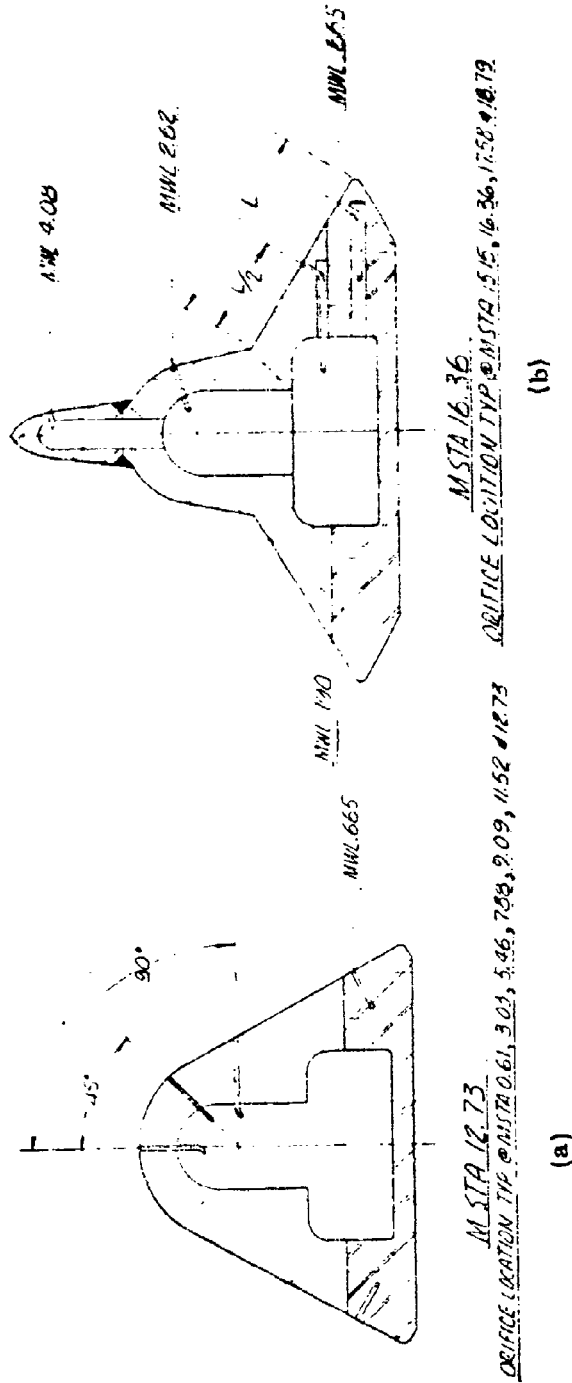


Figure 12. Upper Surface Pressure Tap Circumferential Locations

UNCLASSIFIED

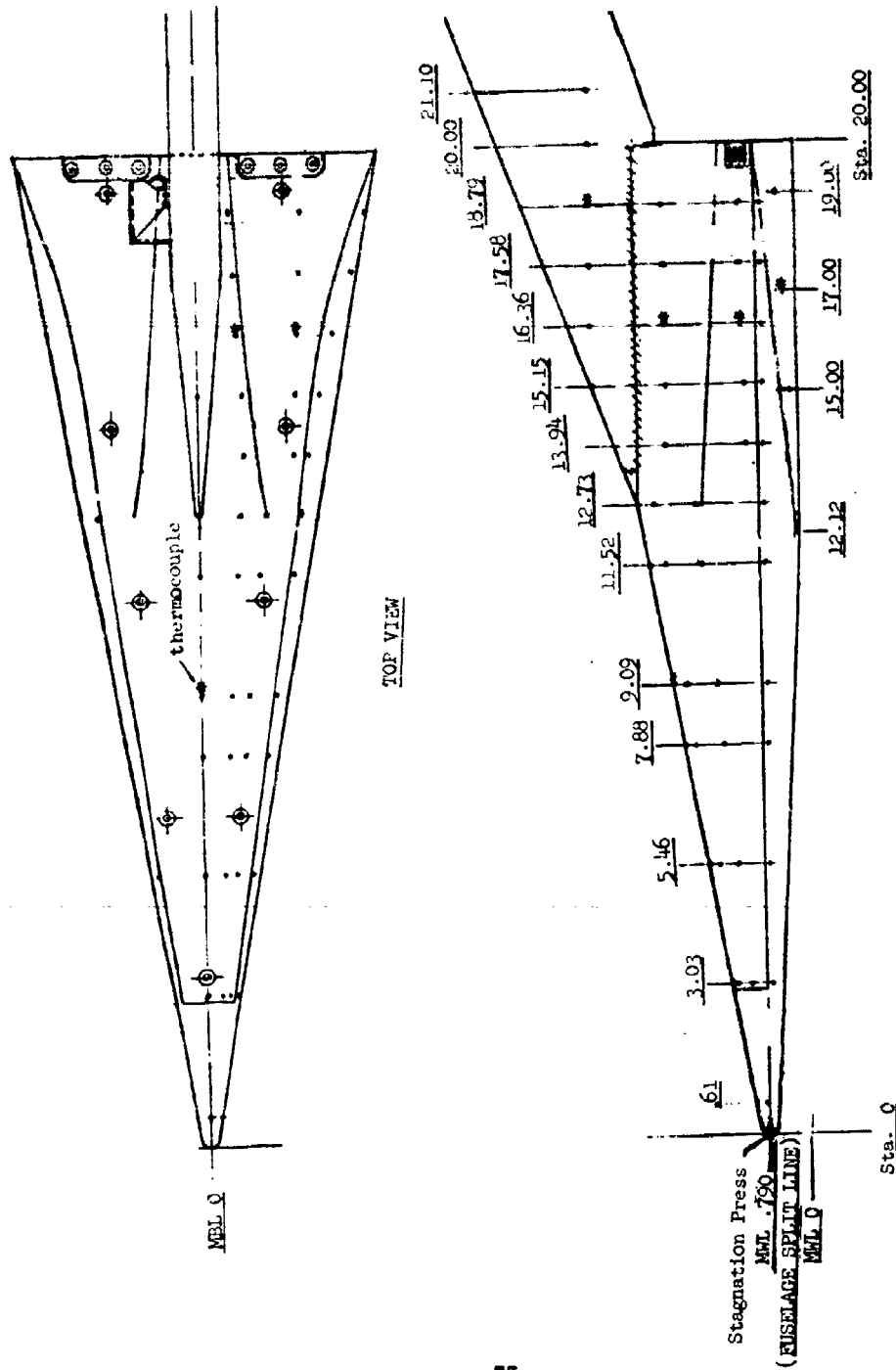
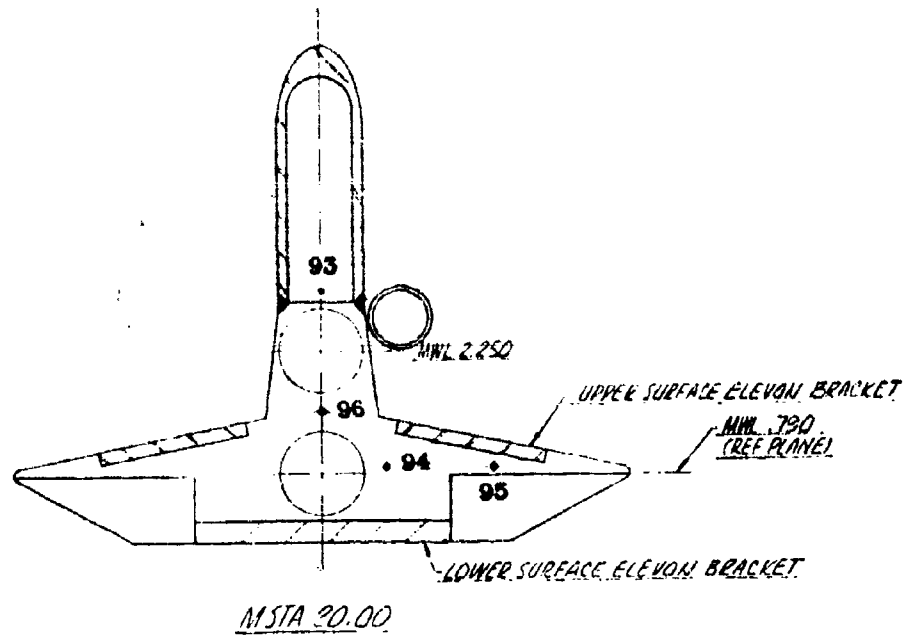


Figure 13. Upper Surface Instrumentation

UNCLASSIFIED

UNCLASSIFIED



LOCATION ~ Inches			
TAP	X	Y	Z
93	20.25	0	3.0
94	20.0	0.81	0.9
95	20.0	2.0	0.9
96	20.0	0	1.55

Figure 14. Base Pressure Instrumentation Locations

74
UNCLASSIFIED

UNCLASSIFIED

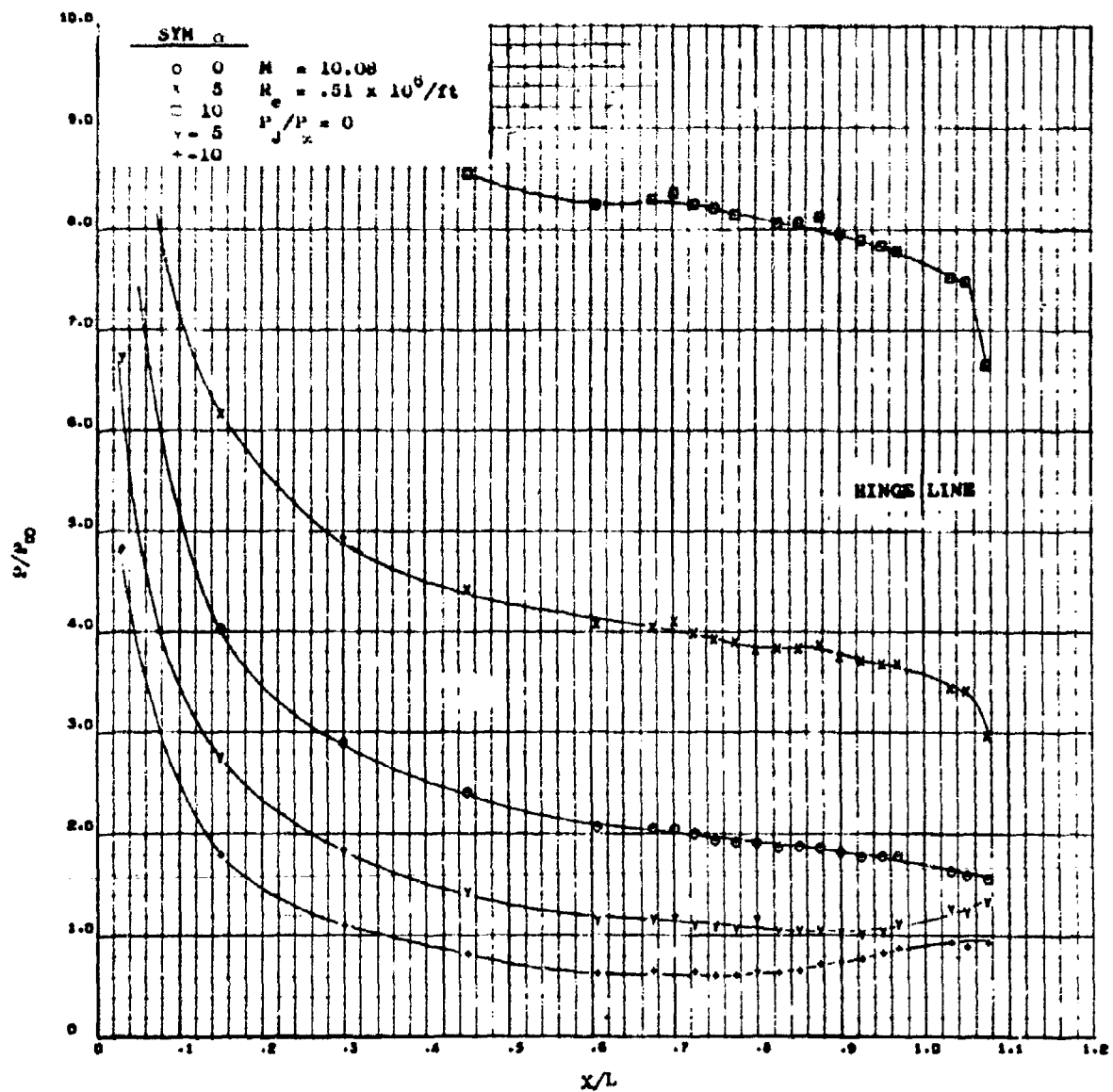


Figure 16. Effect of Angle of Attack on Flat Plate Centerline Pressure at Mach 10 and $R_e = .51 \times 10^6/\text{ft}$

UNCLASSIFIED

UNCLASSIFIED

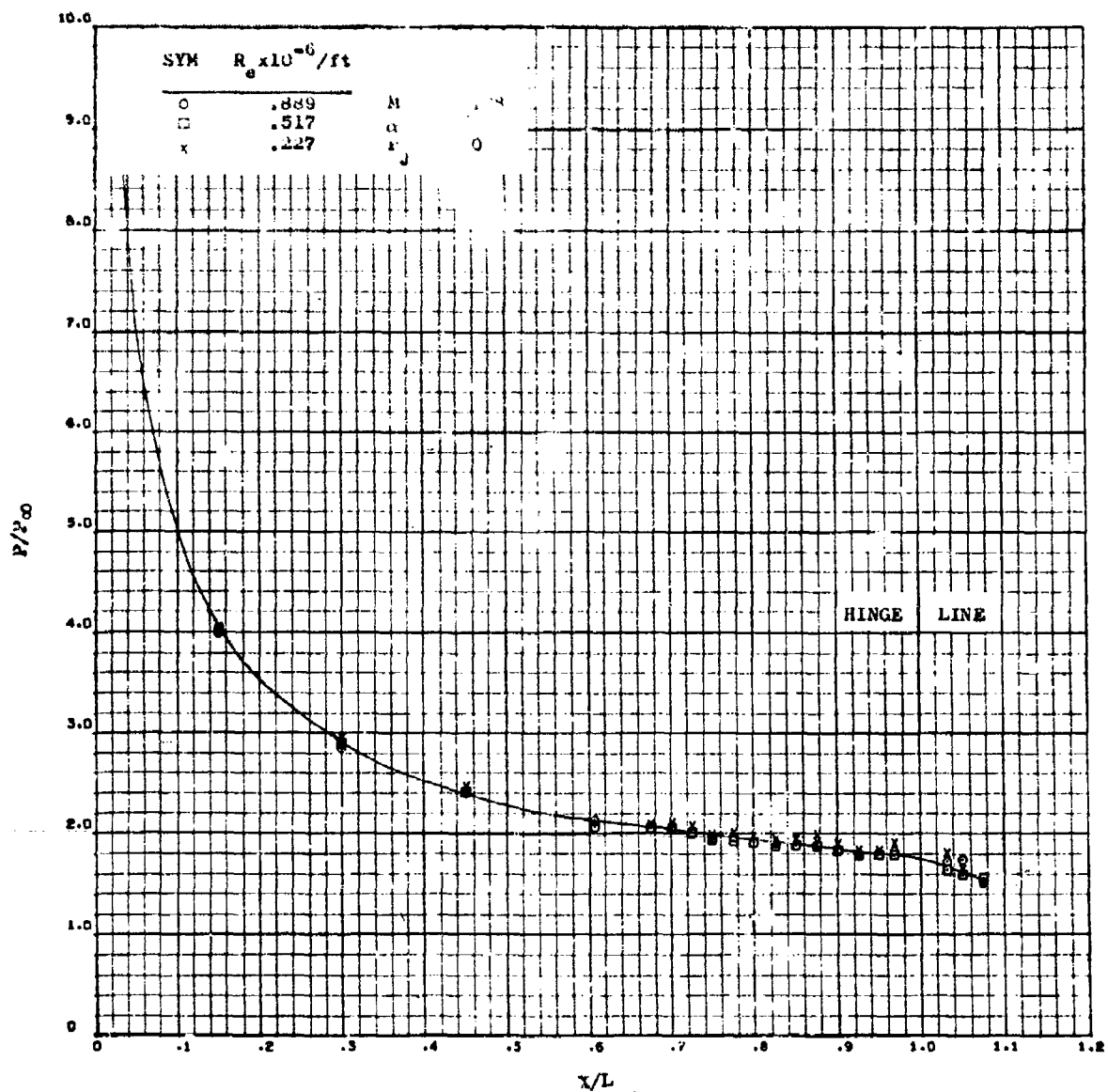


Figure 17. Effect of Reynolds Number on the Flat Plate Centerline Pressure at a Mach Number of 10 and $P_0/P_\infty = 0$

UNCLASSIFIED

UNCLASSIFIED

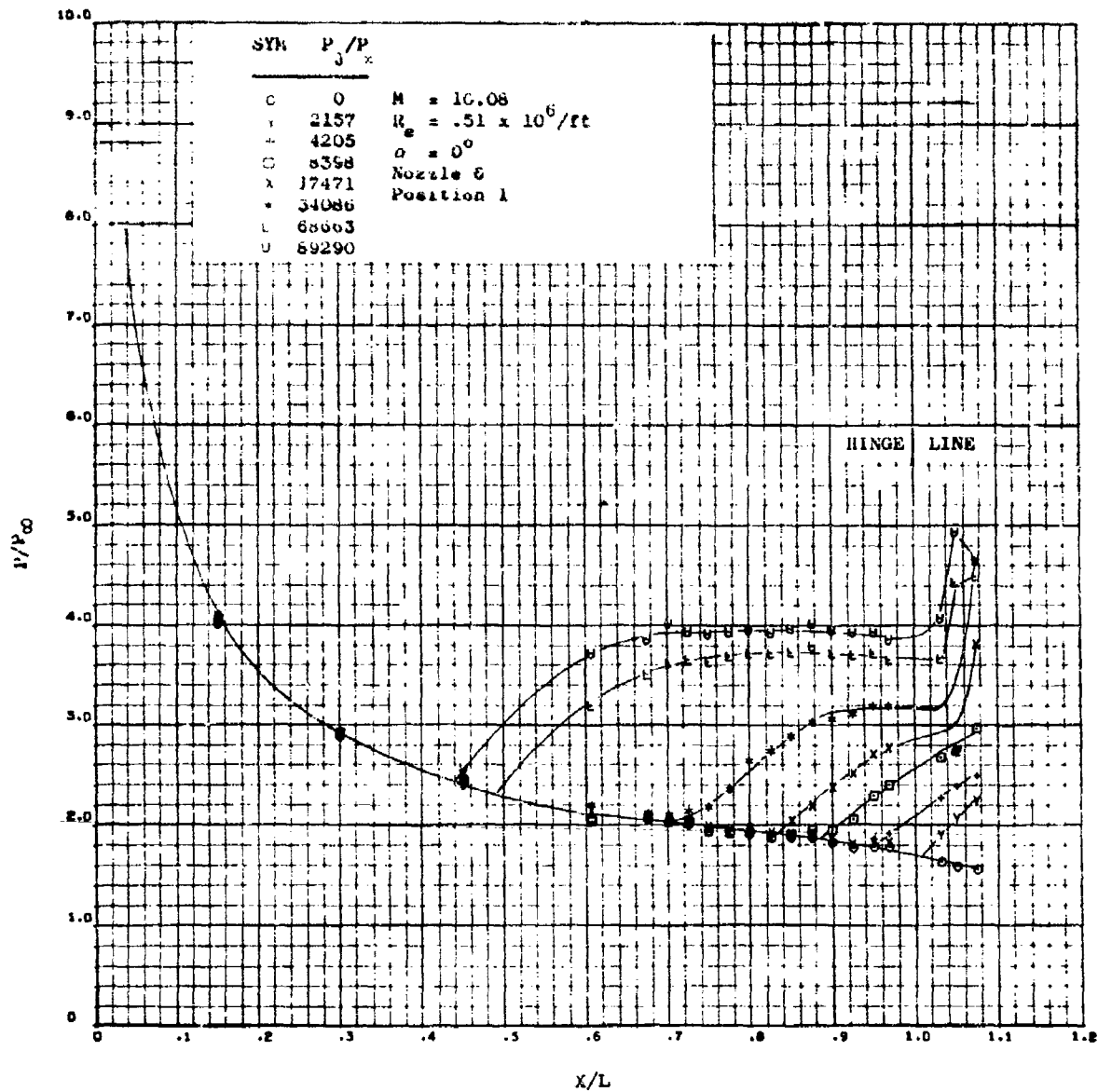
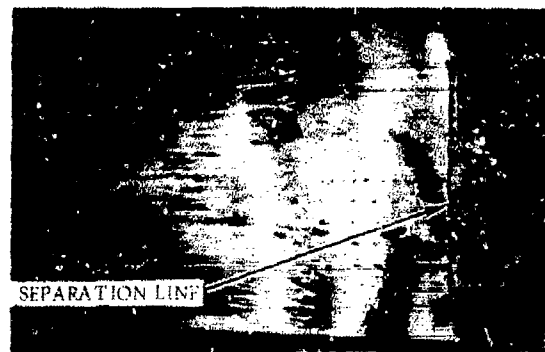


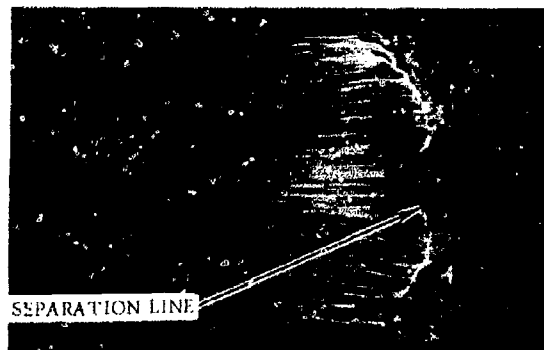
Figure 18. Effect of Jet Pressure Ratio on Flat Plate Centerline Pressure at Zero Angle of Attack for Nozzle 6.

UNCLASSIFIED

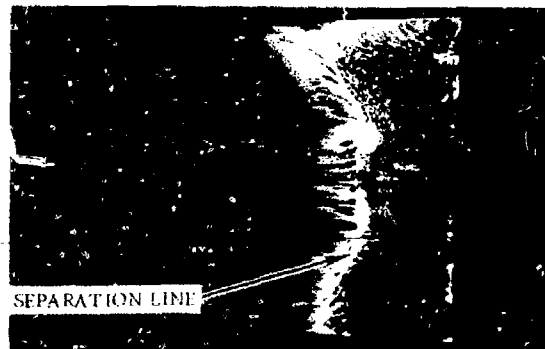
UNCLASSIFIED



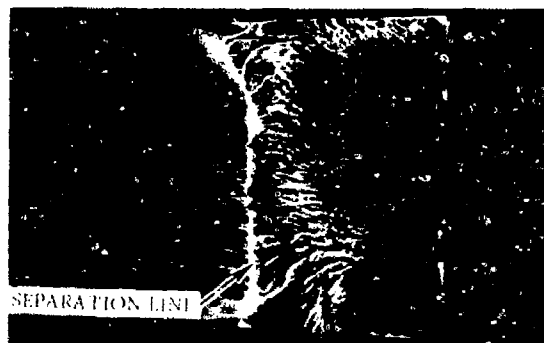
$$P_j/P_\infty = 8500$$



$$P_j/P_\infty = 17000$$



$$P_j/P_\infty = 34000$$



$$P_j/P_\infty = 69000$$

NOZZLE 6
POSITION 1
 $Re = .5 \times 10^6/FT$
 $M_\infty = 10.1$

Figure 19. Flat Plate Oil Flow Visualization of the Effect of Jet Pressure Ratio

UNCLASSIFIED

UNCLASSIFIED

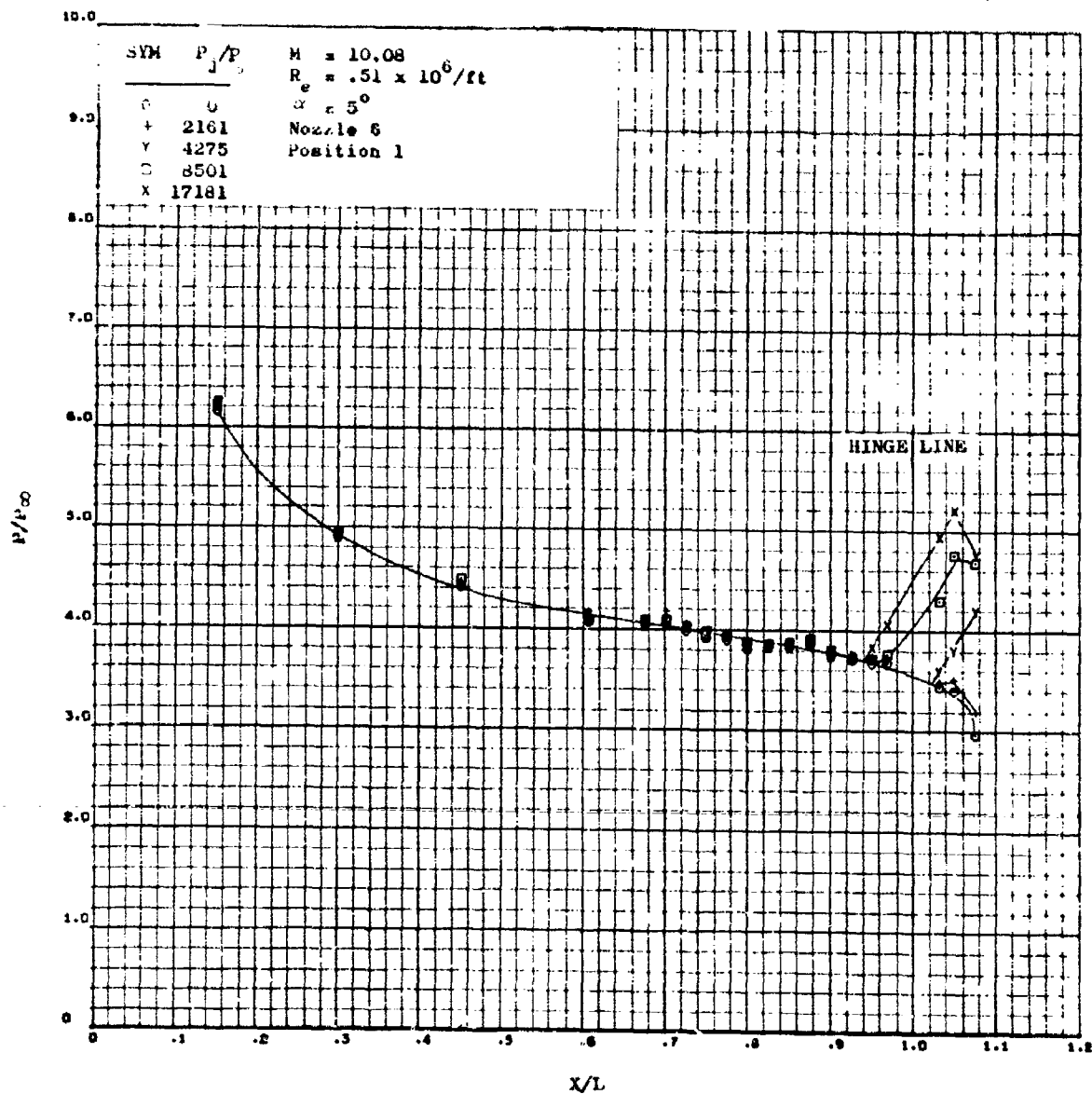


Figure 20. Effect of Jet Pressure Ratio on Flat Plate Centerline Pressure at 5° Angle of Attack for Nozzle 6

UNCLASSIFIED

UNCLASSIFIED

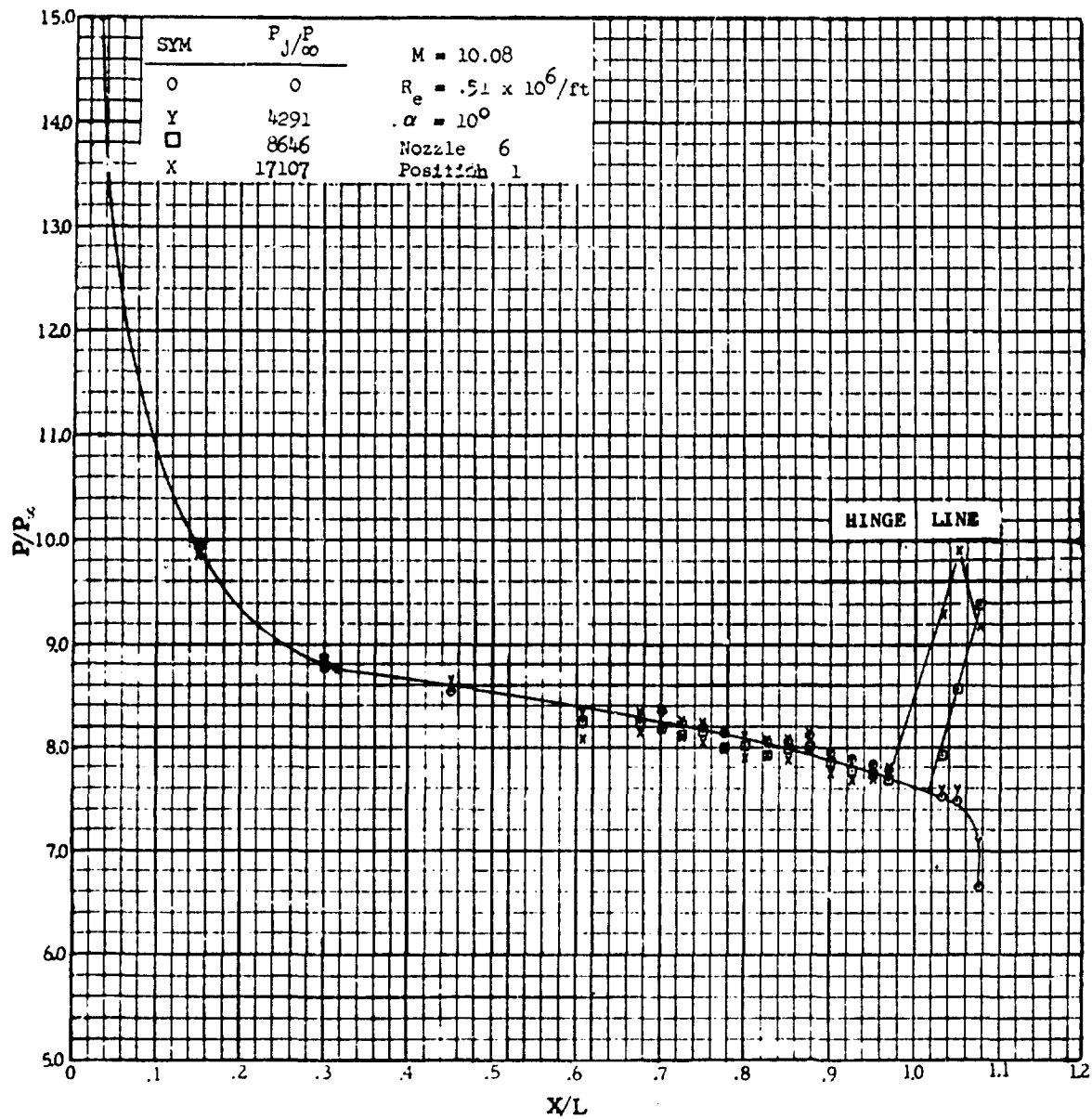


Figure 21. Effect of Jet Pressure Ratios on Flat Plate Centerline Pressure at 10° Angle of Attack for Nozzle 6

UNCLASSIFIED

UNCLASSIFIED

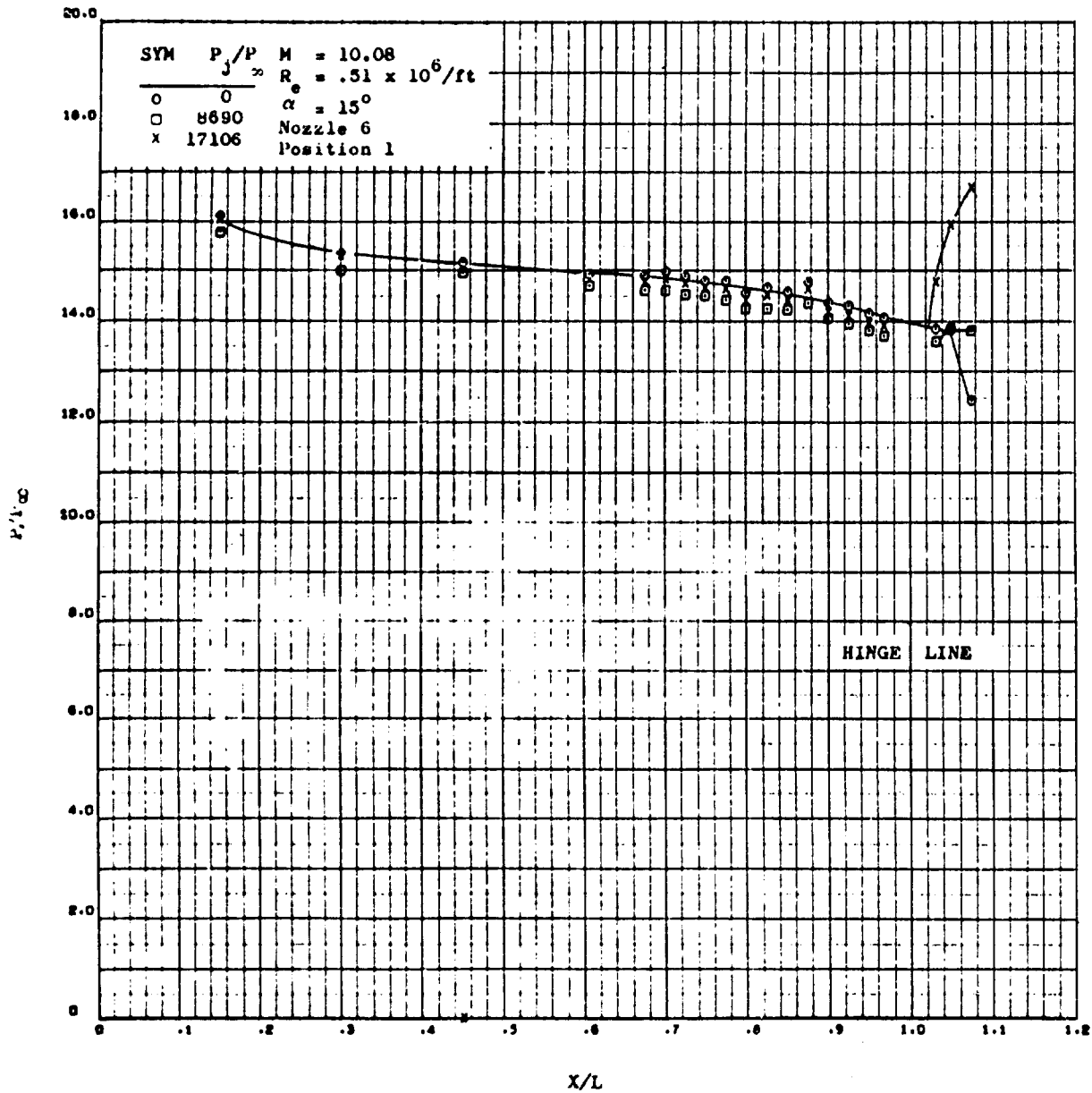


Figure 22. Effect of Jet Pressure Ratio on Flat Plate Centerline Pressure at 15° Angle of Attack for Nozzle 6

UNCLASSIFIED

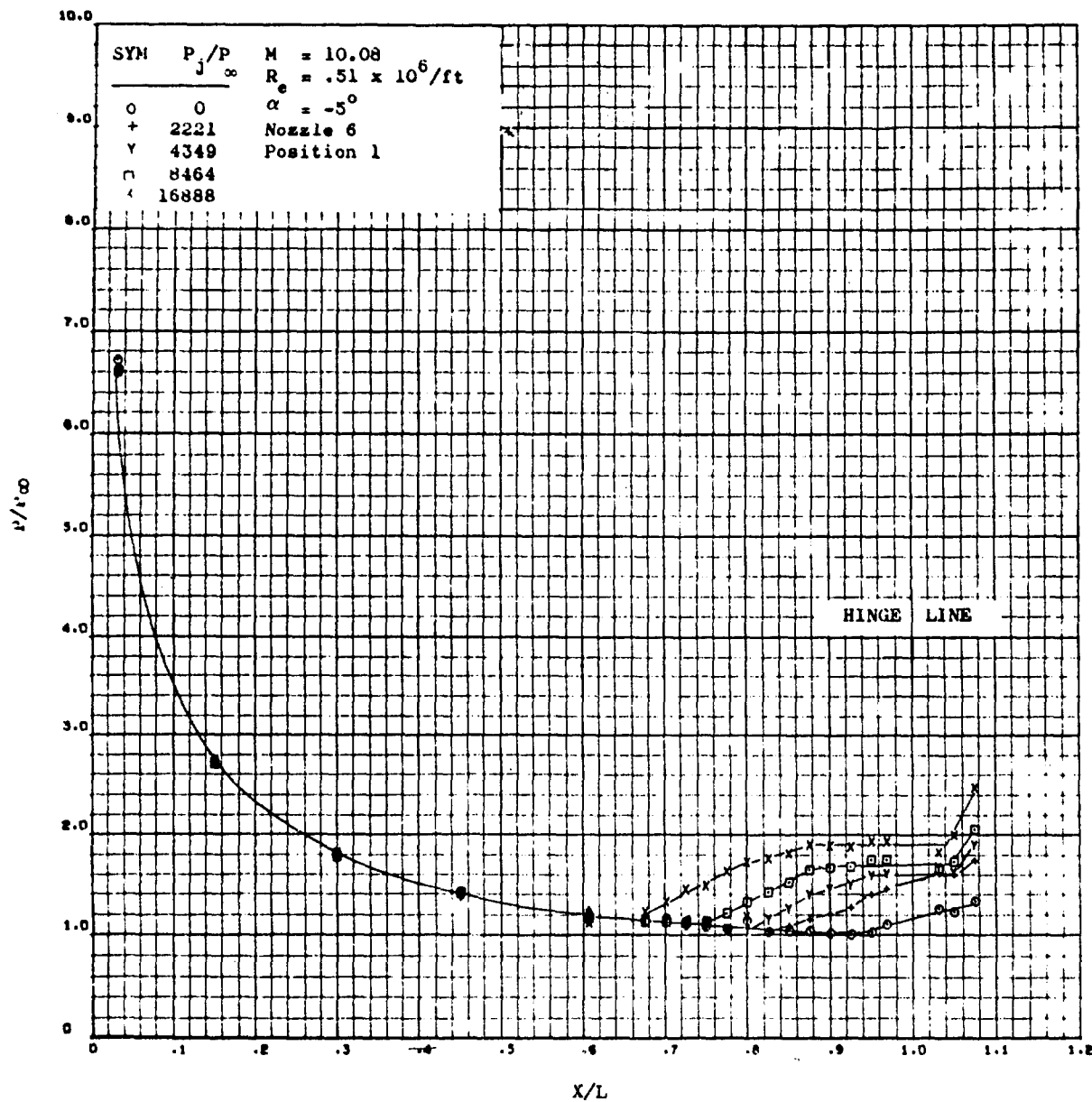


Figure 23. Effect of Jet Pressure Ratio on Flat Plate Centerline Pressure at an Angle of Attack of -5° for Nozzle 6

UNCLASSIFIED

UNCLASSIFIED

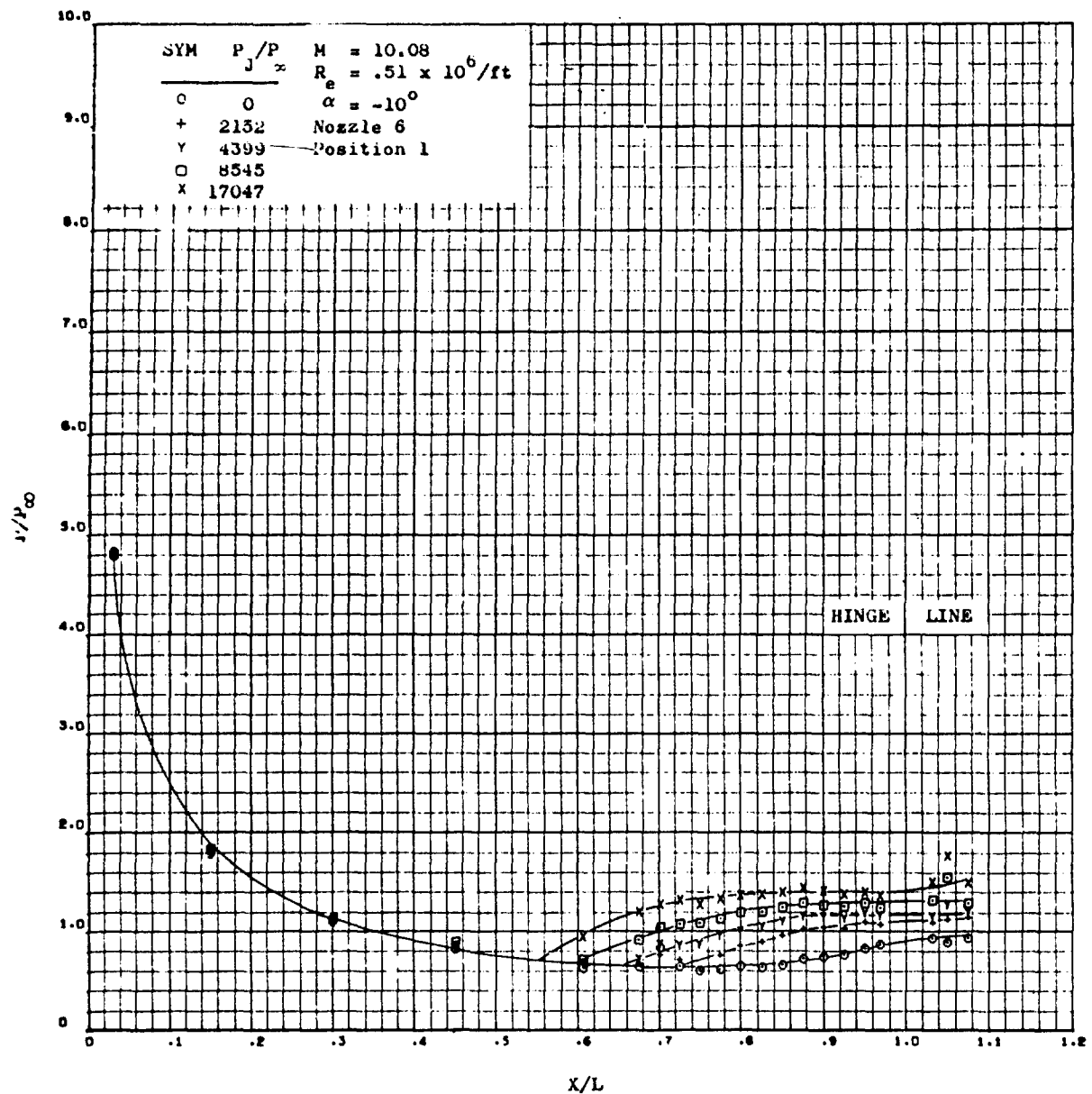


Figure 24. Effect of Jet Pressure Ratio on Flat Plate Centerline Pressure at an Angle of Attack of -10° for Nozzle 6

UNCLASSIFIED

UNCLASSIFIED

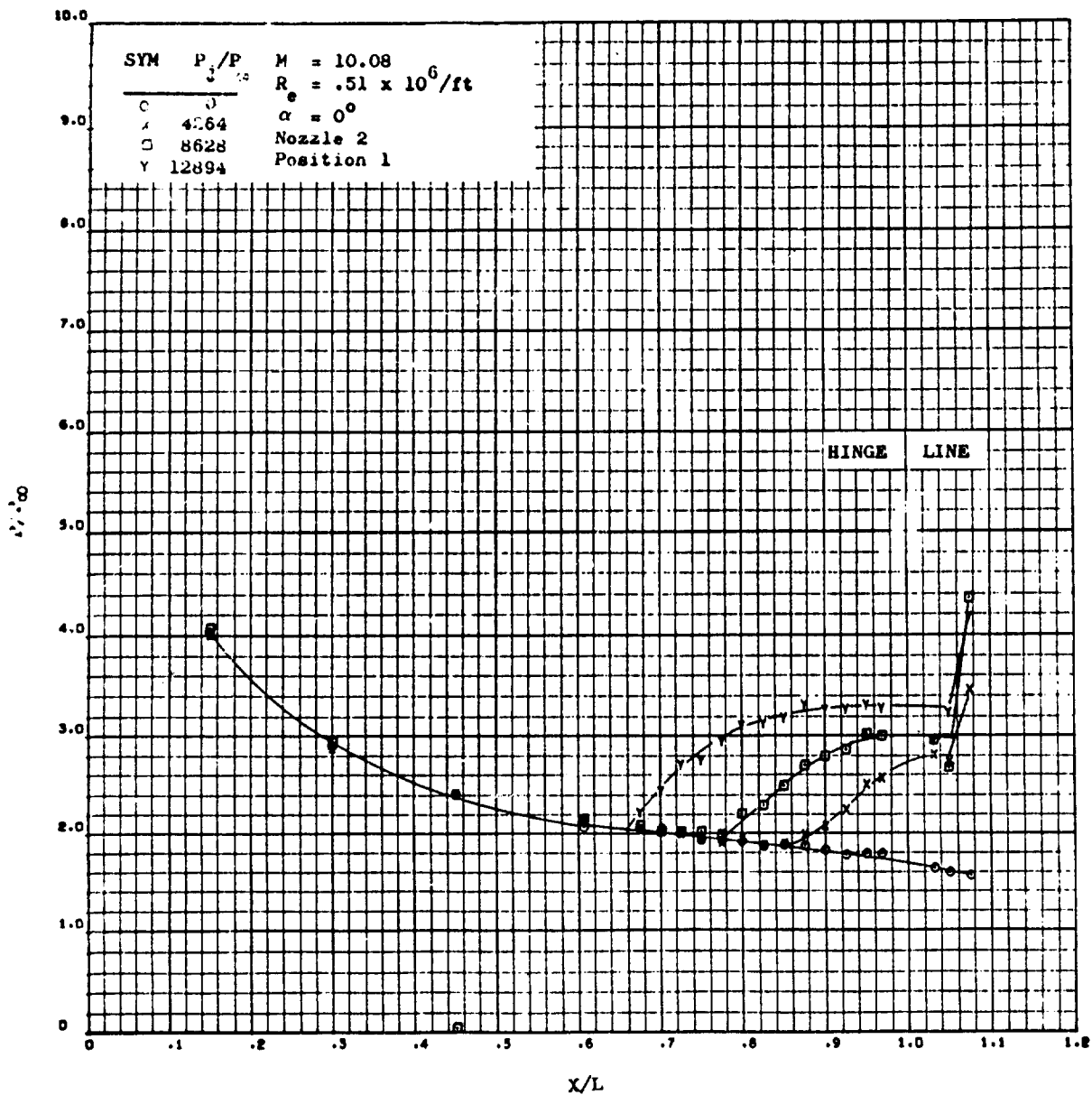
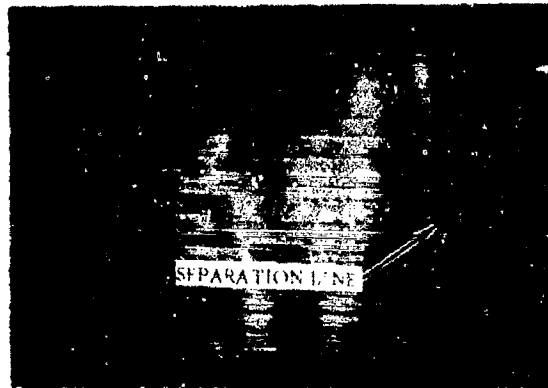


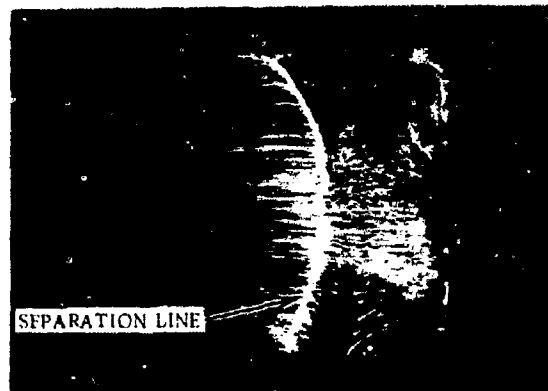
Figure 25. Effect of Jet Pressure Ratio on Flat Plate Centerline Pressure at Zero Angle of Attack for Nozzle 2

UNCLASSIFIED

UNCLASSIFIED



$A/A_0 = 1$



$A/A_0 = 2.25$

NOZZLE POSITION 1
 $\rho_1/P = 8500$
 $\alpha = 6$ DEGREE
 $Re = 0.5 \times 10^6/FT$
 $M = 10.1$

Figure 26. Flat Plate Oil Flow Visualization of the Effect of Nozzle Expansion Ratio

86
UNCLASSIFIED

UNCLASSIFIED

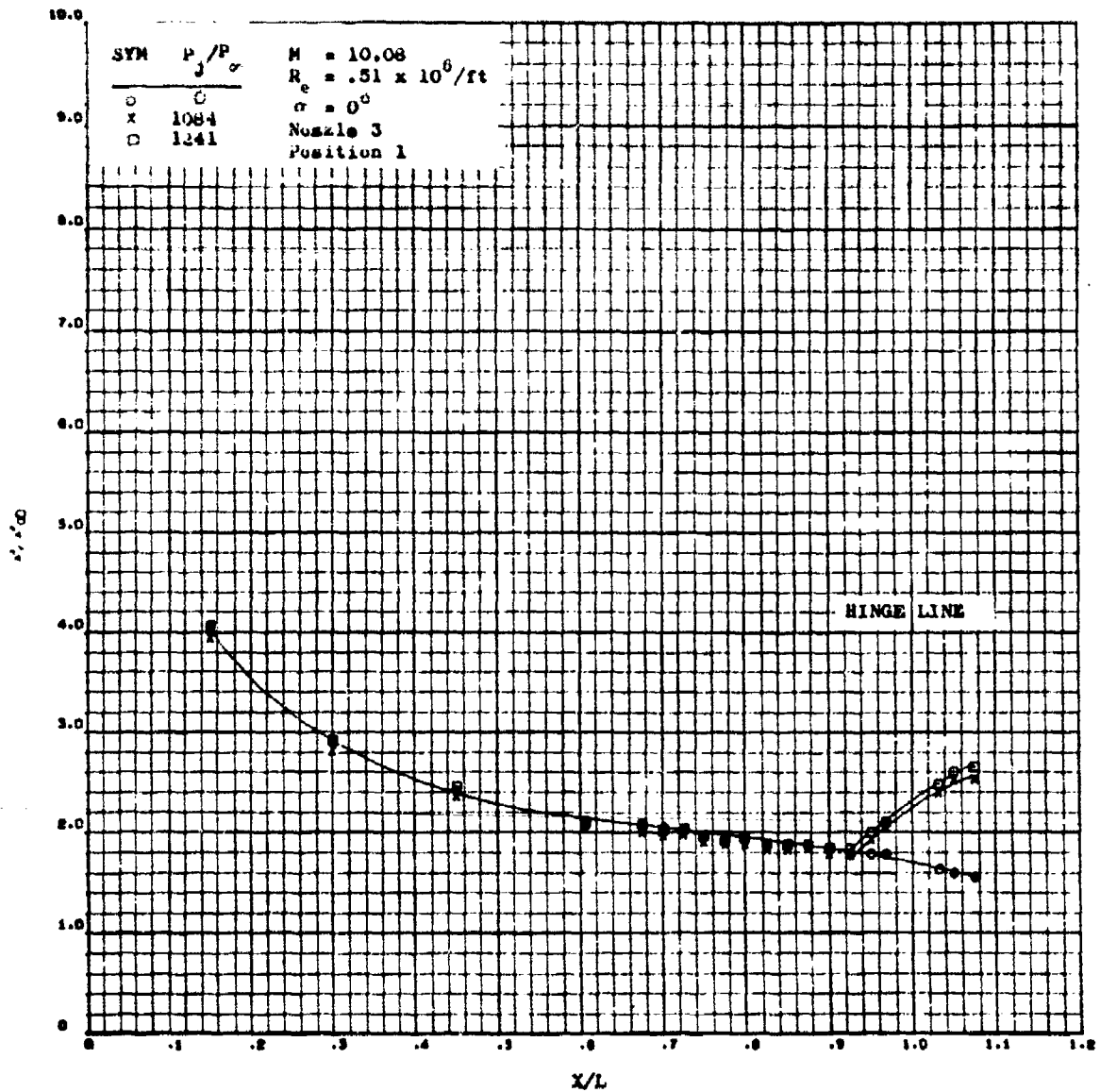


Figure 27. Effect of Jet Pressure Ratio on Flat Plate Centerline Pressure at Zero Angle of Attack for Nozzle 3

UNCLASSIFIED

UNCLASSIFIED

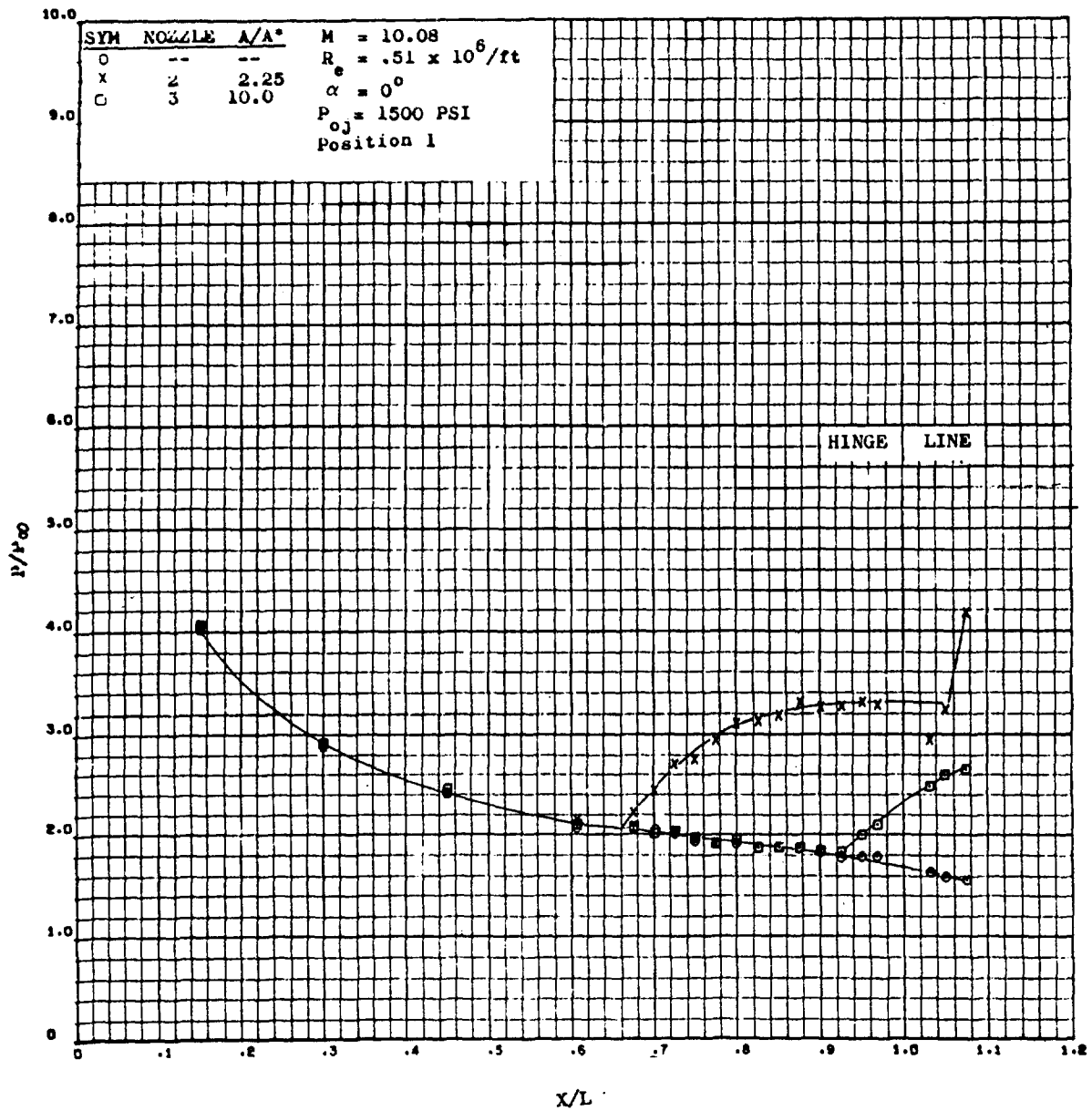


Figure 28. A Comparison of Nozzle Expansion Ratio Effects on Flat Plate Centerline Pressure for Nozzles 2 and 3 at a Chamber Pressure of 1500 psi

UNCLASSIFIED

UNCLASSIFIED

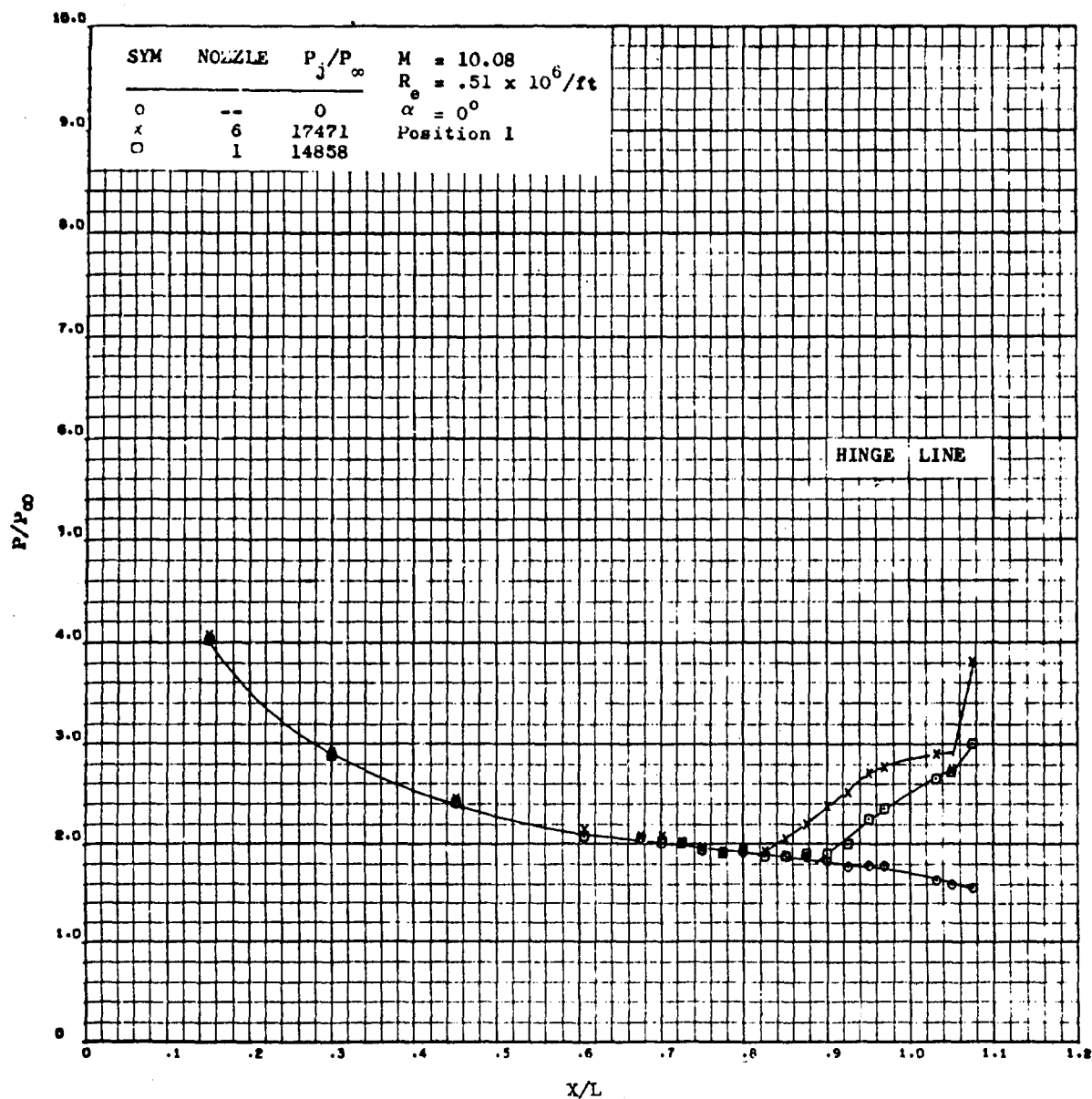


Figure 29. Effect of Nozzle Size on Flat Plate Centerline Pressure at Zero Angle of Attack

89
UNCLASSIFIED

UNCLASSIFIED

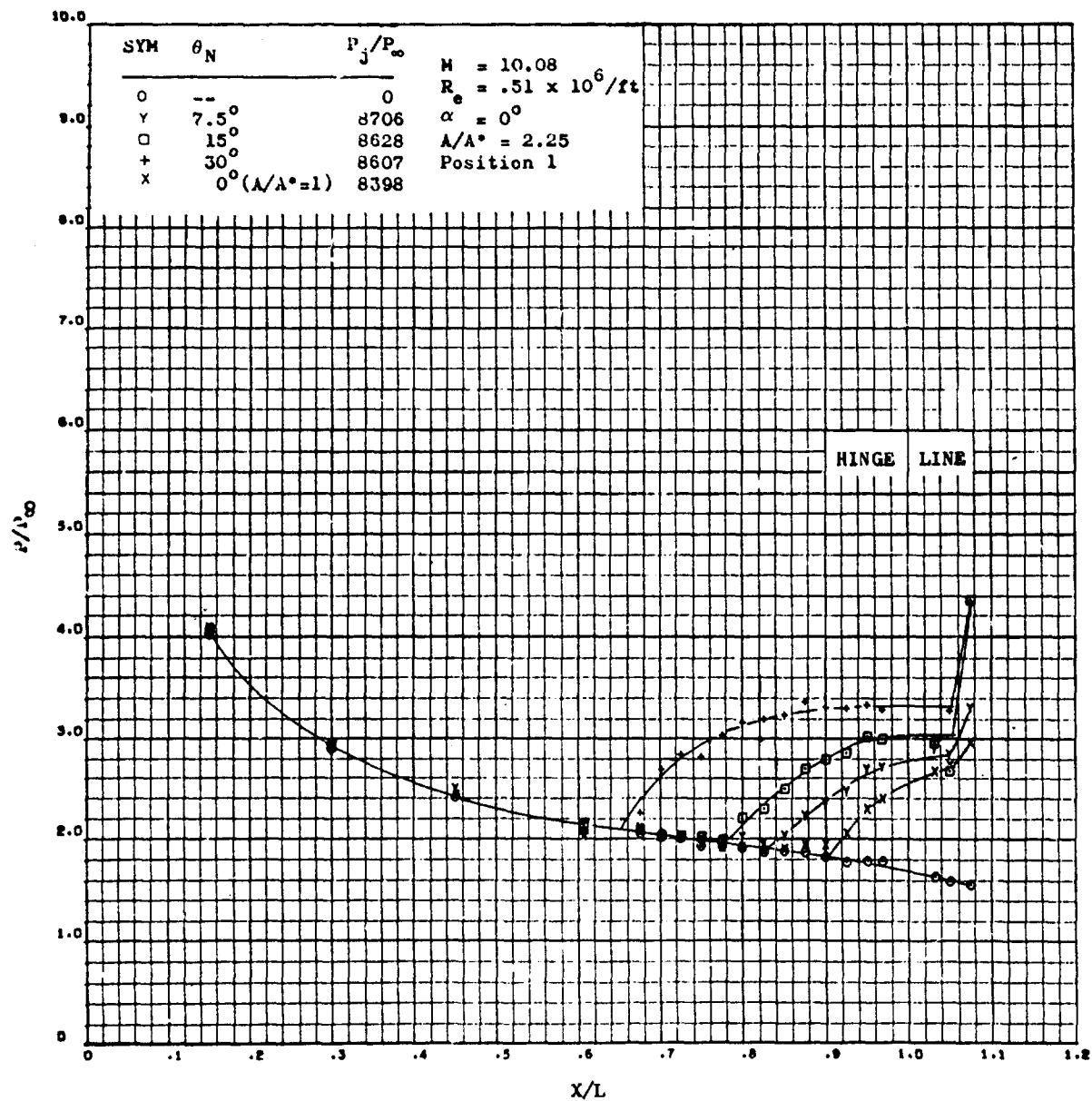


Figure 30. A Comparison of Nozzle Exit Angle Effects on Flat Plate Centerline Pressure at Zero Angle of Attack

UNCLASSIFIED

UNCLASSIFIED

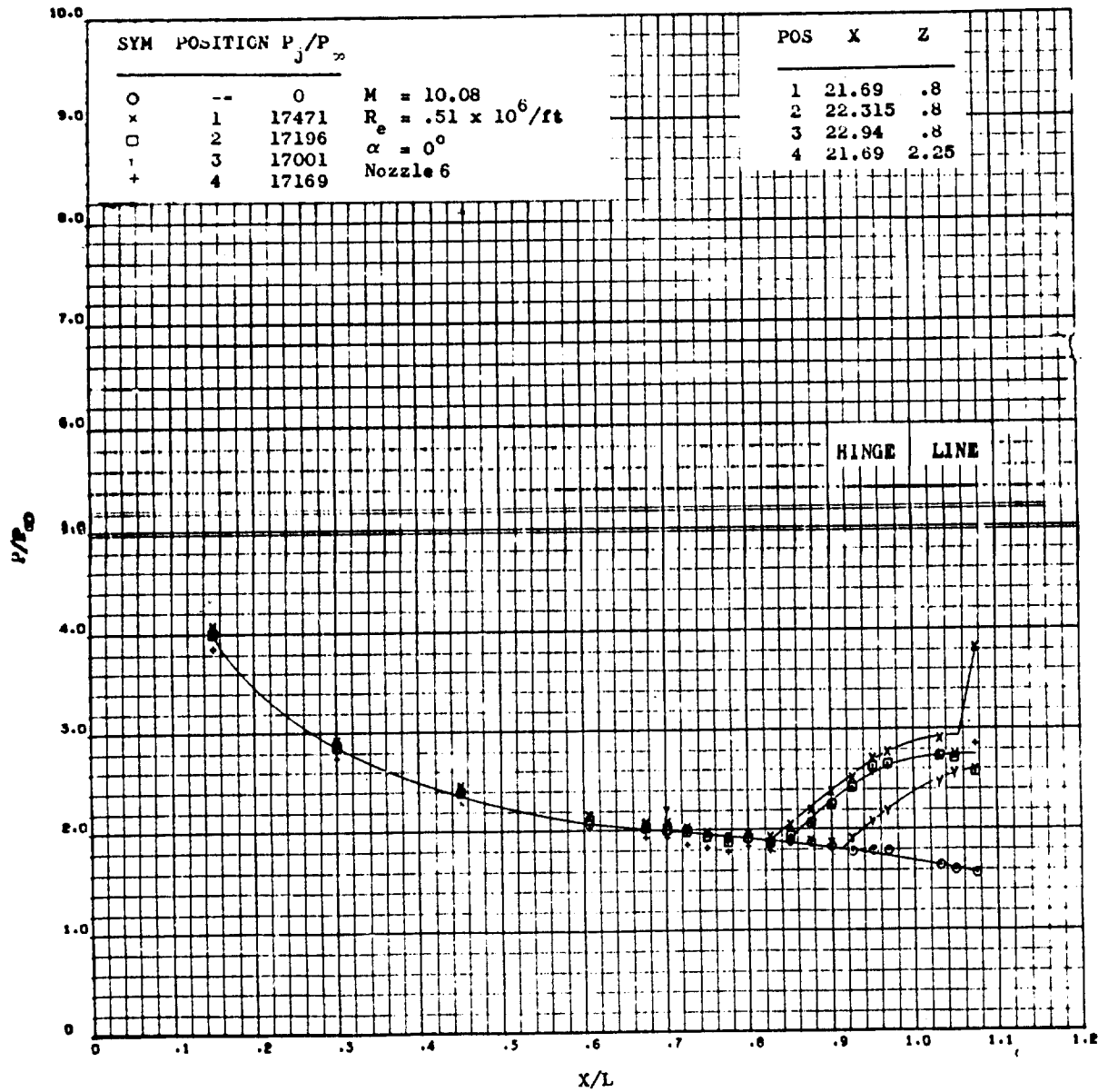


Figure 31. Effect of Nozzle Position on Flat Plate Centerline Pressure for Nozzle 6

UNCLASSIFIED

UNCLASSIFIED

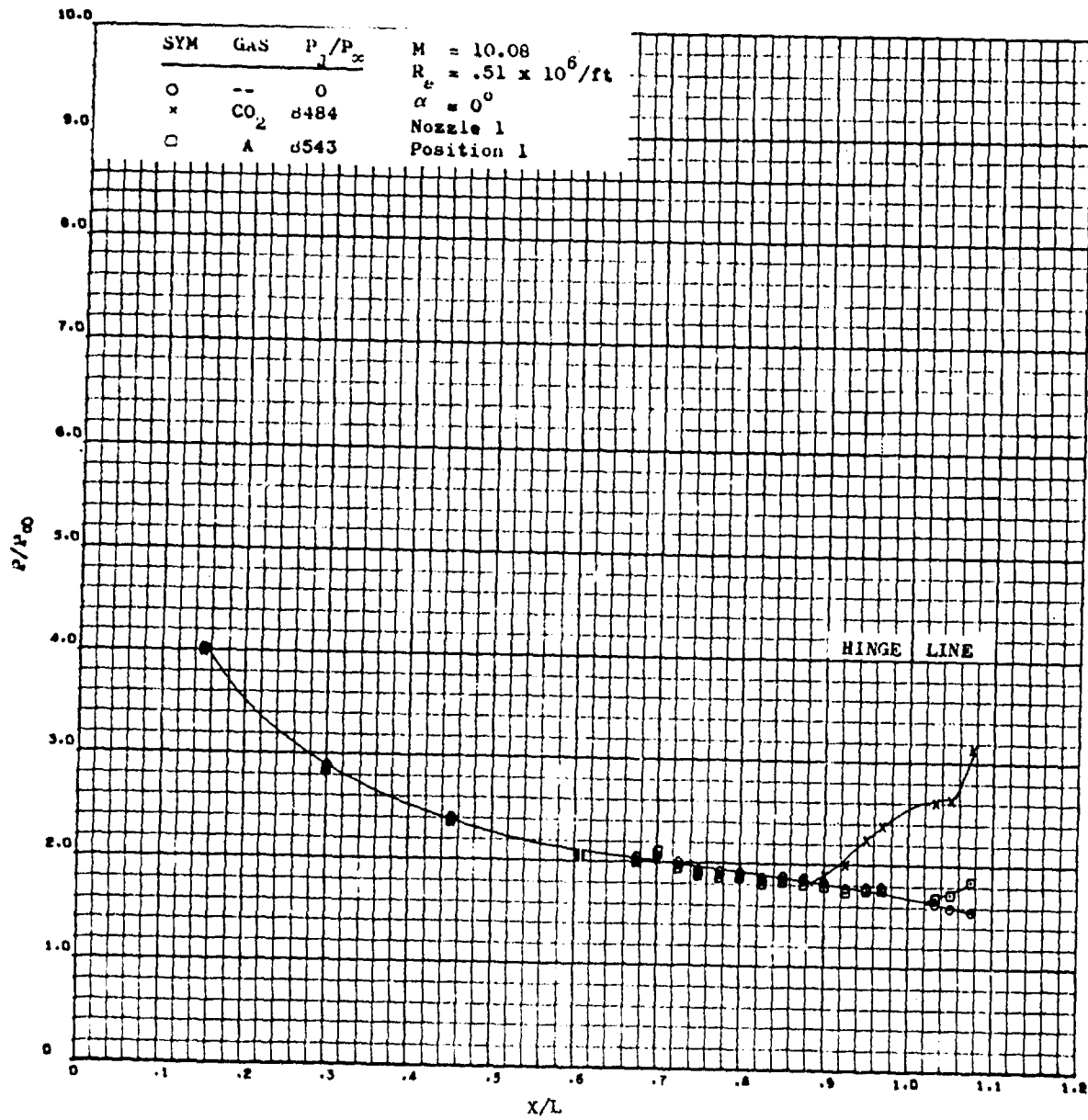


Figure 32. A Comparison of Exhaust Gas Effects on Flat Plate Centerline Pressure at Zero Angle of Attack

UNCLASSIFIED

UNCLASSIFIED

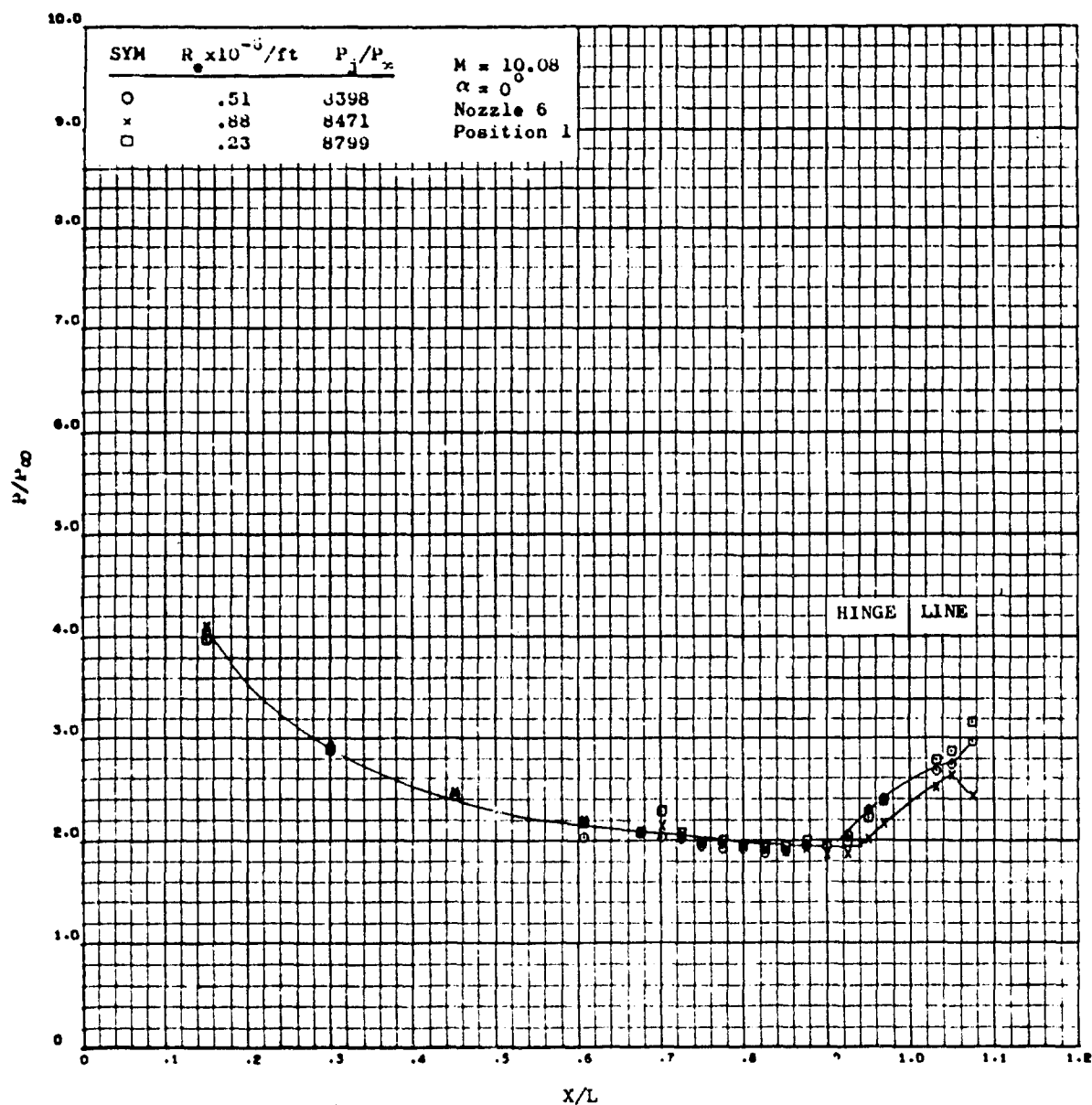


Figure 53. Effect of Reynolds Number on Flat Plate Centerline Pressure at Zero Angle of Attack and a Jet Pressure Ratio of 8000 for Nozzle 6

UNCLASSIFIED

UNCLASSIFIED

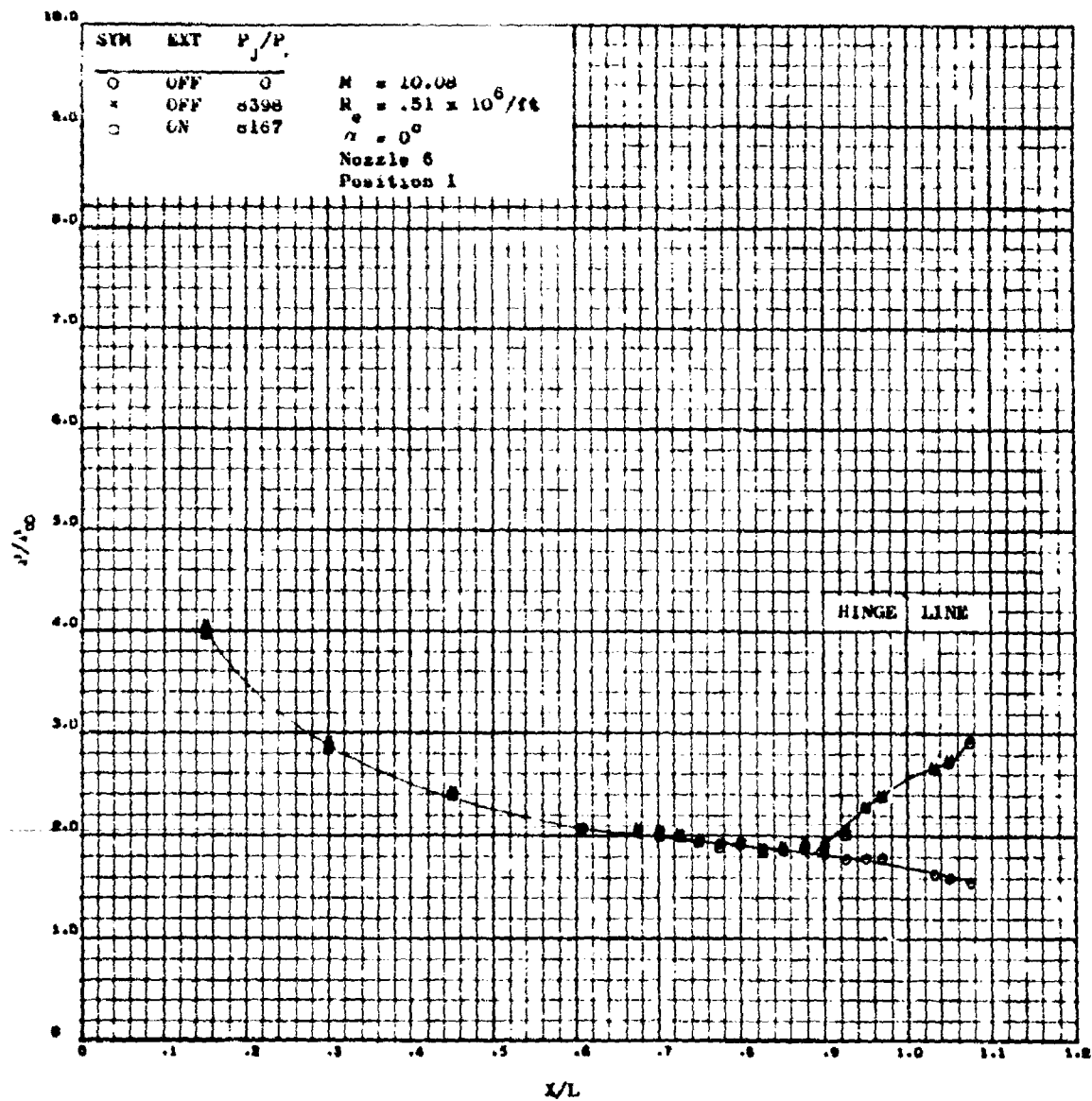
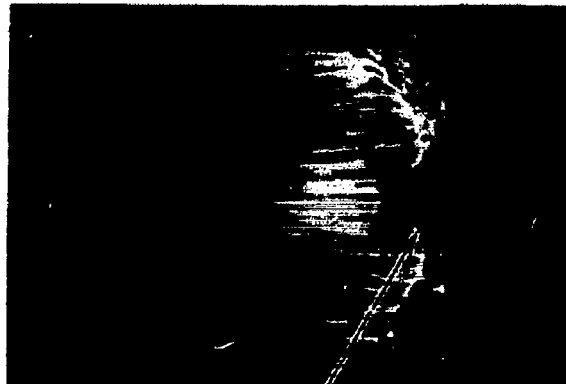


Figure 34. Effect of Eleven Extensions on Flat Plate Centerline Pressure at Zero Angle of Attack and a Jet Pressure Ratio of 3000 for Nozzle 6

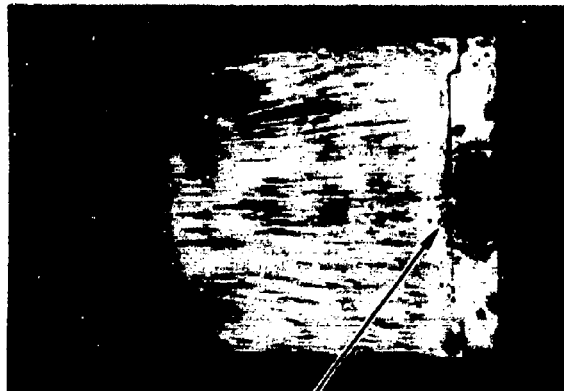
UNCLASSIFIED

UNCLASSIFIED



EXTENSIONS
OFF

SEPARATION LINE



EXTENSIONS
ON

SEPARATION LINE

NOZZLE 6
POSITION 1
 $\alpha = 0$ DEGREE
 $P_1/P_0 = 17000$
 $Re = 1.5 \times 10^5$
 $M = 1.1$

Figure 35. Flat Plate Oil Flow Visualization of the Effect of the Elevon

95
UNCLASSIFIED

UNCLASSIFIED

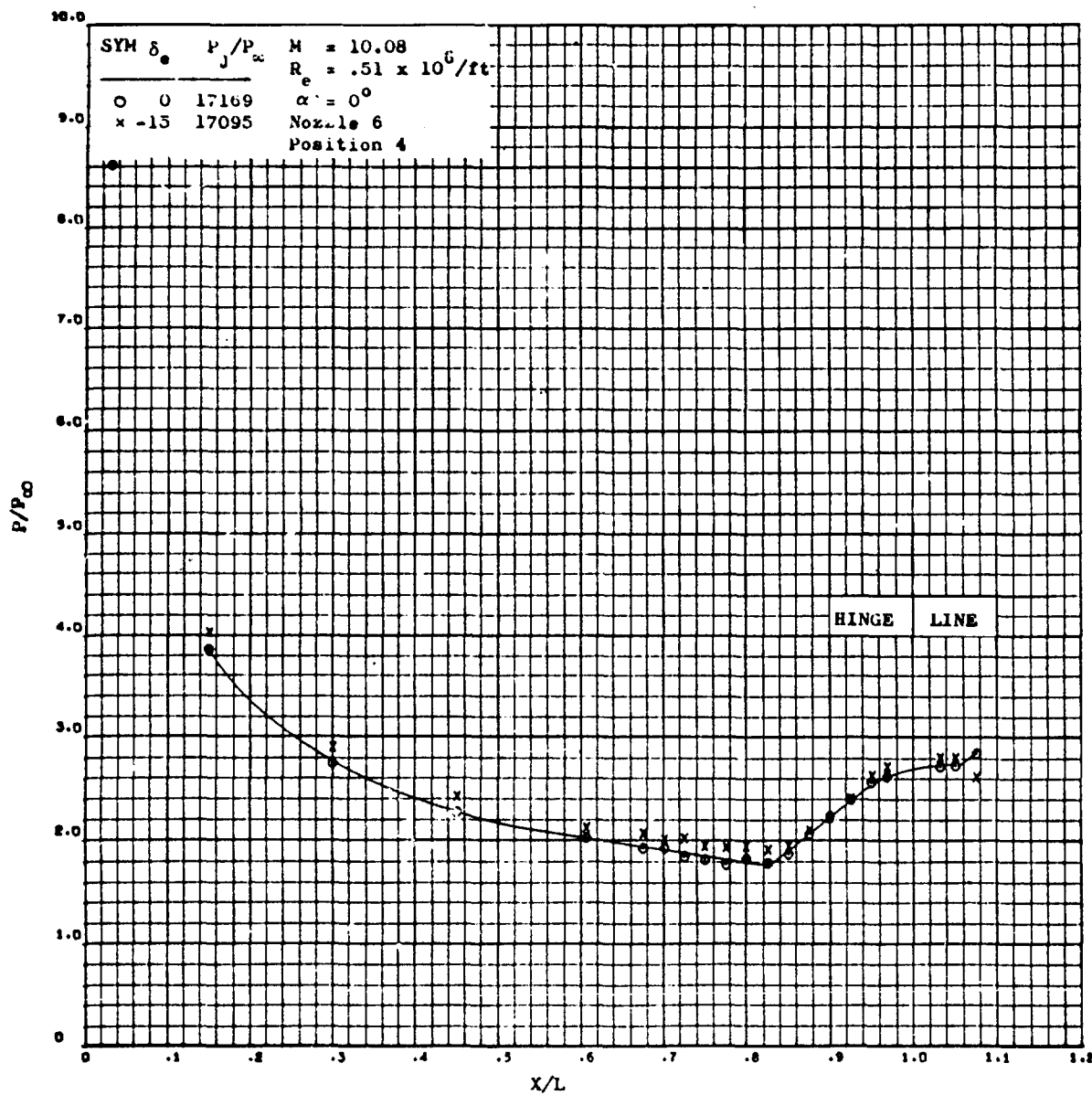


Figure 36. Effect of a Control Deflection of -15° on Flat Plate Centerline Pressure at Zero Angle of Attack and a Jet Pressure Ratio of 17000 for Nozzle 6

UNCLASSIFIED

UNCLASSIFIED

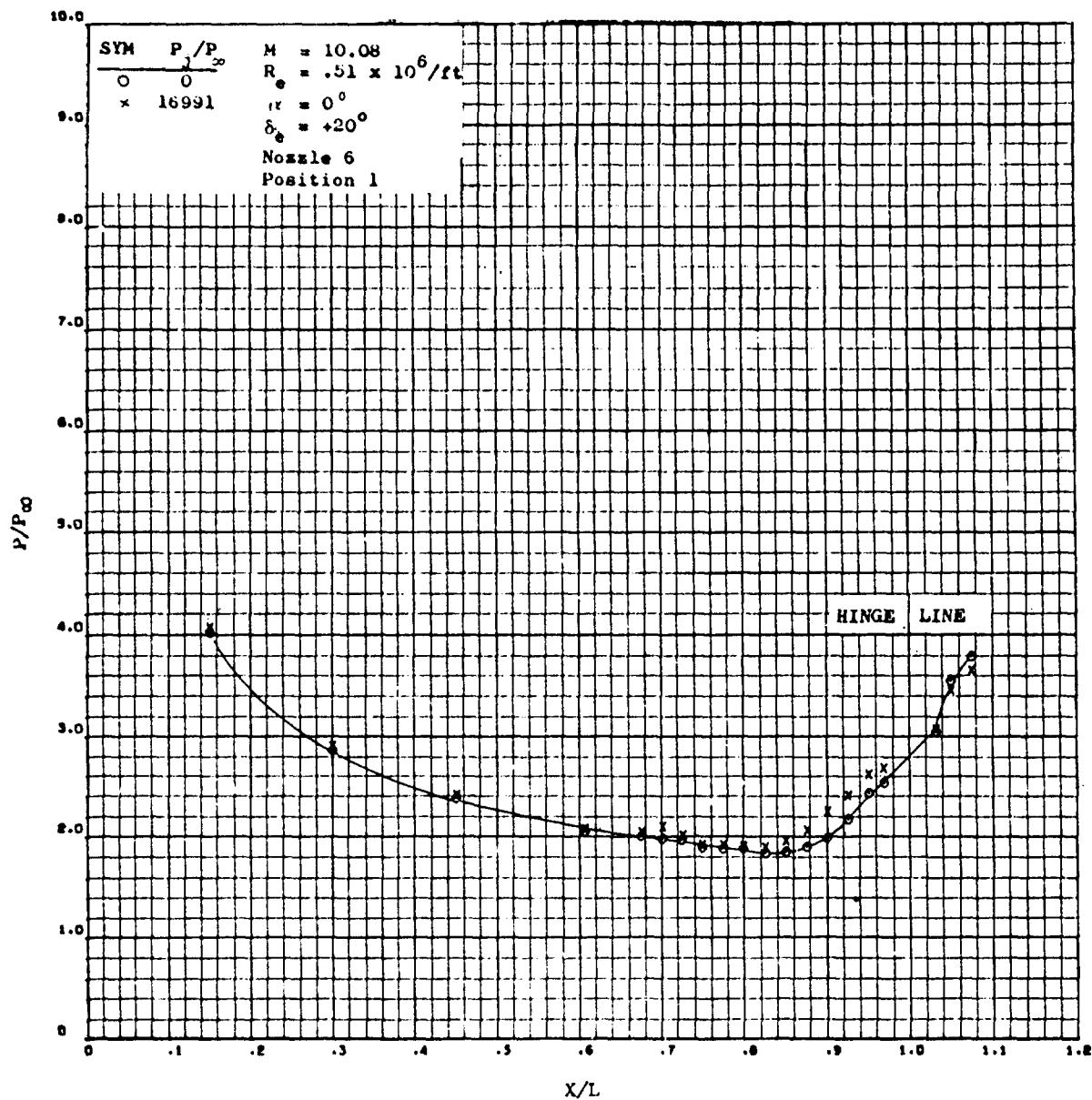


Figure 37. Effect of Plume Combined with $+20^\circ$ Control Deflection on Flat Plate Centerline Pressure

UNCLASSIFIED

UNCLASSIFIED

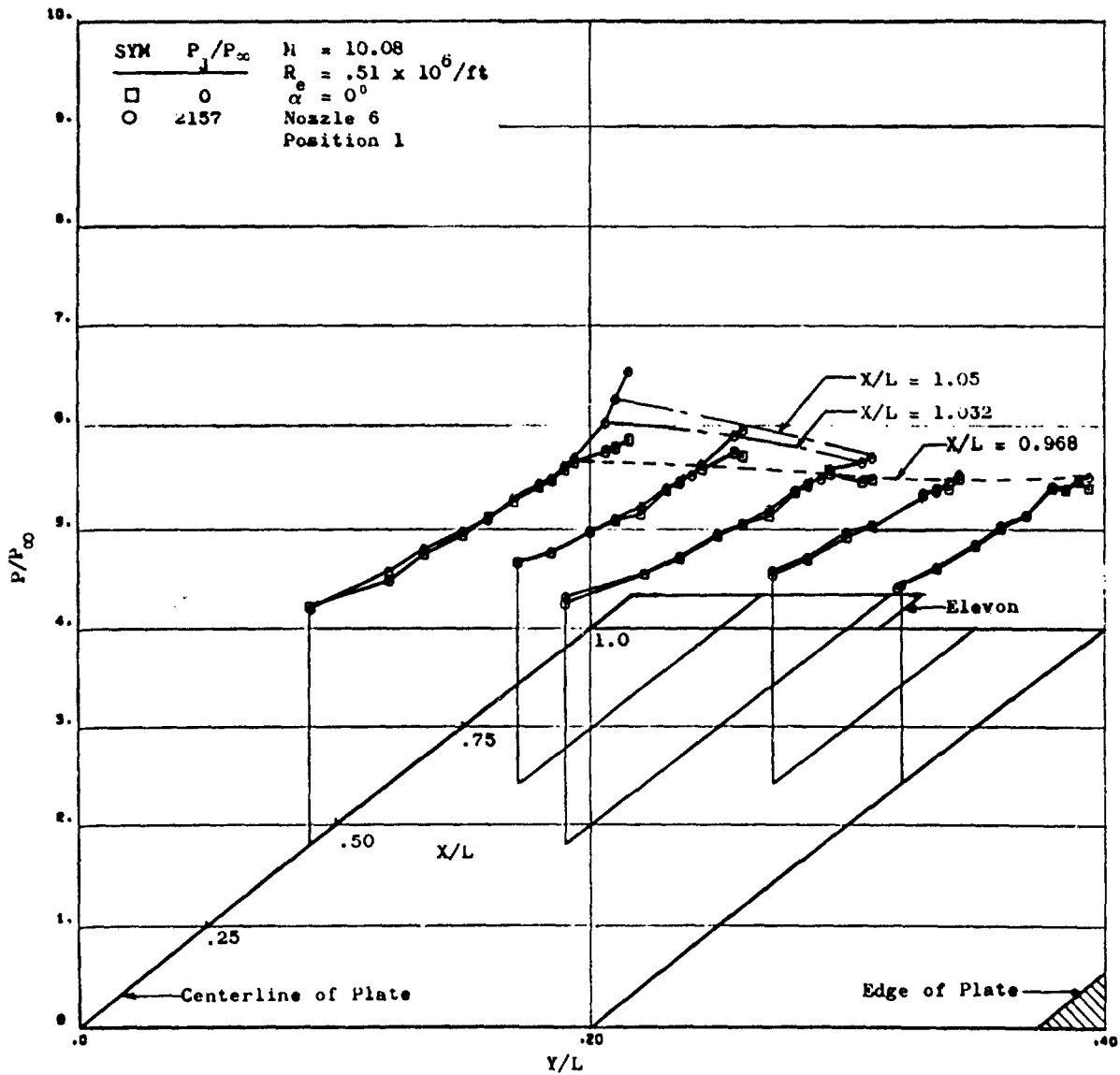


Figure 38. Flat Plate Spanwise Pressure Distribution for $P_j/P_\infty = 2157$

UNCLASSIFIED

UNCLASSIFIED

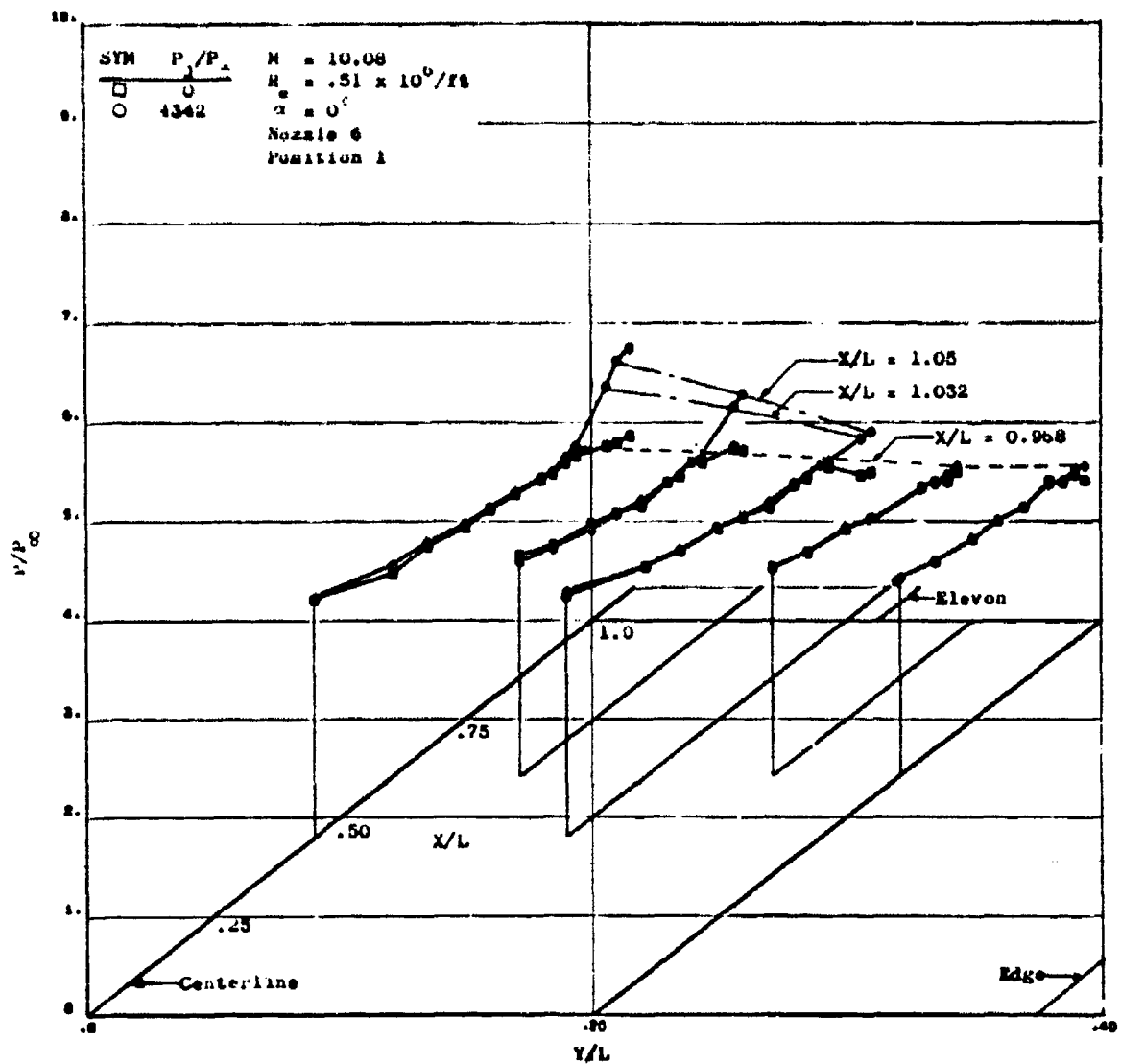


Figure 32. Flat Plate Spanwise Pressure Distribution for $P_{\infty}/P_{\infty} = 4342$

99
UNCLASSIFIED

UNCLASSIFIED

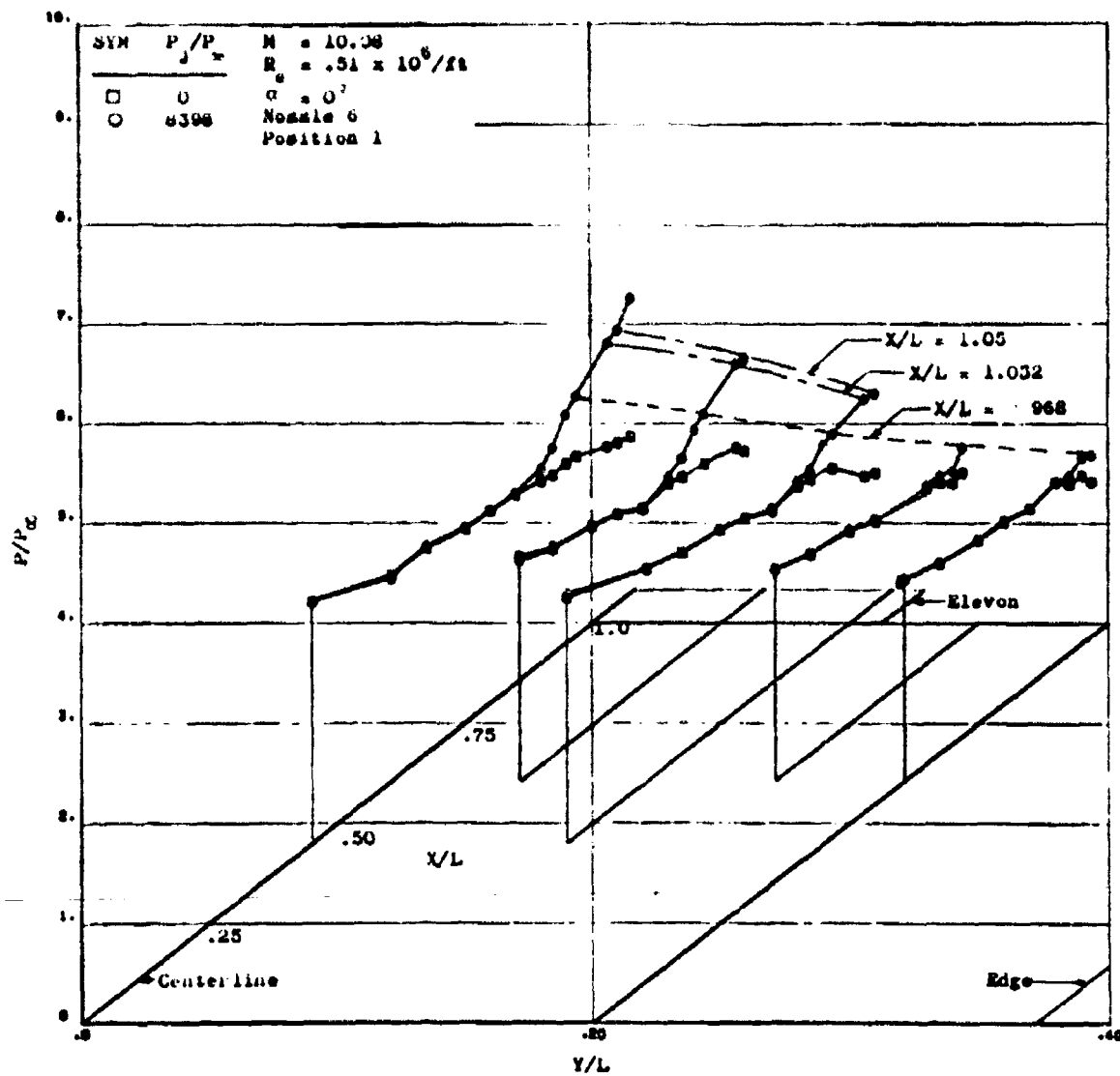


Figure 42. Flat Plate Spanwise Pressure Distribution for $P_j/P_\infty = 8398$

100
UNCLASSIFIED

UNCLASSIFIED

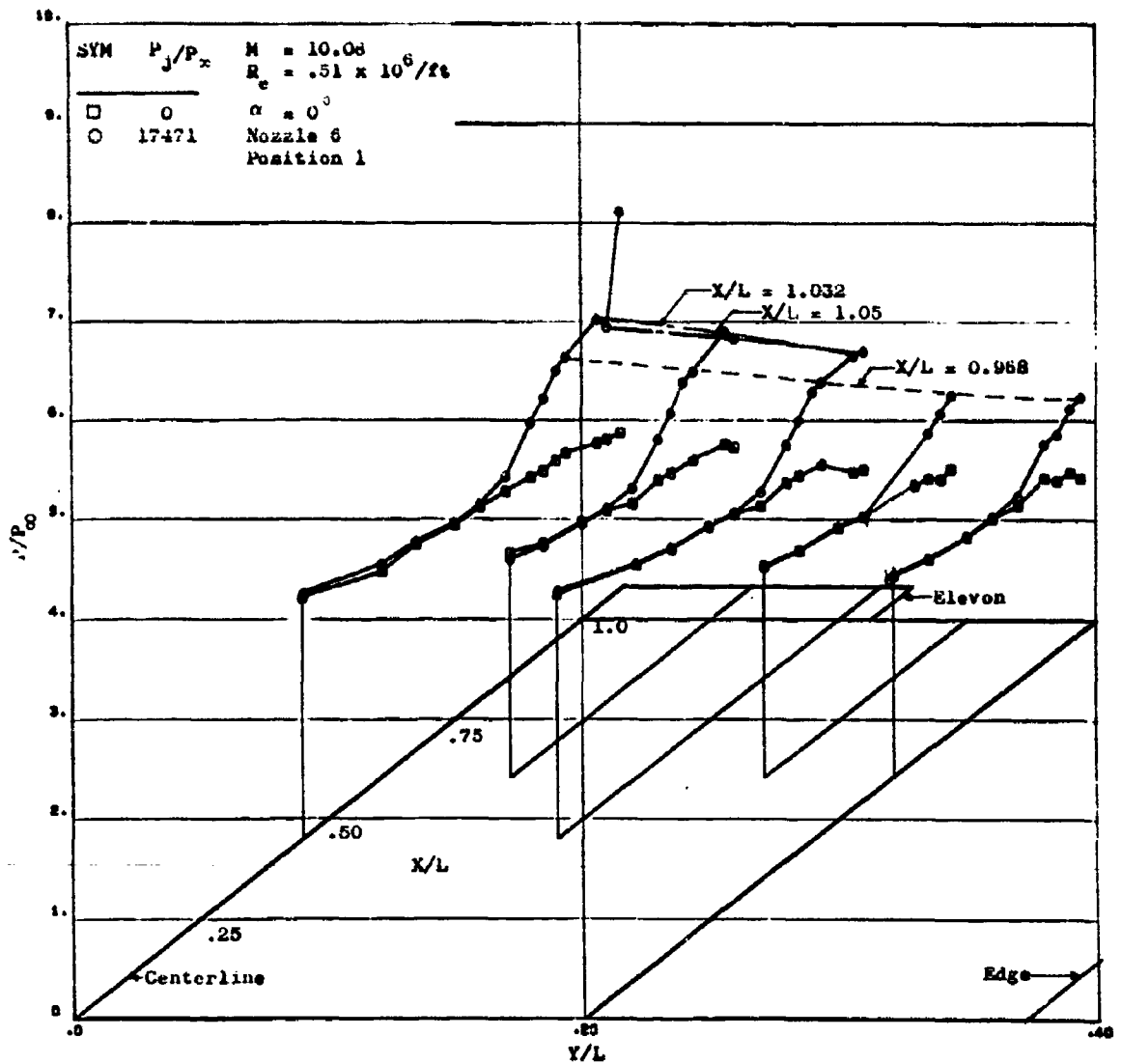


Figure 41. Flat Plate Spanwise Distribution for $P_j/P_\infty = 17471$

101
UNCLASSIFIED

UNCLASSIFIED

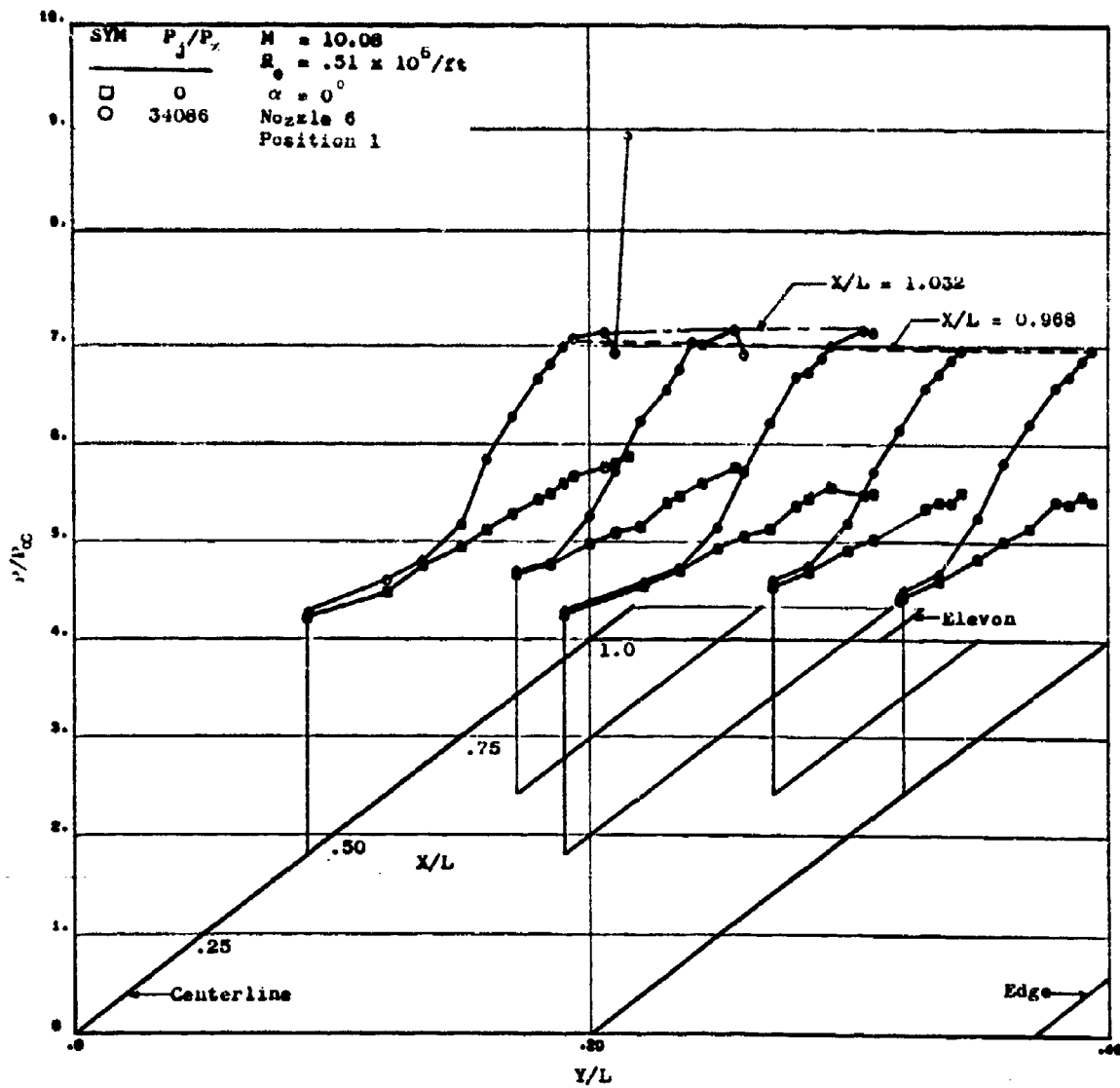


Figure 42. Flat Plate Spanwise Distribution for $P_j/P_\infty = 34086$

UNCLASSIFIED

UNCLASSIFIED

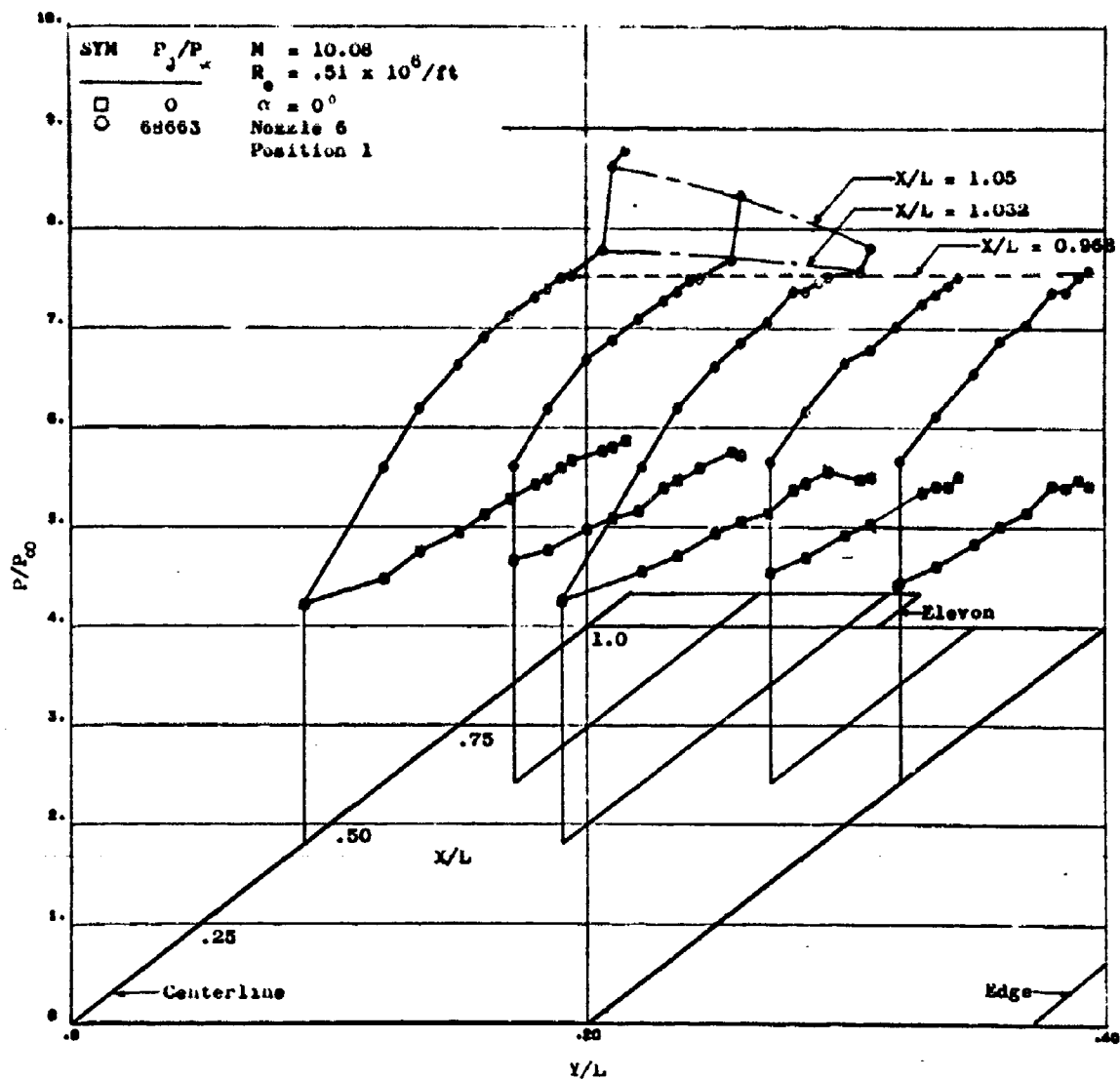


Figure 43. Flat Plate Spanwise Pressure Distribution for $P_j/P_\infty = 68663$

UNCLASSIFIED

UNCLASSIFIED

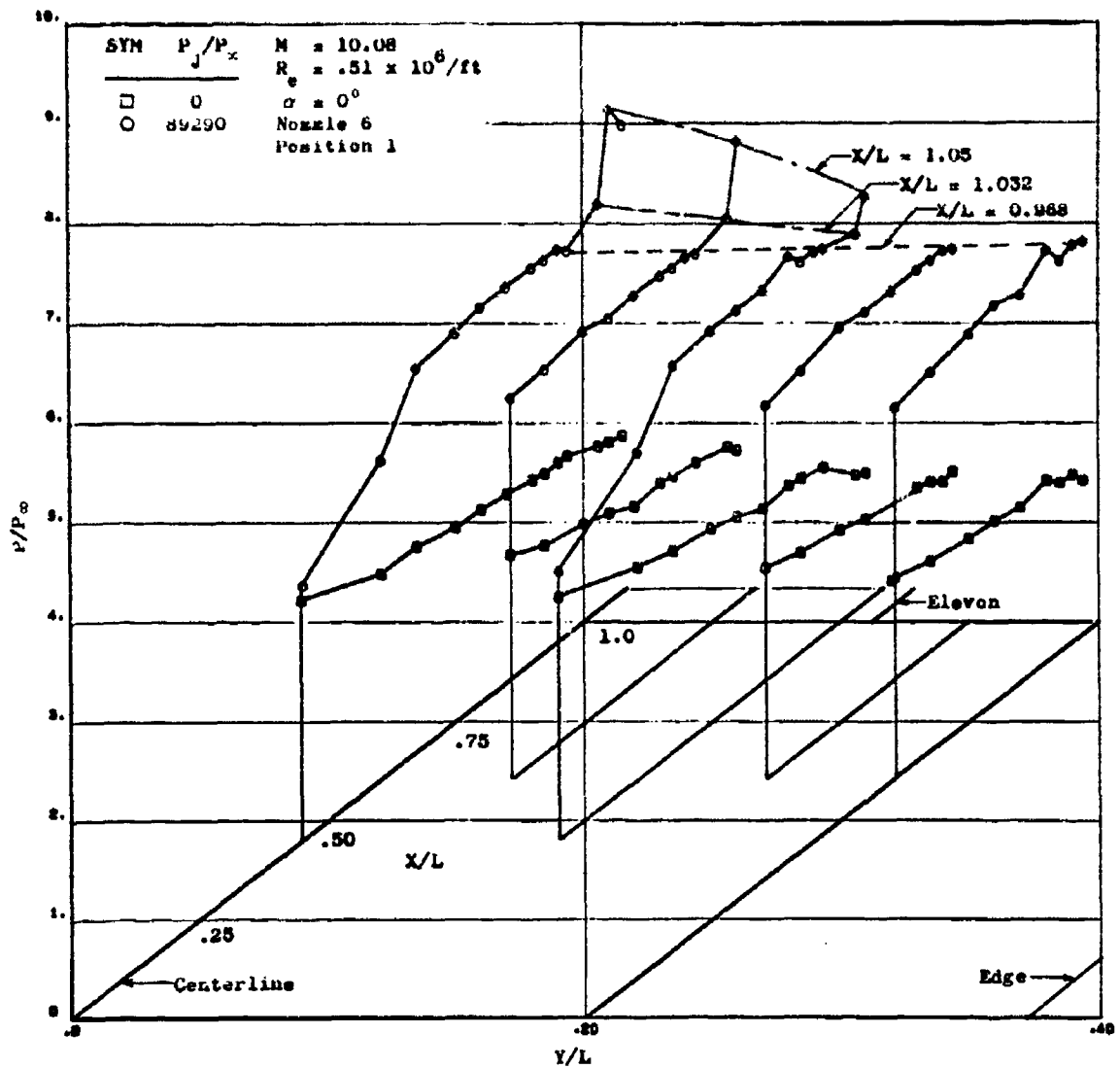


Figure 44. Flat Plate Spanwise Pressure Distribution for $P_j/P_\infty = 89290$

104
UNCLASSIFIED

UNCLASSIFIED

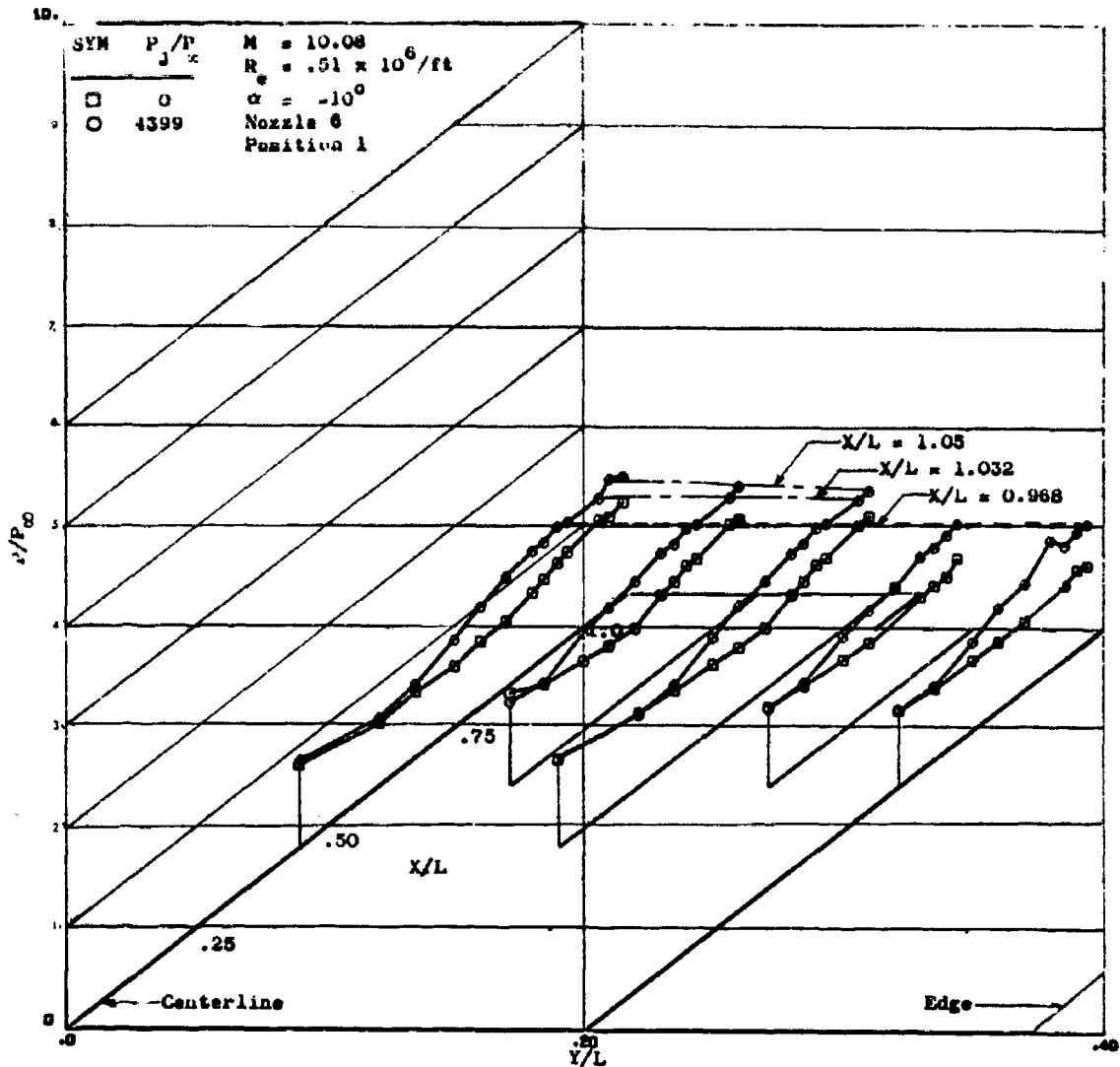


Figure 45. Flat Plate Pressure Distribution at $\alpha = -10^\circ$ and $P_j/P_\infty = 4399$

UNCLASSIFIED

UNCLASSIFIED

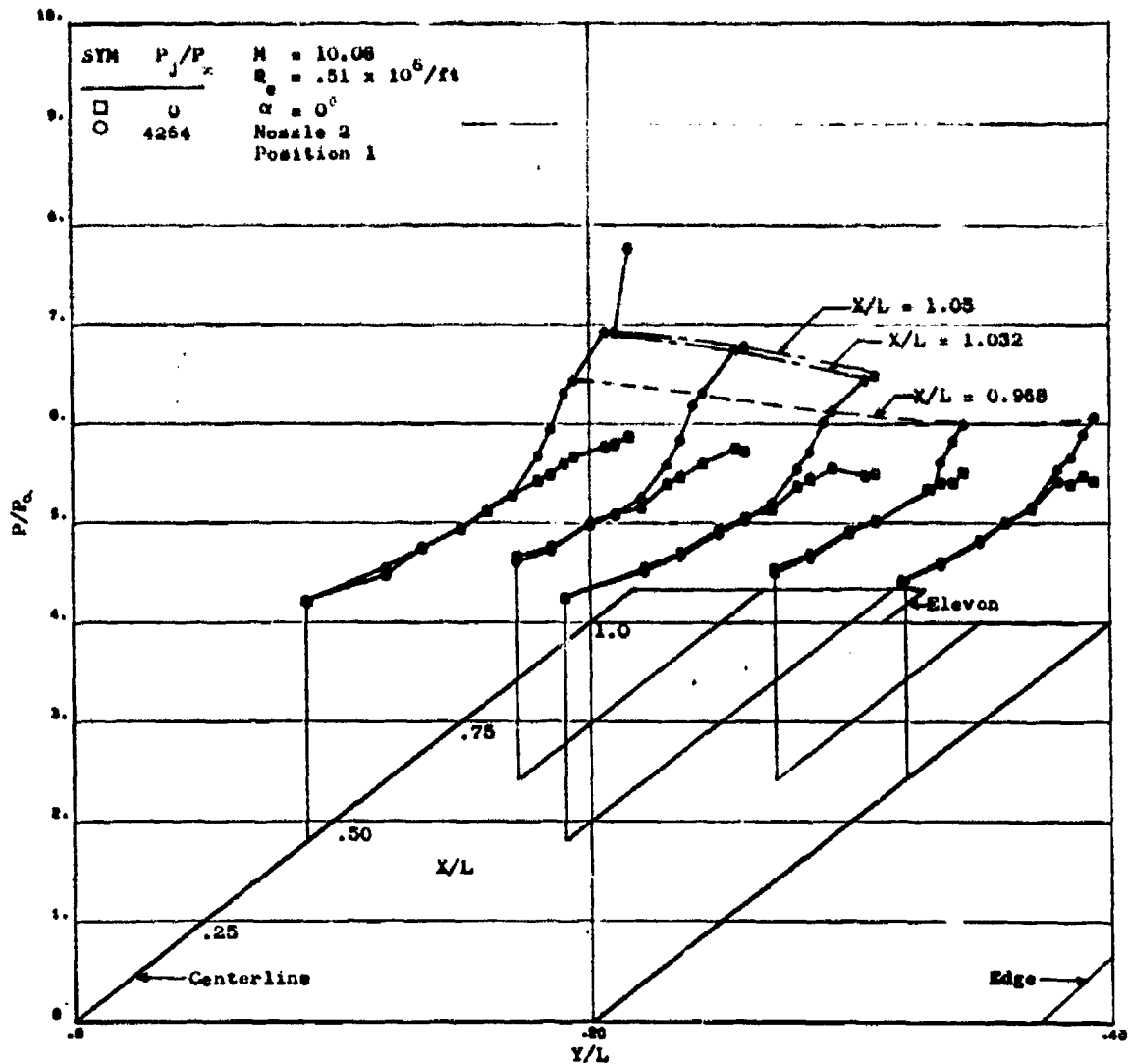


Figure 46. Flat Plate Spanwise Distribution for Nozzle 2 and $P_j/P_\infty = 4264$

UNCLASSIFIED

UNCLASSIFIED

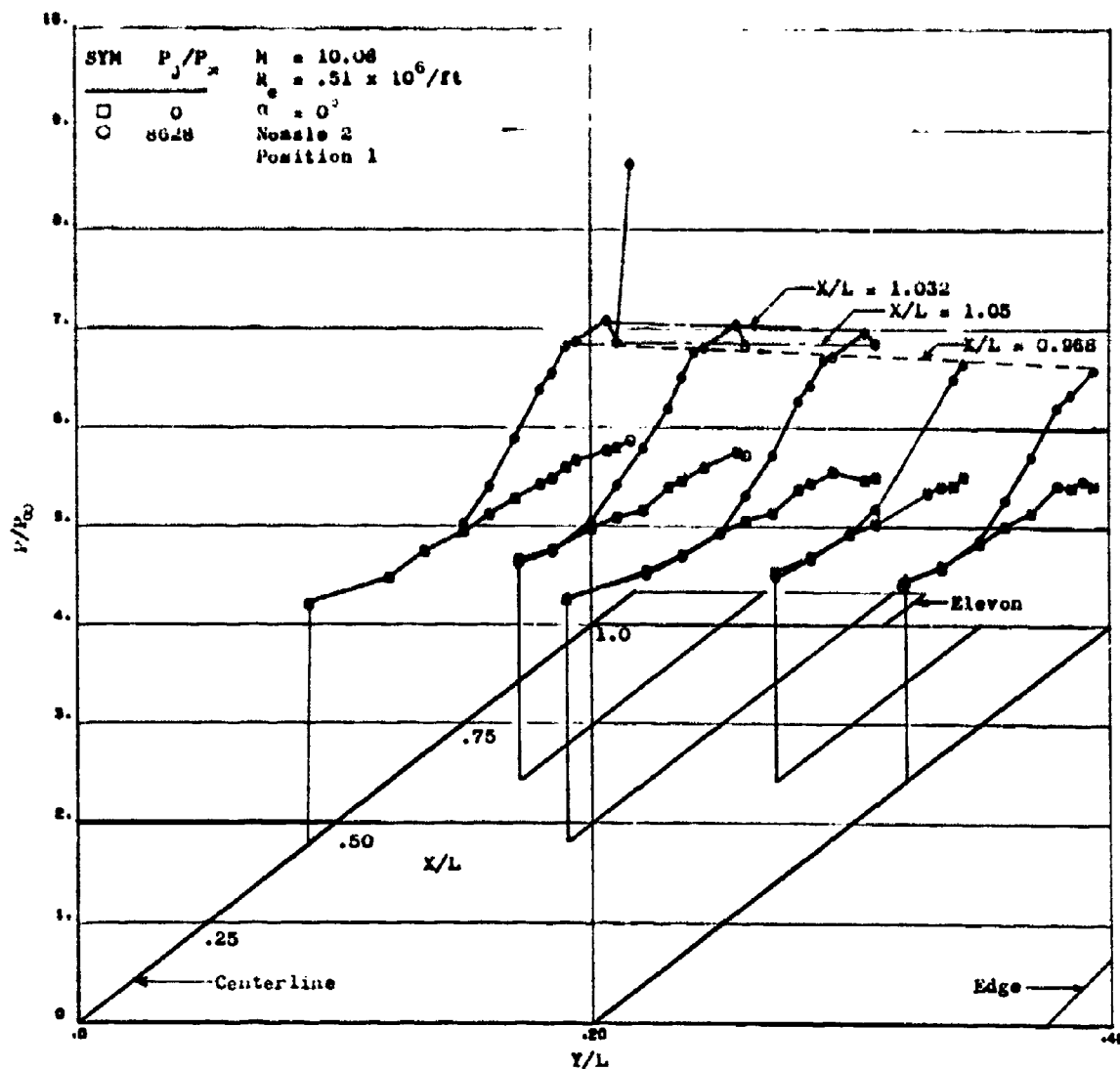


Figure 47. Spanwise Pressure Distribution for Nozzle 2 and $P_j/P_\infty = 8628$

107
UNCLASSIFIED

UNCLASSIFIED

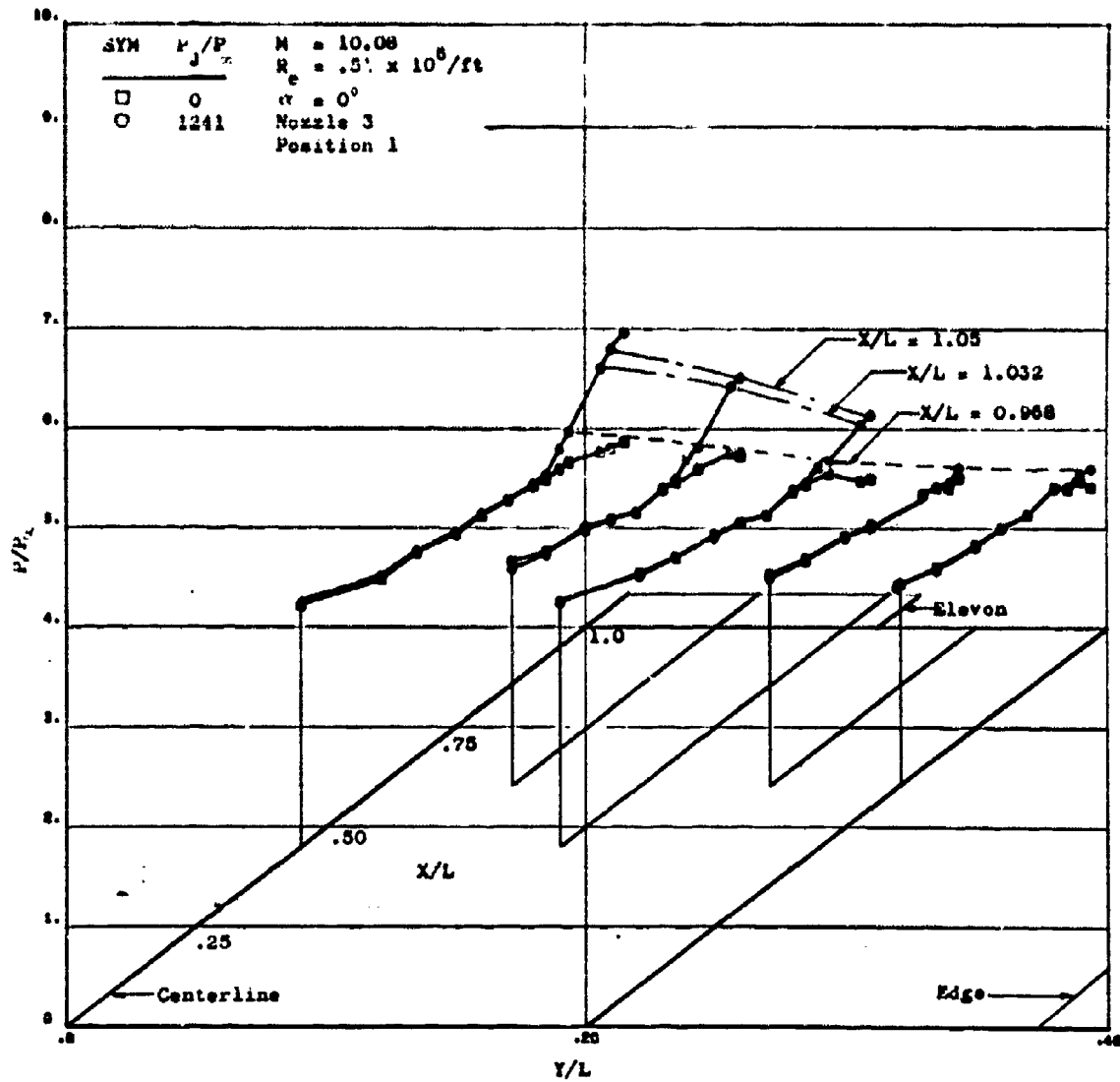


Figure 48. Flat Plate Spanwise Pressure Distribution for Nozzle 3 and $P_j/P_\infty = 1241$

UNCLASSIFIED

UNCLASSIFIED

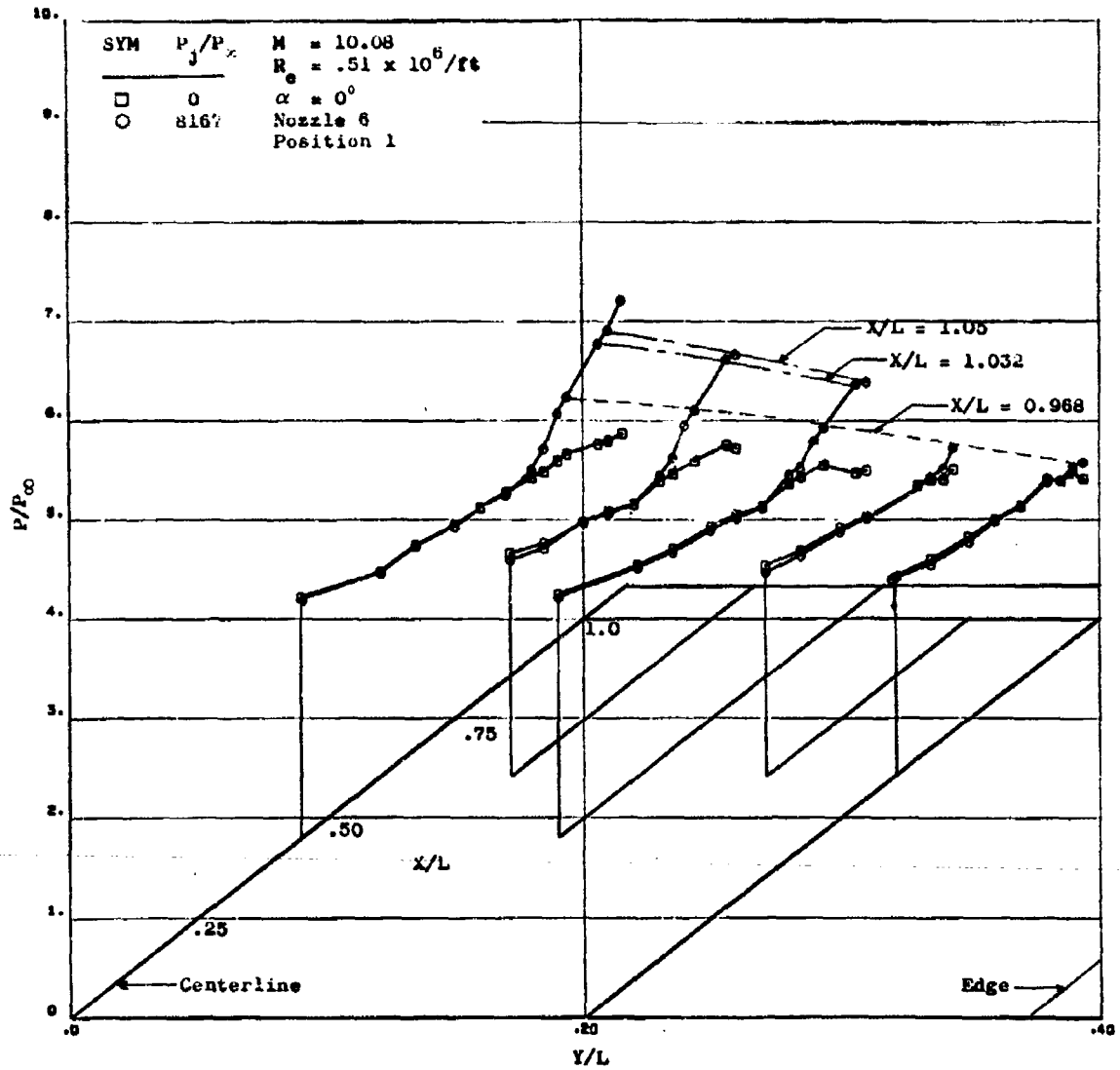


Figure 49. Flat Plate Spanwise Distribution with Extension Installed.

UNCLASSIFIED

UNCLASSIFIED

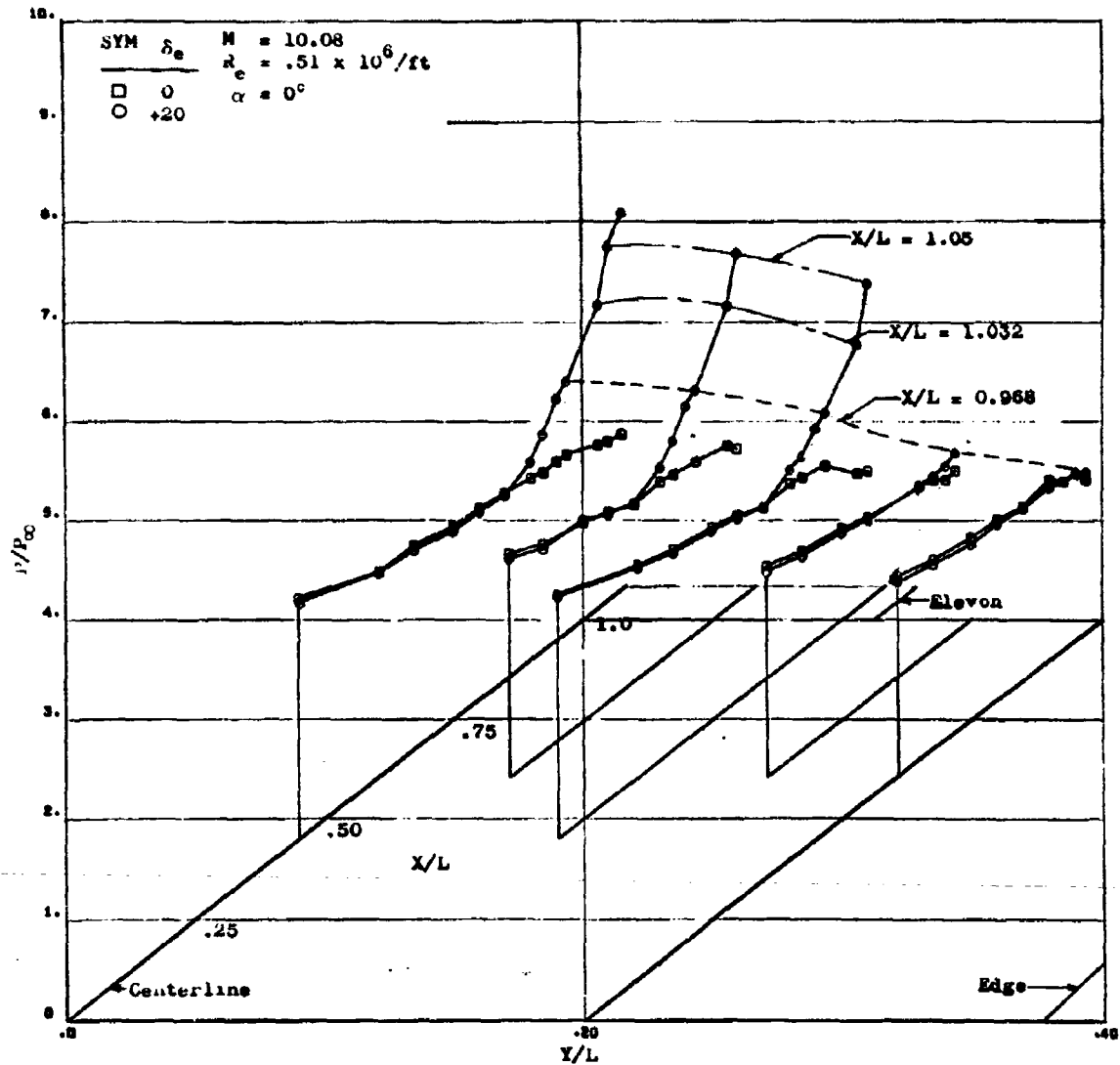


Figure 50. Effect of Control Surface Deflection on the Flat Plate Spanwise Pressure Distribution

110
UNCLASSIFIED

CONFIDENTIAL

(This page is Unclassified)

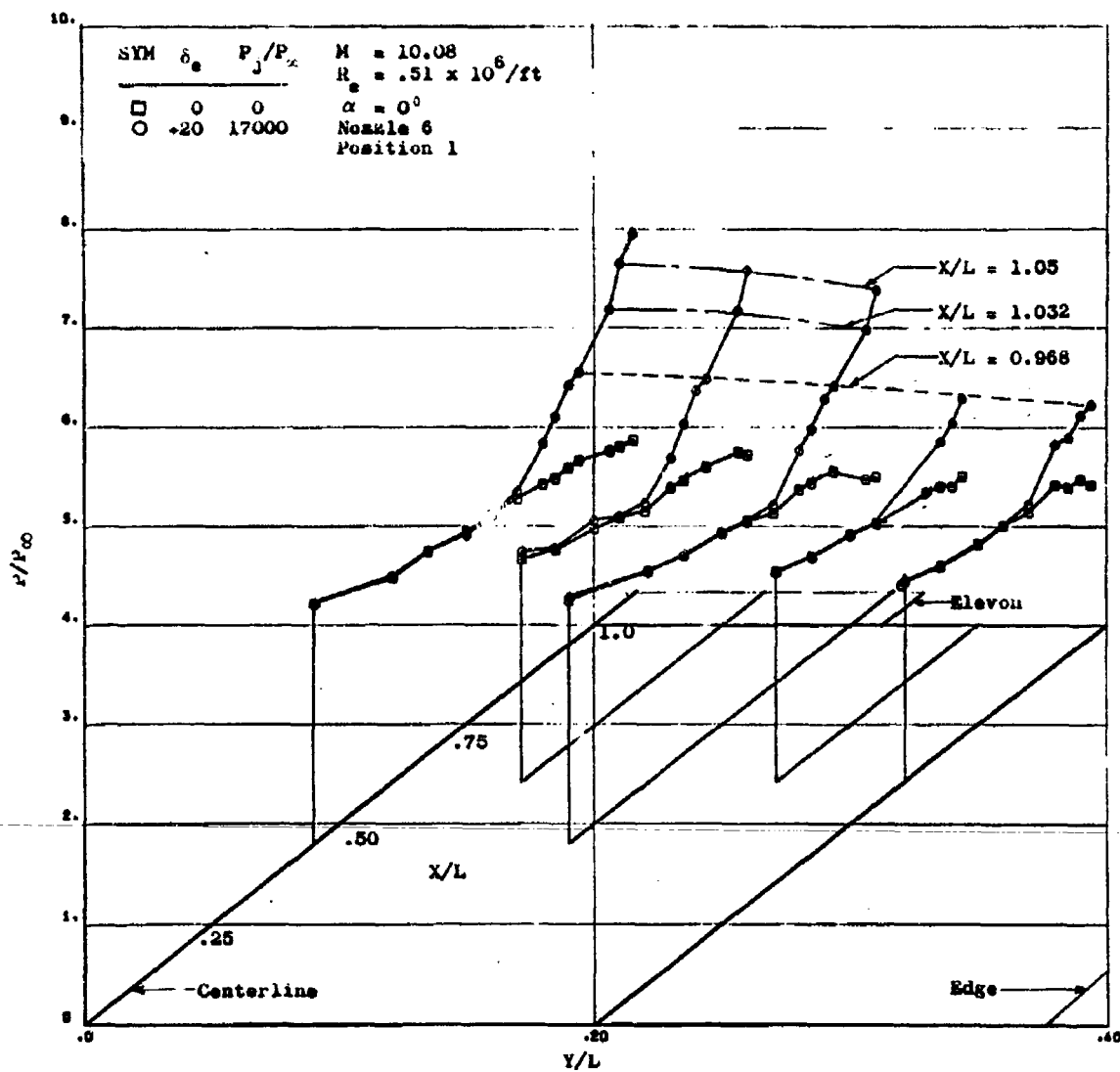


Figure 51. Flat Plate Spanwise Pressure Distribution with Control Deflection and Plume

111
CONFIDENTIAL
(This page is Unclassified)

CONFIDENTIAL

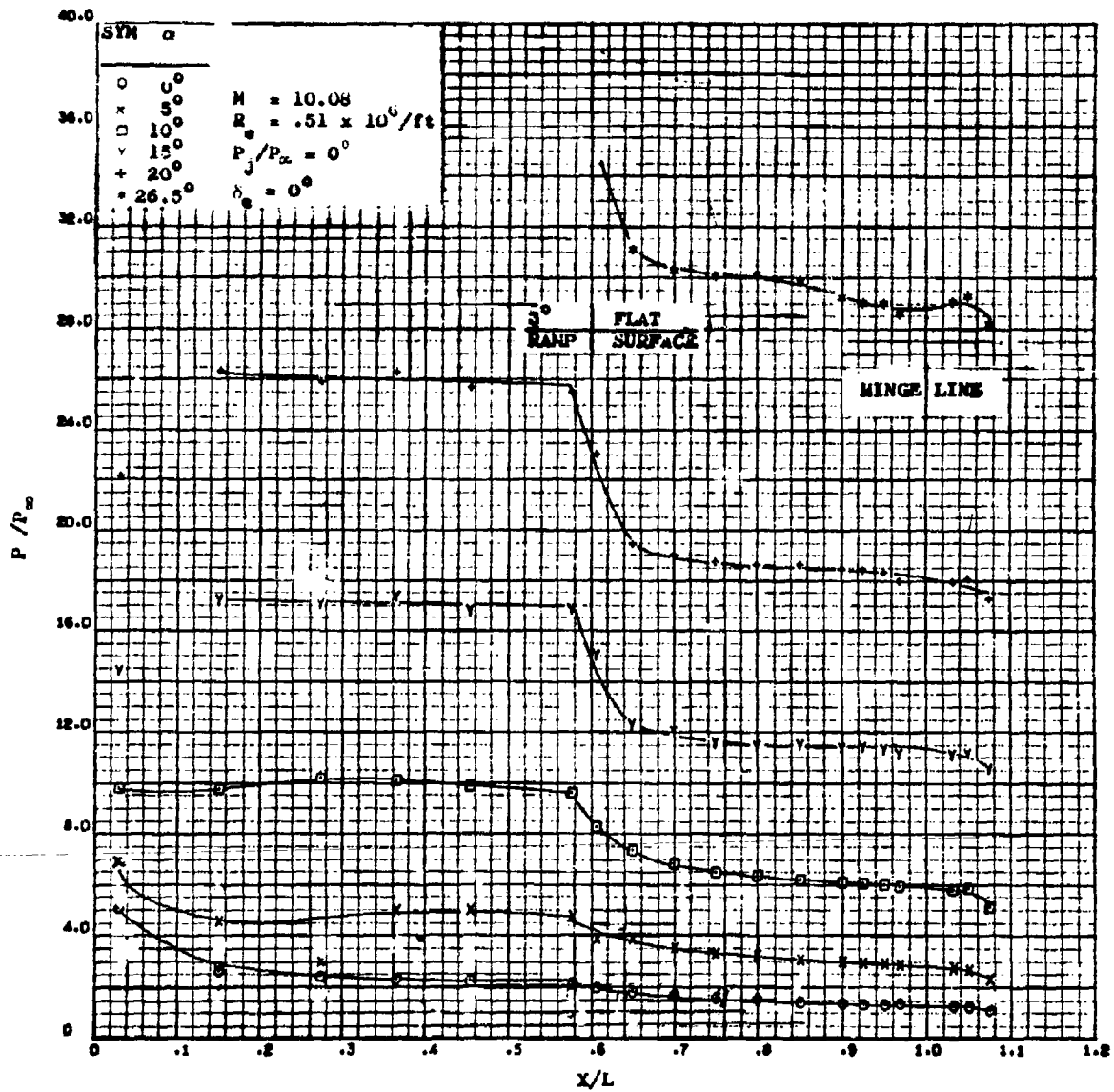


Figure 52. Delta Bottom Centerline Pressure Without a Plume at a Mach Number of 10

CONFIDENTIAL

CONFIDENTIAL

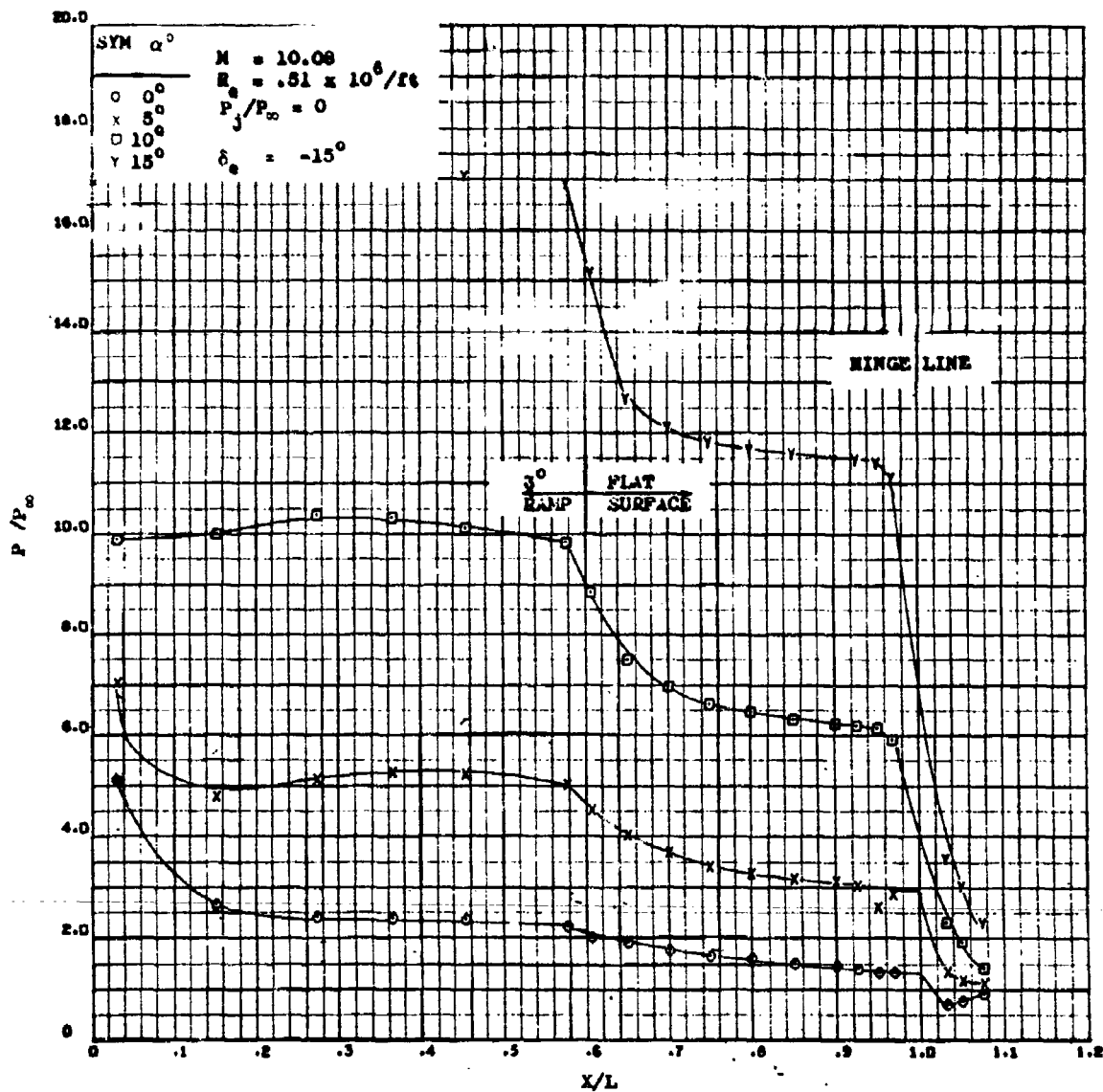


Figure 53. Effect of a -15 Degree Control Deflection on Delta Planform Bottom Centerline Pressure at Mach 10

CONFIDENTIAL

CONFIDENTIAL

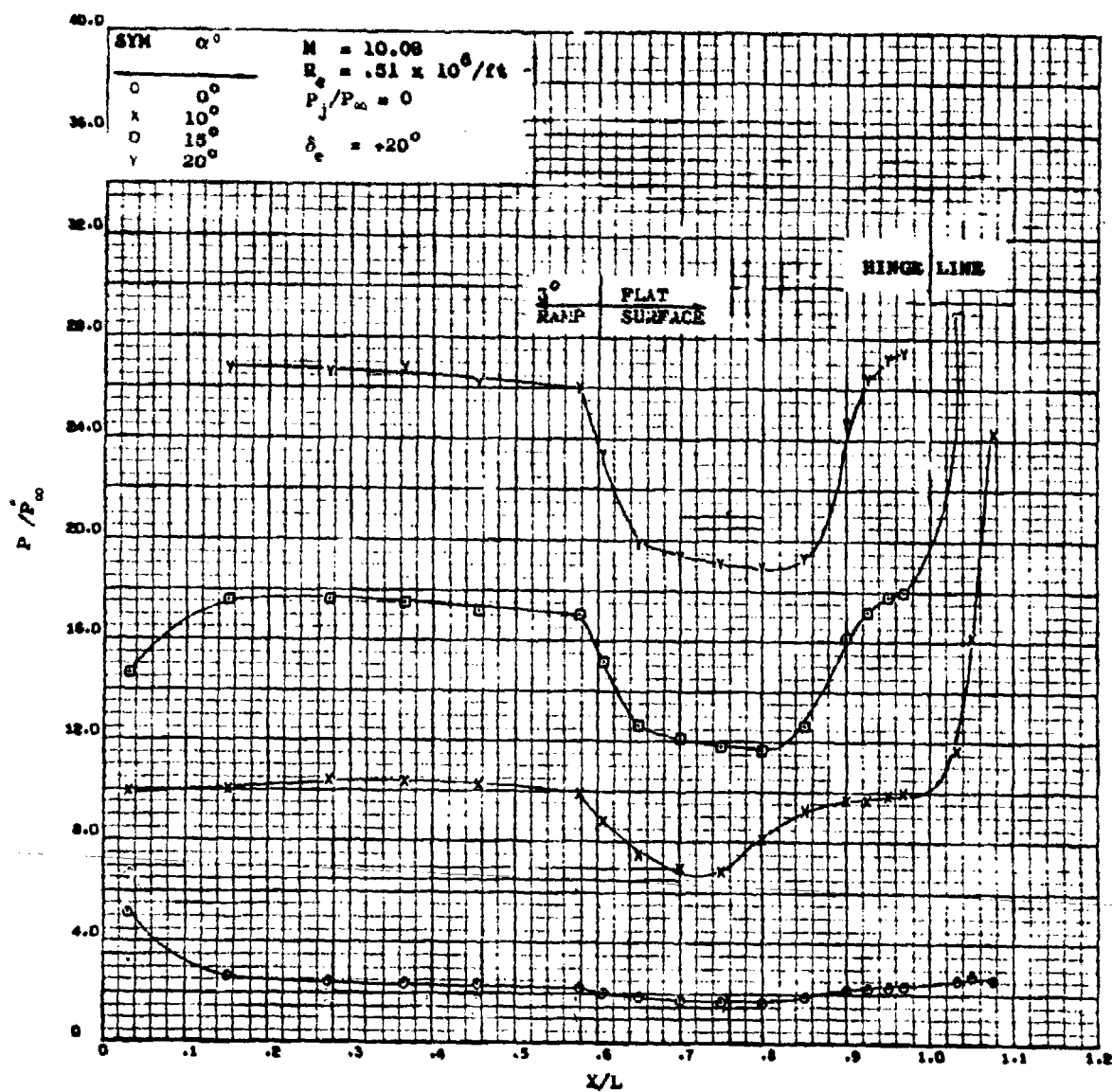


Figure 54. Effect of a +20 Degree Control Deflection on Delta Planform Bottom Centerline Pressure at a Mach Number of 10 and $P_j / P_\infty = 0$

CONFIDENTIAL

CONFIDENTIAL

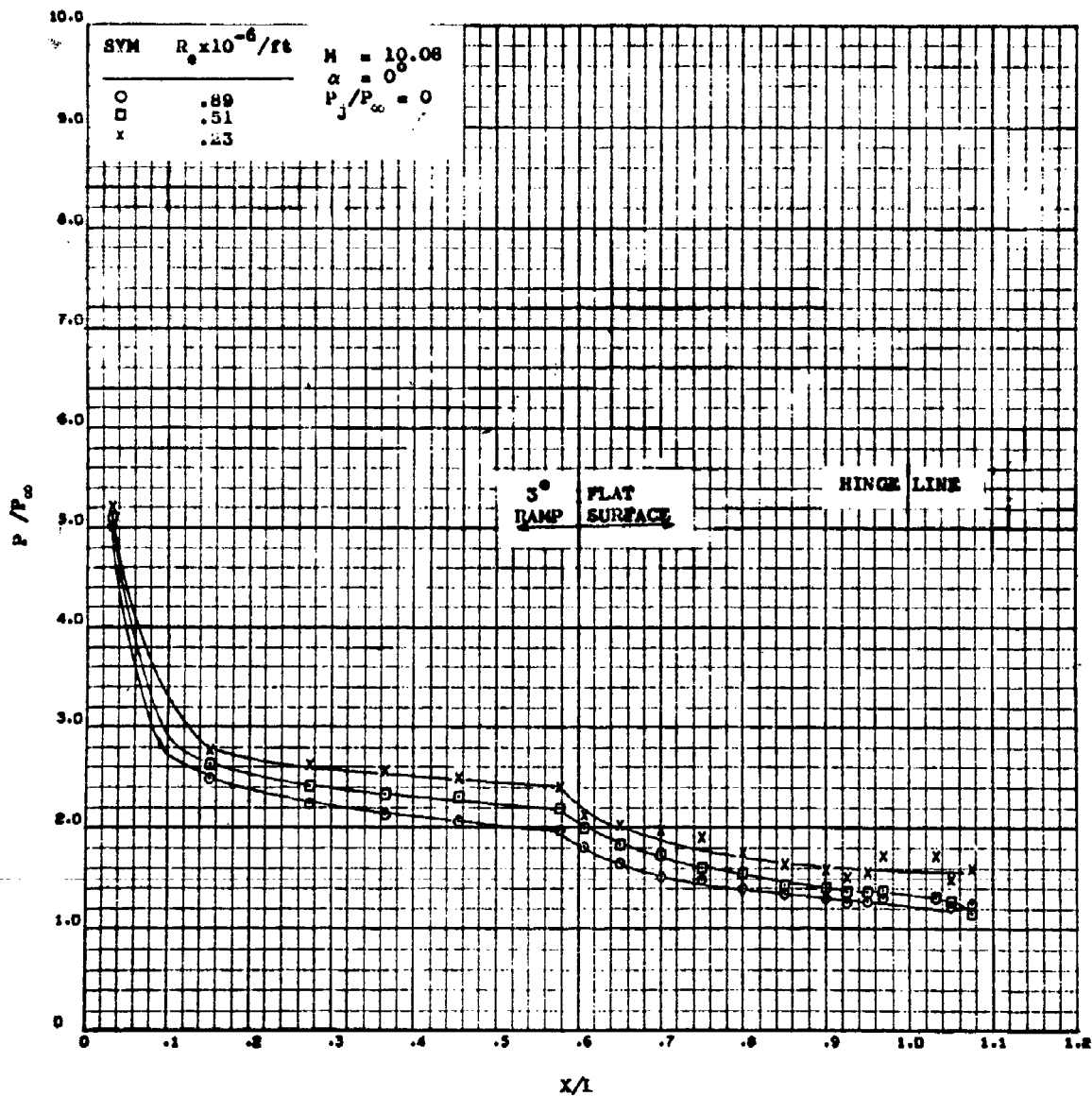


Figure 55. Effect of Reynolds Number on the Delta Planform Bottom Centerline Pressure at a Mach Number of 10 and $P_j/P_\infty = 0$

CONFIDENTIAL

CONFIDENTIAL

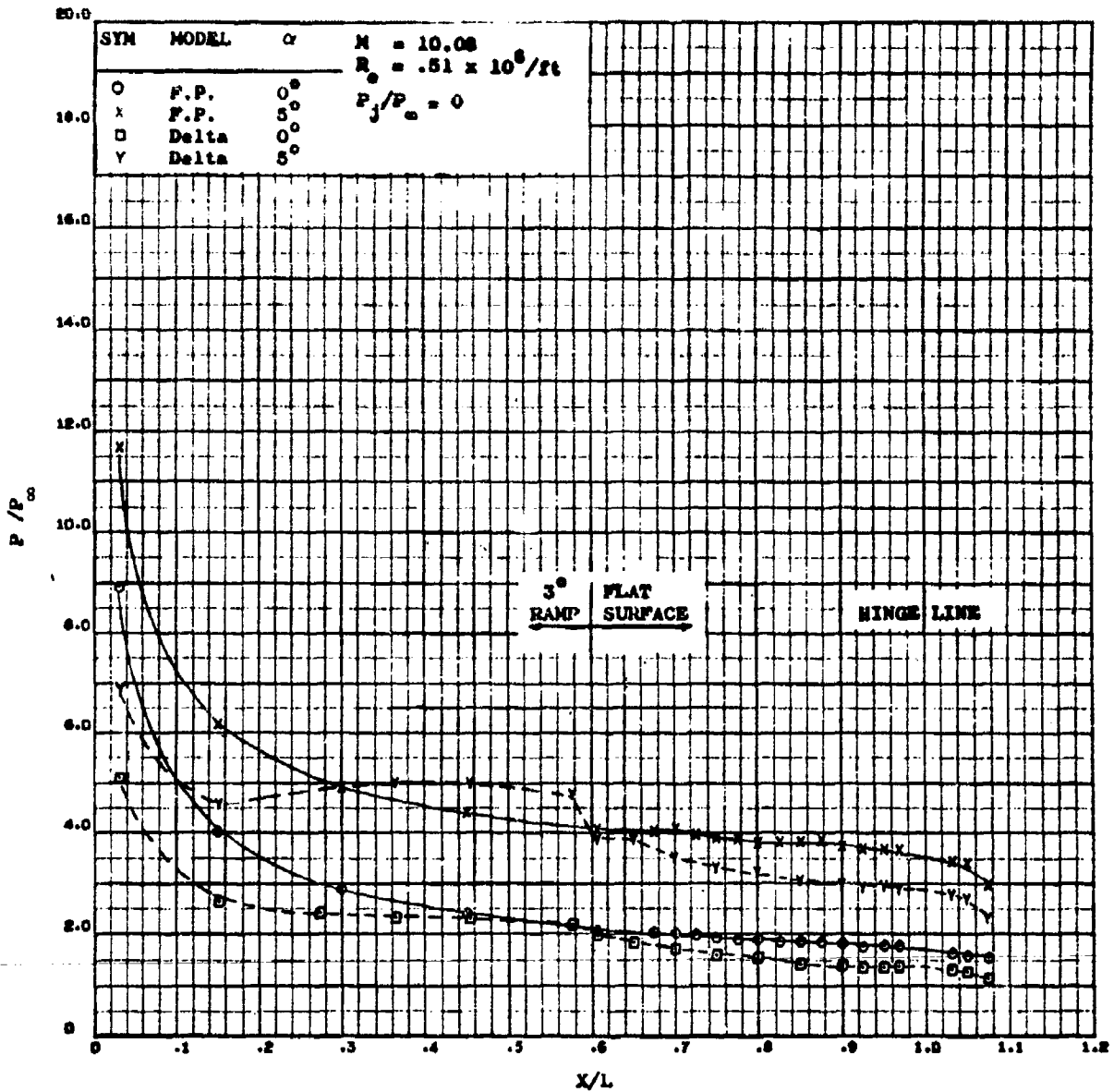


Figure 56. A Comparison of Centerline Pressure on the Bottom Centerline of the Flat Plate and Delta Configurations at $M = 10$ and $R_e = .5 \times 10^6 / ft$

CONFIDENTIAL

CONFIDENTIAL

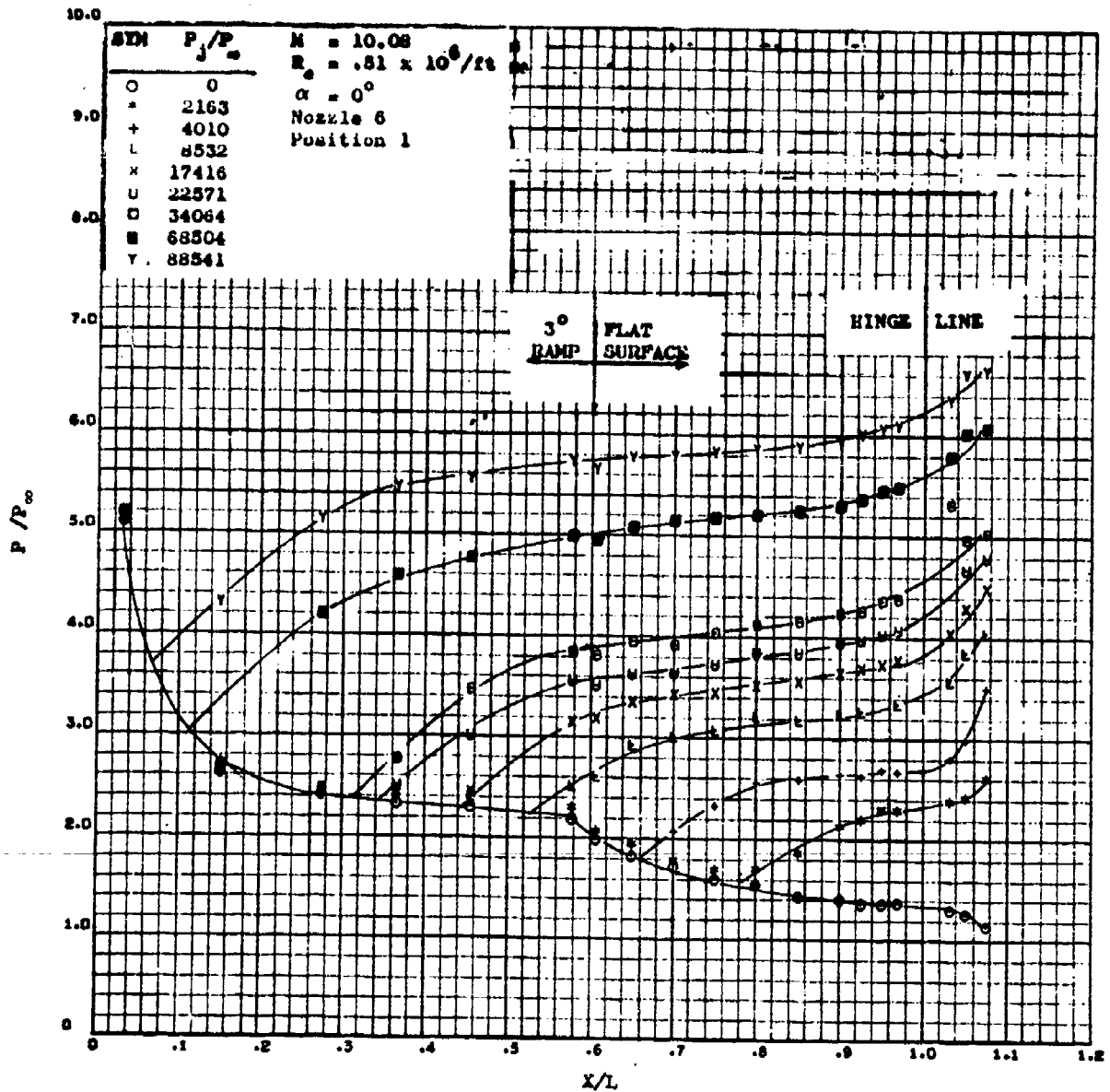
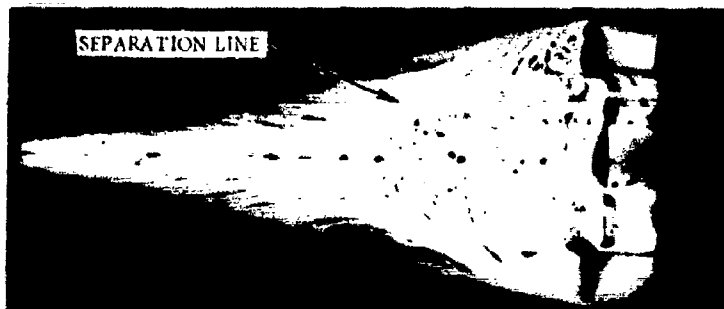


Figure 57. Effect of Jet Pressure Ratio on Bottom Centerline Pressure on the Delta Planform at a Mach Number of 10 and Zero Angle of Attack for Nozzle 6

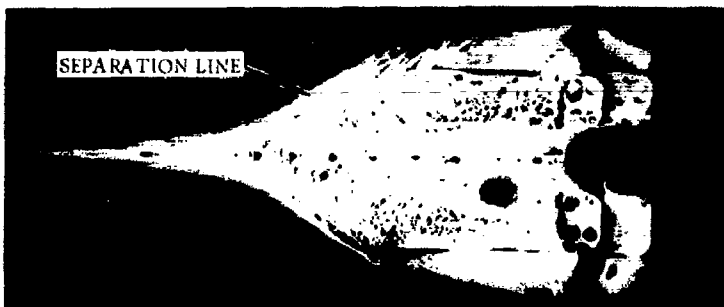
CONFIDENTIAL

CONFIDENTIAL

(This page is Unclassified)



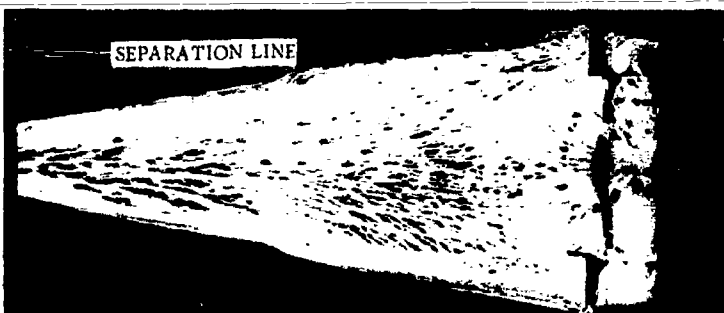
$$P_j/P_\infty = 8500$$



$$P_j/P_\infty = 17000$$



$$P_j/P_\infty = 34000$$



$$P_j/P_\infty = 89000$$

NOZZLE 6, POSITION 1
 $\alpha = 0^\circ$, $Re = 0.5 \times 10^6$, $M_\infty = 10.1$

Figure 58. Oil Flow Visualization of the Effect of Jet Pressure Ratio on the Delta Configuration

118
 CONFIDENTIAL
 (This page is Unclassified)

CONFIDENTIAL

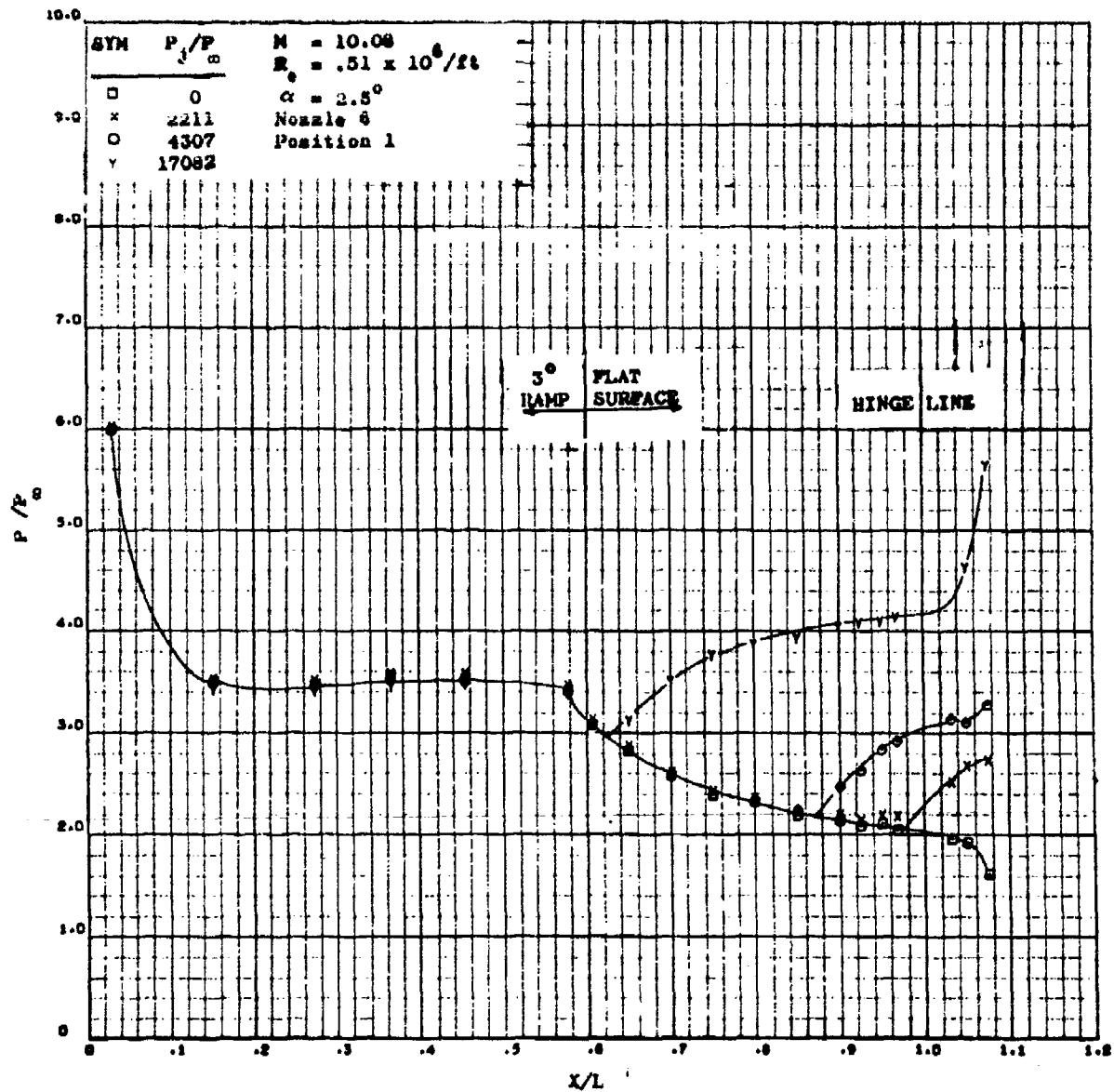


Figure 59. Effect of Jet Pressure Ratio on Bottom Centerline Pressure on the Delta Planform at a Mach Number of 10 and 2.5° Angle of Attack for Nozzle 6

CONFIDENTIAL

CONFIDENTIAL

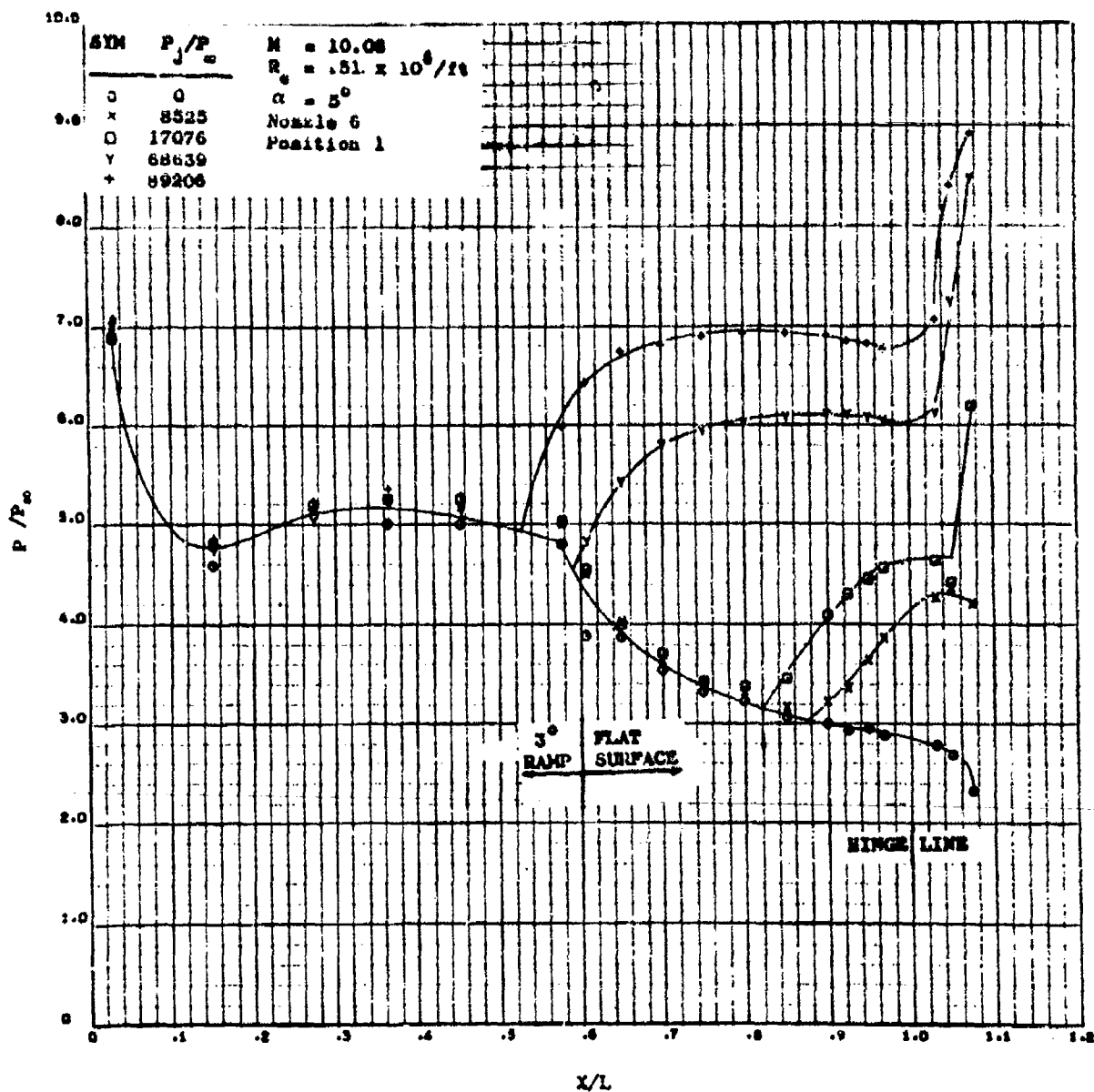


Figure 60. Effect of Jet Pressure Ratio on Bottom Centerline Pressure on the Delta Planform at Mach 10 and 5° Angle of Attack

CONFIDENTIAL

CONFIDENTIAL

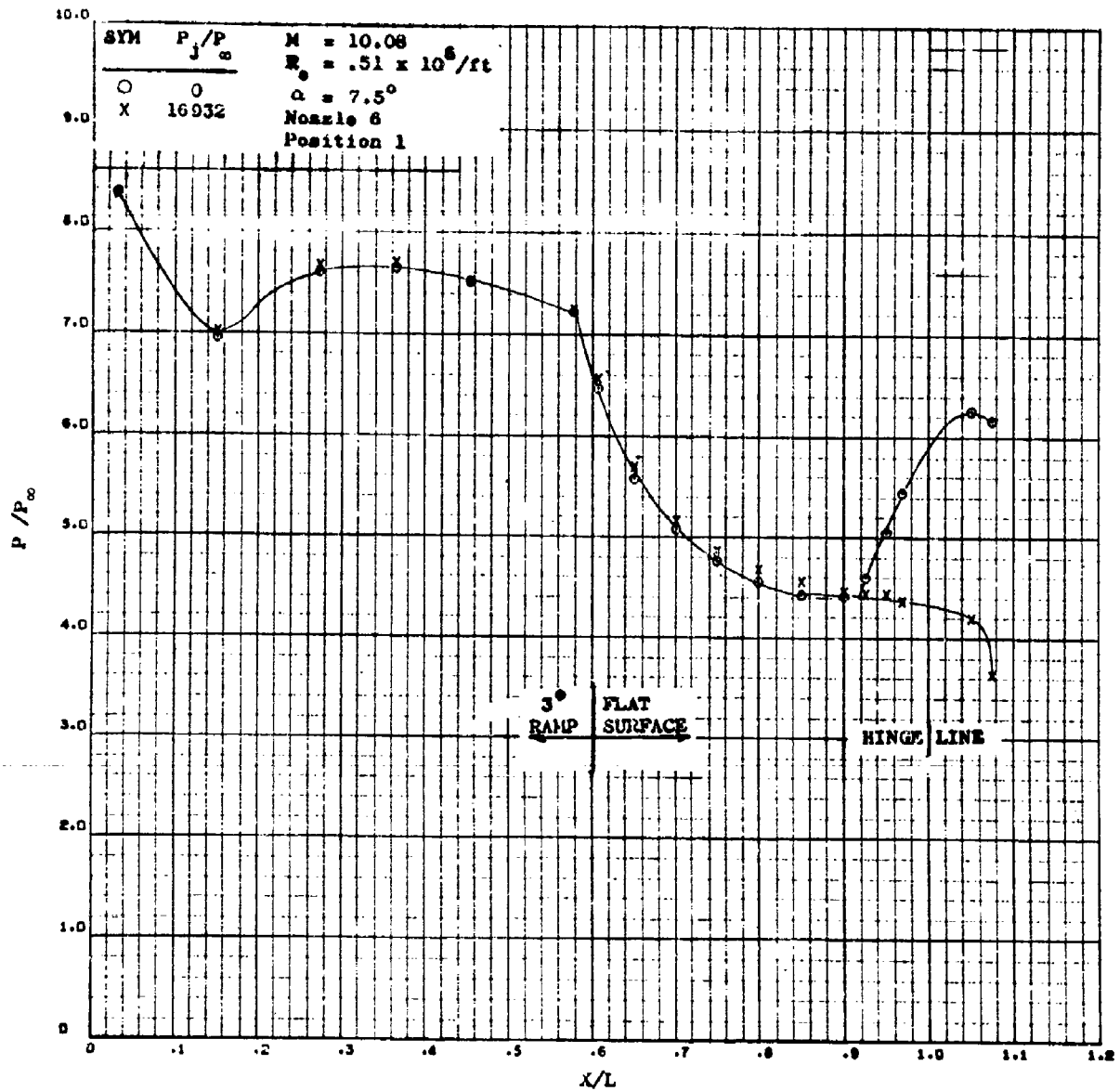


Figure 21. Effect of Jet Pressure Ratio on Bottom Centerline Pressure, on the Delta Planform at Mach 10 and 7.5 degree Angle of Attack

CONFIDENTIAL

CONFIDENTIAL

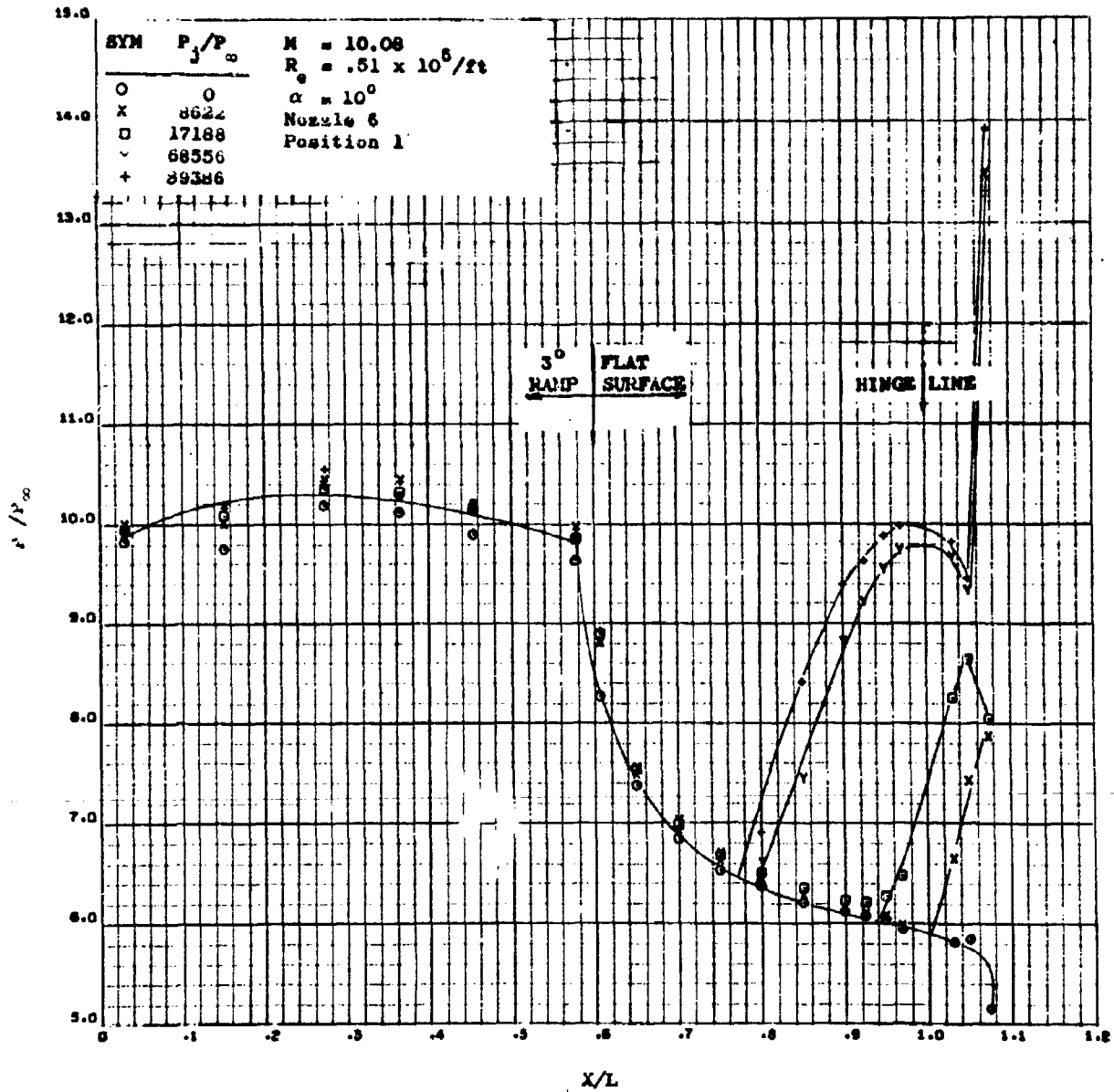


Figure 62. Effect of Jet Pressure Ratio on Delta Bottom Centerline Pressure at Mach 10 and 10° Angle of Attack

CONFIDENTIAL

CONFIDENTIAL

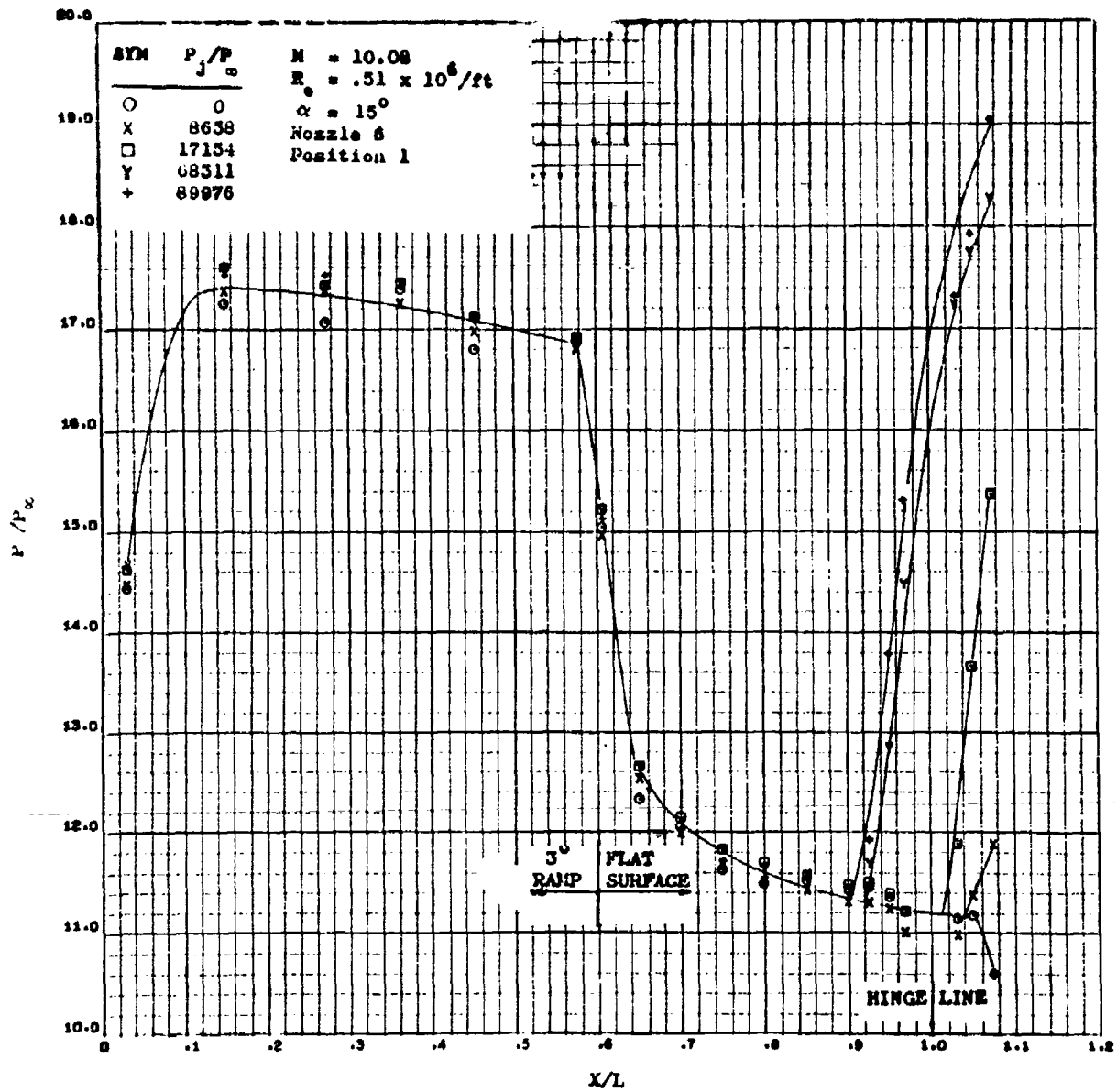


Figure 63. Effect of Jet Pressure Ratio in Delta Bottom Centerline Pressure at Mach 10 and 15° Angle of Attack

CONFIDENTIAL

CONFIDENTIAL

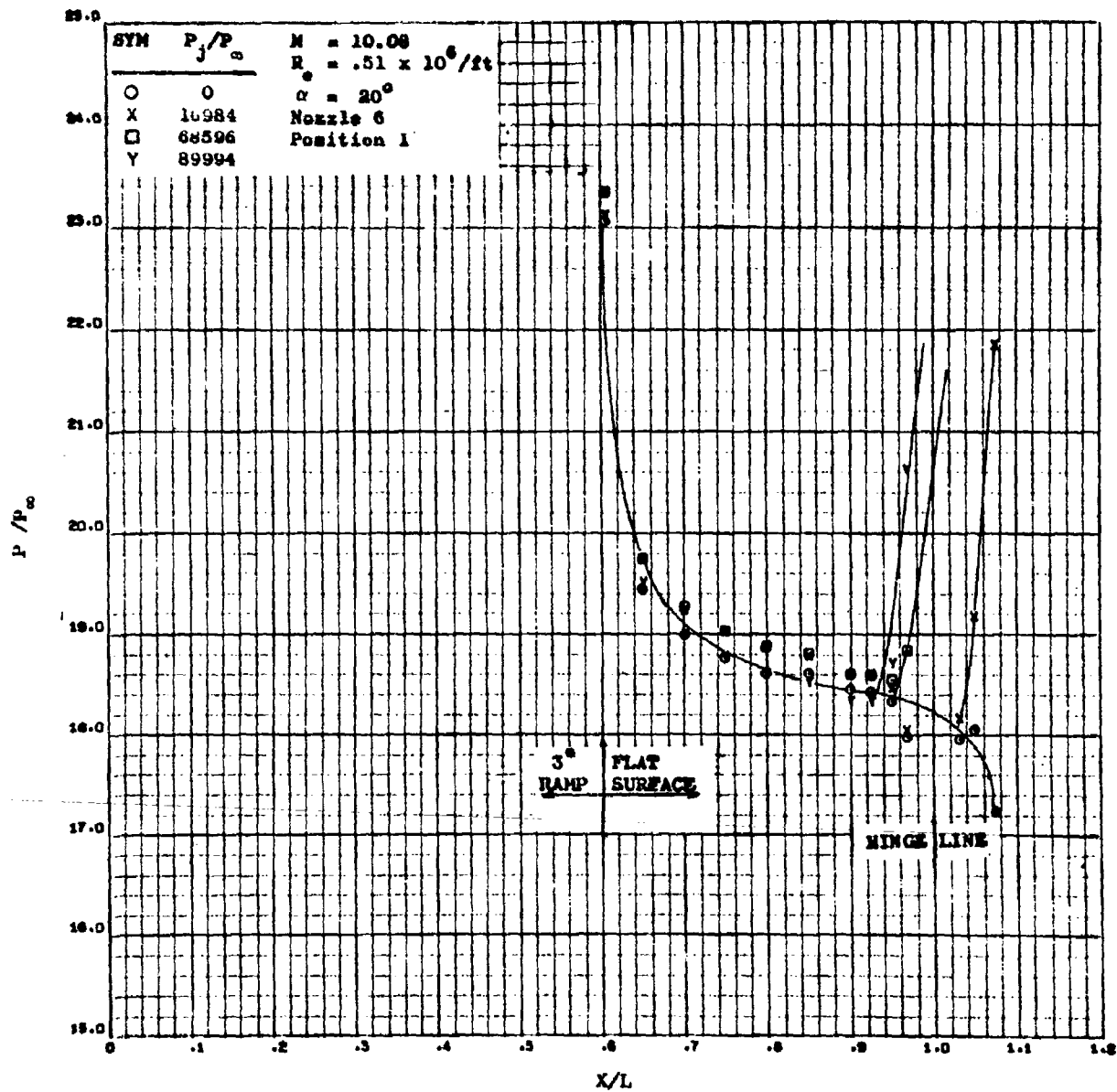


Figure 64. Effect of Jet Pressure Ratio on Delta Bottom Centerline Pressure at Mach 10 and 20° Angle of Attack

CONFIDENTIAL

CONFIDENTIAL

$M = 10.08$
 $R_e = .51 \times 10^6 / ft$
Nozzle 6
Position 1

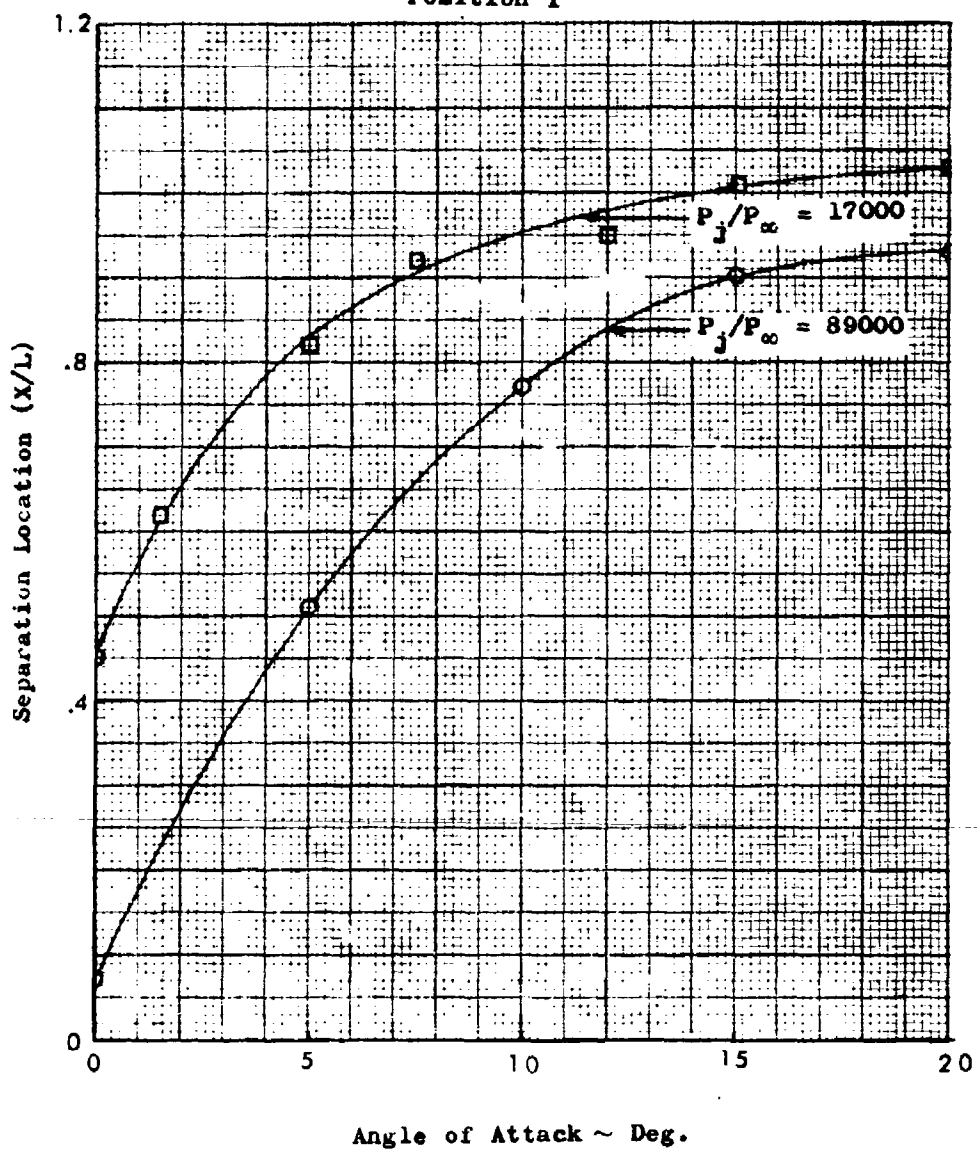
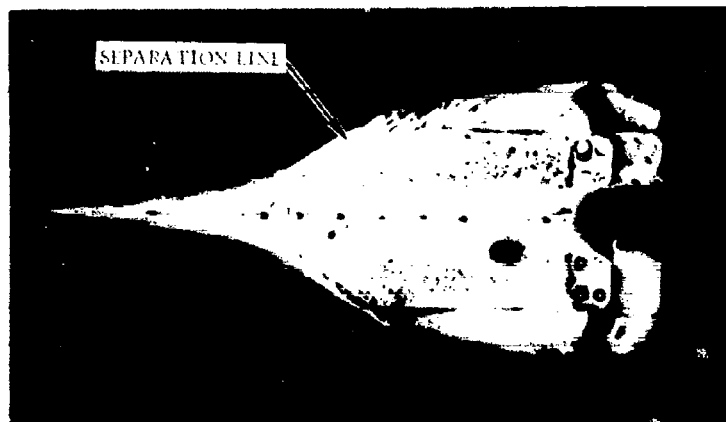


Figure 65. Angle of Attack Effect on Separation Location at Mach 10

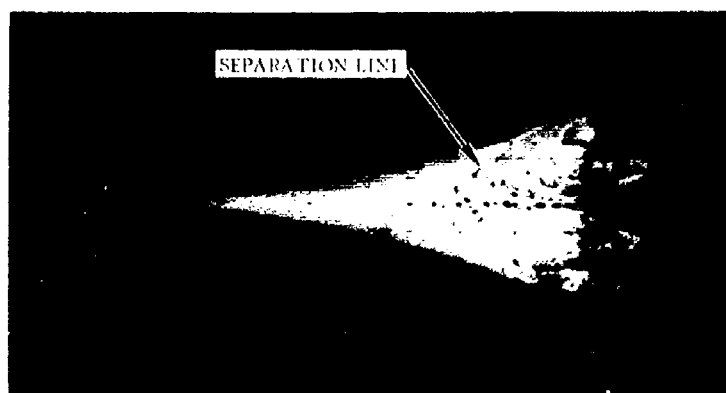
CONFIDENTIAL

CONFIDENTIAL

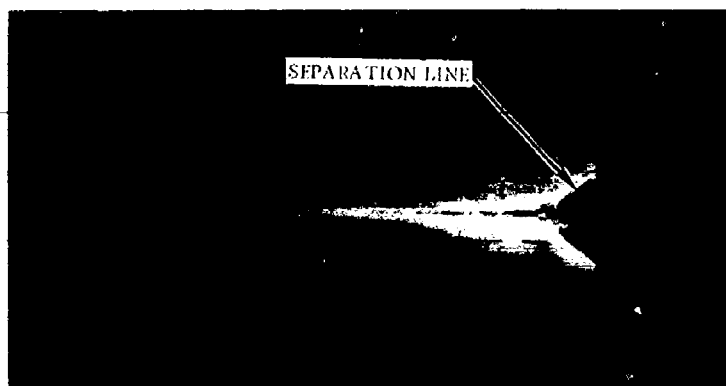
(This page is Unclassified)



$\alpha = 0^\circ$



$\alpha = 2.5^\circ$



$\alpha = 5^\circ$

NOZZLE 6, POSITION 1

$P_j/P_\infty = 1.600$, $Re = 0.5 \times 10^6$, $M = 10.1$

Figure 66. Flow Visualization of the Effect of Angle of Attack on Plume-induced Separation

126

CONFIDENTIAL

(This page is Unclassified)

CONFIDENTIAL

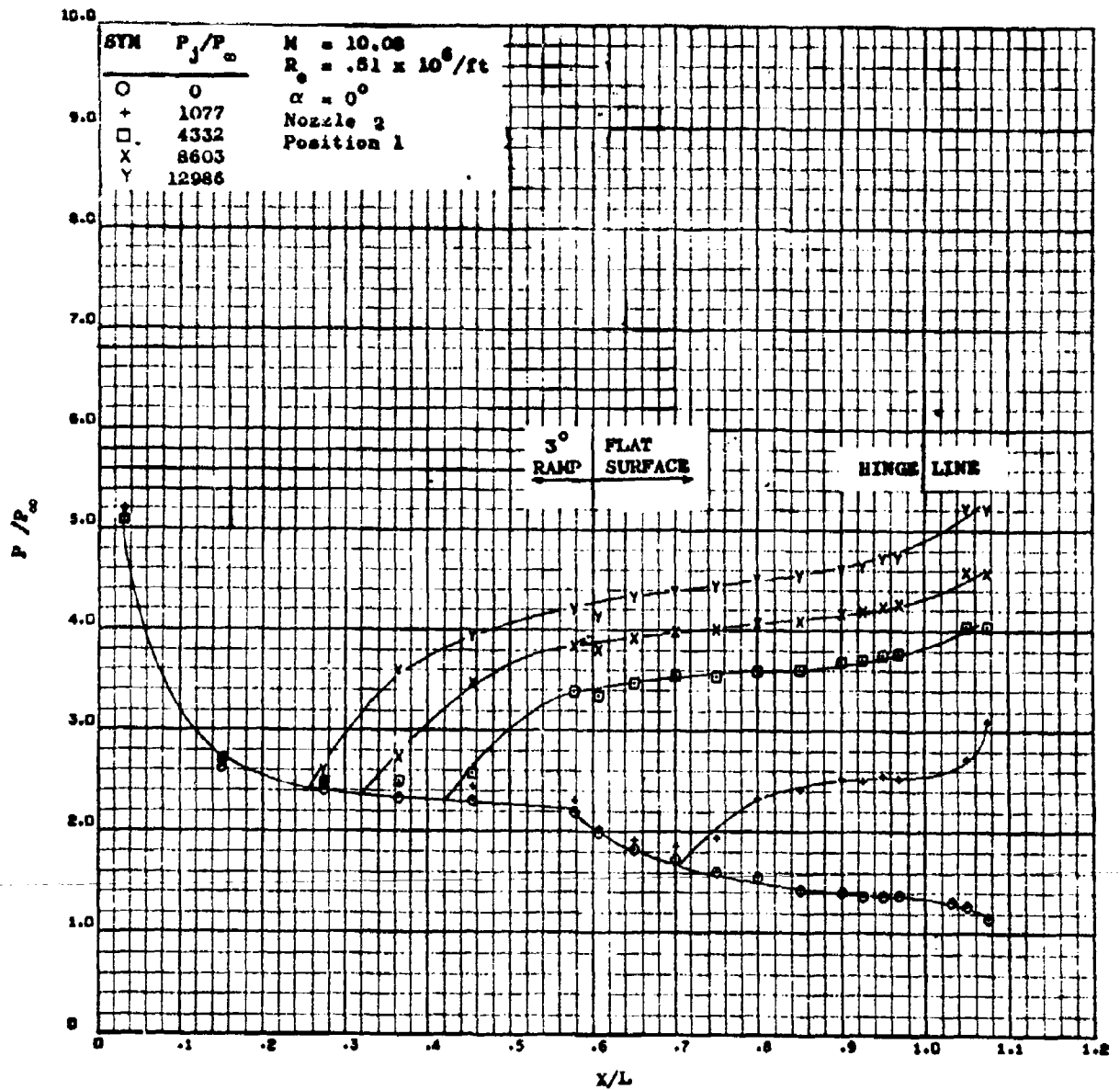
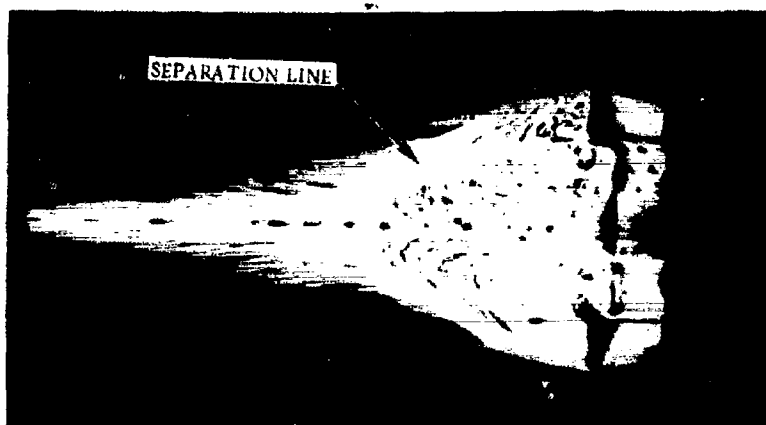


Figure 67. Effect of Jet Pressure Ratio on Bottom Centerline Pressure on the Delta Planform at a Mach Number of 10 and Zero Angle of Attack for Nozzle 2

CONFIDENTIAL

CONFIDENTIAL

(This page is Unclassified)



$$A/A_0 = 1$$



$$\frac{A}{A_0} = 2.25$$

NOZZLE POSITION 1

P_j/P_∞ 8500

α 0 DEGREE

Re 0.5×10^6 /FT

M 10.1

Figure 68. Flow Visualization of the Effect of Nozzle Expansion Ratio on Plume-Induced Separation

128
CONFIDENTIAL
(This page is Unclassified)

CONFIDENTIAL

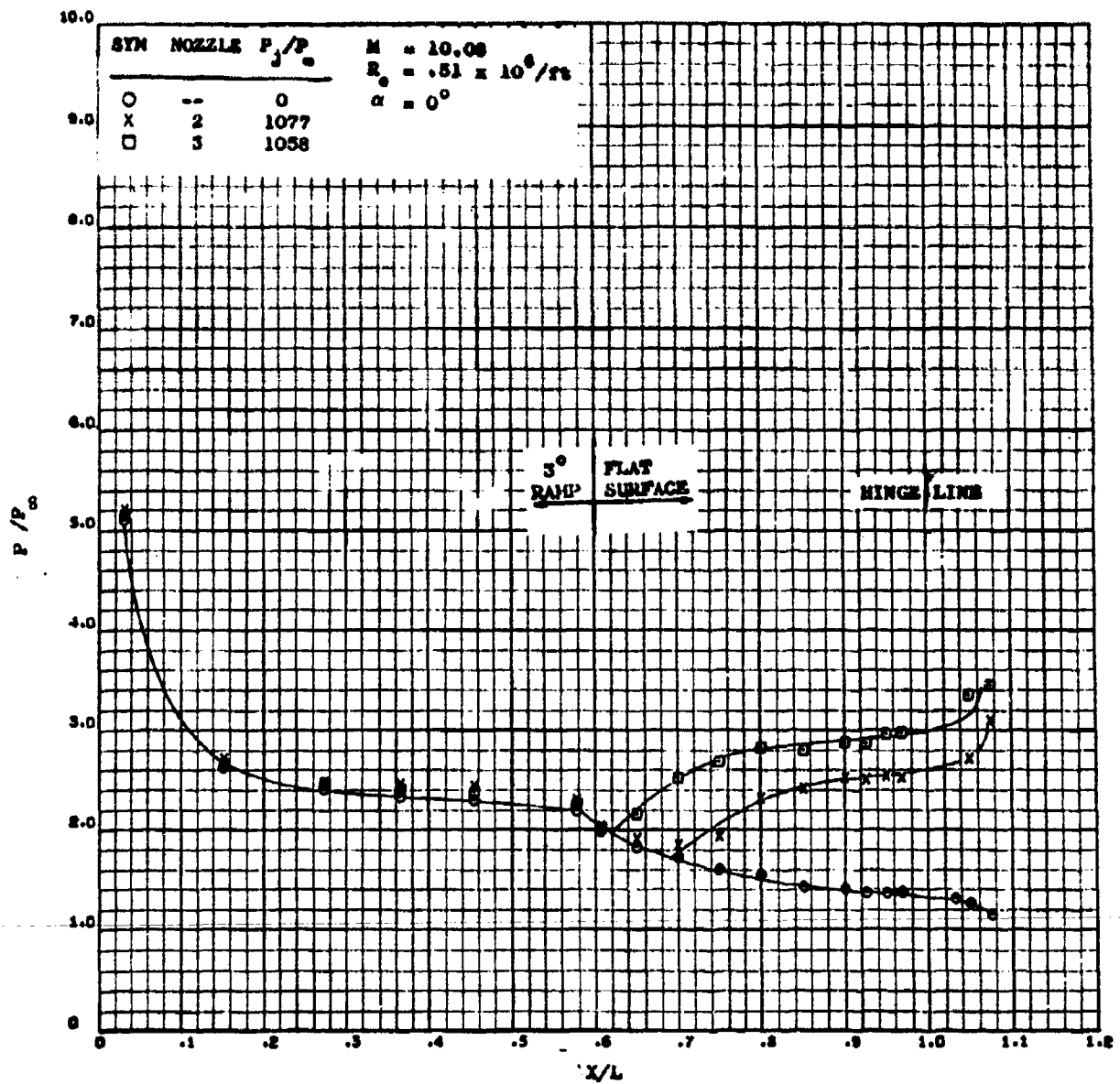


Figure 69. Effect of Nozzle Expansion Ratio on Bottom Centerline

CONFIDENTIAL

CONFIDENTIAL

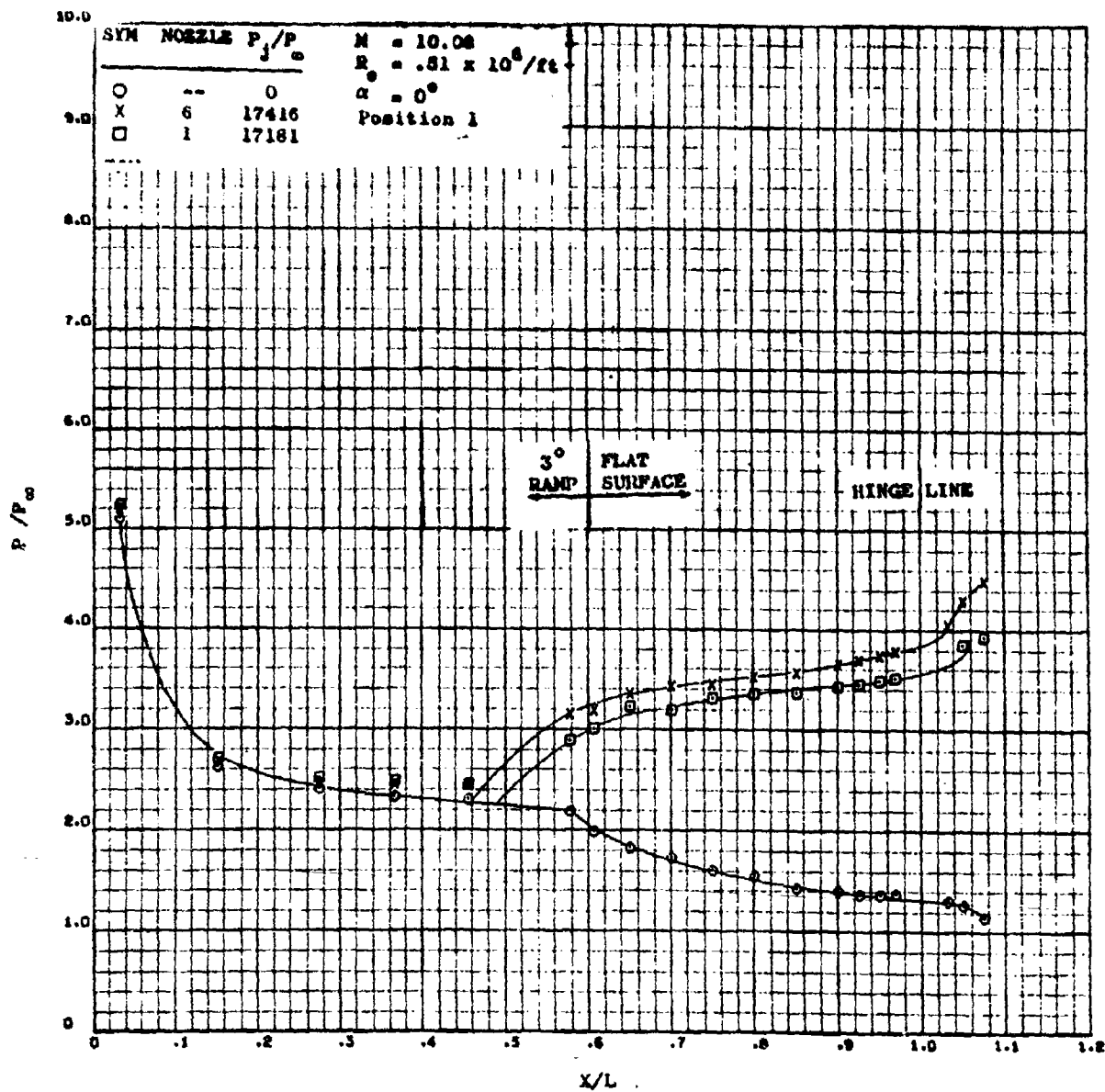


Figure 70. Effect of Nozzle Size on Bottom Centerline Pressure on the Delta Planform at a Mach Number of 10 and Zero Angle of Attack

CONFIDENTIAL

CONFIDENTIAL

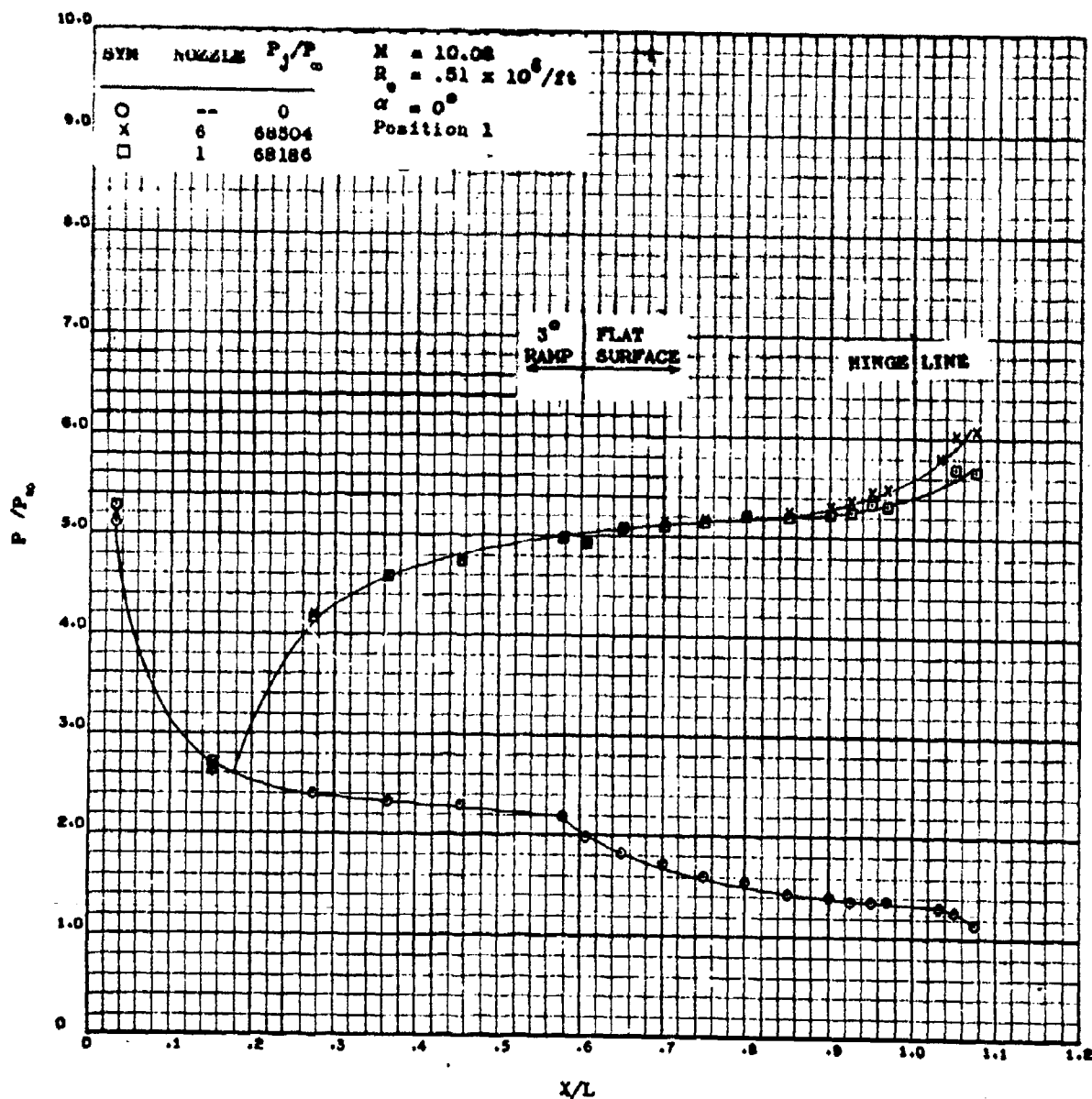


Figure 71. Effect of Nozzle Size on Bottom Centerline Pressure on the Delta Planform at a Mach Number of 10 and Zero Angle of Attack

CONFIDENTIAL

CONFIDENTIAL

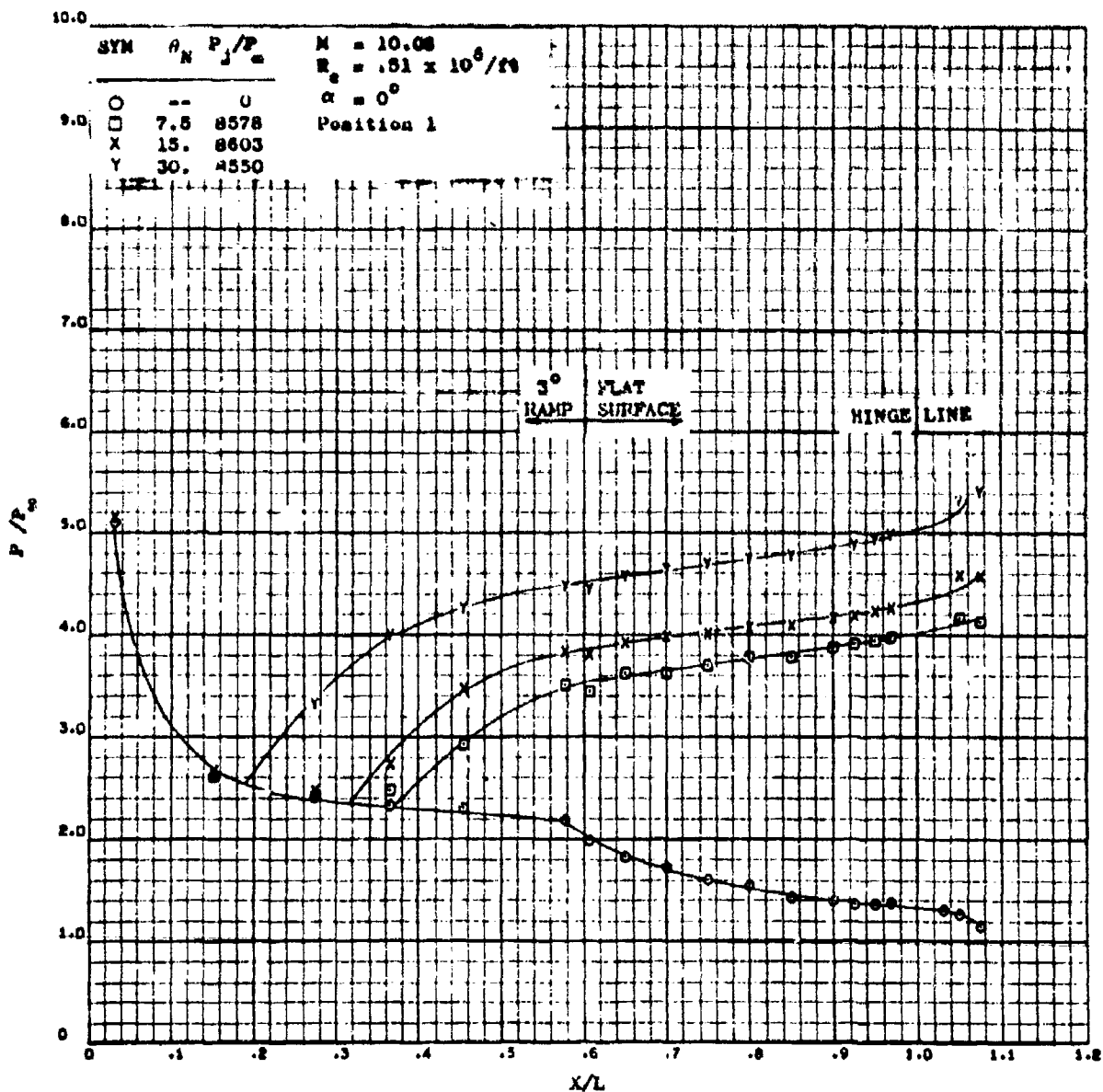


Figure 72. Effect of Nozzle Exit Angle on Bottom Centerline Pressure on the Delta Planform at a Mach Number of 10 and Zero Angle of Attack

CONFIDENTIAL

CONFIDENTIAL

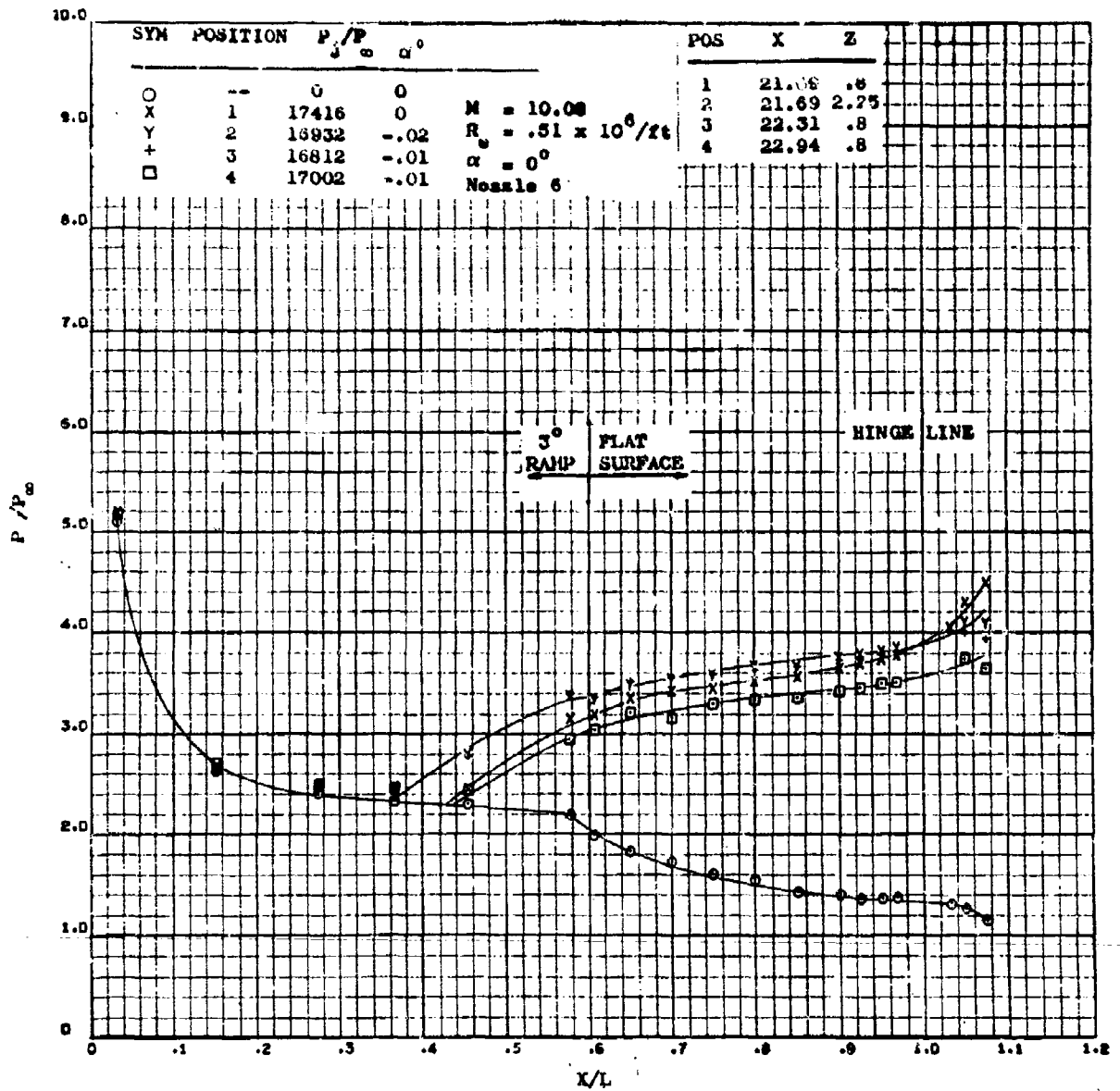
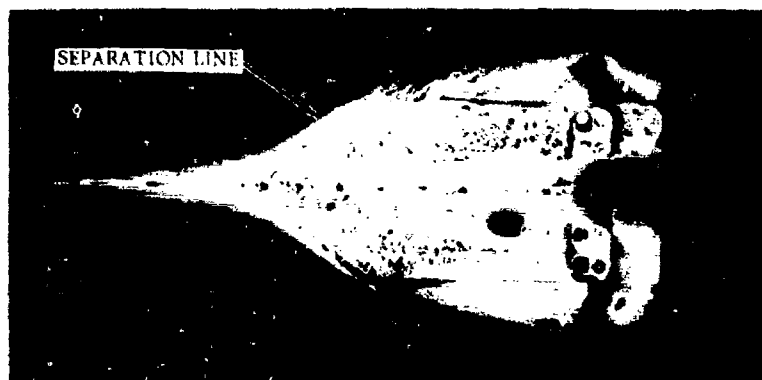


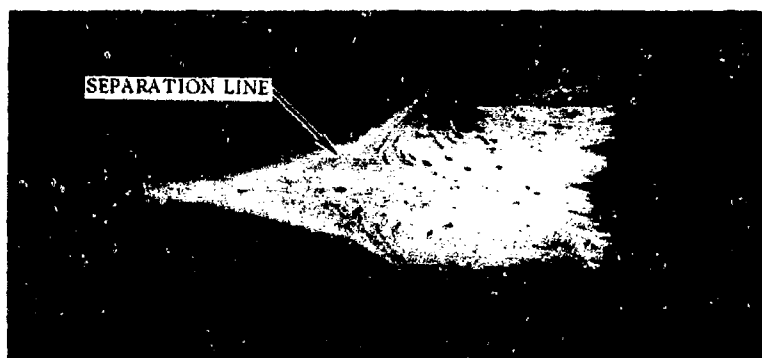
Figure 73. Effect Nozzle Position on Bottom Centerline Pressure on the Delta Planform at a Mach Number of 10 and Zero Angle of Attack

CONFIDENTIAL

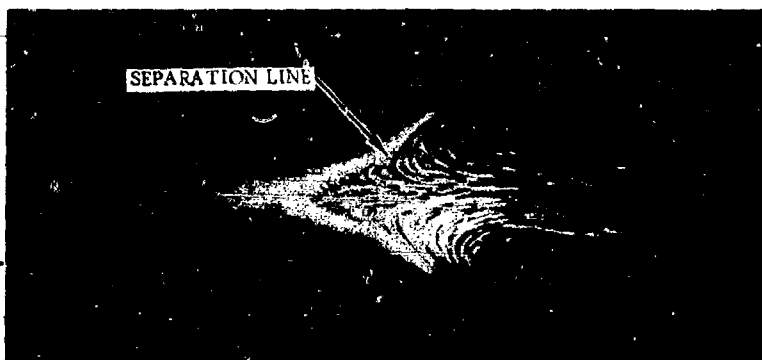
CONFIDENTIAL
(This page is Unclassified)



NOZZLE EXIT
STATION 21.69



STATION 22.315



STATION 22.94

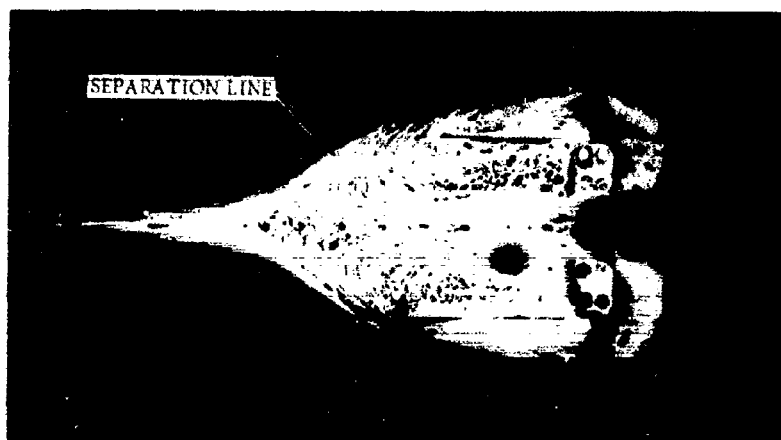
NOZZLE 6, VERTICAL POSITION ON MWL
 $\alpha = 0^\circ$, $Re = 1.5 \times 10^6/ft$
 $M = 10.1$, $P_j/P_\infty = 17000$

Figure 74. Oil Flow Visualization of the Effect of Nozzle Axial
Location on Separation on the Delta Configuration

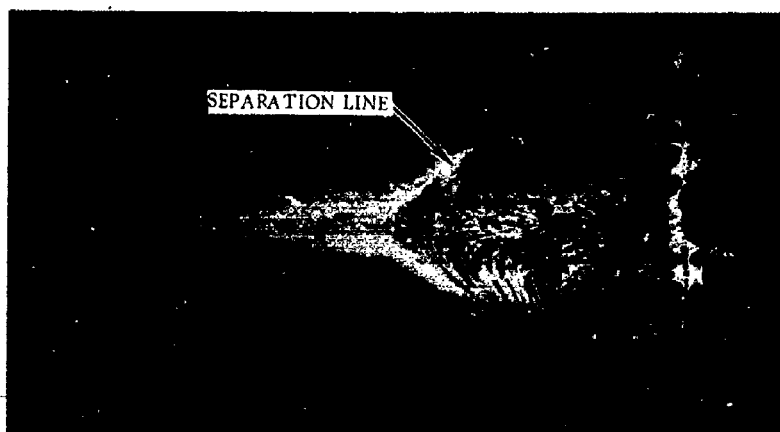
134

CONFIDENTIAL
(This page is Unclassified)

CONFIDENTIAL
(This page is Unclassified)



NOZZLE VERTICAL
POSITION
MWL .8



MWL 2.25

NOZZLE EXIT AT 21.69, NOZZLE 6
 $\alpha = 0$ DEGREE
 $P_1/P_\infty = 17000$
 $Re = 1.5 \times 10^6/FT$
 $M = 10.1$

Figure 75. Oil Flow Visualization of the Effect of Nozzle Vertical Position on the Separation of the Delta Configuration

135
CONFIDENTIAL
(This page is Unclassified)

CONFIDENTIAL

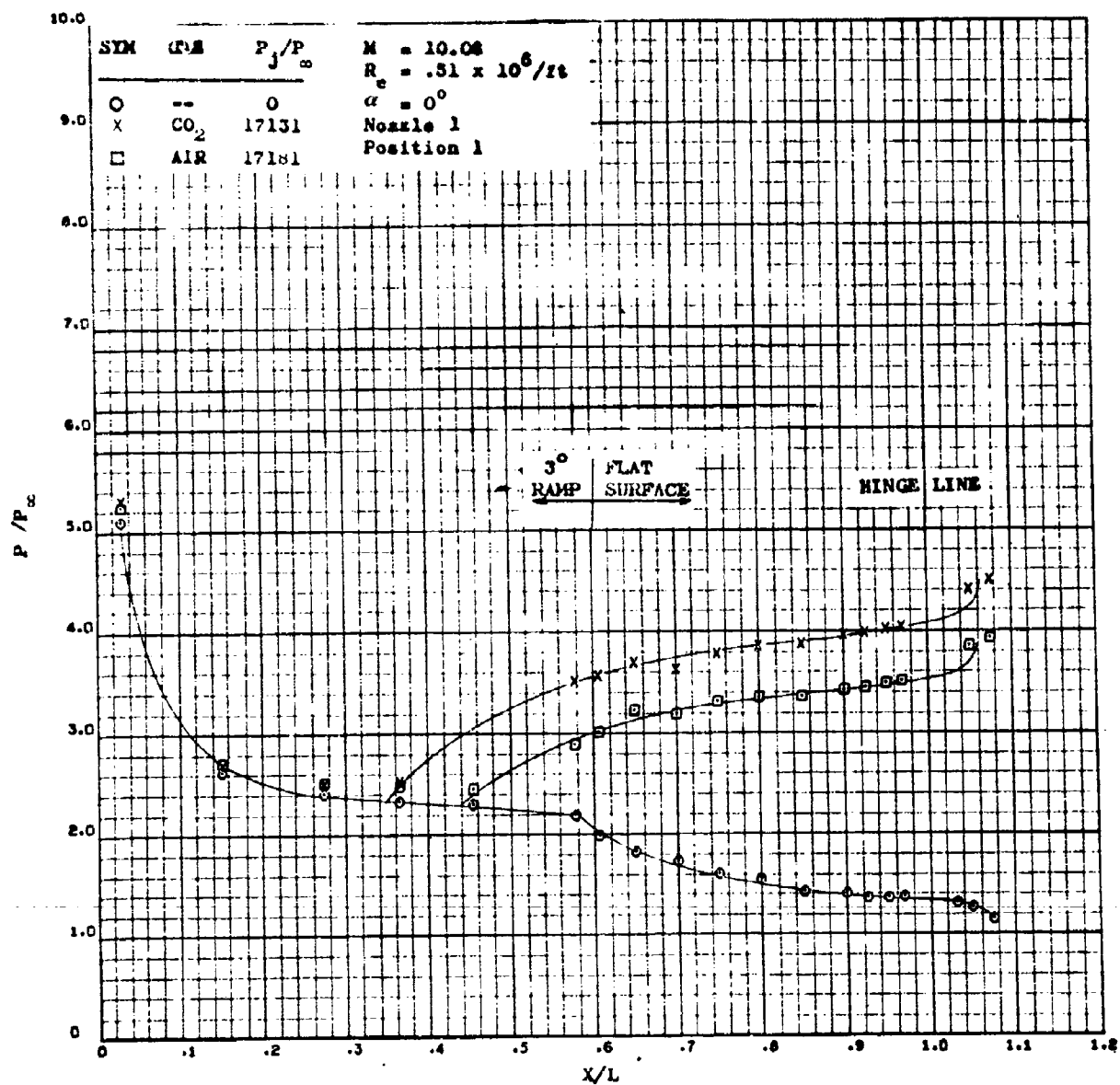


Figure 76. Effect of Exhaust Gas on Bottom Centerline Pressure on the Delta Planform at a Mach Number of 10 and Zero Angle of Attack

CONFIDENTIAL

CONFIDENTIAL

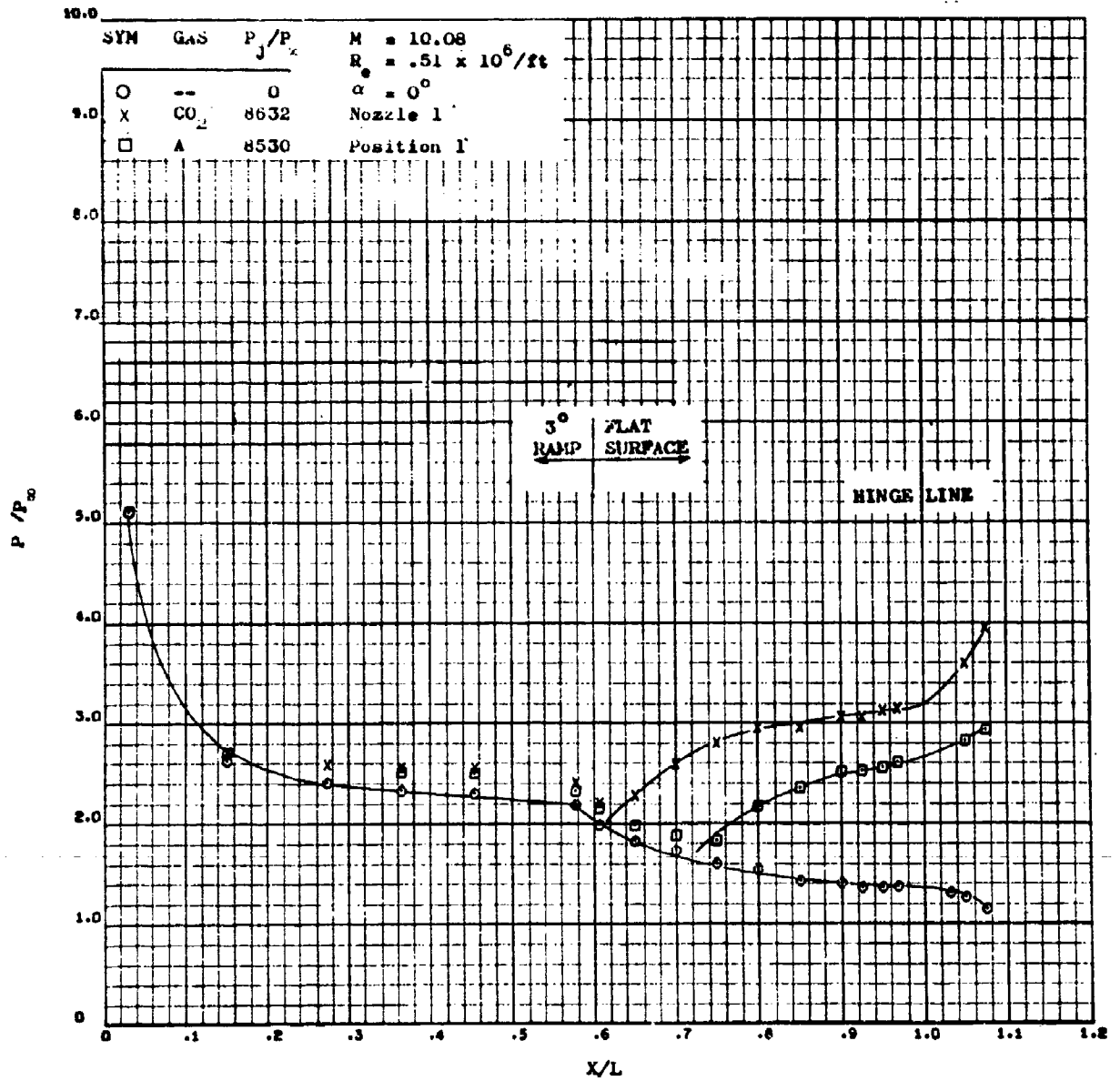


Figure 77. Effect of Exhaust Gas on Bottom Centerline Pressure on the Delta Planform at a Mach Number of 10 and Zero Angle of Attack

CONFIDENTIAL

CONFIDENTIAL

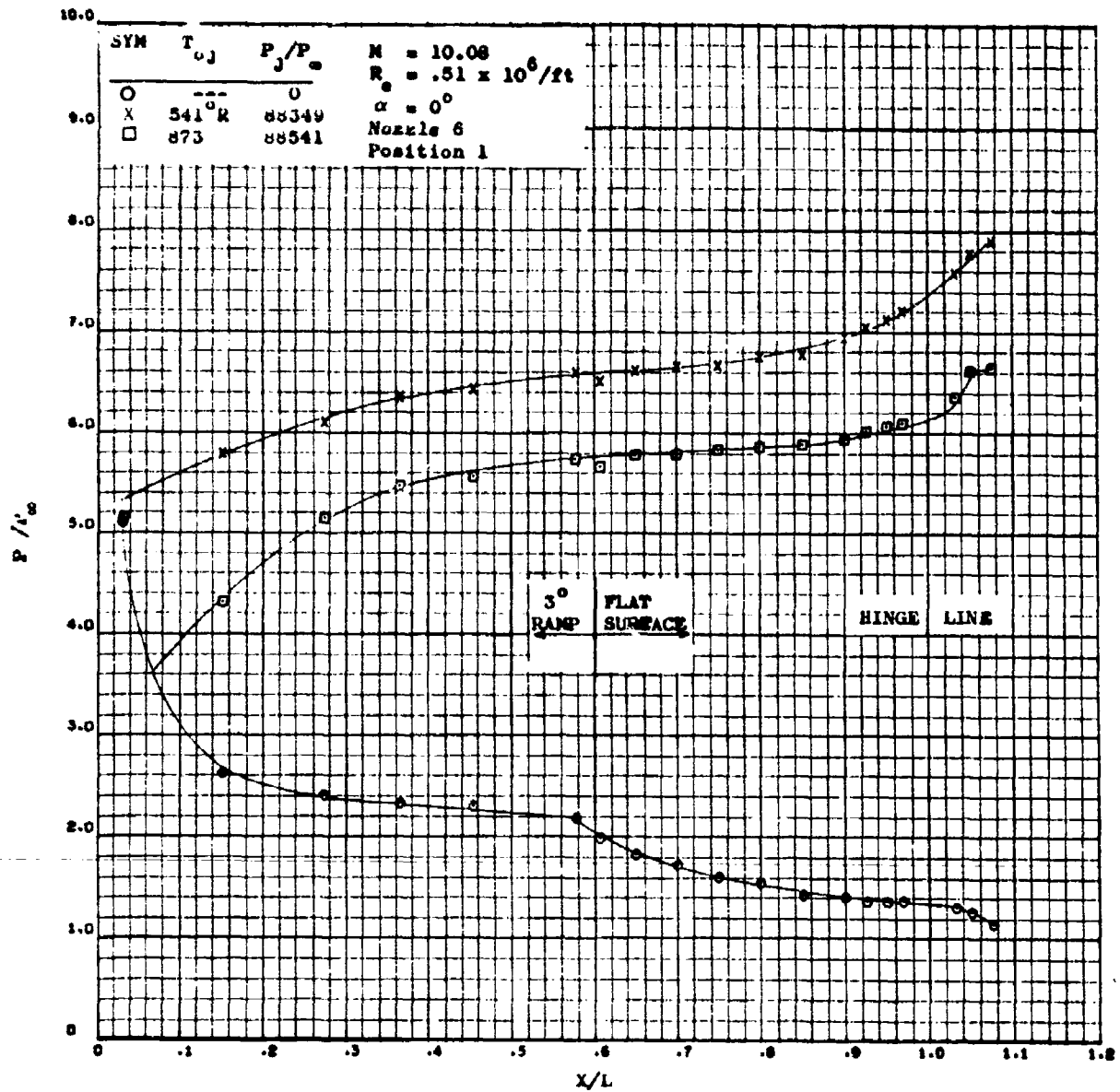


Figure 7B. Effect of Gas Supply Temperature on Plume Induced Separation at Mach 10 for $P_j/P_\infty = 88500$

CONFIDENTIAL

CONFIDENTIAL

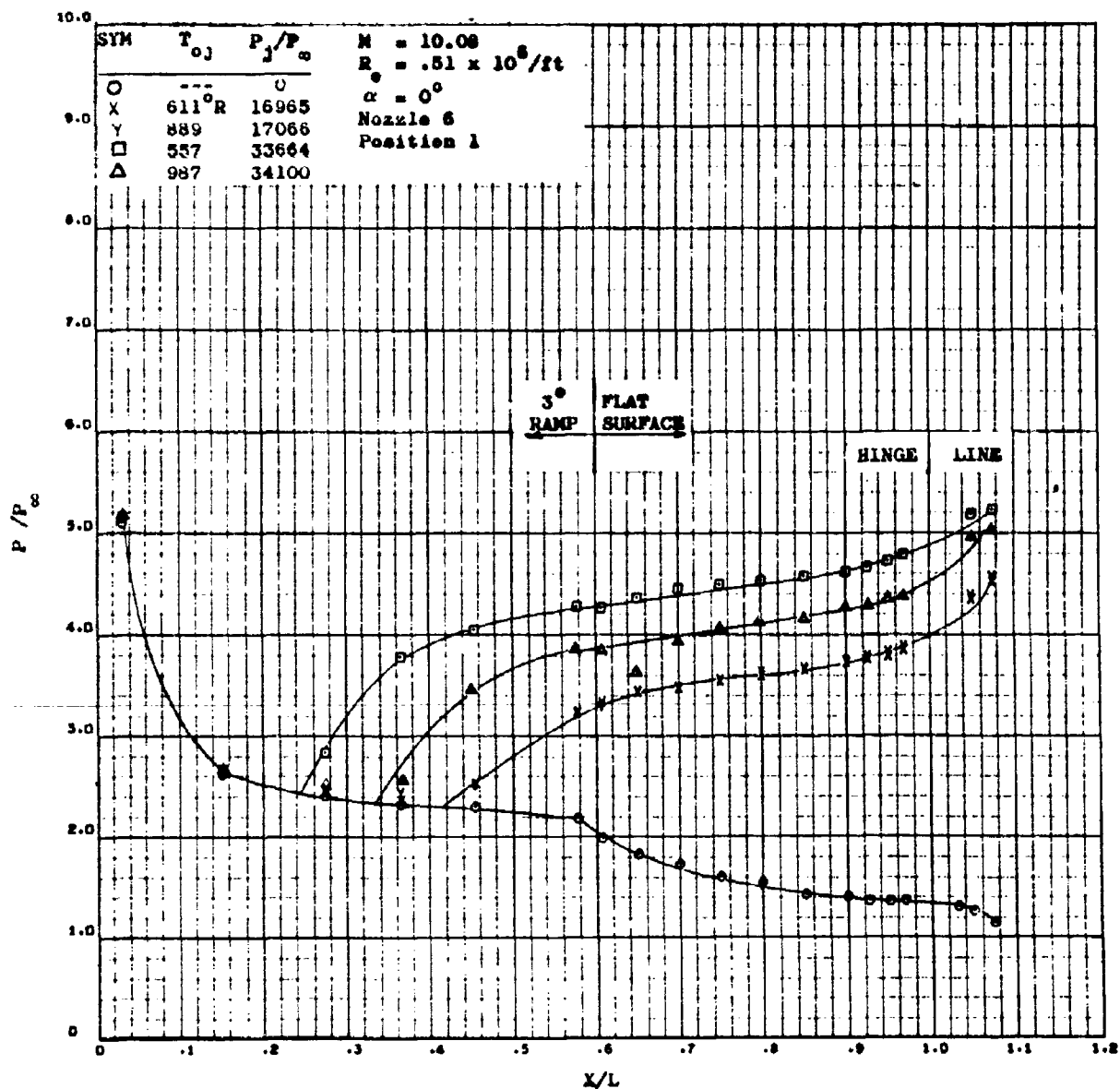


FIGURE 70. Effect of Gas Supply Temperature on Plume Induced Separation at Mach 10.

CONFIDENTIAL

CONFIDENTIAL

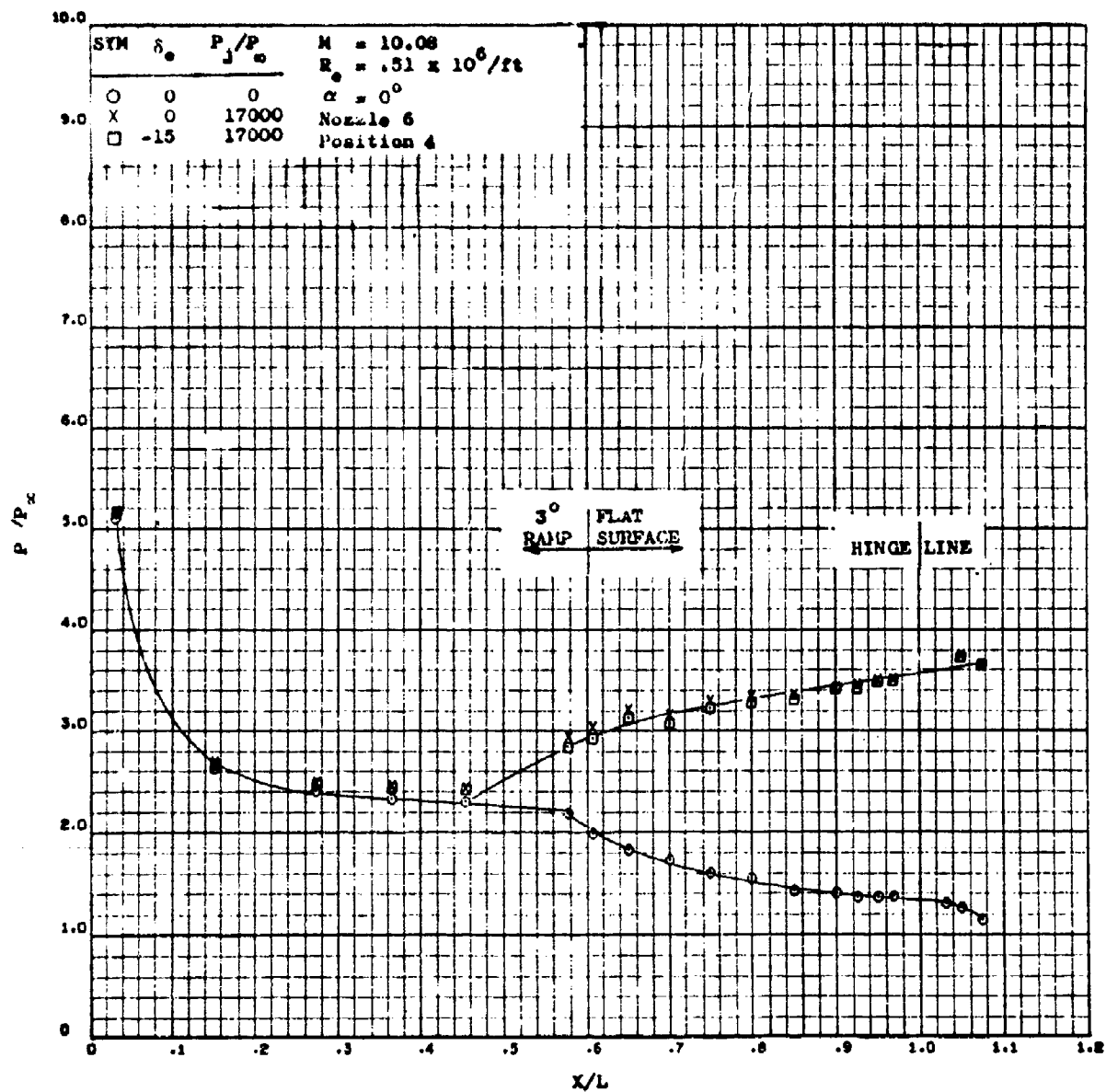


Figure 50. Effect of a -15° Control Deflection on Bottom Centerline Pressure on the Delta Platform at Mach 10 and Zero Angle of Attack

CONFIDENTIAL

CONFIDENTIAL

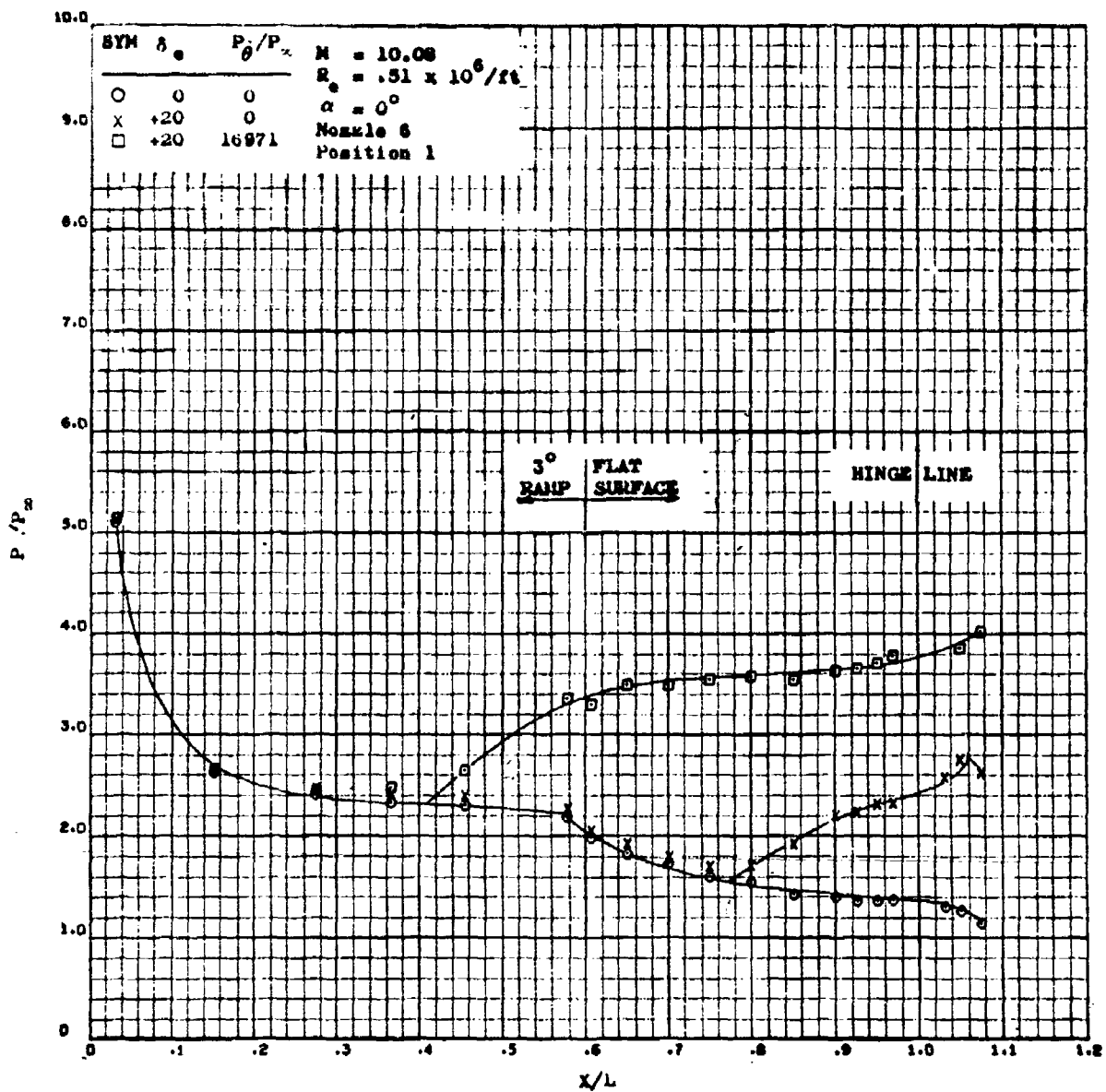
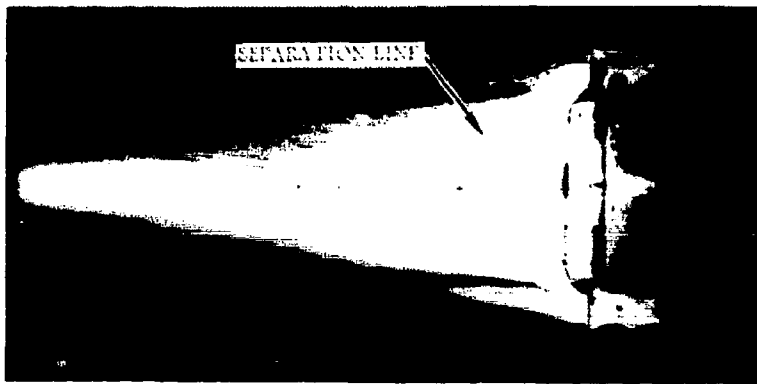


Figure 31. Effect of a +20° Control Deflection on Bottom Centerline Pressure. Mach 10

CONFIDENTIAL

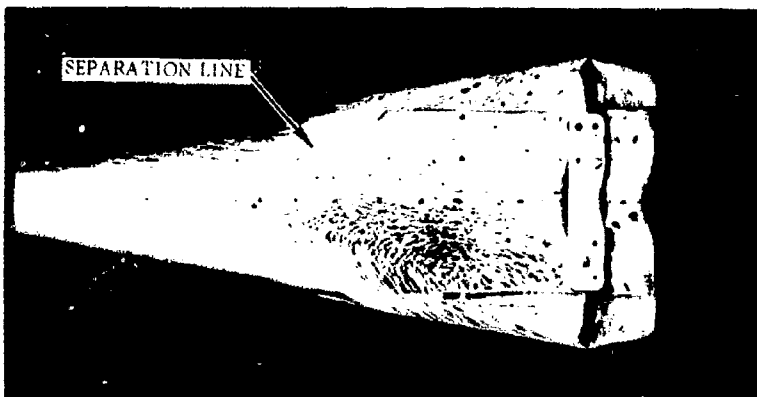
CONFIDENTIAL

(This page is Unclassified)



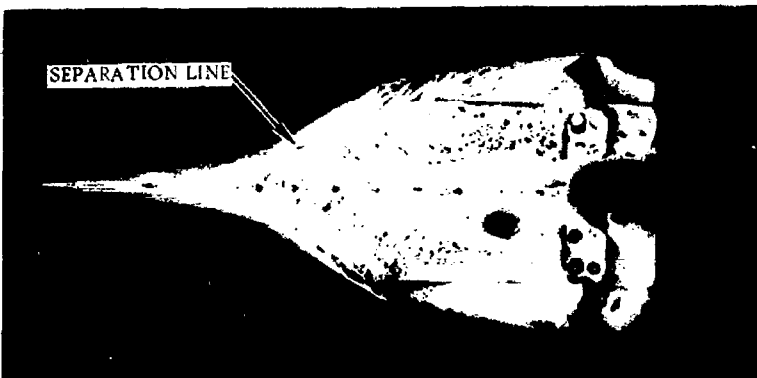
$$\delta e = +20^\circ$$

$$P_j/P_\infty = 0$$



$$\delta e = +20^\circ$$

$$P_j/P_\infty = 17000$$



$$\delta e = +20^\circ$$

$$P_j/P_\infty = 17000$$

NOZZLE 6, POSITION 1

$\alpha = 0^\circ$, $Re = 0.5 \times 10^6/ft$, $M = 10.1$

Figure 82. Flow Visualization of the Effect of Plume with Control Deflection at Zero Angle of Attack

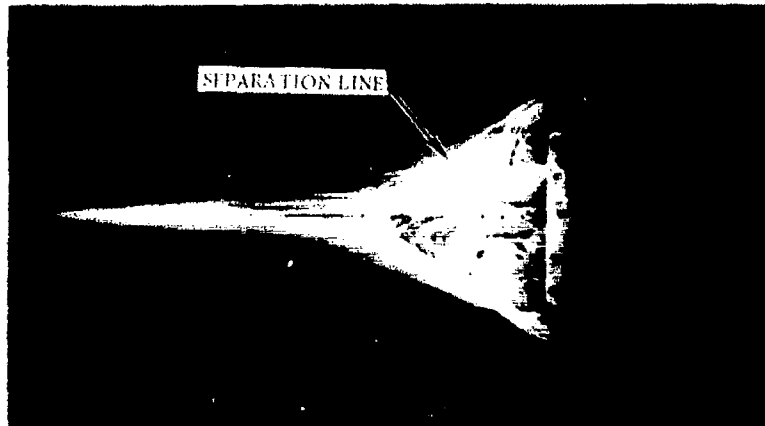
142

CONFIDENTIAL

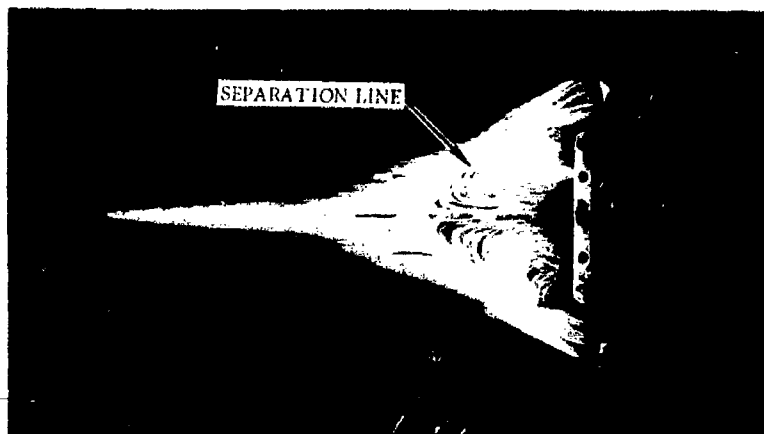
(This page is Unclassified)

CONFIDENTIAL

(This page is Unclassified)



$$\delta e = +20^\circ$$
$$P_j/P_\infty = 0$$



$$\delta e = +20^\circ$$
$$P_j/P_\infty = 17000$$

NOZZLE G
POSITION 1
 α 10 DEGREE
Re 0.5×10^6 / ft
M 10.1

Figure 83. Flow Visualization of the Effect of Plume with Control
Deflection at 10 Degree Angle of Attack

143

CONFIDENTIAL

(This page is Unclassified)

CONFIDENTIAL

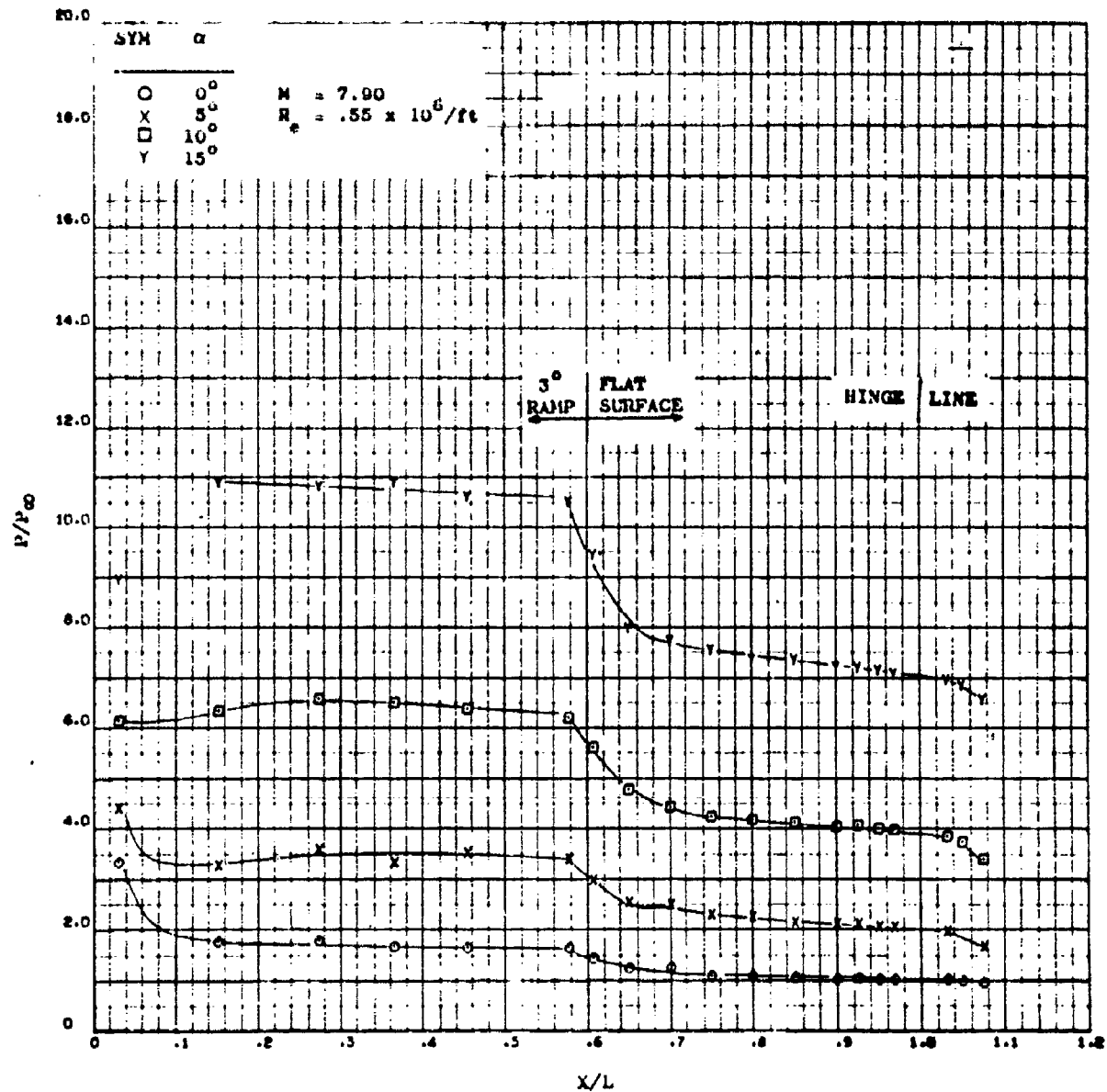


Figure 94. Effect of Angle of Attack on Bottom Centerline Pressure on the Delta Platform and a Mach number of 7.0, $P_{\infty}/P_0 = 0$.

CONFIDENTIAL

CONFIDENTIAL

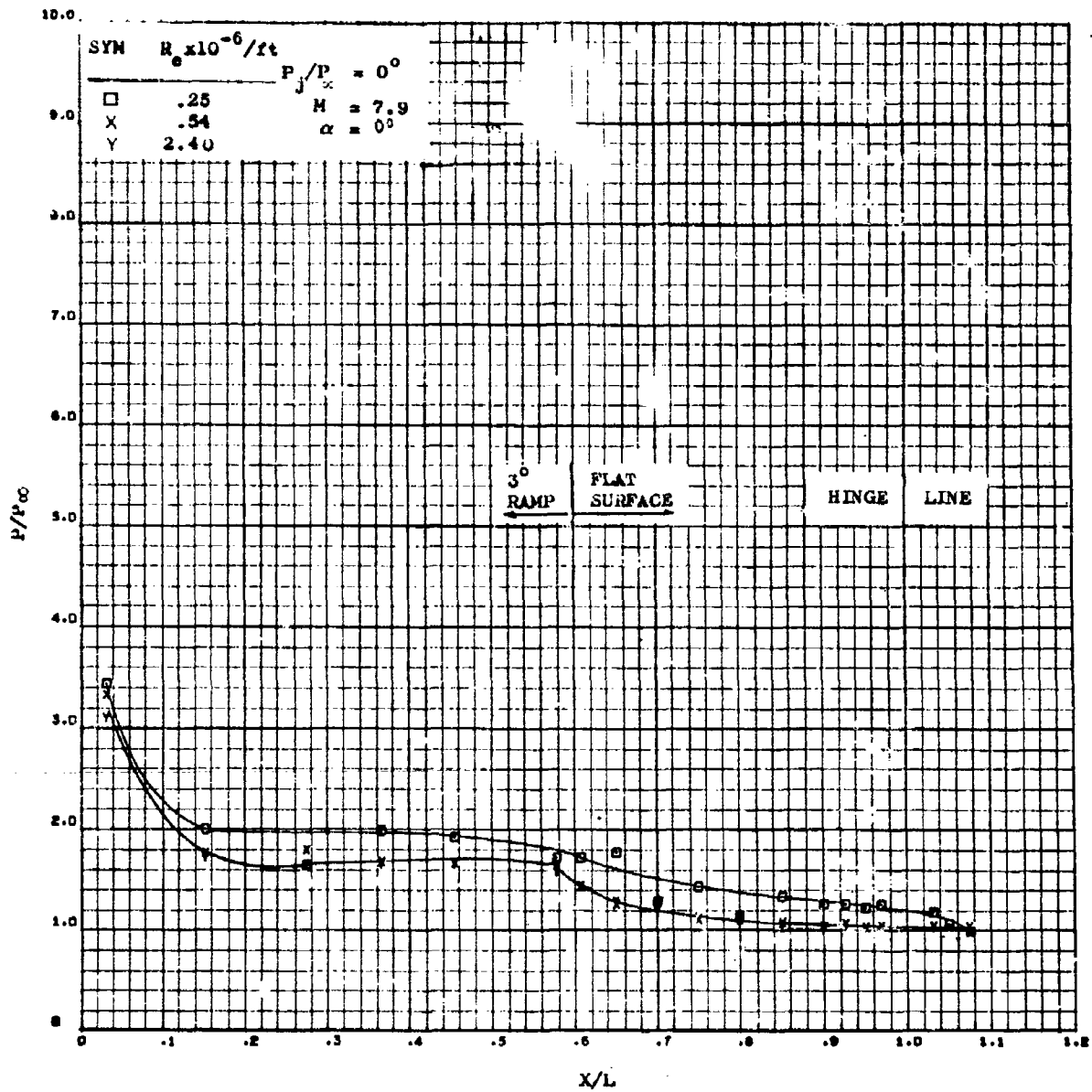


Figure 85. Effect of Reynolds Number on the Delta Planform Bottom Centerline Pressure at a Mach Number of 7.9

CONFIDENTIAL

CONFIDENTIAL

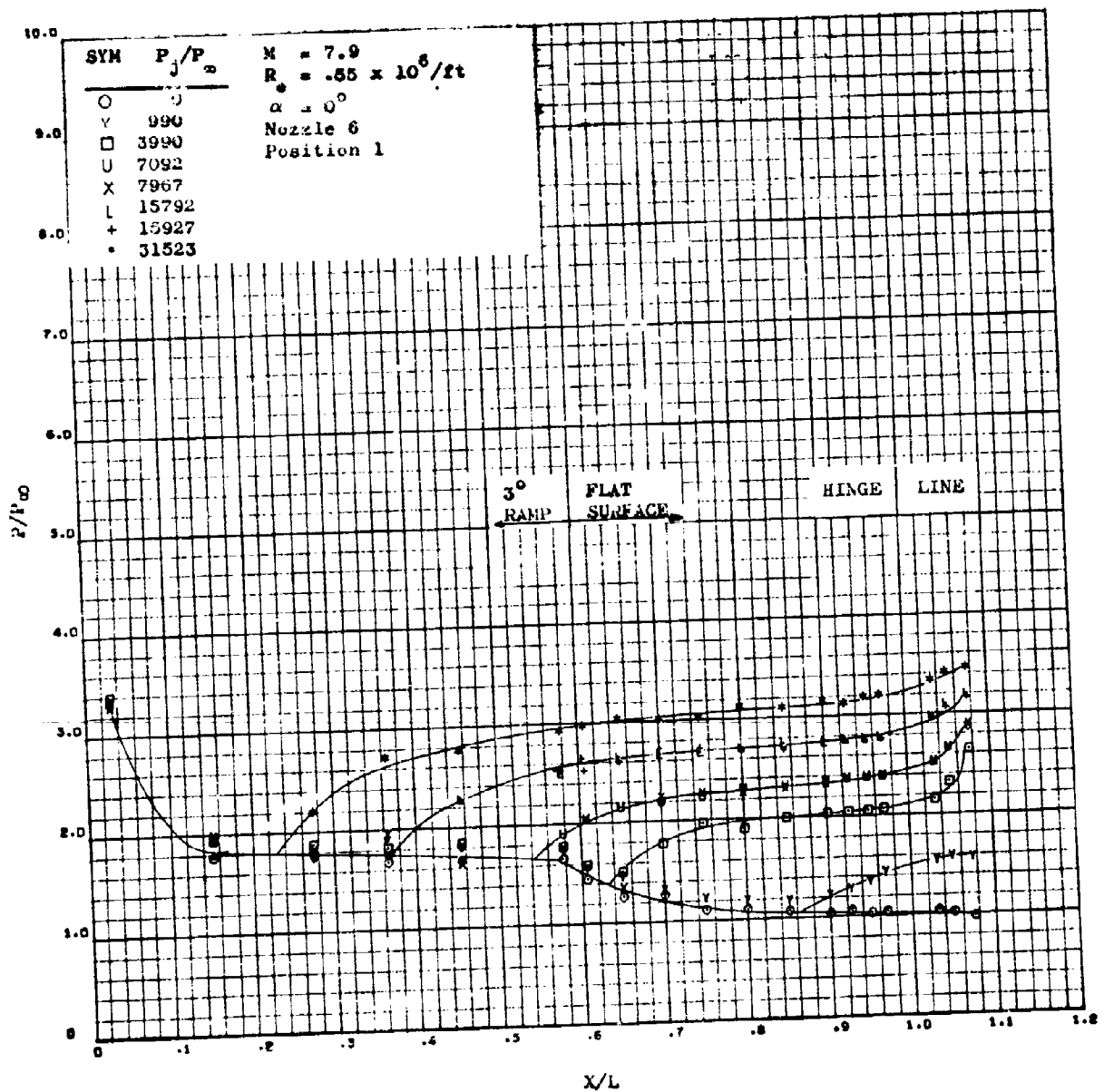


Figure 50. Effect of Jet Pressure Ratio on Plume Induced Separation at Mach 7.9 with Nozzle 6 at Zero Angle of Attack

CONFIDENTIAL

CONFIDENTIAL

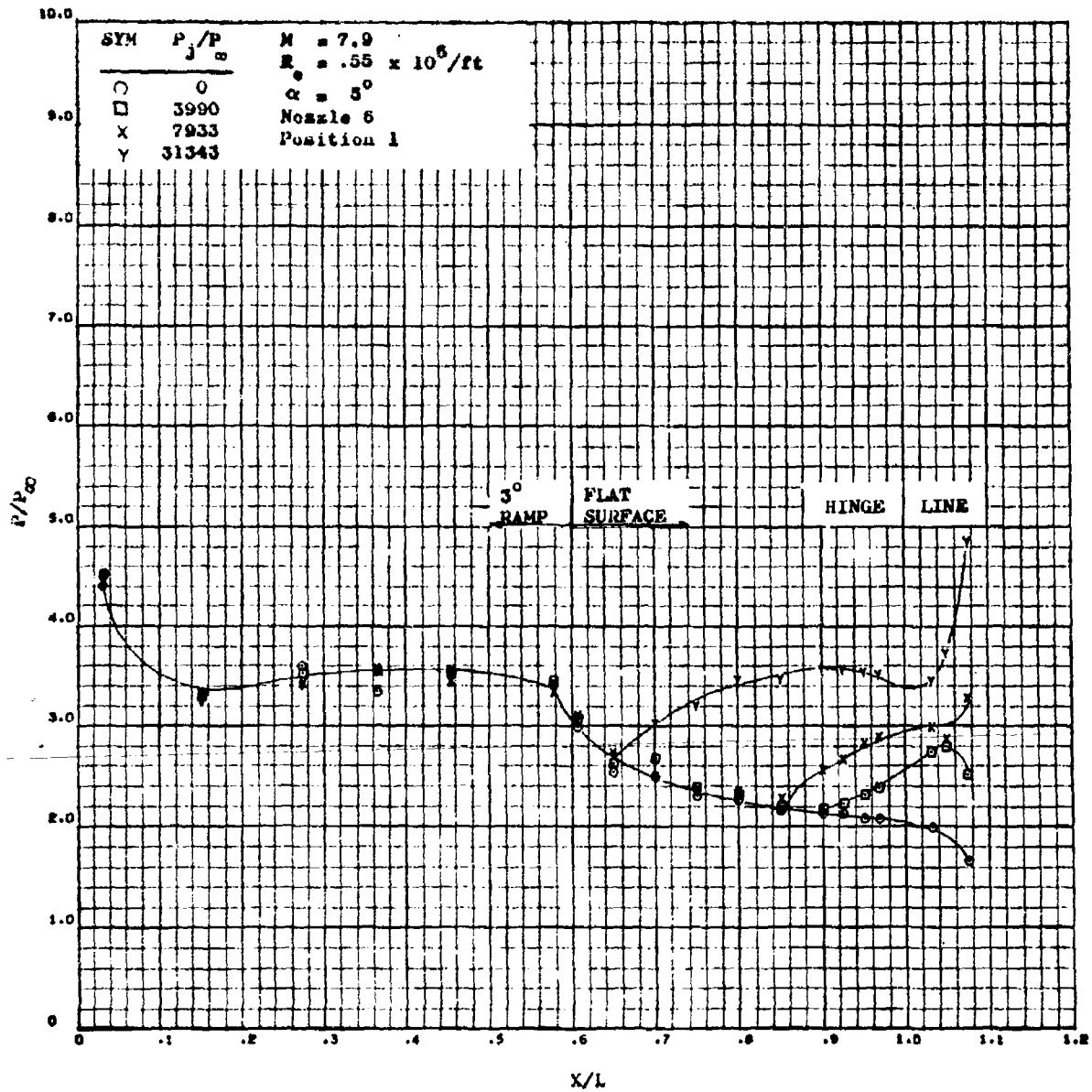


Figure 17. Effect of Jet Pressure Ratio on Plume Induced Separation at Mach 7.9 and 5° Angle of Attack

CONFIDENTIAL

CONFIDENTIAL

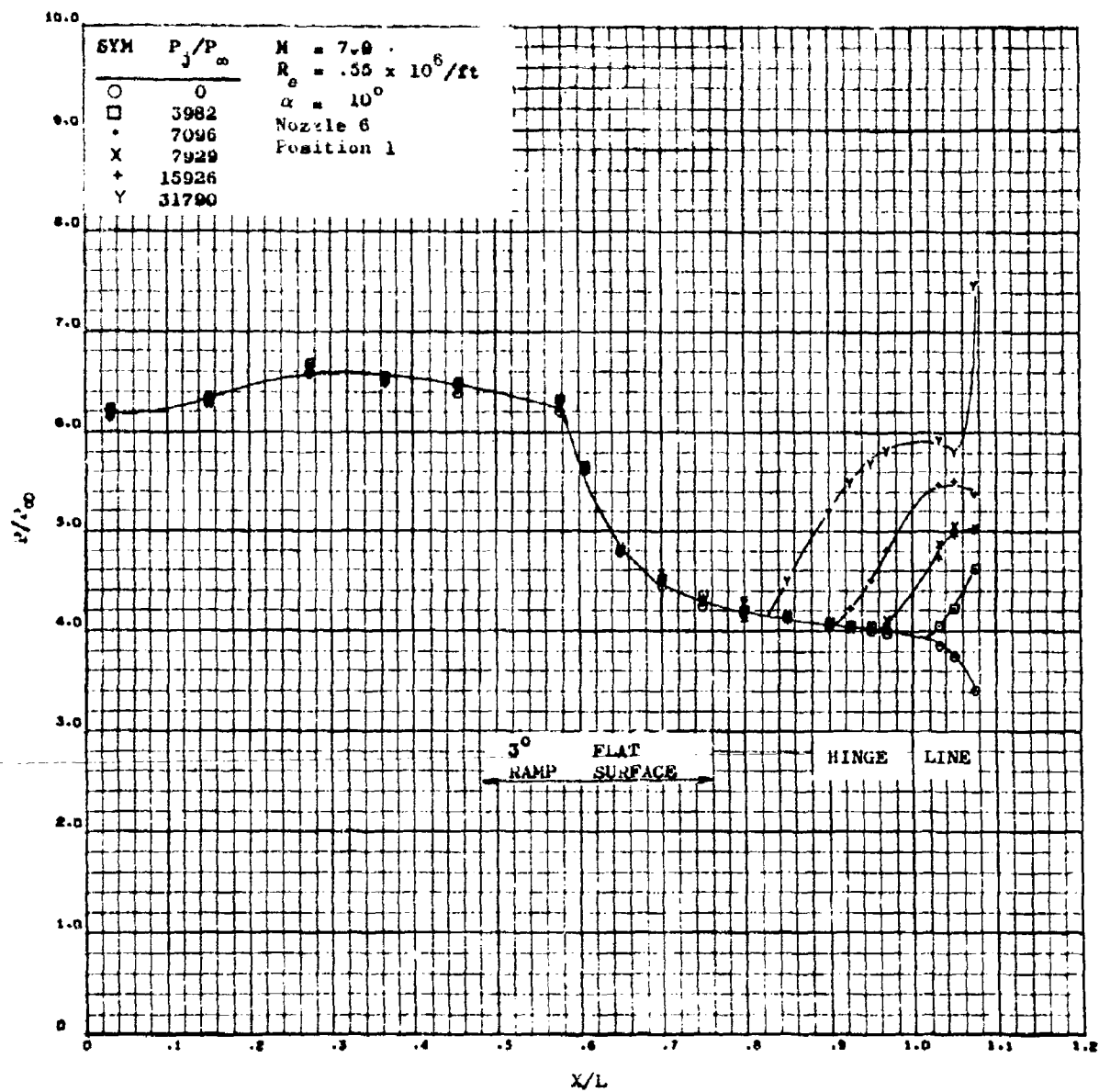


Figure 10. Effect of Jet Pressure Ratio on Flow Induced Separation at Mach 7.0 and 10° Angle of Attack

CONFIDENTIAL

CONFIDENTIAL

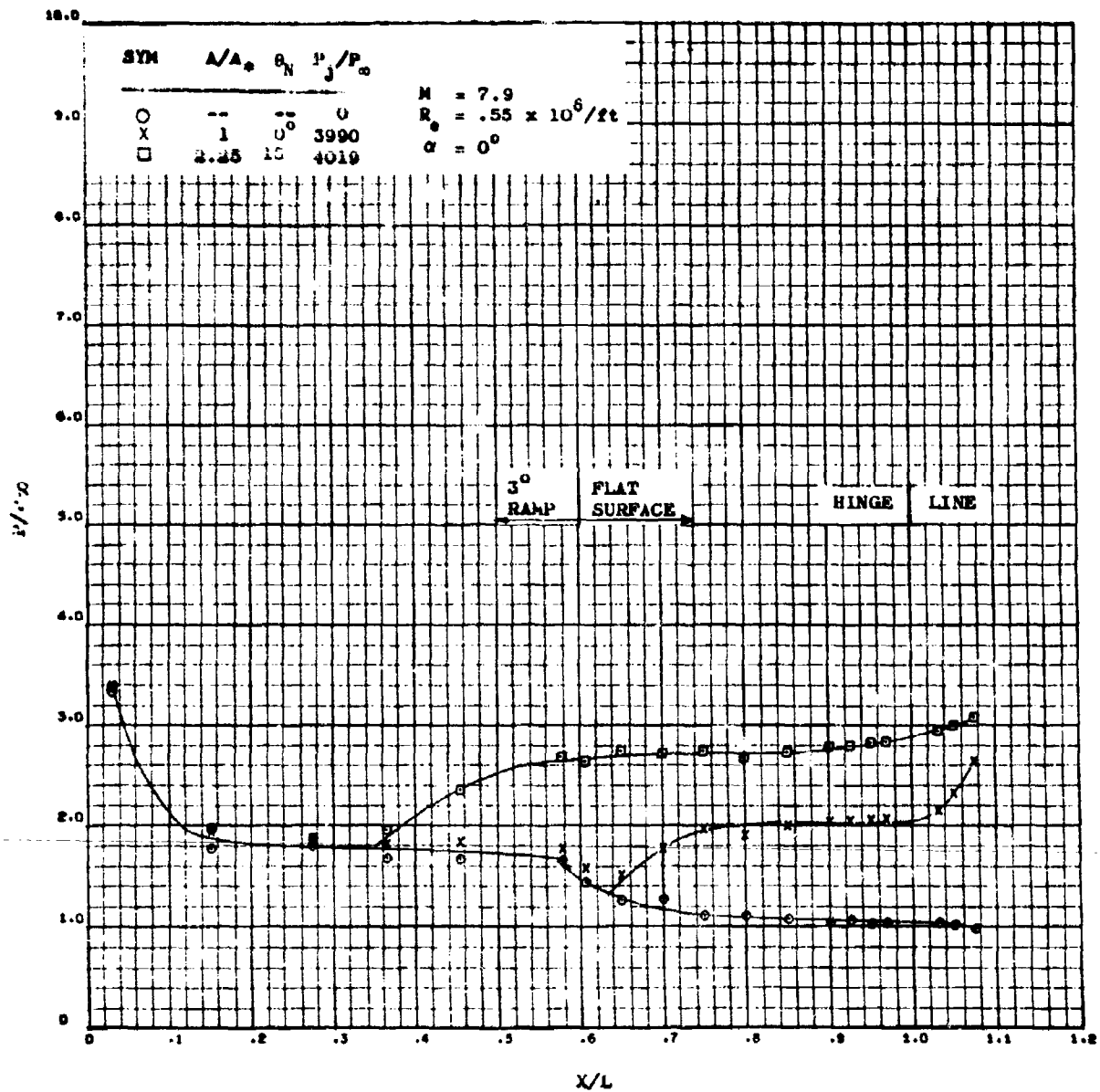


Figure 10. A Comparison of Sonic Nozzle Data with that of an Expansion Ratio of 2.25 at Mach 7.9.

CONFIDENTIAL

CONFIDENTIAL

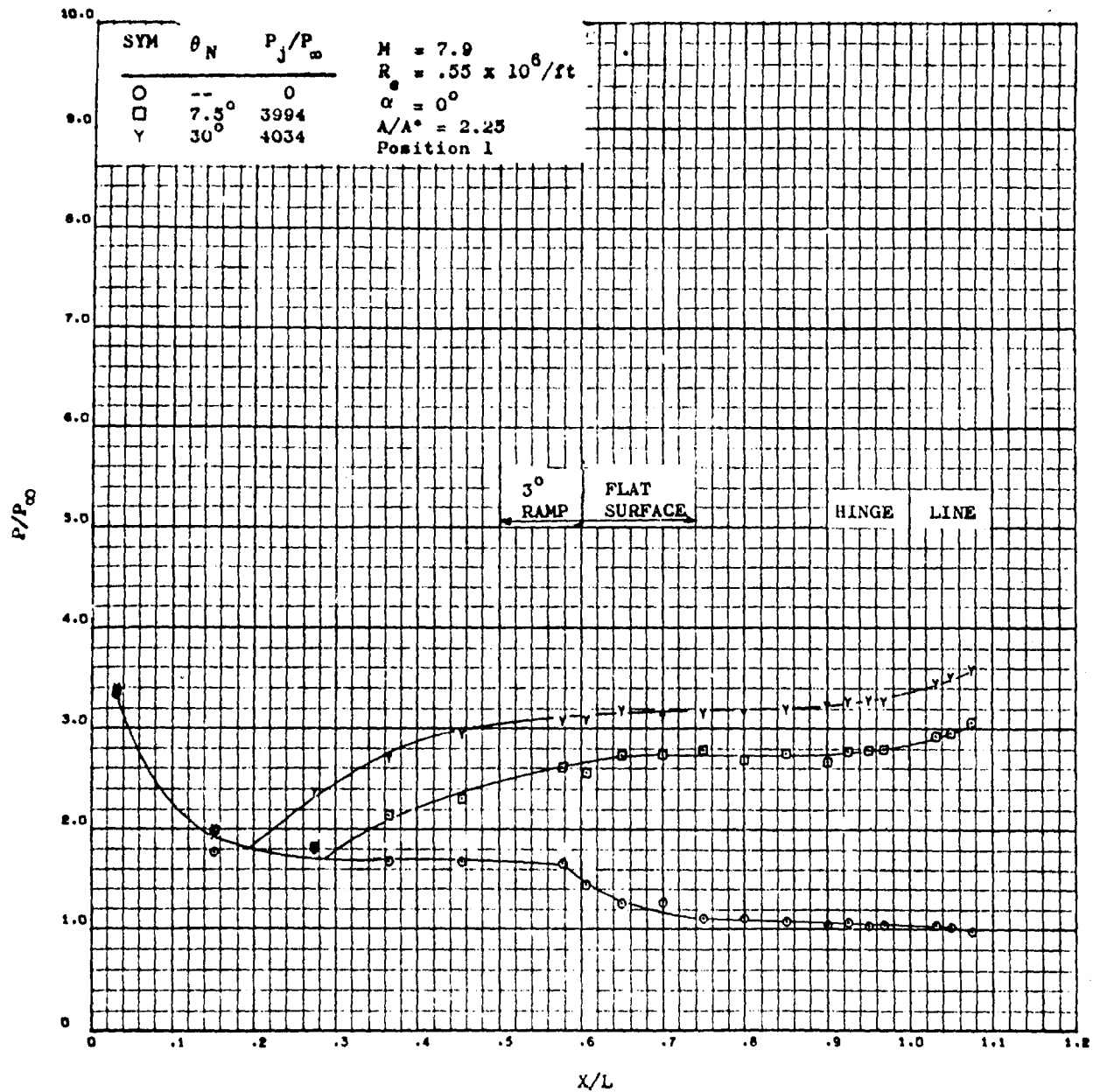


Figure 90. Effect of Nozzle Exit Angle at Mach 7.9 and Zero Angle of Attack

CONFIDENTIAL

CONFIDENTIAL

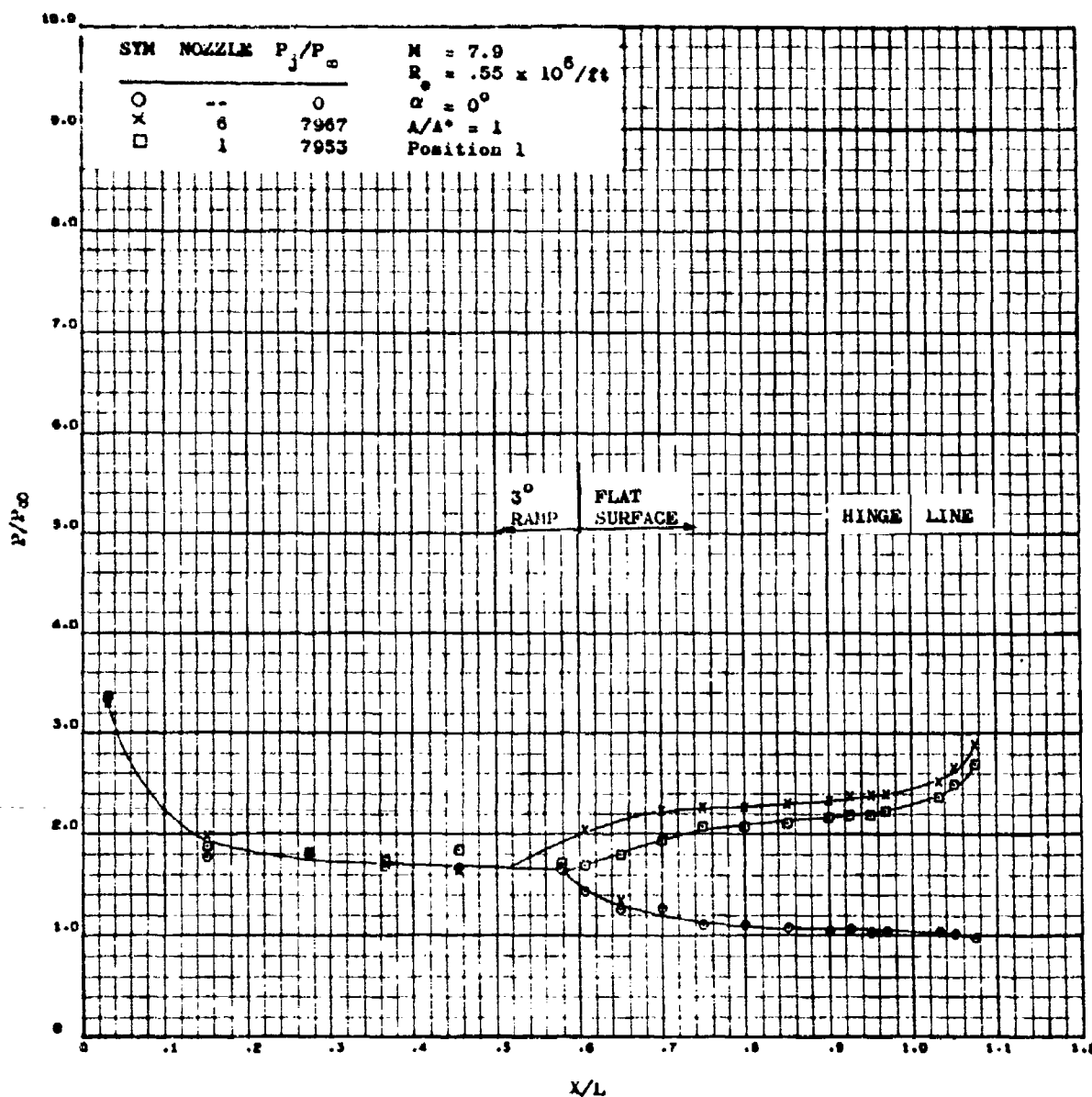


Figure 91. Effect of Nozzle Size on Plume Induced Separation at Mach 7.9

CONFIDENTIAL

CONFIDENTIAL

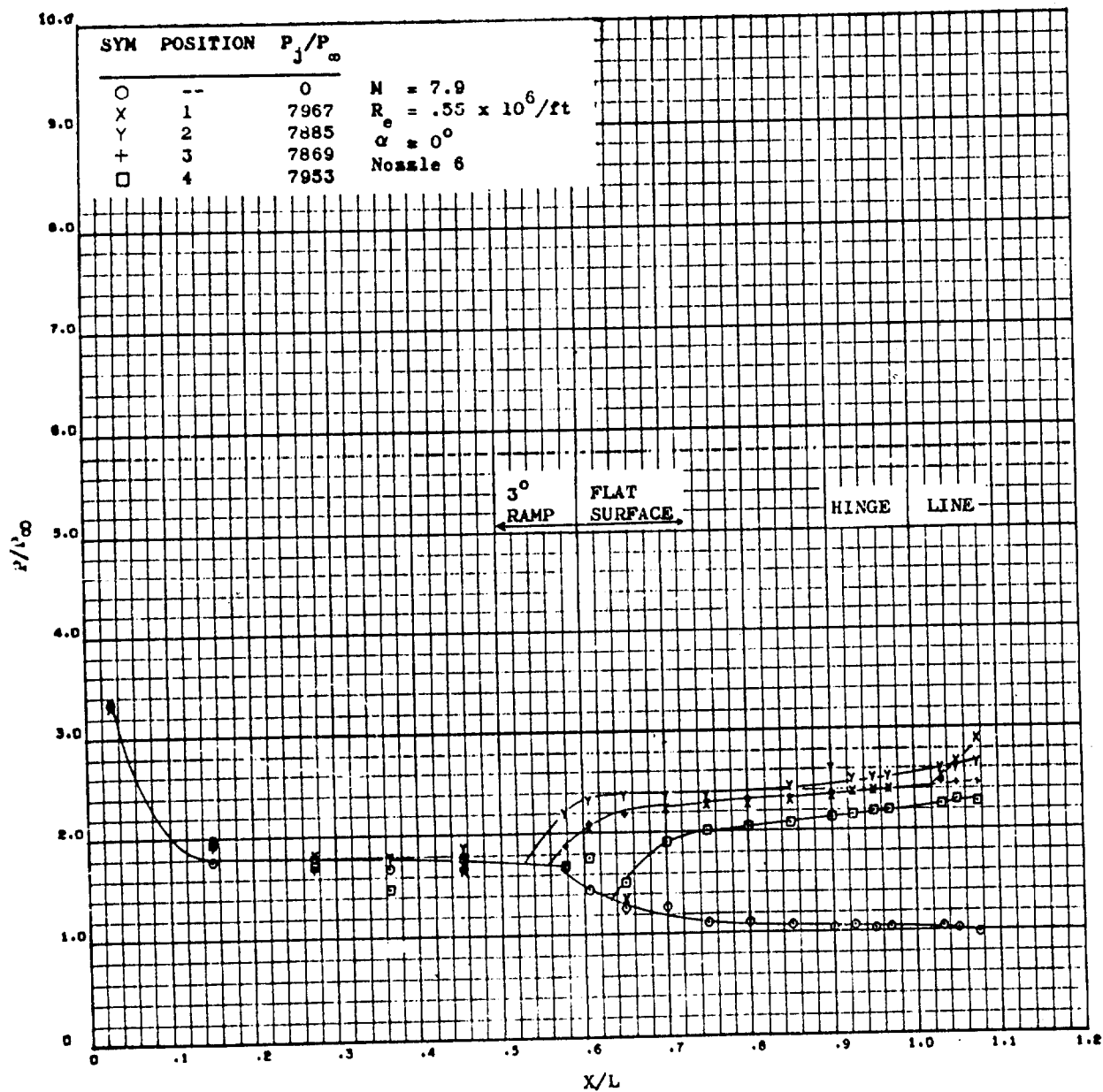


Figure 92. Effect of Nozzle Position on Plume Induced Separation at Mach 7.9

CONFIDENTIAL

CONFIDENTIAL

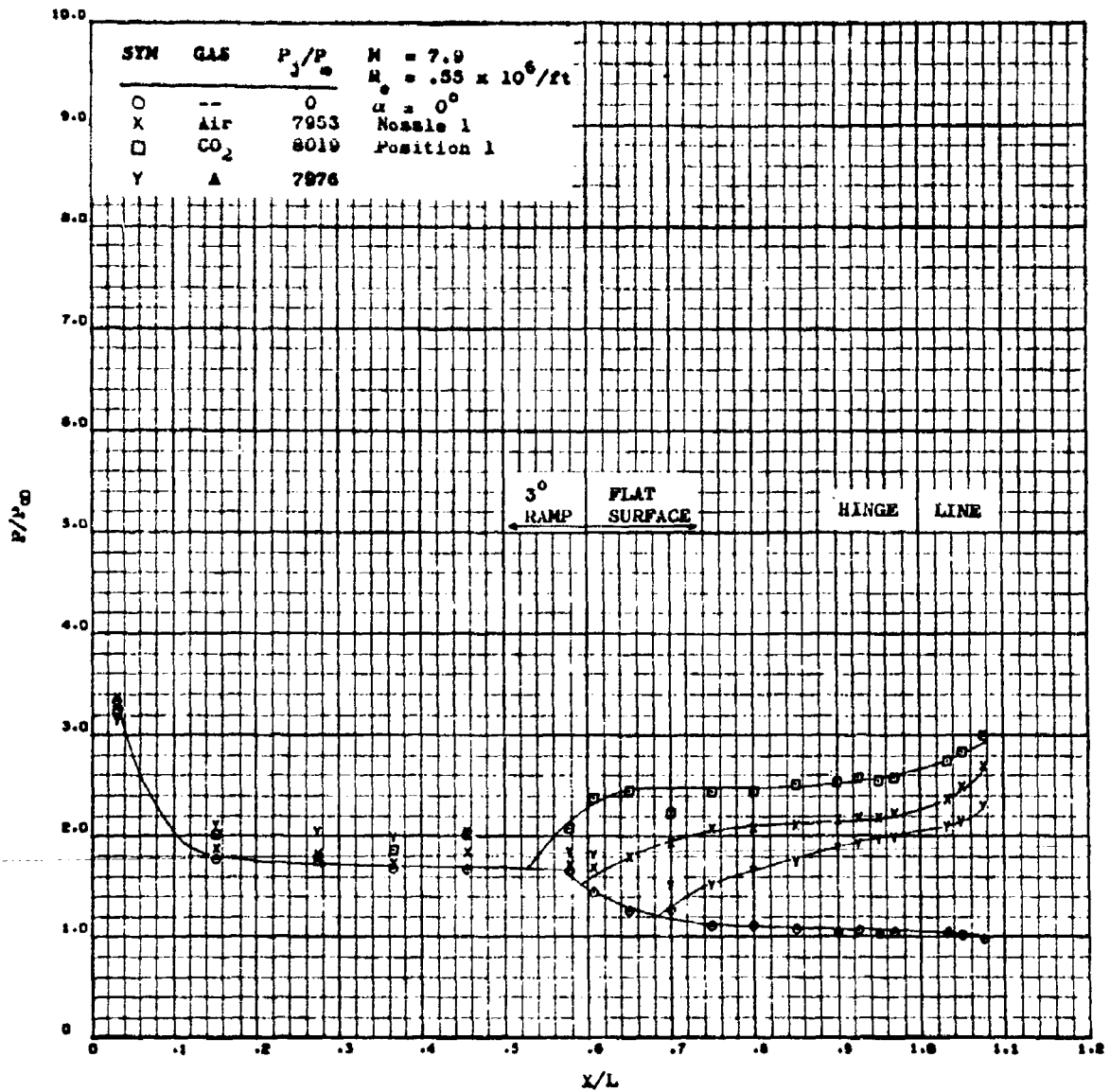


Figure 91. Effect of Exhaust Gas on Plume Induced Separation
at Mach 7.9 and $P_3/P_0 = 8000$

CONFIDENTIAL

CONFIDENTIAL

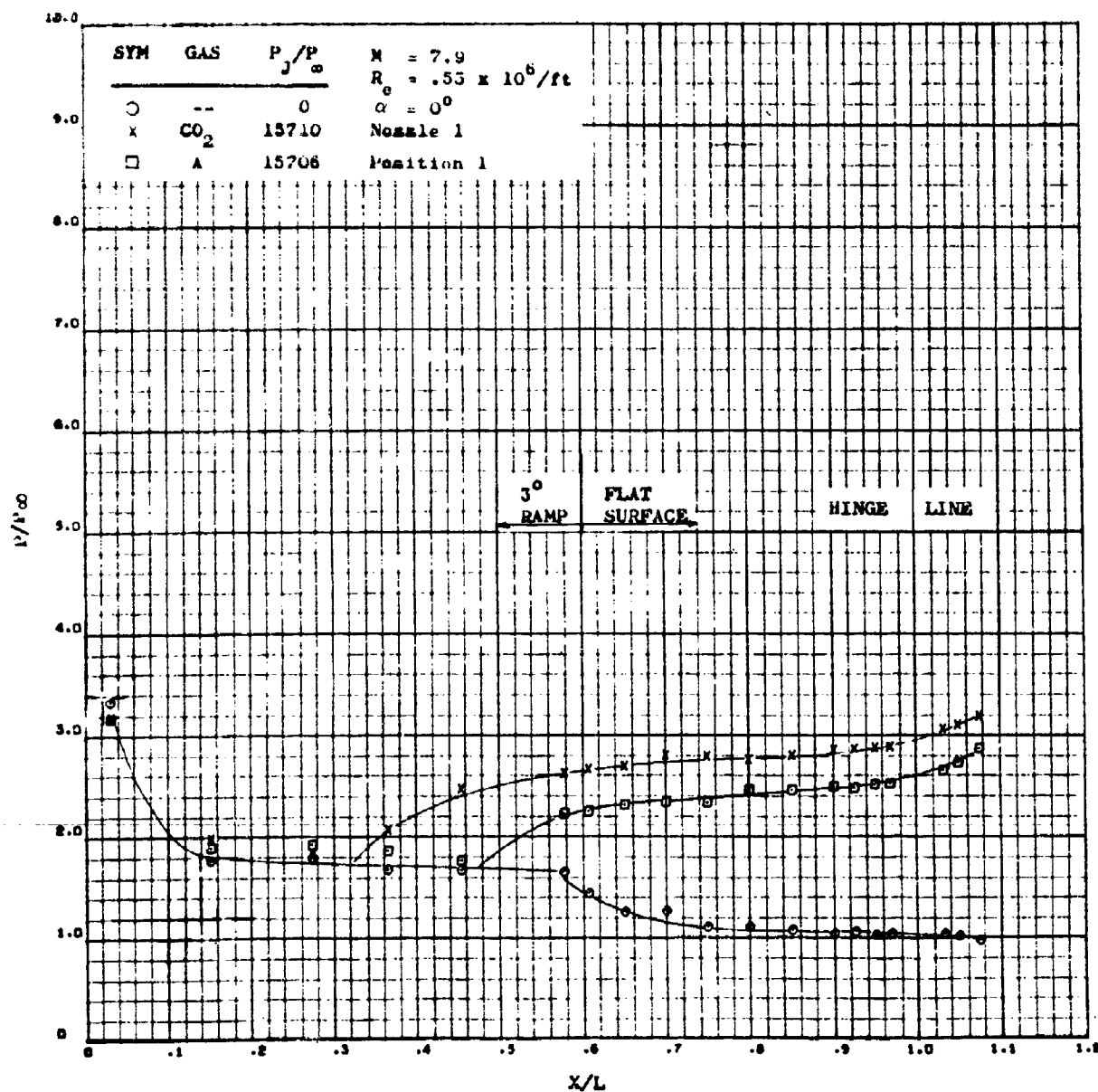


Figure 9b. Effect of Exhaust Gas on Plume Induced Separation
at Mach 7.9 and $P_j/P_\infty = 15700$

CONFIDENTIAL

CONFIDENTIAL

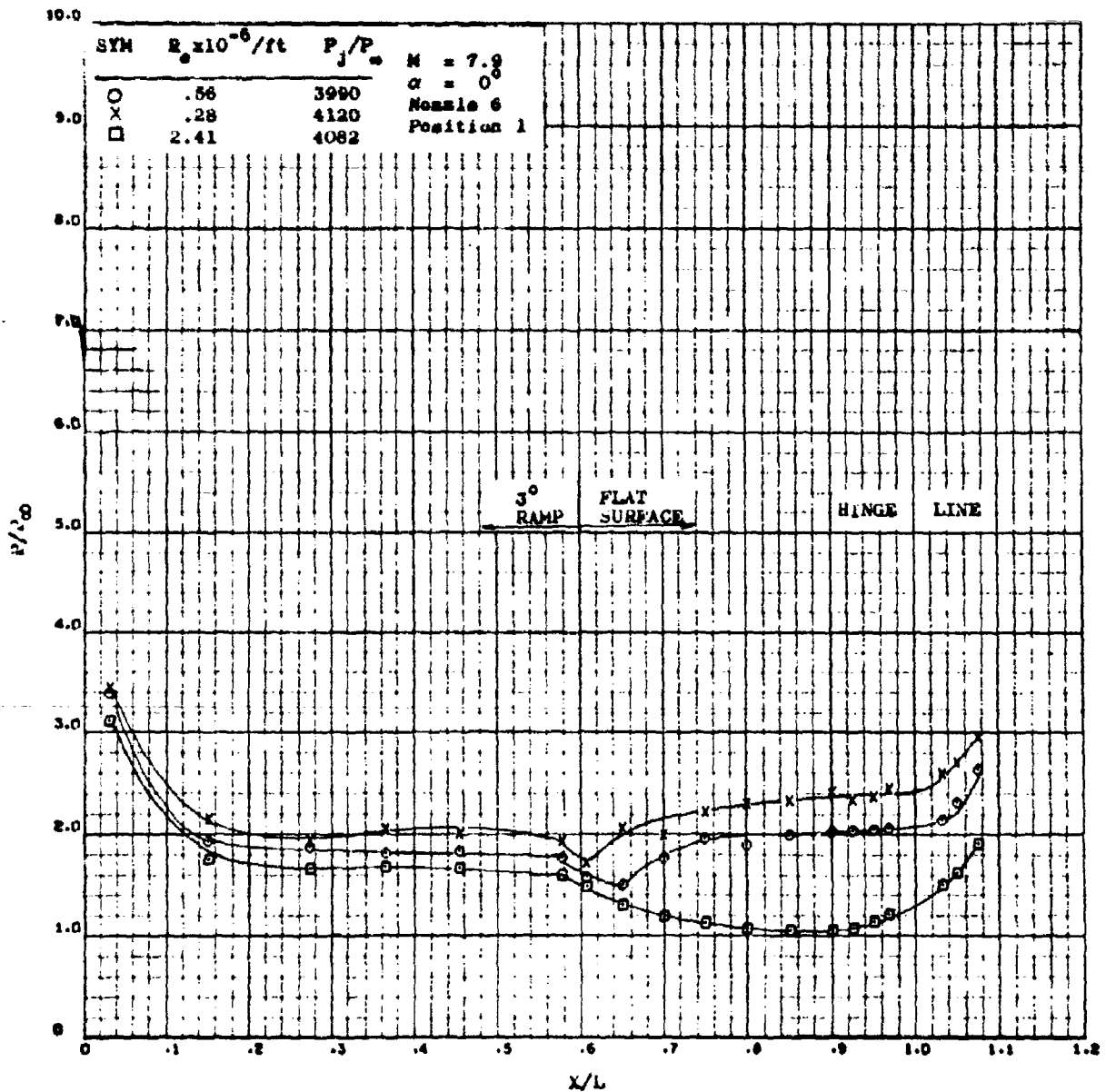


Figure 1. Effect of Free Stream Reynolds Number on Plume Induced Separation
 at Mach 7.9 and $P_j/P_\infty = 1.000$

CONFIDENTIAL

CONFIDENTIAL

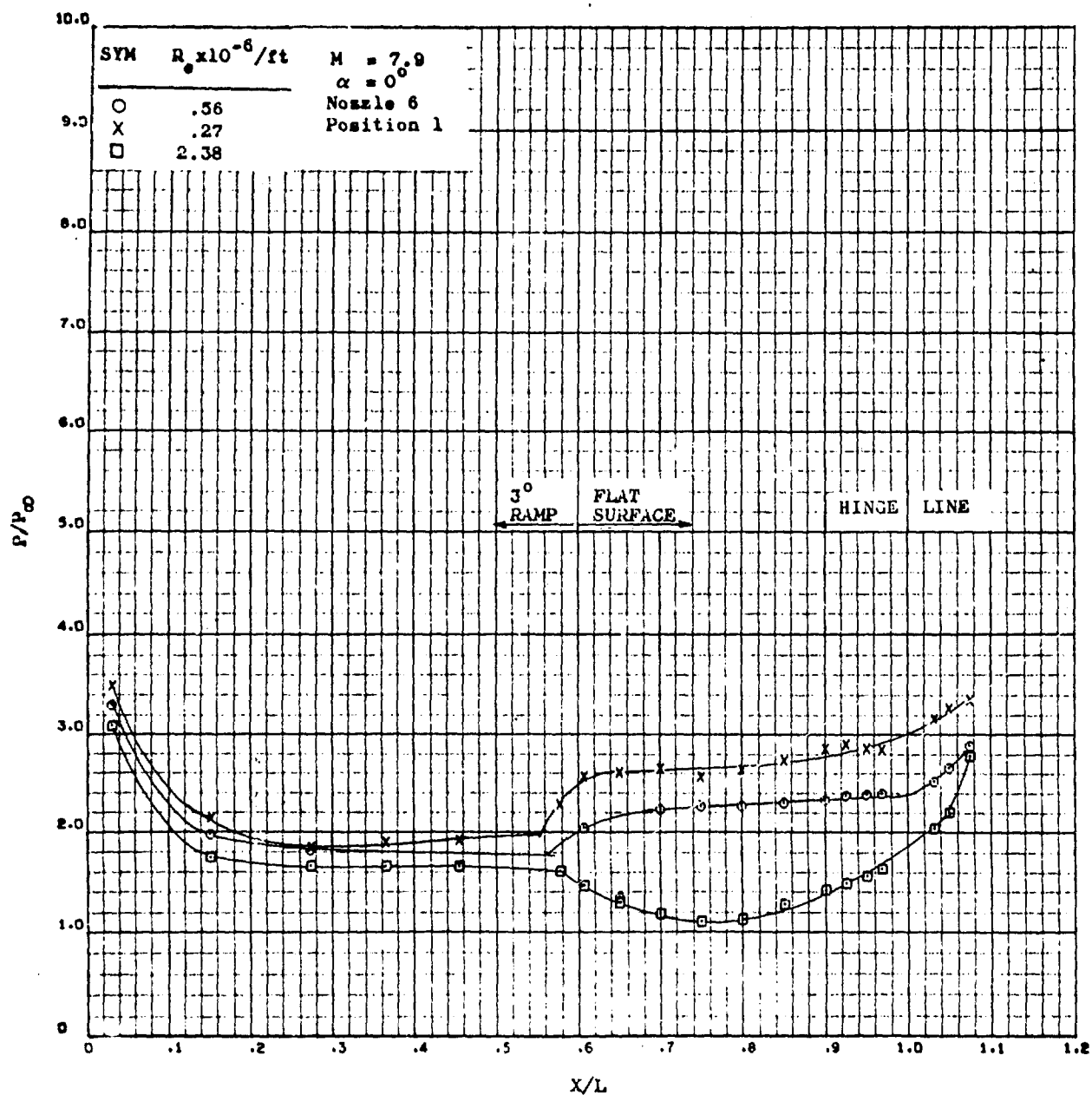


Figure 96. Effect of Free Stream Reynolds Number on Plume Induced Separation at Mach 7.9 and $P_j/P_\infty = 8000$

CONFIDENTIAL

CONFIDENTIAL

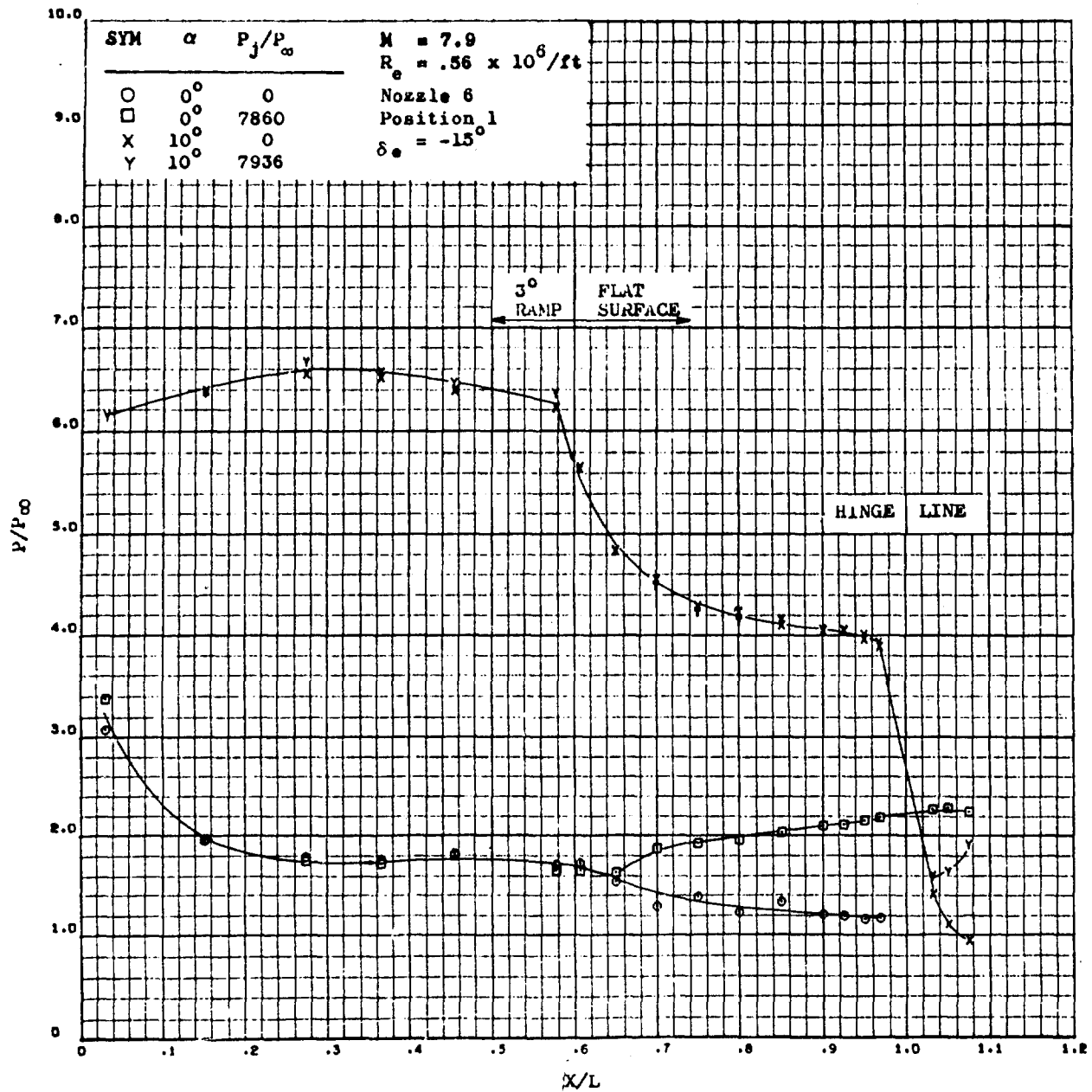


Figure 97. Effect of a -15° Elevon Deflection on Plume Induced Separation at Mach 7.9

CONFIDENTIAL

CONFIDENTIAL

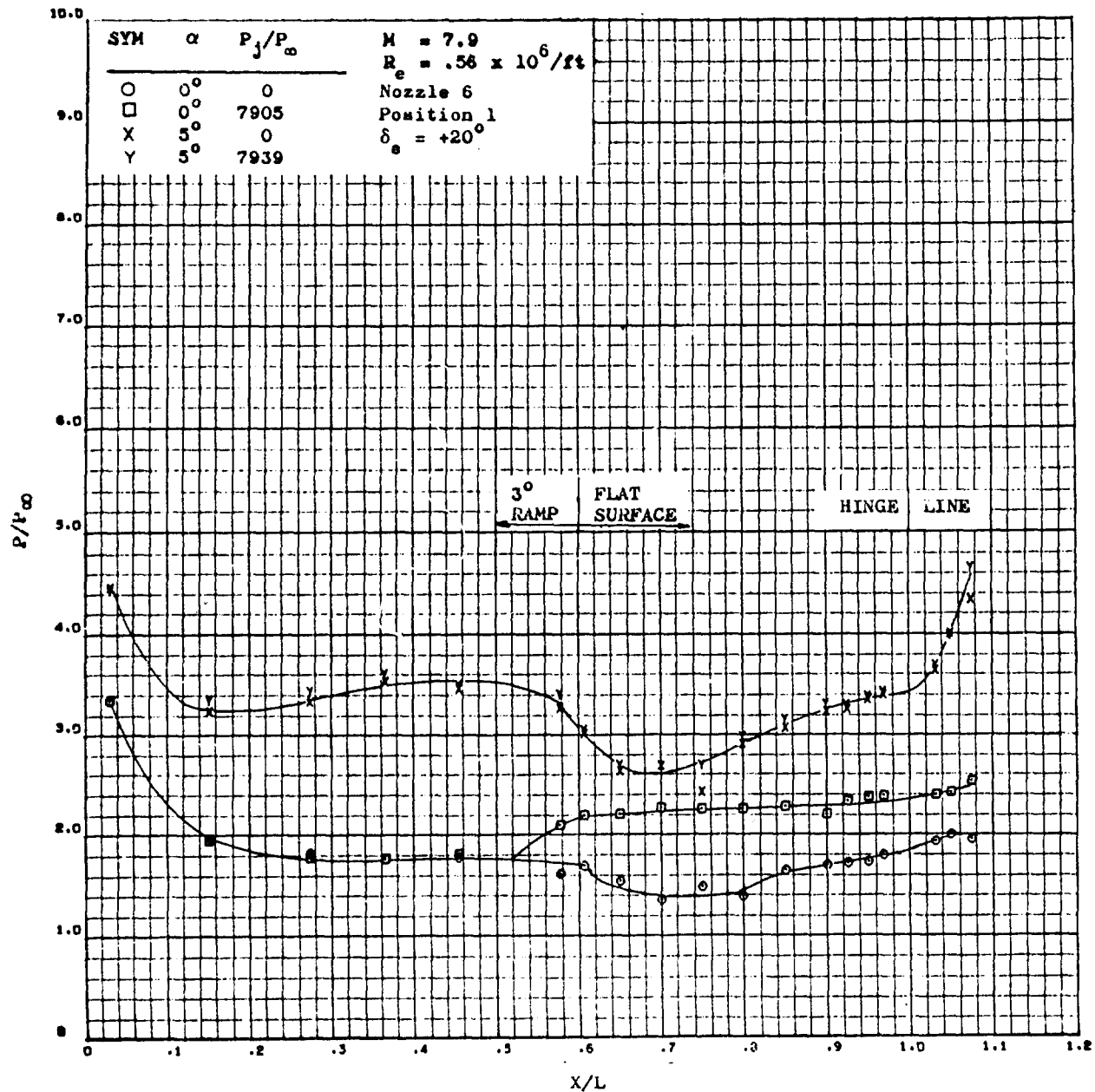


Figure 98. Effect of a $+20^\circ$ Control Deflection on Plume Induced Separation at Mach 7.9

CONFIDENTIAL

CONFIDENTIAL

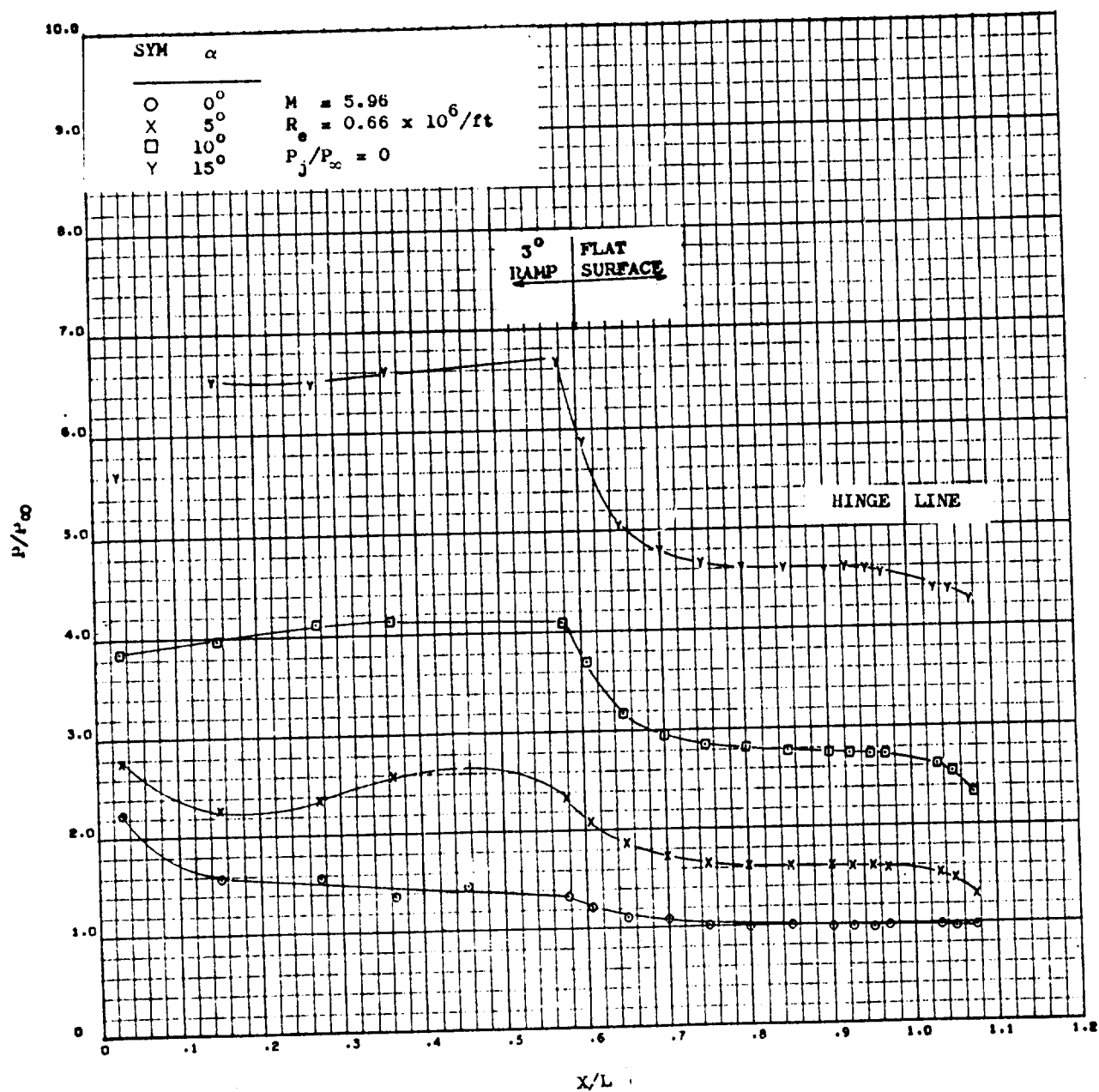


Figure 20. Effect of Angle of Attack on Bottom Centerline Pressure on the Delta Planform at a Mach Number of 5.9, $P_j / P_\infty = 0$

CONFIDENTIAL

CONFIDENTIAL

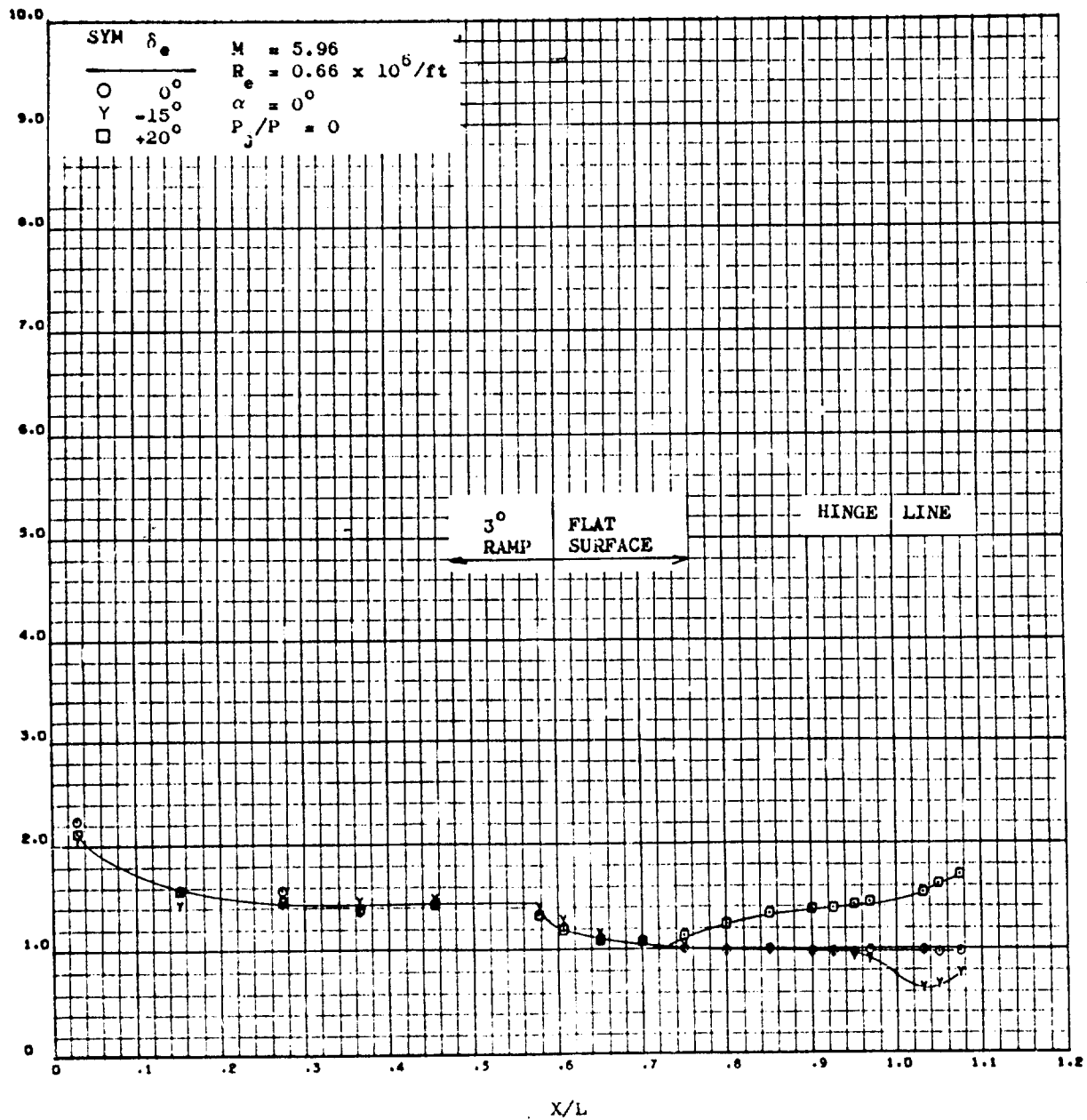


Figure 100. Effect of Control Deflection on Bottom Centerline Pressure on the Delta Planform at $M = 5.96$, $P_j / P_\infty = 0$

CONFIDENTIAL

CONFIDENTIAL

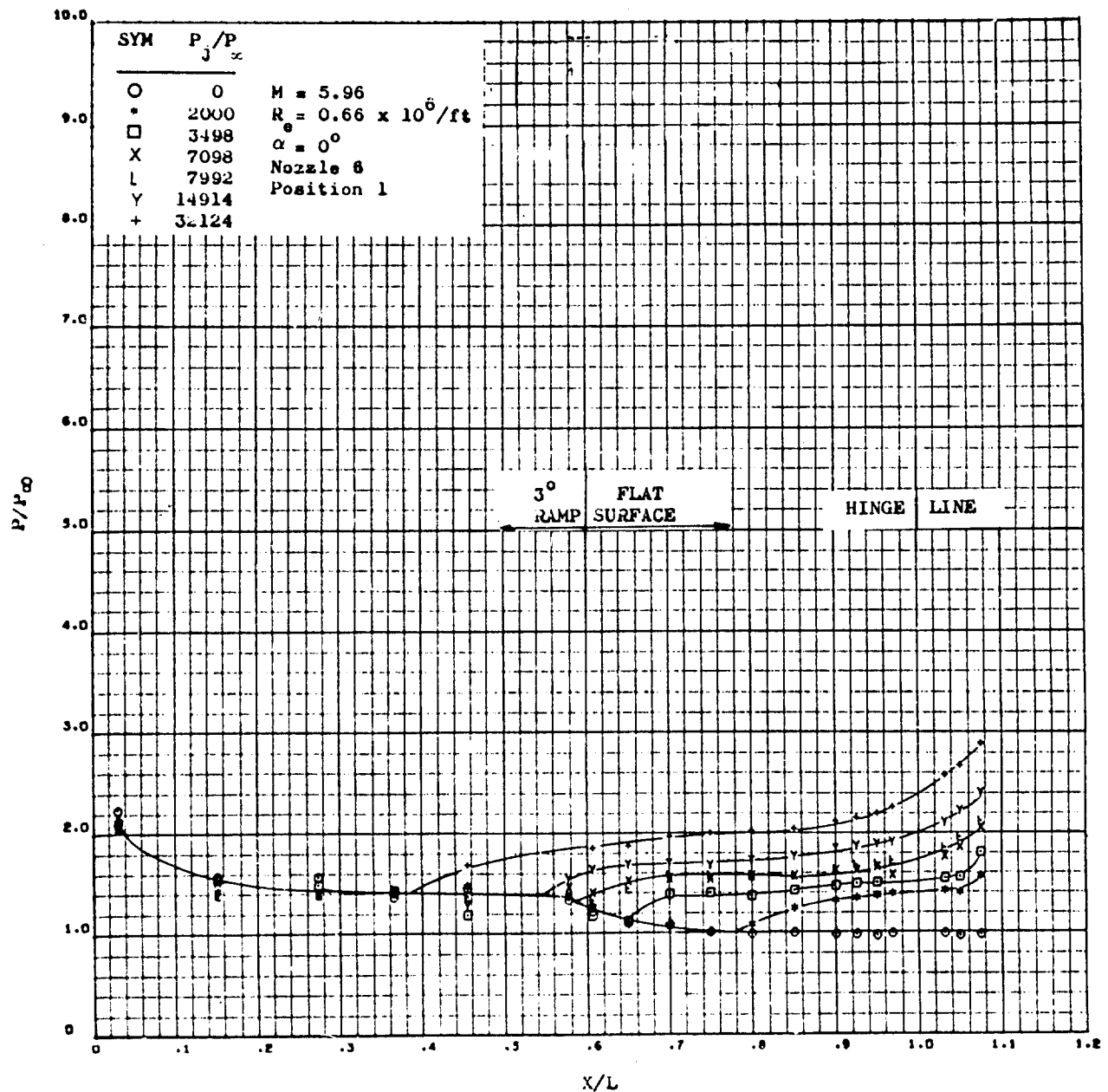


Figure 101. Effect of Jet Pressure Ratio on Bottom Centerline Pressure at Mach 5.96

CONFIDENTIAL

CONFIDENTIAL

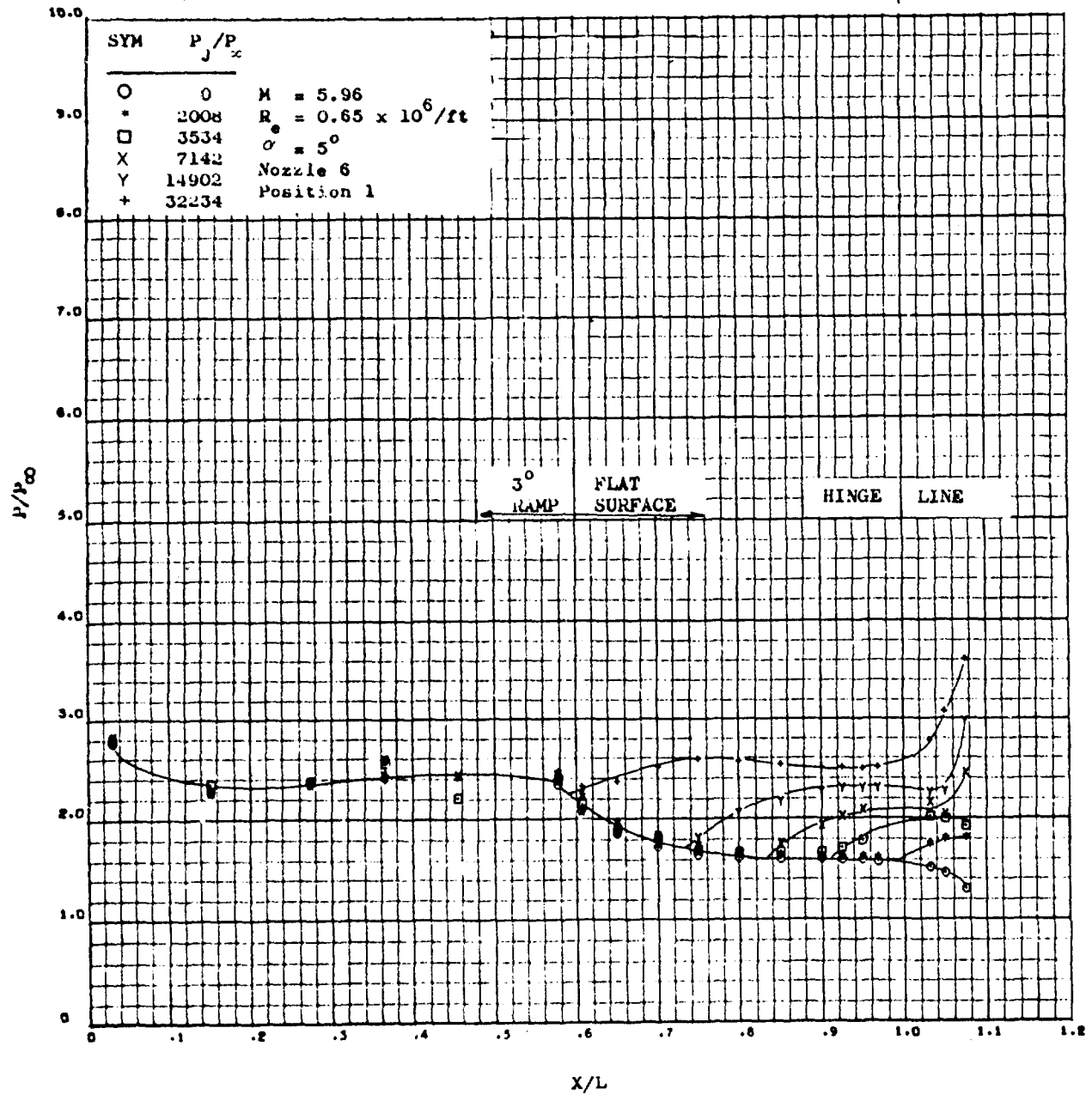


Figure 104. Effect of Jet Pressure Ratio on Bottom Centerline Pressure at Mach 5.96 and 5° Angle of Attack

CONFIDENTIAL

CONFIDENTIAL

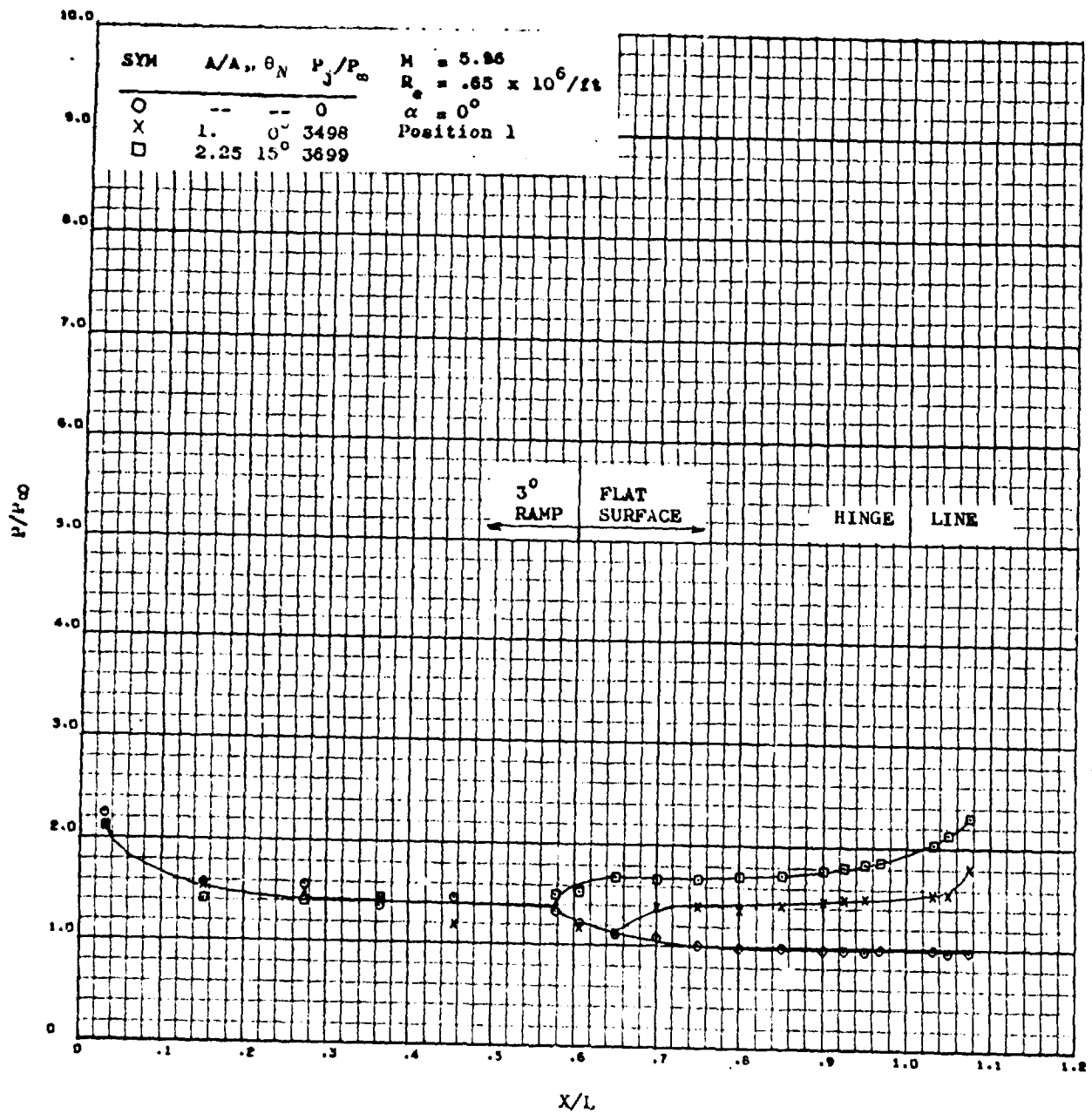


Figure 103. A Comparison of Sonic Orifice Nozzle Data with an Expansion Ratio 2.25 Nozzle at Mach 5.96.

CONFIDENTIAL

CONFIDENTIAL

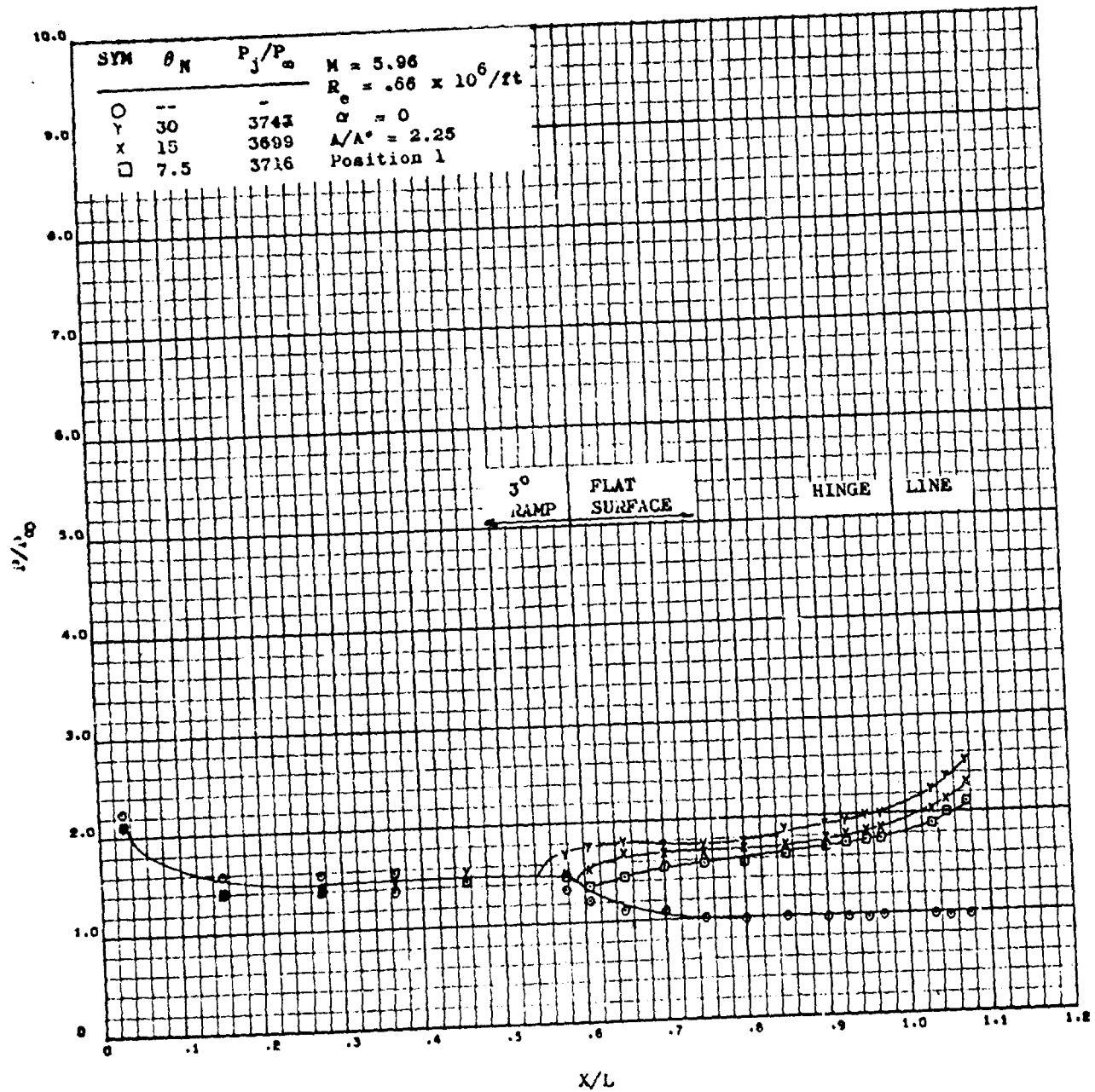


Figure 104. Effect of Hinge Exit Angle on Bottom Centerline Pressure at Mach 5.96

CONFIDENTIAL

CONFIDENTIAL

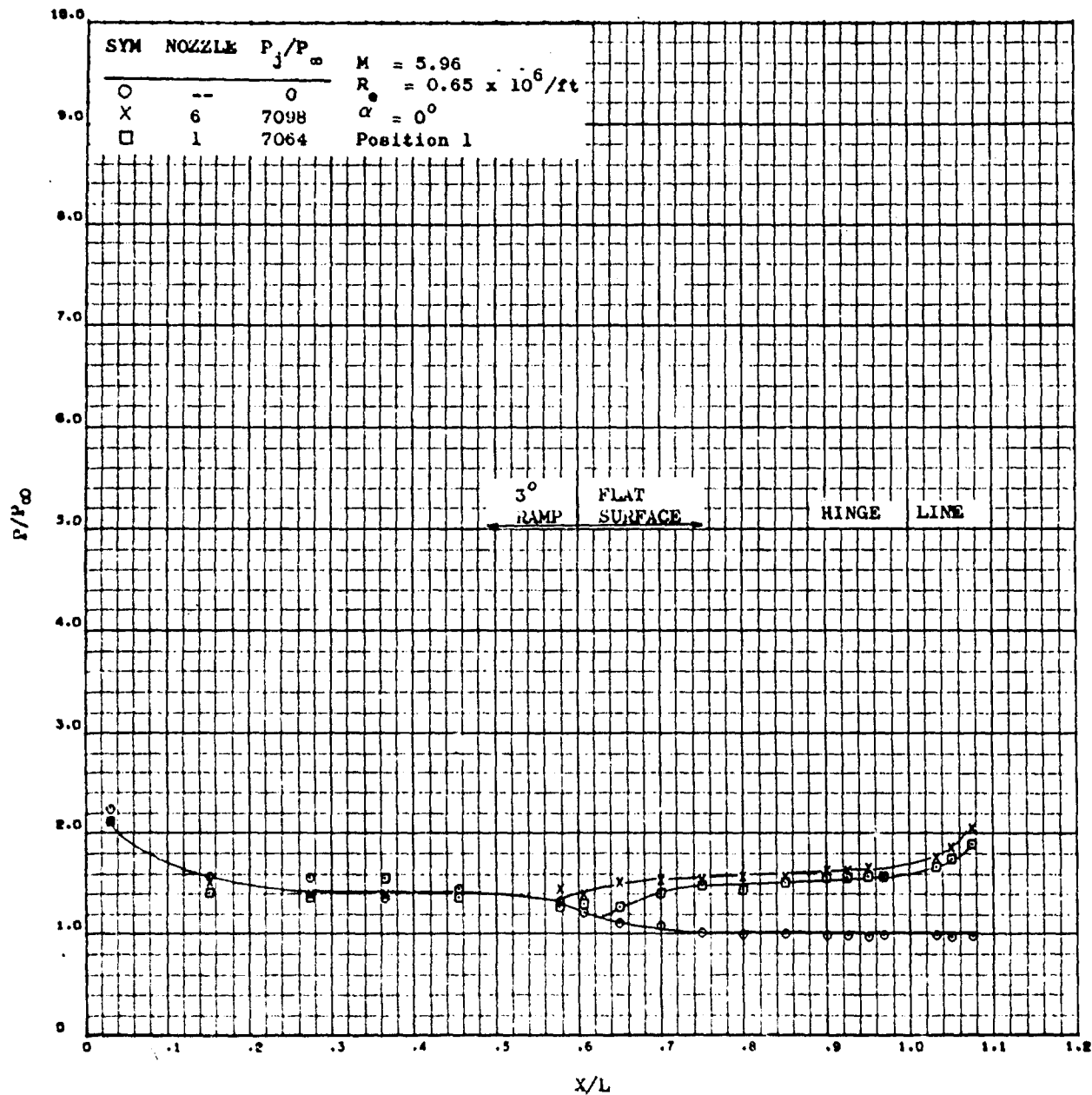


Figure 105. Effect of Nozzle Size on Bottom Centerline Pressure at Mach 5.96

CONFIDENTIAL

CONFIDENTIAL

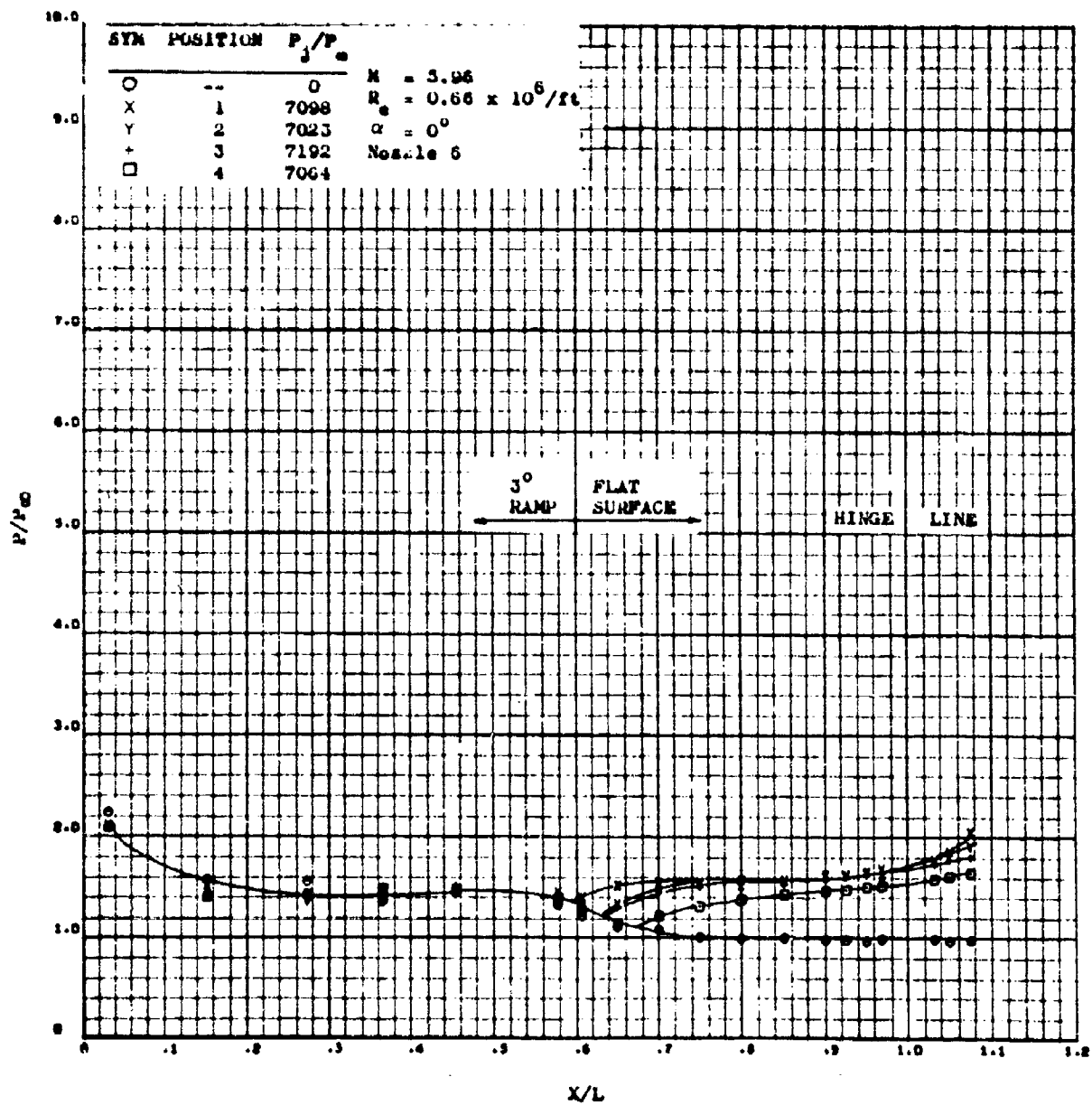


Figure 10. Effect of N-zile location on time induced separation at Mach 5.96

CONFIDENTIAL

CONFIDENTIAL

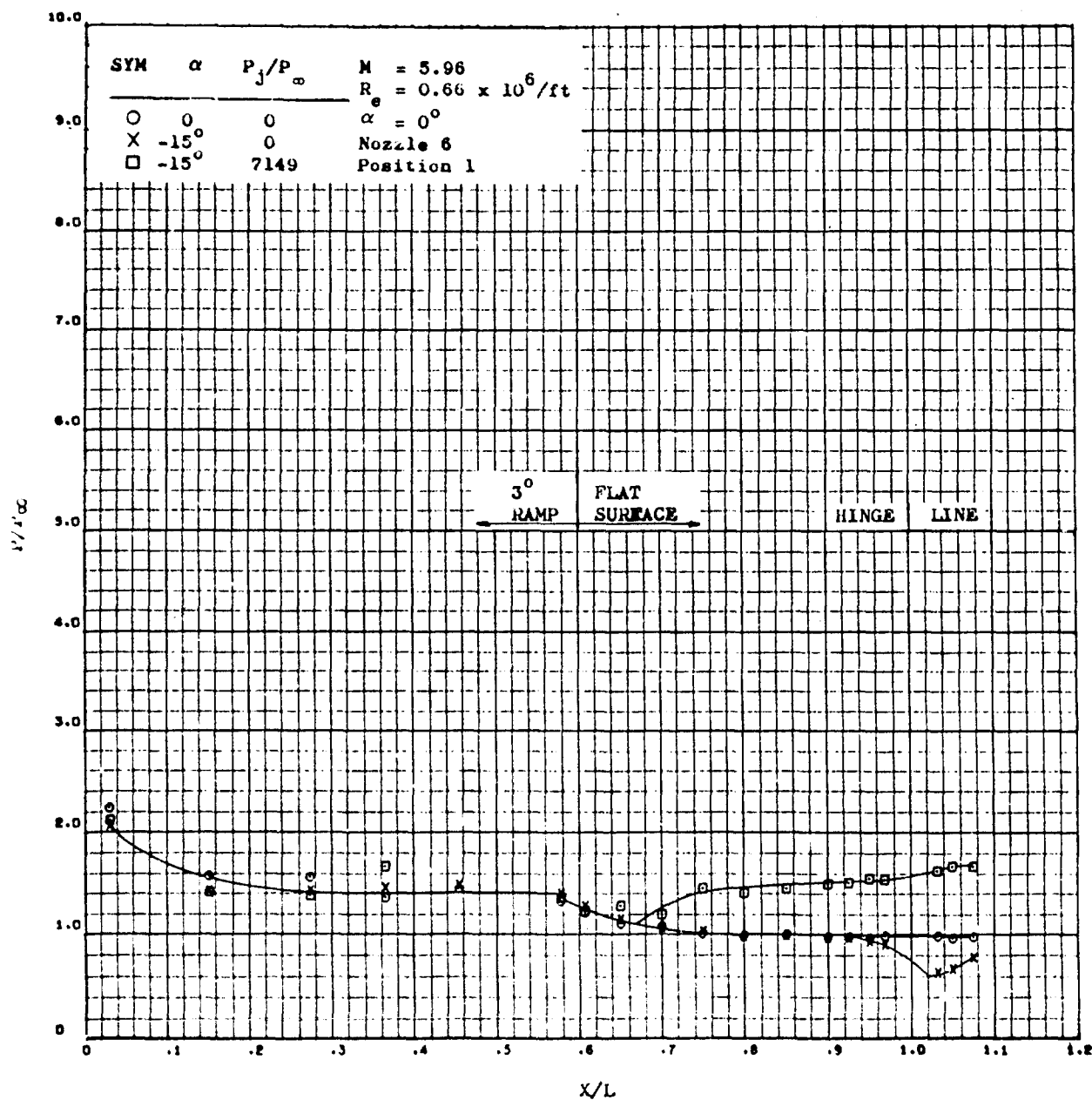


Figure 107. Effect of a -15° Elevon Deflection with Plume on Bottom Centerline Pressure at Mach 5.96

CONFIDENTIAL

CONFIDENTIAL

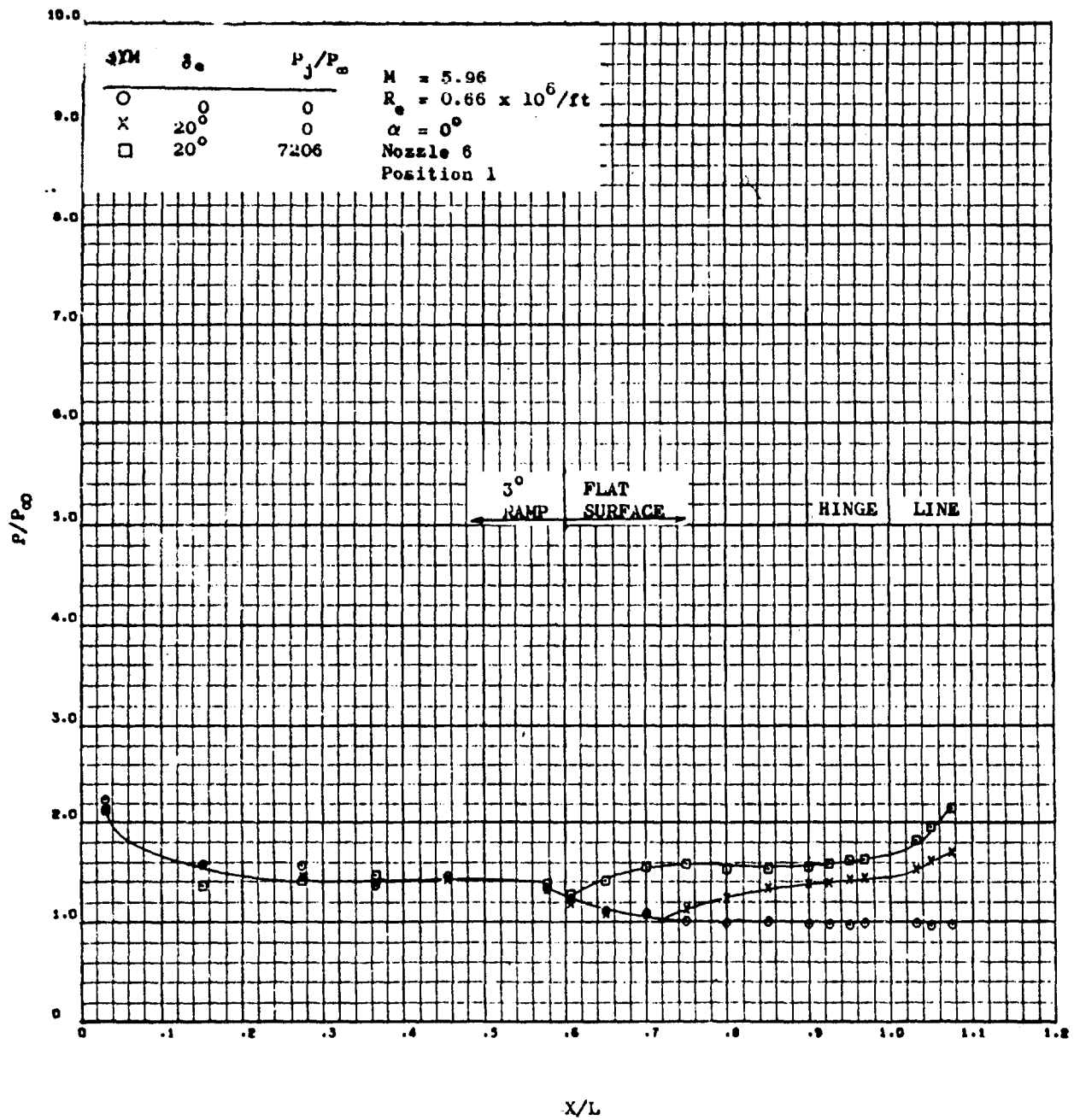


Figure 108. Effect of a +20° Elevon and Plume on Bottom Centerline Pressure at Mach 5.96

CONFIDENTIAL

CONFIDENTIAL

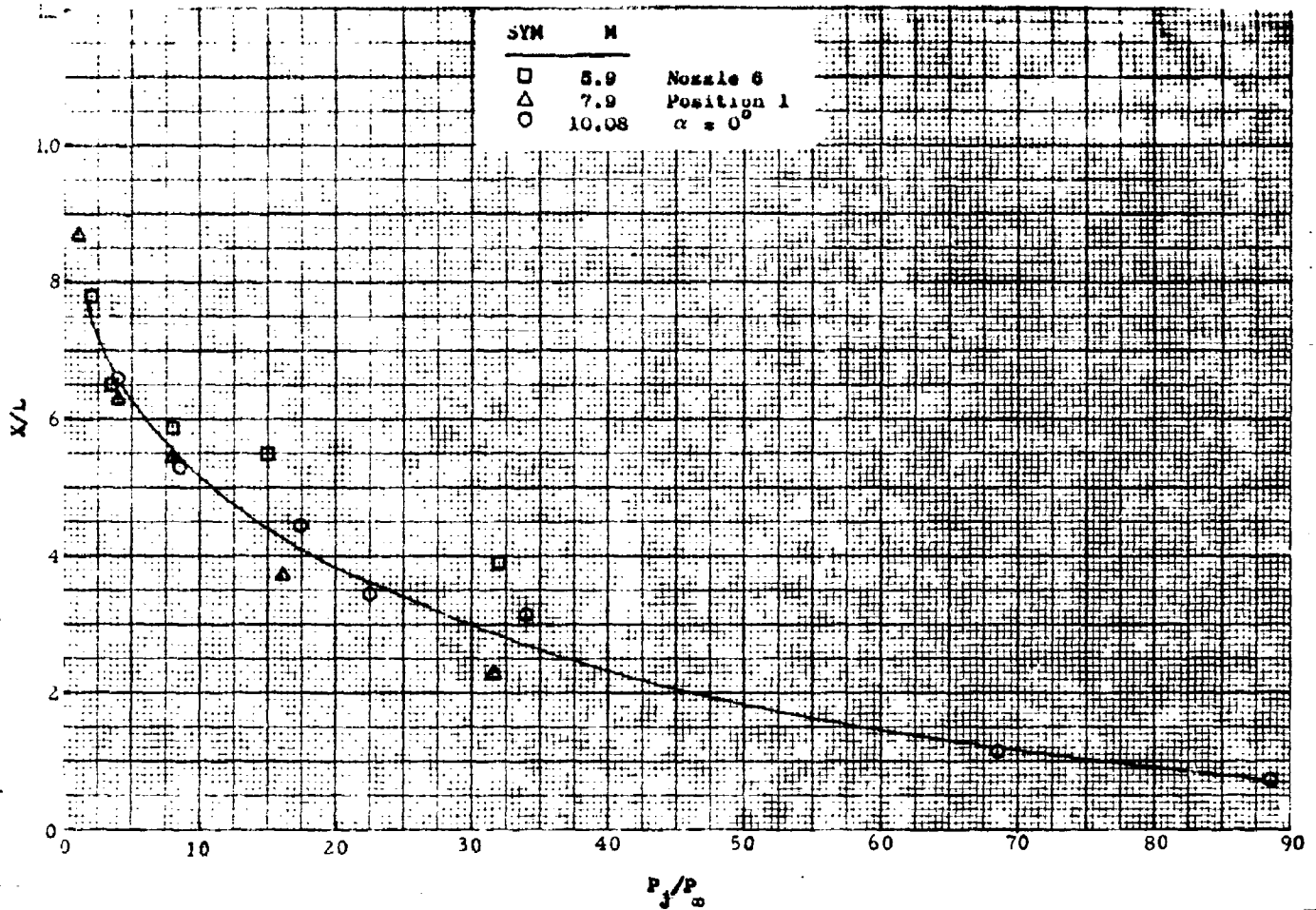


Figure 109. Effect of Mach Number on Separation Location

CONFIDENTIAL

CONFIDENTIAL

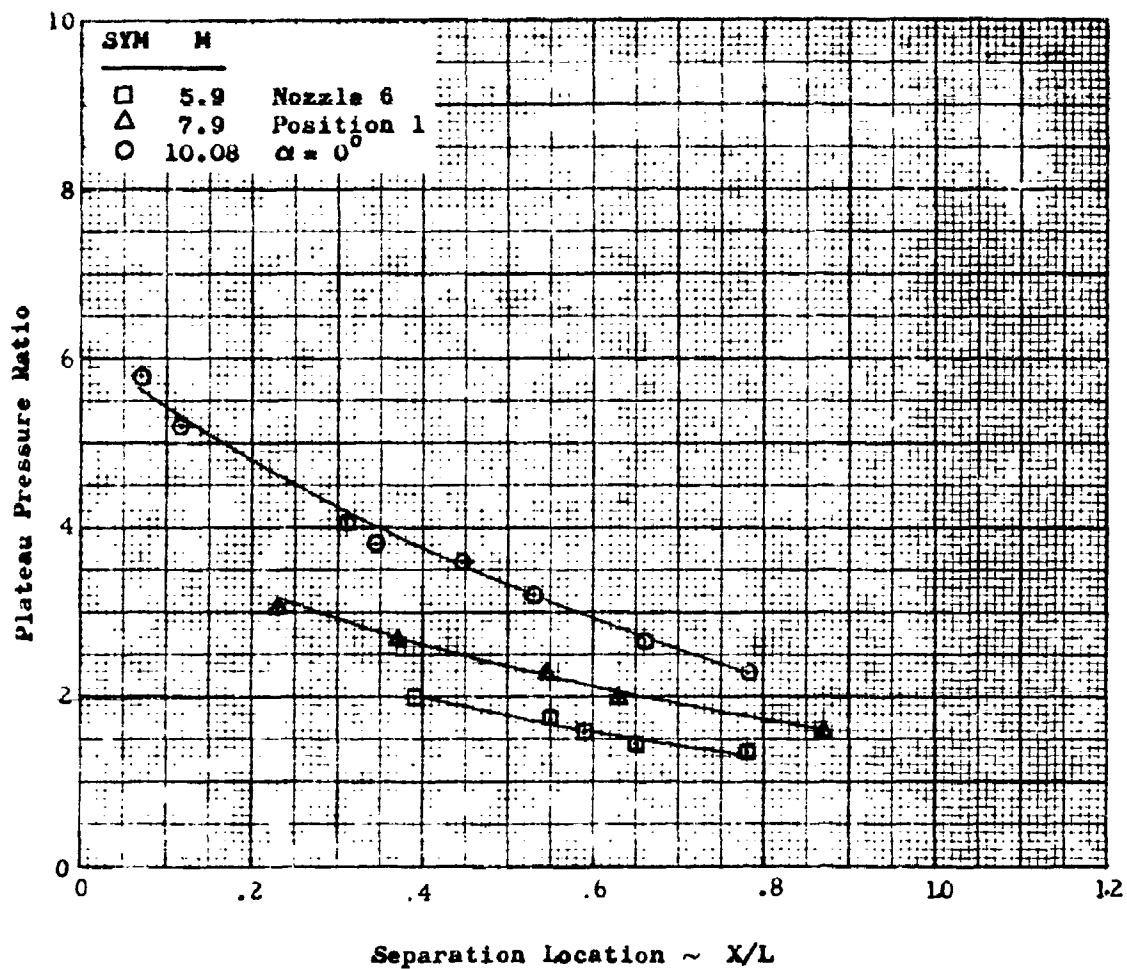


Figure 110. Mach Number Effect on Plateau Pressure Ratio

CONFIDENTIAL

CONFIDENTIAL

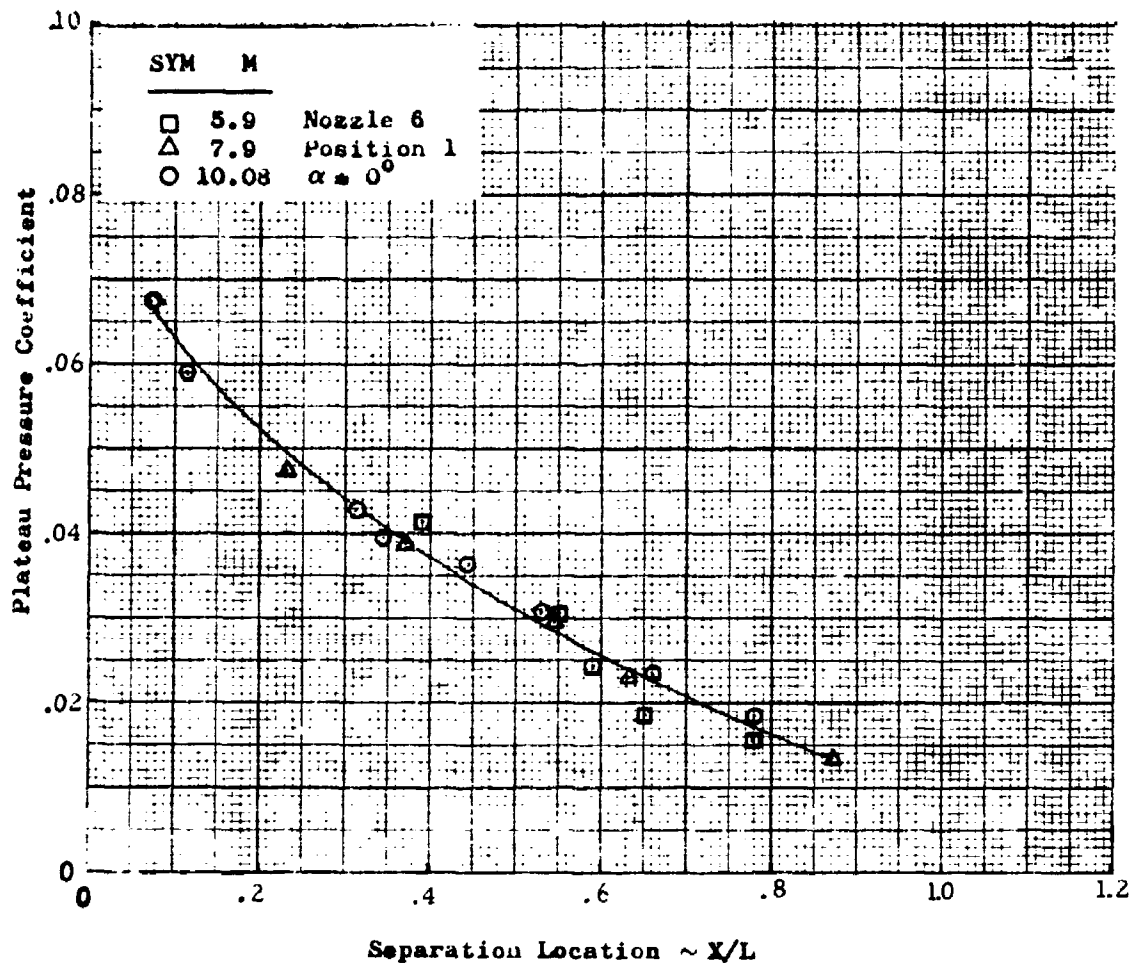


Figure 111. Mach Number Effect on Plateau Pressure Coefficient

CONFIDENTIAL

CONFIDENTIAL

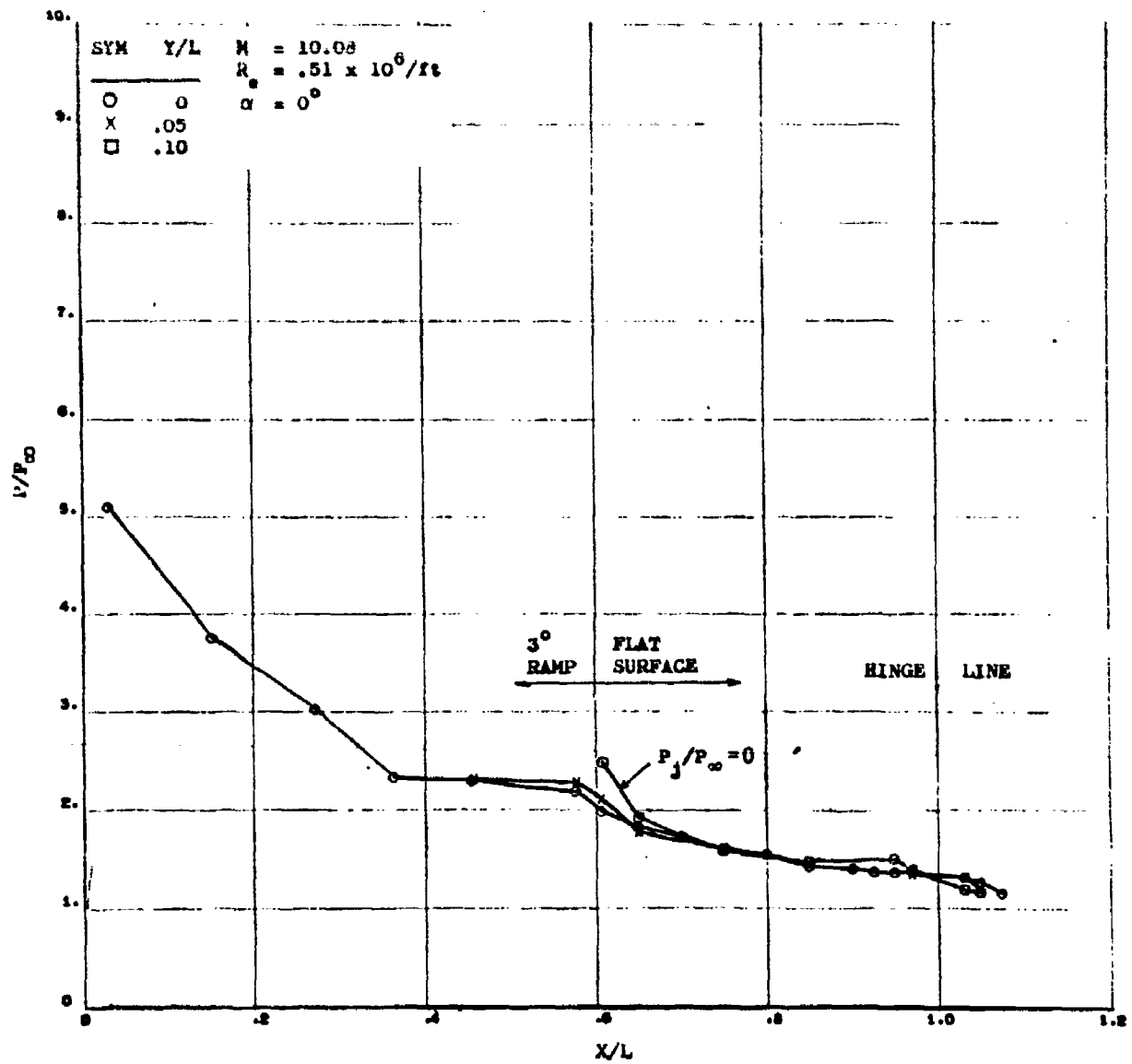


Figure 112. Delta Bottom Pressures at Mach = 10.08

CONFIDENTIAL

CONFIDENTIAL

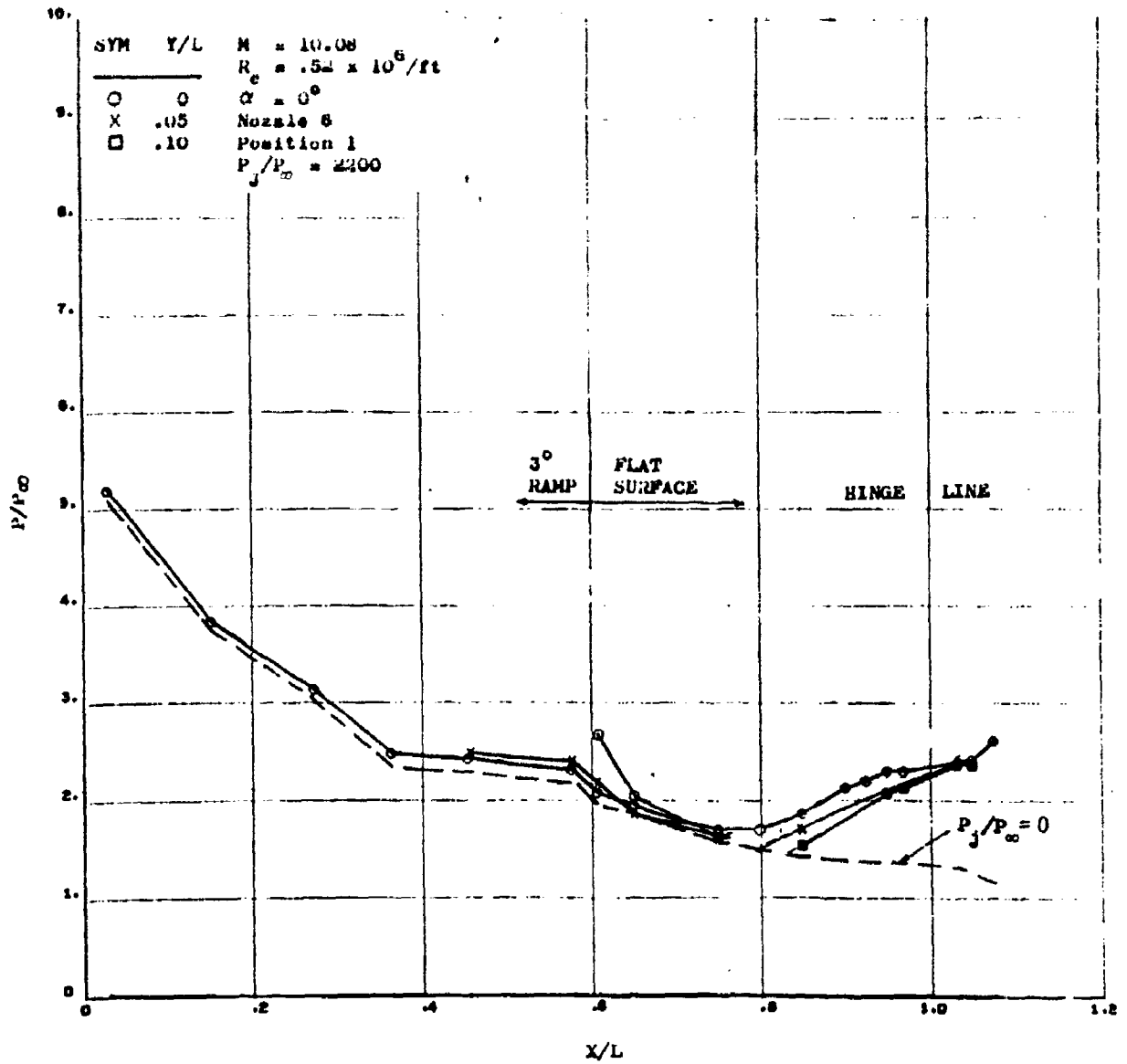


Figure 113. Bottom Pressure Distribution at Mach = 10.08 and $P_j / P_\infty = 2200$

CONFIDENTIAL

CONFIDENTIAL

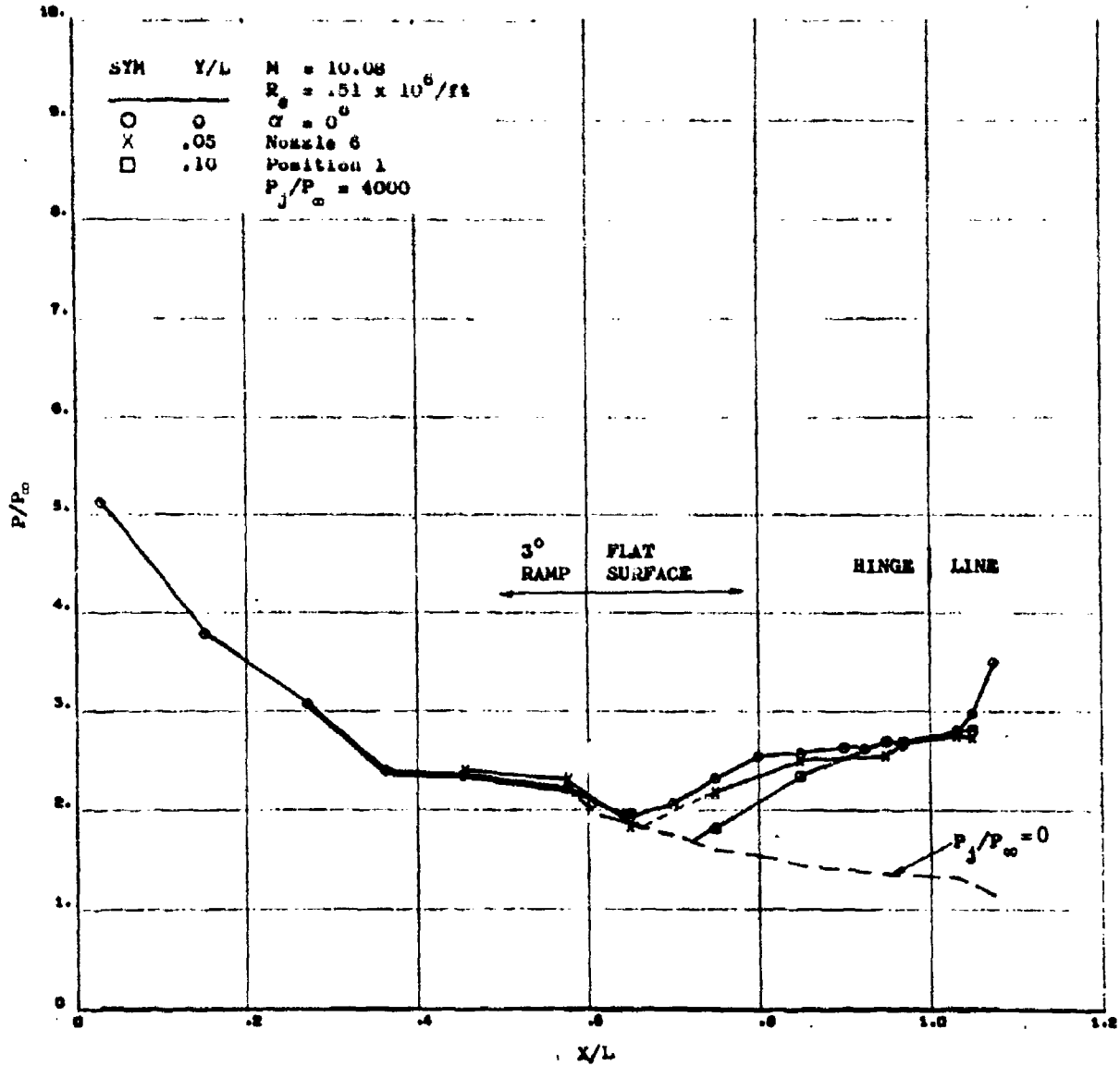


Figure 114. Bottom Pressure Distribution at Mach = 10.08 and $P_j/P_\infty = 4000$

CONFIDENTIAL

CONFIDENTIAL

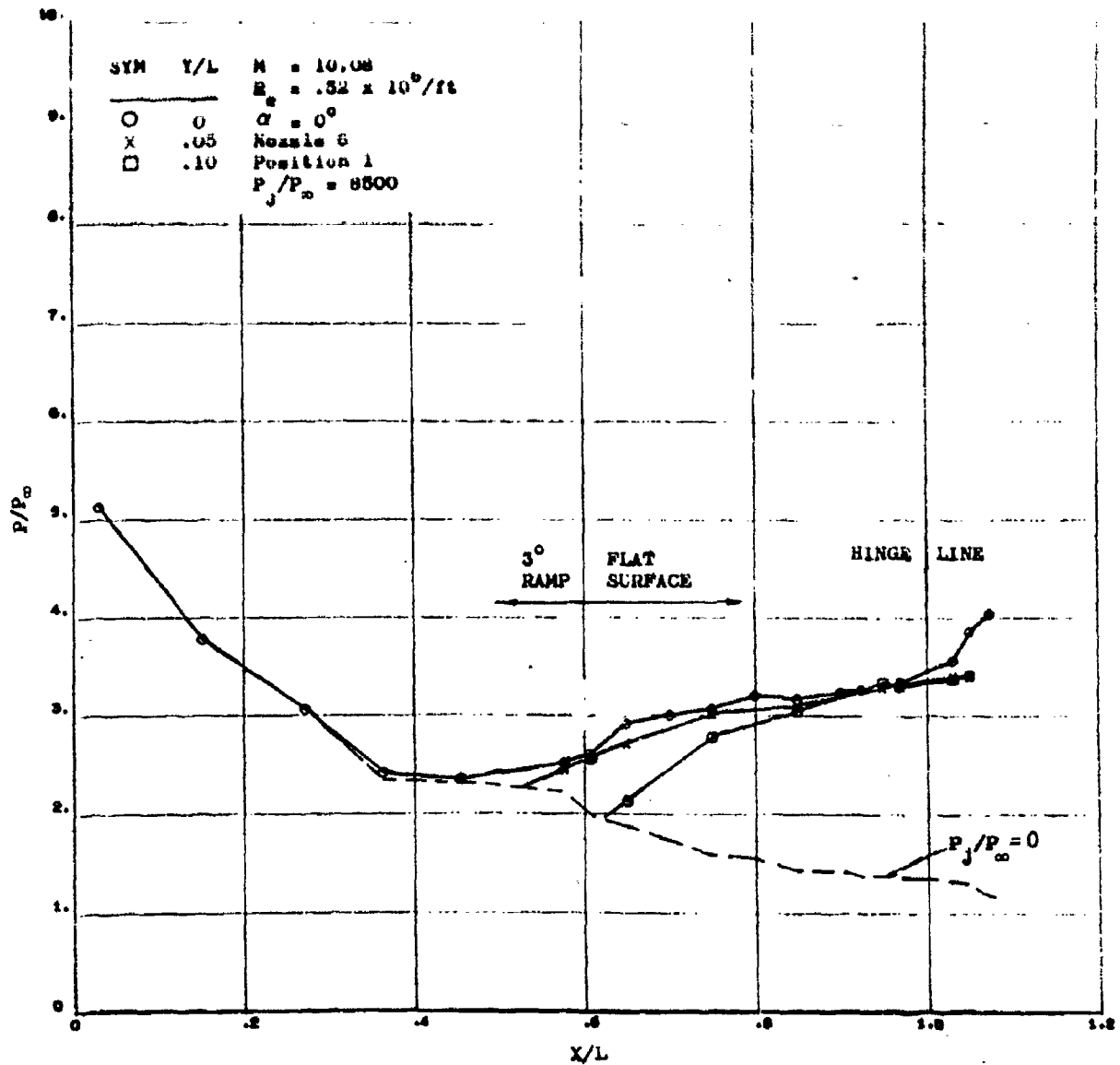


Figure 115. Bottom Pressure Distribution at Mach = 10.08 and $P_j/P_\infty = 8500$

CONFIDENTIAL

CONFIDENTIAL

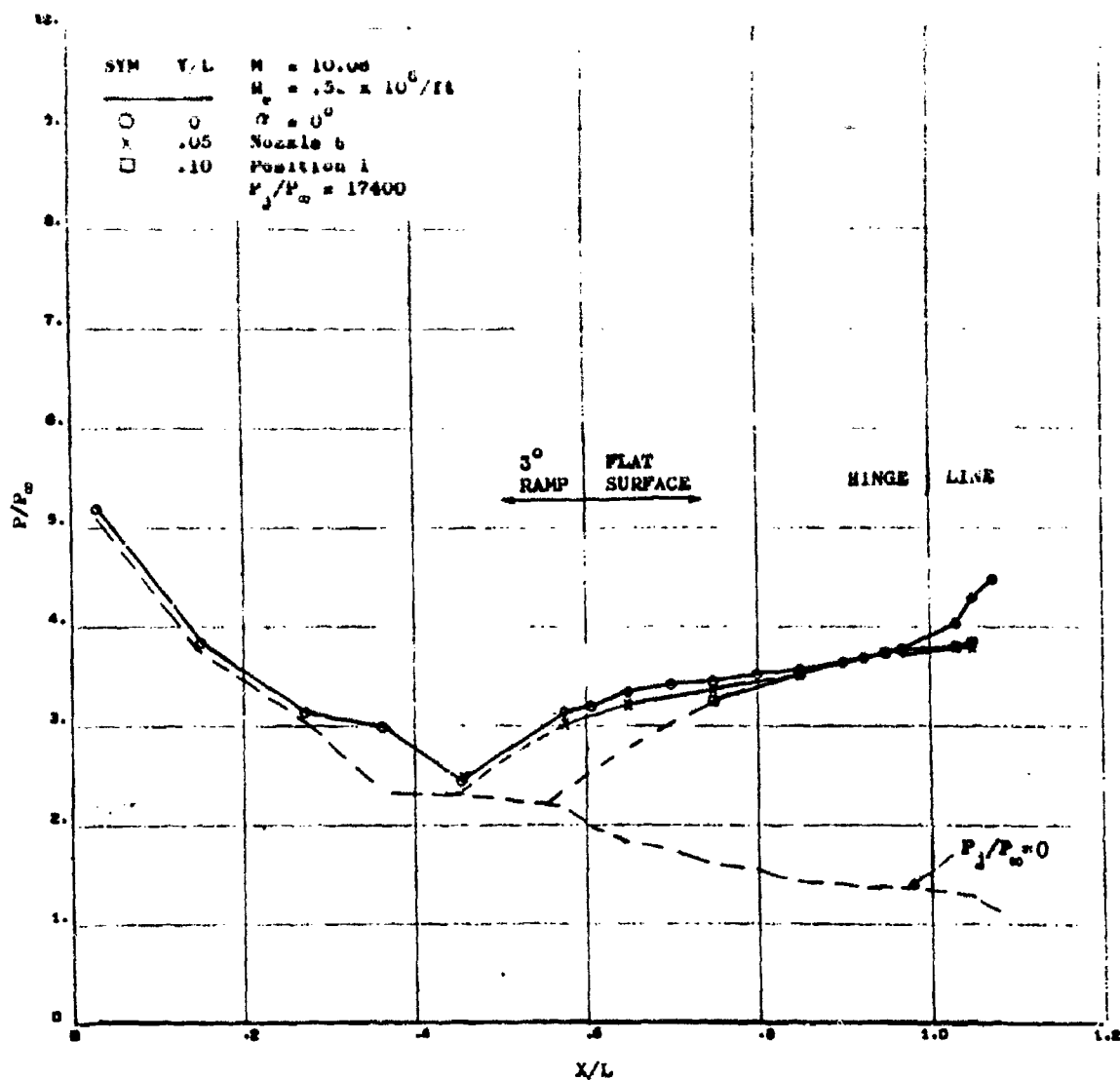


Figure 116. Bottom Pressure Distribution at Mach = 10.08 and $P_j/P_\infty = 17400$

CONFIDENTIAL

CONFIDENTIAL

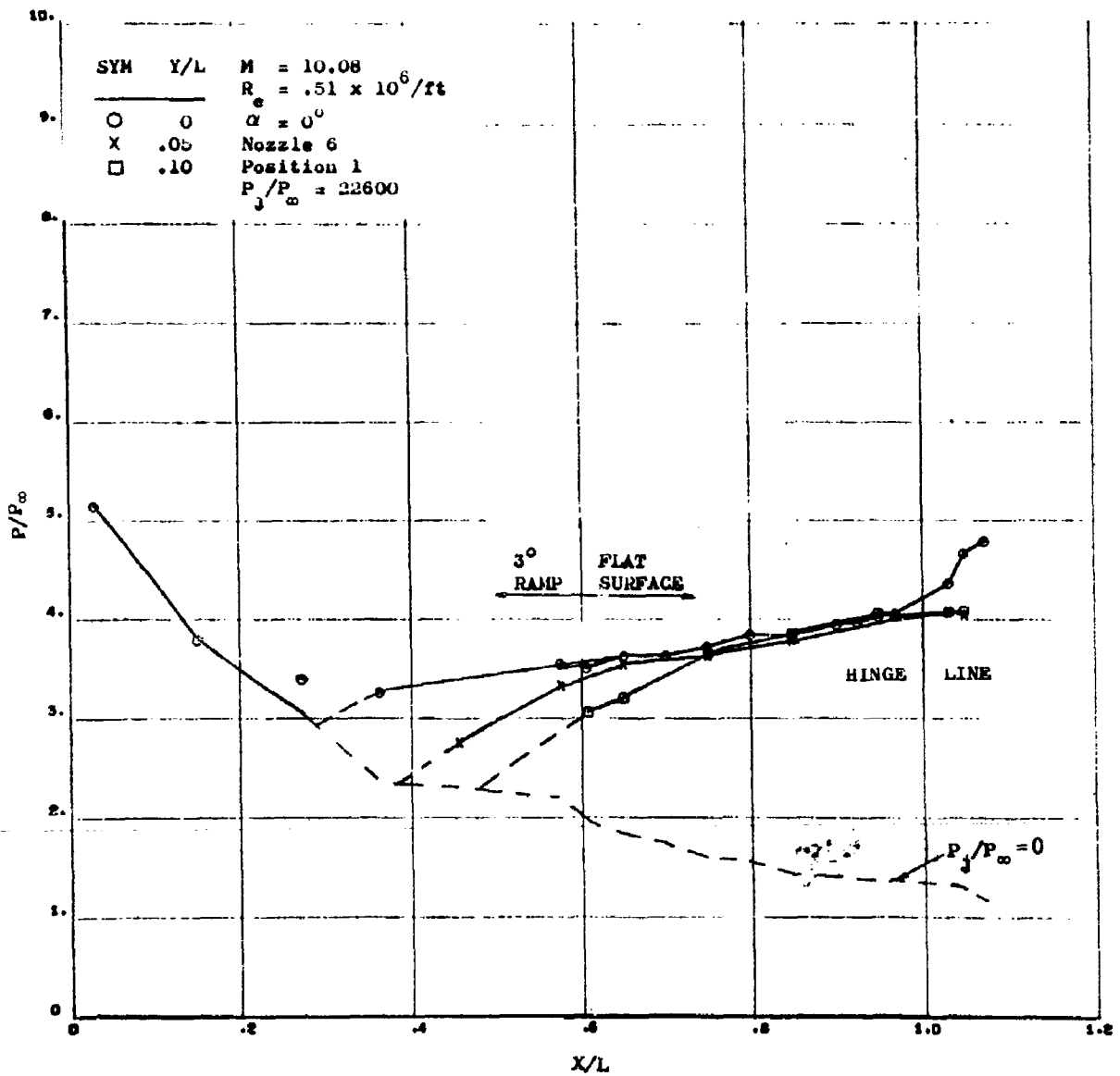


Figure 117. Bottom Pressure Distribution at Mach = 10.08 and $P_j / P_\infty = 22600$

CONFIDENTIAL

CONFIDENTIAL

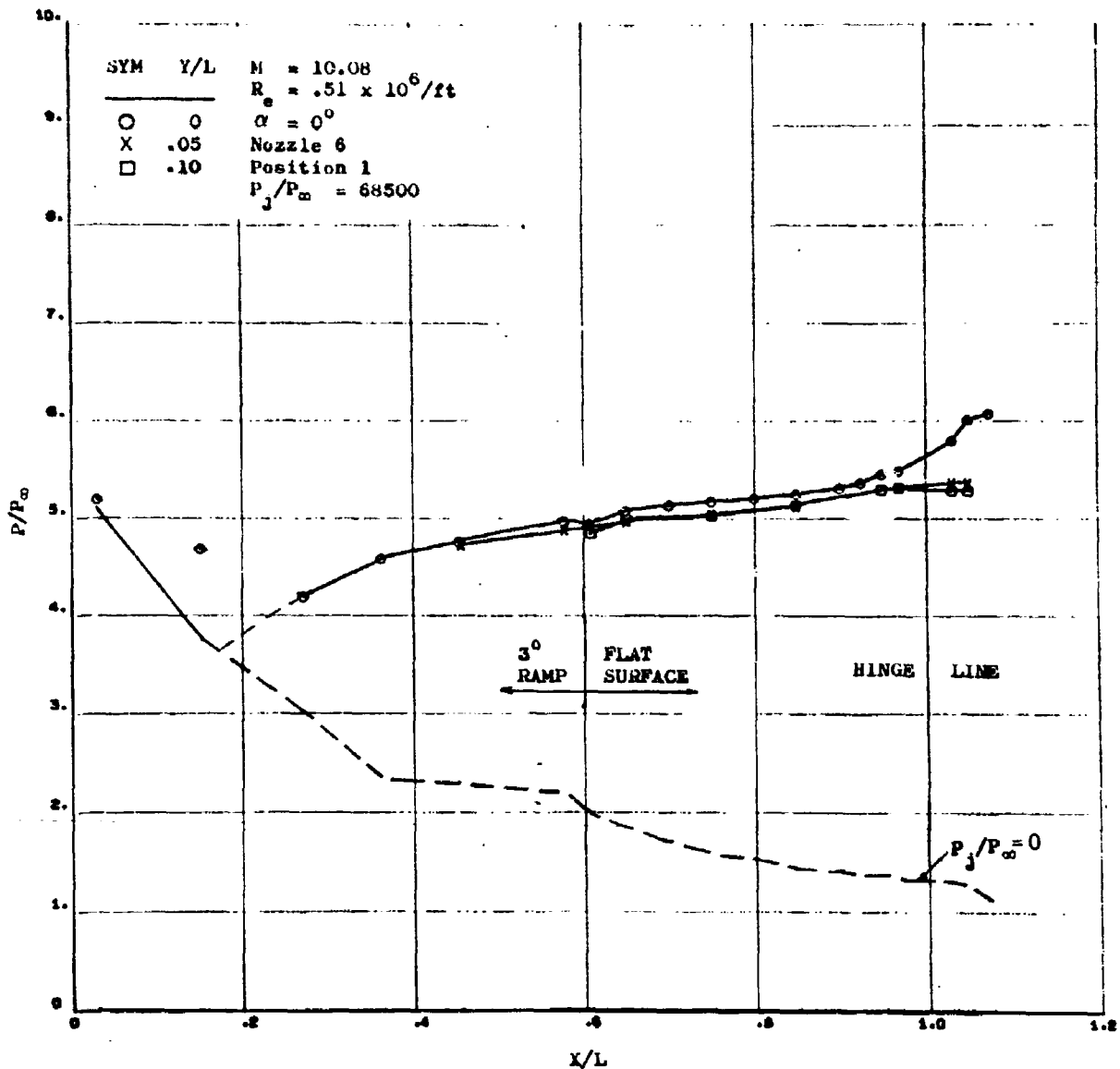


Figure 118. Bottom Pressure Distribution at Mach = 10.08 and P_j/P_∞ = 68500

CONFIDENTIAL

CONFIDENTIAL

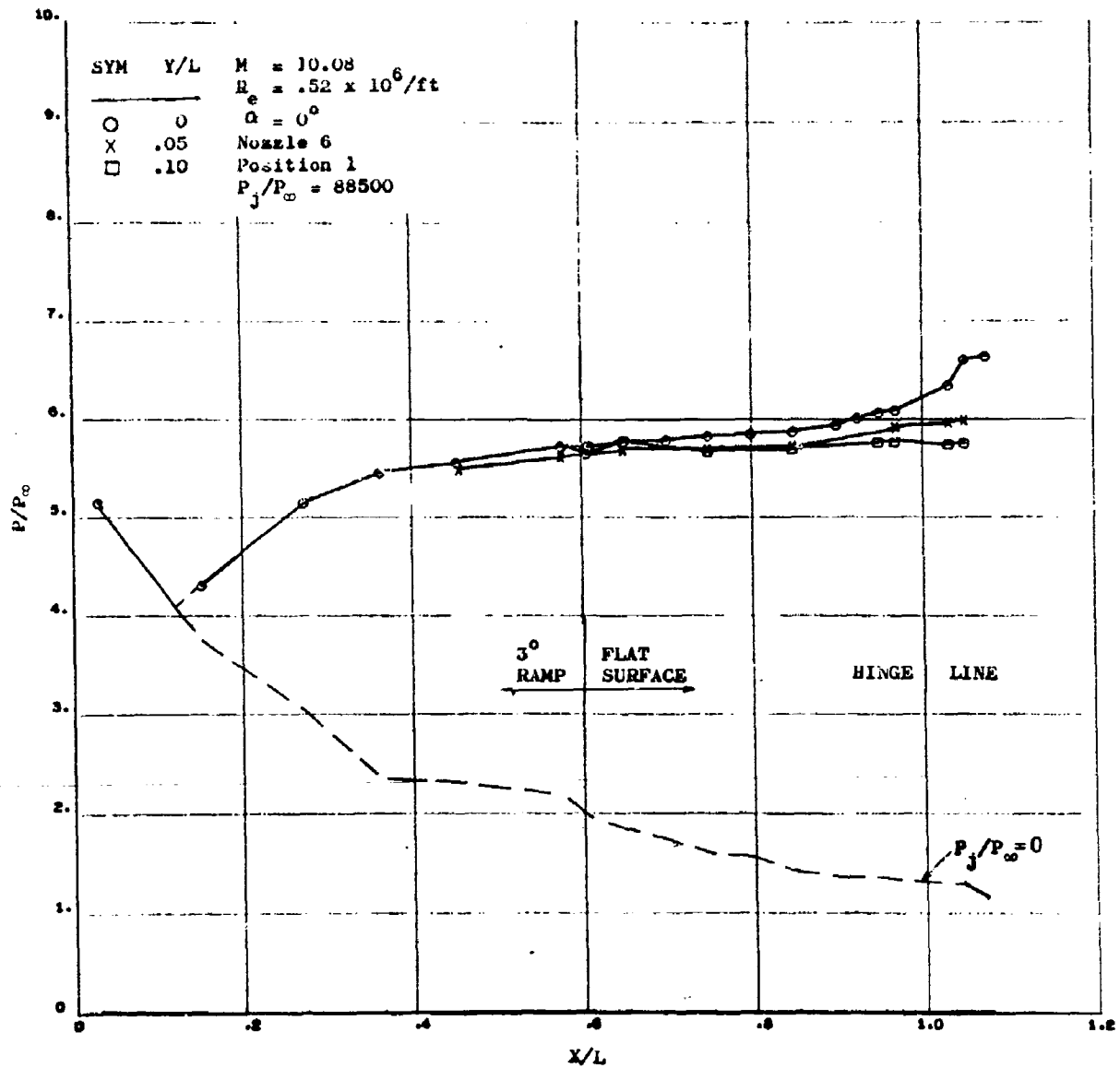


Figure 119. Bottom Pressure Distribution at Mach = 10.08 and $P_j/P_\infty = 88500$

CONFIDENTIAL

CONFIDENTIAL

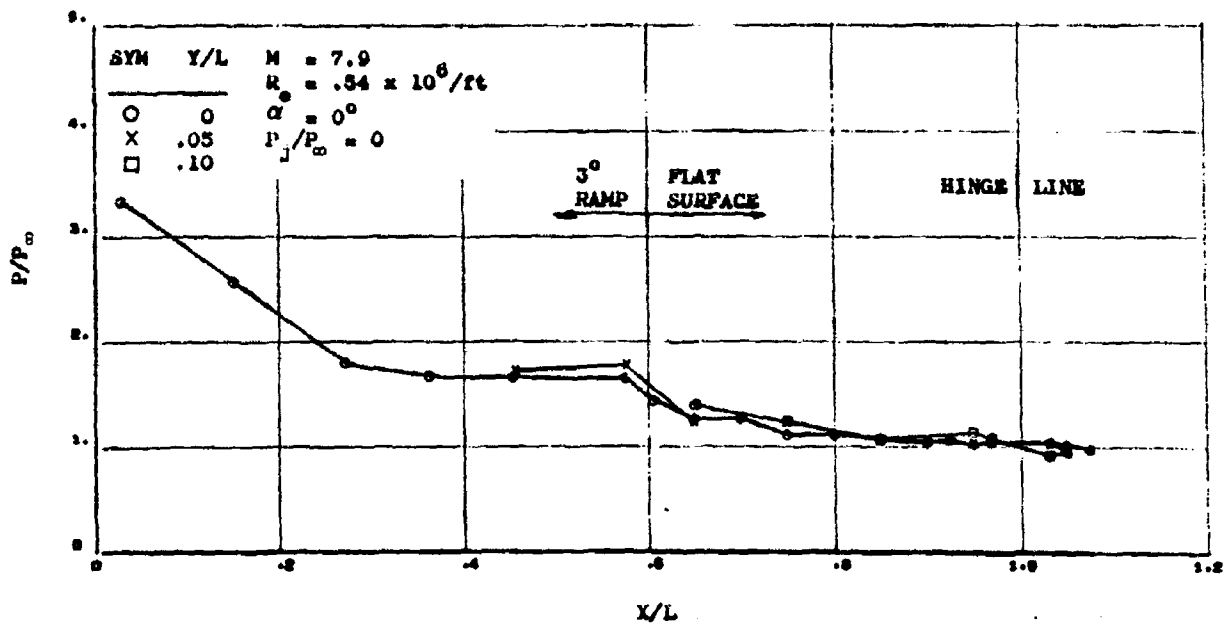


Figure 120. Bottom Pressure Distribution at Mach 7.9

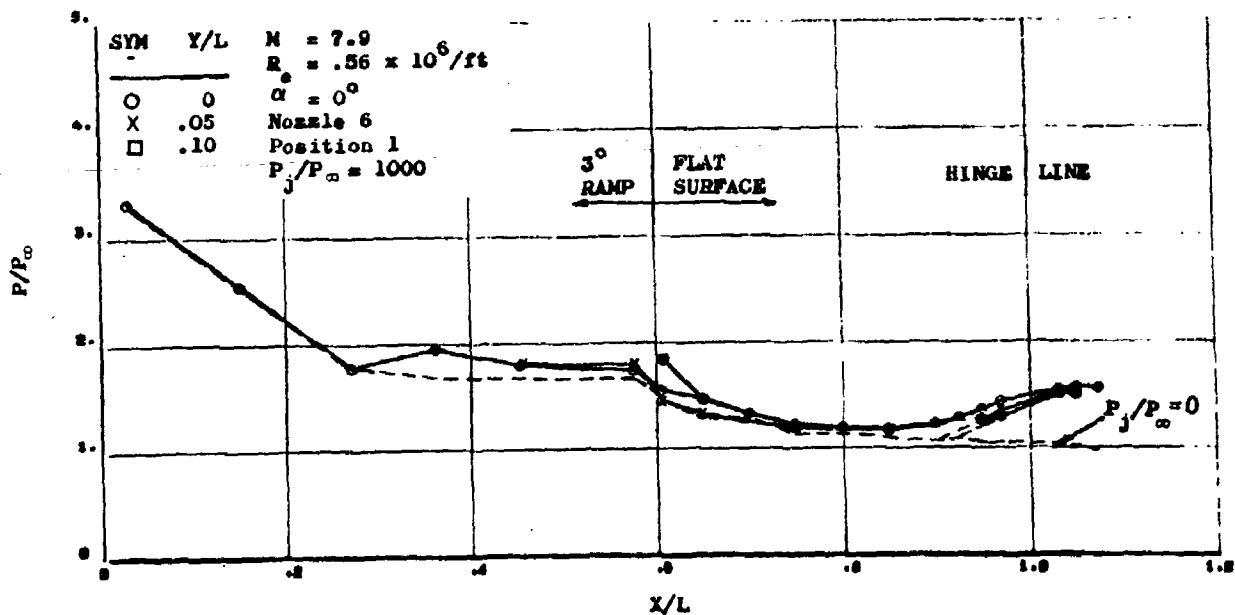


Figure 121. Bottom Pressures at Mach = 7.9 and $P_j/P_\infty = 1000$

CONFIDENTIAL

CONFIDENTIAL

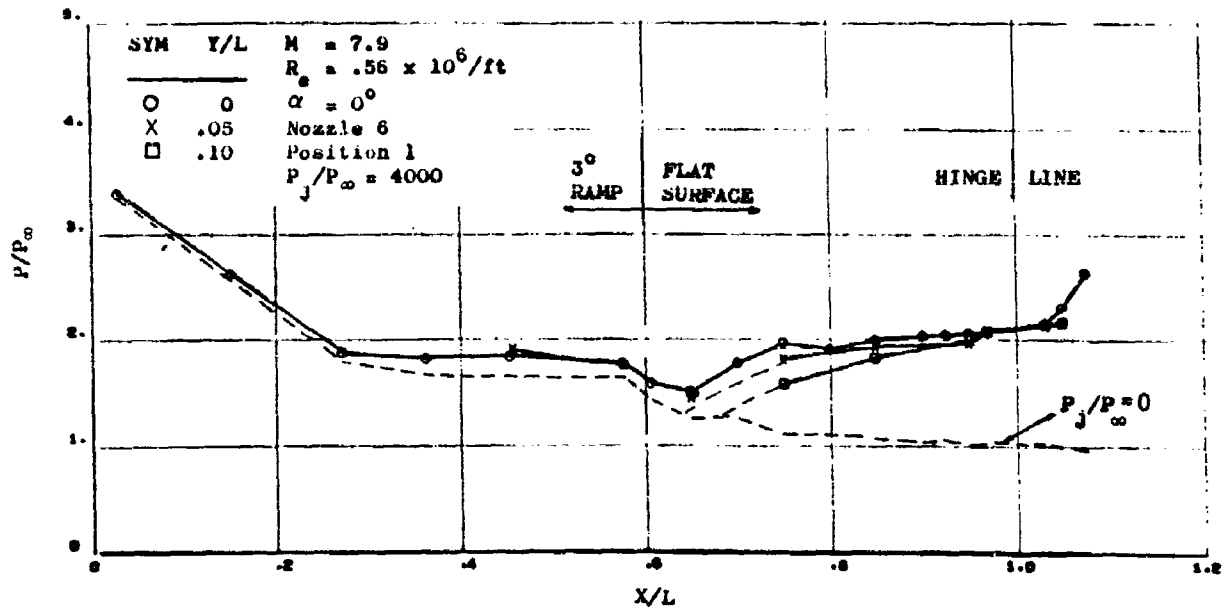


Figure 122. Bottom Pressures at Mach = 7.9 and $P_j/P_\infty = 4000$

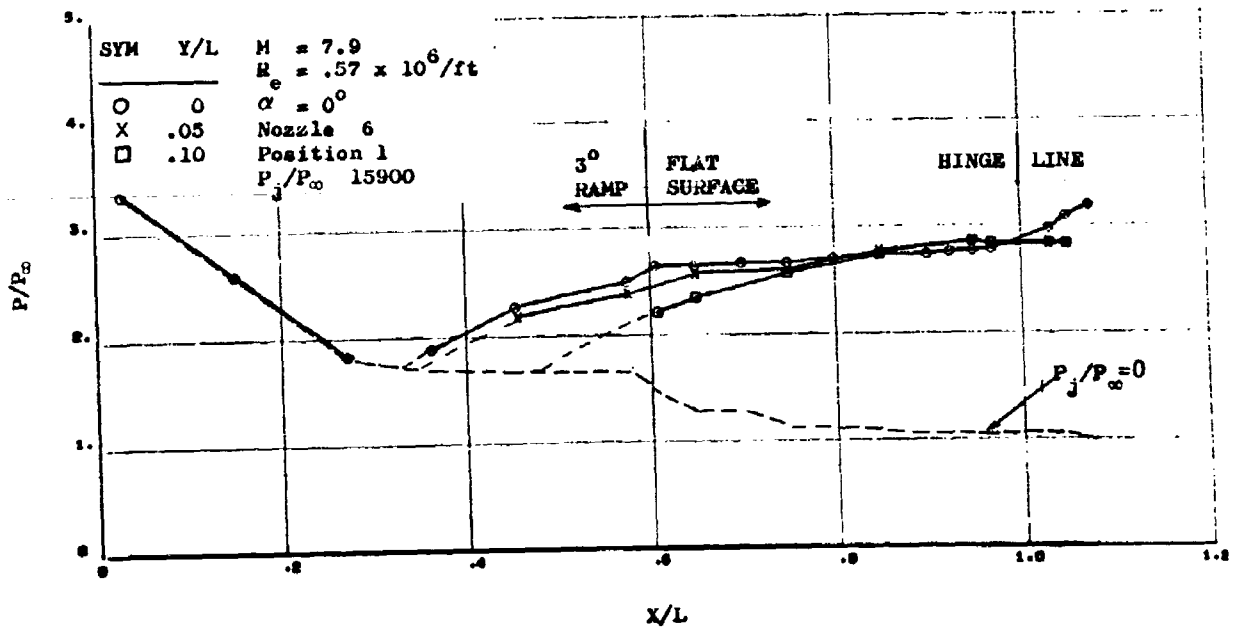


Figure 123. Bottom Pressures at Mach = 7.9 and $P_j/P_\infty = 15900$

CONFIDENTIAL

CONFIDENTIAL

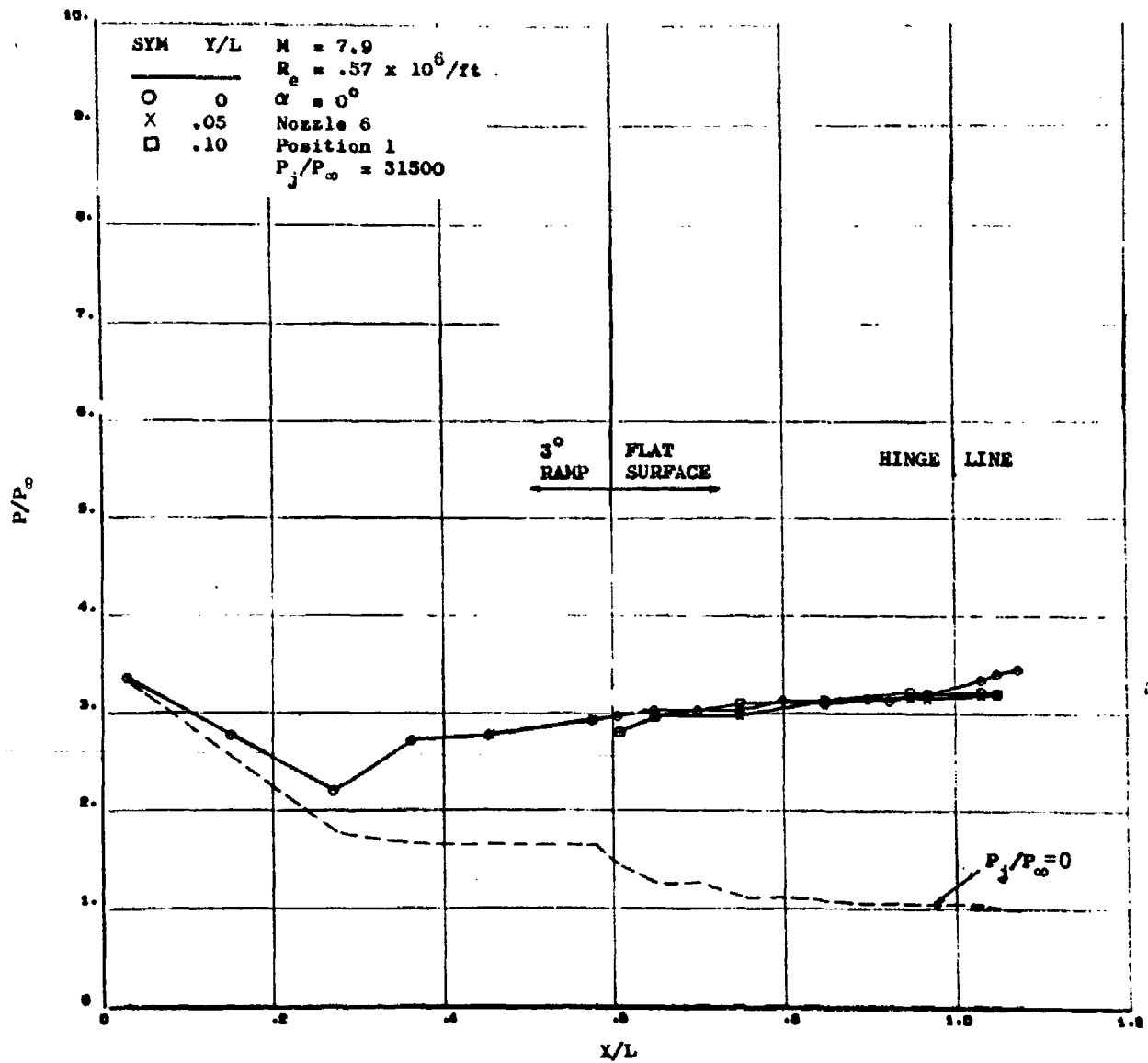


Figure 124. Bottom Pressures at Mach = 7.9 and $P_j/P_\infty = 31500$

CONFIDENTIAL

CONFIDENTIAL

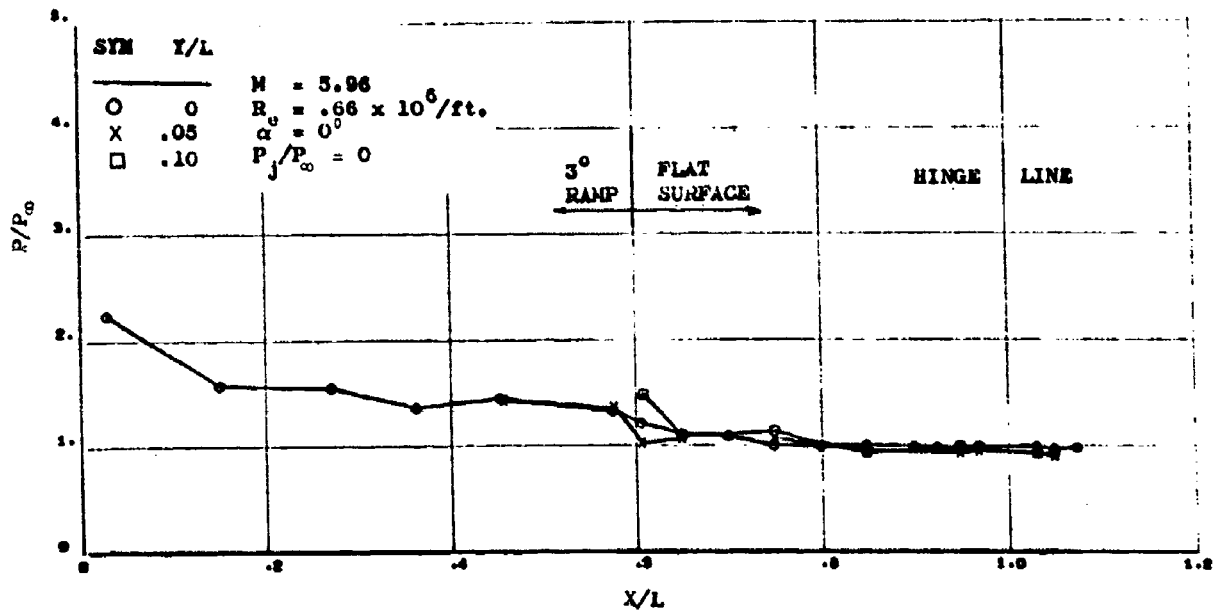


Figure 125. Bottom Pressures at Mach = 5.96

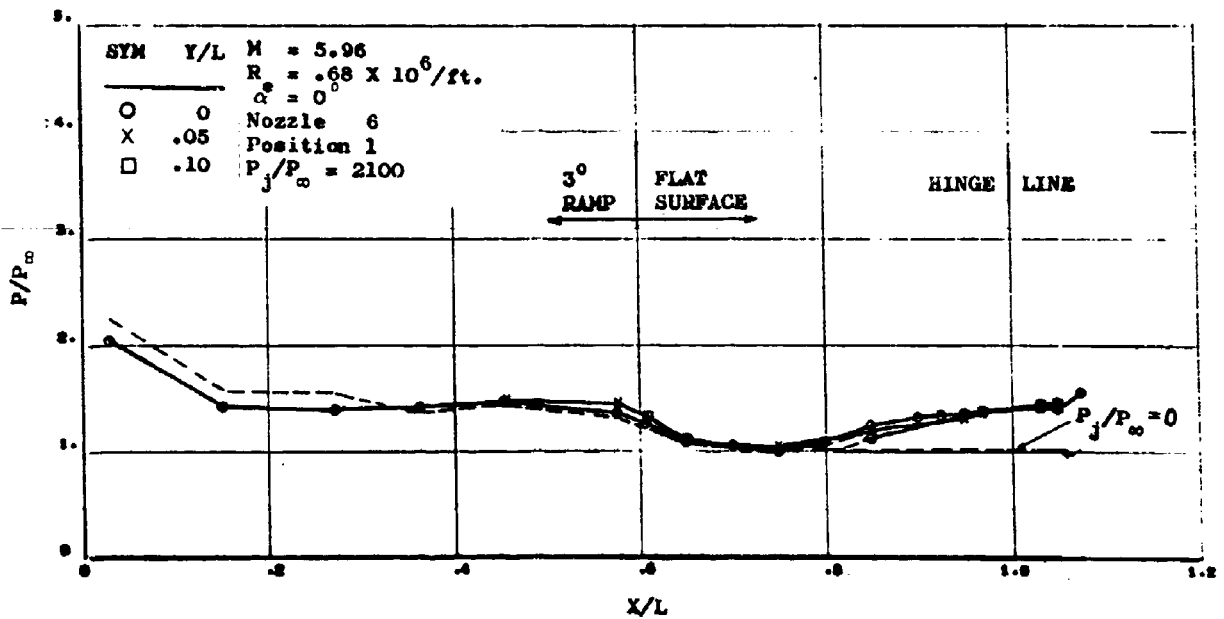


Figure 126. Bottom Pressures at Mach = 5.96 and $P_j/P_\infty = 2100$

CONFIDENTIAL

CONFIDENTIAL

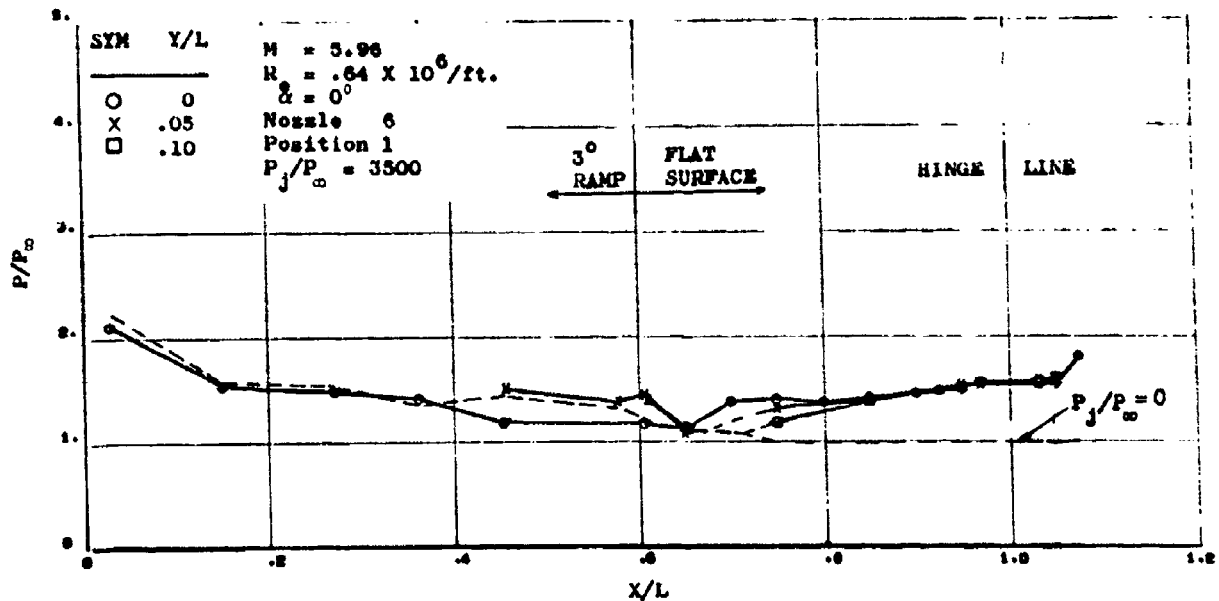


Figure 127. Bottom Pressures at Mach = 5.96 and $P_j/P_\infty = 3500$

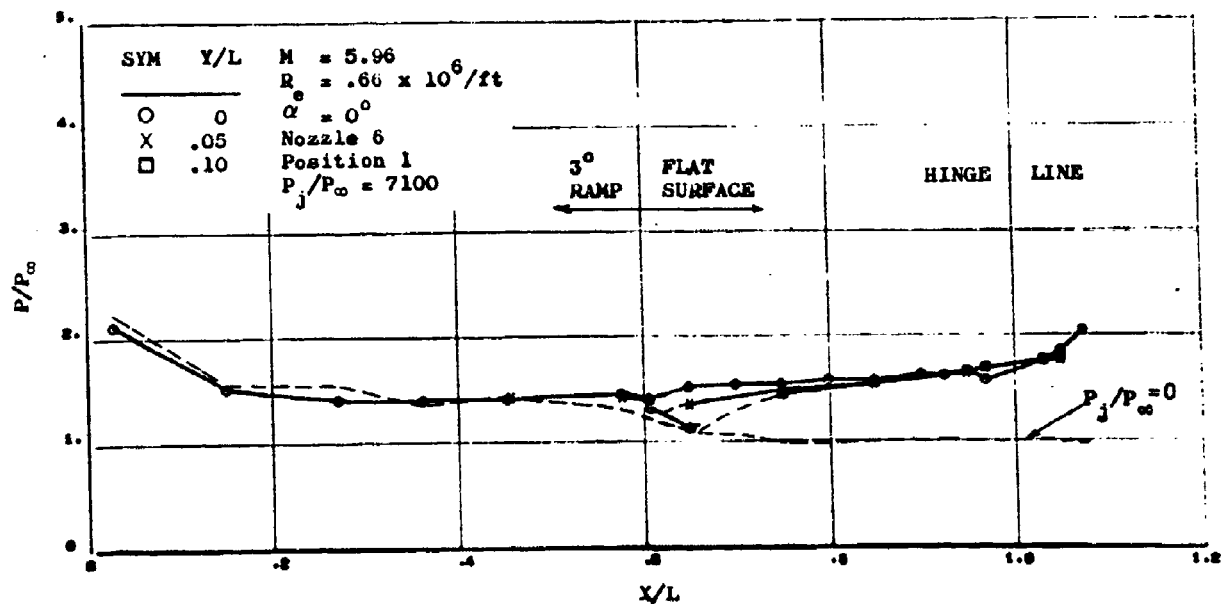


Figure 128. Bottom Pressures at Mach = 5.96 and $P_j/P_\infty = 7100$

CONFIDENTIAL

CONFIDENTIAL

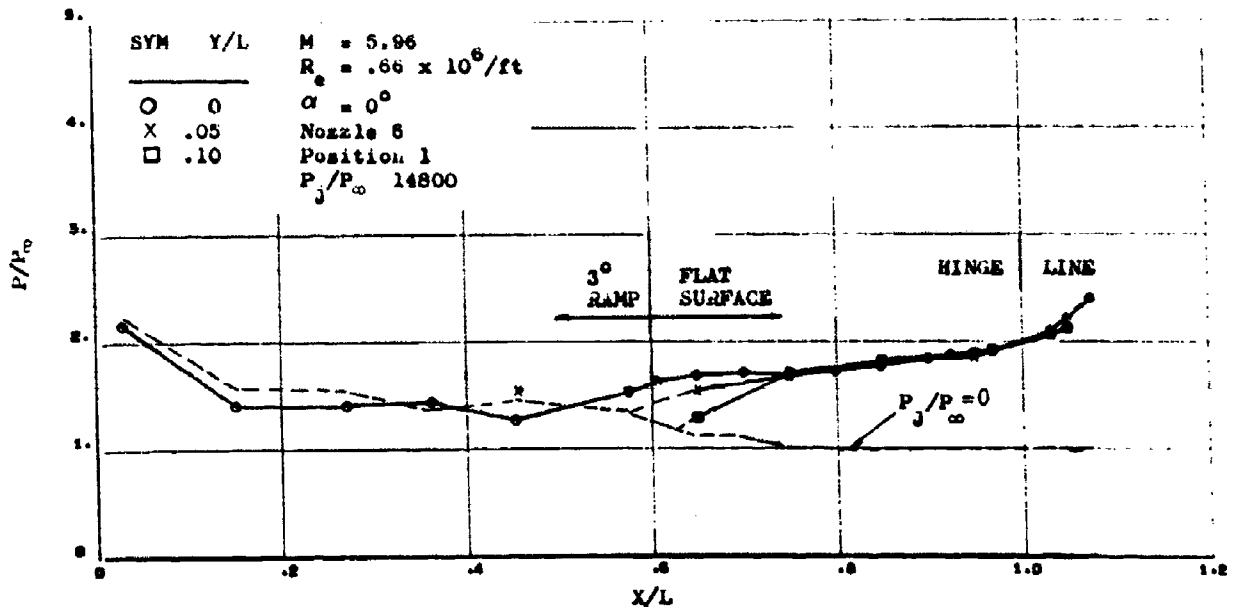


Figure 129. Bottom Pressures at Mach = 5.96 and $P_j/P_\infty = 14800$

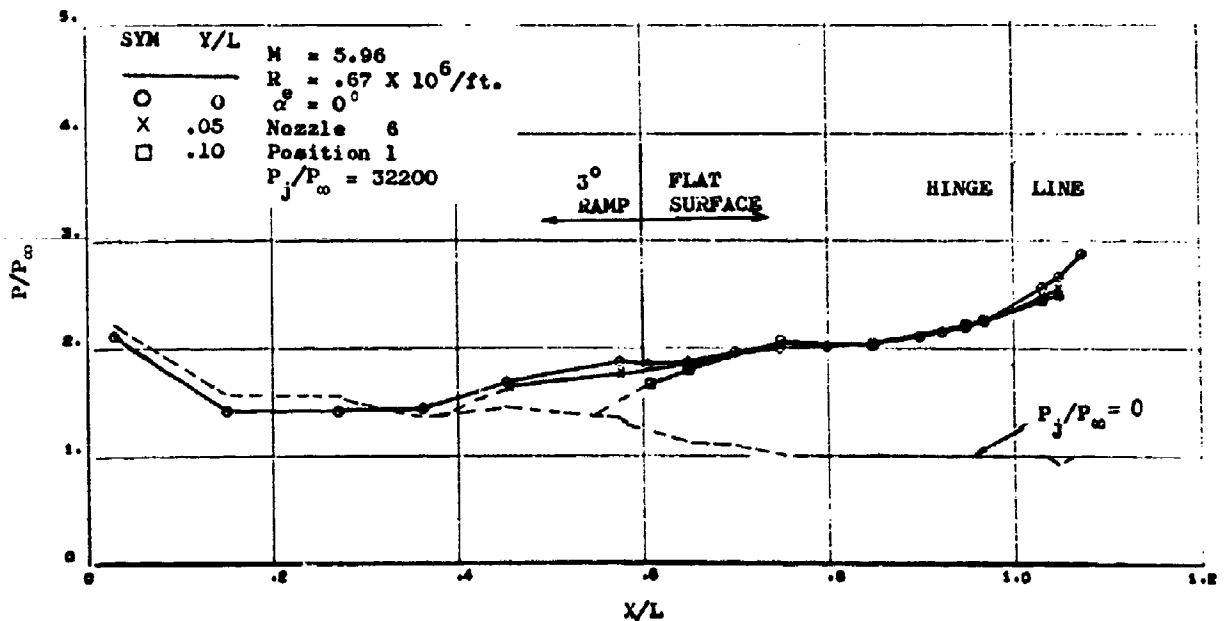


Figure 130. Bottom Pressures at Mach = 5.96 and $P_j/P_\infty = 32200$

CONFIDENTIAL

CONFIDENTIAL

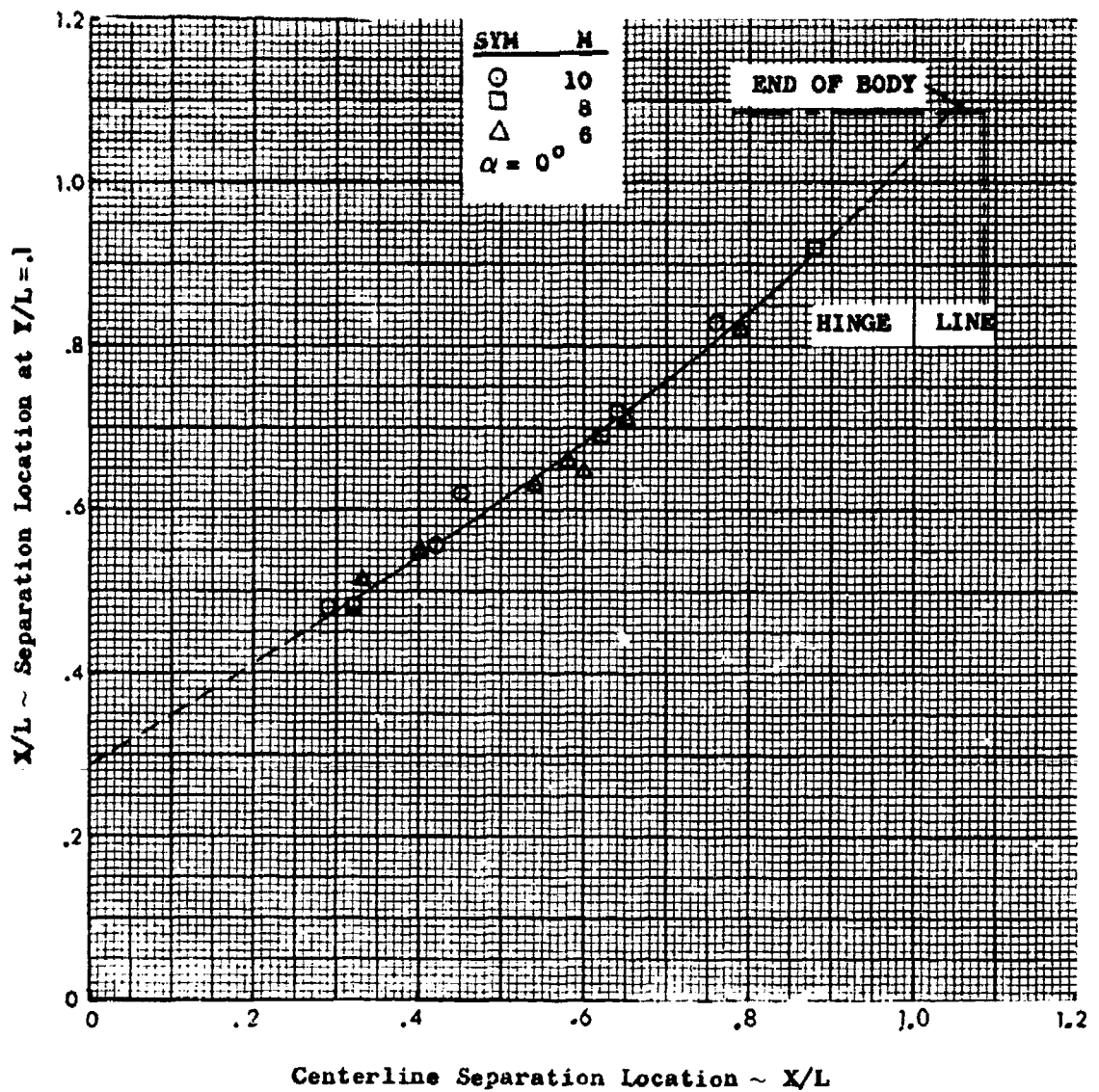


Figure 131. A Comparison of Separation Locations on the Bottom of the Delta Configuration

CONFIDENTIAL

CONFIDENTIAL

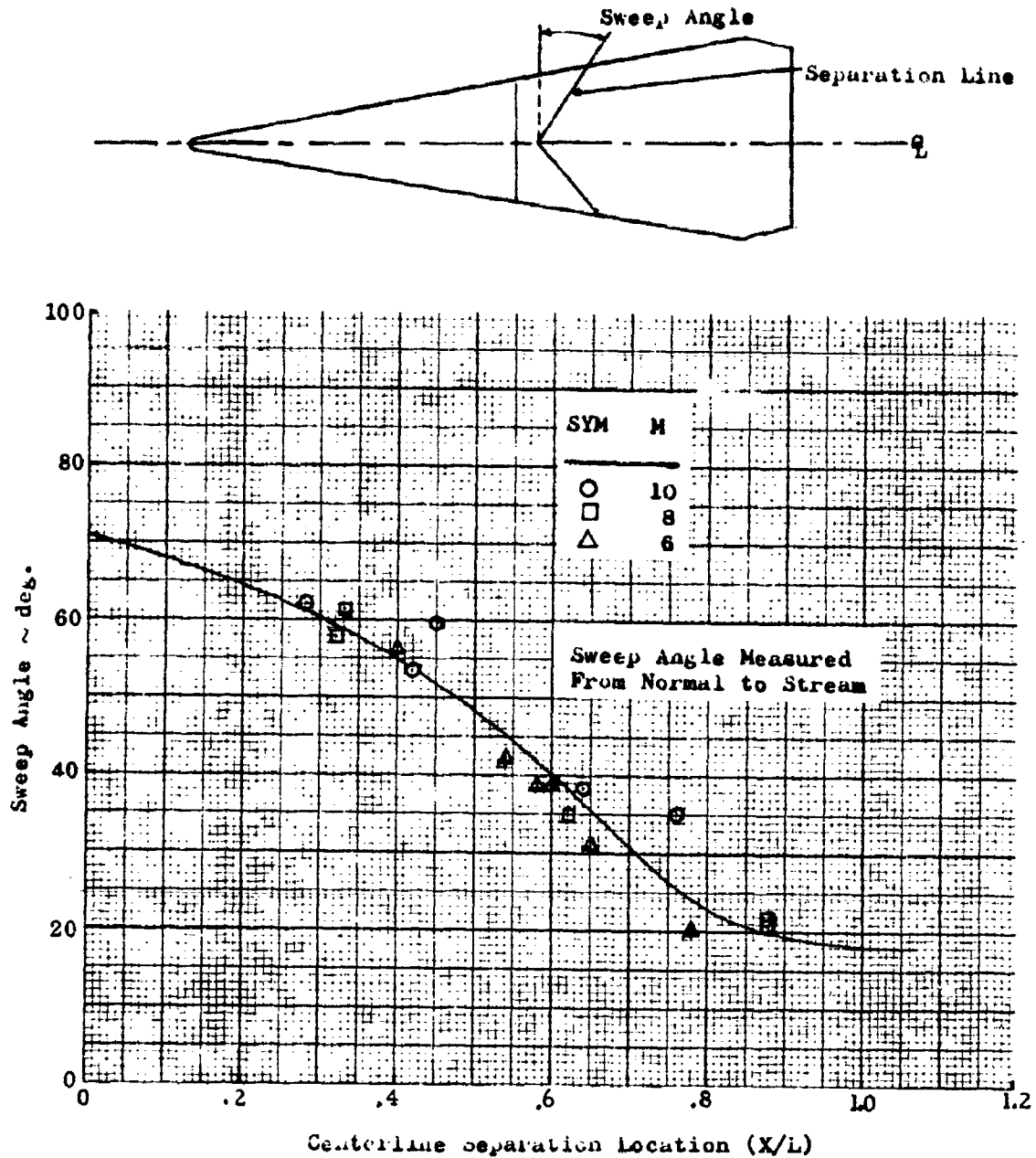


Figure 132. Sweep Angle of Spanwise Separation Location

CONFIDENTIAL

CONFIDENTIAL

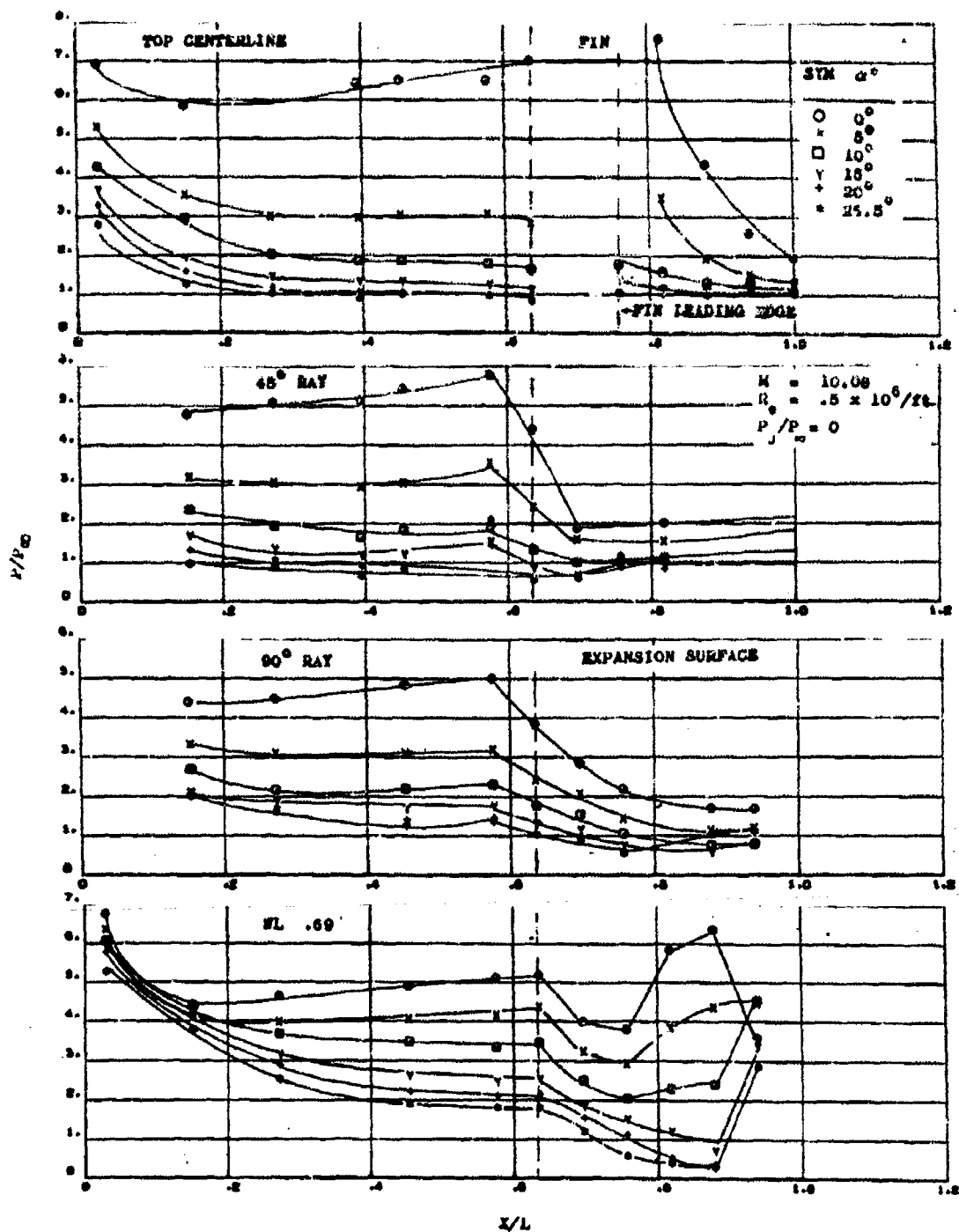


Figure 133. Upper Surface Pressures without Plume at $M = 10.08$

CONFIDENTIAL

CONFIDENTIAL

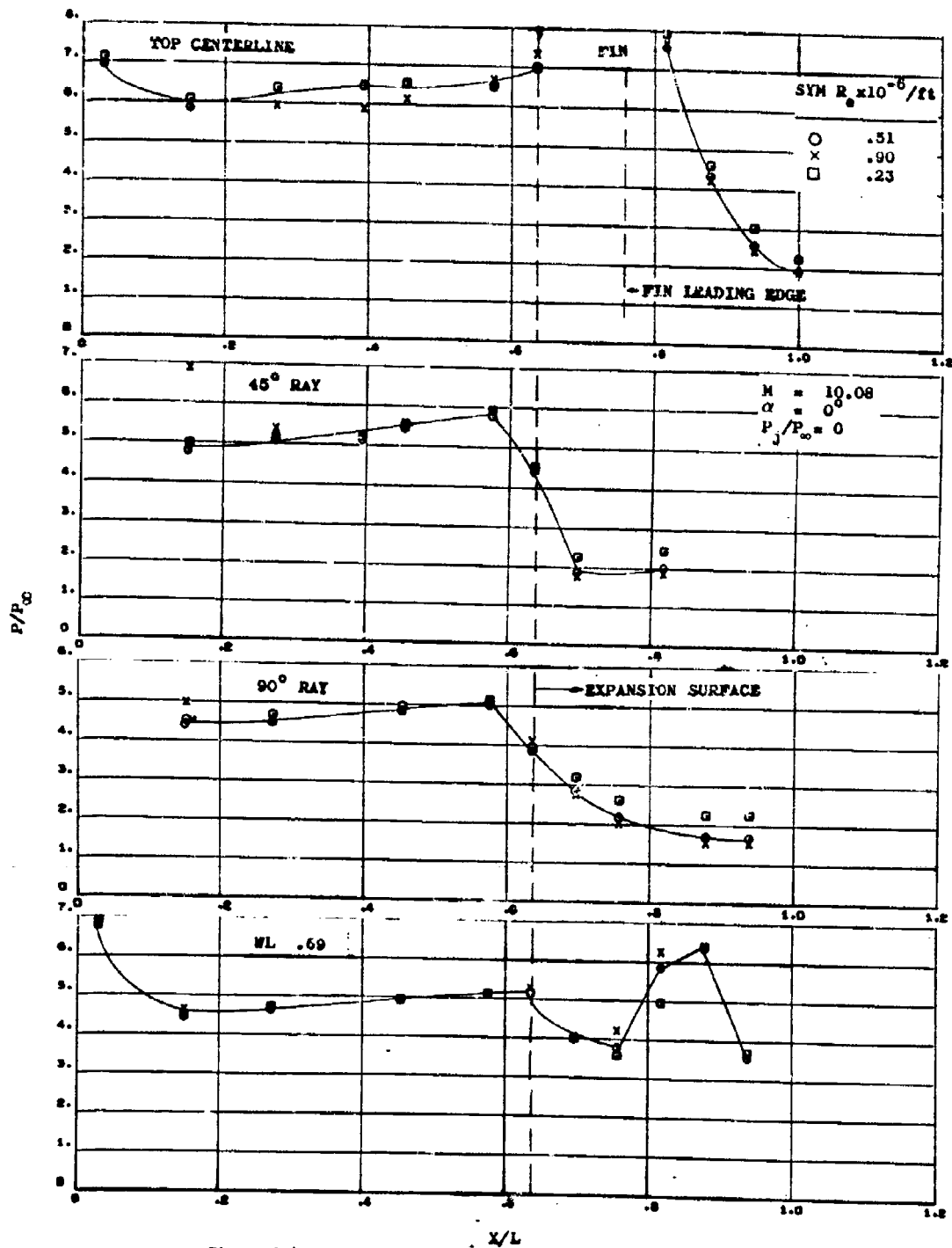


Figure 134. Effect of Reynolds Number on Upper Surface Pressure at $M = 10.08$

CONFIDENTIAL

CONFIDENTIAL

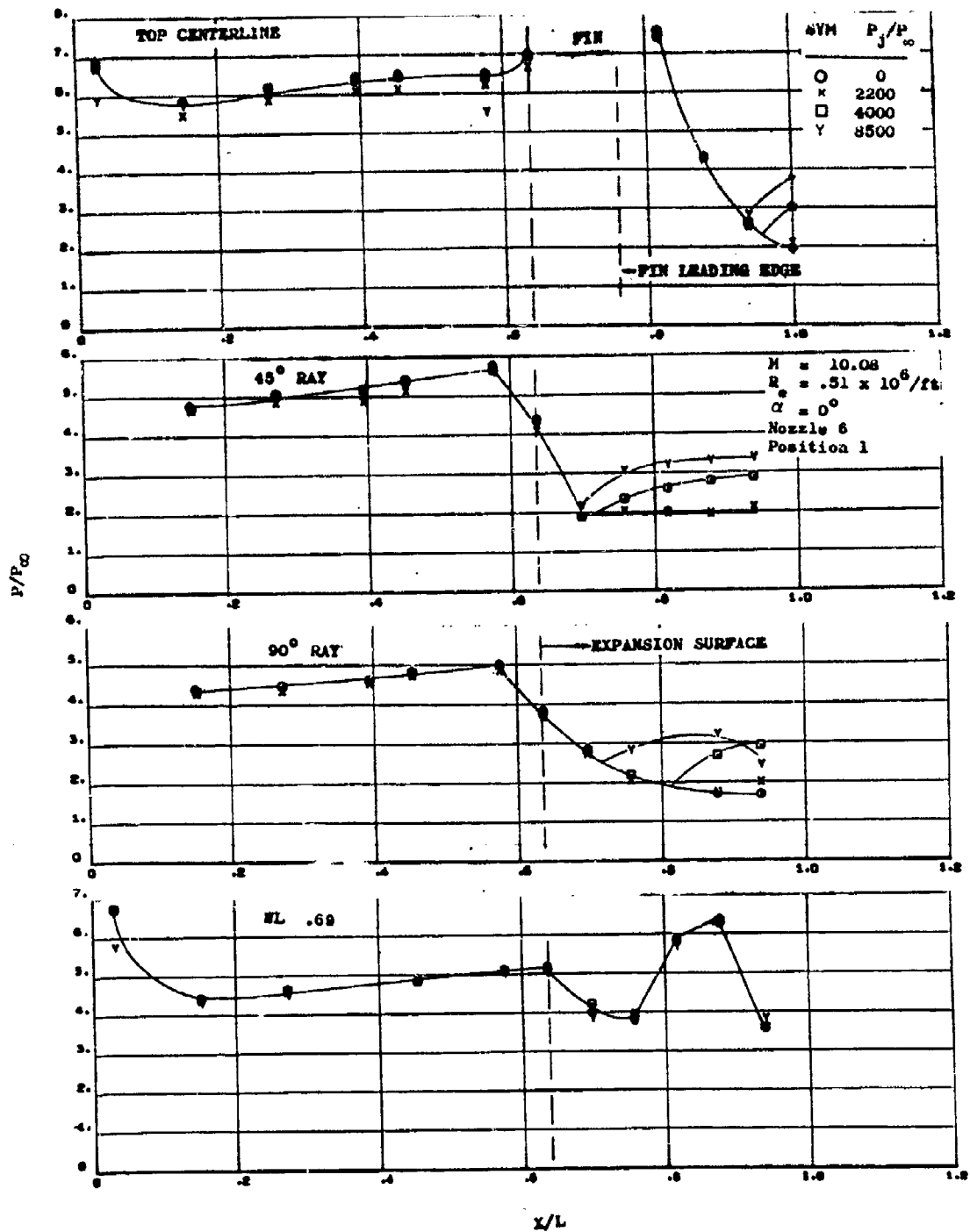


Figure 135a. Effect of Jet Pressure Ratio on Upper Surface Pressures
at $\alpha = 0^\circ$ and $M = 10.08$

190

CONFIDENTIAL

CONFIDENTIAL

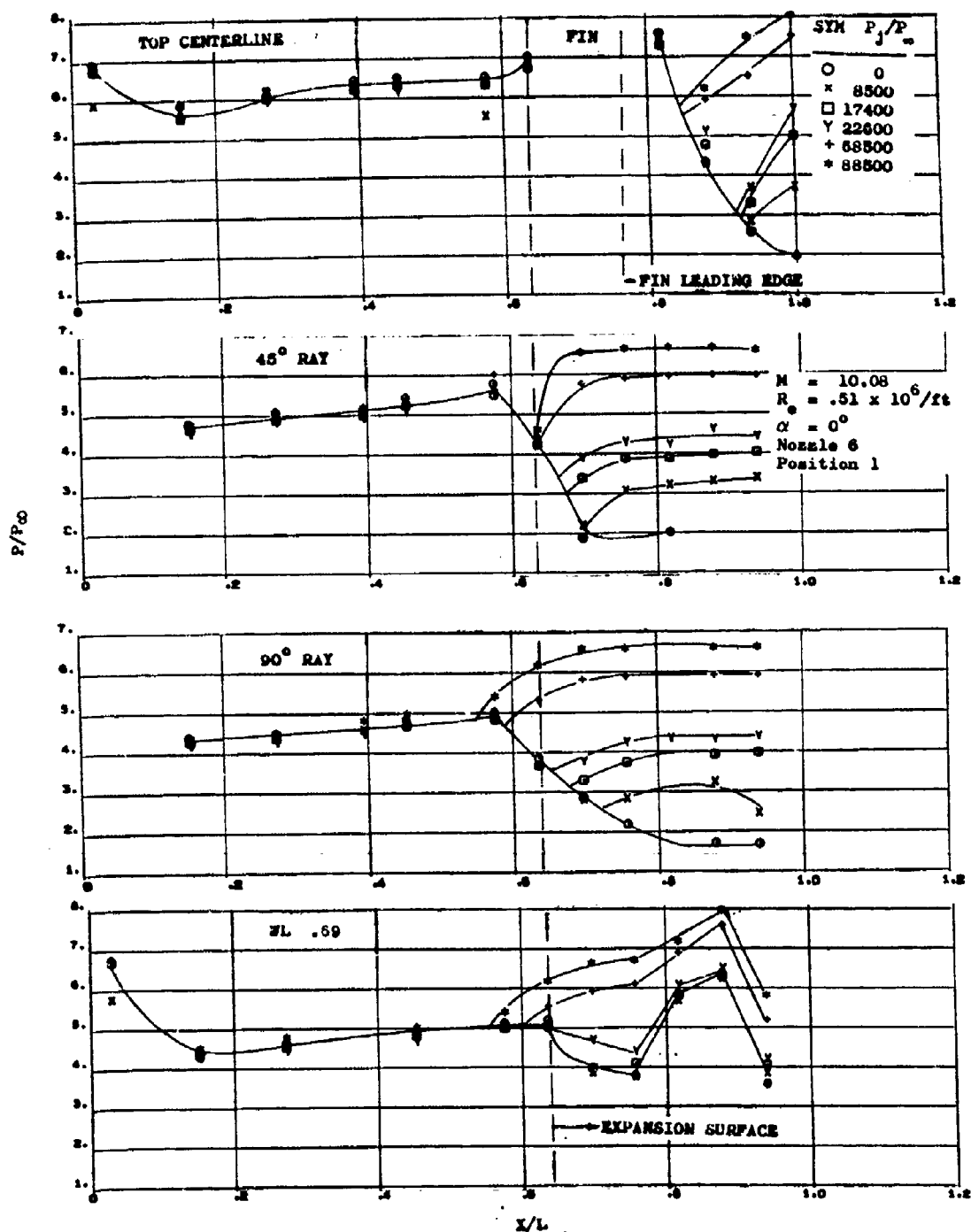
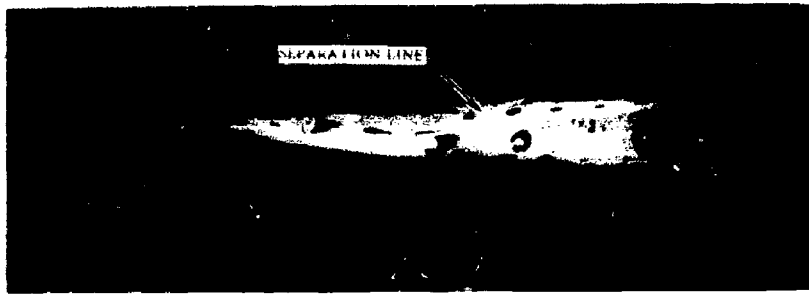


Figure 135b. Effect of Jet Pressure Ratio on Upper Surface Pressures at $\alpha = 0^\circ$ and $M = 10.08$

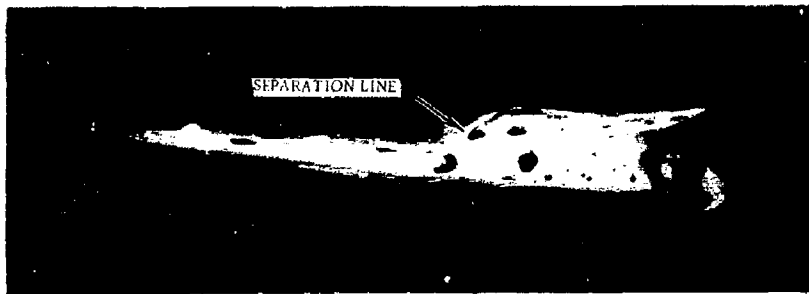
CONFIDENTIAL

CONFIDENTIAL

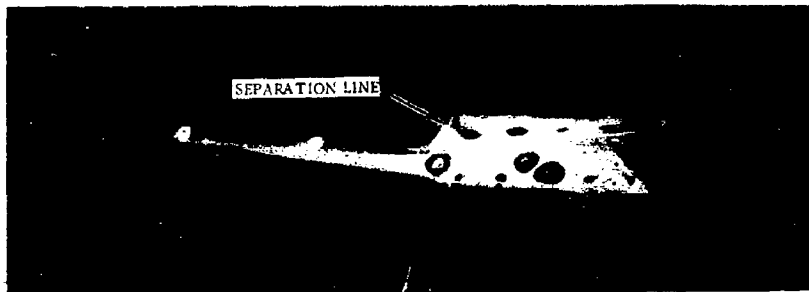
(This page is Unclassified)



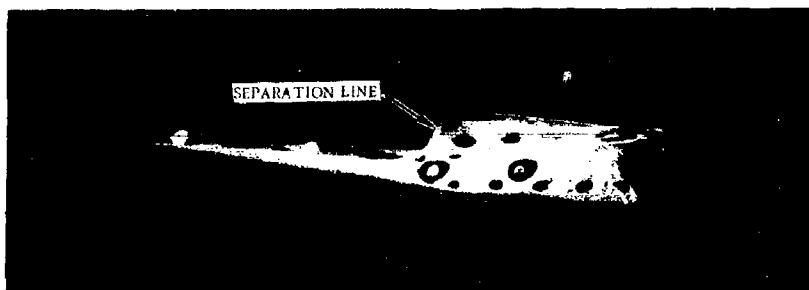
$$P_j/P_\infty = 8500$$



$$P_j/P_\infty = 17000$$



$$P_j/P_\infty = 68000$$



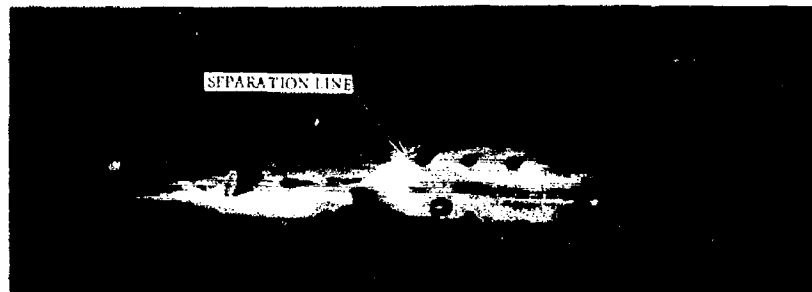
$$P_j/P_\infty = 89000$$

NOZZLE 6, POSITION 1
 $\alpha = 0$ DEGREE
 $Re = 0.5 \times 10^{-6}/FT$
 $M = 10.1$

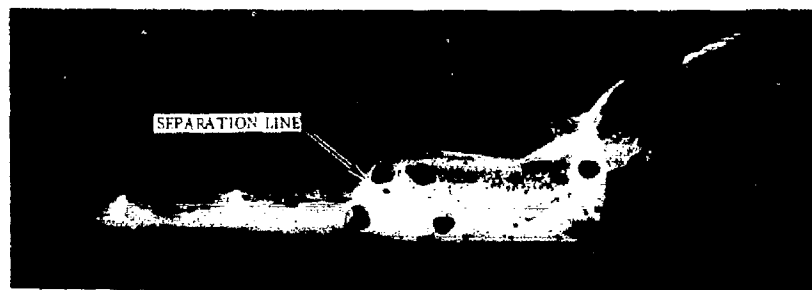
Figure 136a. Delta Oil Flow Visualization, Effect of Jet Pressure Ratio (top view)

192
CONFIDENTIAL
(This page is Unclassified)

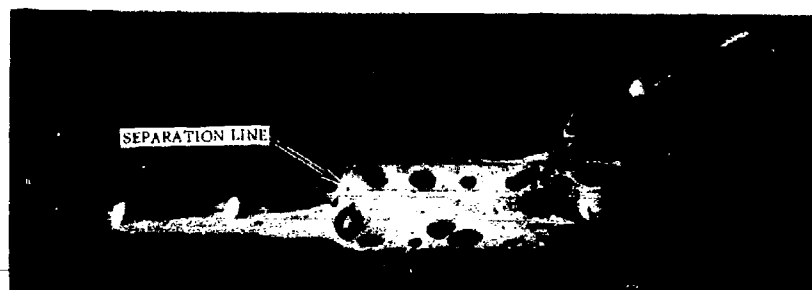
CONFIDENTIAL
(This page is Unclassified)



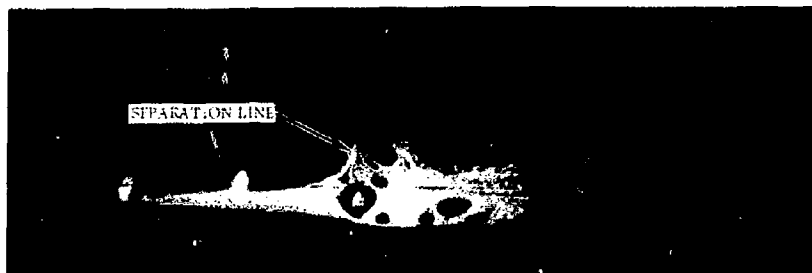
$P_j/P_\infty = 8500$



$P_j/P_\infty = 17000$



$P_j/P_\infty = 68000$



$P_j/P_\infty = 89000$

NOZZLE 6, POSITION 1
 $\alpha = 0$ DEGREE
 $Re = 0.5 \times 10^{-6}/FT$
 $M = 10.1$

Figure 136b. Delta Oil Flow Visualization, Effect of Jet Pressure Ratio (side view)

CONFIDENTIAL

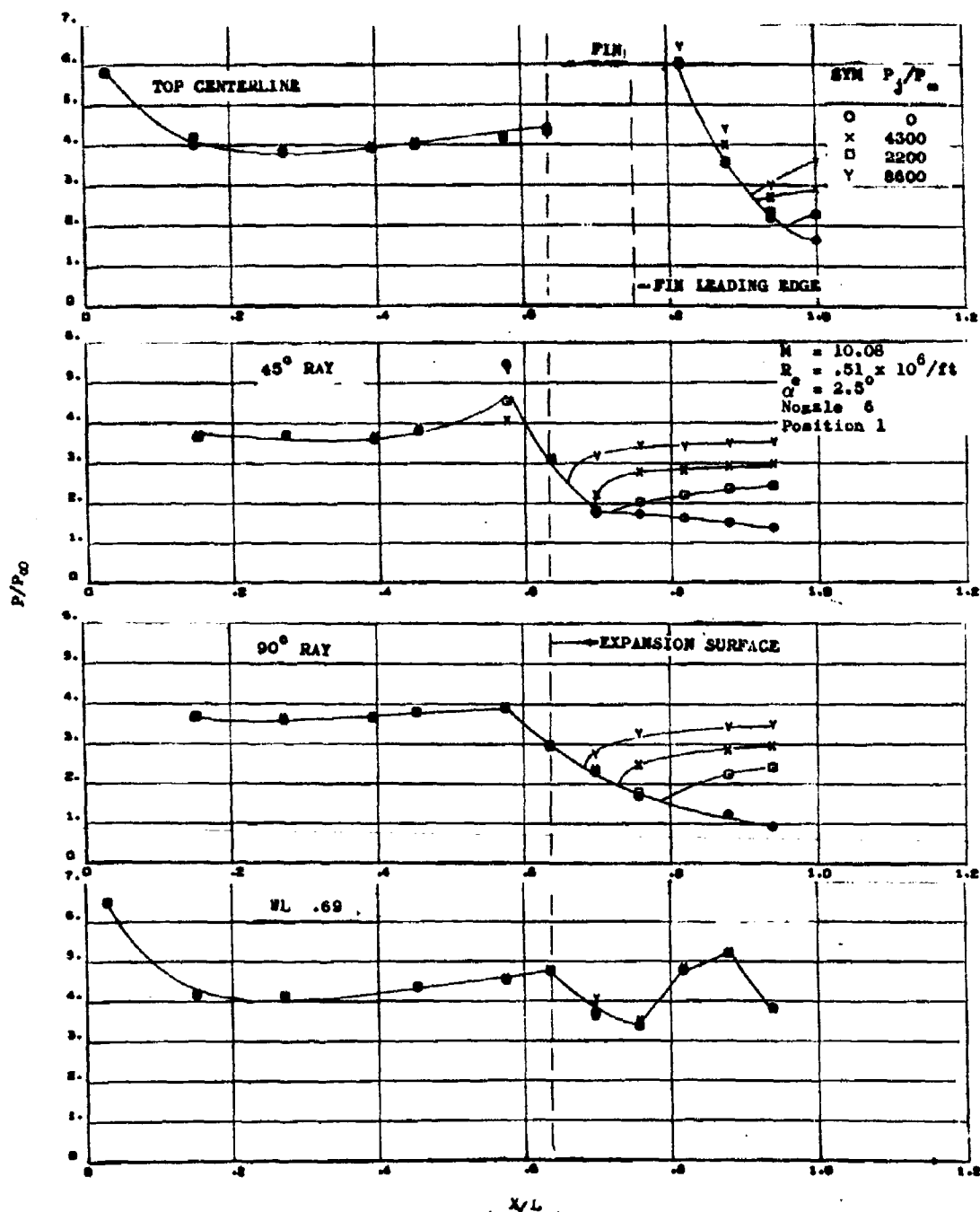


Figure 137. Effect of Jet Pressure Ratio on Upper Surface Pressures at $\alpha = 2.5^\circ$ and $M = 10.08$

CONFIDENTIAL

CONFIDENTIAL

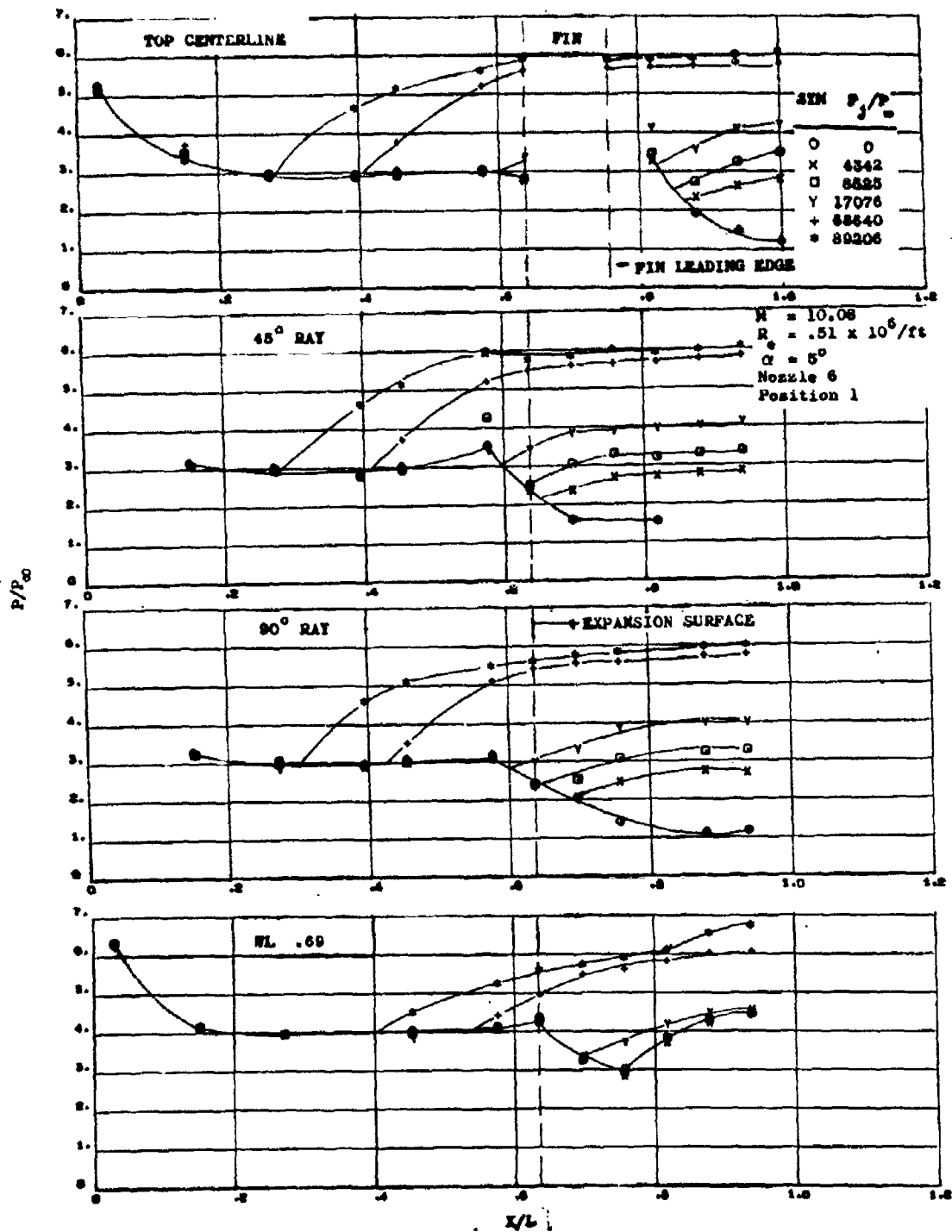


Figure 138. Effect of Jet Pressure Ratio on Upper Surface Pressures at $\alpha = 5^\circ$ and $M = 10.08$

CONFIDENTIAL

CONFIDENTIAL

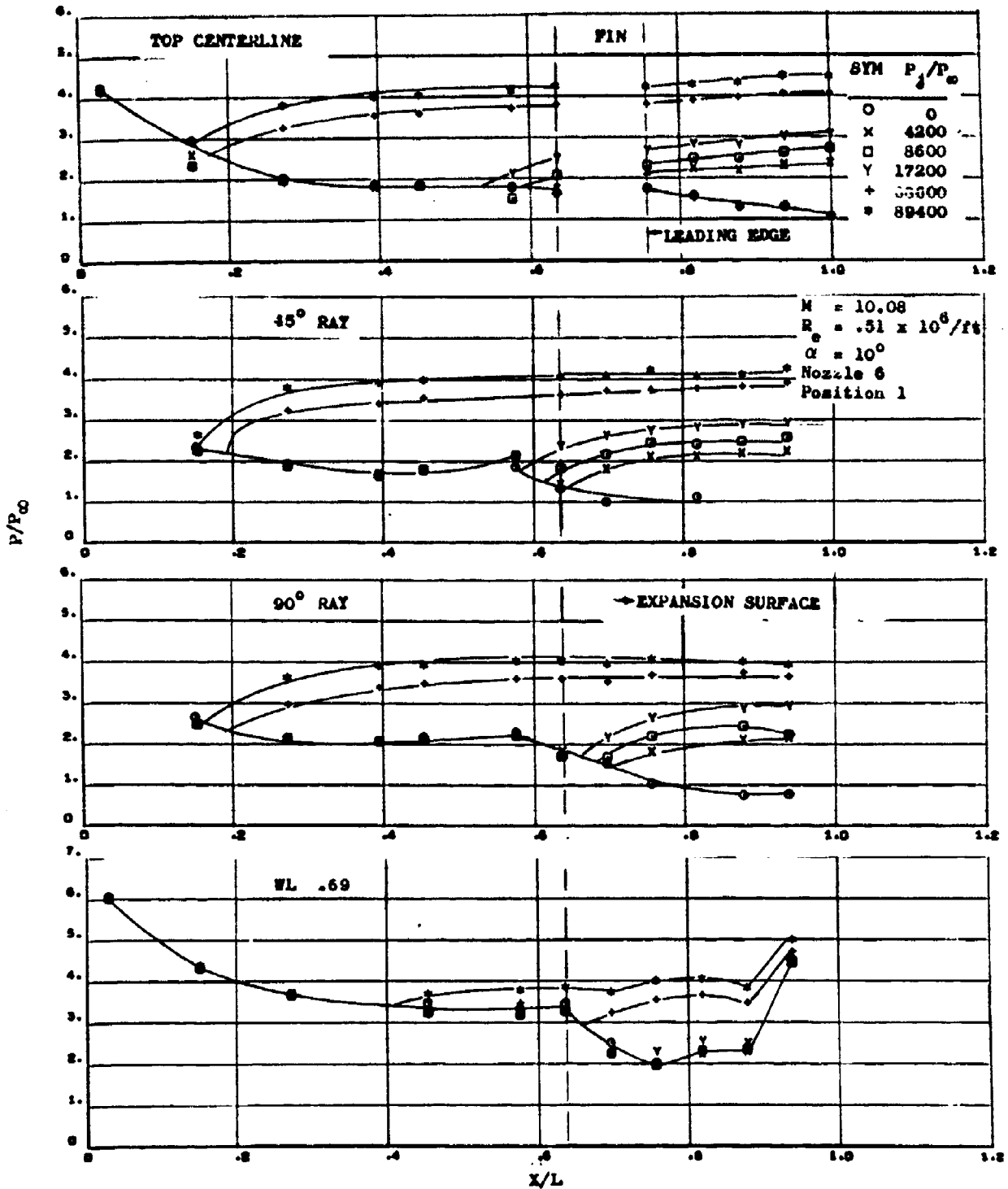


Figure 139. Effect of Jet Pressure Ratio on Upper Surface Pressure
at $\alpha = 10^\circ$ and $M = 10.08$

CONFIDENTIAL

CONFIDENTIAL

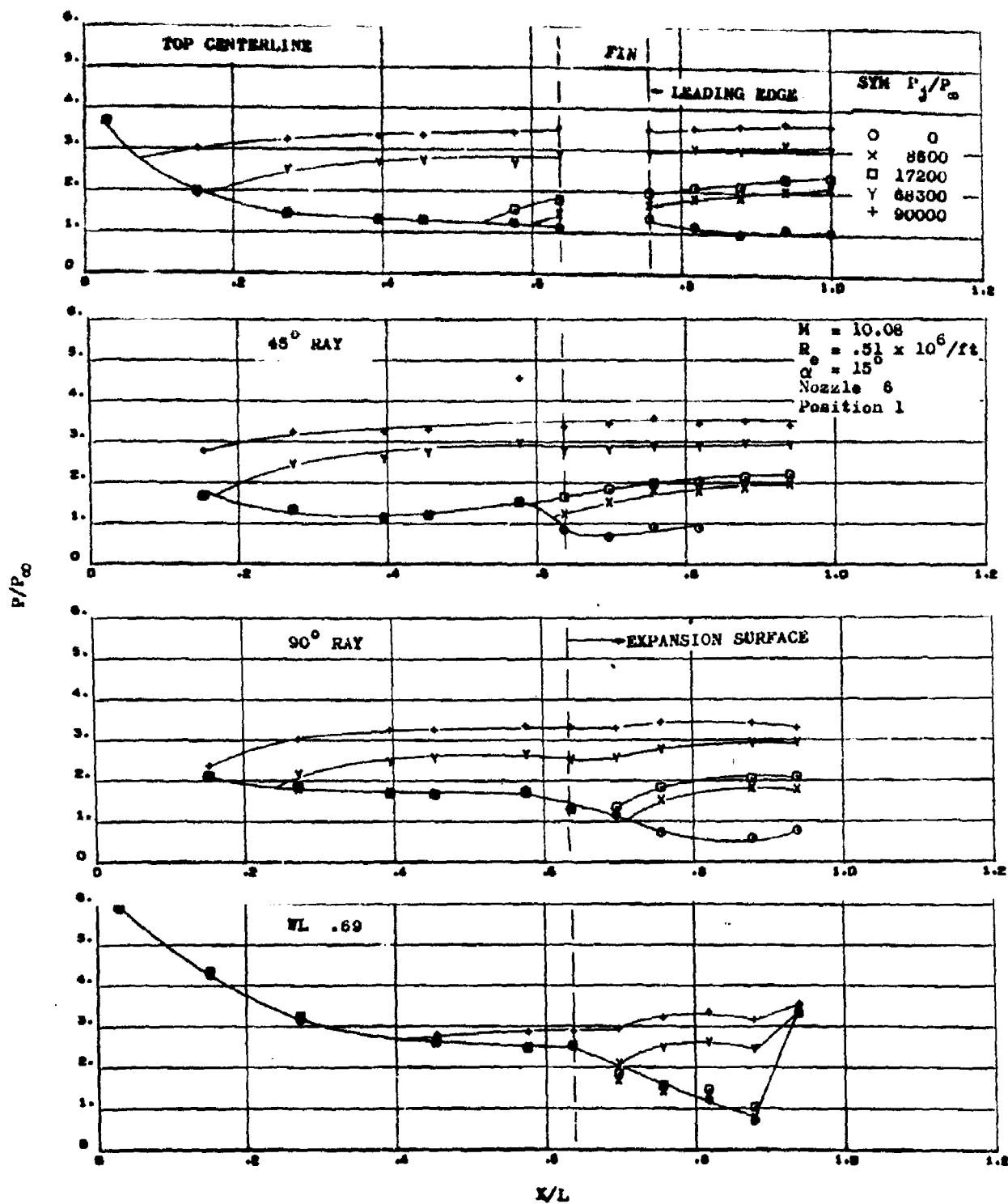


Figure 140. Effect of Jet Pressure Ratio on Upper Surface Pressures at $\alpha = 15^\circ$ and $M = 10.08$

CONFIDENTIAL

CONFIDENTIAL

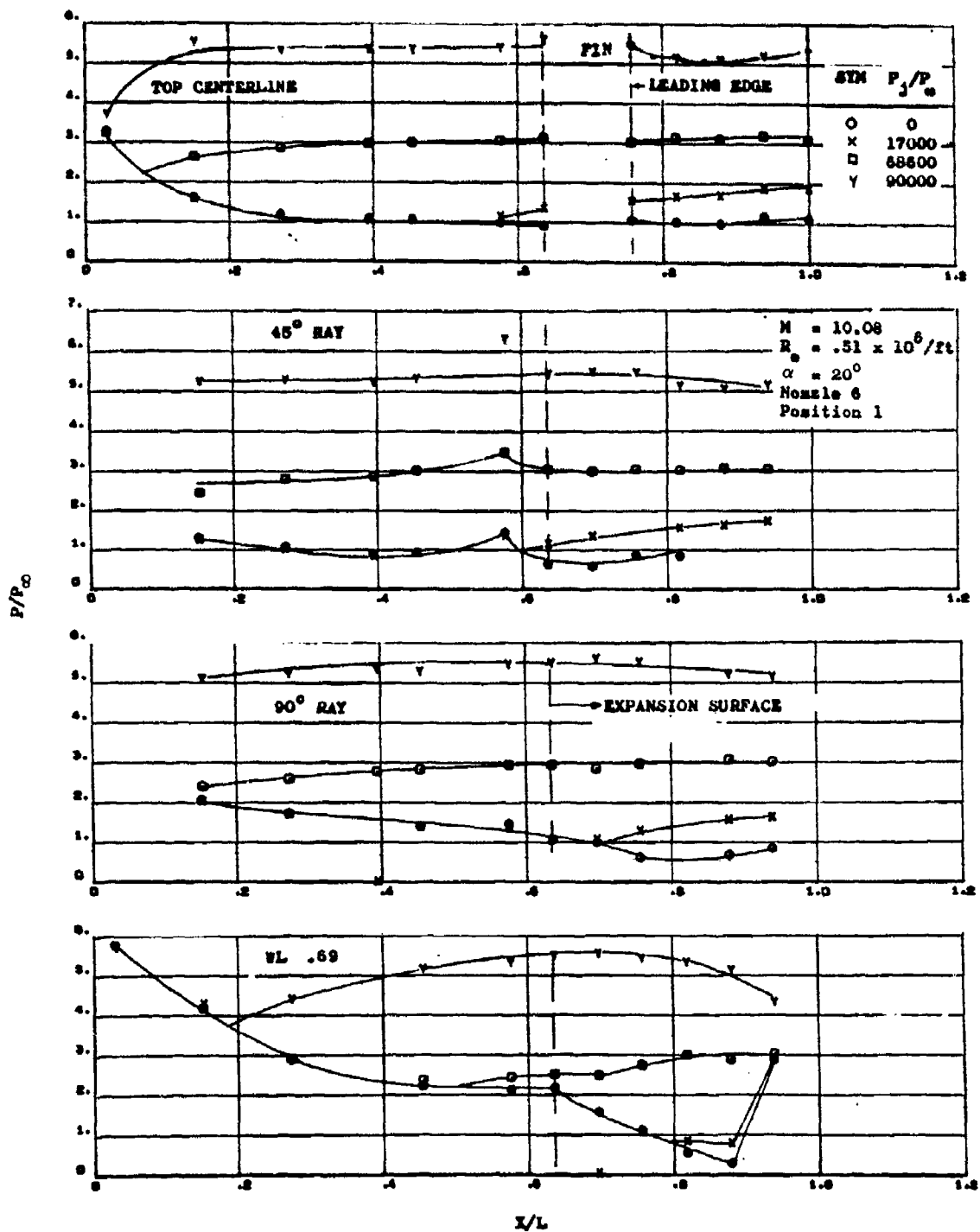


Figure 141. Effect of Jet Pressure Ratio on Upper Surface Pressures
at $\alpha = 20^\circ$ and $M = 10.08$

CONFIDENTIAL

CONFIDENTIAL

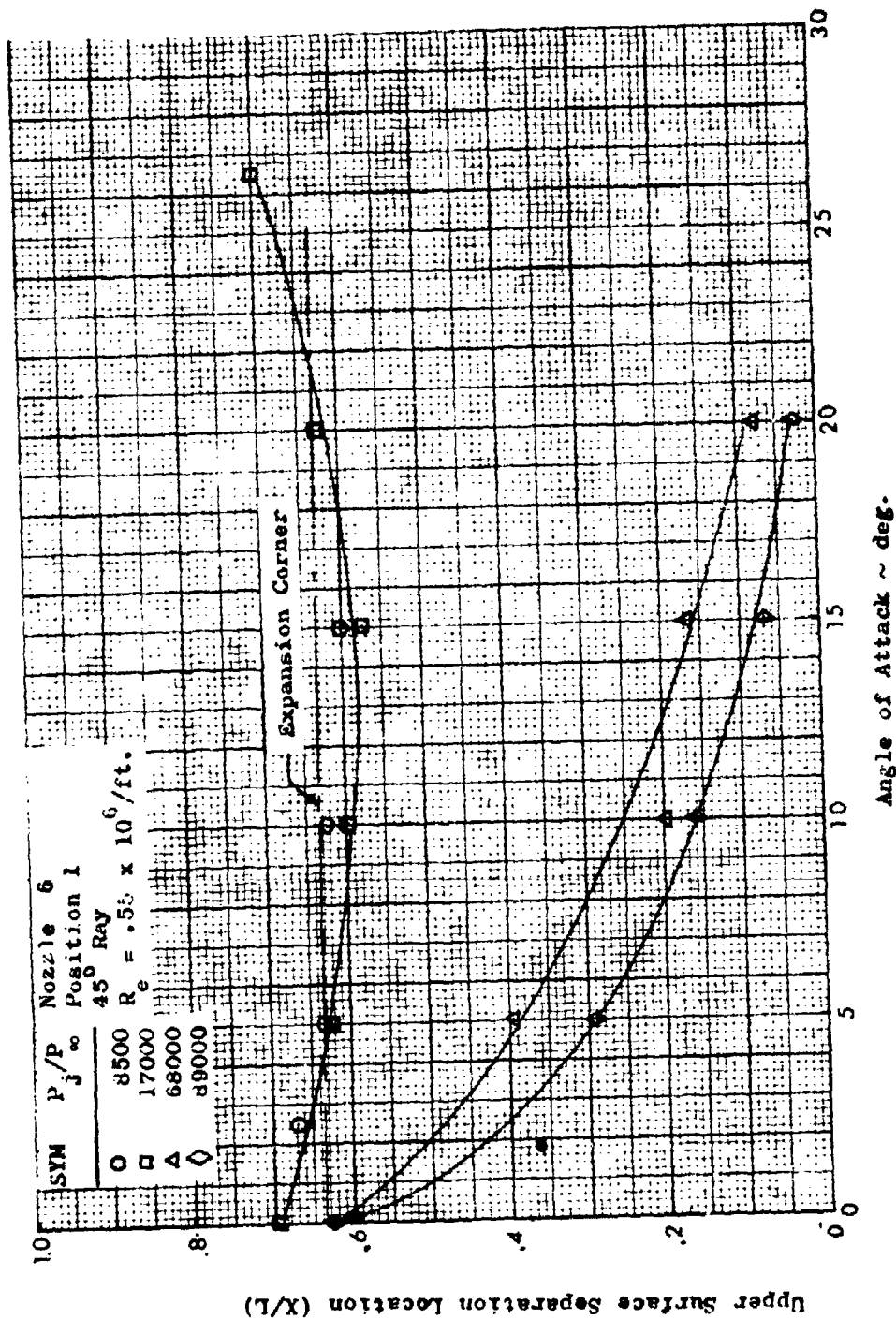


Figure 142. Angle of Attack Effect on Separation Location at $M = 10$

CONFIDENTIAL

CONFIDENTIAL

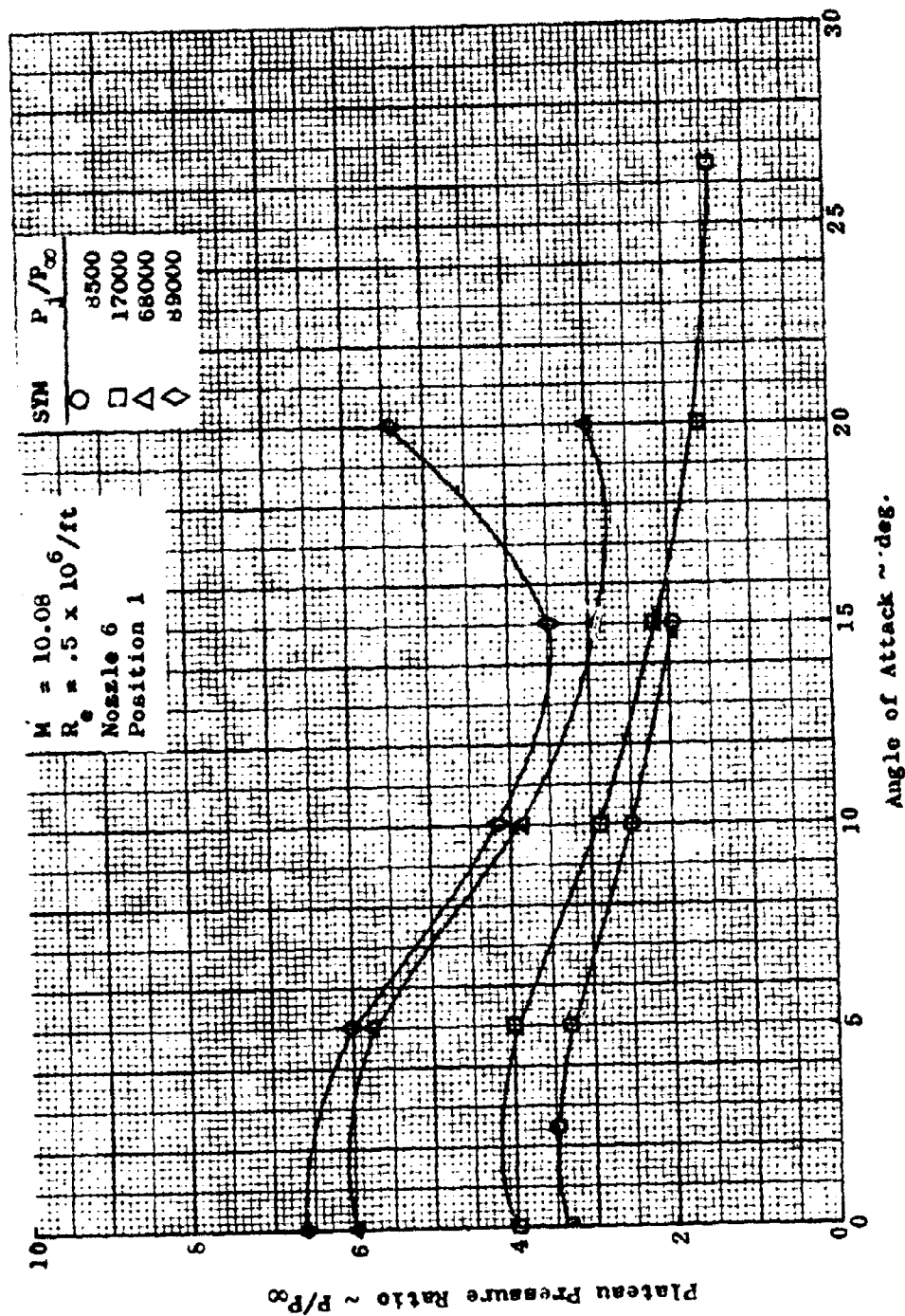


Figure 143. Angle of Attack Effect on Upper Surface Plateau Pressure at $M = 10$

200
CONFIDENTIAL

CONFIDENTIAL

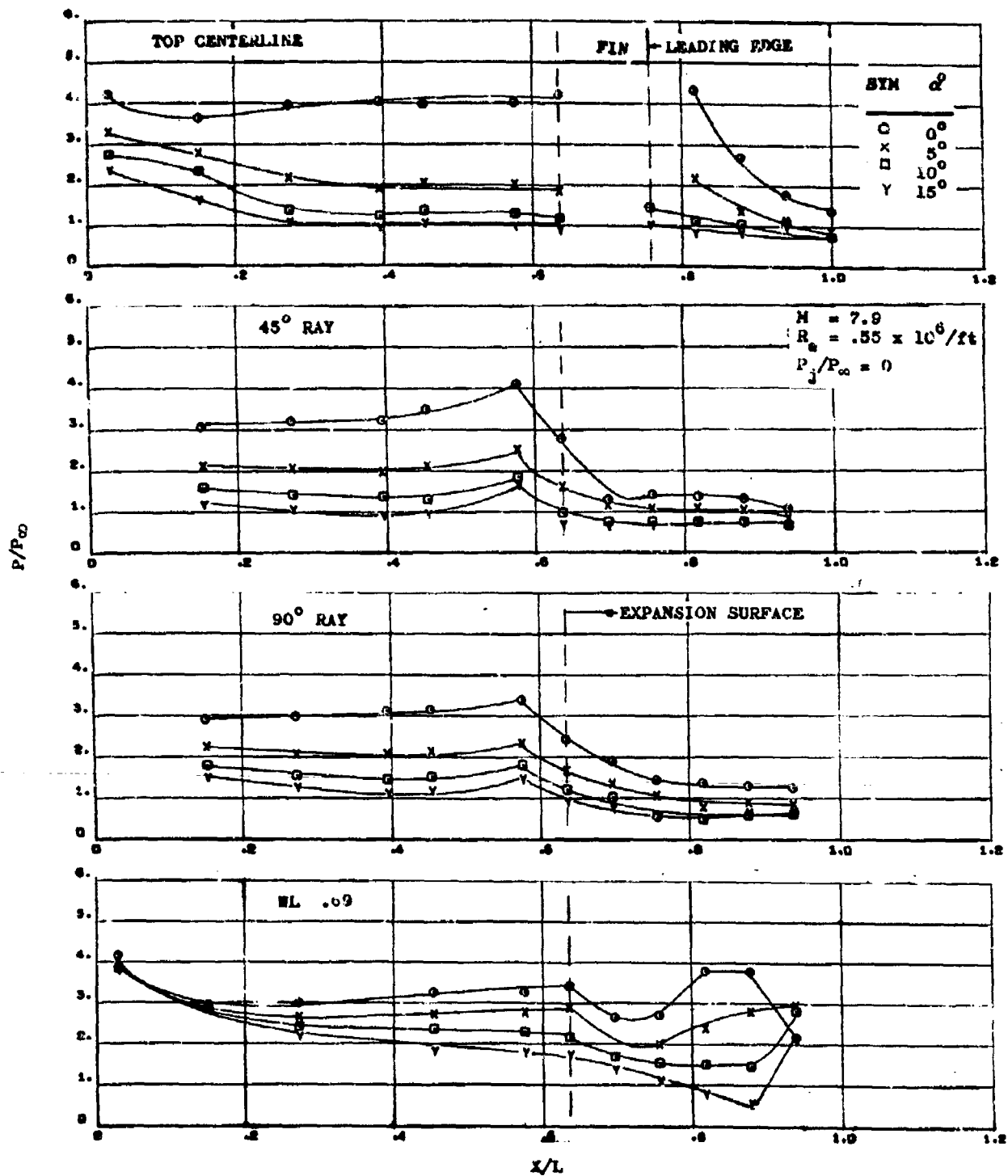


Figure 144. Upper Surface Pressures at $M = 7.9$

CONFIDENTIAL

CONFIDENTIAL

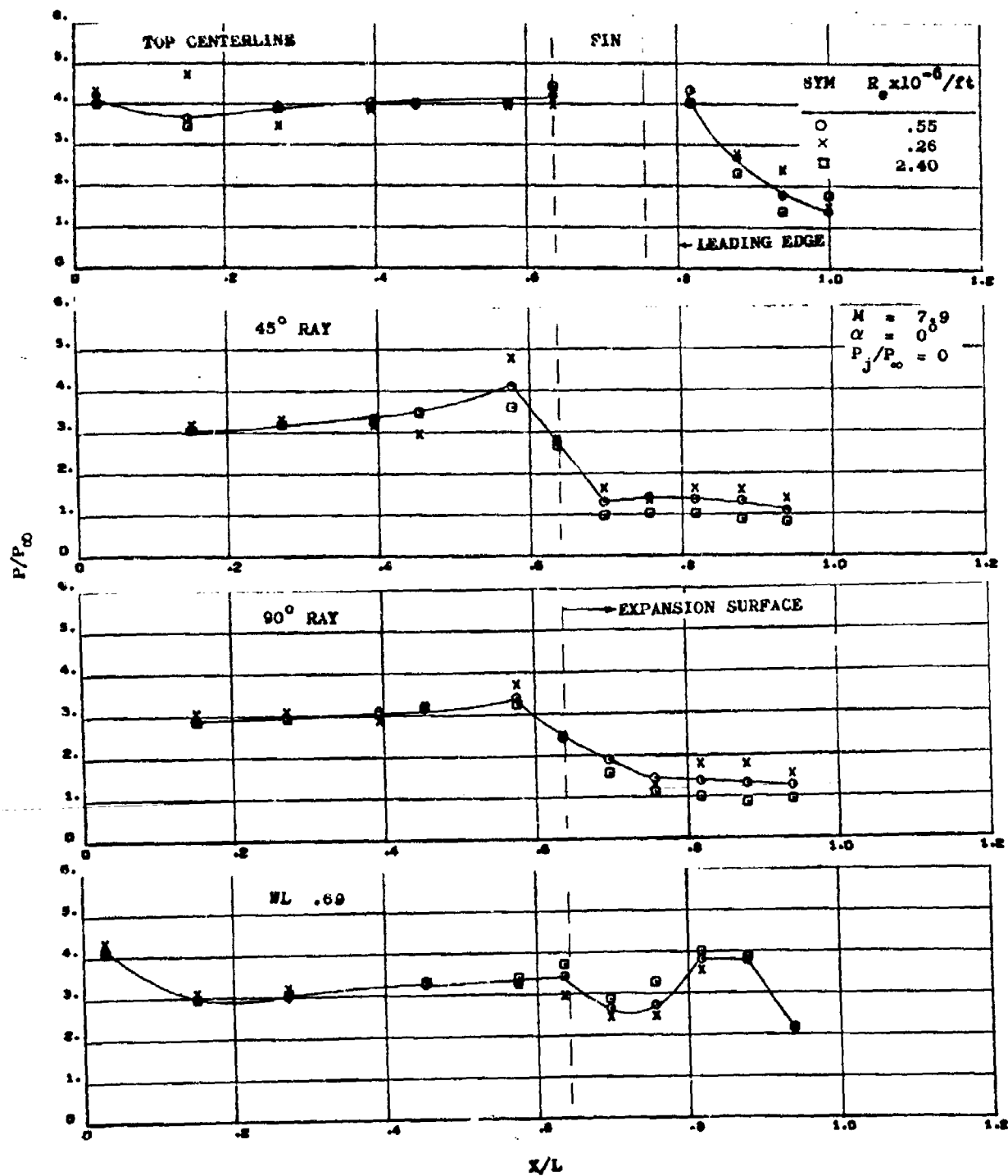


Figure 145. Effect of Reynolds Number on Upper Surface Pressures at $M = 7.9$

CONFIDENTIAL

CONFIDENTIAL

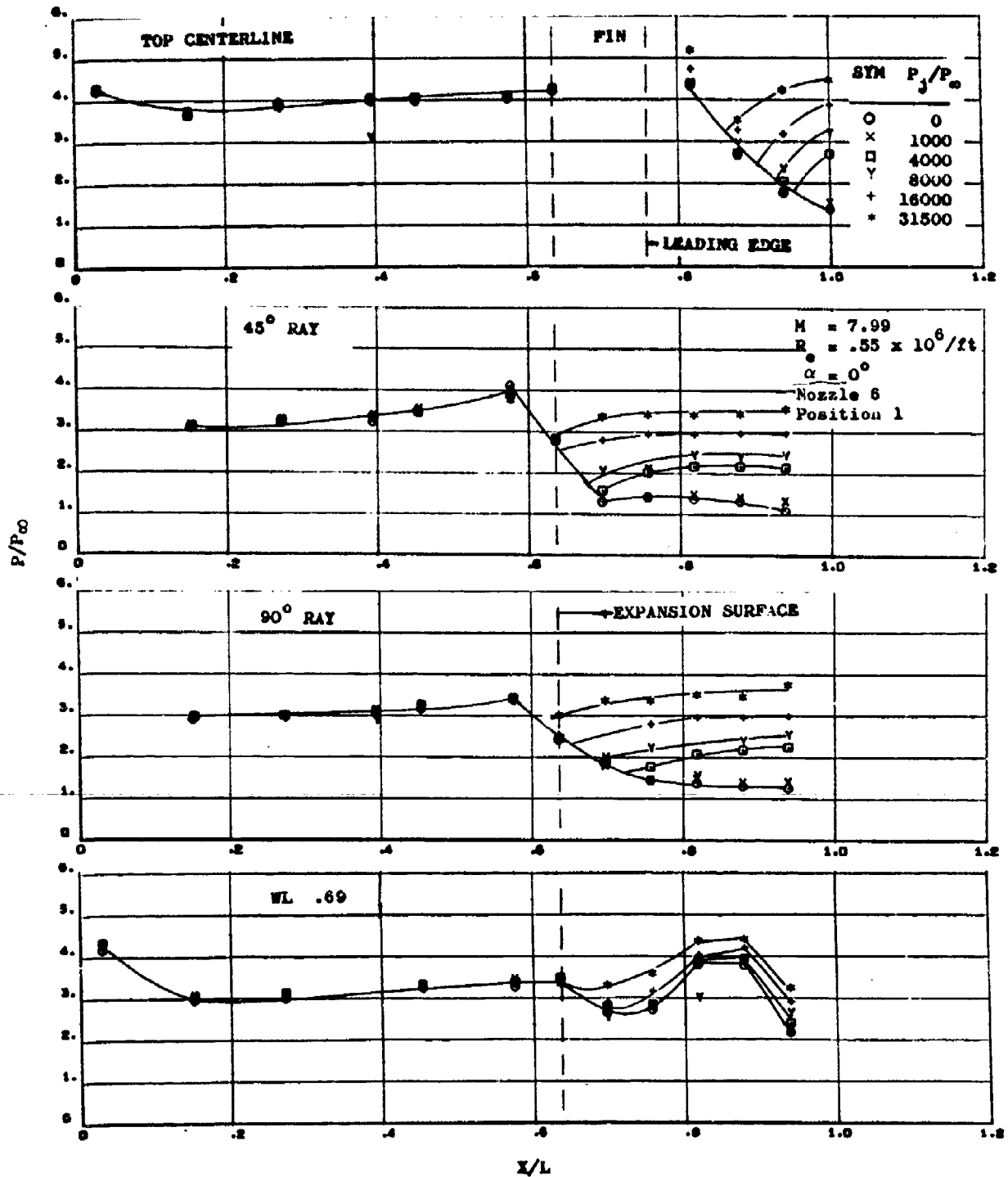


Figure 146. Effect of Jet Pressure Ratio on Upper Surface Pressures at $\alpha = 0^\circ$ and $M = 7.9$

CONFIDENTIAL

CONFIDENTIAL

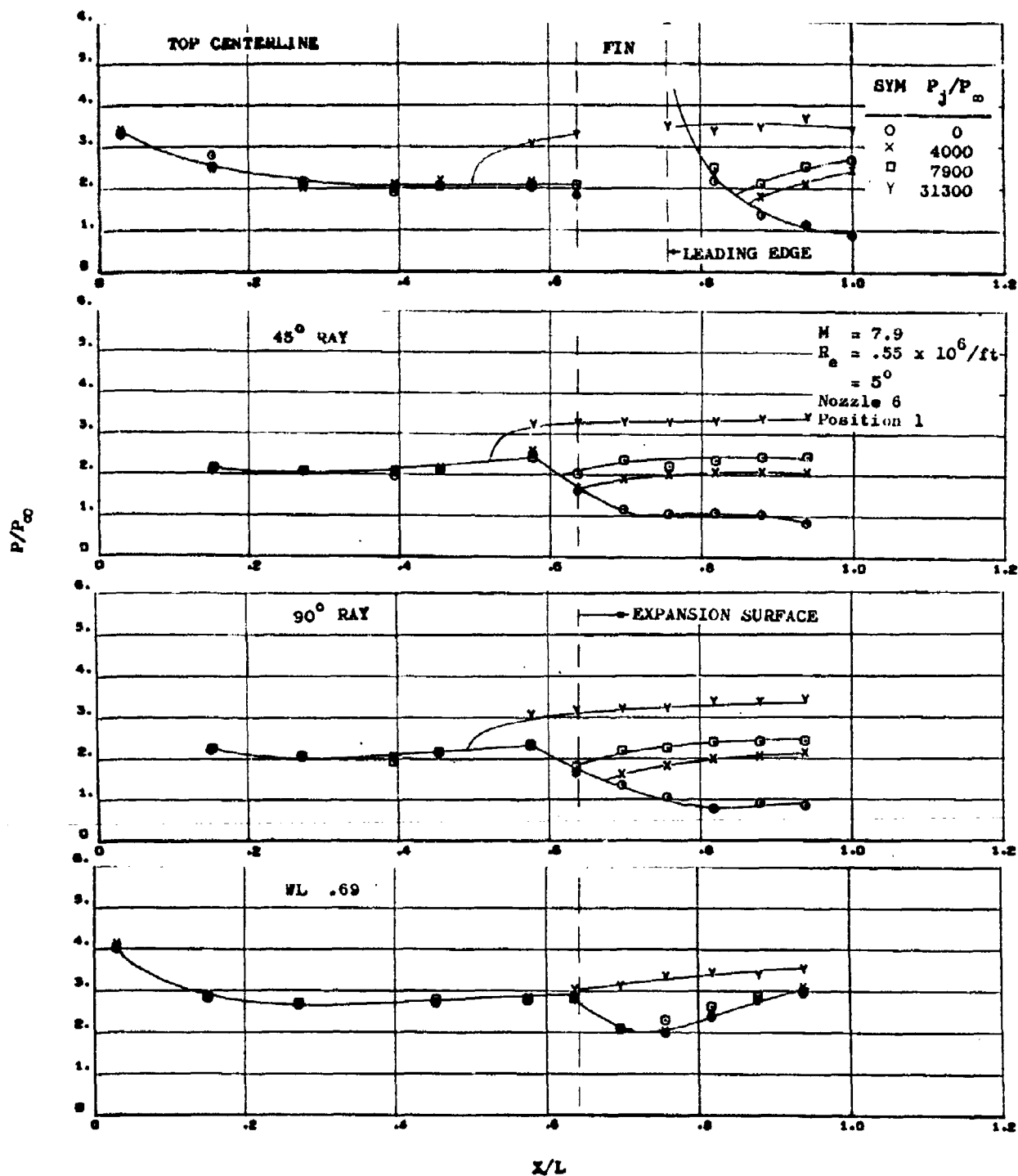


Figure 147. Effect of Jet Pressure Ratio on Upper Surface Pressures at $\gamma = 5^\circ$ and $M = 7.9$

CONFIDENTIAL

CONFIDENTIAL

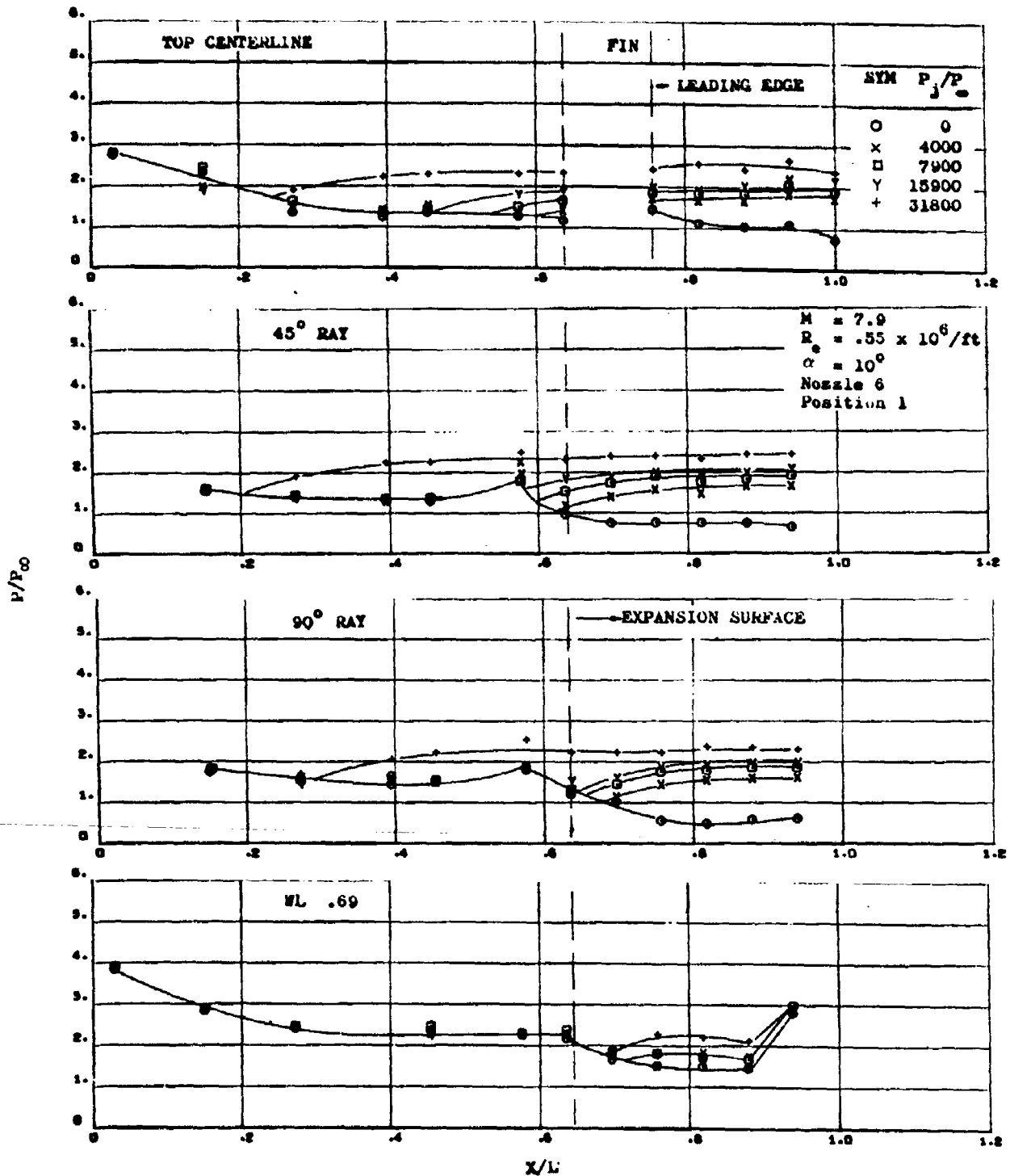


Figure 148. Effect of Jet Pressure Ratio on Upper Surface Pressures
at $\alpha = 10^\circ$ and $M = 7.9$

CONFIDENTIAL

CONFIDENTIAL

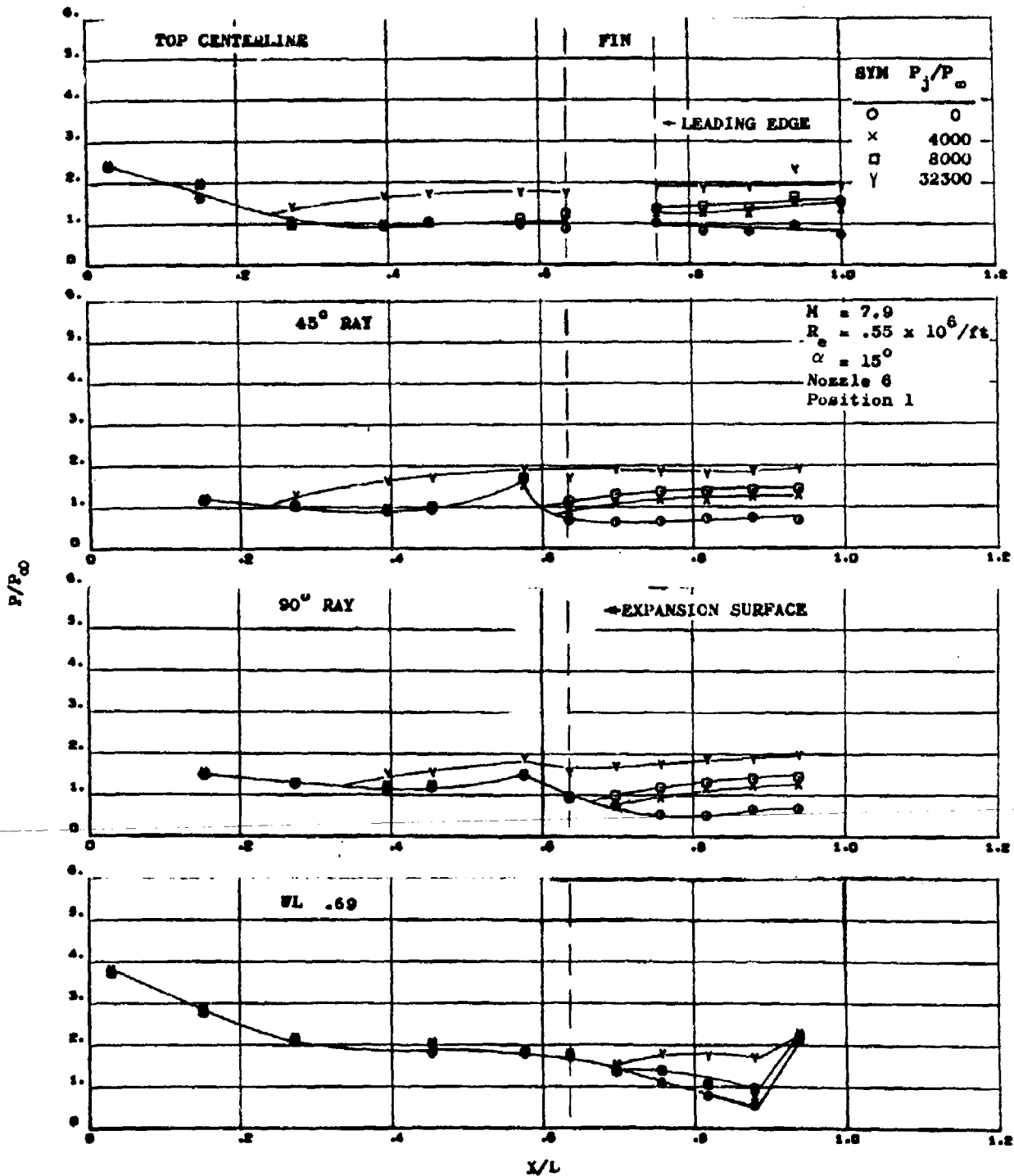


Figure 149. Effect of Jet Pressure Ratio on Upper Surface Pressures at $\alpha = 15^\circ$ and $M = 7.9$

CONFIDENTIAL

CONFIDENTIAL

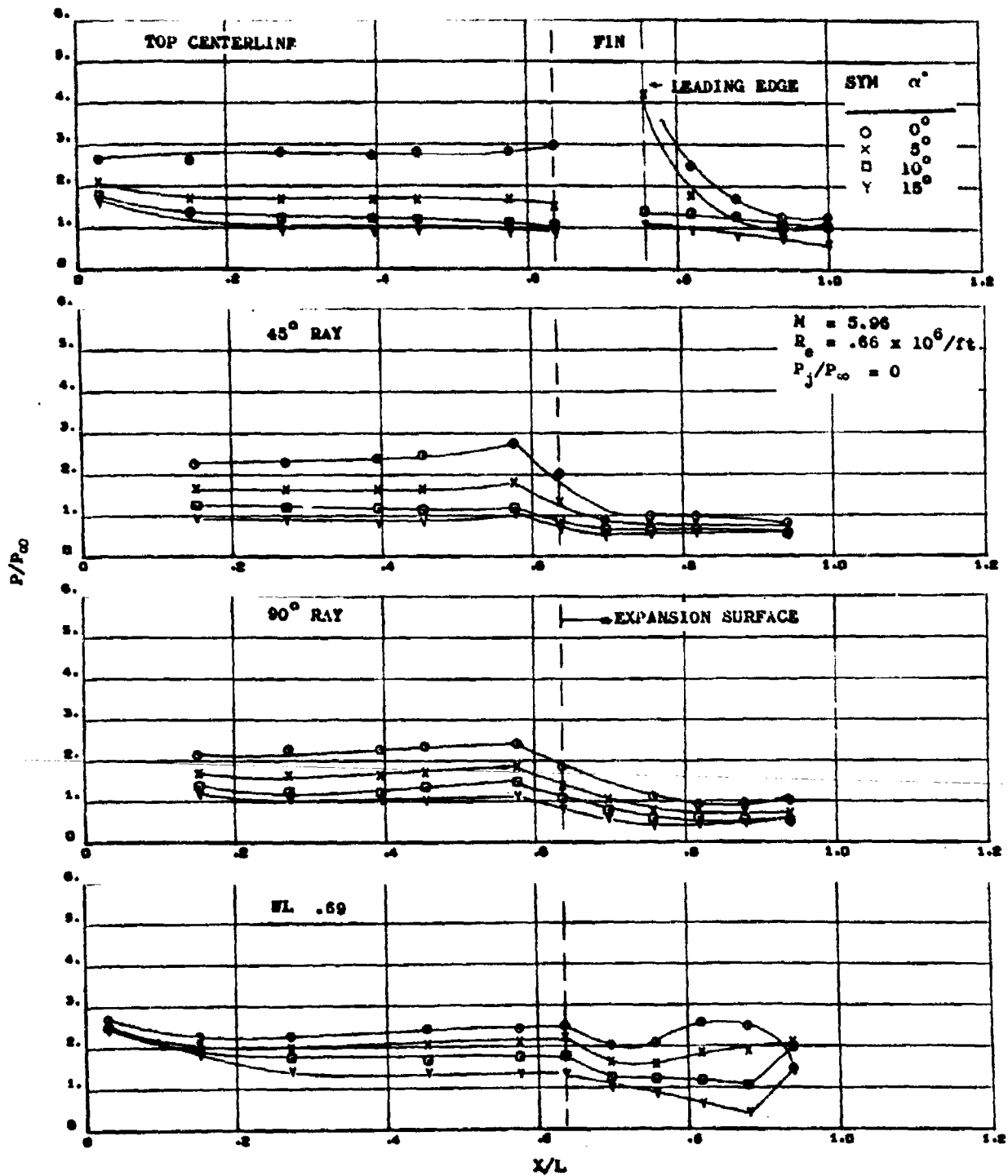


Figure 150. Upper Surface Pressures at $M = 5.96$

CONFIDENTIAL

CONFIDENTIAL

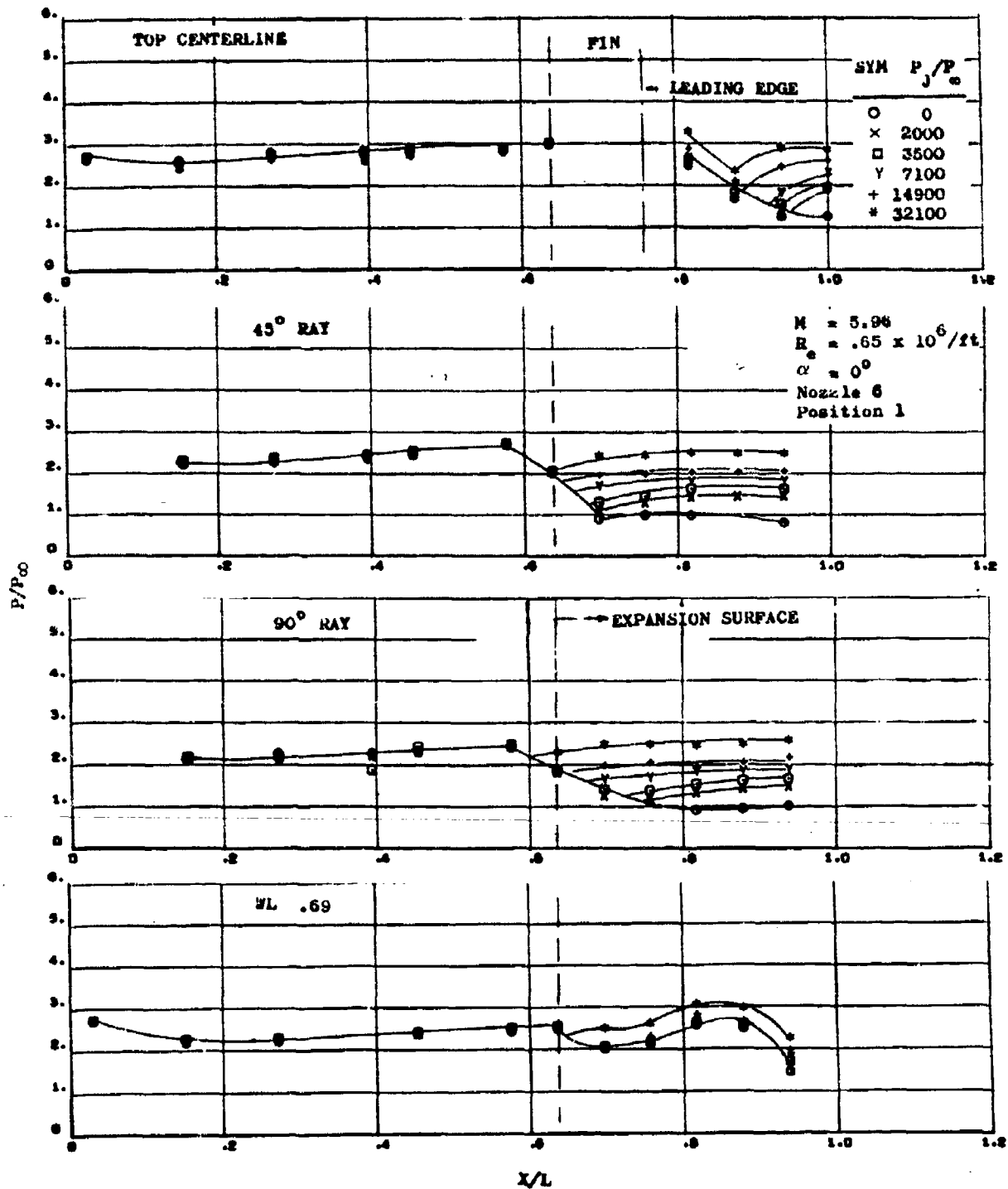


Figure 151. Effect of Jet Pressure Ratio on Upper Surface Pressures at $\alpha = 0^\circ$ and $M = 5.96$

CONFIDENTIAL

CONFIDENTIAL

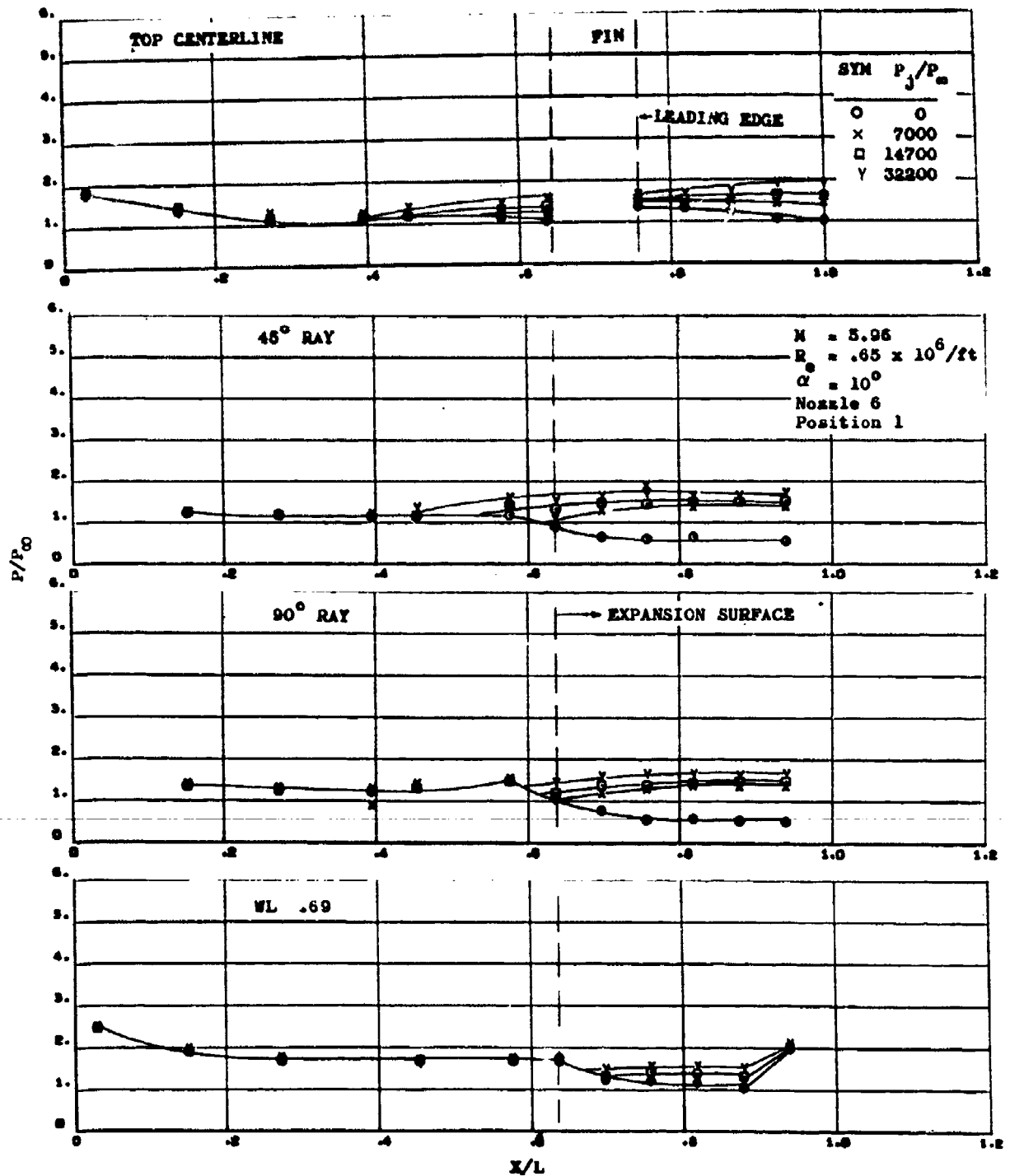


Figure 152. Effect of Jet Pressure Ratio on Upper Surface Pressure at $\alpha = 10^\circ$ and $M = 5.96$

CONFIDENTIAL

CONFIDENTIAL

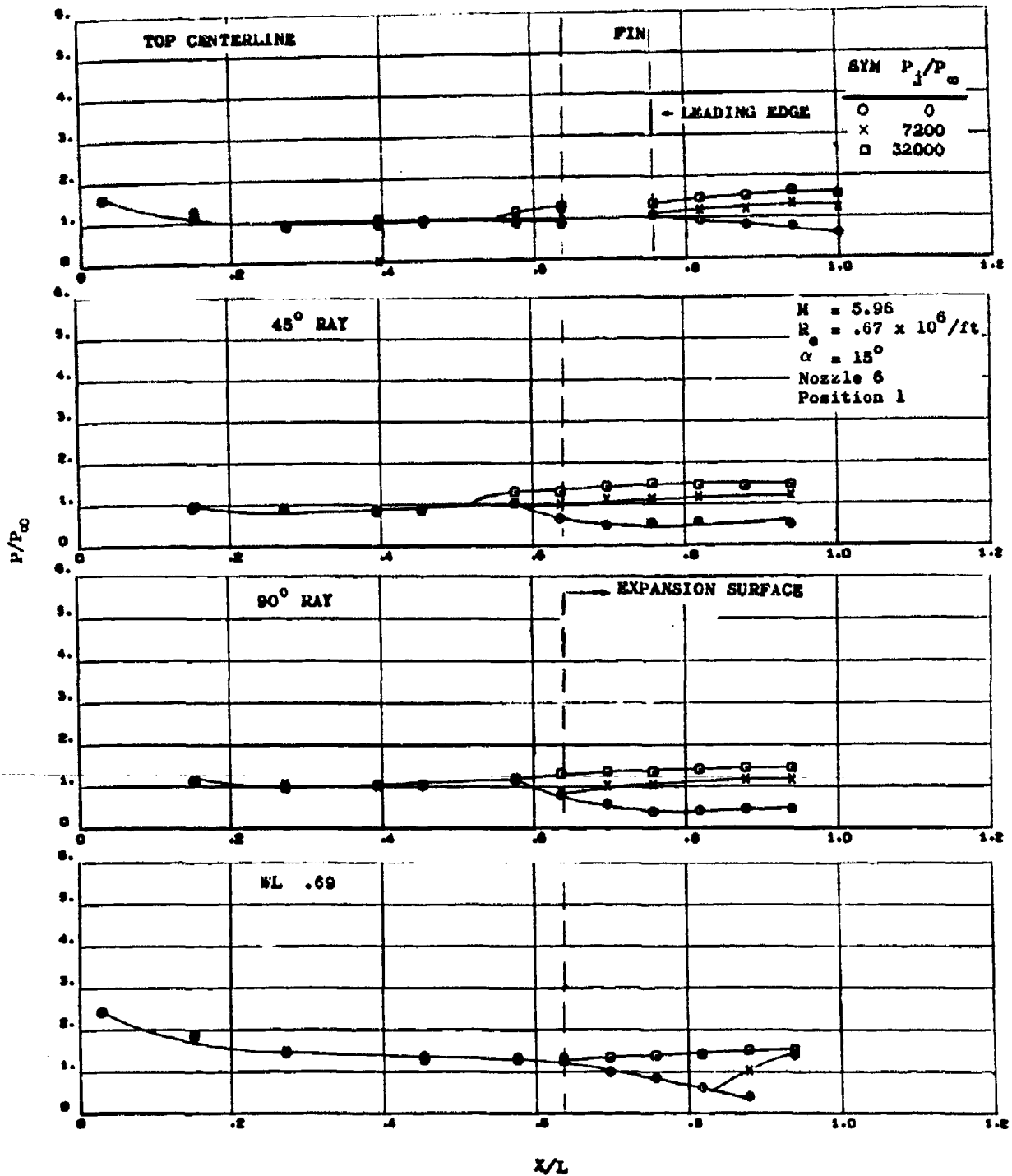


Figure 153. Effect of Jet Pressure Ratios on Upper Surface Pressures at $\alpha = 15^\circ$ and $M = 5.96$

CONFIDENTIAL

CONFIDENTIAL

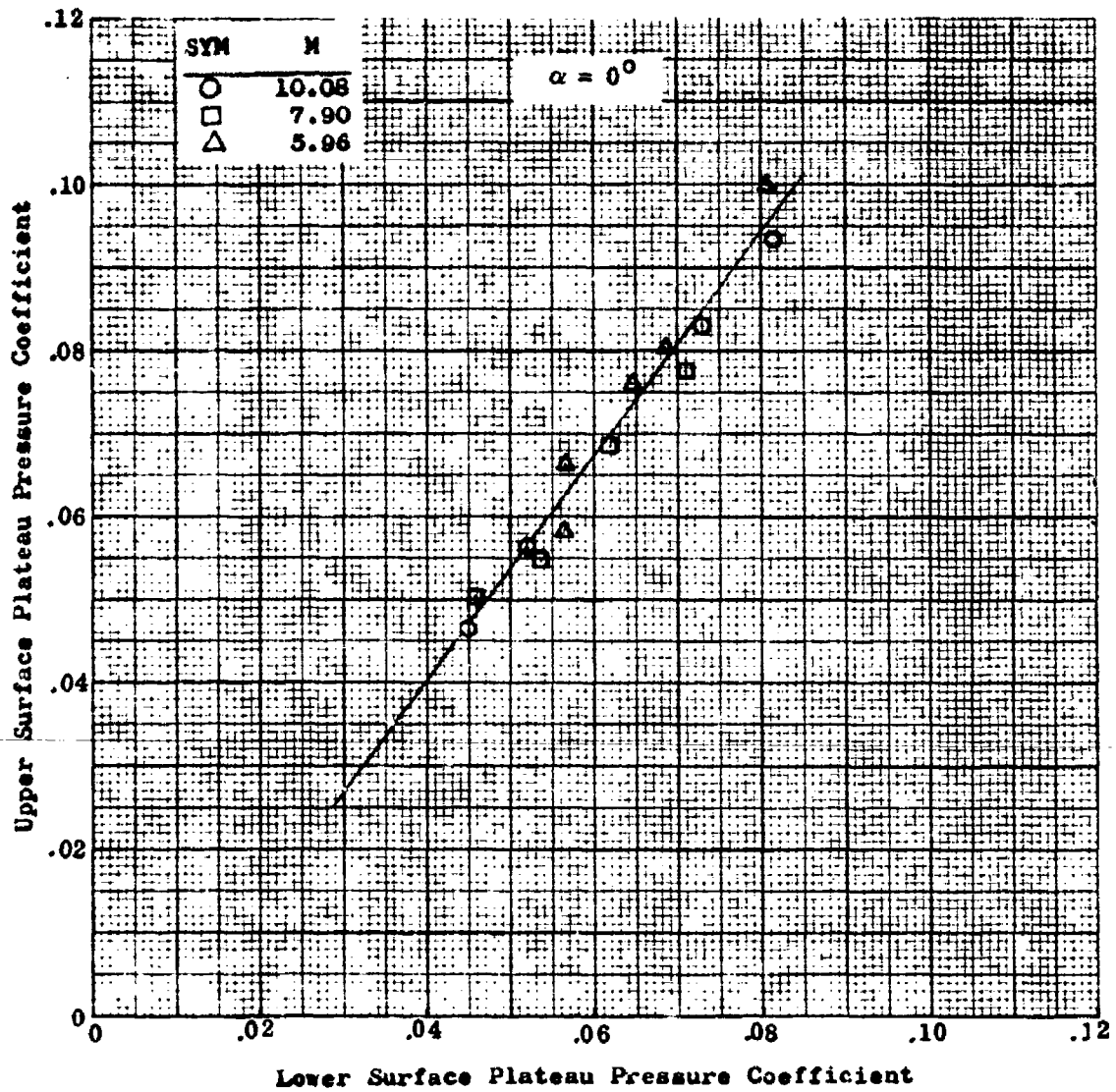


Figure 154. A Comparison of Upper and Lower Surface Plateau Pressures

CONFIDENTIAL

CONFIDENTIAL

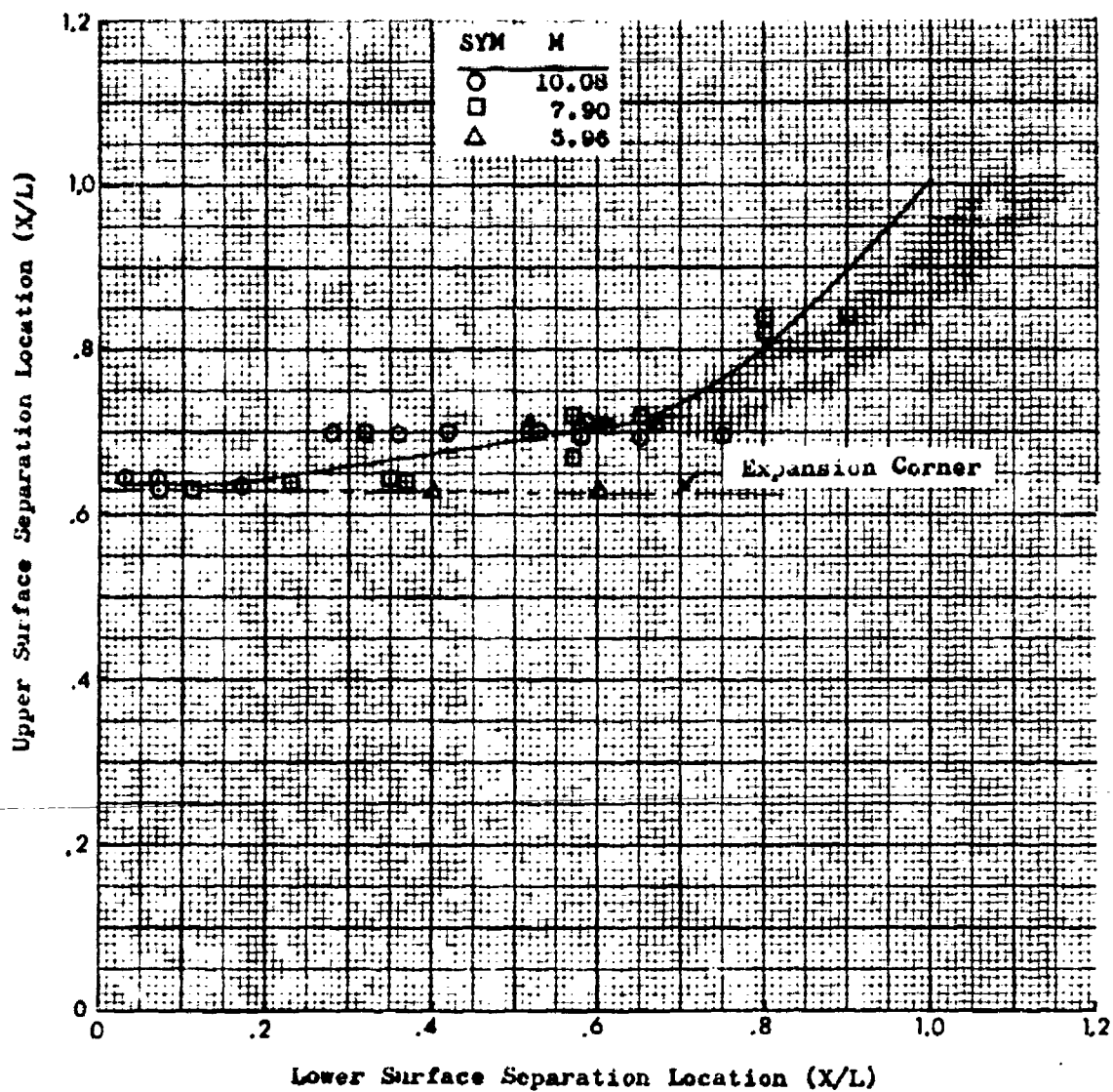


Figure 155. A Comparison of Upper and Lower Surface Separation Locations at $\alpha = 0^\circ$

CONFIDENTIAL

CONFIDENTIAL

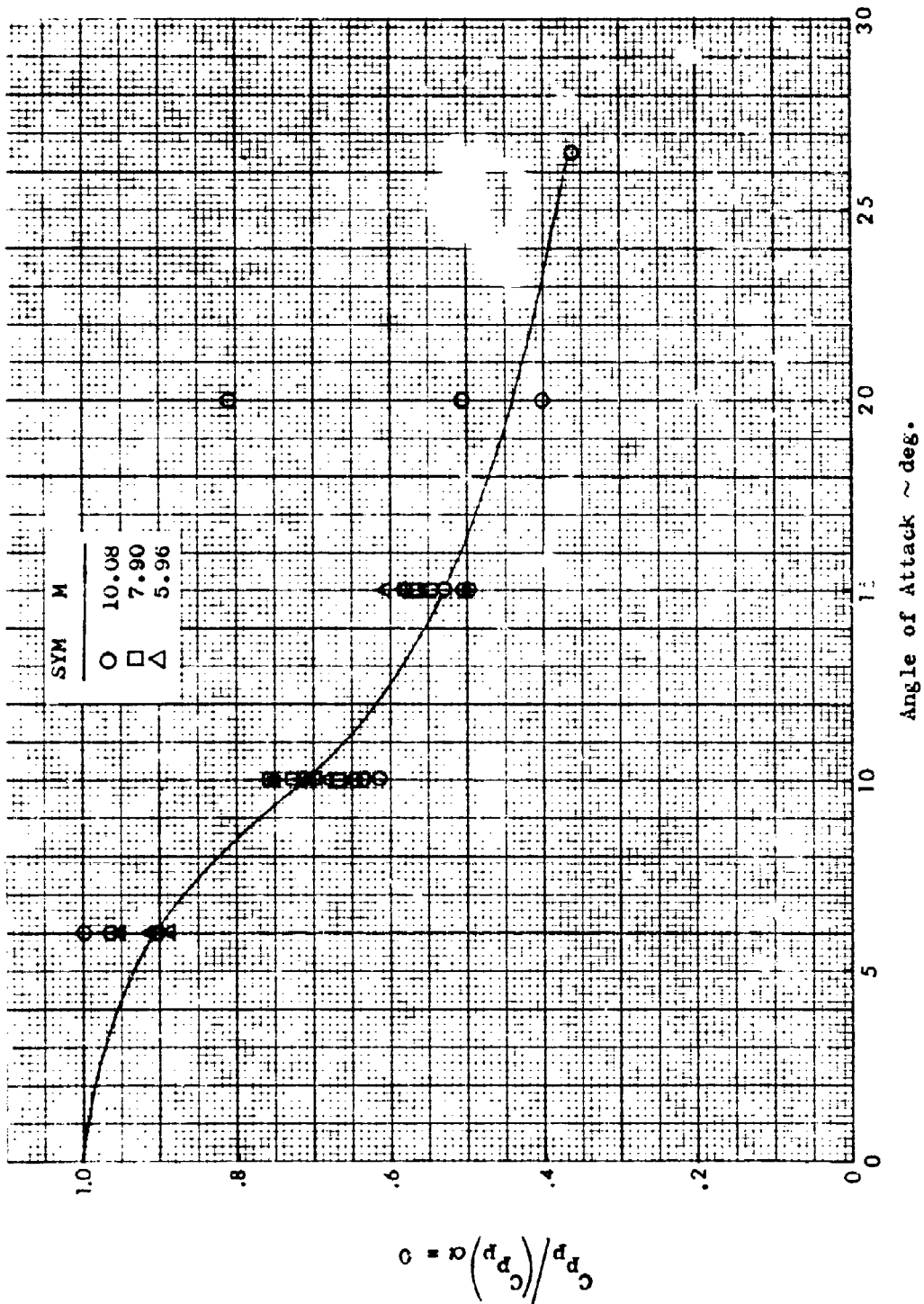


Figure 156. Angle of Attack Affects on Upper Surface Plateau Pressure

CONFIDENTIAL

CONFIDENTIAL

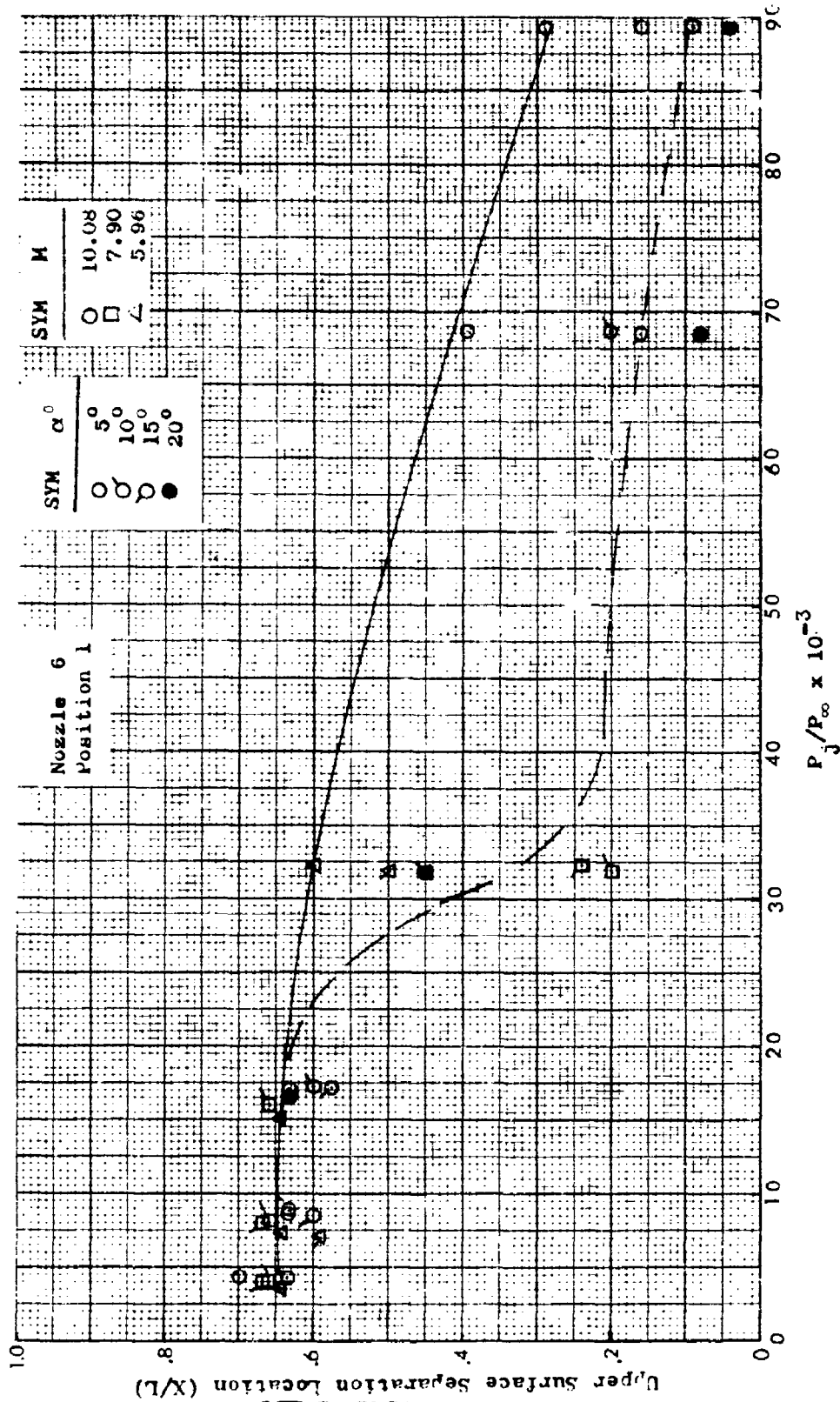


Figure 157. Angle of Attack Effect on Upper Surface Separation Location

CONFIDENTIAL

CONFIDENTIAL

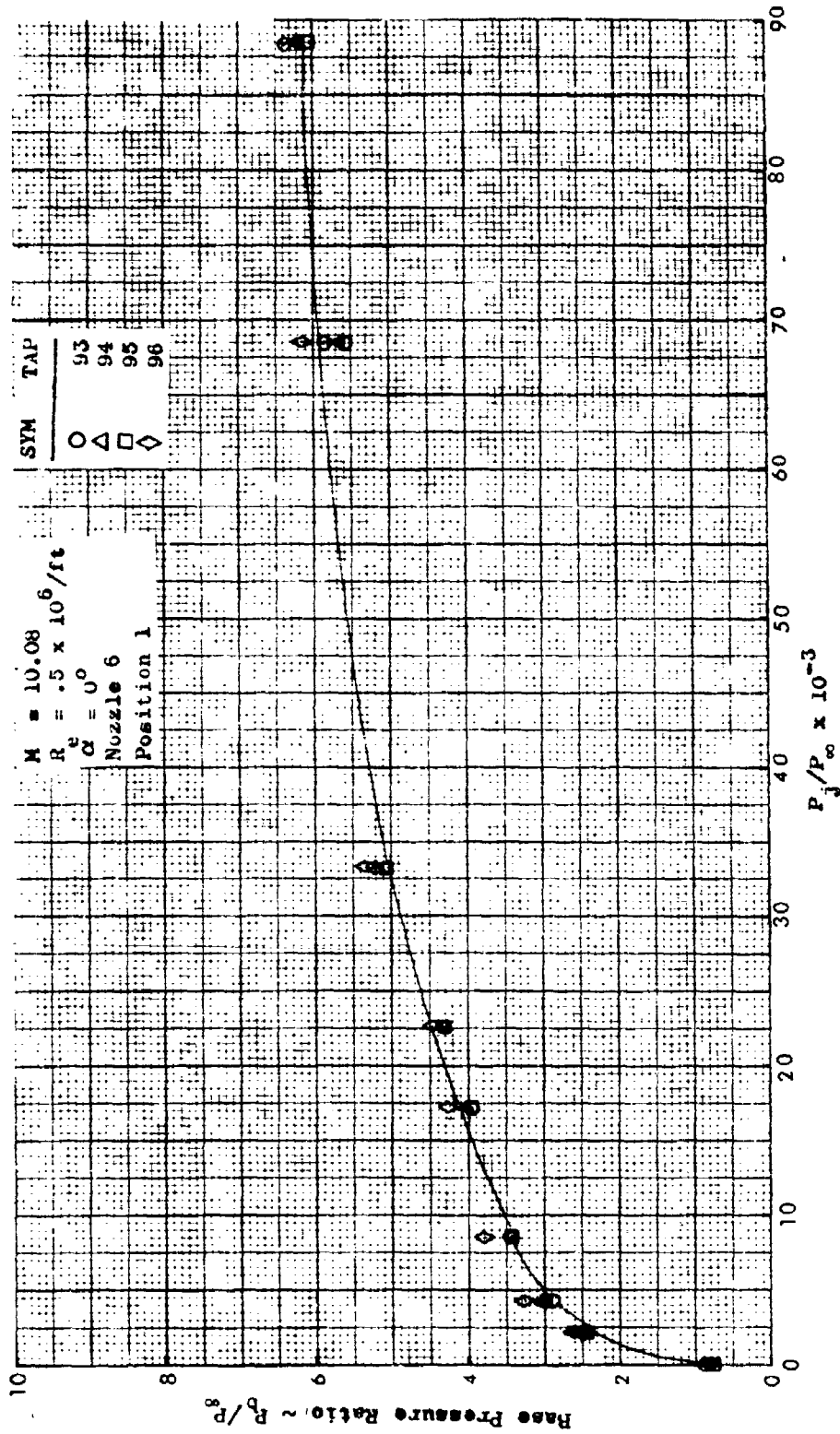


Figure 158. Effect of Jet Pressure Ratio on Base Pressure at $M = 10.08$

CONFIDENTIAL

CONFIDENTIAL

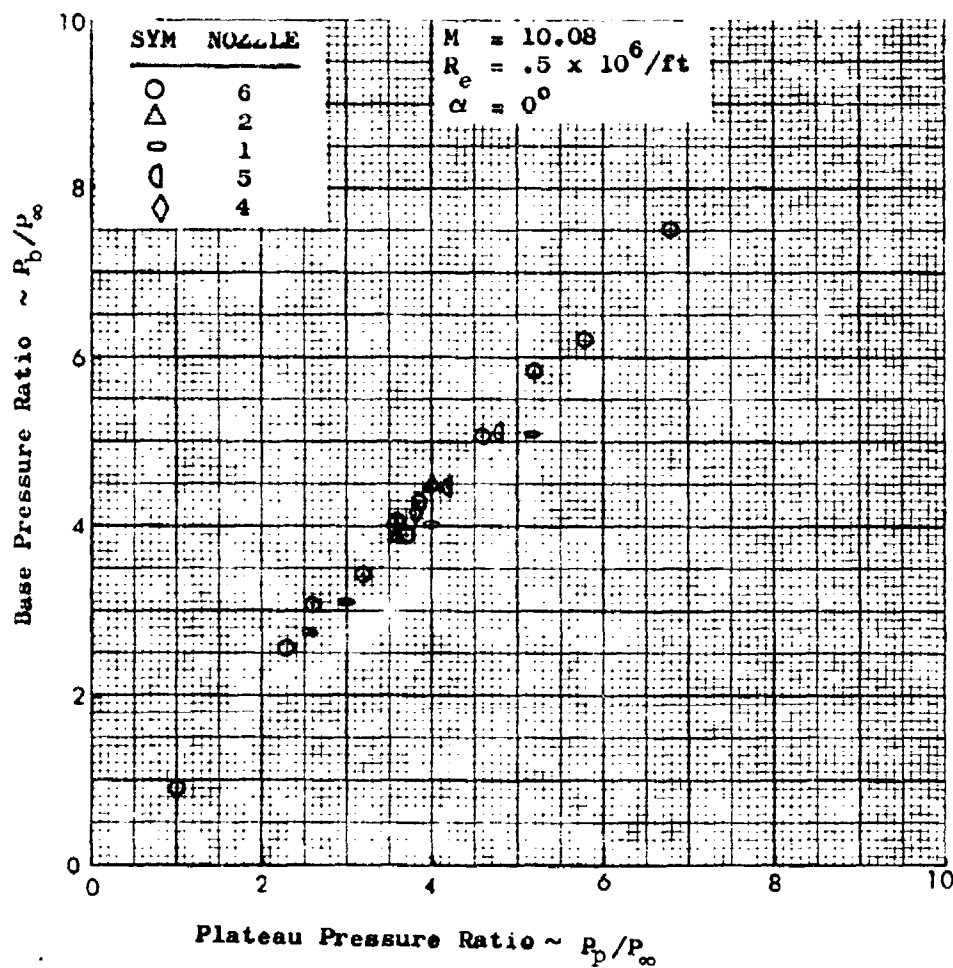


Figure 159. A Comparison of Base Pressure and Lower Surface Plateau Pressure at $M = 10.08$

CONFIDENTIAL

CONFIDENTIAL

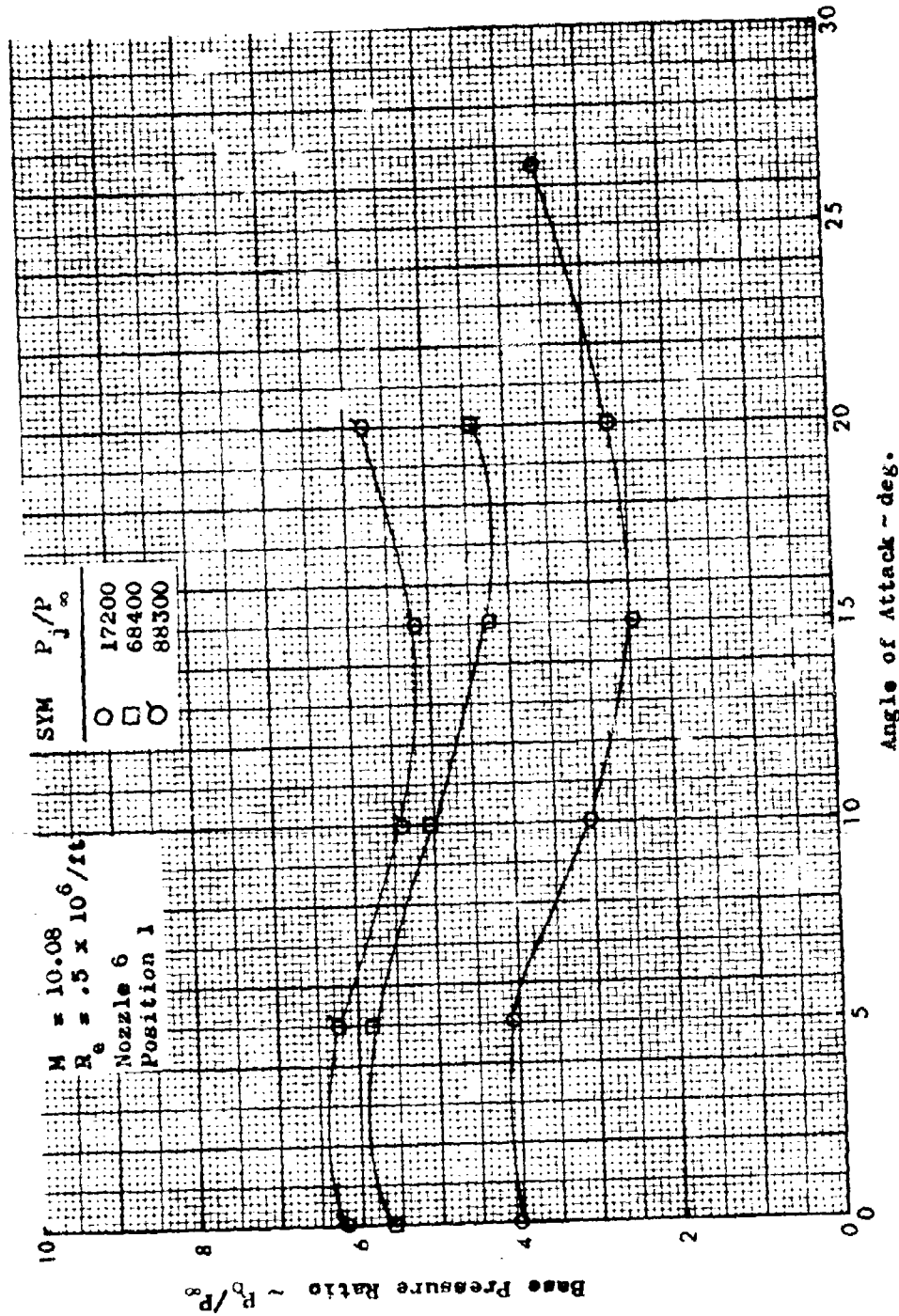


Figure 160. Angle of Attack Effect on Base Pressure at $M = 10.08$

CONFIDENTIAL

CONFIDENTIAL

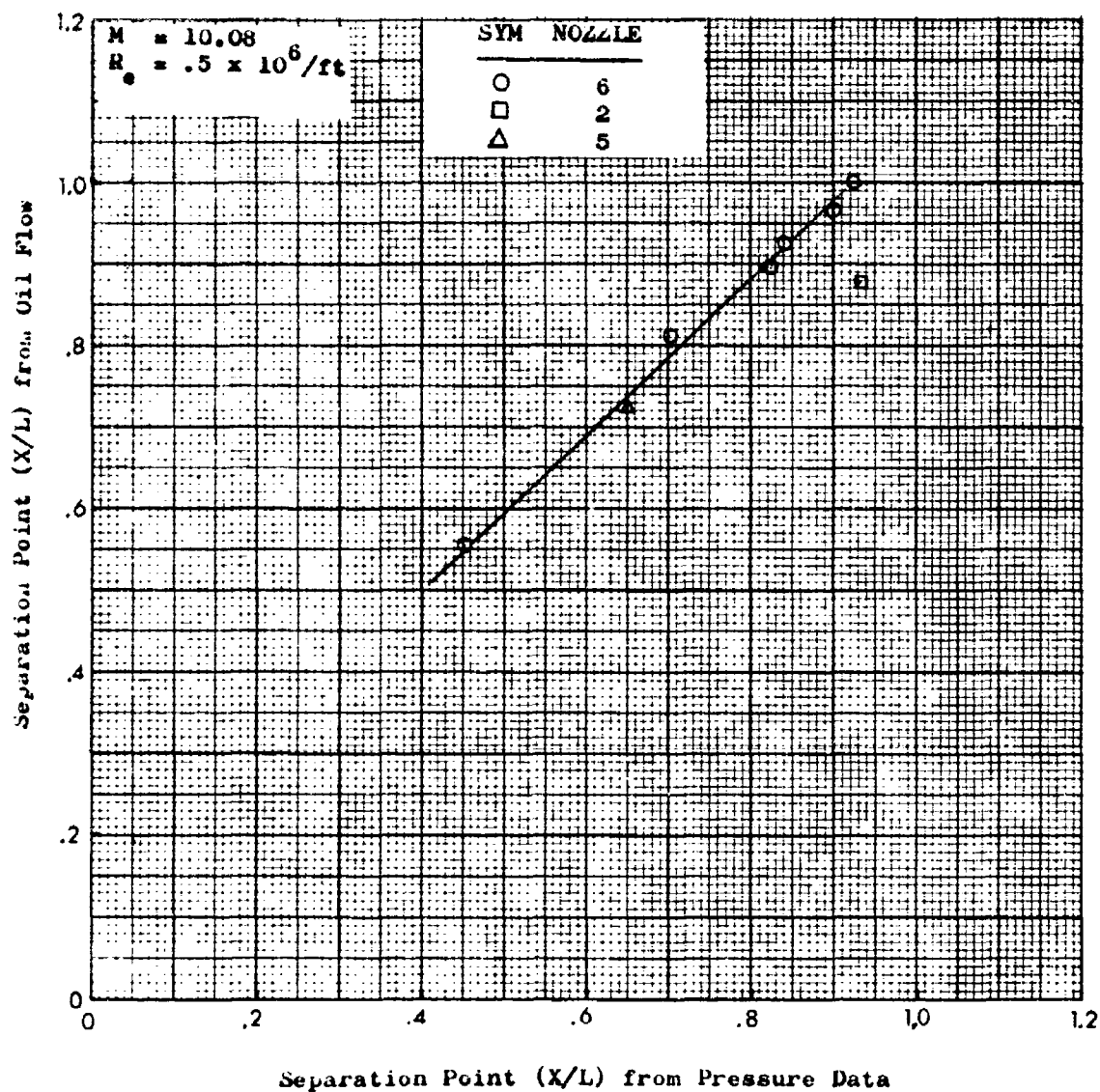


Figure 101. A Comparison of Oil Flow Versus Pressure Results on Separation Point on Flat Plate Centerline

CONFIDENTIAL

CONFIDENTIAL

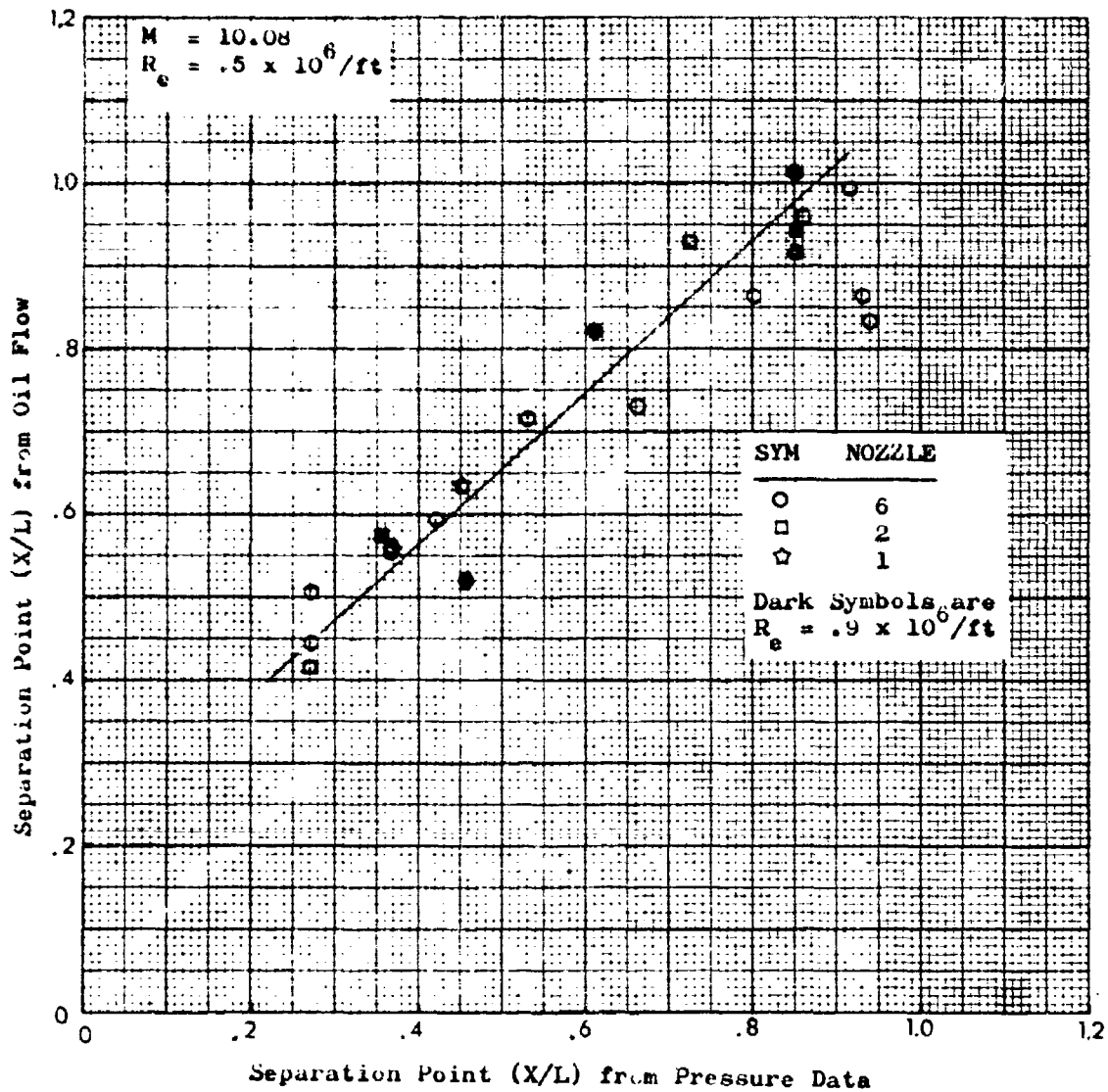


Figure 162. A Comparison of Separation Points from Oil Flow and Pressure Data on Delta Centerline

CONFIDENTIAL

CONFIDENTIAL

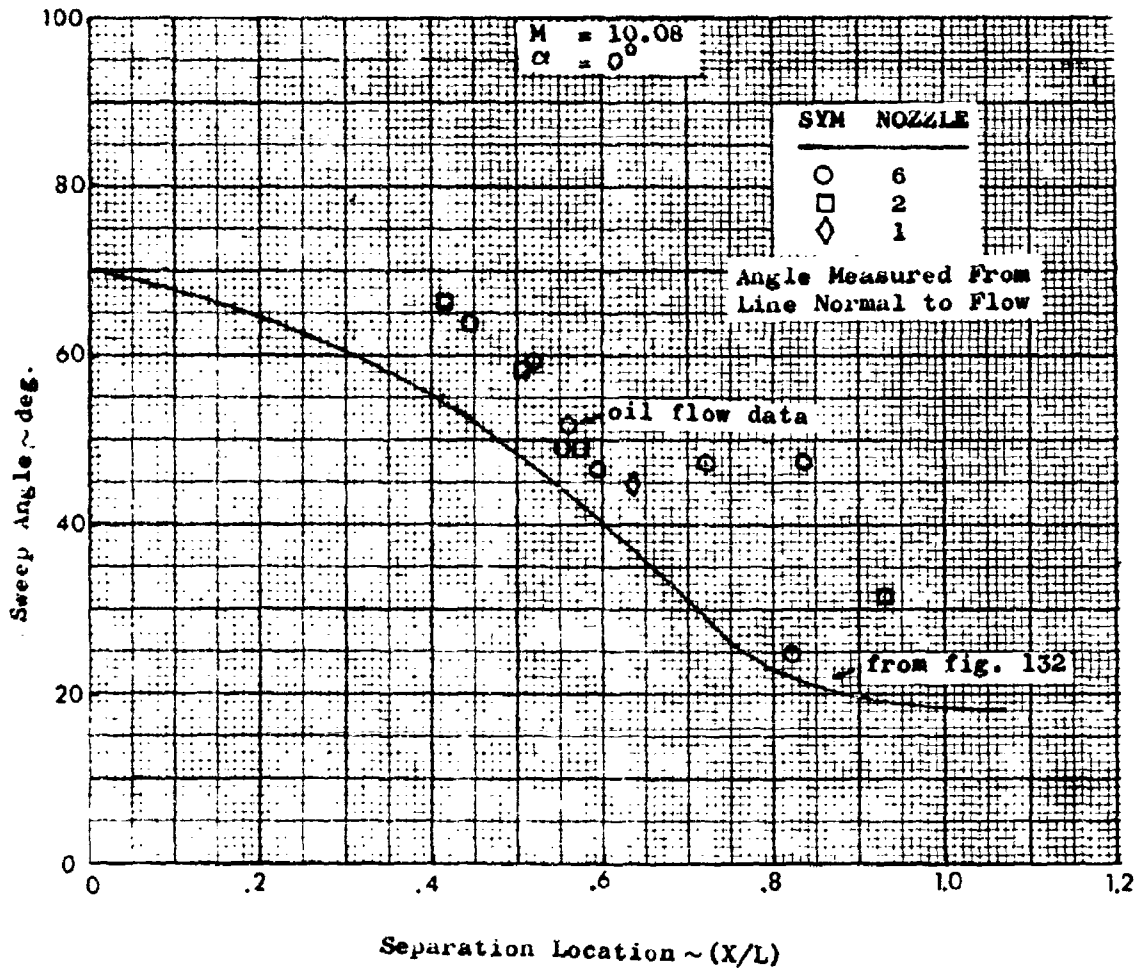
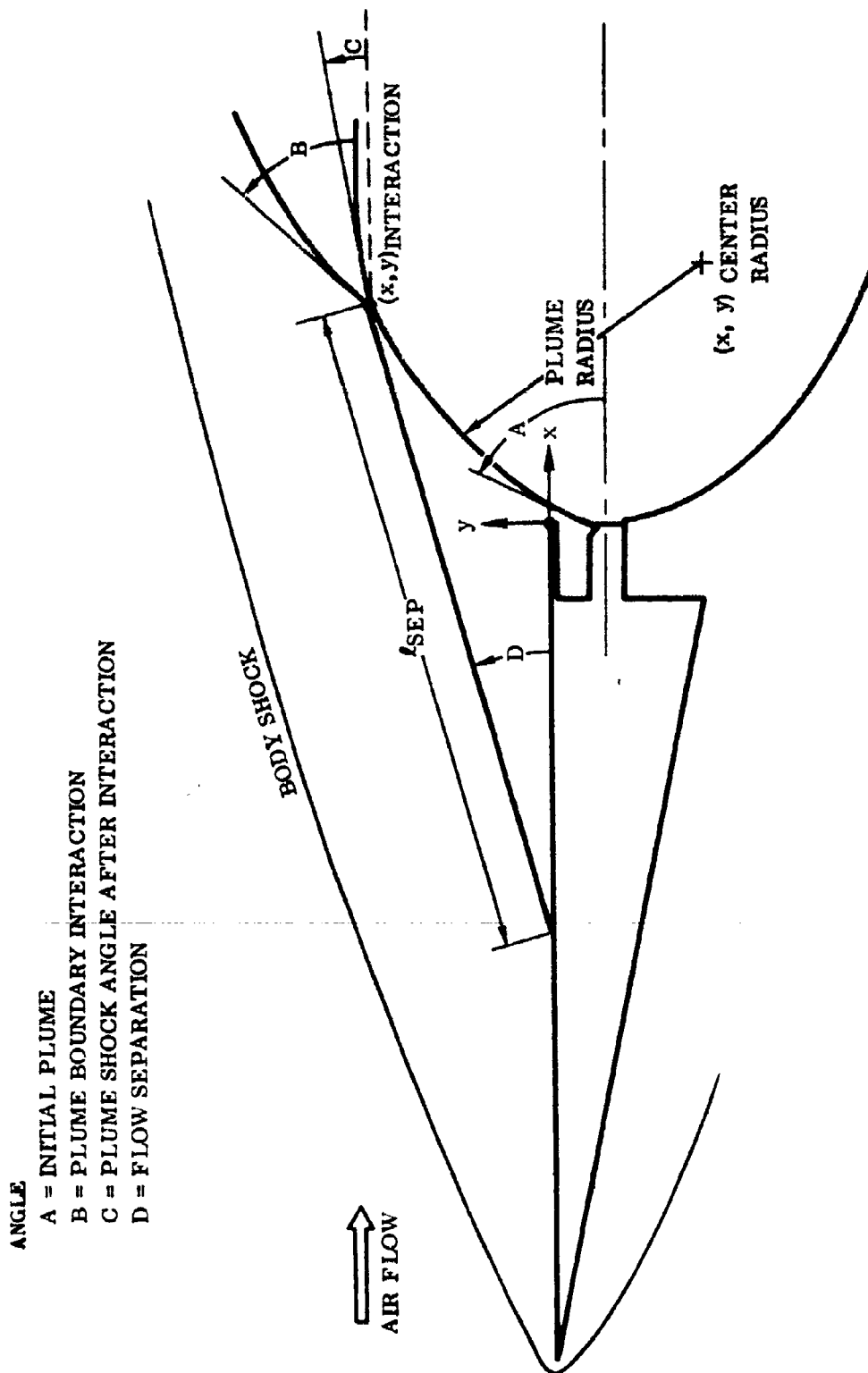


Figure 163. Delta Configuration Spanwise Separation Line Sweep Angle Comparison

CONFIDENTIAL

UNCLASSIFIED



ANGLE

A = INITIAL PLUME

B = PLUME BOUNDARY INTERACTION

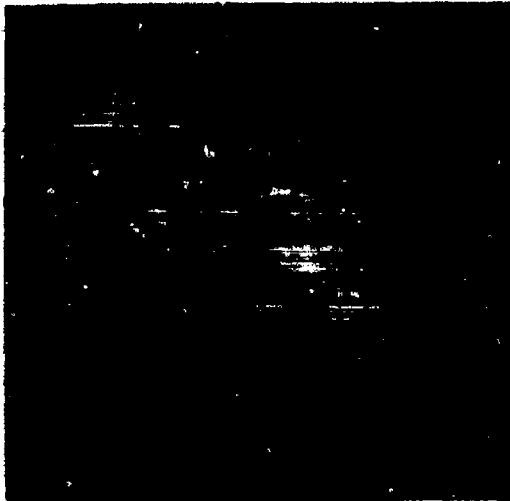
C = PLUME SHOCK ANGLE AFTER INTERACTION

D = FLOW SEPARATION

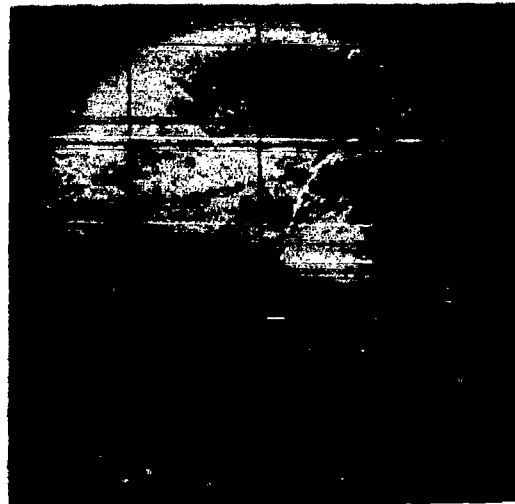
Figure 164. Schematic of Plume Interaction Measurements

UNCLASSIFIED

UNCLASSIFIED



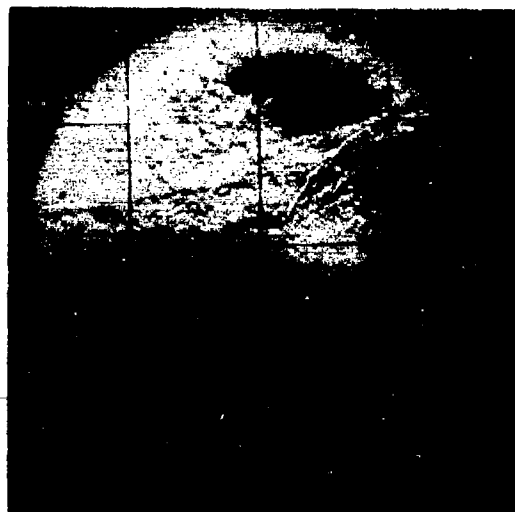
$P_j/P_\infty = 17200$



$P_j/P_\infty = 68500$



$P_j/P_\infty = 22600$



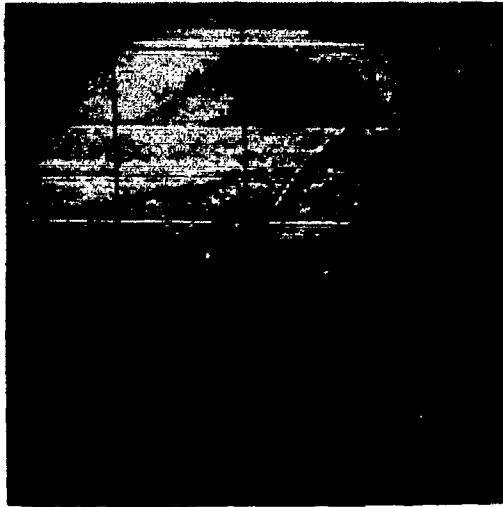
$P_j/P_\infty = 89200$

NOZZLE G, POSITION 1
 $\alpha = 0$ DEGREE
 $Re = 1.51 \times 10^6/FT$
 $M = 10.08$

Figure 165. Effect of Jet Pressure Ratio on Plume at $M = 10.08$ and $\alpha = 0^\circ$

UNCLASSIFIED

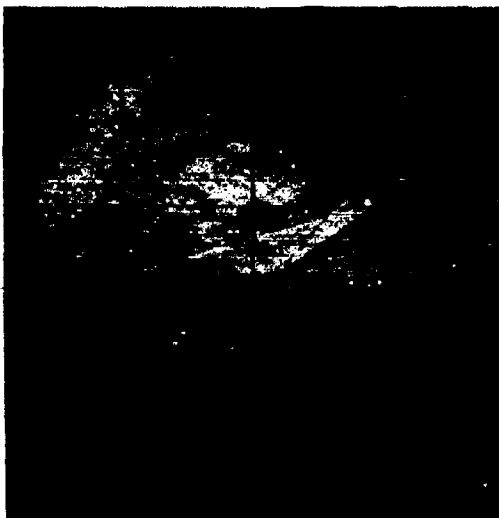
UNCLASSIFIED



$\alpha = 0^\circ$



$\alpha = 5^\circ$



$\alpha = 10^\circ$



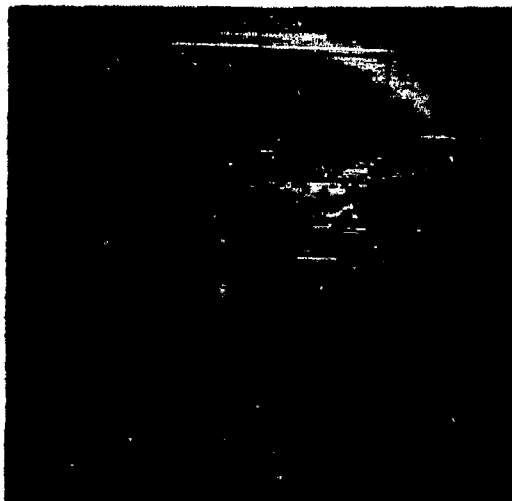
$\alpha = 15^\circ$

NOZZLE 6, POSITION 1
 $P_1/P_\infty = 89.500$
 $Re = 0.51 \times 10^{-6}/FT$
 $M = 10.08$

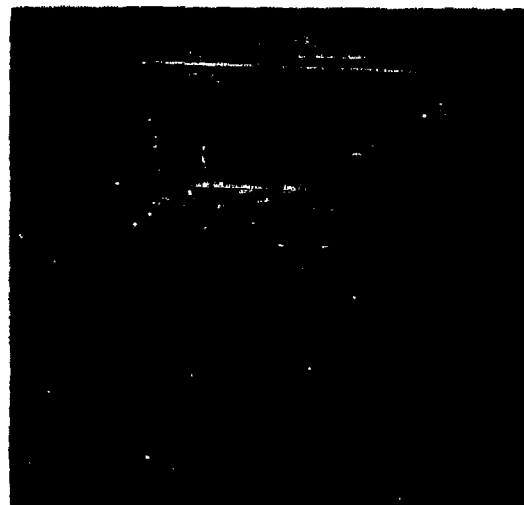
Figure 166. Effect of Angle of Attack on Plume at $M = 10.08$

UNCLASSIFIED

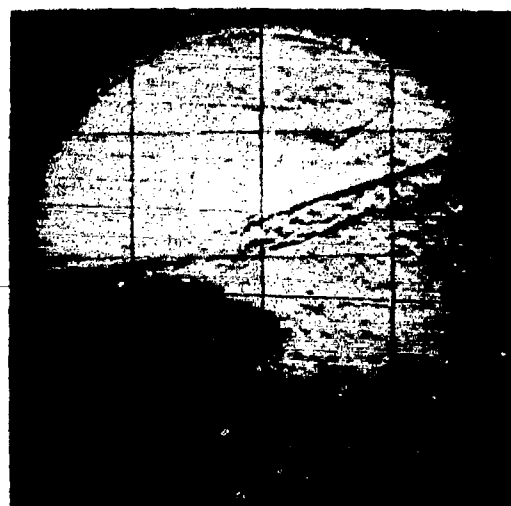
UNCLASSIFIED



$M = 10.08$



$M = 7.9$



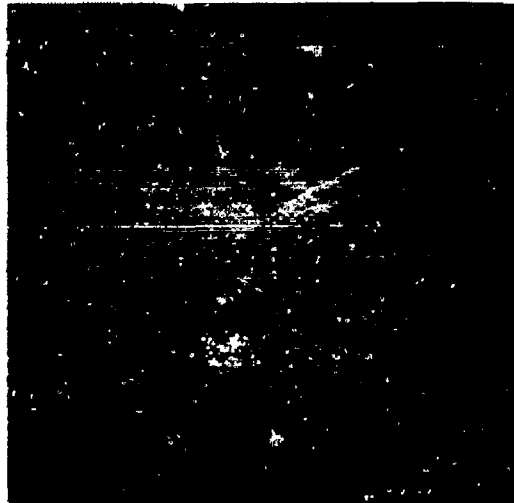
$M = 5.96$

NOZZLE 6, POSITION 1
 $\alpha = 0.1$ DEGREE
 $P_t/P_\infty = 2.000$

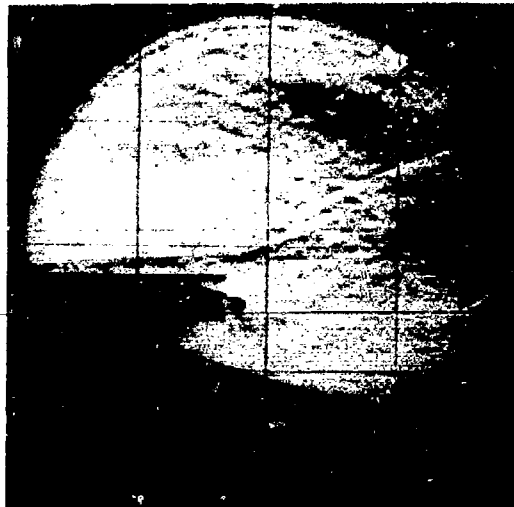
Figure 167. A Comparison of Plumes at Mach 6, 8, and Mach 10

UNCLASSIFIED

UNCLASSIFIED



NOZZLE 6



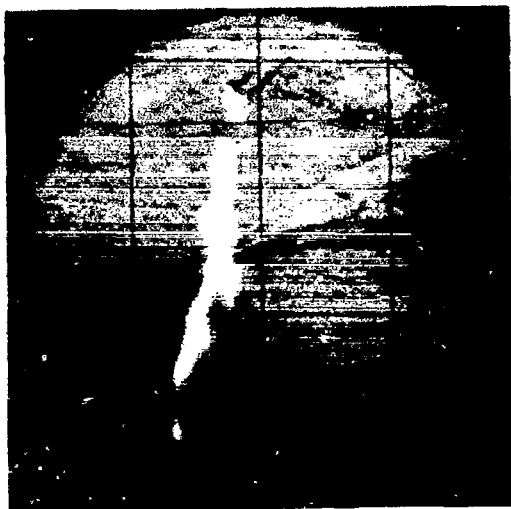
NOZZLE 1

POSITION 1
 α 0 DEGREE
 P_1/P_∞ 7500
 Re 1.0×10^6 FT
 M 5.96

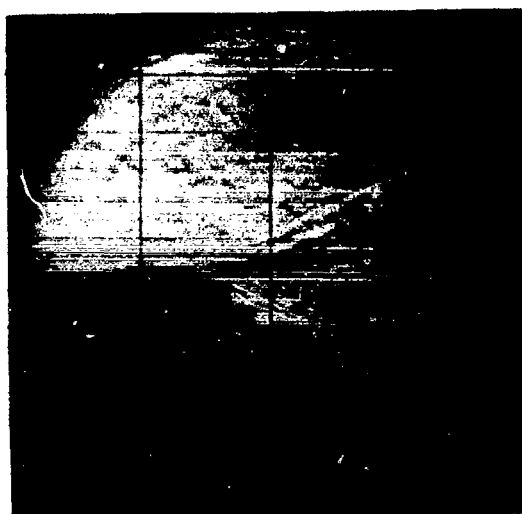
Figure 168. Effect of Nozzle Size on the Plume at $M = 5.96$

UNCLASSIFIED

UNCLASSIFIED



CO₂



AIR



ARGON

NOZZLE 1, POSITION 1

$\alpha = 0$ DEGREE

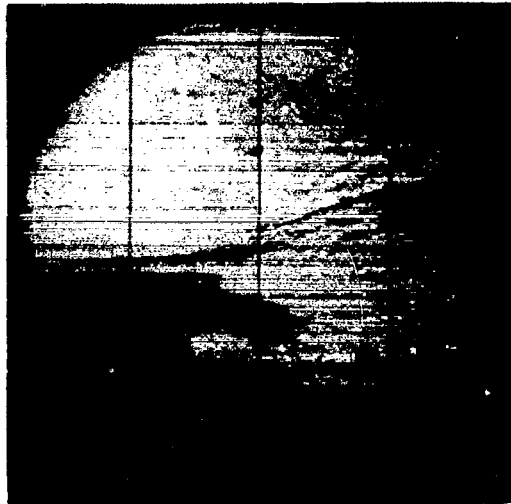
$Re = 1.66 \times 10^6 / FT$

$M = 5.96$

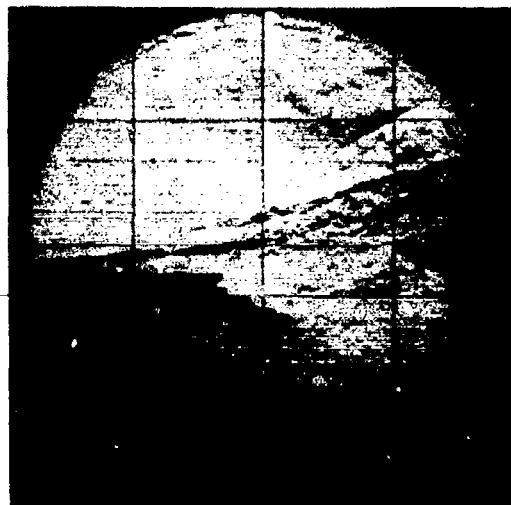
Figure 169. A Comparison of Exhaust Gas on the Plume at $M = 5.96$

UNCLASSIFIED

UNCLASSIFIED



$\theta_N = 7.5$ DEGREE



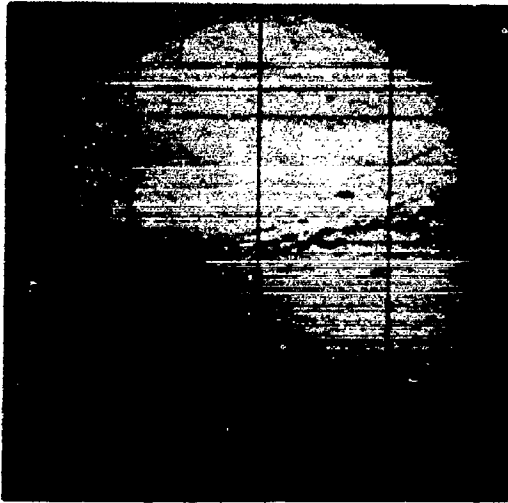
$\theta_N = 30$ DEGREE

POSITION 1
 $\alpha = 0$ DEGREE
 $Re = 0.8 \times 10^6$, FT
 $A/A_\infty = 2.25$
 $M = 5.96$

Figure 170. A Comparison of Exit Angle Effects at $M = 5.96$

UNCLASSIFIED

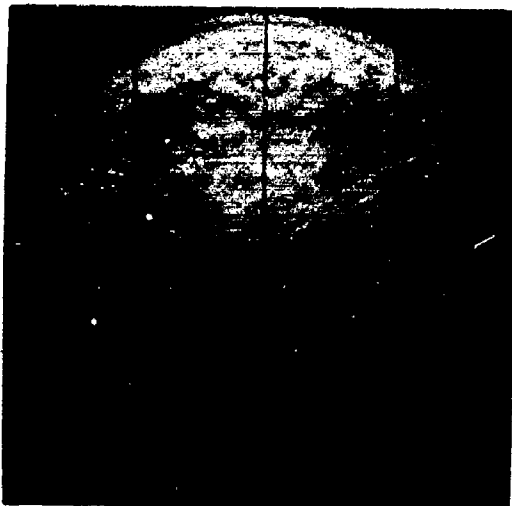
UNCLASSIFIED



POSITION 1



POSITION 4



POSITION 2



POSITION 3

Figure 171. Effect of Nozzle Location on Plume at M 5, 96

228
UNCLASSIFIED

CONFIDENTIAL

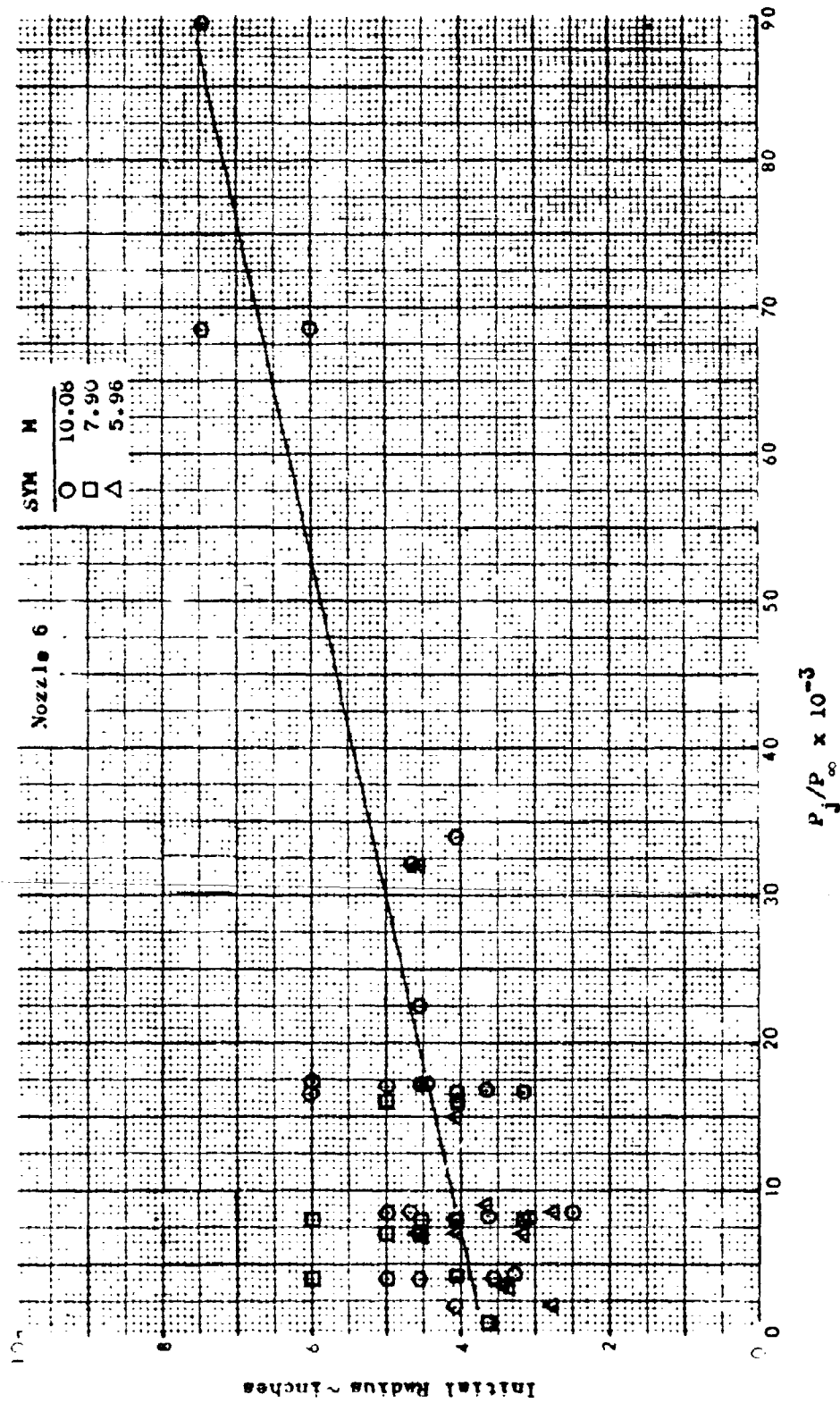


Figure 172. Measured Plume Initial Radius as a Function of Jet Pressure Ratio

CONFIDENTIAL

CONFIDENTIAL

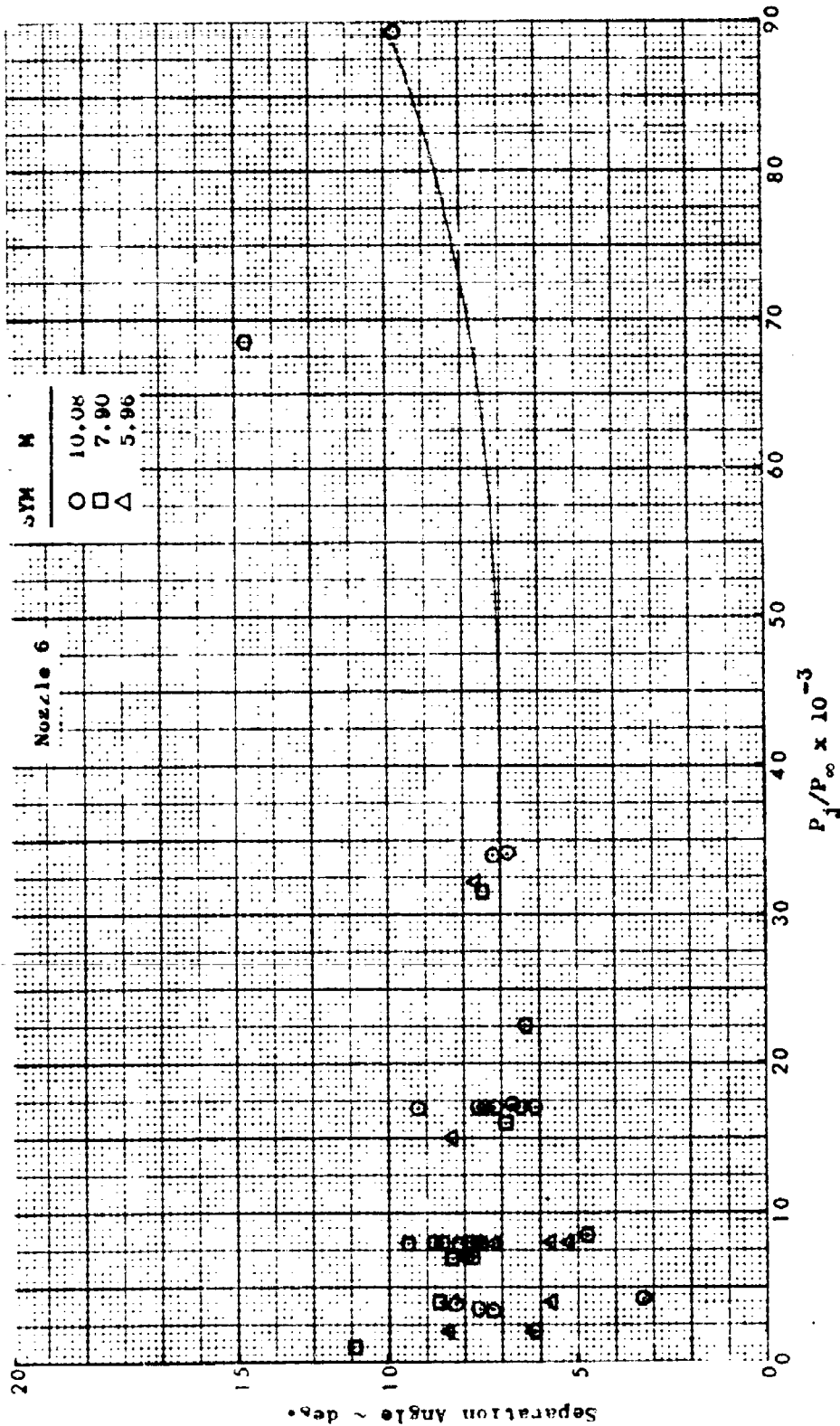


Figure 173. Measured Flow Separation Angle as a Function of Jet Pressure Ratio

CONFIDENTIAL

CONFIDENTIAL

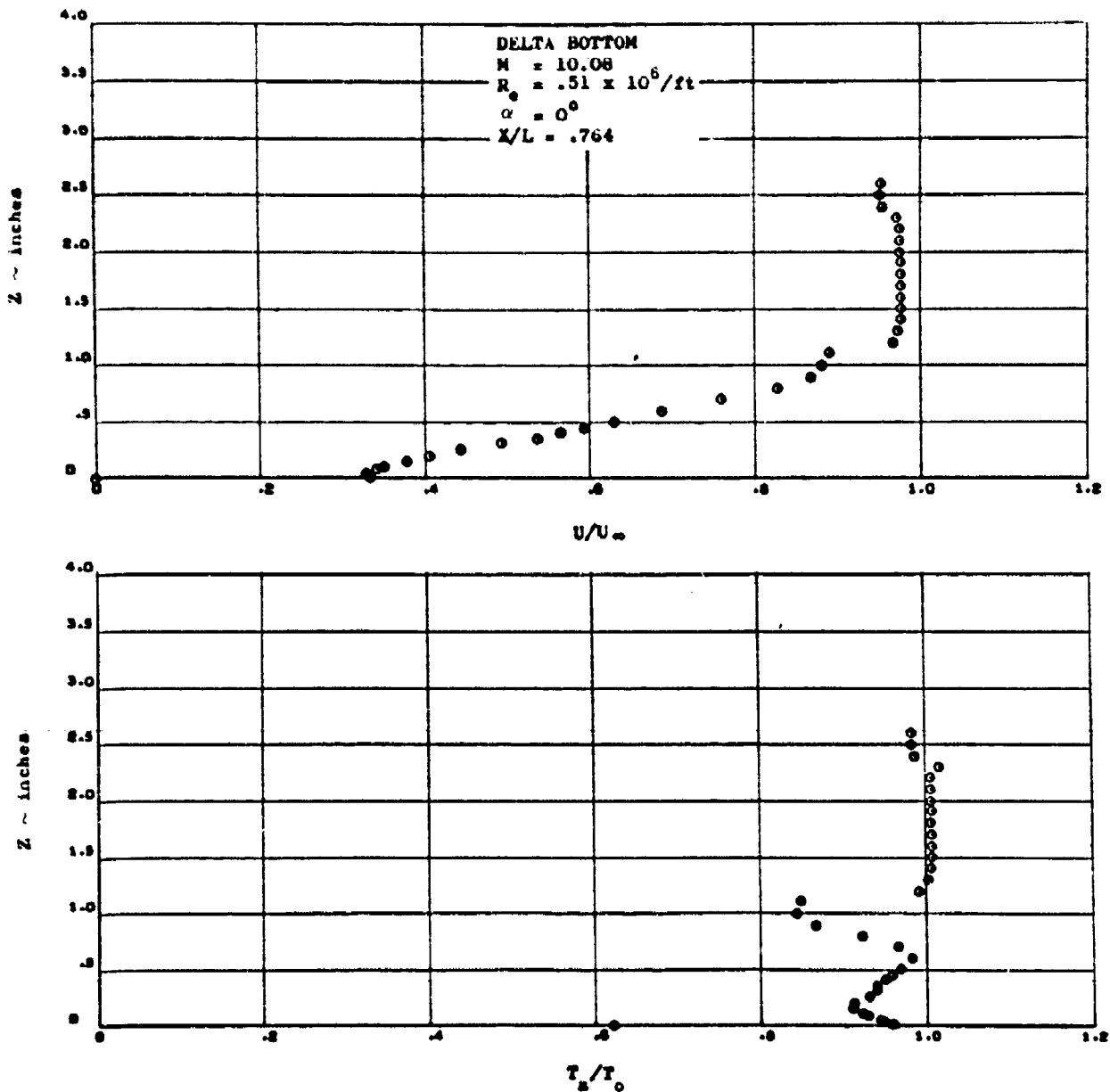


Figure 174a. Flow Surveys at Mach 10 without a Plume

CONFIDENTIAL

CONFIDENTIAL

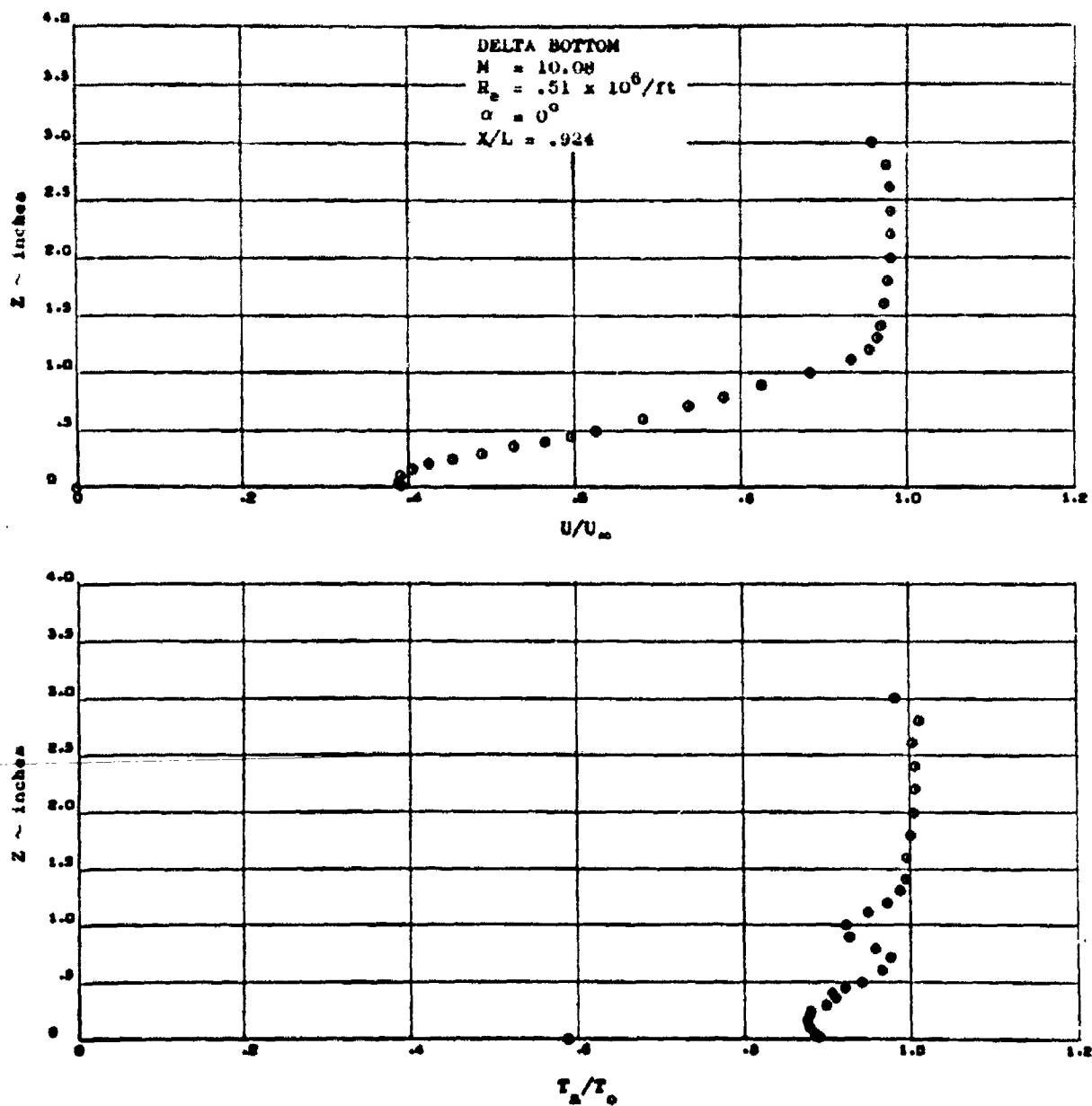


Figure 1741. Flow Surveys at Mach 10 without a Plume

CONFIDENTIAL

CONFIDENTIAL

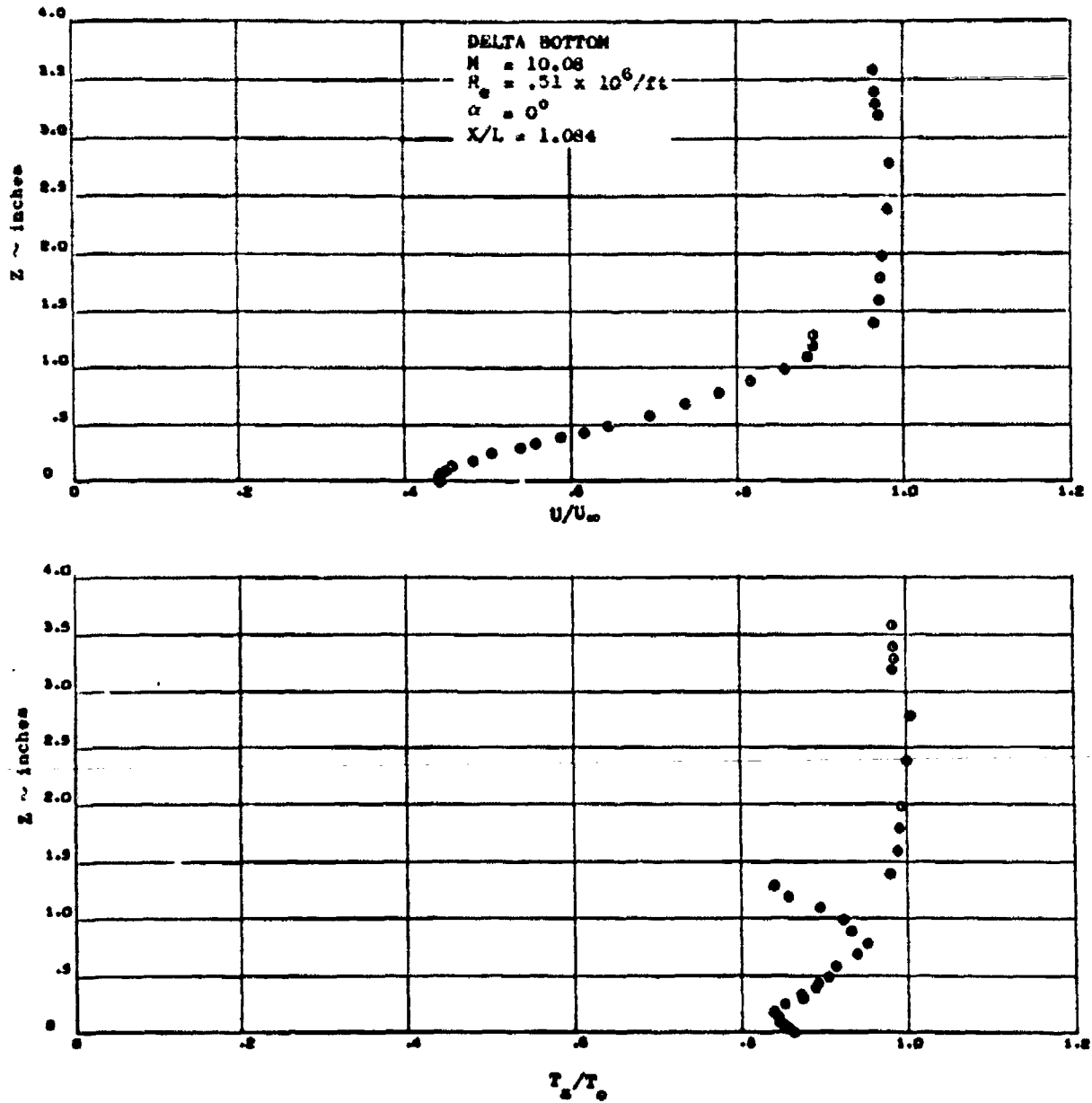


Figure 174c. Flow Surveys at Mach 10 without a Plume

CONFIDENTIAL

CONFIDENTIAL

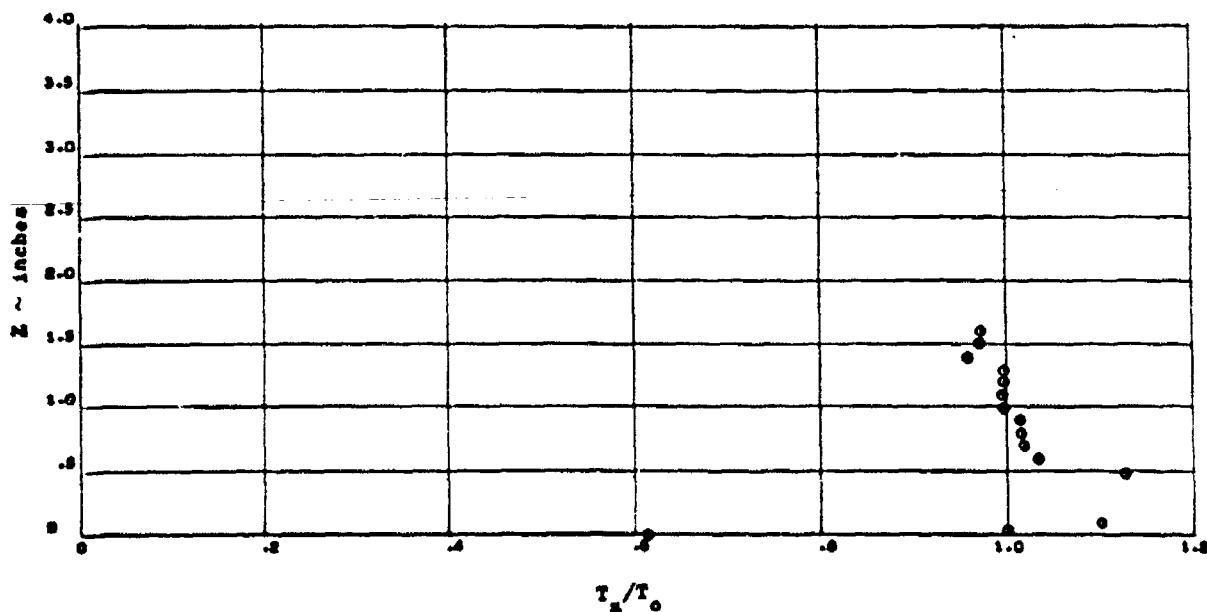
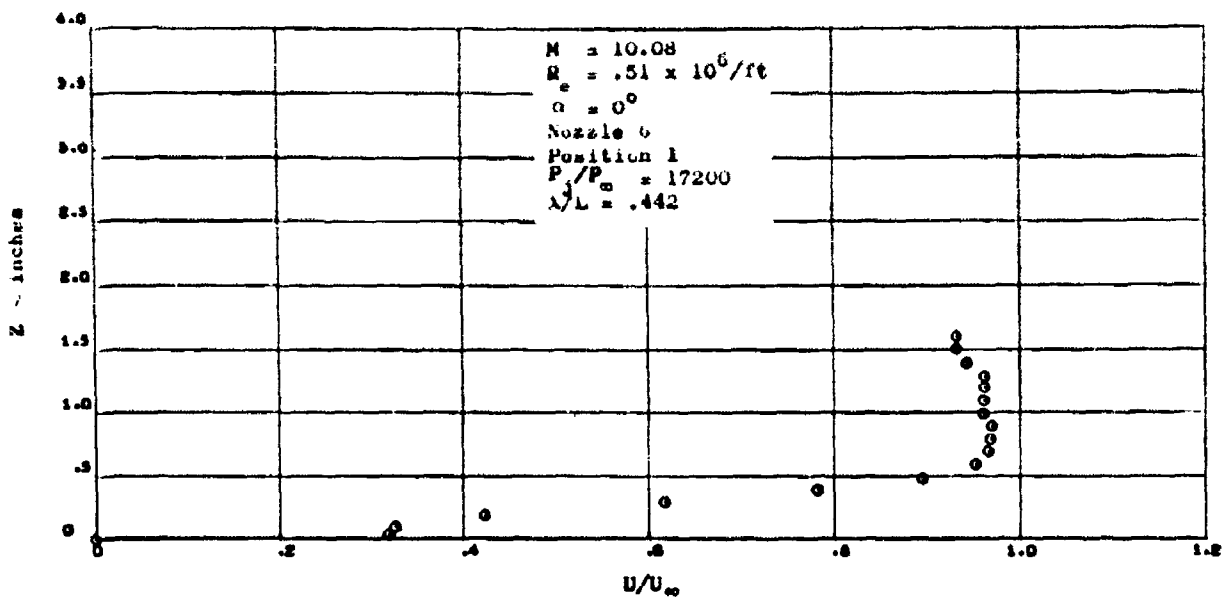


Figure 11(a). Flow Survey at Mach 10 with $P_1/P_\infty = 17200$, $X/L = .442$

CONFIDENTIAL

CONFIDENTIAL

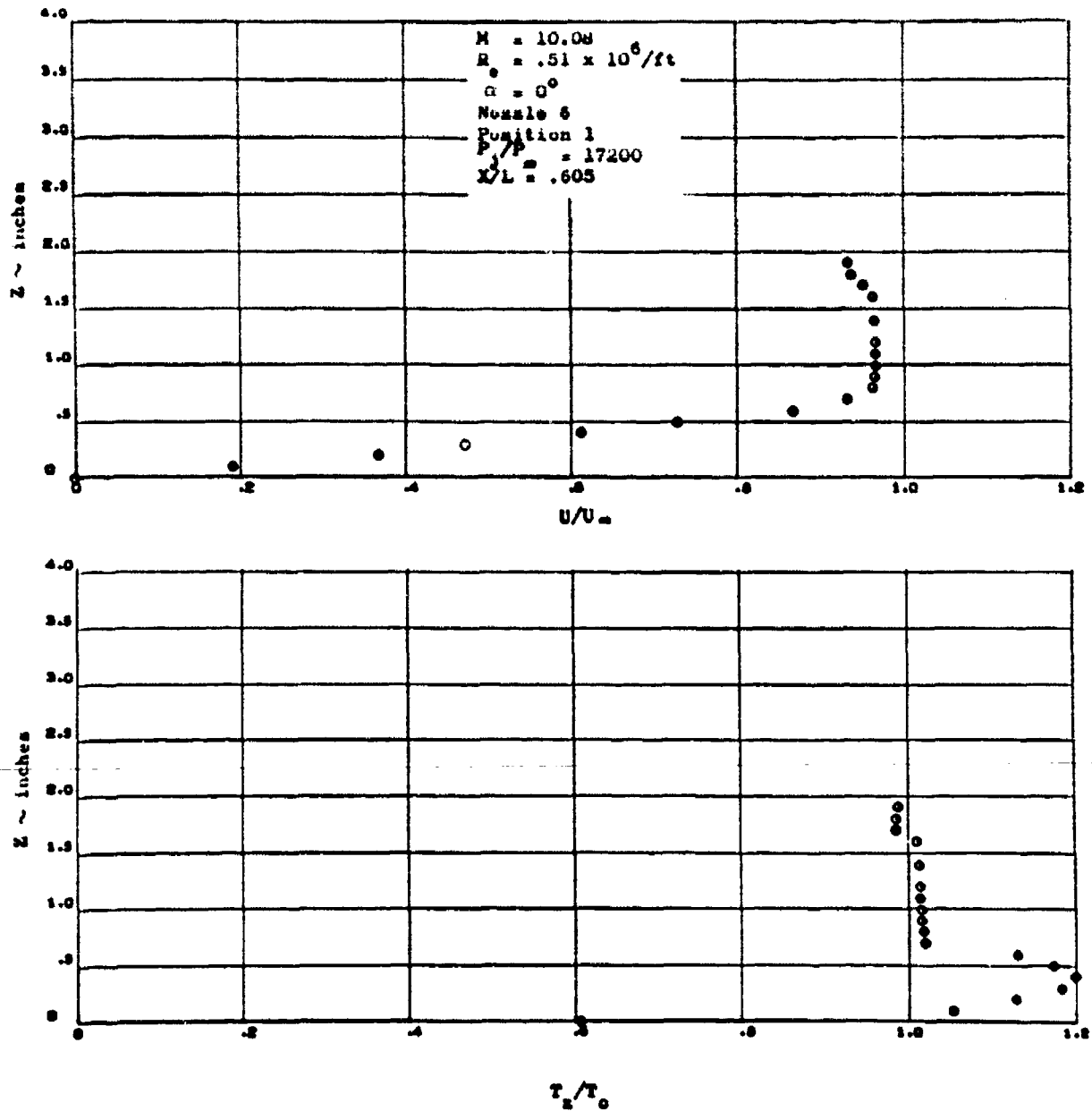


Figure 175b. Flow Survey at Mach 10 with $P_j/P_\infty = 17200$, $x/L = .605$

CONFIDENTIAL

CONFIDENTIAL

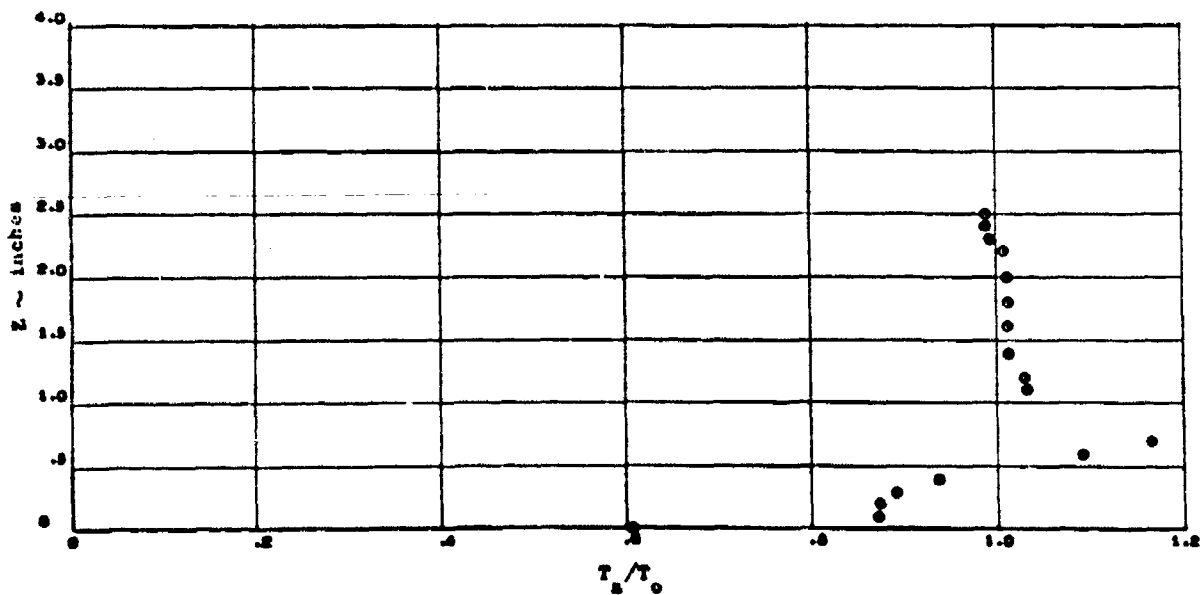
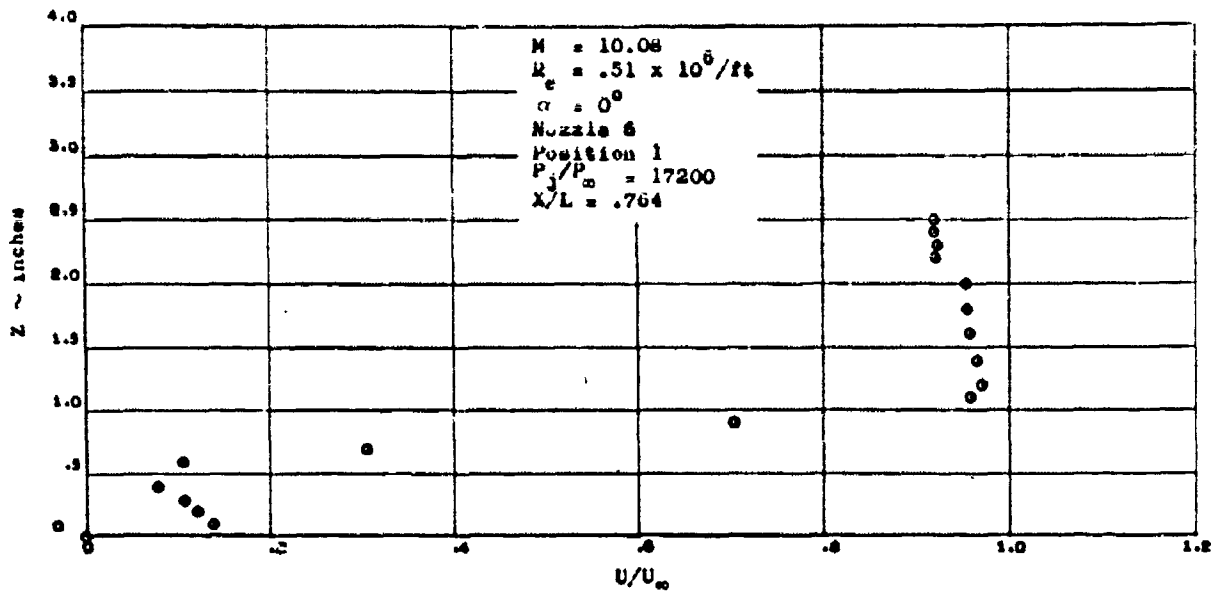


Figure 17b. Flow Survey at Mach 10 with $P_j/P_\infty = 17200$, $X/L = .764$.

CONFIDENTIAL

CONFIDENTIAL

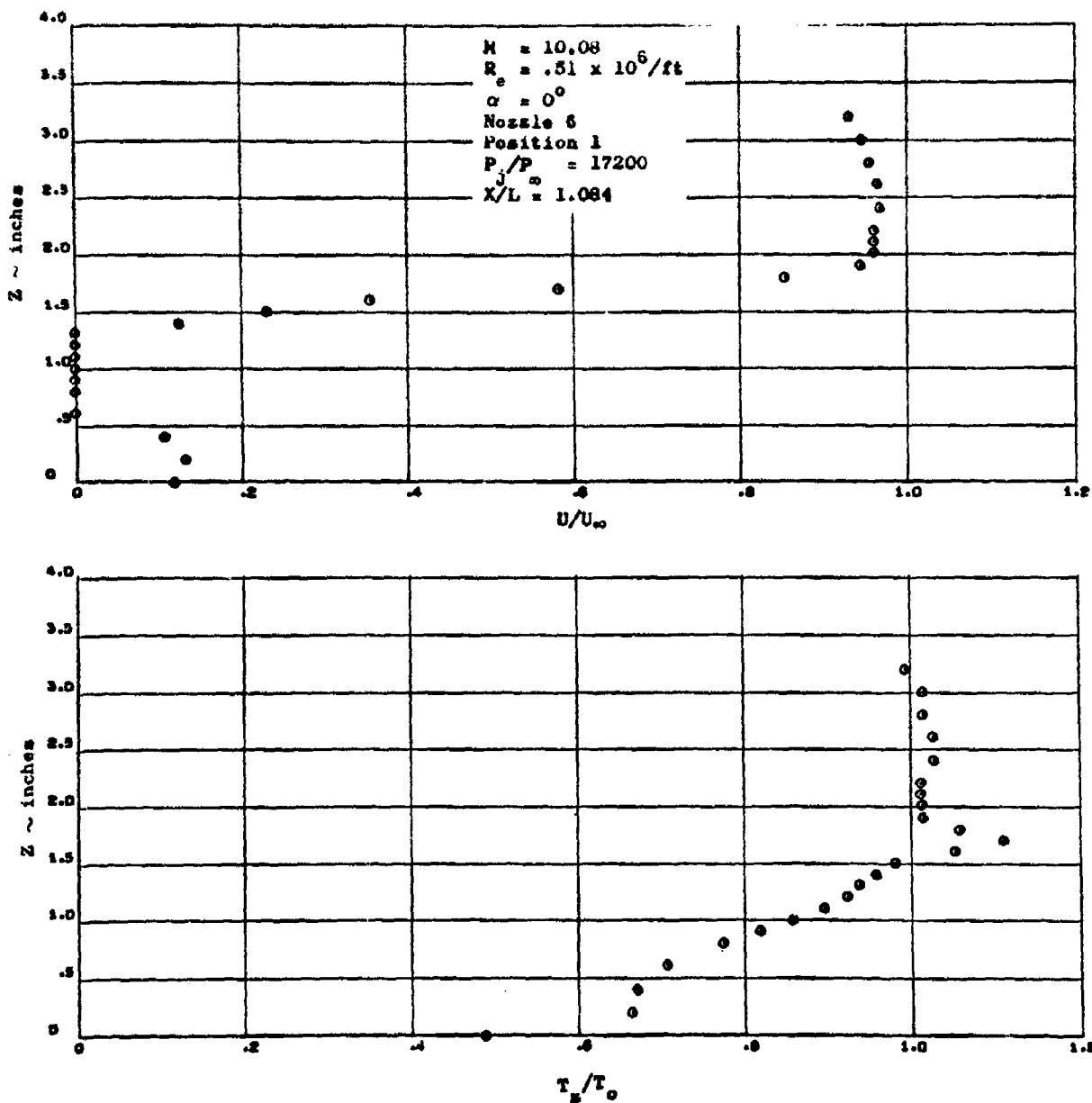


Figure 175d. Flow Survey at Mach 10 with $P_j/P_\infty = 17200$, $X/L = 1.084$

CONFIDENTIAL

CONFIDENTIAL

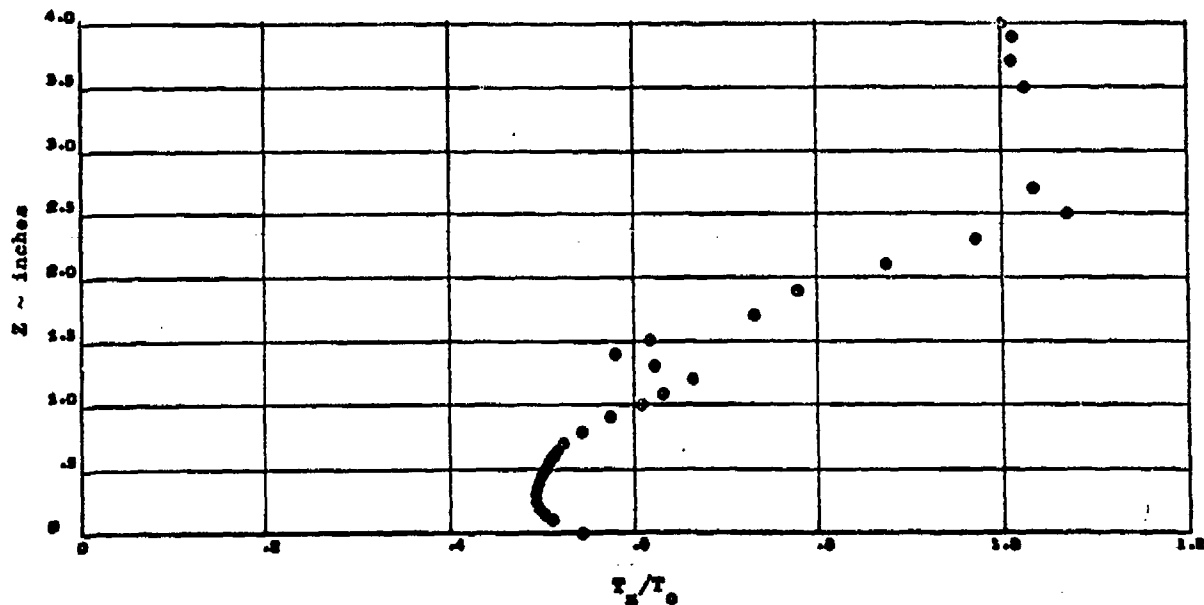
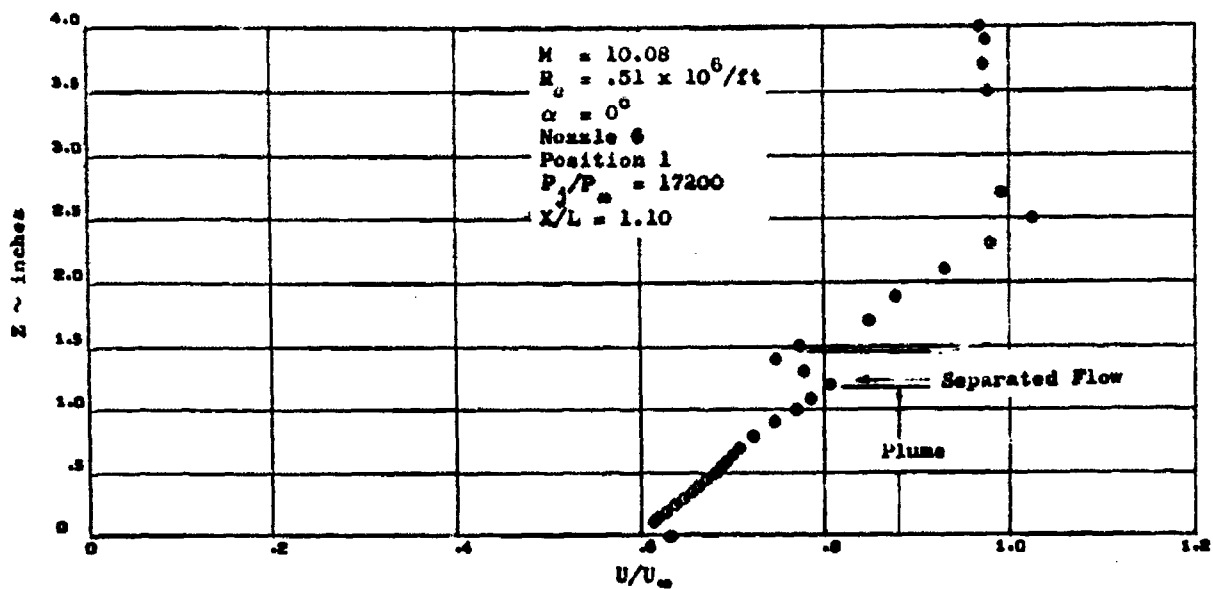


Figure 175e. Flow Survey at Mach 10 with $P_j/P_\infty = 17200$, $X/L = 1.10$

CONFIDENTIAL

CONFIDENTIAL

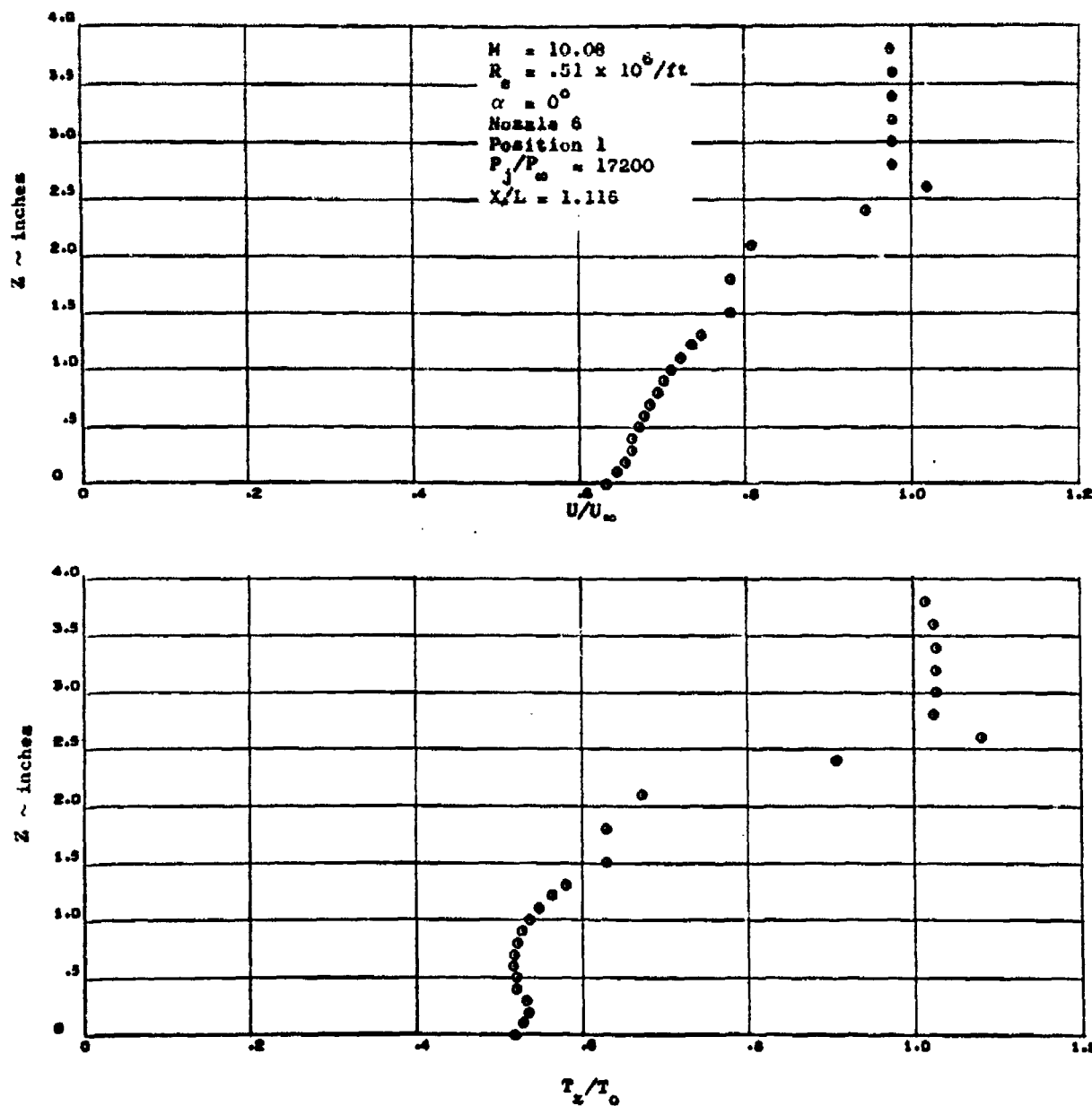


Figure 175f. Flow Survey at Mach 10 with $P_j/P_\infty = 17200$, $X/L = 1.116$

CONFIDENTIAL

CONFIDENTIAL

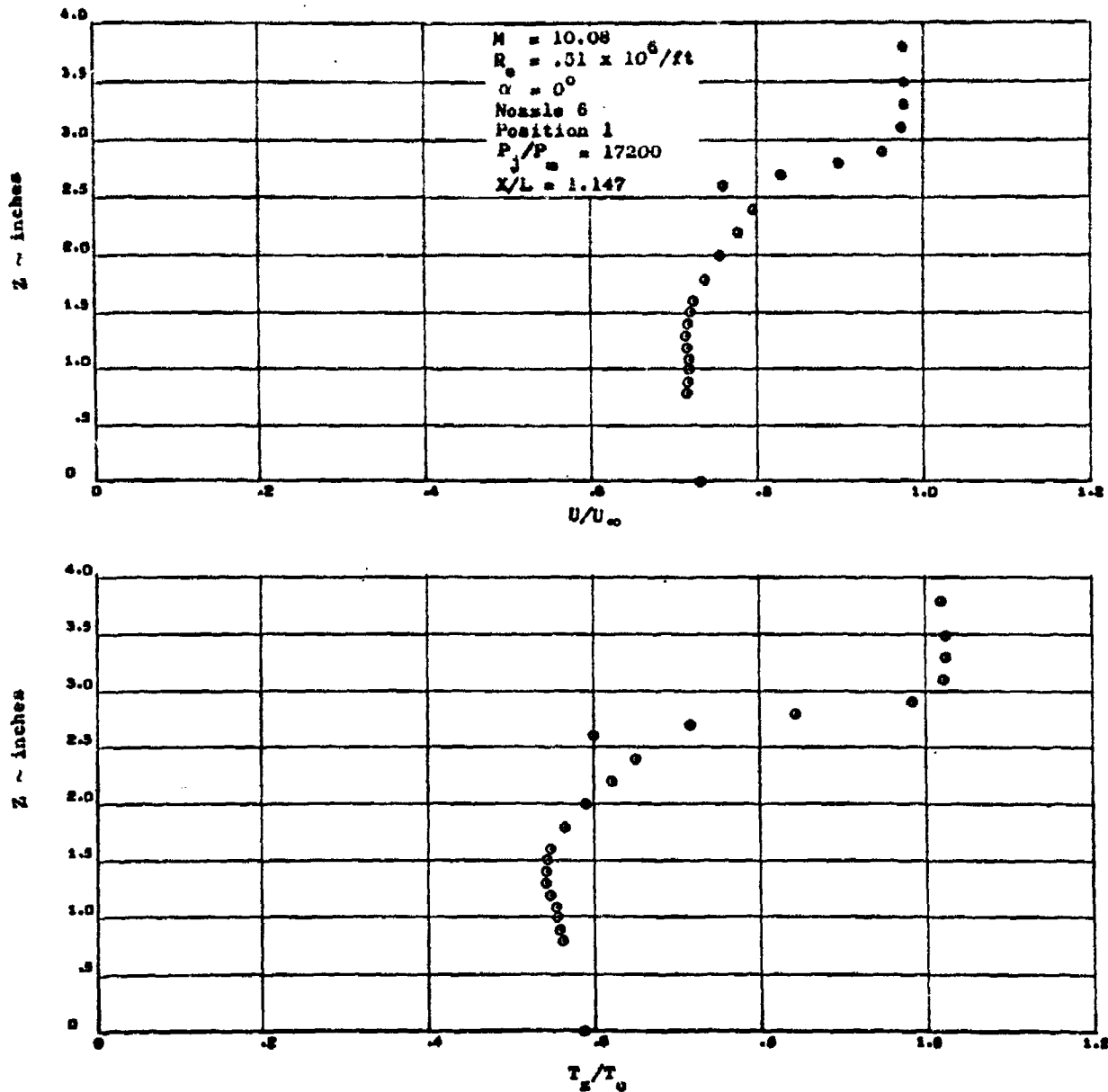


Figure 175g. Flow Survey at Mach 10 with $P_j/P_\infty = 17200$, $X/L = 1.147$

CONFIDENTIAL

CONFIDENTIAL

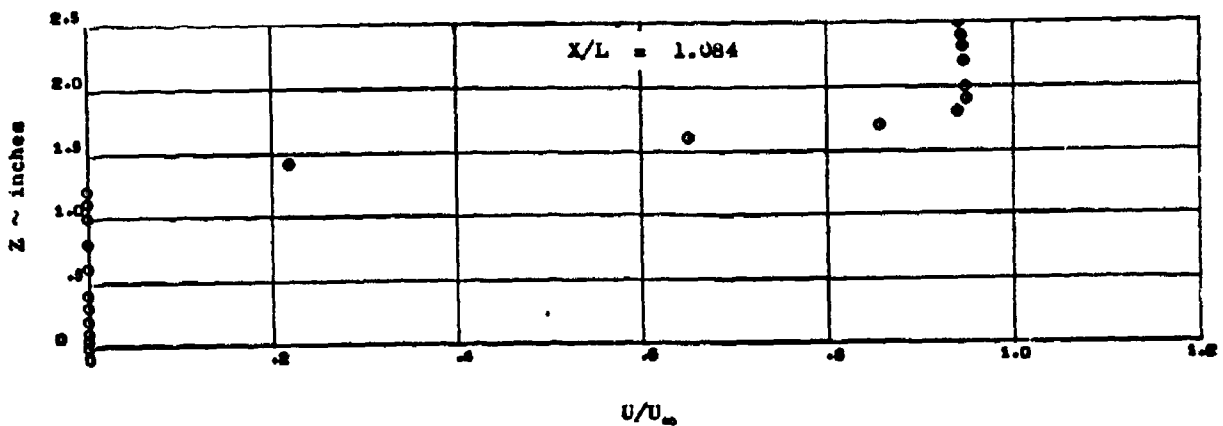
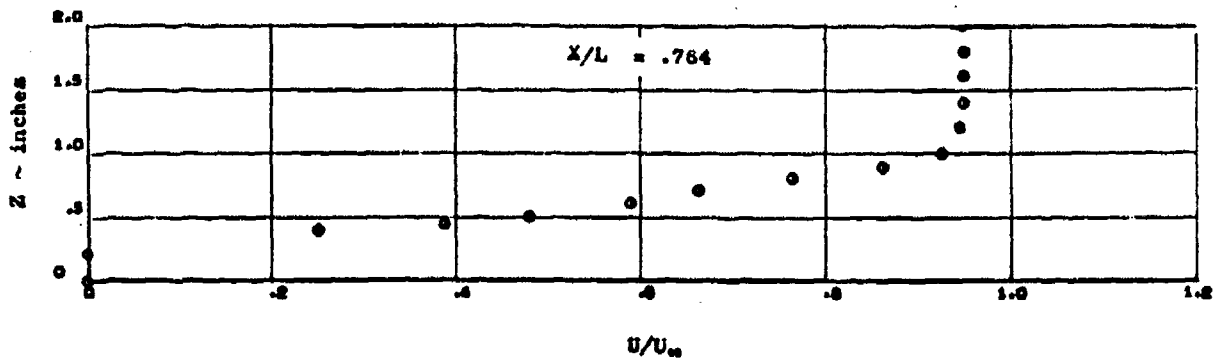
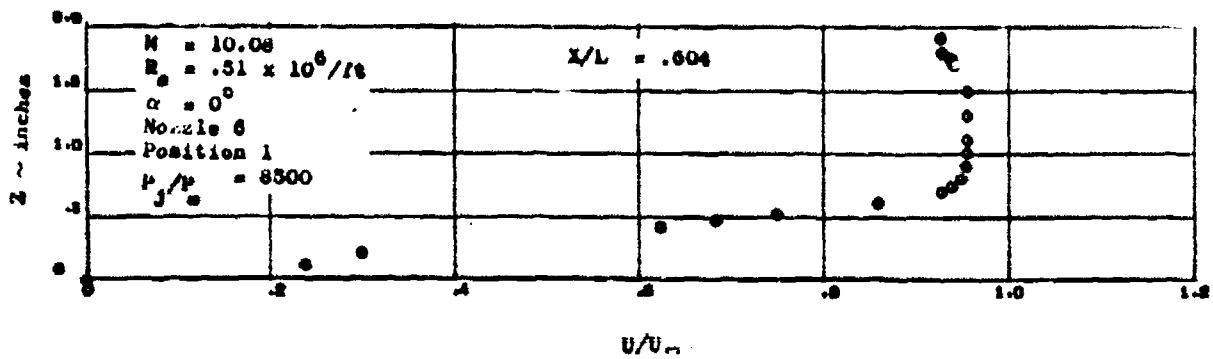
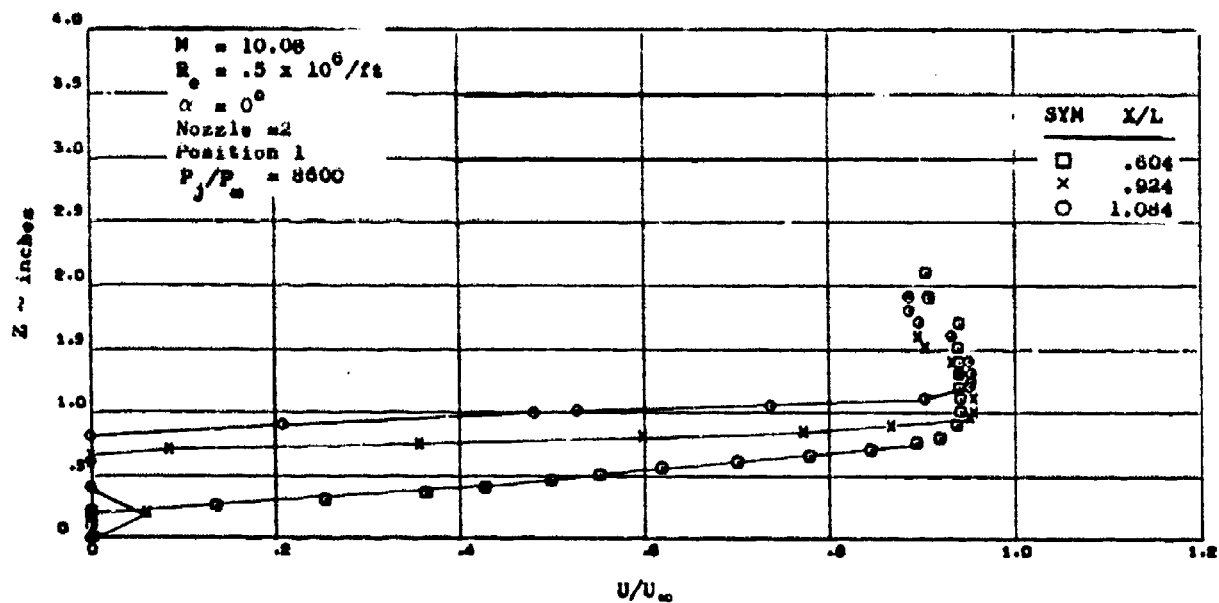


Figure 176 Flow Surveys at Mach 10 and $P_j/P_\infty = 8500$

CONFIDENTIAL

CONFIDENTIAL



177a

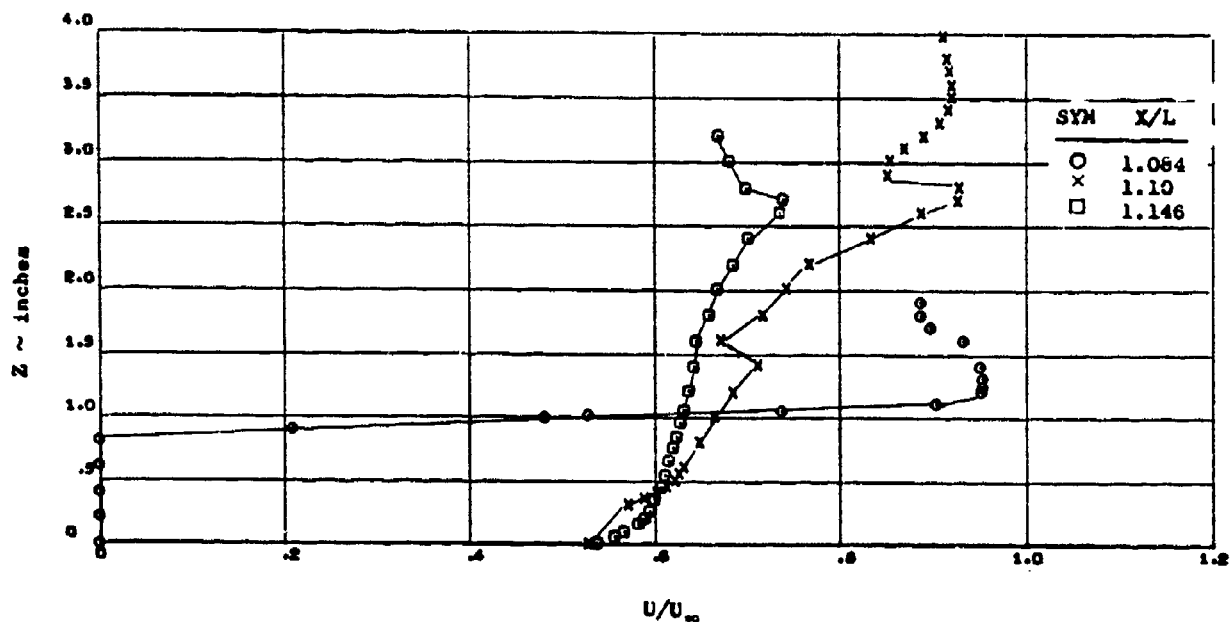


Figure 177 Effect of the Nozzle 2 Plume at 5 Axial Locations on Bottom Surface of Delta Planform

242

CONFIDENTIAL

CONFIDENTIAL

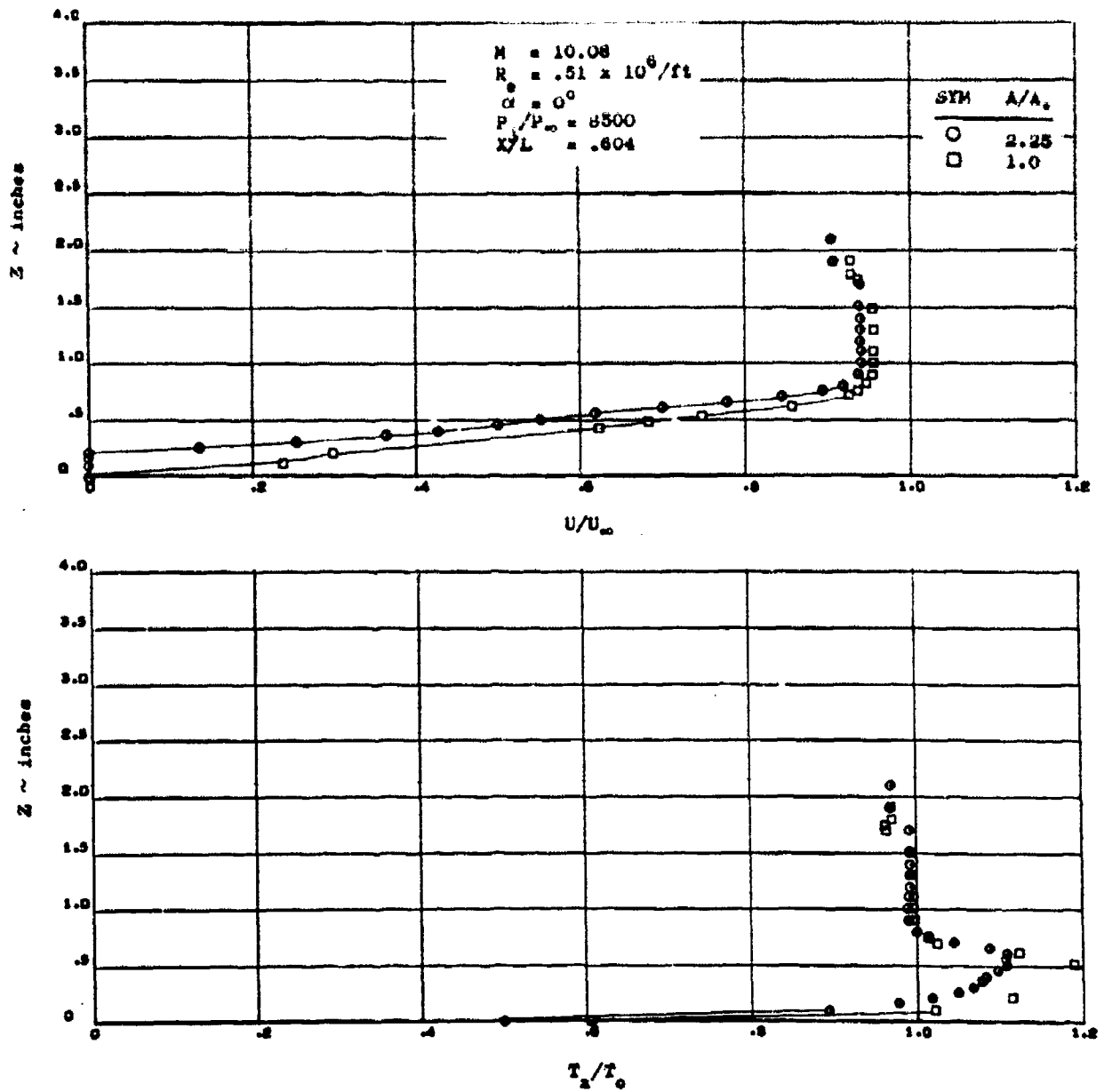


Figure 178a. Expansion Ratio Effect on Flow Surveys at $M = 10$, $X/L = .604$

CONFIDENTIAL

CONFIDENTIAL

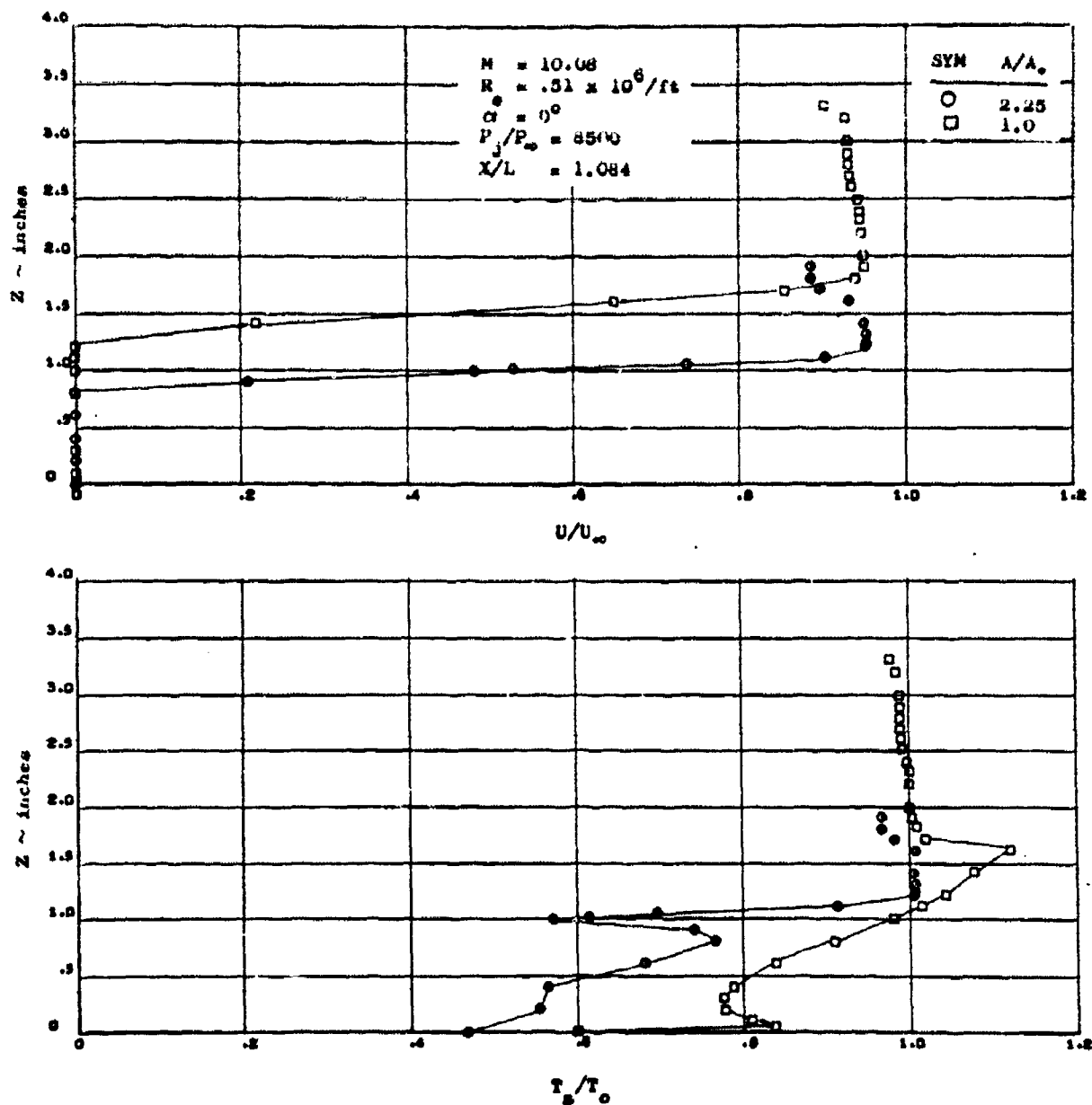


Figure 178b. Expansion Ratio Effect on Flow Surveys at $M = 10$, $X/L = 1.084$

CONFIDENTIAL

CONFIDENTIAL

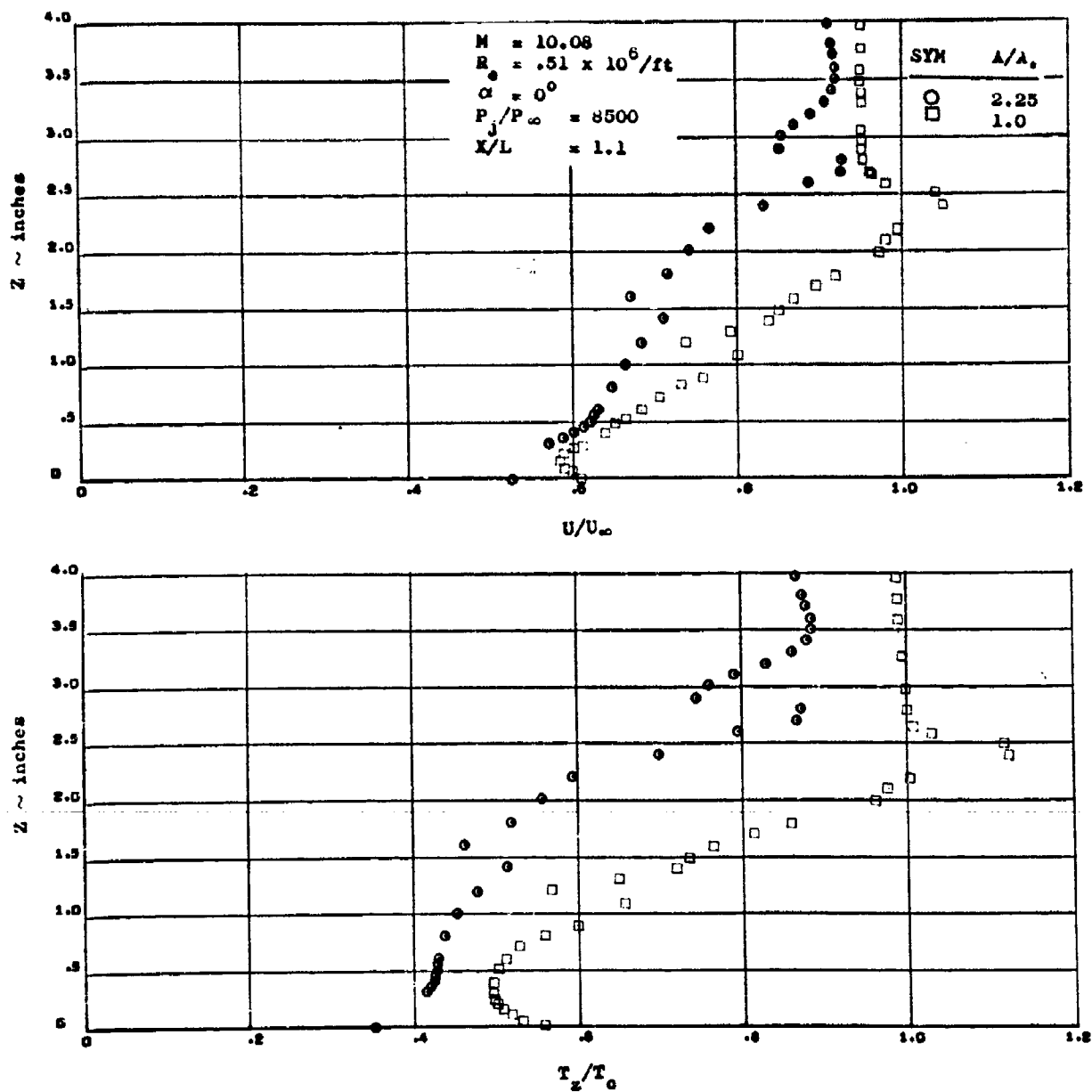
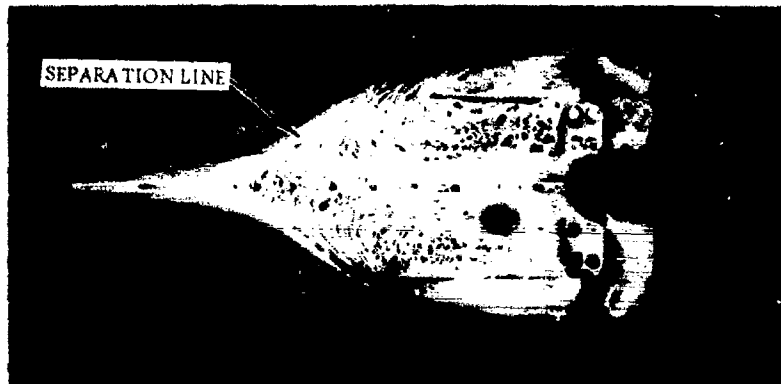


Figure 178c. Expansion Ratio Effect on Flow Surveys at $M = 10$, $X/L = 1.1$

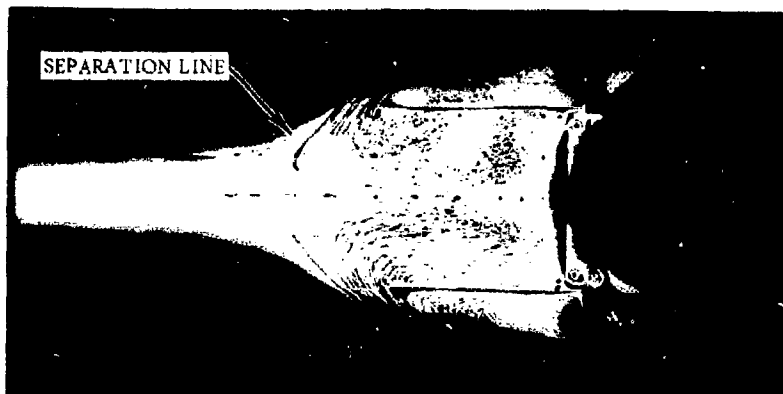
CONFIDENTIAL

CONFIDENTIAL

(This page is Unclassified)



NOZZLE 6
POSITION 1
 $P_j/P_\infty = 17000$



5.3" DISK
AT STATION 22.94

$M = 10.1$
 $Re = 0.5 \times 10^6 / FT$
 $\alpha = 0$ DEGREE

Figure 179. A Comparison of Flow Separation Caused by a Disk
Representing a Plume

246

CONFIDENTIAL

(This page is Unclassified)

CONFIDENTIAL

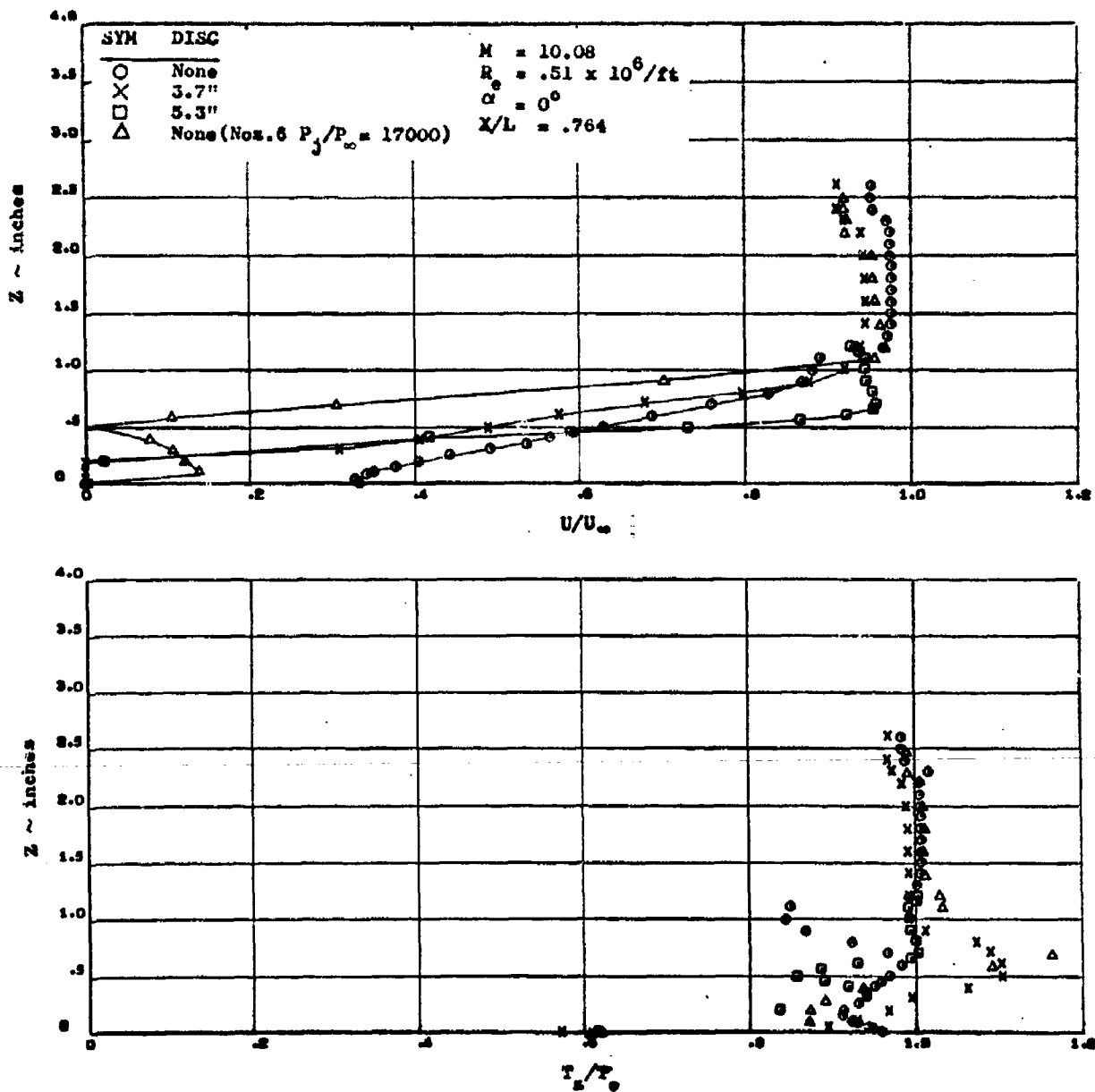


Figure 180. A Comparison of Flow Surveys with a Disc Representing a Plume

CONFIDENTIAL

CONFIDENTIAL

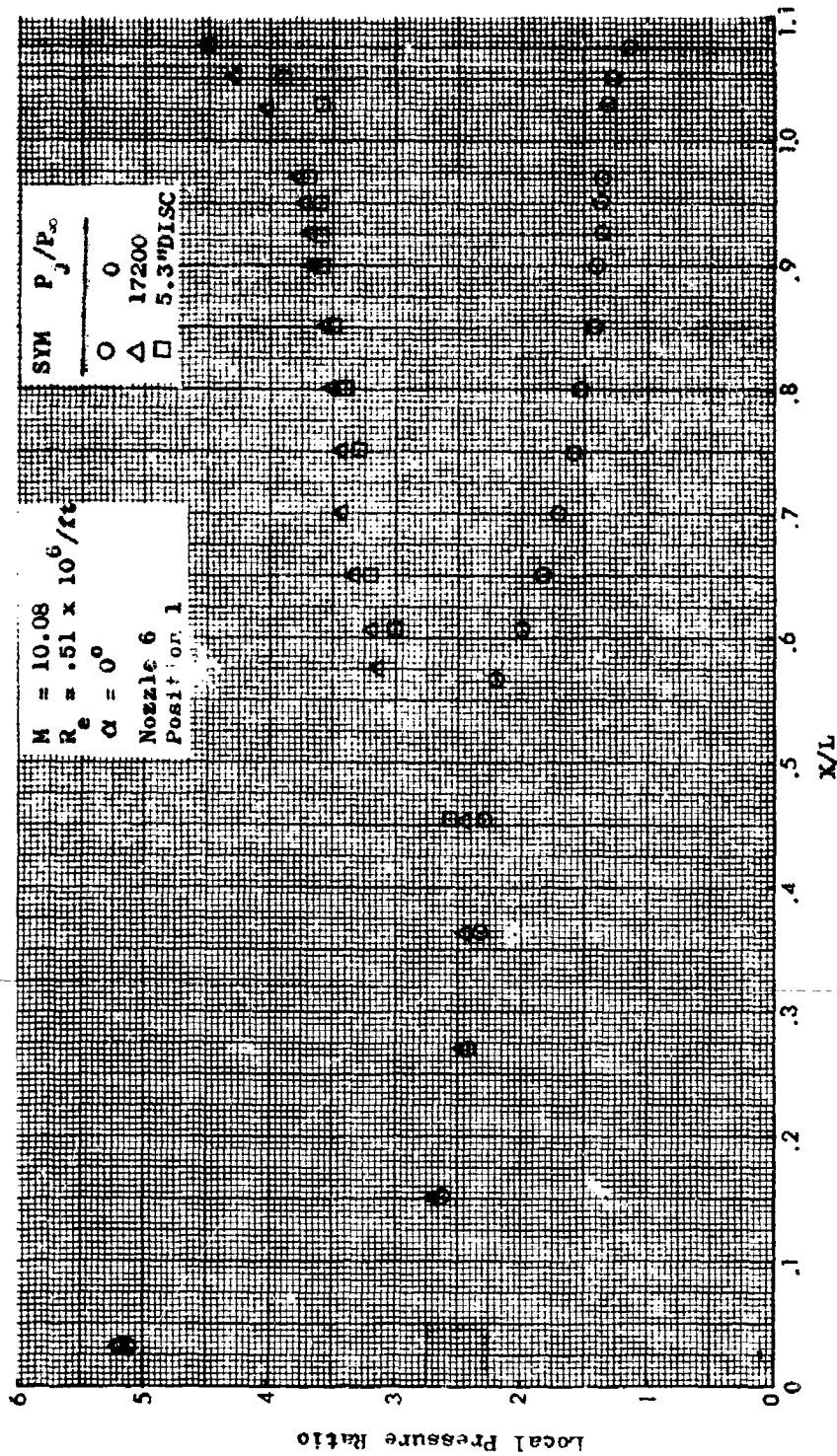


Figure 181. Centerline Pressure Distribution Using Large Disc for Plume Simulation

CONFIDENTIAL

CONFIDENTIAL

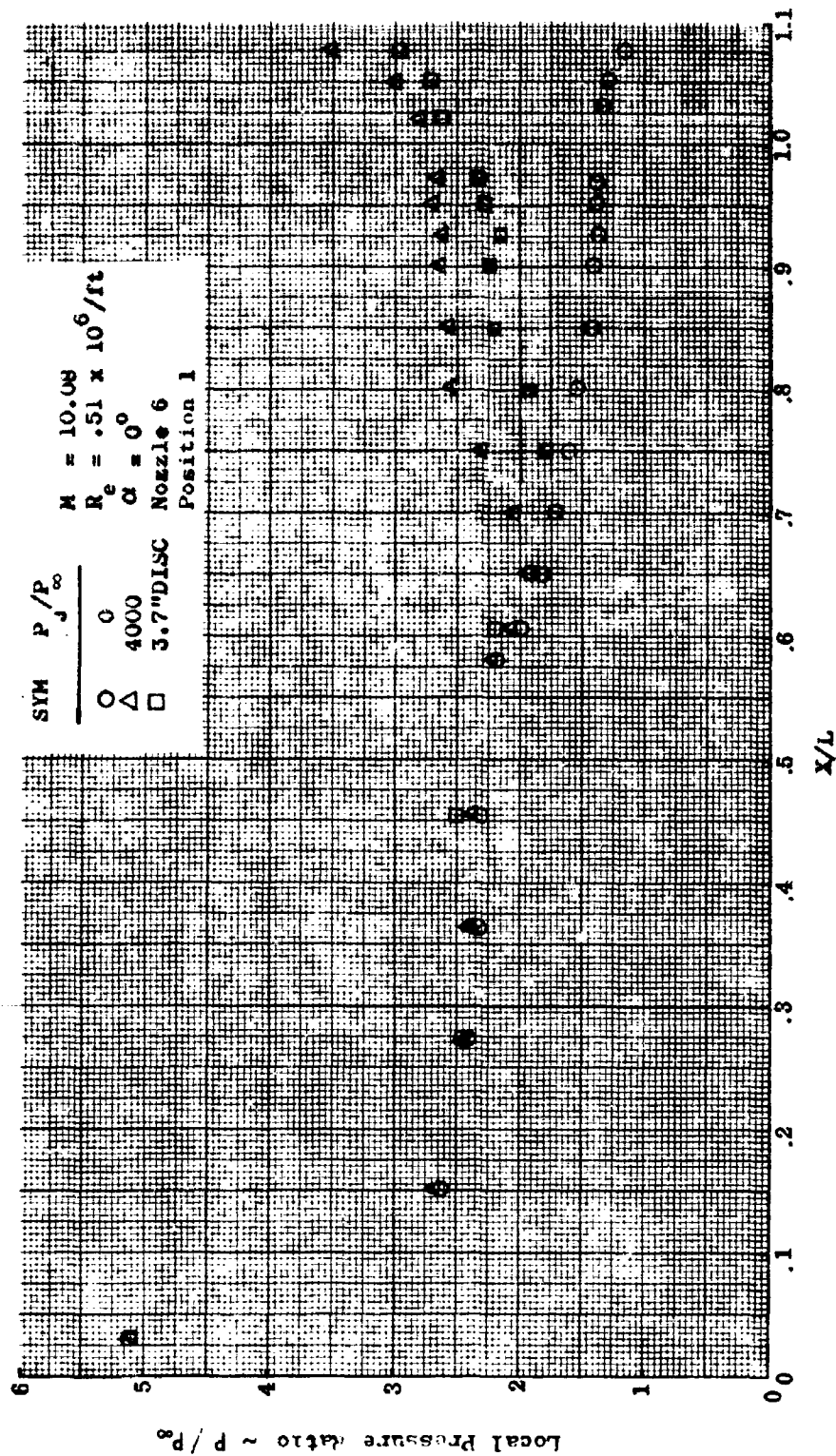


Figure 182. Centerline Pressure Distribution Using Small Disc for Plume Simulation

CONFIDENTIAL

CONFIDENTIAL

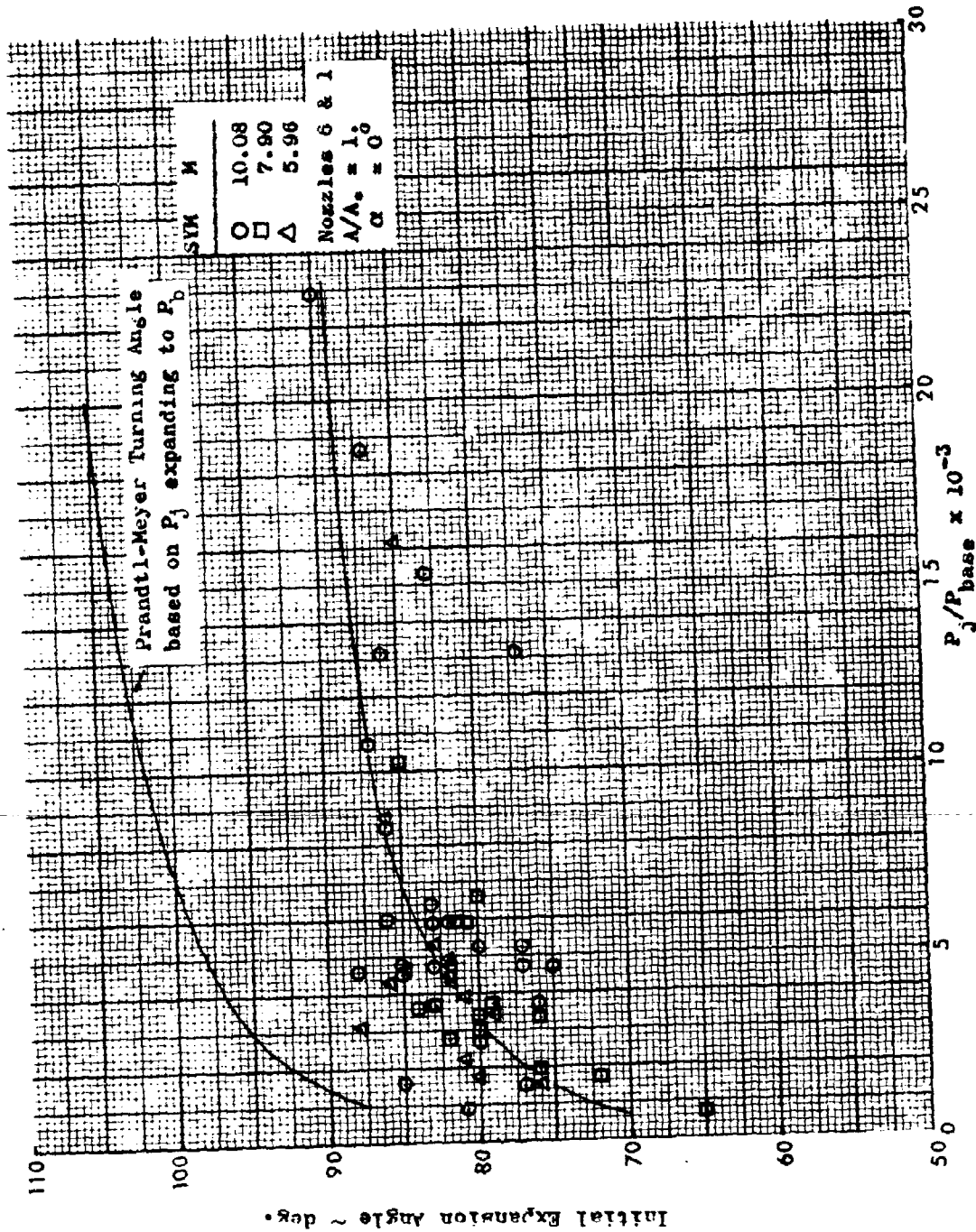


Figure 183. Plume Initial Turning Angle for the Sonic Nozzles

CONFIDENTIAL

CONFIDENTIAL

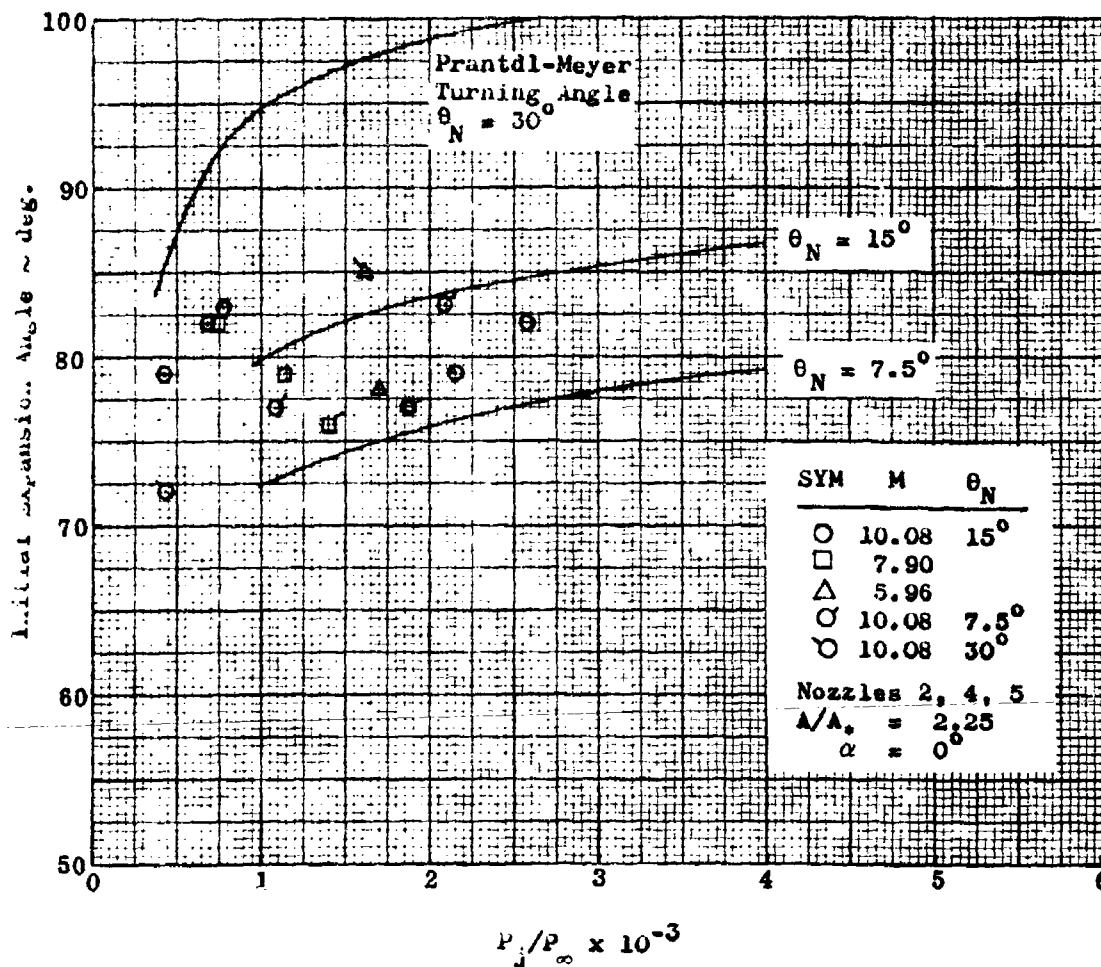


Figure 184. Plume Initial Turning Angle for the $A/A_* = 2.25$ Nozzles

CONFIDENTIAL

CONFIDENTIAL

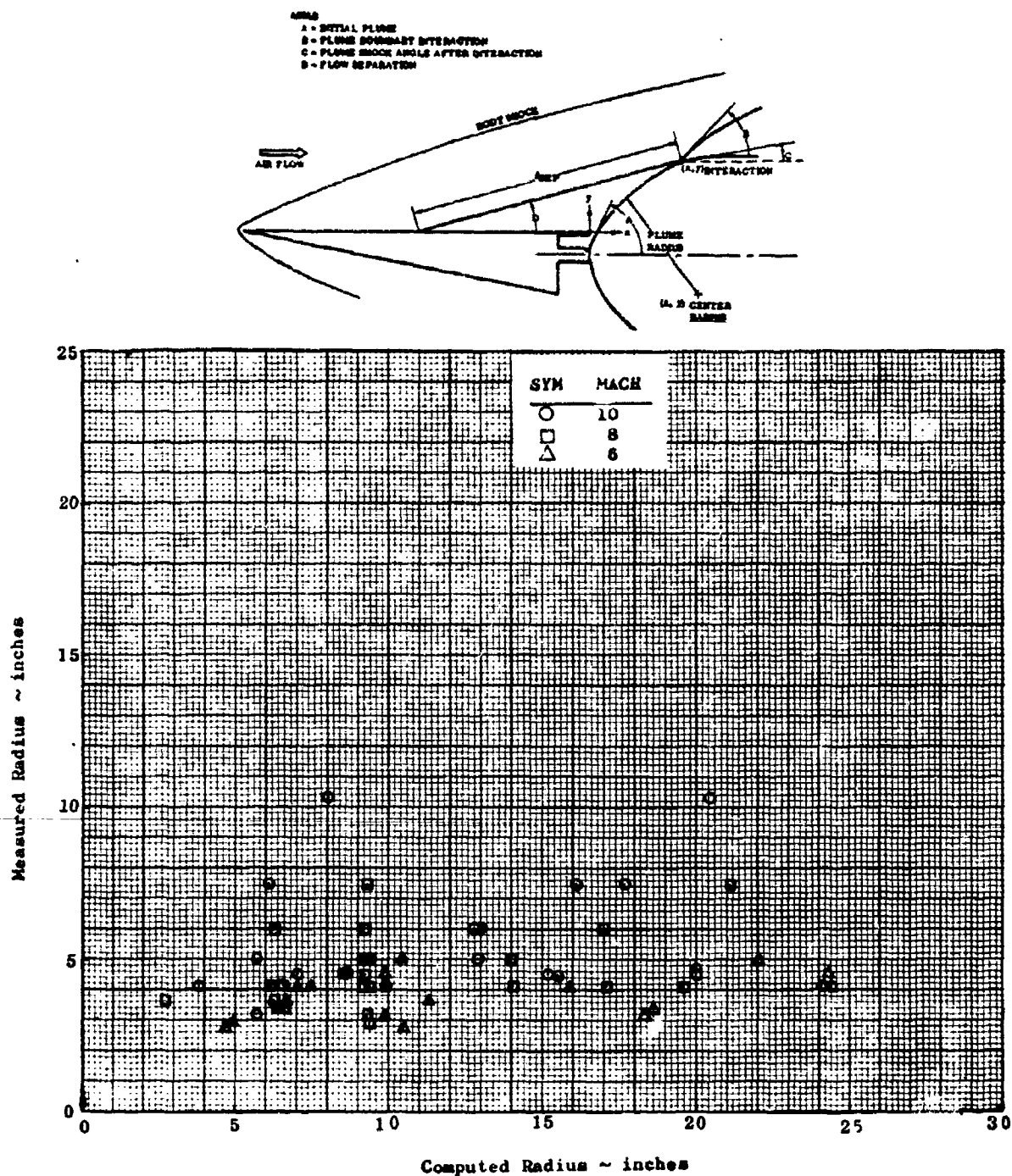


Figure 185. A Comparison of Plume Initial Radii by Mach Number

CONFIDENTIAL

CONFIDENTIAL

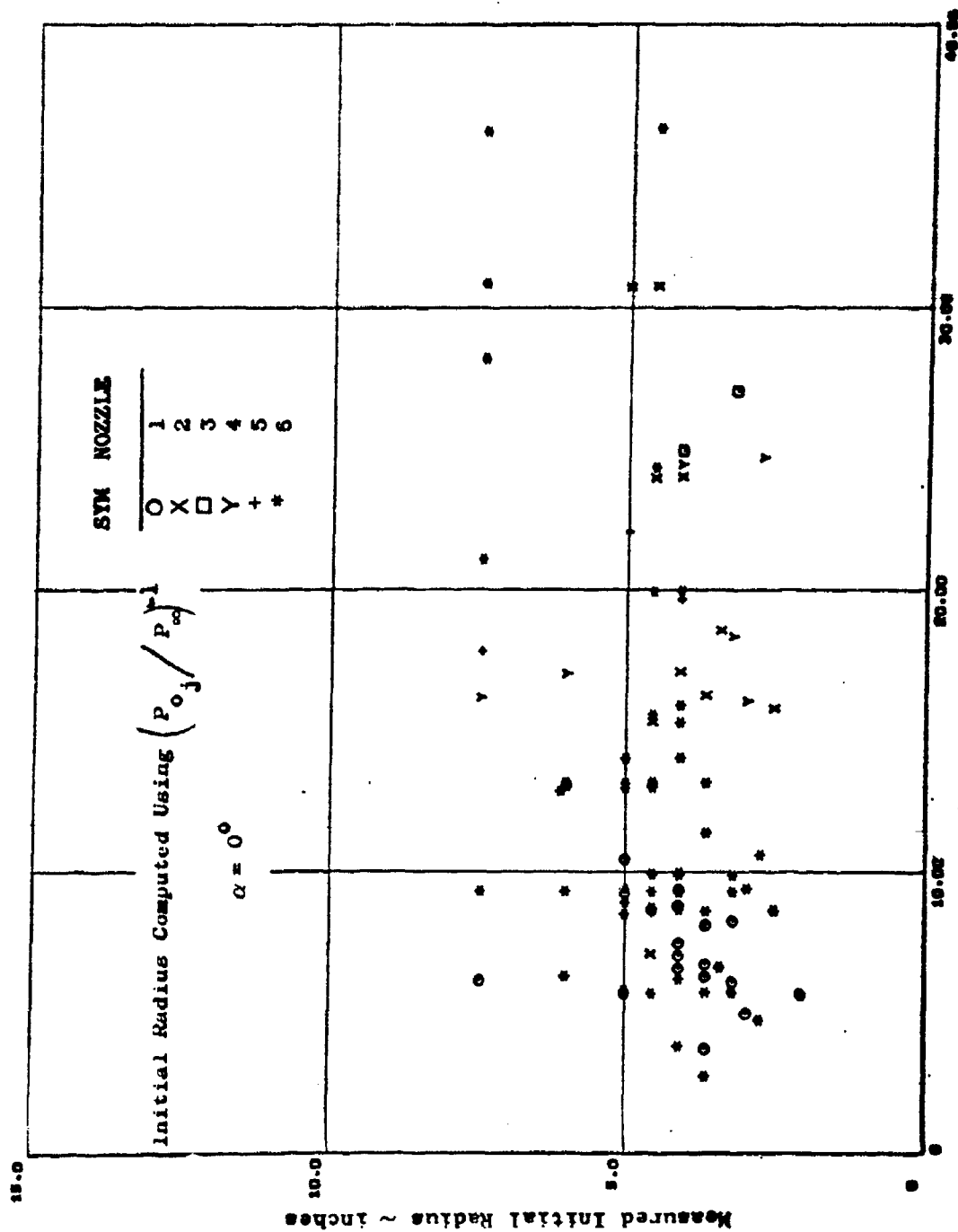


Figure 186. Plume Radius Comparison Based on Jet Pressure Ratioed to Ambient Pressure

CONFIDENTIAL

CONFIDENTIAL

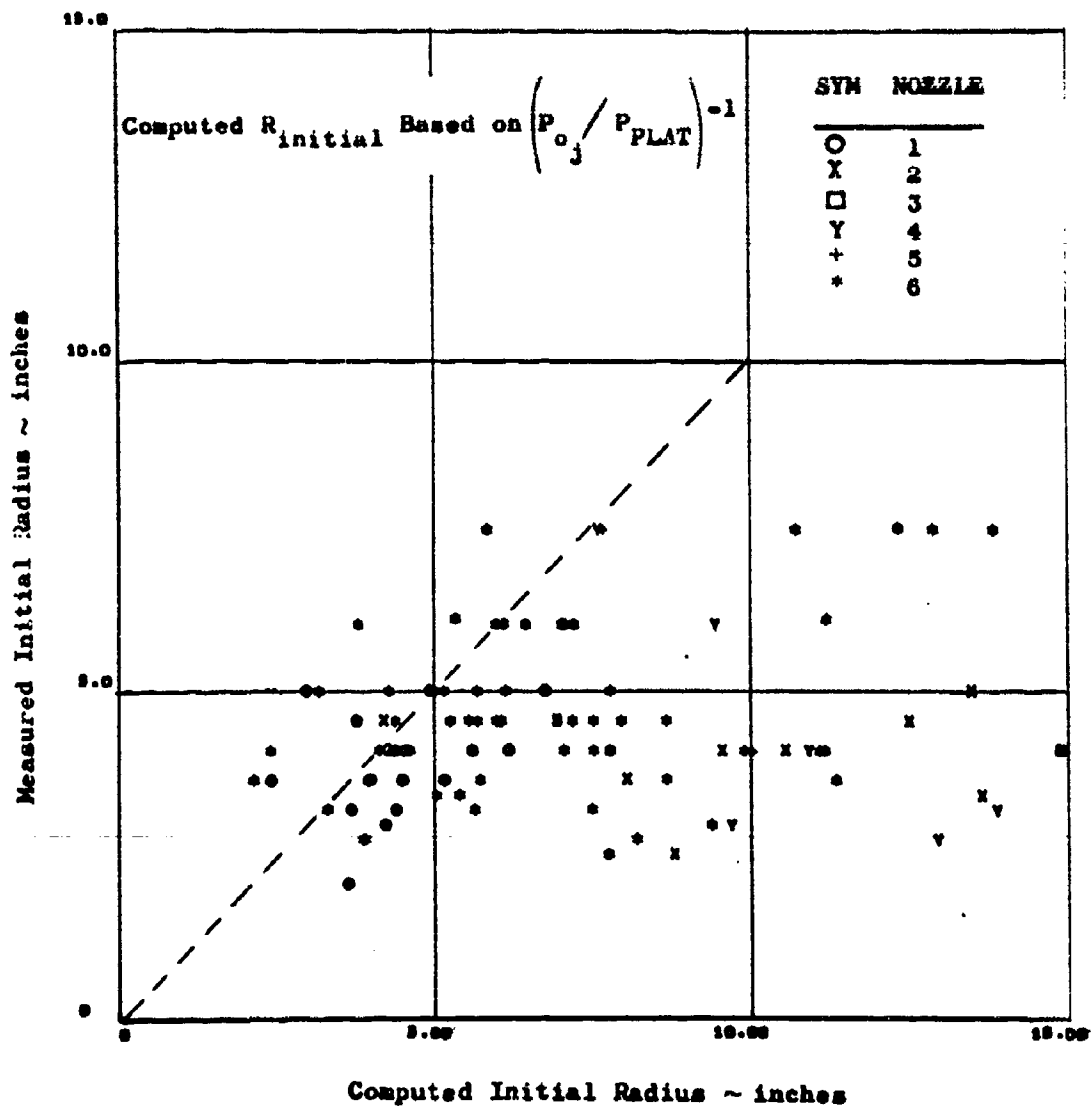


Figure 187. Plume Comparisons Using Plateau Pressure

CONFIDENTIAL

CONFIDENTIAL

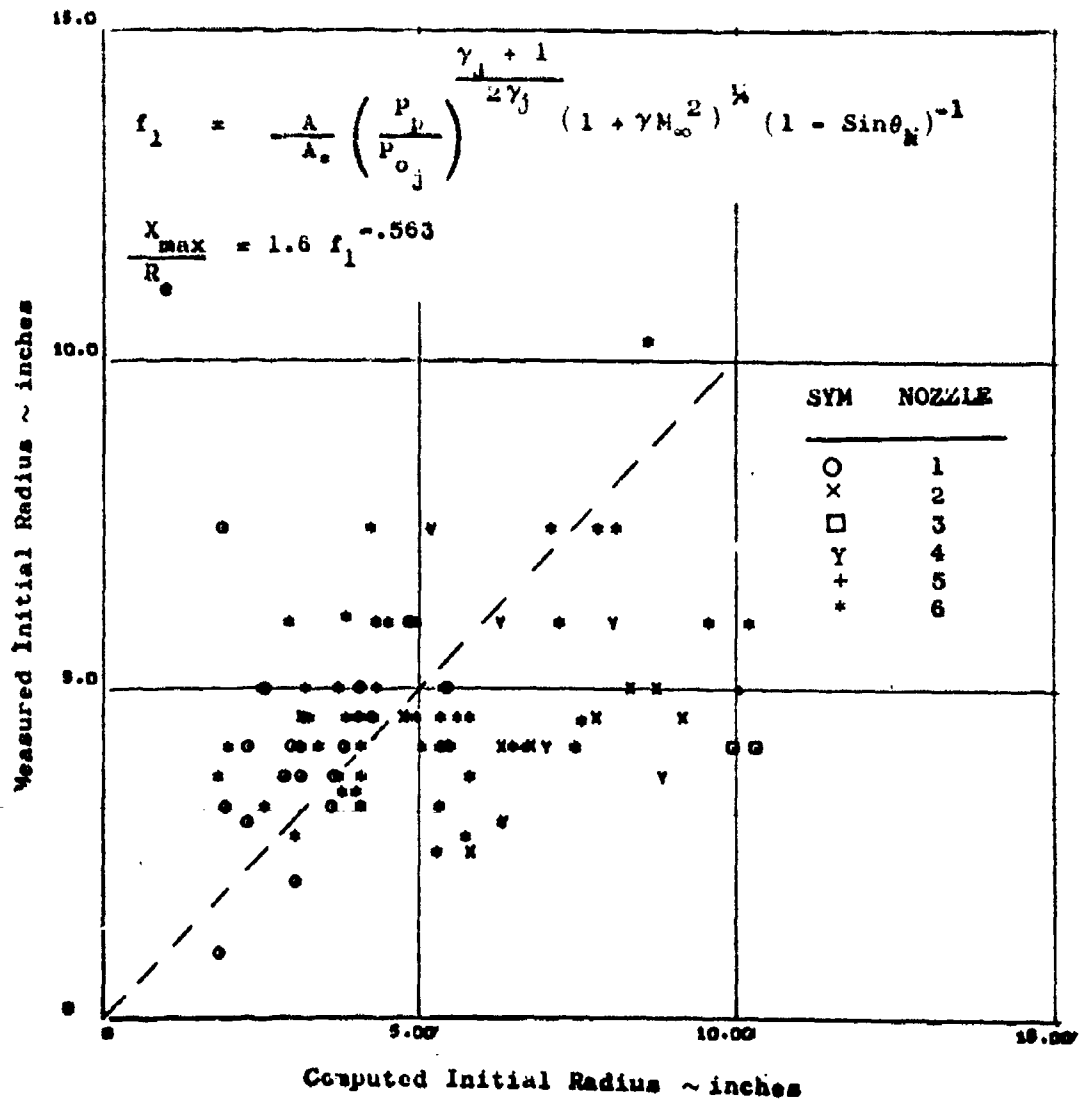


Figure 188a. Plume Comparison Based on Modified Model - Effect of Nozzle

CONFIDENTIAL

CONFIDENTIAL

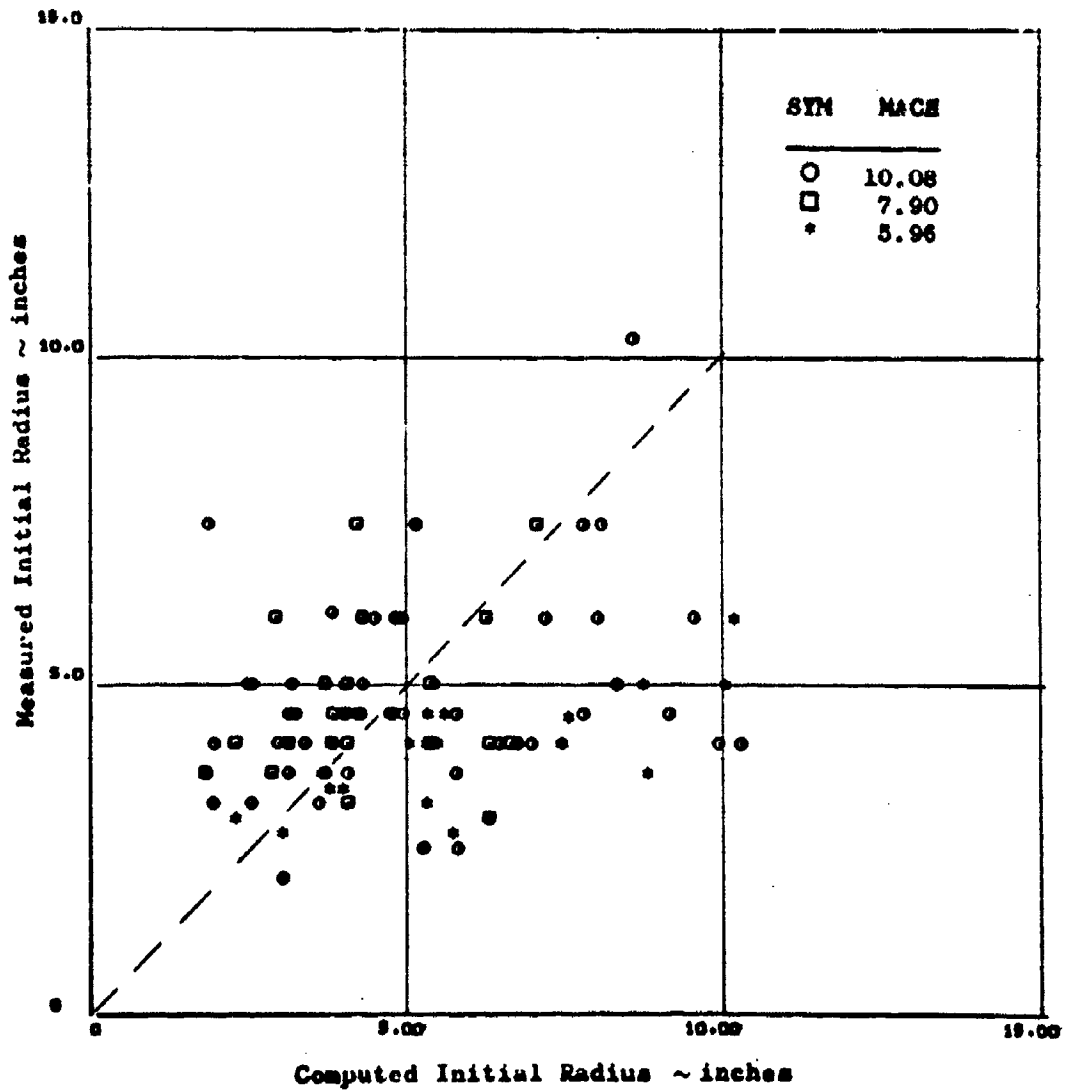


Figure 188b. Plume Comparison Based on Modified Model - Effect of Mach

256
CONFIDENTIAL

CONFIDENTIAL

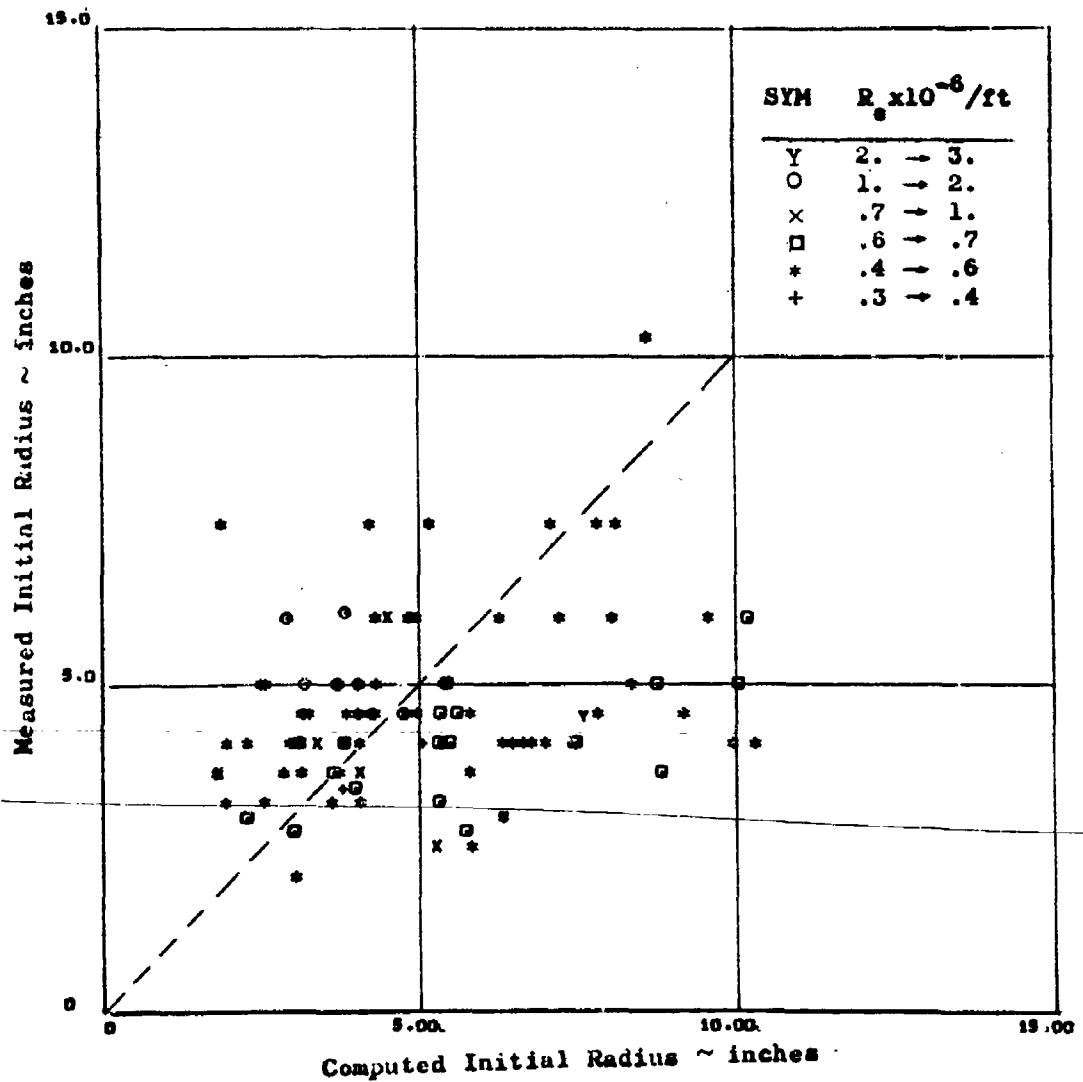


Figure 188c. Plume Comparison Based on Modified Model -
Effect of Reynolds Number

CONFIDENTIAL

CONFIDENTIAL

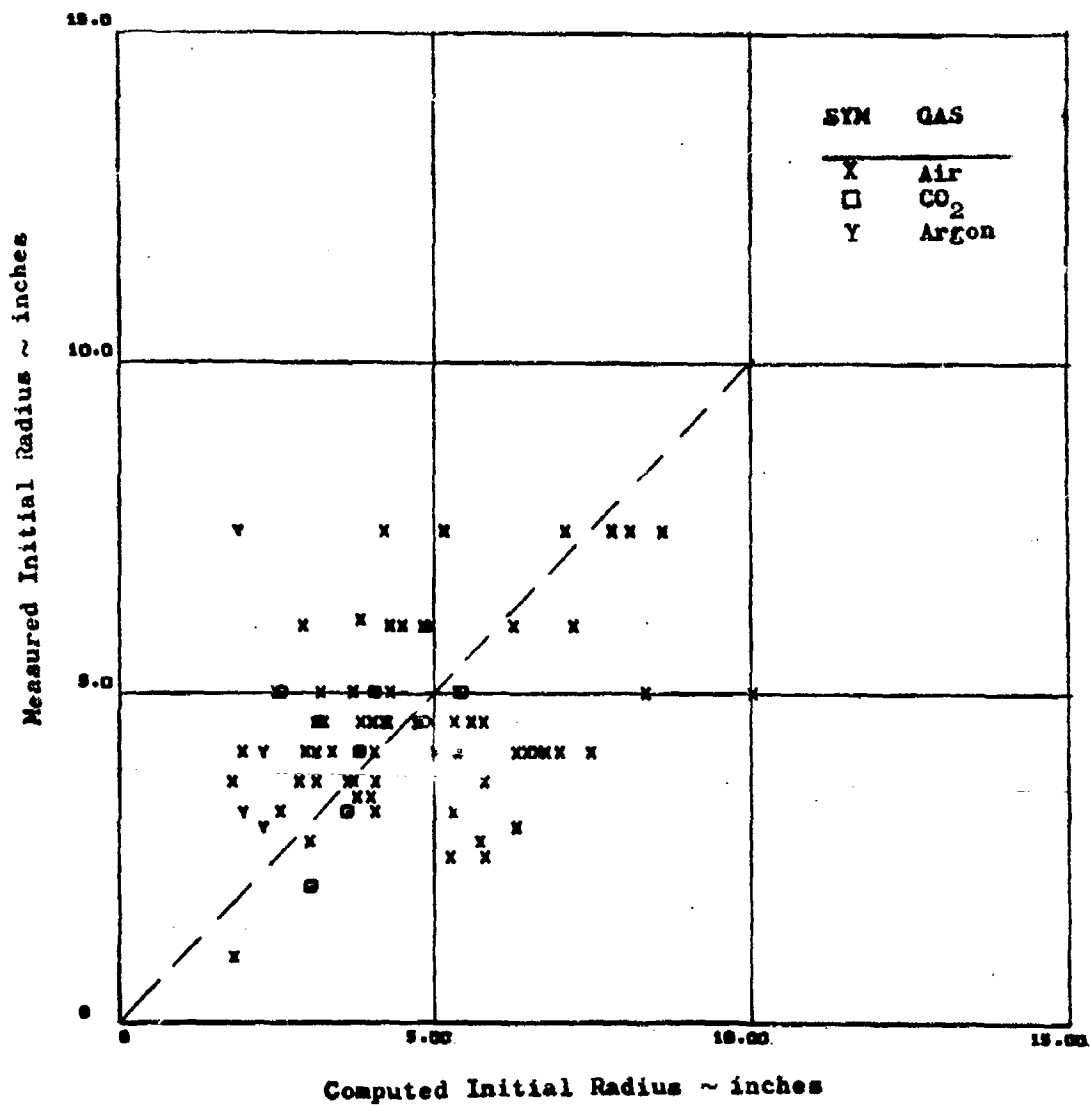


Figure 188d. Plume Comparison Based on Modified Model -
Effect of Exhaust Gas

CONFIDENTIAL

CONFIDENTIAL

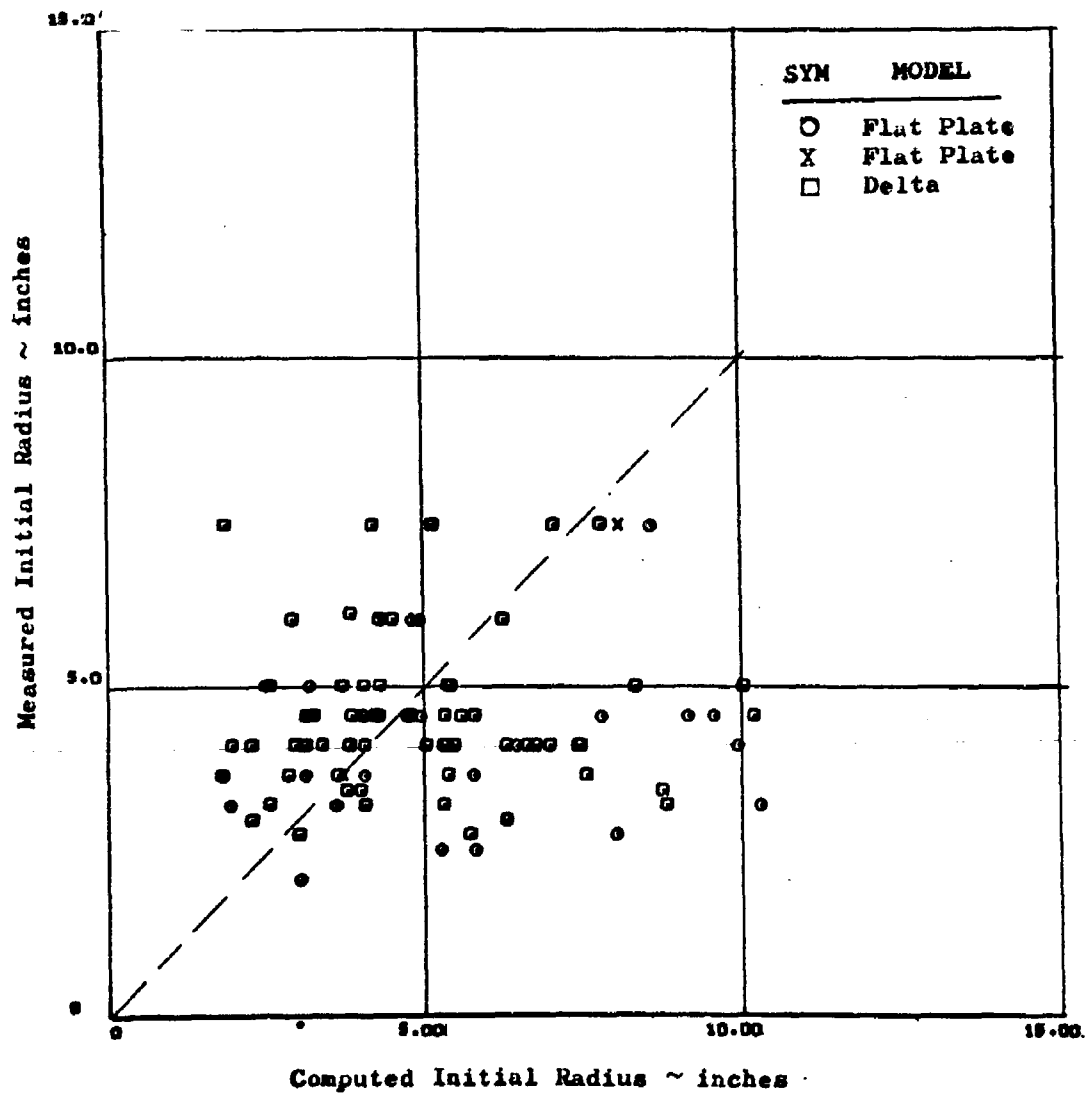


Figure 188e. Plume Comparison Based on Modified Model -
Effect of Model Geometry

CONFIDENTIAL

CONFIDENTIAL

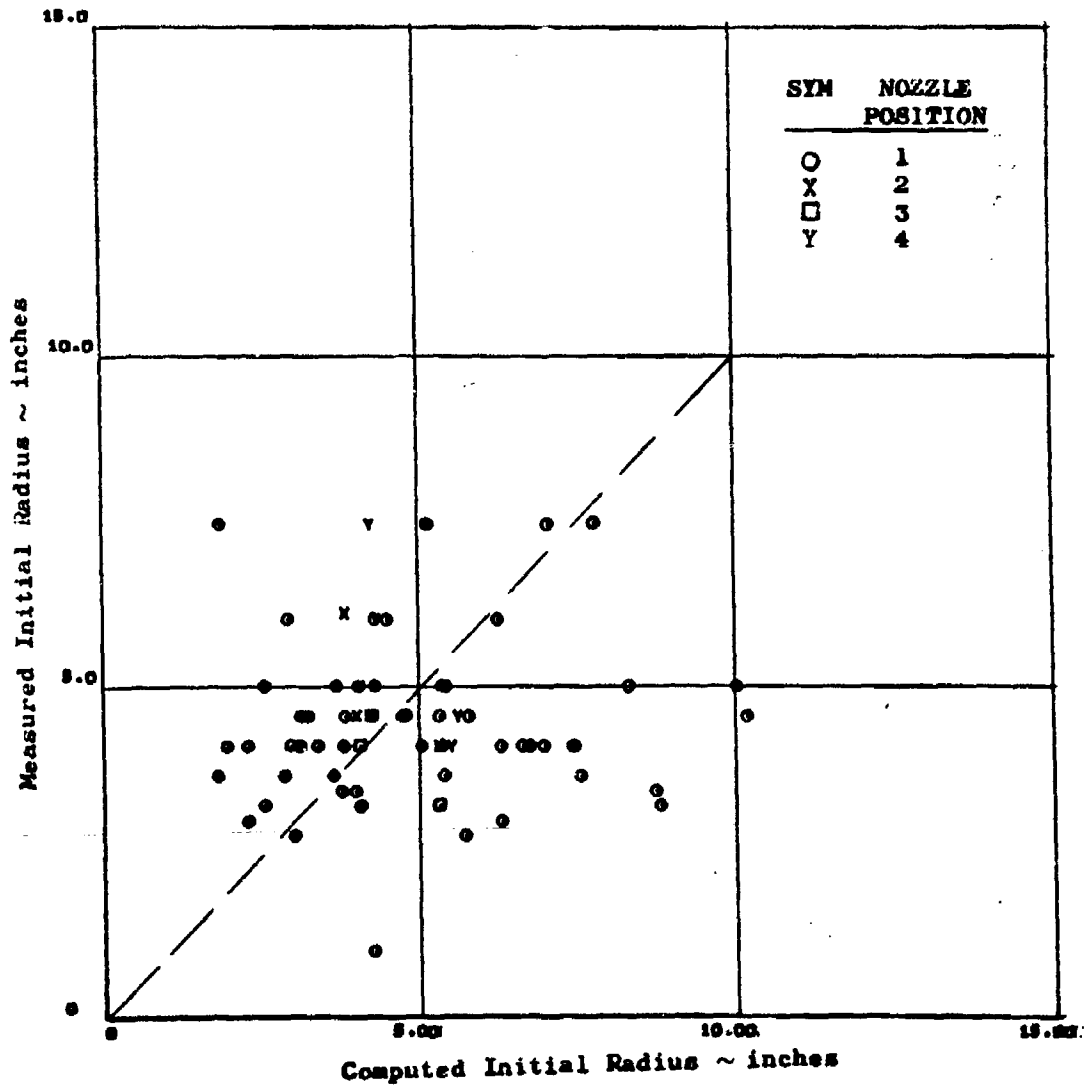


Figure 188f. Plume Comparison Based on Modified Model -
Effect of Nozzle Position

CONFIDENTIAL

CONFIDENTIAL

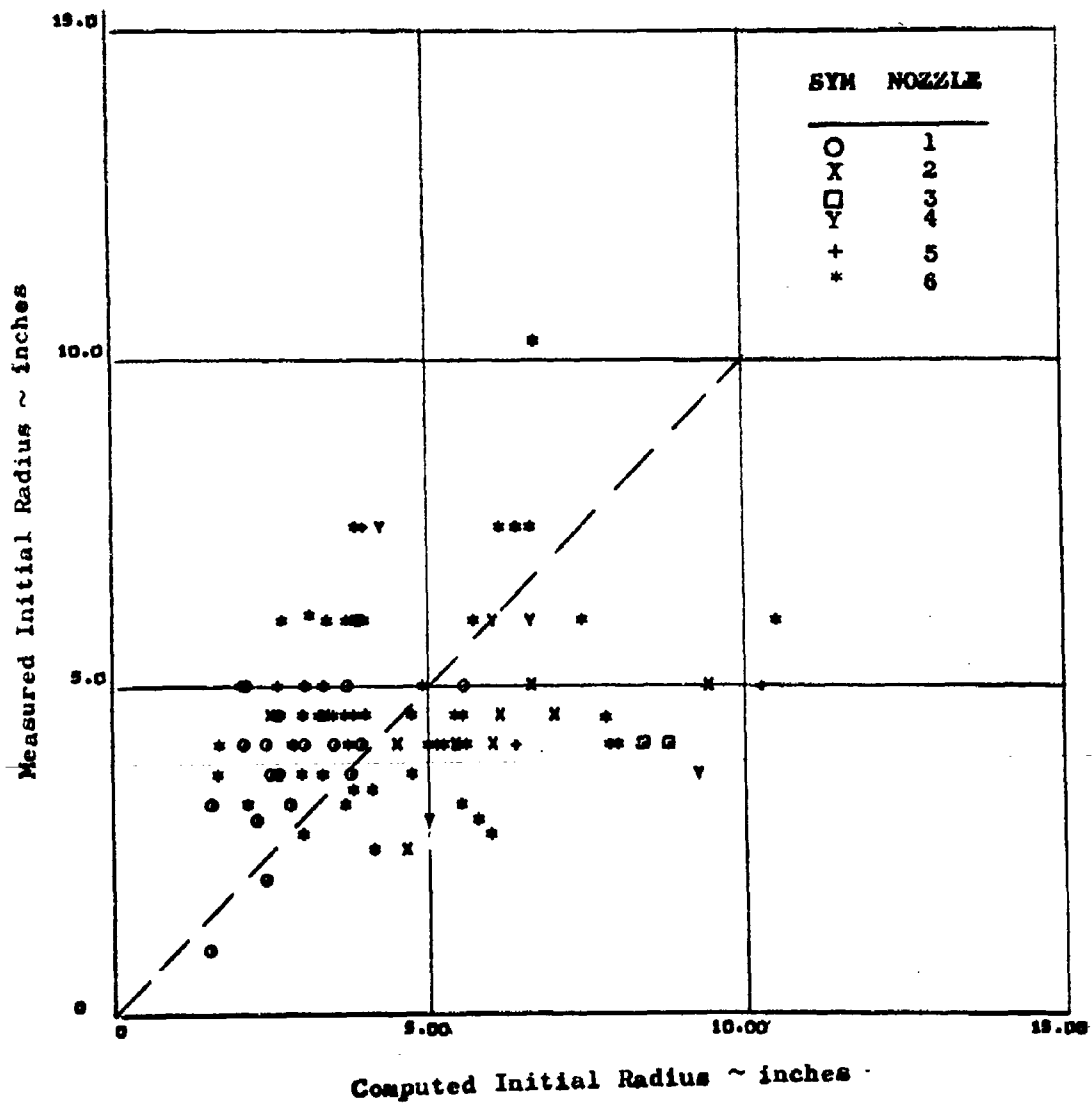


Figure 189a. Plume Comparison with Total Temperature Ratio Correction - Effect of Nozzle

CONFIDENTIAL

CONFIDENTIAL

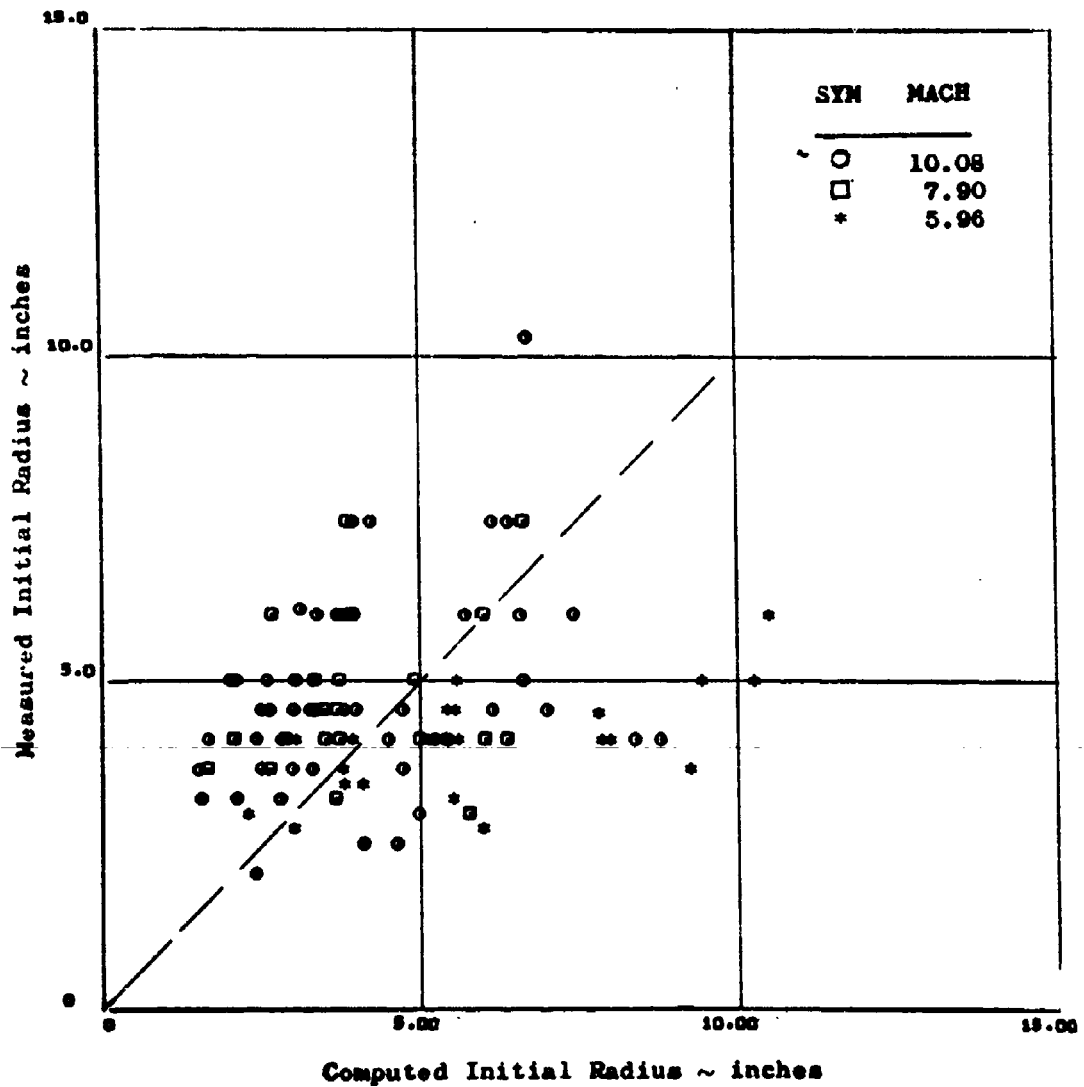


Figure 189b. Plume Comparison with Total Temperature Ratio Correction - Effect of Mach Number

CONFIDENTIAL

CONFIDENTIAL

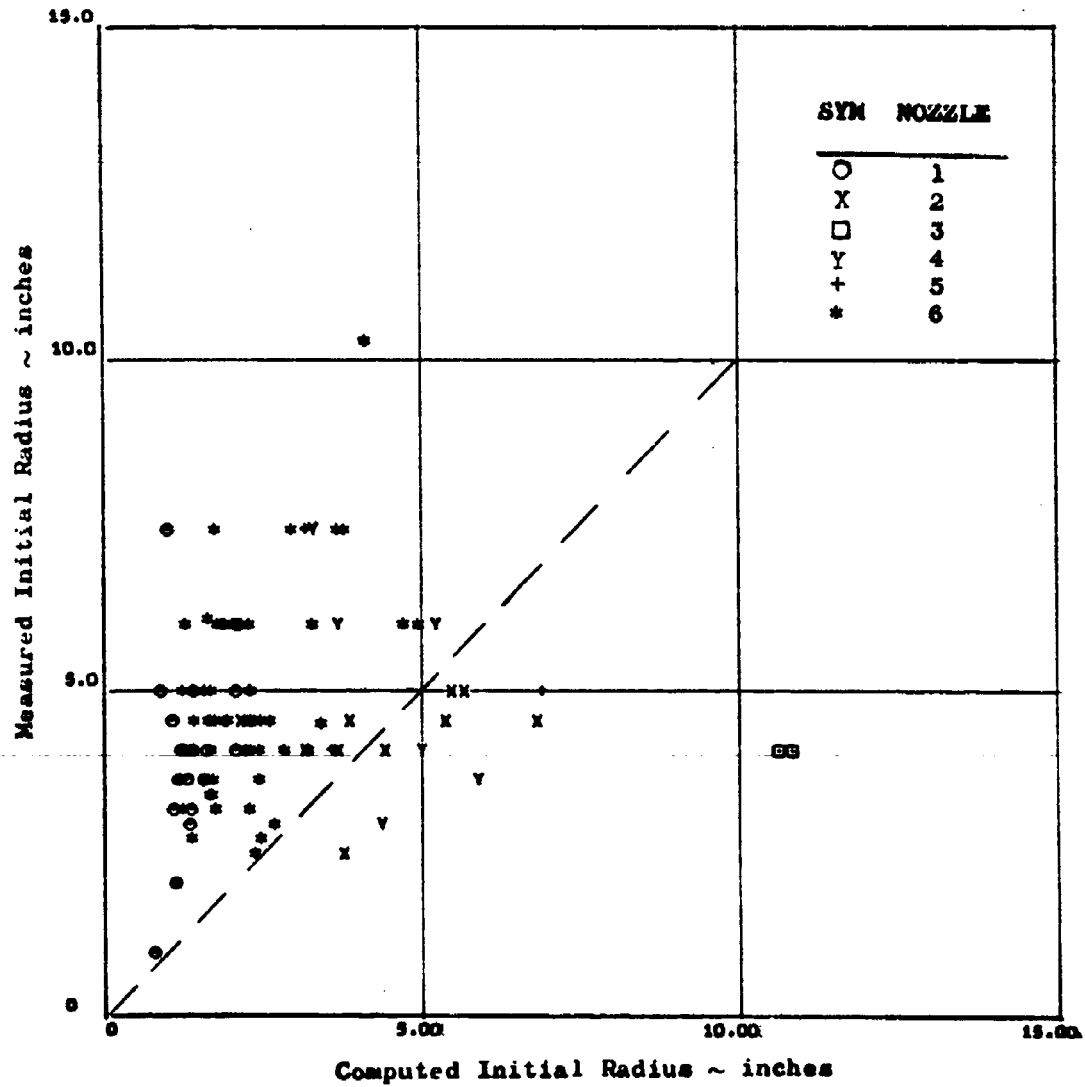


Figure 190. A Comparison of Plume Shapes with Ambient Temperature Ratio Correction

CONFIDENTIAL

CONFIDENTIAL

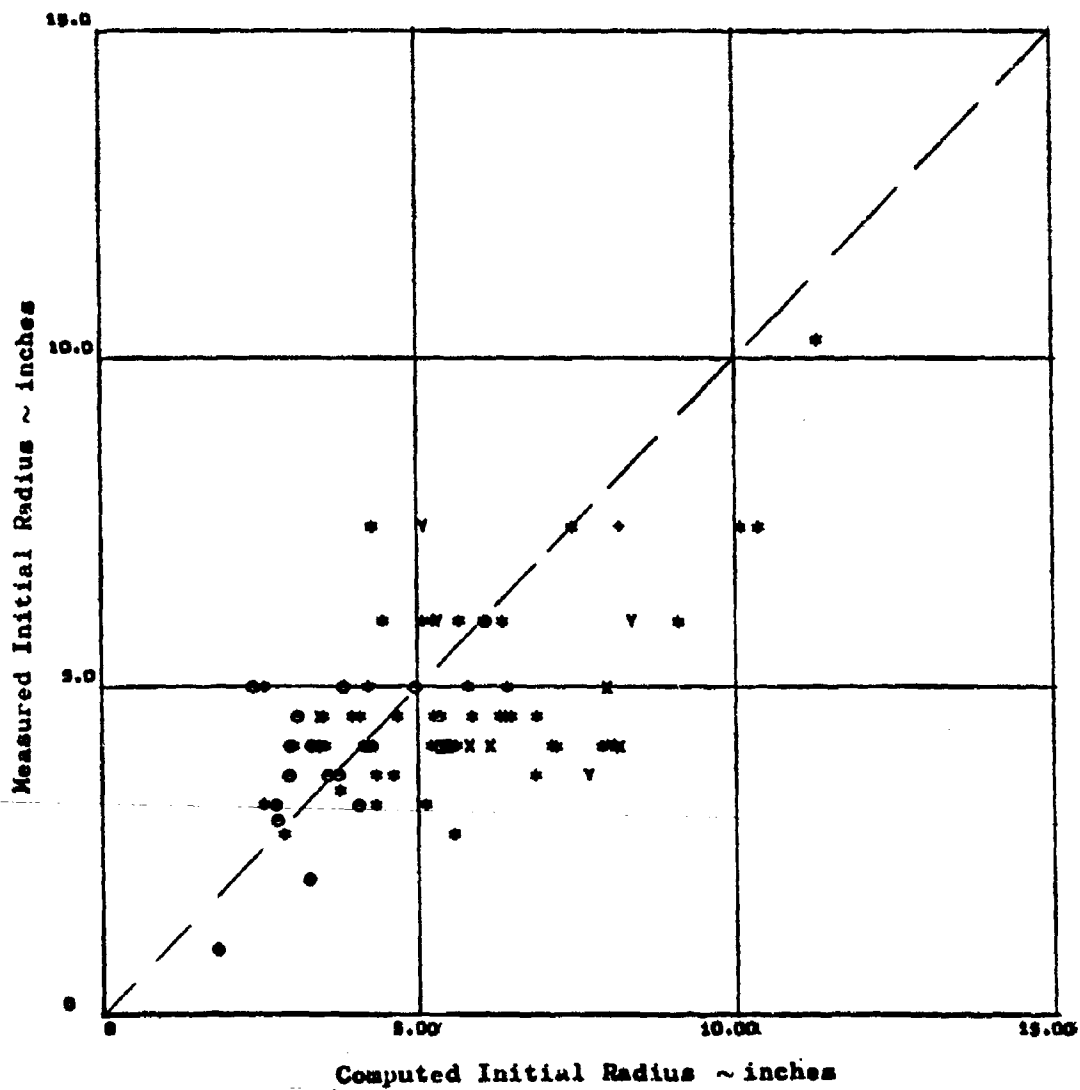
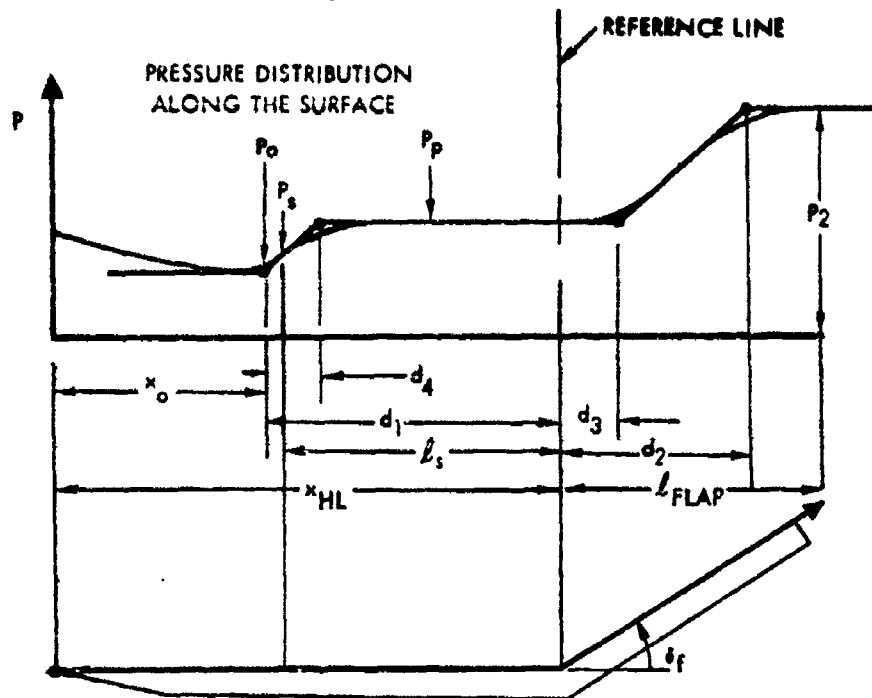


Figure 191. A Comparison of Plume Shape with Expansion Ratio and Mach Corrections

CONFIDENTIAL

UNCLASSIFIED



From AFFDL-TR-66-85

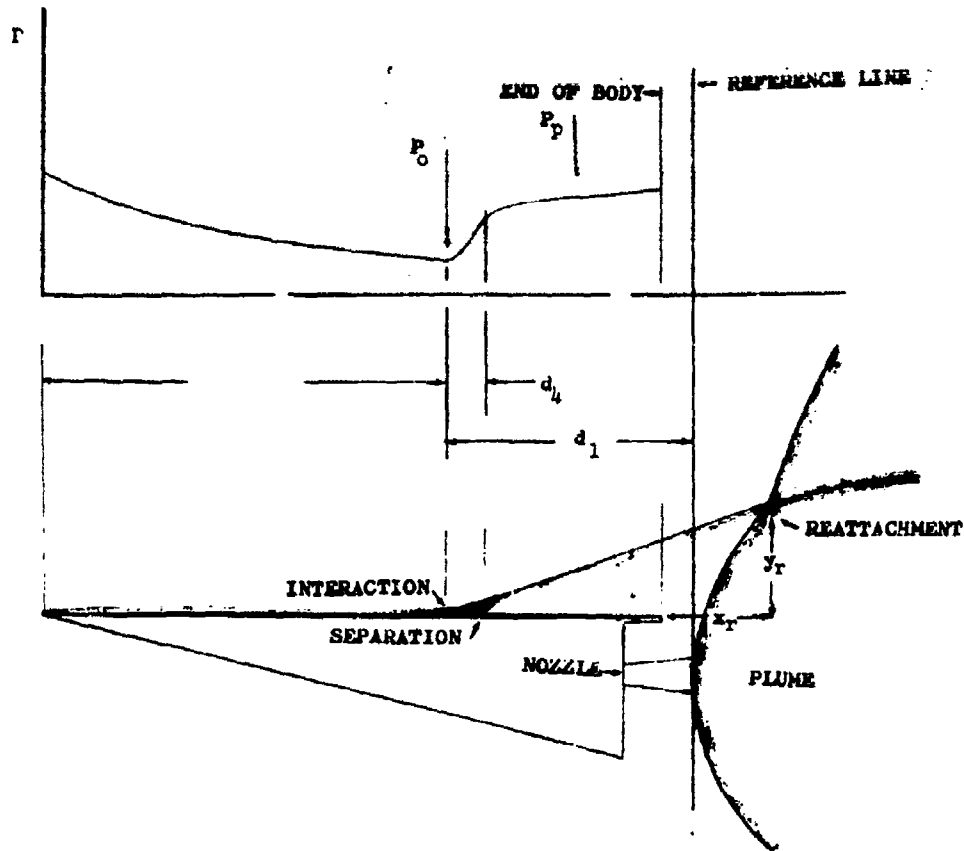
- P = Pressure
- P_0 = Pressure at Upstream Interaction Point
- P_s = Pressure at Separation
- P_p = Plateau Pressure
- P_2 = Reattachment Pressure
- d_1 = Upstream Interaction Distance
- d_2 = Downstream Interaction Distance to Peak Pressure
- d_3 = Downstream Interaction Distance to Pressure Rise
- d_4 = Free Interaction Length
- l_s = Separation Length
- l_{FLAP} = Flap Length
- x_0 = Interaction Location
- x_{HL} = Hinge Line Location
- δ_f = Flap Angle

(a) Control Surface Separation

Figure 192. Definition of Interaction Parameters for Separated Flow

UNCLASSIFIED

UNCLASSIFIED



(b) Plume Induced Separation

Figure 192. Definition of Interaction Parameters for Separated Flow

UNCLASSIFIED

CONFIDENTIAL

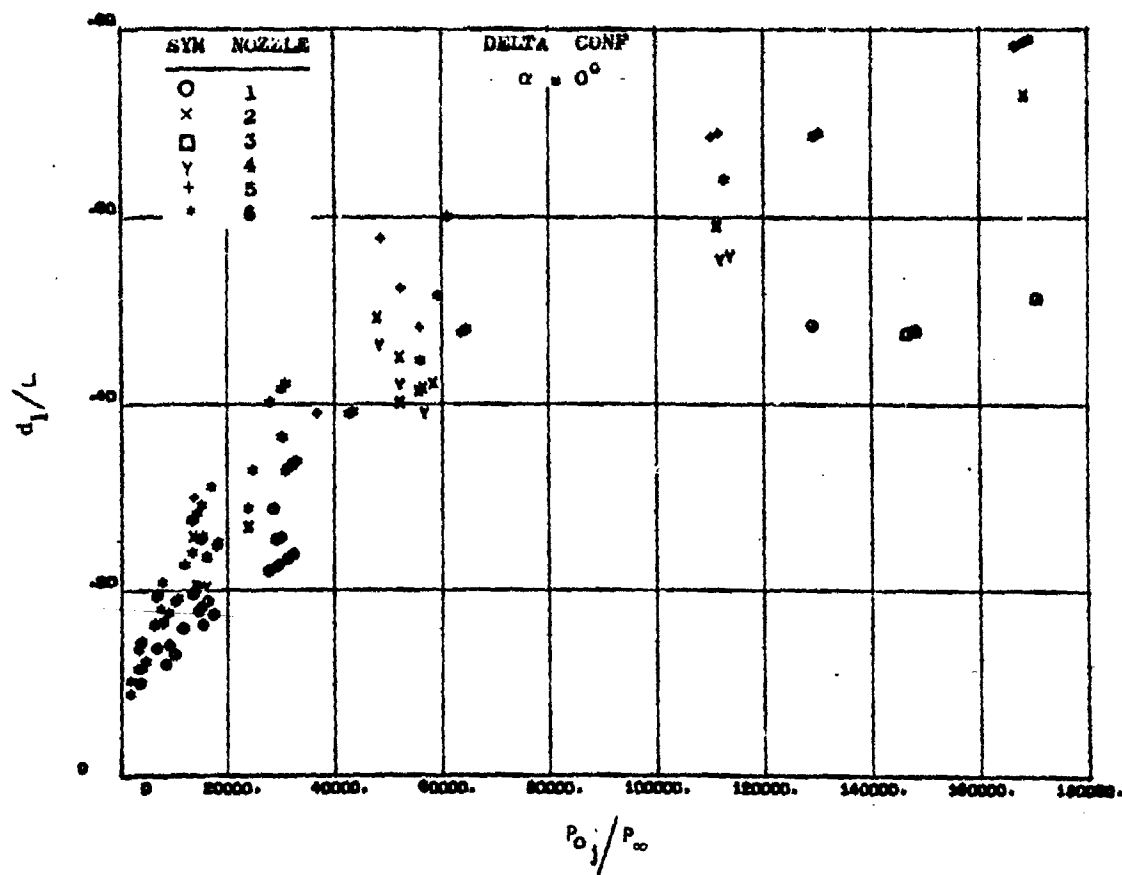


Figure 193. Upstream Interaction Length as a Function of Nozzle Total Pressure Ratio.

CONFIDENTIAL

CONFIDENTIAL

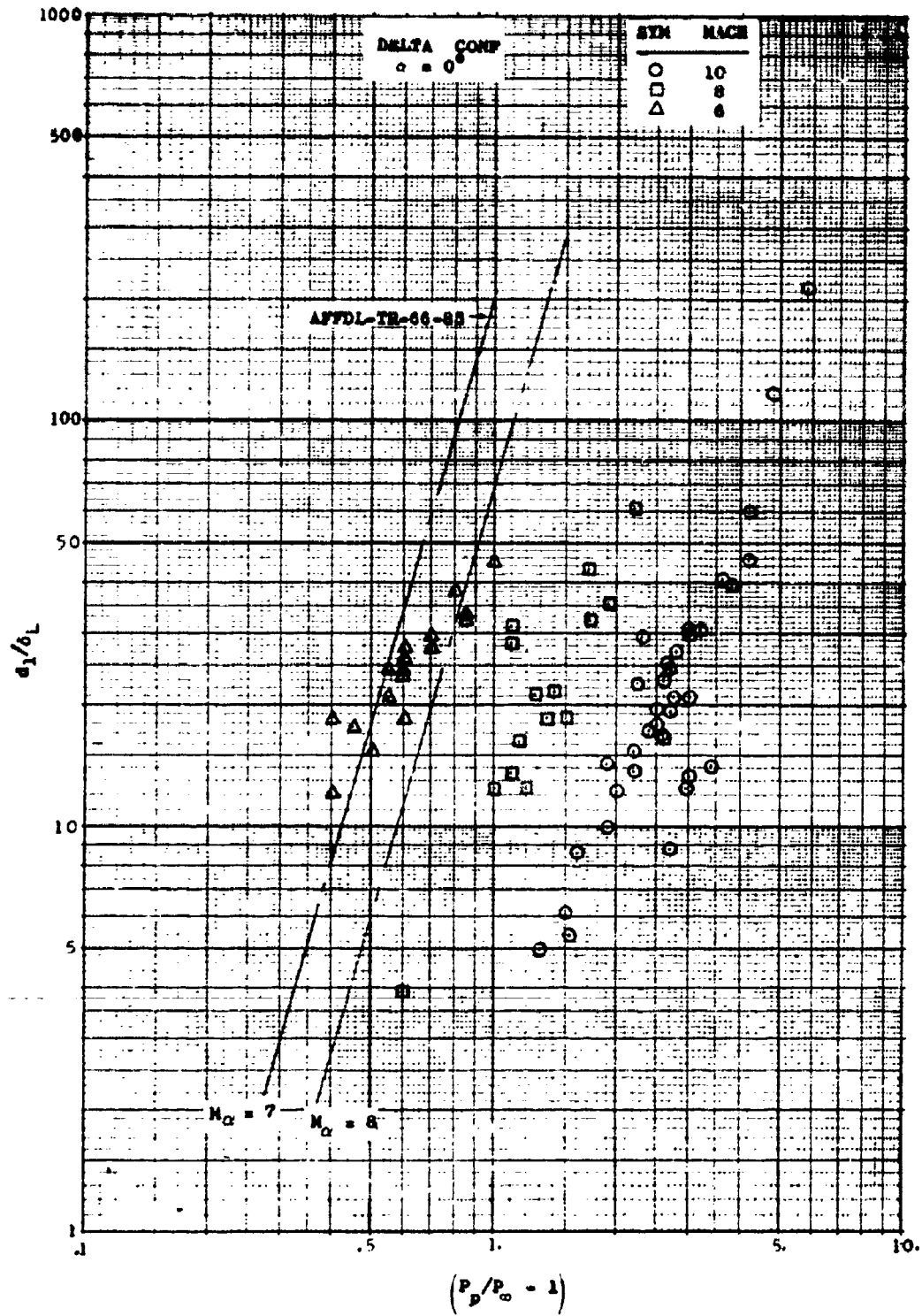


Figure 194. A Comparison of Upstream Interaction Length with Laminar Control Separation Correlations.

268

CONFIDENTIAL

CONFIDENTIAL

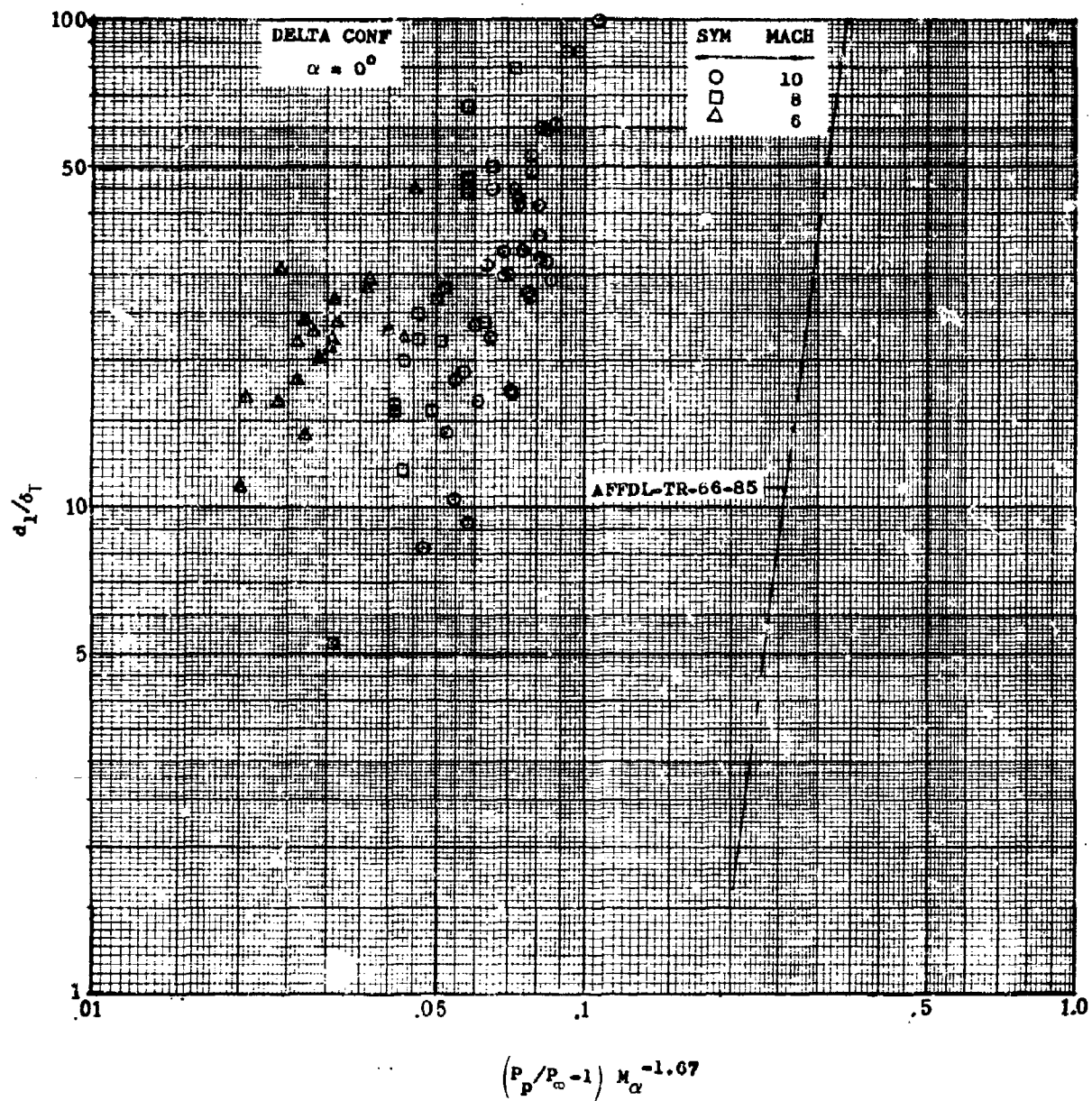


Figure 195. A Comparison of Upstream Interaction Length with a Turbulent Control Separation Correlation.

CONFIDENTIAL

CONFIDENTIAL

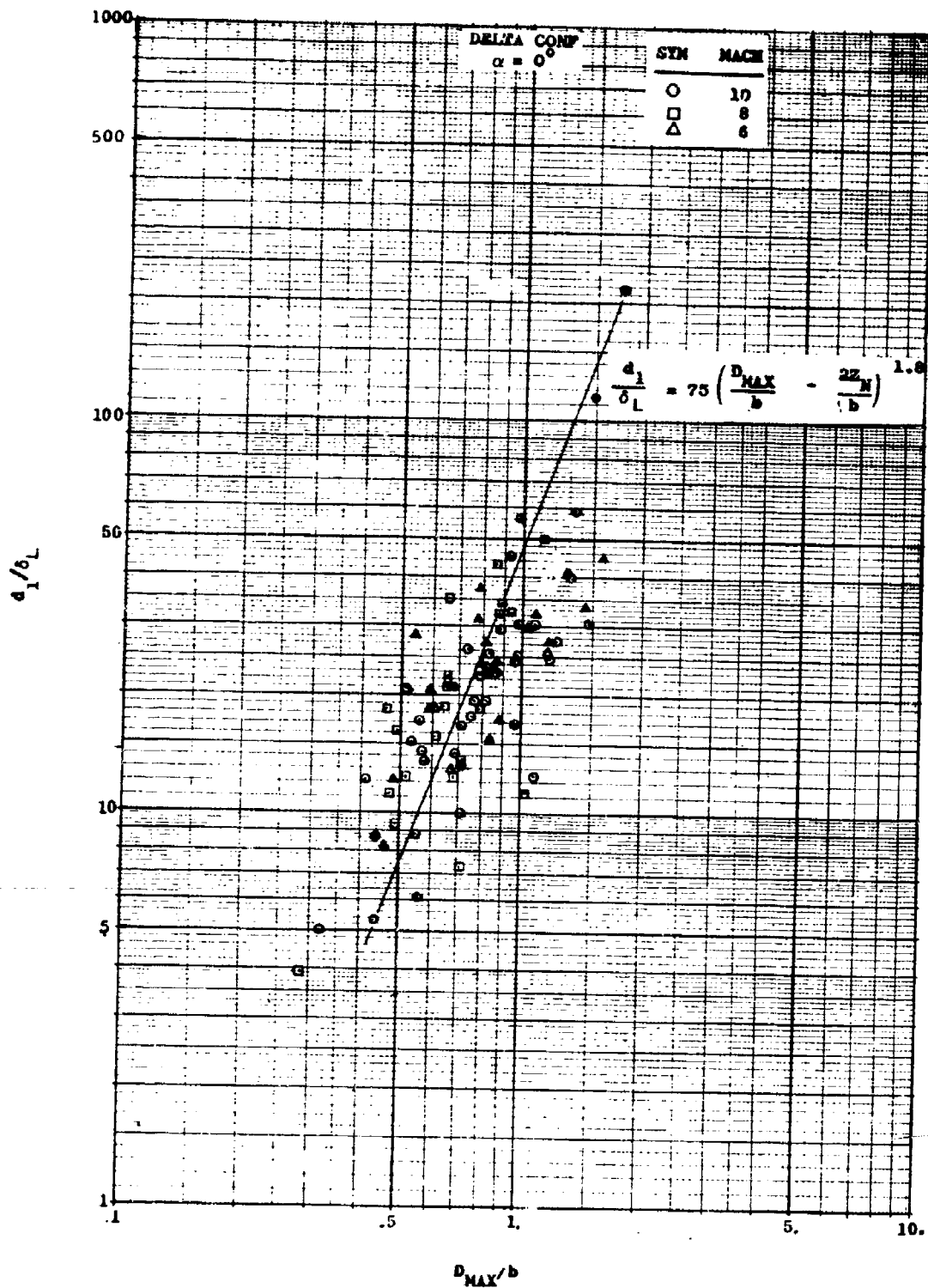


Figure 196. A Correlation of Upstream Interaction Length Based on a Laminar Boundary Layer.

270

CONFIDENTIAL

CONFIDENTIAL

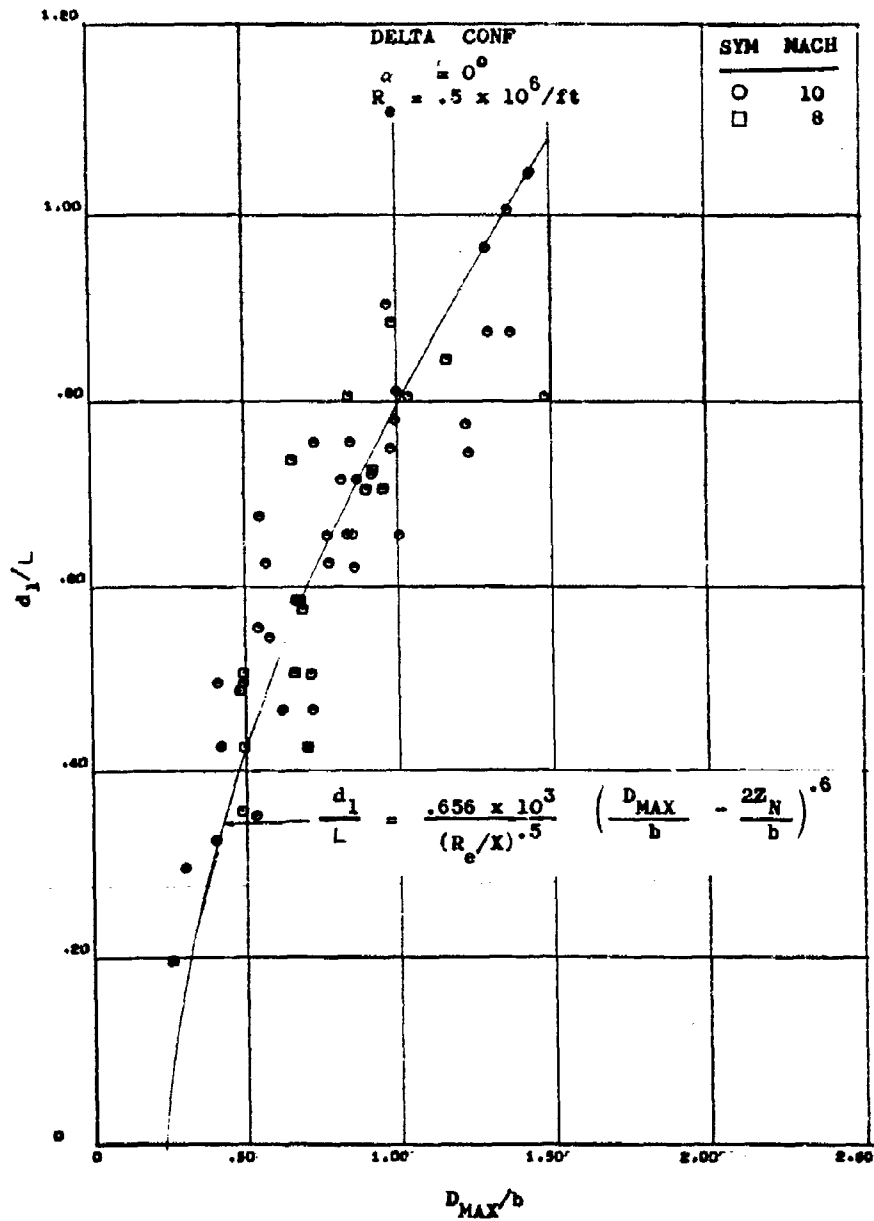


Figure 197. Upstream Interaction Length at $\alpha = 0$ and $R_e = 0.5 \times 10^6 / \text{ft}$.
 271

CONFIDENTIAL

CONFIDENTIAL

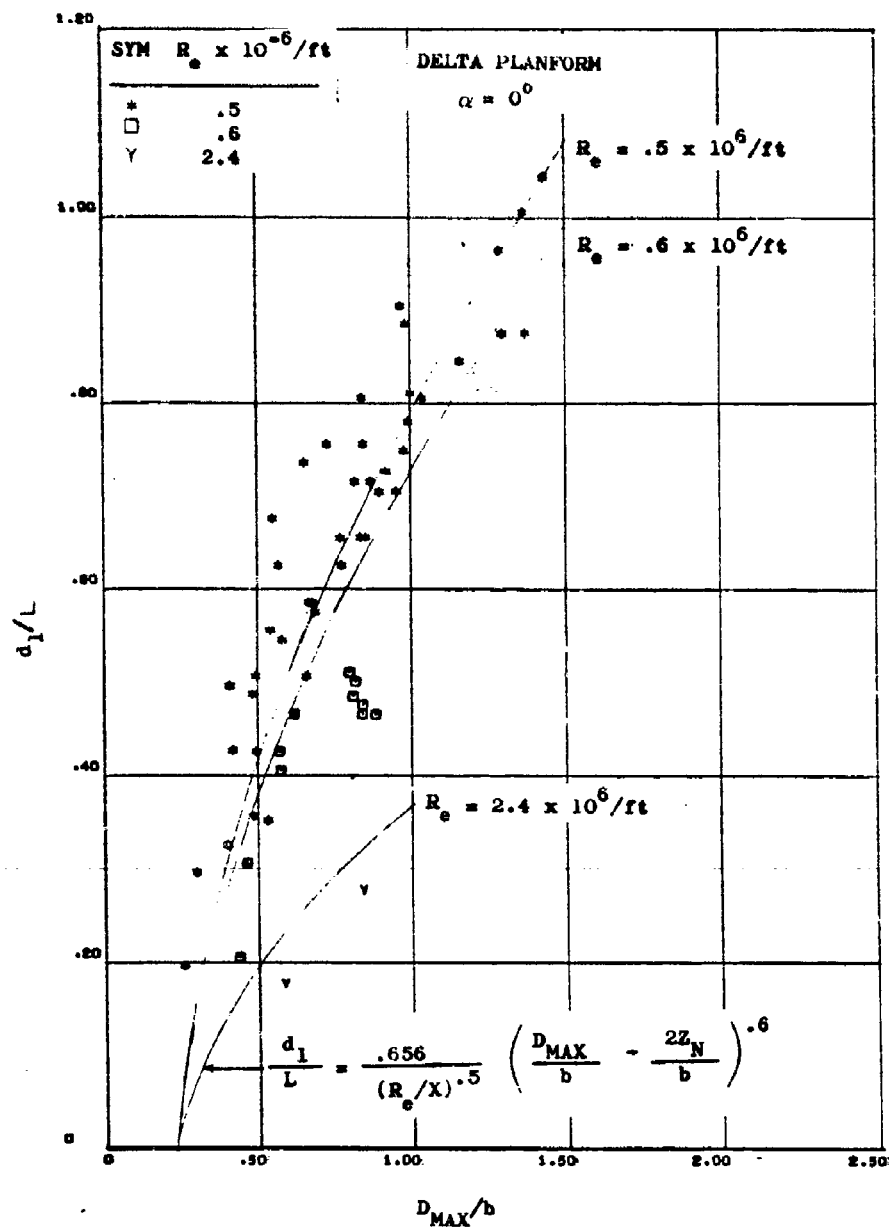


Figure 198. Upstream Interaction Length Correlations with Reynolds Number.

CONFIDENTIAL

CONFIDENTIAL

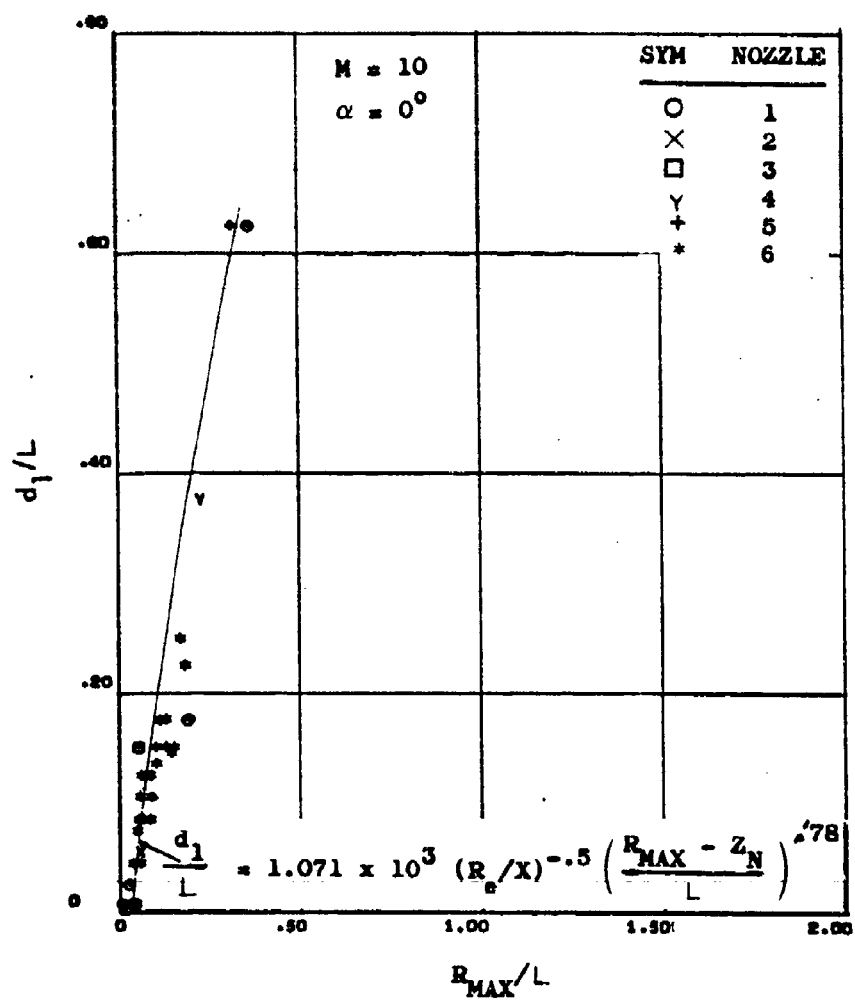


Figure 199. Flat Plate Upstream Interaction Length
at $\alpha = 0^\circ$.

CONFIDENTIAL

CONFIDENTIAL

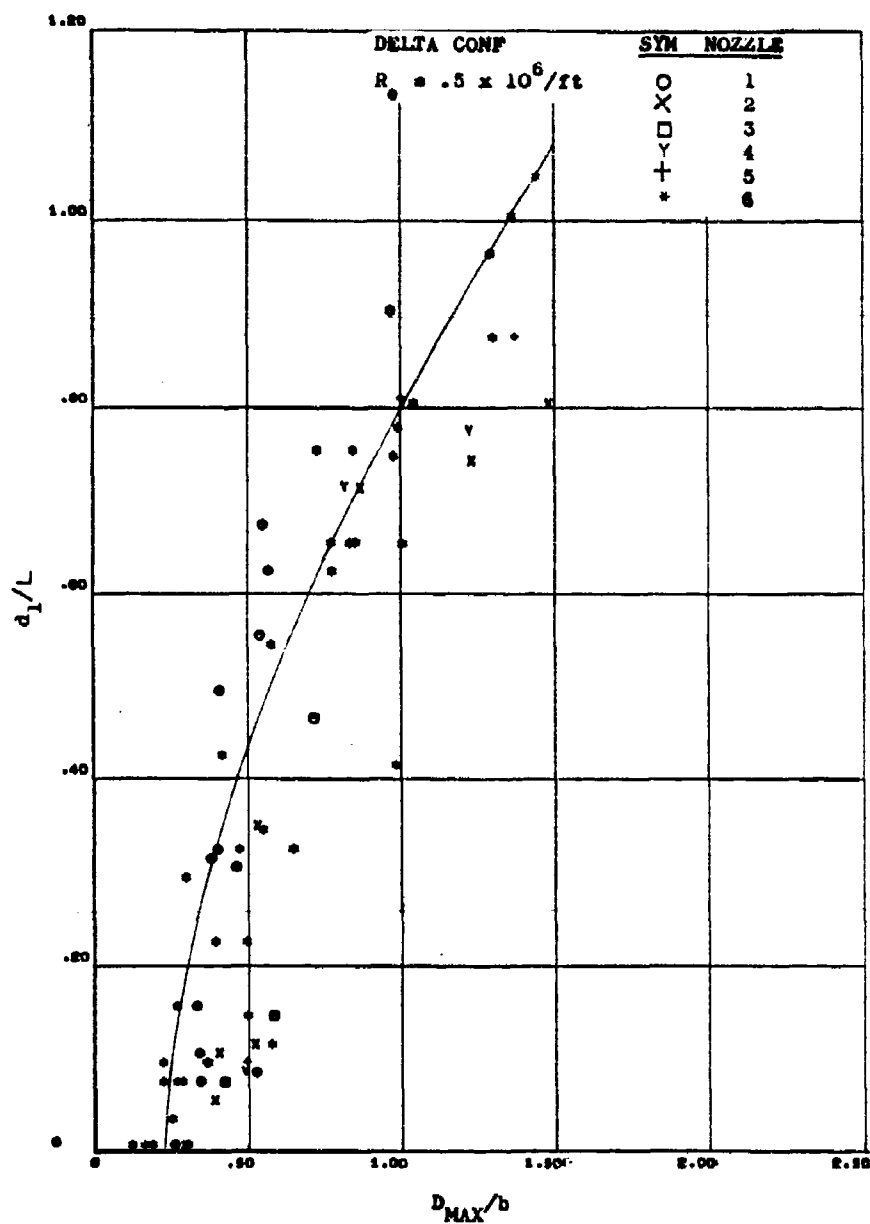


Figure 200. Upstream Interaction Length Correlation at Positive Angle of Attack.

CONFIDENTIAL

CONFIDENTIAL
(This page is Unclassified)

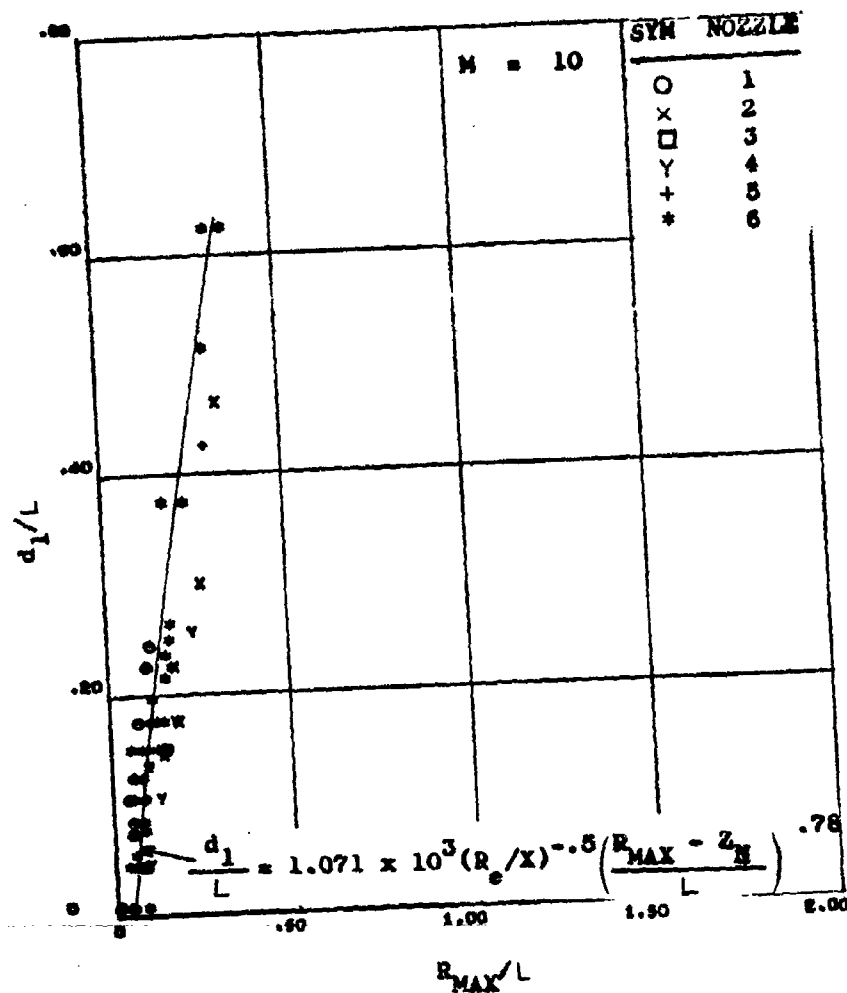


Figure 201. Flat Plate Upstream Interaction Length Correlation at Mach 10.

²⁷⁵
CONFIDENTIAL
(This page is Unclassified)

CONFIDENTIAL

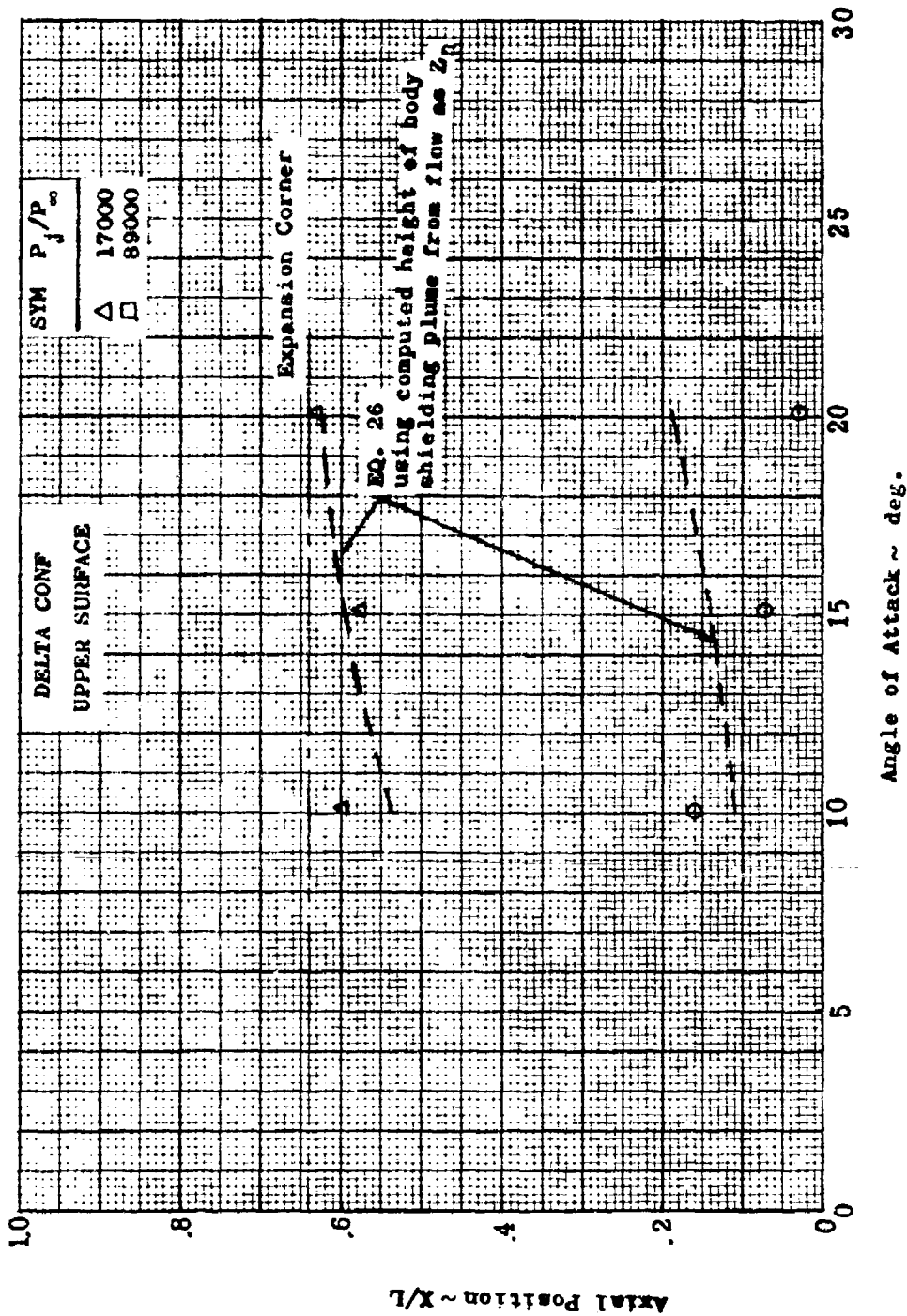


Figure 202. Upper Surface Interaction Location Comparison.

CONFIDENTIAL

CONFIDENTIAL

(This page is Unclassified)

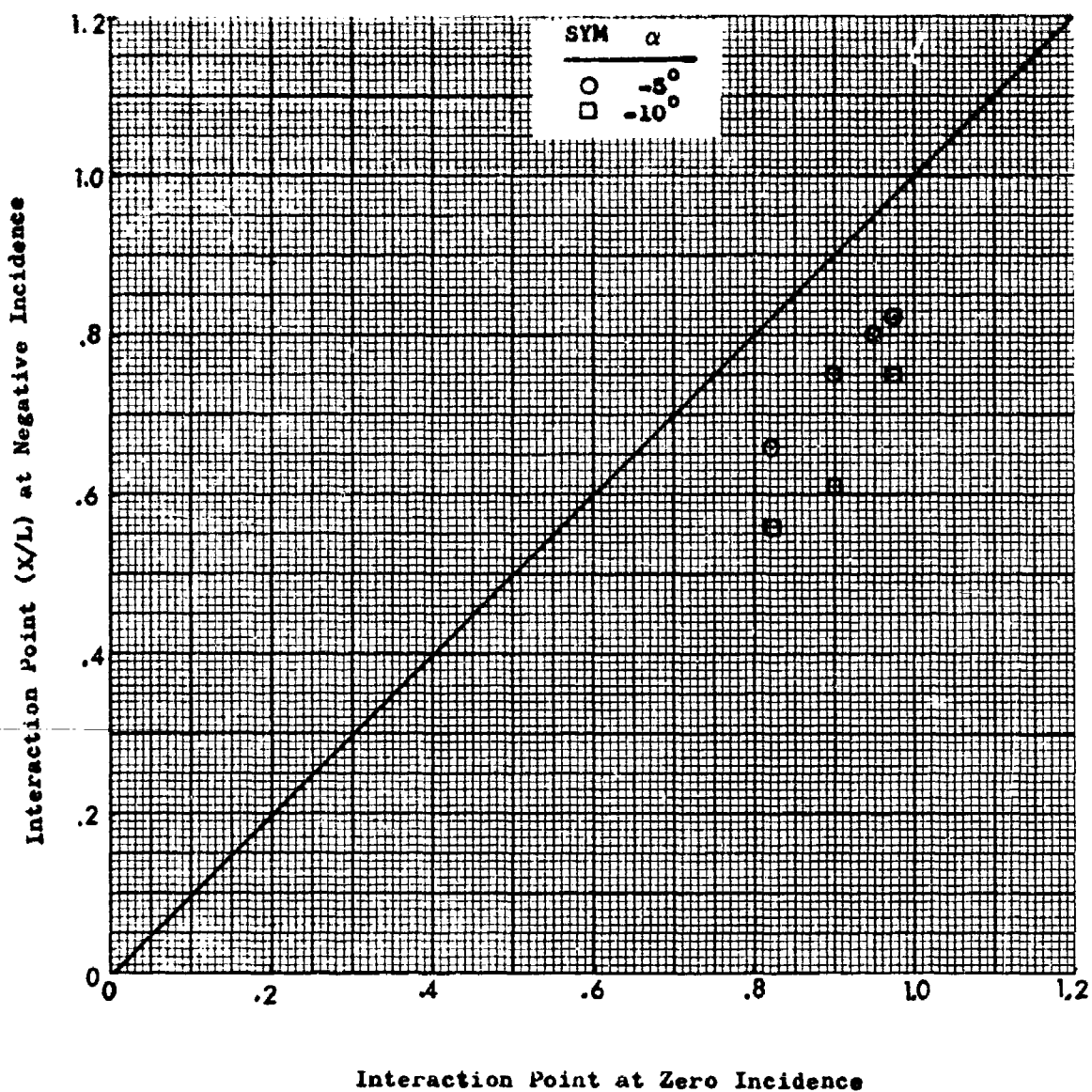


Figure 203. A Comparison of Flat Plate Interaction Points at Negative Incidence.

277

CONFIDENTIAL

(This page is Unclassified)

CONFIDENTIAL

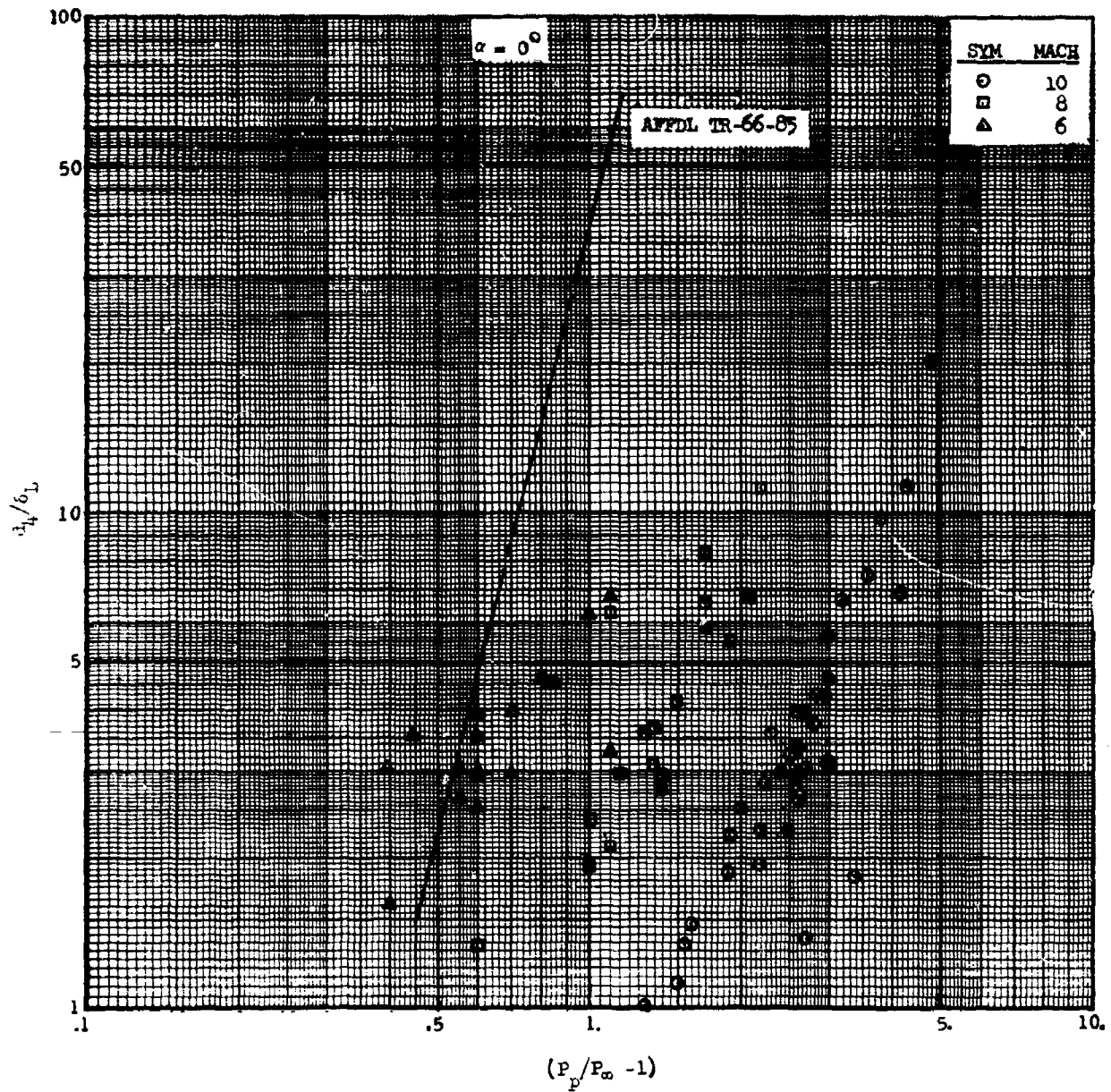


Figure 204. Free Interaction Length Correlation Based on a Laminar Boundary Layer.

CONFIDENTIAL

CONFIDENTIAL

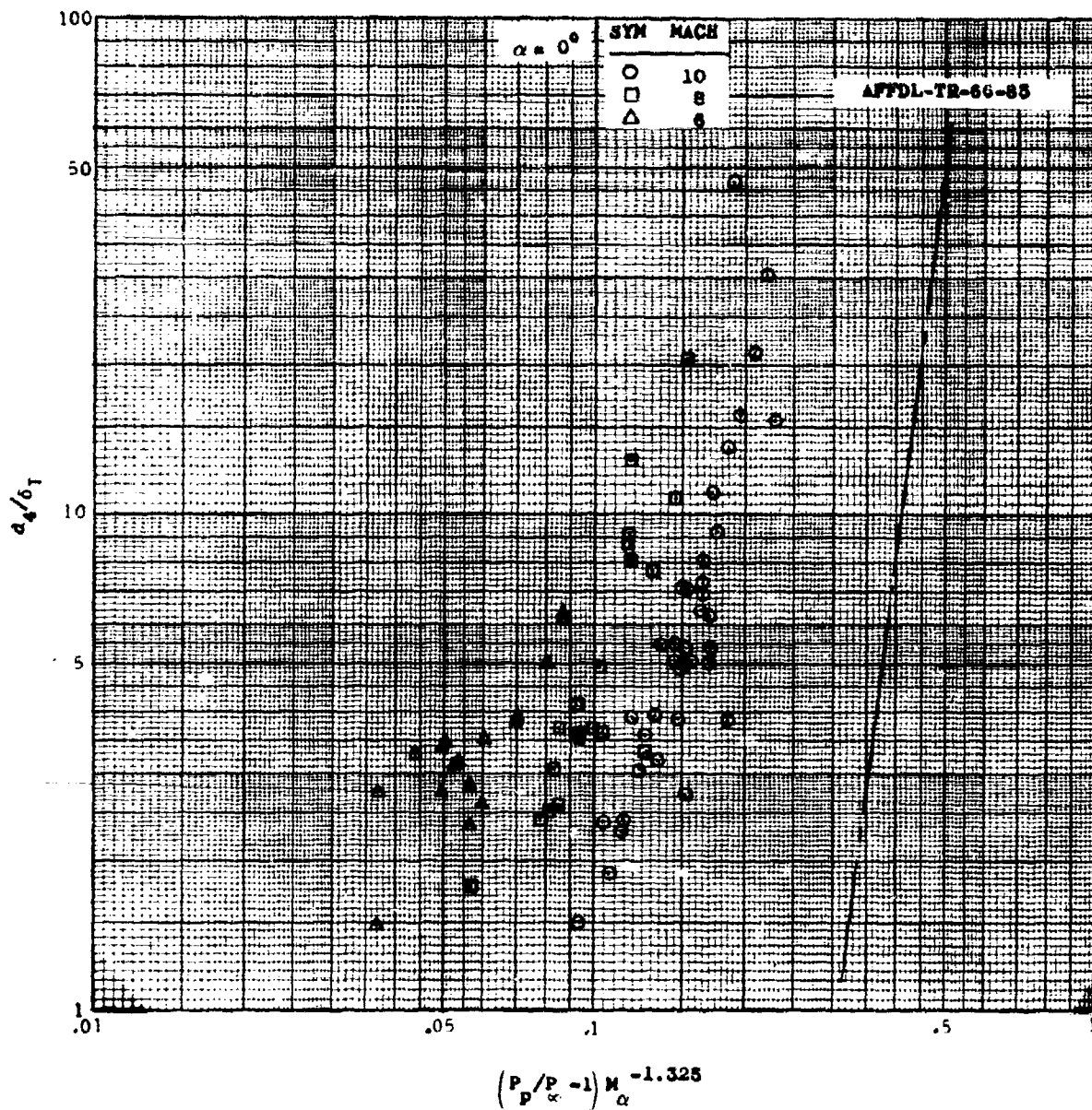


Figure 205. Free Interaction Length Correlation Based on a Turbulent Boundary Layer Thickness.

CONFIDENTIAL

CONFIDENTIAL

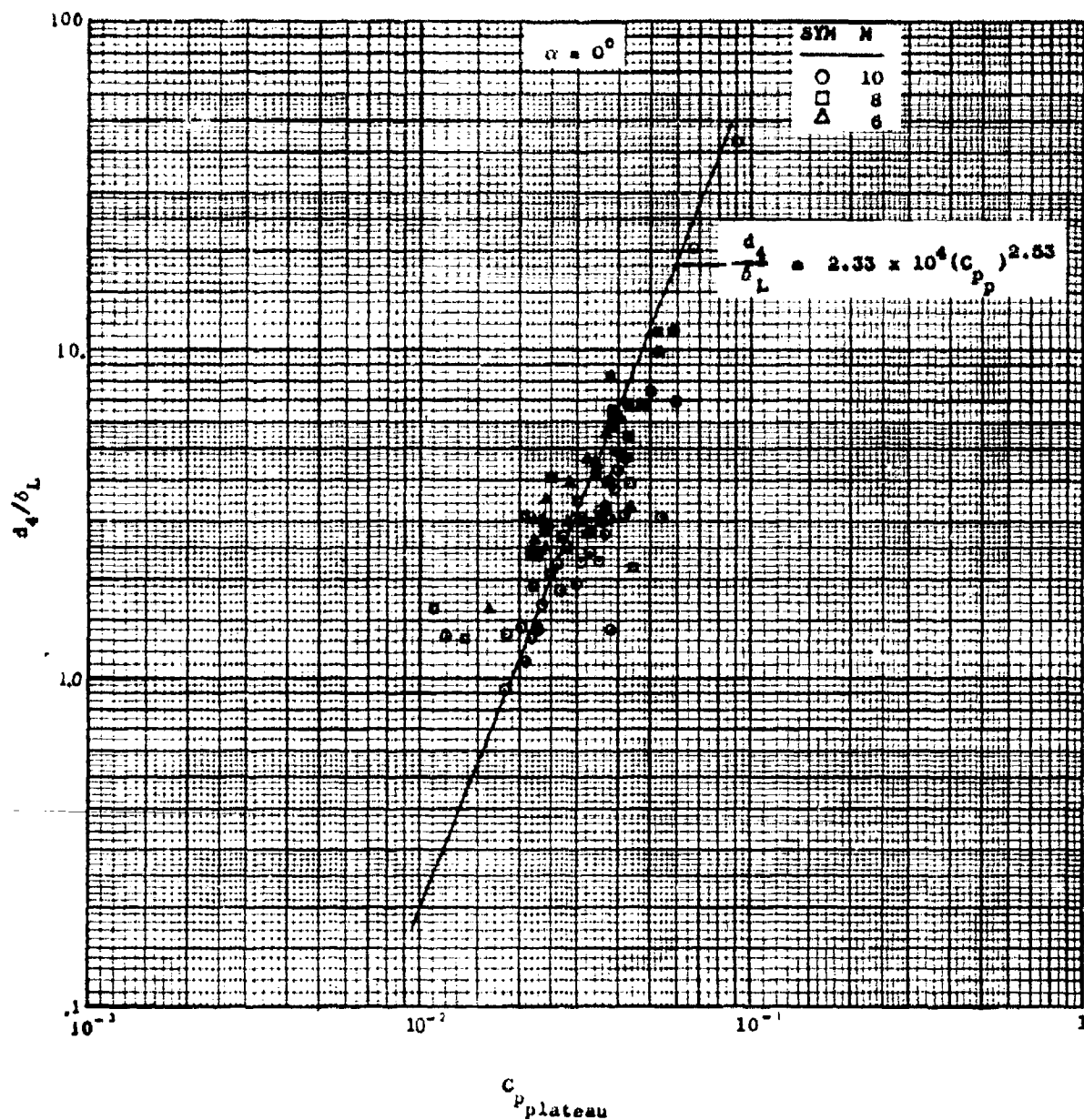


Figure 206. Free Interaction Length Correlation Against Plateau Pressure Coefficient.

CONFIDENTIAL

CONFIDENTIAL

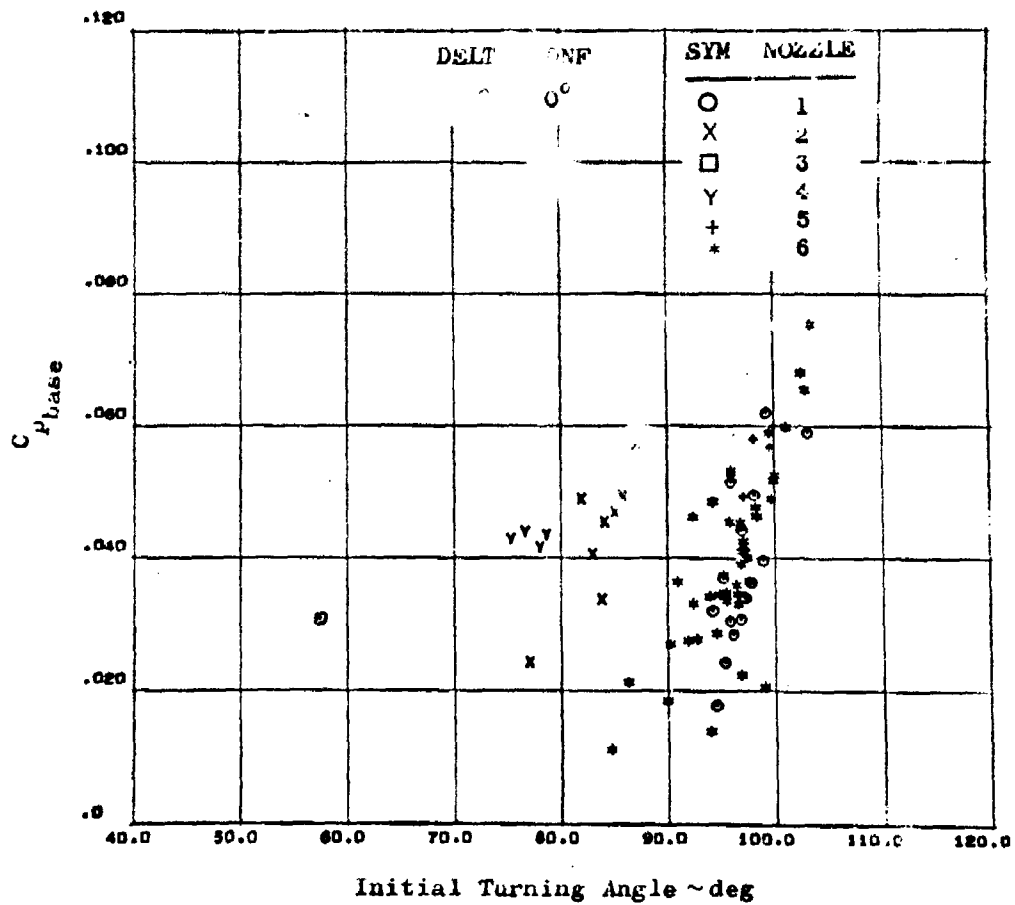


Figure 207. Base Pressure Correlated with Plume Initial Turning Angle

CONFIDENTIAL

CONFIDENTIAL

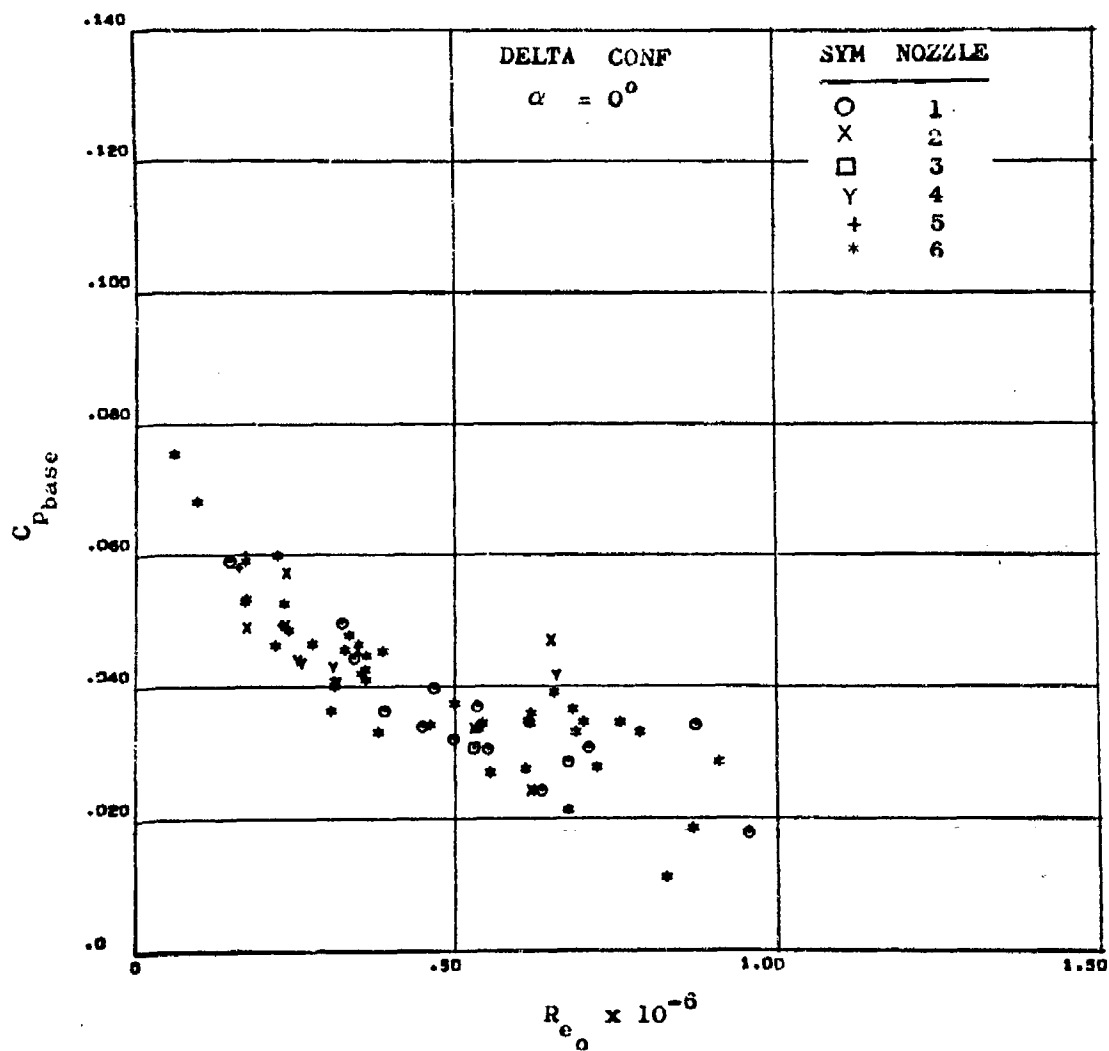


Figure 208. Base Pressure Correlated by Reynolds Number at the Interaction Point

CONFIDENTIAL

CONFIDENTIAL

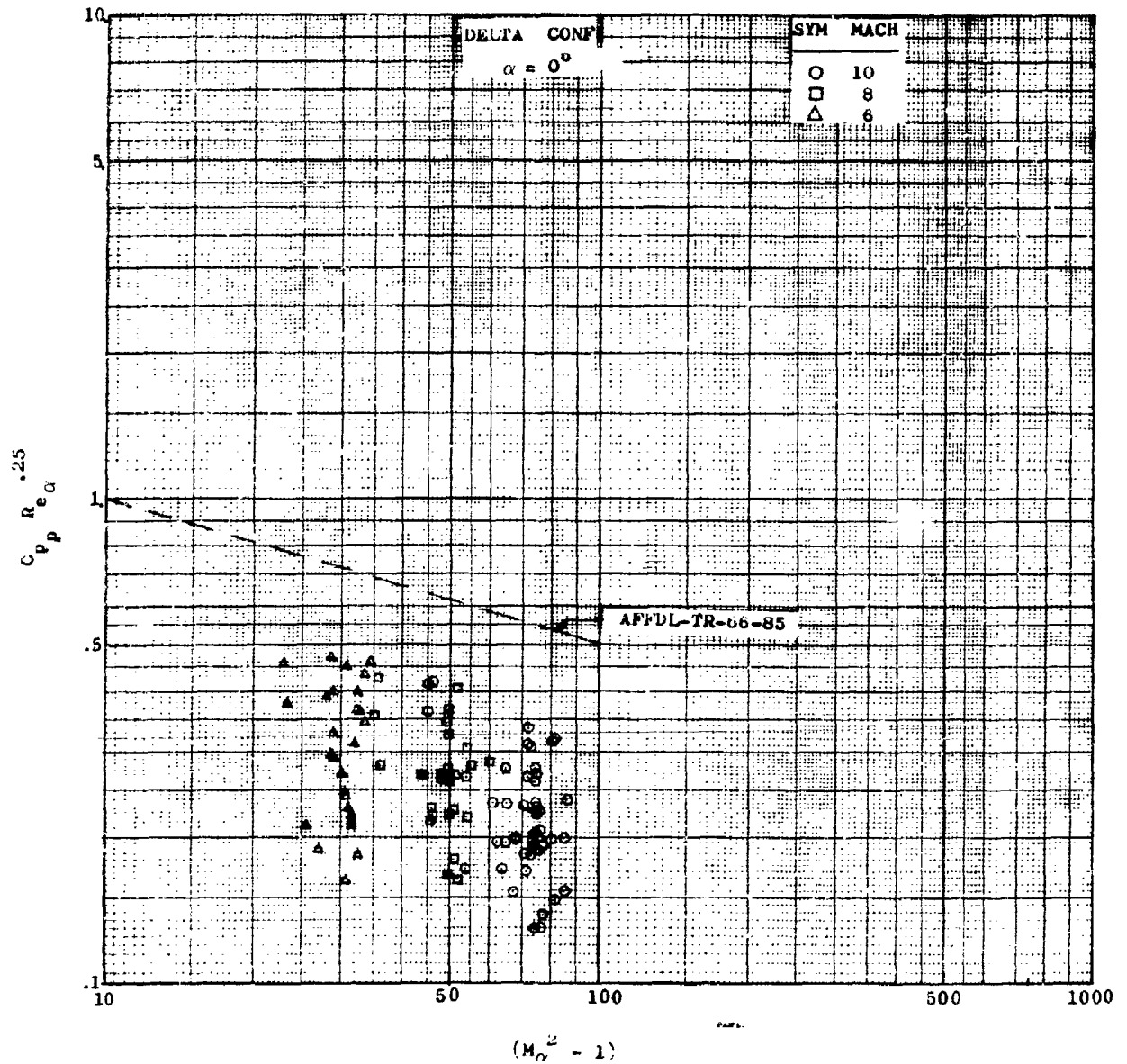


Figure 20). Plateau Pressure Correlation Based on a Laminar Boundary Layer

CONFIDENTIAL

CONFIDENTIAL

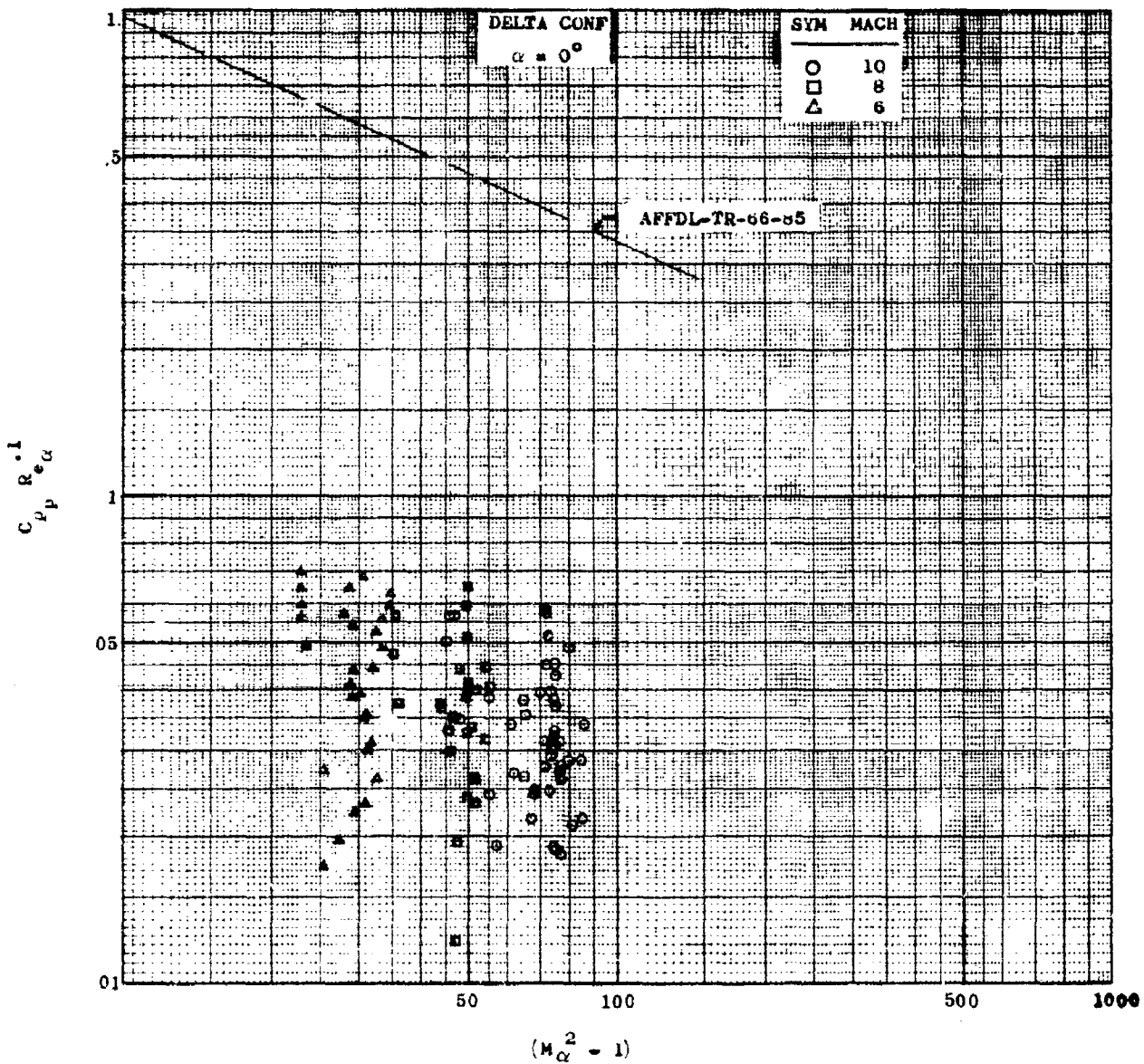


Figure 210. Plateau Pressure Correlation Based on a Turbulent Boundary Layer Assumption

CONFIDENTIAL

CONFIDENTIAL

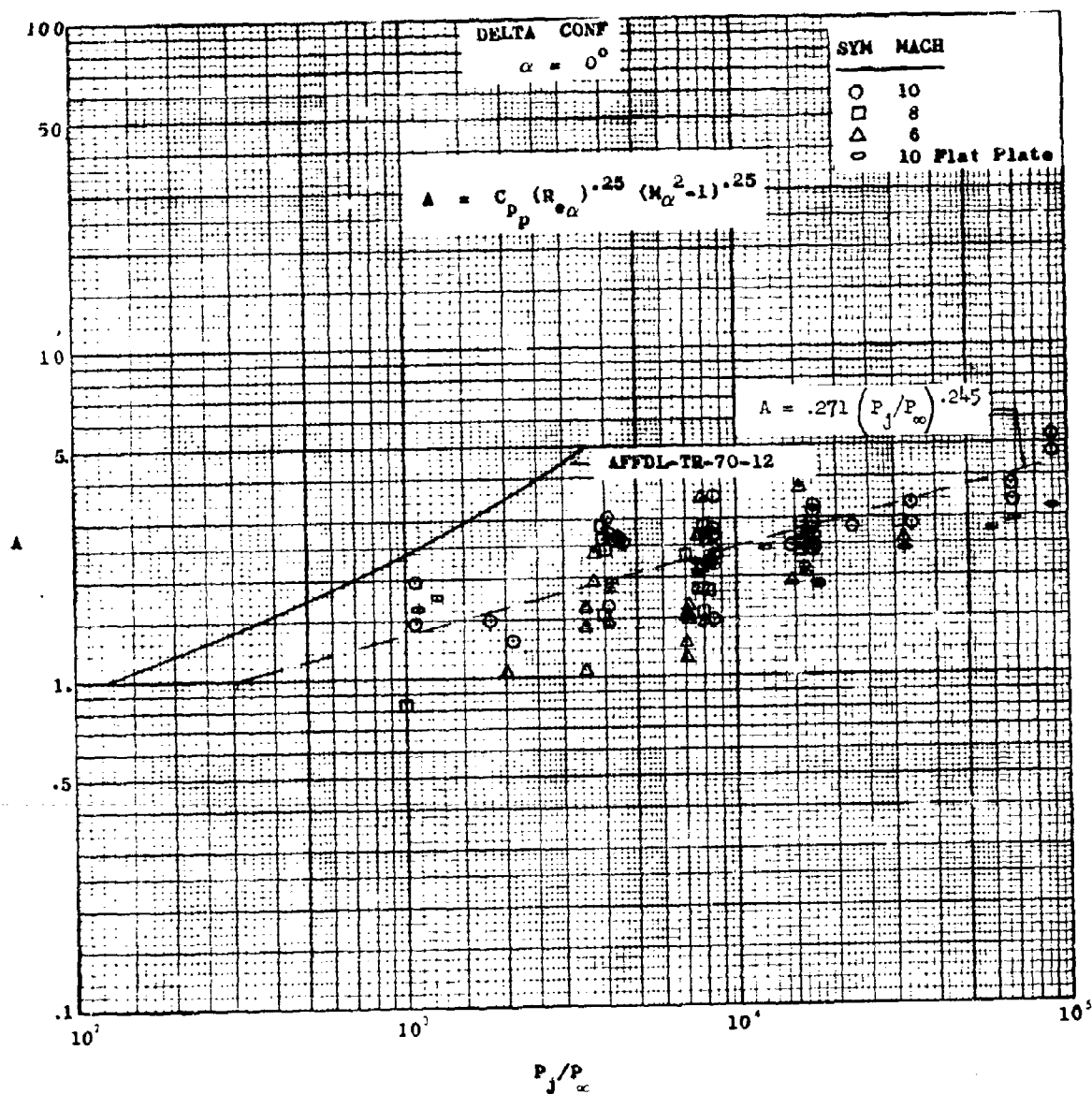


Figure 211. Plateau Pressure Correlated with Jet Pressure Ratio.

CONFIDENTIAL

CONFIDENTIAL

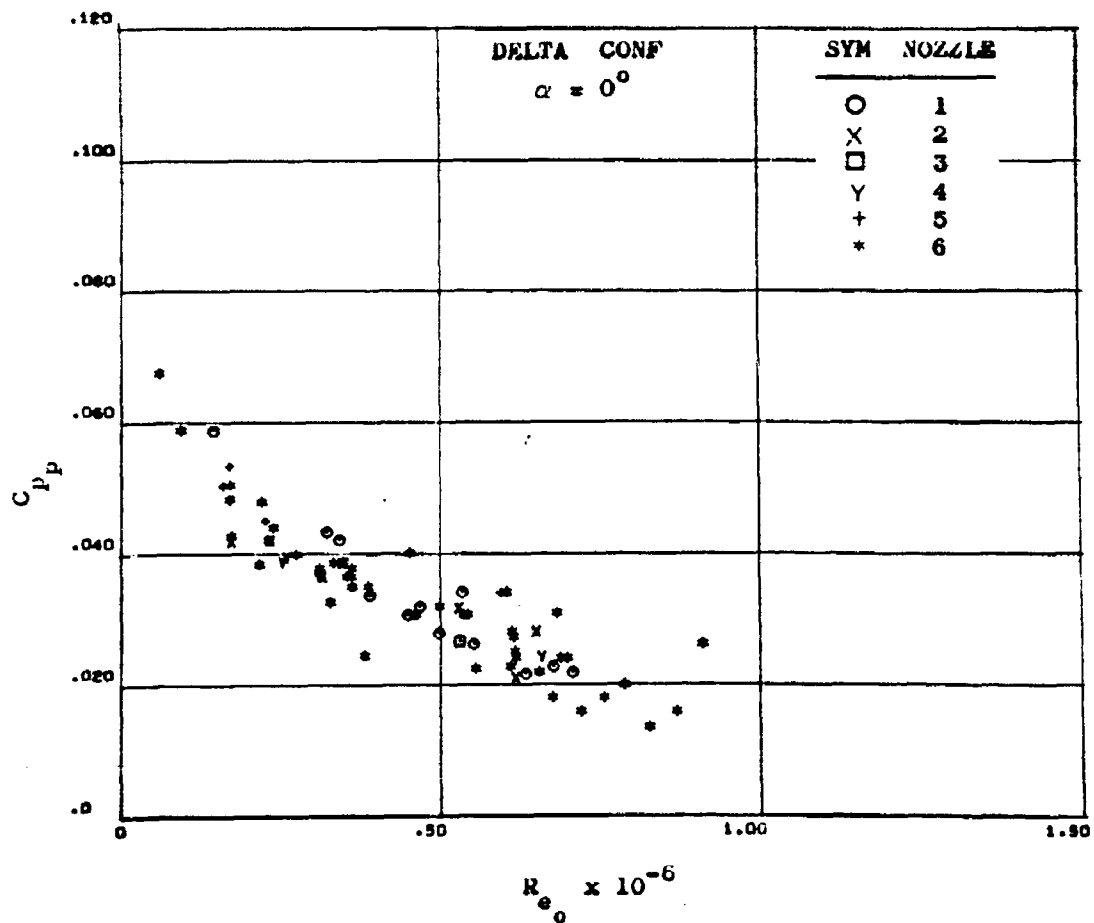


Figure 212. Plateau Pressure Correlated with Reynolds Number at Interaction Point

CONFIDENTIAL

CONFIDENTIAL

(This page is Unclassified)

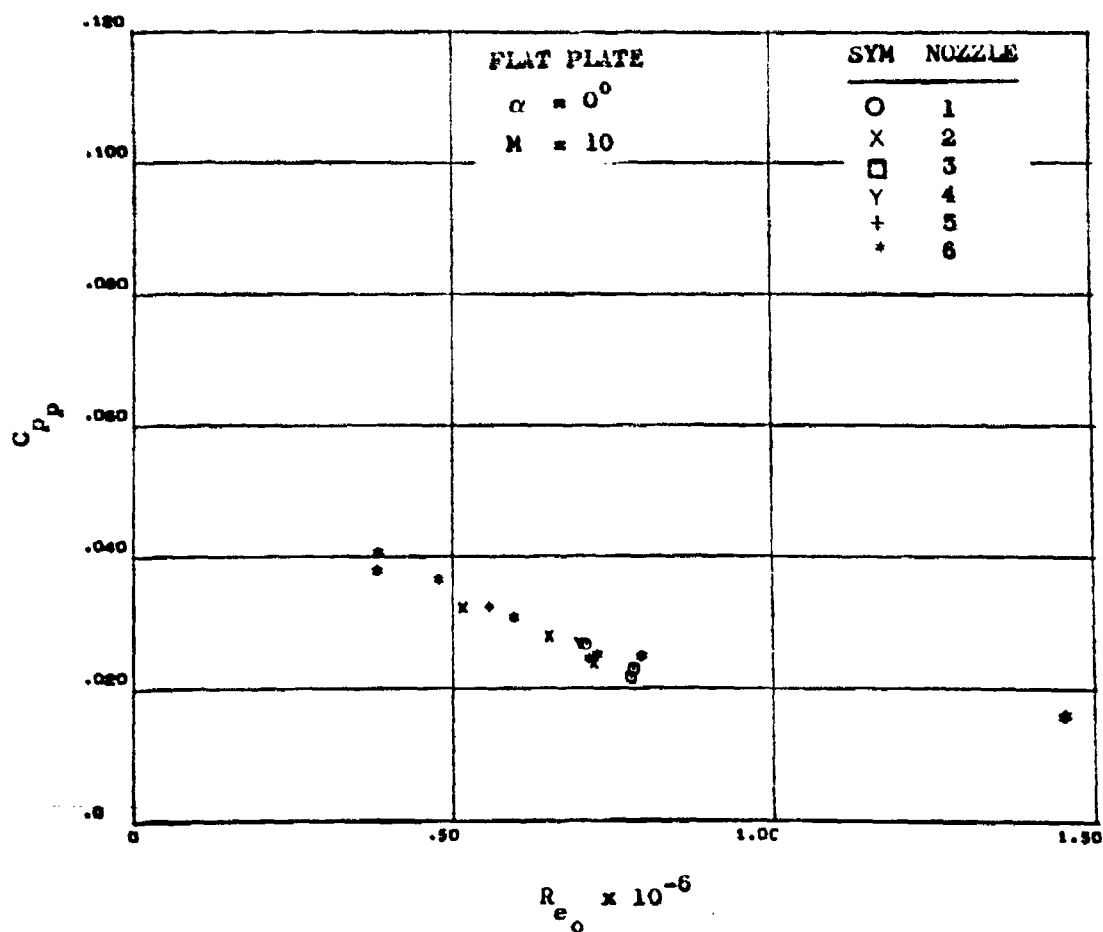


Figure 213. Flat Plate Pressure Correlation at a Mach Number of 10.

287

CONFIDENTIAL

(This page is Unclassified)

CONFIDENTIAL

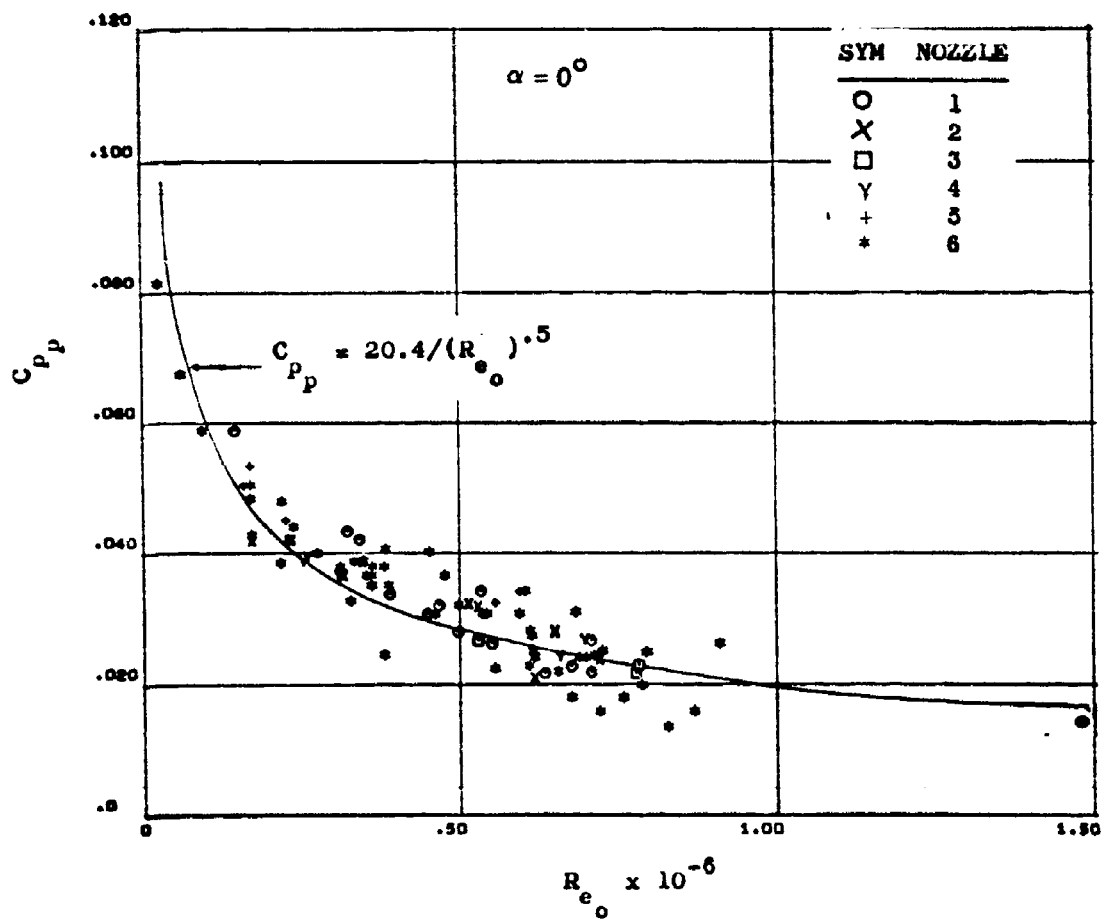


Figure 214. Plateau Pressure Correlation at $\alpha = 0^\circ$.

CONFIDENTIAL

CONFIDENTIAL

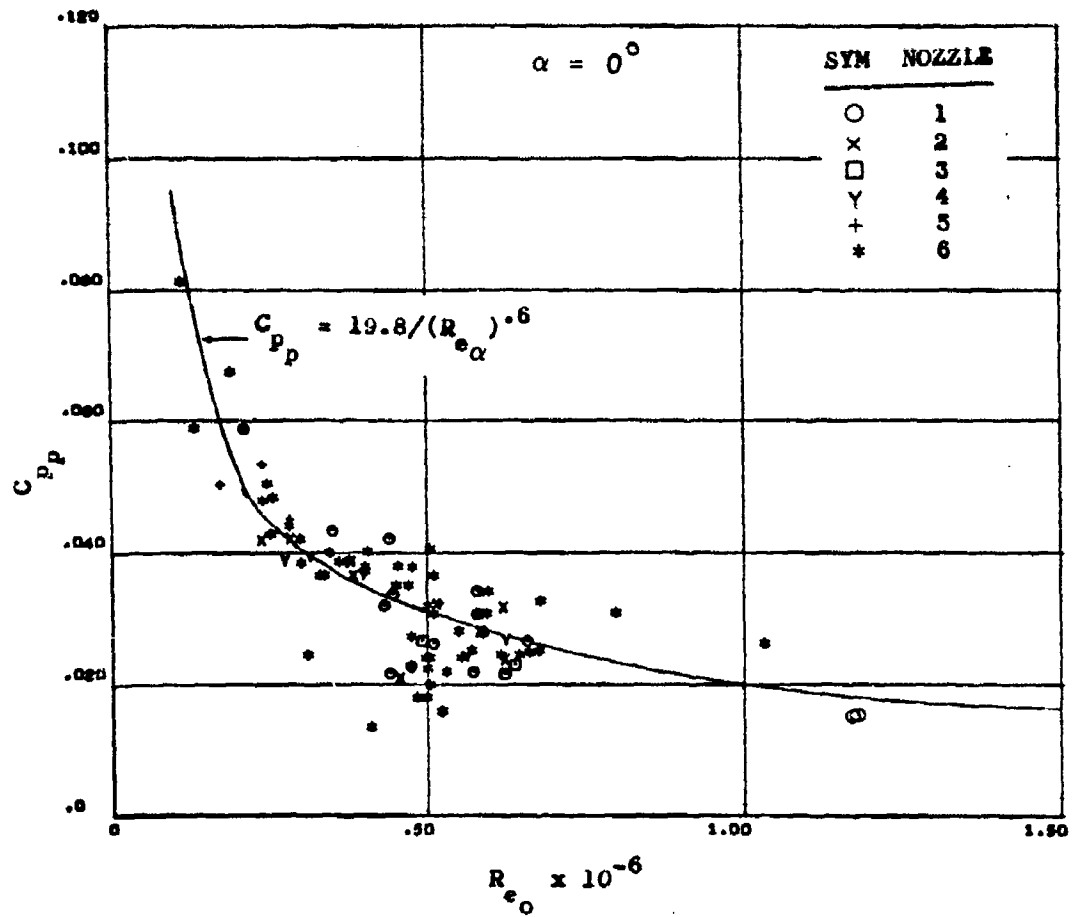


Figure 215. Plateau Pressure Correlated with Reynolds Number
Based on Local Condition

CONFIDENTIAL

CONFIDENTIAL

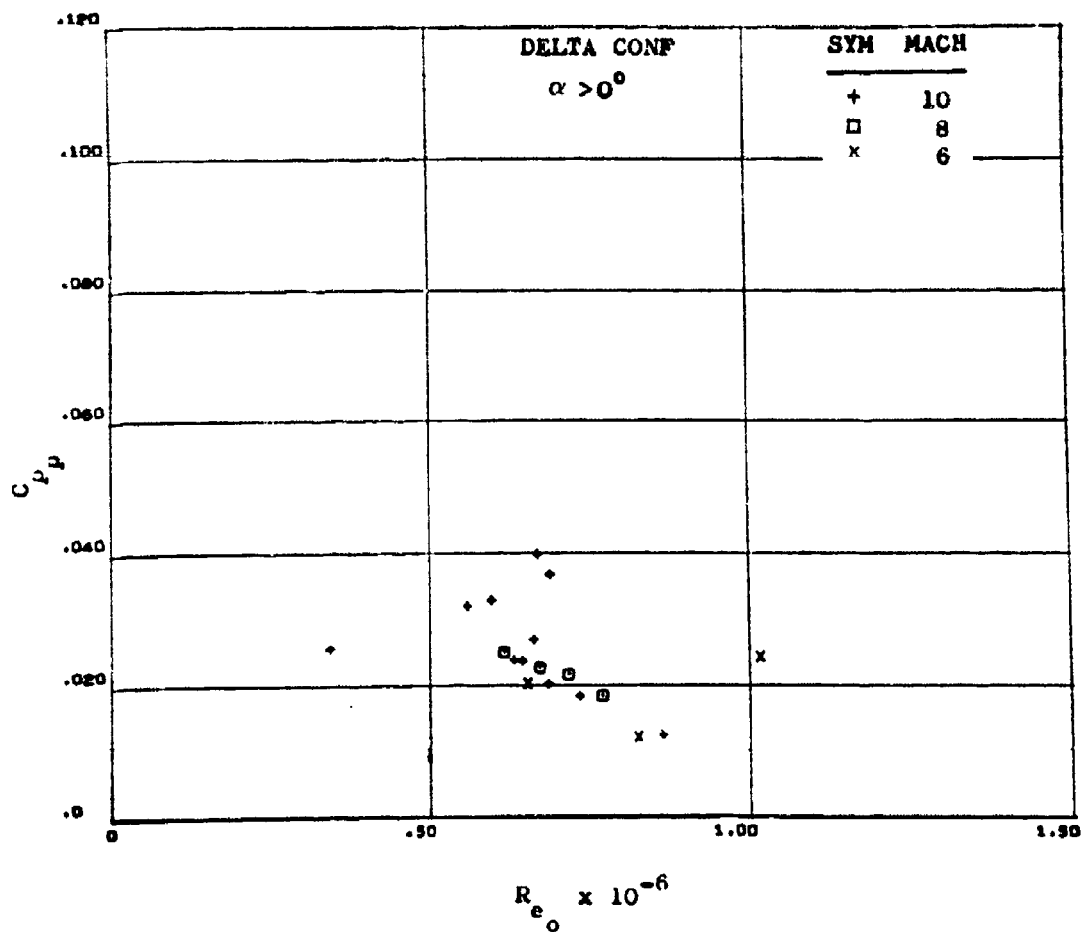


Figure 216. Plateau Pressure at Positive Angles of Attack

CONFIDENTIAL

UNCLASSIFIED

APPENDIX I TEST CONDITIONS

The test conditions for all of the pressure runs are specified in the following table. The configuration code in the table is a four digit code

ABCD

where

A = model geometry

- 1 = flat plate
- 2 = flat plate plus extensions
- 3 = delta conf.
- 4 = delta configuration with upper surface elevons off

B = nozzle code as specified in Table 1 of text

C = nozzle position code as shown in Figure 8 of text

D = lower elevon deflection

- 1 = 0°
- 2 = -15°
- 3 = -20°

UNCLASSIFIED

APPENDIX I (continued)

Run	Conf Code	M _∞	R _e x 10 ⁻⁶ /ft	α Deg	P ₀ PSI	T ₀ ~ R°
1	1111	10.150	.889	0.000	.015	92.470
2	1111	10.150	.887	10.010	.015	92.470
3	1111	10.150	.887	15.020	.015	92.870
4	1111	10.150	.890	.010	.015	92.790
5	1111	10.150	.893	10.020	.015	92.670
6	1111	10.150	.898	15.020	.015	92.670
7	1111	10.150	.891	-10.030	.015	92.660
8	1111	10.150	.863	-10.060	.015	92.800
9	1111	10.910	.227	0.000	.004	95.270
10	1111	10.910	.224	10.000	.004	95.060
11	1111	10.910	.226	.020	.004	94.970
12	9	0.000	0.000	0.000	0.000	0.000
13	1111	10.150	.899	-0.000	.015	92.470
14	1611	10.150	.891	0.000	.015	92.670
15	1611	10.150	.885	0.000	.015	92.660
16	1611	10.000	.517	-0.010	.009	92.970
17	1611	10.000	.515	4.980	.009	92.880
18	1611	10.000	.517	10.000	.009	92.780
19	1611	10.000	.516	15.020	.009	92.730
20	1611	10.000	.519	-4.980	.009	92.490
21	1611	10.000	.514	-10.030	.009	93.500
22	1611	10.000	.507	.090	.009	93.730
23	1611	10.000	.508	5.020	.009	93.780
24	1611	10.000	.508	10.080	.009	93.660
25	1611	10.000	.506	15.110	.009	94.120
26	1611	10.000	.506	-4.930	.009	93.910
27	1611	10.000	.502	-9.910	.009	94.030
28	1611	10.000	.506	.090	.009	93.450
29	1611	10.000	.508	5.090	.009	93.800
30	1611	10.000	.505	10.090	.009	93.790
31	1611	10.000	.512	15.050	.009	92.790
32	1611	10.000	.512	-4.910	.009	93.730
33	1611	10.000	.505	-9.890	.009	94.160
34	1611	10.000	.502	.050	.009	93.760
35	1611	10.000	.509	5.090	.009	93.600
36	1611	10.000	.510	10.090	.009	93.520
37	1611	10.000	.507	-4.920	.009	93.800
38	1611	10.000	.512	-9.950	.009	93.800
39	1611	10.000	.506	.080	.009	94.480
40	1611	10.000	.503	5.070	.009	94.490
41	1611	10.000	.502	-4.920	.009	94.370
42	1611	10.000	.502	-9.920	.009	94.350
43	1611	10.000	.509	0.000	.009	93.760
44	1611	10.000	.508	0.000	.009	93.870
45	1611	10.000	.506	0.000	.009	94.020
46	1611	10.000	.507	0.000	.009	93.970
47	1611	10.150	.885	-0.010	.015	92.800
48	1611	10.150	.887	10.010	.015	92.990
49	1611	10.010	.231	0.000	.004	94.550
50	1611	10.010	.228	10.010	.004	95.040
51	1211	10.000	.508	0.000	.009	93.990
52	1211	10.000	.500	10.010	.009	94.160
53	1211	10.000	.505	10.000	.009	94.010
54	1211	10.000	.501	.010	.009	94.040
55	1211	10.000	.504	.010	.009	93.910
56	1211	10.000	.504	9.990	.009	93.940
57	1211	10.000	.505	-0.020	.009	93.900
58	1211	10.000	.507	10.000	.009	93.740
59	1211	10.000	.509	10.010	.009	93.670
60	1211	10.000	.507	0.000	.009	93.750
61	1411	10.000	.515	-0.010	.009	93.890

END

UNCLASSIFIED

UNCLASSIFIED

APPENDIX 1 (continued)

Run	Conf Code	M _∞	R _e × 10 ⁻⁶ /ft	α Deg	P ₀ PSI	T ₀ ~ R°
62	1411	10.080	.503	10.020	.000	93.810
63	1411	10.080	.514	10.020	.009	93.540
64	1411	10.080	.509	0.000	.009	93.760
65	1511	10.080	.512	0.000	.009	93.660
66	1511	10.080	.509	9.480	.009	93.780
67	1311	10.080	.512	-.010	.009	93.760
68	1111	10.080	.502	10.010	.009	93.810
69	2611	10.080	.515	-.030	.009	93.610
70	2611	10.080	.510	10.000	.009	93.810
71	2611	10.080	.509	10.010	.009	93.660
72	2611	10.080	.513	0.000	.009	93.740
73	1621	10.080	.506	-.020	.009	93.730
74	1621	10.080	.509	10.010	.009	93.740
75	1631	10.080	.512	-.020	.009	93.550
76	1631	10.080	.504	10.010	.009	93.740
77	1641	10.080	.502	0.000	.009	94.080
78	1641	10.080	.508	10.610	.009	93.460
79	1642	10.080	.505	0.000	.009	93.790
80	1642	10.080	.510	10.020	.009	93.590
81	2611	10.080	.509	0.000	.009	93.690
82	1111	10.080	.506	0.000	.009	93.660
83	1111	10.080	.511	0.000	.009	93.460
84	1111	10.080	.508	10.040	.009	93.480
85	1111	10.080	.508	0.000	.009	93.660
86	1111	10.080	.508	10.040	.009	93.810
87	1613	10.080	.505	0.000	.009	93.680
88	1613	10.080	.505	9.990	.009	93.920
89	1613	10.080	.505	.010	.009	93.860
90	1611	10.080	.510	7.510	.009	93.580
91	1611	10.080	.506	7.530	.009	93.720
92	3611	10.150	.899	0.000	.015	92.140
93	3611	10.150	.892	10.020	.015	92.420
94	3611	10.150	.896	20.040	.015	92.220
95	3611	10.010	.729	0.000	.004	94.560
96	3611	10.010	.728	10.000	.004	94.560
97	3611	10.010	.724	20.020	.004	94.530
98	3611	10.080	.509	0.000	.009	93.570
99	3611	10.080	.513	5.000	.009	93.350
100	3611	10.080	.509	10.020	.009	93.630
101	3611	10.080	.504	14.990	.009	93.880
102	3611	10.080	.506	19.980	.009	93.710
103	3611	10.080	.509	26.500	.009	93.780
104	3611	10.080	.506	-.040	.009	93.940
105	3611	10.080	.516	0.000	.009	92.930
106	3611	10.080	.514	5.030	.009	92.990
107	3611	10.080	.514	10.030	.009	92.850
108	3611	10.080	.513	15.020	.009	92.780
109	3611	10.080	.513	20.040	.009	92.870
110	3611	10.080	.514	26.530	.009	92.710
111	3611	10.080	.514	0.000	.009	92.810
112	3611	10.080	.518	4.960	.009	92.530
113	3611	10.080	.517	10.000	.009	92.710
114	3611	10.080	.516	14.990	.009	92.530
115	3611	10.080	.519	19.990	.009	92.620
116	3611	10.080	.517	-.010	.009	92.590
117	3611	10.080	.516	5.000	.009	92.800
118	3611	10.080	.515	10.030	.009	92.760
119	3611	10.080	.516	15.020	.009	92.720
120	3611	10.080	.516	20.010	.009	92.790
121	3611	10.080	.513	-.030	.009	92.670
122	3611	10.080	.517	2.500	.009	92.650
123	3611	10.080	.520	5.020	.009	92.260

UNCLASSIFIED

APPENDIX 1 (continued)

Run	Conf Code	M _∞	R _e x 10 ⁻⁶ /ft	α Deg	P _∞ PSI	T _∞ ~ R°
124	3611	10.020	.521	10.020	.009	92.190
125	3611	10.020	.520	15.020	.009	92.270
126	3611	10.020	.519	.020	.009	92.340
127	3611	10.020	.522	2.520	.009	92.190
128	3611	10.020	.514	5.010	.009	92.680
129	3611	10.020	.520	9.990	.009	92.430
130	3611	10.020	.517	15.010	.009	92.510
131	3611	10.020	.519	0.000	.009	92.420
132	3611	10.020	.518	2.510	.009	92.340
133	3611	10.020	.517	5.020	.009	92.360
134	3611	10.020	.522	10.020	.009	92.310
135	3611	10.020	.520	15.000	.009	92.510
136	3611	10.020	.520	2.510	.009	92.370
137	3612	10.020	.516	.010	.009	92.470
138	3612	10.020	.522	4.990	.009	91.960
139	3612	10.020	.527	10.010	.009	91.740
140	3612	10.020	.525	15.020	.009	92.410
141	3613	10.020	.519	0.000	.009	92.340
142	3613	10.020	.519	10.040	.009	92.240
143	3613	10.020	.520	15.000	.009	92.230
144	3613	10.020	.523	20.030	.009	92.290
145	3211	10.020	.516	.010	.009	92.570
146	3211	10.020	.517	10.020	.009	92.480
147	3211	10.020	.519	15.000	.009	92.260
148	3211	10.020	.524	0.000	.009	91.690
149	3211	10.020	.526	10.010	.009	91.540
150	3211	10.020	.525	14.990	.009	91.860
151	3211	10.020	.523	0.000	.009	91.910
152	3211	10.020	.528	10.060	.009	91.740
153	3211	10.020	.511	0.000	.009	93.220
154	3211	10.020	.512	5.010	.009	93.000
155	3211	10.020	.515	10.000	.009	92.850
156	3411	10.020	.514	-.010	.009	92.870
157	3411	10.020	.518	4.980	.009	92.960
158	3411	10.020	.507	9.990	.009	93.740
159	3611	10.010	.225	0.000	.004	95.060
160	3611	10.010	.231	5.000	.004	94.460
161	3111	10.020	.513	0.000	.009	93.220
162	3111	10.020	.516	5.080	.009	92.740
163	3111	10.020	.515	.020	.009	93.300
164	3111	10.020	.507	5.060	.009	93.690
165	3111	10.020	.508	2.540	.009	93.670
166	3111	10.020	.506	0.000	.009	93.740
167	3111	10.020	.504	2.490	.009	94.070
168	3111	10.020	.516	-.010	.009	92.720
169	3111	10.020	.518	-.010	.009	92.640
170	3111	10.020	.513	9.970	.009	93.020
171	3111	10.020	.513	14.960	.009	93.000
172	3111	10.020	.515	0.000	.009	92.890
173	3111	10.020	.515	10.020	.009	92.790
174	3111	10.020	.517	15.030	.009	92.700
175	3511	10.020	.511	0.000	.009	93.250
176	3511	10.020	.509	9.970	.009	93.340
177	3511	10.020	.514	14.970	.009	92.840
178	3611	10.020	.514	0.000	.009	92.950
179	3611	10.150	.496	0.000	.015	92.090
180	3611	10.150	.499	5.020	.015	92.090
181	3611	10.150	.495	10.030	.015	92.010
182	3611	10.150	.491	15.020	.015	92.720
183	3641	10.020	.512	-.010	.009	93.220
184	3641	10.020	.513	5.050	.009	93.280
185	3641	10.020	.511	10.050	.009	93.530

UNCLASSIFIED

UNCLASSIFIED

APPENDIX 1 (CONTINUED)

Run	Conf Code	M_{∞}	$R_e \times 10^{-6}/ft$	α Deg	P_r PSI	$T_{\infty} - R^{\circ}$
186	3642	10.000	.514	0.000	.009	93.220
187	3642	10.000	.514	5.000	.009	93.130
188	3642	10.000	.513	9.900	.009	93.070
189	3613	10.000	.517	0.000	.009	92.860
190	3613	10.000	.515	5.000	.009	93.070
191	3613	10.000	.513	10.050	.009	93.090
192	3711	10.000	.519	0.000	.009	92.770
193	3711	10.000	.517	4.990	.009	93.230
194	3711	10.000	.512	9.990	.009	93.390
195	3411	10.000	.516	0.000	.009	93.020
196	3411	10.000	.514	4.990	.009	93.030
197	3411	10.000	.517	9.990	.009	92.930
198	3611	10.010	.252	9.990	.004	88.480
199	3611	10.050	.512	0.000	.009	93.110
200	3611	10.000	.509	0.000	.009	93.690
201	3611	10.000	.509	-0.050	.009	93.330
202	3611	10.000	.510	5.020	.009	93.630
203	3611	10.000	.509	10.000	.009	93.800
204	4611	10.000	.504	.010	.009	94.220
205	4611	10.000	.507	5.010	.009	94.040
206	4611	10.000	.507	10.000	.009	94.010
207	4611	10.000	.505	-2.040	.009	94.030
208	3621	10.000	.508	-0.020	.009	93.800
209	3621	10.000	.510	5.020	.009	93.630
210	3621	10.000	.508	10.000	.009	93.800
211	3631	10.000	.508	-0.010	.009	93.800
212	3631	10.000	.506	5.020	.009	93.970
213	3631	10.000	.508	10.000	.009	93.810
214	3611	10.000	.508	-2.000	.009	93.890
215	3611	10.000	.506	2.530	.009	93.880
216	3611	10.000	.509	7.540	.009	93.630
217	3611	10.010	.234	10.010	.004	94.430
218	3211	10.010	.228	-0.090	.004	95.080
219	3211	10.010	.232	5.030	.004	93.660
220	3211	10.010	.235	10.010	.004	93.020
221	3211	10.150	.895	0.000	.015	92.430
222	3211	10.150	.896	4.970	.015	92.370
223	3211	10.150	.896	9.980	.015	92.390
224	3611	10.150	.898	0.000	.015	92.270
225	3611	10.150	.896	5.070	.015	92.350
226	3611	10.150	.898	10.040	.015	92.270
227	3611	10.000	.510	-0.010	.009	93.360
228	3611	10.000	.518	7.560	.009	92.870
229	3642	10.000	.514	15.040	.009	93.350
230	3642	10.000	.513	20.000	.009	93.490
231	3641	10.010	.231	0.000	.004	94.090
232	3641	10.010	.228	5.060	.004	94.710
233	3641	10.010	.231	10.050	.004	94.490
234	3621	10.010	.228	0.000	.004	95.130
235	3621	10.010	.229	5.100	.004	94.810
236	3621	10.010	.228	10.110	.004	94.740
237	3611	5.960	.657	0.000	.022	101.190
238	3611	5.960	.662	4.990	.022	101.390
239	3611	5.960	.663	10.010	.022	101.500
240	3611	5.960	.660	14.980	.022	102.000
241	3611	5.960	.643	0.000	.022	103.300
242	3611	5.960	.639	5.030	.022	103.400
243	3611	5.960	.642	10.000	.022	104.170
244	3611	5.970	.639	15.000	.022	103.290
245	3611	5.960	.644	-0.010	.022	104.000
246	3611	5.960	.642	5.000	.022	104.190
247	3611	5.900	.355	.010	.013	104.590

UNCLASSIFIED

UNCLASSIFIED

APPENDIX 1 (continued)

Run	Conf Code	M _∞	R _e × 10 ⁻⁶ /ft	α Deg	P _∞ PSI	T _∞ ~ R°
24 8	3611	5.900	.370	4.990	.013	104.100
24 9	3611	5.900	.376	4.980	.013	103.500
25 0	3611	5.900	.376	.010	.013	103.300
25 1	3611	5.900	.375	.010	.013	103.000
25 2	3613	5.960	.651	0.000	.022	102.500
25 3	3613	5.960	.645	5.010	.022	103.100
25 4	3613	5.960	.664	0.000	.022	100.000
25 5	3613	5.960	.668	5.010	.022	100.500
25 6	3611	5.960	.655	0.000	.022	100.600
25 7	3611	5.960	.660	5.010	.022	100.700
25 8	3611	5.960	.667	10.000	.022	100.700
25 9	3211	5.960	.670	-.020	.022	100.800
26 0	3211	5.960	.662	10.020	.022	100.700
26 1	3411	5.960	.669	.010	.022	100.200
26 2	3411	5.960	.674	10.020	.022	100.200
26 3	3511	5.960	.670	.010	.022	100.200
26 4	3511	5.960	.676	10.010	.022	100.200
26 5	3811	5.960	.675	-.010	.022	100.200
26 6	3611	5.960	.673	5.010	.022	100.200
26 7	3611	5.960	.674	10.010	.022	100.200
26 8	3611	5.960	.676	14.990	.022	100.200
26 9	3611	5.960	.677	-.010	.022	100.200
27 0	3611	5.960	.675	5.000	.022	100.200
27 1	3641	5.960	.676	-.010	.022	100.300
27 2	3641	5.960	.671	5.000	.022	100.300
27 3	3641	5.960	.671	10.000	.022	100.300
27 4	3642	5.960	.672	-0.000	.022	100.300
27 5	3642	5.960	.671	10.000	.022	100.400
27 6	3642	5.960	.665	0.000	.022	100.400
27 7	3642	5.960	.669	10.010	.022	101.200
27 8	3621	5.960	.663	.010	.022	101.800
27 9	3621	5.960	.655	10.020	.022	101.900
28 0	3631	5.960	.648	-.020	.022	101.900
28 1	3631	5.960	.662	10.000	.022	102.000
28 2	3611	5.960	.653	-.050	.022	102.000
28 3	3611	5.960	.668	-.050	.022	102.200
28 4	3111	5.960	.652	0.000	.022	102.200
28 5	3111	5.960	.658	5.010	.022	102.200
28 6	3111	5.960	.659	10.000	.022	102.200
28 7	3111	5.960	.660	-.010	.022	102.200
28 8	3111	5.960	.653	-.010	.022	102.200
28 9	3111	5.960	.662	4.990	.022	102.200
29 0	3111	5.960	.655	-.010	.022	102.200
29 1	3111	5.960	.659	-.010	.022	102.200
29 2	3611	6.040	2.348	-.030	.079	101.300
29 3	3611	6.040	2.348	-.040	.078	101.800
29 4	3611	7.900	.537	0.000	.012	88.290
29 5	3611	7.900	.548	5.010	.012	89.530
29 6	3611	7.900	.556	10.000	.012	88.640
29 7	3611	7.900	.564	15.000	.012	87.850
29 8	3611	7.900	.563	0.000	.012	88.360
29 9	3611	7.900	.563	5.010	.012	88.410
30 0	3611	7.900	.563	9.990	.012	88.410
30 1	3611	7.900	.564	15.000	.012	88.490
30 2	3611	7.900	.562	0.000	.012	88.540
30 3	3611	7.900	.562	5.020	.012	88.560
30 4	3611	7.900	.562	10.010	.012	88.560
30 5	3611	7.900	.563	15.000	.012	88.560
30 6	3611	7.900	.563	-0.000	.012	88.560
30 7	3611	7.900	.561	-.010	.012	88.560
30 8	3211	7.900	.563	.020	.012	88.640
30 9	3211	7.900	.563	9.990	.012	88.640

26

UNCLASSIFIED

UNCLASSIFIED

APPENDIX 1 (continued)

Run	Conf Code	M _u	R _c × 10 ⁻⁶ /ft	α Deg	P _o PSI	T _u ~ R°
710	7411	7.900	.561	.010	.012	88.560
711	7411	7.900	.563	10.010	.012	88.450
712	7511	7.900	.562	.010	.012	88.340
713	7511	7.900	.561	10.030	.012	88.450
714	7111	7.900	.559	-.010	.012	88.710
715	7111	7.900	.562	5.000	.012	88.710
716	7611	7.900	.559	0.000	.012	88.580
717	7611	7.900	.562	5.010	.012	88.380
718	7611	7.900	.566	0.000	.012	88.190
719	7611	7.900	.563	5.030	.012	88.120
720	7641	7.900	.566	-.010	.012	88.020
721	7641	7.900	.568	5.020	.012	87.970
722	7641	7.900	.559	9.990	.012	87.970
723	7642	7.900	.566	-.050	.012	87.970
724	7642	7.900	.568	10.010	.012	87.990
725	7642	7.900	.568	.010	.012	88.170
726	7642	7.900	.564	10.000	.012	88.290
727	7621	7.900	.564	-.010	.012	88.530
728	7621	7.900	.563	10.030	.012	88.560
729	7671	7.900	.563	-.030	.012	88.460
730	7671	7.900	.563	10.010	.012	88.410
731	7111	7.900	.568	-.010	.012	88.340
732	7111	7.900	.561	-.010	.012	88.270
733	7111	7.900	.559	2.520	.012	88.340
734	7111	7.900	.563	5.010	.012	88.340
735	7111	7.900	.565	5.020	.012	88.340
736	7111	7.900	.563	.010	.012	88.270
737	7111	7.900	.563	2.520	.012	88.270
738	7111	7.900	.561	2.520	.012	88.270
739	7111	7.900	.569	0.000	.012	88.270
740	7611	7.840	.255	-.030	.005	86.860
741	7611	7.840	.262	5.020	.005	85.620
742	7611	7.840	.274	.010	.005	83.440
743	7611	7.840	.277	5.020	.005	82.670
744	7611	7.840	.280	0.000	.005	82.500
745	7611	7.840	.277	5.020	.005	83.140
746	7611	7.900	.574	-.030	.012	88.530
747	7611	7.900	.567	5.020	.012	89.250
748	7611	7.900	.555	10.030	.012	88.880
749	7611	7.900	.558	15.030	.012	87.820
750	7611	7.900	.569	.020	.012	87.090
751	7611	7.900	.575	9.990	.012	87.250
752	7611	7.900	.569	.010	.012	87.650
753	7611	7.900	.569	10.020	.012	87.700
754	7611	7.990	2.396	-.010	.054	94.620
755	7611	7.990	2.418	9.990	.054	94.630
756	7611	7.990	2.381	.010	.054	95.030
757	7611	7.990	2.413	10.030	.054	94.330
758	7611	7.990	2.410	.010	.054	94.660
759	7611	7.990	2.392	5.020	.054	95.170
760	7611	7.990	2.394	10.030	.054	94.290

UNCLASSIFIED

UNCLASSIFIED

APPENDIX II

FLAT PLATE AND BOTTOM CENTERLINE DATA

The interaction lengths as well as the plateau pressure and separation pressure on the flat plate and on bottom centerline of the delta model are presented in this table. The up-stream interaction length (d_1) is measured forward of the plane of the nozzle exit and is non-dimensionalized by the reference length (L) which is 20 inches. Free interaction length (d_f) is non-dimensionalized by the same length. Plateau pressure and separation pressure are presented as ratios to the tunnel ambient pressure. Runs for which interaction length is zero indicate that values were not read, not that the length is zero.

UNCLASSIFIED

APPENDIX II (Continued)

Run	Calc Code	P _{0j}	T _{0j}	Y _j	d ₁ /L	d ₂ /L	P _{FLAT} P ₀	P _{SEP} P ₀
1	1111	0.000	0.000					
2	1111	0.000	0.000					
3	1111	0.000	0.000					
4	1111	70.100	1147.000	1.400	.026	0.000	0.000	1.750
5	1111	70.110	1163.000	1.410	0.000	0.000	0.000	0.000
6	1111	70.310	1177.000	1.400	0.000	0.000	0.000	0.000
7	1111	70.710	1290.000	1.400	0.000	0.000	0.000	0.000
8	1111	0.000	0.000					
9	1111	0.000	0.000					
10	1111	0.000	0.000					
11	1111	32.640	966.000	1.400	.076	0.000	0.000	1.900
12	7	0.000	0.000					
13	1111	116.990	1070.000	1.400	.086	0.000	2.100	1.800
14	1611	123.400	974.000	1.400	.086	0.000	0.000	1.900
15	1611	70.750	1114.000	1.400	.046	0.000	0.000	1.750
16	1611	0.000	0.000					
17	1611	0.000	0.000					
18	1611	0.000	0.000					
19	1611	0.000	0.000					
20	1611	0.000	0.000					
21	1611	0.000	0.000					
22	1611	293.000	463.000	1.400	.251	.160	0.000	1.900
23	1611	291.000	454.000	1.400	.151	.130	0.000	3.750
24	1611	290.200	916.000	1.400	.106	0.000	0.000	.780
25	1611	297.400	944.000	1.400	.086	0.000	0.000	14.000
26	1611	247.600	955.000	1.400	.416	.200	1.900	1.200
27	1611	746.300	973.000	1.400	.516	.100	1.400	.750
28	1611	142.700	964.000	1.400	.176	0.000	0.000	1.900
29	1611	144.500	936.000	1.400	.126	0.000	0.000	3.700
30	1611	145.400	937.000	1.400	.126	0.000	0.000	7.700
31	1611	145.000	925.000	1.400	.000	0.000	0.000	0.000
32	1611	143.500	921.000	1.400	.326	.120	1.850	1.100
33	1611	143.400	939.000	1.400	.466	.100	1.300	.750
34	1611	72.950	946.000	1.400	.126	.095	2.800	1.850
35	1611	73.020	928.000	1.400	.056	0.000	0.000	3.600
36	1611	72.830	931.000	1.400	0.000	0.000	0.000	0.000
37	1611	72.870	935.000	1.400	.276	.135	1.065	1.100
38	1611	75.940	974.000	1.400	.466	.110	1.150	.700
39	1611	36.550	1005.000	1.400	.151	0.000	0.000	1.400
40	1611	36.280	998.000	1.400	0.000	0.000	0.000	0.000
41	1611	36.760	998.000	1.400	.251	0.000	0.000	1.500
42	1611	36.490	1071.000	1.400	.326	.100	1.100	.600
43	1611	70.710	948.000	1.400	.151	0.000	0.000	1.800
44	1611	579.100	959.000	1.400	.376	.145	3.200	2.100
45	1611	1167.000	869.000	1.400	.626	.230	3.700	2.450
46	1611	1517.000	858.000	1.400	.626	.210	3.900	2.550
47	1611	244.700	854.000	1.400	.176	0.000	0.000	1.900
48	1611	245.900	1023.000	1.400	.106	0.000	0.000	7.800
49	1611	68.840	986.000	1.400	.151	0.000	0.000	2.000
50	1611	66.950	970.000	1.400	.046	0.000	0.000	8.250
51	1211	495.000	911.000	1.400	.226	.125	2.700	1.900
52	1211	488.800	887.000	1.400	.136	0.000	0.000	7.600
53	1211	1002.000	887.000	1.400	.146	0.000	0.000	7.450
54	1211	998.100	882.000	1.400	.301	.150	3.000	1.950
55	1211	1513.000	803.000	1.400	.466	.200	3.300	2.100
56	1211	1510.000	791.000	1.400	.176	.130	9.950	7.750
57	1311	1731.000	739.000	1.400	.151	.115	2.550	1.800
58	1311	1733.000	827.000	1.400	.046	0.000	0.000	7.500
59	1311	1527.000	817.000	1.400	.046	0.000	0.000	7.600
60	1311	1529.000	853.000	1.400	.151	.115	2.650	1.825
61	1411	498.000	851.000	1.400	.176	0.000	0.000	1.900

UNCLASSIFIED

CONFIDENTIAL

APPENDIX II (Continued)

Run	Conf Code	P ₀₁	T ₀₁	Y ₁	d ₁ /L	d ₂ /L	$\frac{P_{PLAT}}{P_a}$	$\frac{P_{SEP}}{P_a}$
62	1411	500.100	832.000	1.400	.046	0.000	0.000	7.400
63	1411	1015.000	954.000	1.400	.106	0.000	0.000	7.700
64	1411	1020.000	996.000	1.400	.256	.145	2.900	1.950
65	1511	1005.000	957.000	1.400	.426	.115	3.300	2.000
66	1511	1015.000	851.000	1.400	.726	0.000	0.000	7.650
67	1111	252.200	0.000	1.400	0.000	.135	0.000	0.000
68	1111	244.100	954.000	1.400	.126	0.000	0.000	7.700
69	2611	143.400	921.000	1.400	.196	0.000	0.000	1.950
70	2611	144.600	957.000	1.400	.076	0.000	0.000	7.700
71	2611	287.200	942.000	1.400	.151	0.000	0.000	7.850
72	2611	298.800	944.000	1.400	.236	.125	0.000	2.000
73	1621	289.900	815.000	1.400	.265	.095	2.750	1.950
74	1621	298.400	940.000	1.400	0.000	0.000	0.000	0.000
75	1631	290.300	992.000	1.400	.031	0.000	0.000	1.950
76	1631	291.900	1015.000	1.400	.031	0.000	0.000	0.000
77	1641	298.200	935.000	1.400	.226	.145	2.750	1.900
78	1641	298.600	924.000	1.400	0.000	0.000	0.000	0.000
79	1642	297.600	1004.000	1.400	.216	.145	2.900	2.000
80	1642	298.500	1046.000	1.400	0.000	0.000	0.000	0.000
81	2611	1008.000	902.000	1.400	.516	.142	3.600	2.200
82	1111	136.600	903.000	1.290	.046	0.000	0.000	1.070
83	1111	276.200	854.000	1.290	.246	.132	2.900	2.000
84	1111	137.500	897.000	1.290	.106	0.000	0.000	7.450
85	1111	156.100	942.000	1.666	.176	0.000	0.000	1.900
86	1111	155.500	931.000	1.666	0.000	0.000	0.000	0.000
87	1613	0.000	0.000					
88	1613	0.000	0.000					
89	1613	296.000	816.000	1.400	.376	0.000	0.000	2.100
90	1611	288.600	896.000	1.400	.176	.130	0.000	2.600
91	1611	297.100	951.000	1.400	.136	0.000	0.000	5.400
92	3611	0.000	0.000					
93	3611	0.000	0.000					
94	3611	0.000	0.000					
95	3611	0.000	0.000					
96	3611	0.000	0.000					
97	3611	0.000	0.000					
98	3611	0.000	0.000					
99	3611	0.000	0.000					
100	3611	0.000	0.000					
101	3611	0.000	0.000					
102	3611	0.000	0.000					
103	3611	0.000	0.000					
104	3611	1503.000	541.000	1.400	1.046	.350	6.800	5.000
105	3611	291.100	858.000	1.400	.656	.170	3.700	2.450
106	3611	289.600	954.000	1.400	.276	.095	4.500	3.500
107	3611	290.700	951.000	1.400	.146	0.000	0.000	6.250
108	3611	299.300	1010.000	1.400	.096	0.000	0.000	11.250
109	3611	287.700	1024.000	1.400	.076	0.000	0.000	18.000
110	3611	298.700	1036.000	1.400	.096	0.000	0.000	28.500
111	3611	1159.000	905.000	1.400	.966	.310	5.200	2.650
112	3611	1161.000	920.000	1.400	.466	.160	6.100	4.950
113	3611	1162.000	926.000	1.400	.276	.150	9.750	6.500
114	3611	1159.000	926.000	1.400	.176	.170	0.000	11.500
115	3611	1159.000	933.000	1.400	.126	0.000	0.000	19.500
116	3611	1509.000	873.000	1.400	1.006	.290	5.800	4.600
117	3611	1514.000	911.000	1.400	.526	.120	6.900	4.900
118	3611	1517.000	926.000	1.400	.296	.180	10.000	6.700
119	3611	1512.000	926.000	1.400	.176	.120	0.000	11.500
120	3611	1510.000	828.000	1.400	.136	.100	0.000	18.500
121	3611	71.200	992.000	1.400	.426	.120	2.600	1.950
122	3611	73.260	952.000	1.400	.226	.114	3.100	2.750
123	3611	72.840	934.200	1.400	.106	0.000	0.000	3.100

CONFIDENTIAL

CONFIDENTIAL

TABLE 11 (continued)

Run	Conf Code	T_{0j}	T_{0j}	γ_j	d_1/L	d_2/L	$\frac{F_{PLAT}}{F_{\infty}}$	$\frac{F_{SEP}}{F_{\infty}}$
126	3611	72.580	912.000	1.400	.035	0.000	0.000	6.000
125	3611	72.340	916.000	1.400	0.000	0.000	0.000	0.000
126	3611	75.960	1023.000	1.400	.296	.090	2.300	1.700
127	3611	79.400	1077.000	1.400	.156	.000	0.000	2.200
128	3611	76.190	1055.000	1.400	.076	0.000	0.000	3.000
129	3611	76.170	1063.000	1.400	0.000	0.000	0.000	0.000
130	3611	76.140	1059.000	1.400	0.000	0.000	0.000	0.000
131	3611	145.000	970.000	1.400	.946	.130	3.290	2.250
132	3611	145.600	947.000	1.400	.746	.100	3.500	2.600
133	3611	143.600	885.000	1.400	.226	.150	0.000	3.150
134	3611	146.000	856.000	1.400	.096	0.000	0.000	6.000
135	3611	144.360	920.000	1.400	.076	0.000	0.000	10.900
136	3611	0.000	0.000					
137	3612	0.000	0.000					
138	3612	0.000	0.000					
139	3612	0.000	0.000					
140	3612	0.000	0.000					
141	3613	0.000	0.000					
142	3613	0.000	0.000					
143	3613	0.000	0.000					
144	3613	0.000	0.000					
145	3211	1002.000	910.000	1.400	.806	.210	4.000	2.400
146	3211	1006.000	955.000	1.400	.161	0.000	0.000	6.300
147	3211	1006.000	958.000	1.400	.096	0.000	0.000	11.250
148	3211	504.700	954.000	1.400	.716	.155	3.600	2.400
149	3211	503.000	1058.000	1.400	.116	0.000	0.000	6.200
150	3211	501.800	1084.000	1.400	.056	0.000	0.000	11.250
151	3211	1507.000	896.000	1.400	.806	0.000	0.000	2.600
152	3211	1516.000	817.000	1.400	.216	0.000	0.000	6.400
153	3211	125.100	796.000	1.400	.351	.107	2.500	1.700
154	3211	124.600	816.000	1.400	.106	0.000	0.000	3.000
155	3211	125.600	836.000	1.400	0.000	0.000	0.000	0.000
156	3611	505.700	951.000	1.400	.716	.140	3.600	2.500
157	3611	505.600	1053.000	1.400	.276	0.000	0.000	3.300
158	3611	503.900	1084.000	1.400	.086	0.000	0.000	6.300
159	3611	65.250	1062.000	1.400	.496	.130	3.700	2.500
160	3611	65.470	1047.000	1.400	.226	0.000	0.000	3.350
161	3111	278.300	1054.000	1.290	.676	.170	4.000	2.500
162	3111	278.000	1034.000	1.290	.306	.160	5.000	3.400
163	3111	179.600	1063.000	1.290	.496	.170	3.000	2.350
164	3111	179.000	1041.000	1.290	.156	0.000	0.000	3.200
165	3111	178.900	1037.000	1.290	.316	.130	3.500	2.400
166	3111	156.300	1055.000	1.668	.726	.135	2.550	1.630
167	3111	140.400	1063.000	1.668	.106	0.000	0.000	2.150
168	3111	249.500	978.000	1.400	.556	.140	3.200	2.500
169	3111	249.800	987.000	1.400	.626	.160	3.400	2.300
170	3111	289.000	992.000	1.400	.076	0.000	0.000	6.100
171	3111	287.500	994.000	1.400	0.000	0.000	0.000	0.000
172	3111	1158.000	960.000	1.400	.906	.230	5.200	2.700
173	3111	1164.000	968.000	1.400	.256	0.000	0.000	6.750
174	3111	1164.000	1018.000	1.400	.086	0.000	0.000	11.750
175	3511	495.500	865.000	1.400	.911	.300	4.200	2.450
176	3511	499.500	798.000	1.400	.151	0.000	0.000	6.300
177	3511	499.600	931.000	1.400	.096	0.000	0.000	11.500
178	3611	281.700	1045.000	1.400	.756	.210	3.850	2.450
179	3611	245.600	1059.000	1.400	.466	.120	2.900	2.300
180	3611	245.000	1024.000	1.400	.226	.110	0.000	3.100
181	3611	245.700	1020.000	1.400	.086	0.000	0.000	6.100
182	3611	246.400	1026.000	1.400	0.000	0.000	0.000	0.000
183	3641	249.500	1042.000	1.400	.656	.160	3.500	2.450
184	3641	249.500	1052.000	1.400	.146	.110	0.000	3.150
185	3641	240.100	1056.000	1.400	0.000	0.000	0.000	0.000

CONFIDENTIAL

CONFIDENTIAL

API DATA 11 (CONTINUED)

ROW	DATE	APR	TOY	Y	31/2	31/1	PLAT P ₂	PSEP P ₂
196	3642	298.800	1052.000	1.400	.626	.135	3.500	2.400
197	3642	290.800	1053.000	1.400	.226	.155	0.000	3.200
198	3642	289.500	1054.000	1.400	0.000	0.000	0.000	0.000
199	3613	287.000	1050.000	1.400	.756	.225	3.650	2.500
199	3613	289.300	1042.000	1.400	.326	.130	5.000	3.800
191	3613	288.300	1041.000	1.400	.326	.150	9.400	6.450
192	3311	1320.000	904.000	1.400	.466	.145	2.900	2.000
193	3311	1322.000	880.000	1.400	.146	0.000	0.000	3.100
194	3311	1321.000	876.000	1.400	.076	0.000	0.000	6.100
195	3411	1082.000	799.000	1.400	.776	.160	3.800	2.400
196	3411	1004.000	945.000	1.400	.226	.140	0.000	3.250
197	3411	1001.000	984.000	1.400	.076	.060	8.000	6.100
198	3611	64.300	981.000	1.400	.096	0.000	0.000	6.300
199	3611	287.100	611.000	1.400	.656	.215	7.600	2.000
200	3611	568.500	557.000	1.400	.876	.270	4.600	2.700
201	3511	998.000	838.000	1.400	.876	.360	4.800	2.650
202	3511	996.400	876.000	1.400	.376	.125	5.400	3.900
203	3511	997.500	884.000	1.400	.226	.150	0.000	6.100
204	4611	287.800	850.000	1.400	.656	.172	3.600	2.000
205	4611	296.500	833.000	1.400	.216	.130	0.000	3.400
206	4611	298.100	722.000	1.400	.116	0.000	0.000	6.200
207	4611	298.800	631.000	1.400	.756	.215	3.150	2.100
208	3621	295.400	612.000	1.400	.750	.205	3.700	2.500
209	3621	297.400	598.000	1.400	.190	.105	0.000	3.100
210	3621	298.000	582.000	1.400	0.000	0.000	0.000	0.000
211	3631	296.400	594.000	1.400	.781	.205	3.650	2.500
212	3631	299.700	589.000	1.400	.221	0.000	0.000	3.000
213	3631	287.200	578.000	1.400	.031	0.000	0.000	0.000
214	3611	296.200	594.000	1.400	.756	.215	3.100	2.100
215	3611	298.500	587.000	1.400	.416	.145	4.100	3.200
216	3611	298.100	587.000	1.400	.166	.125	0.000	4.500
217	3611	64.160	697.000	1.400	.896	0.000	0.000	6.300
218	3211	220.500	582.000	1.400	.621	.270	3.450	2.600
219	3211	219.800	581.000	1.400	.226	.140	0.000	3.300
220	3211	220.100	575.000	1.400	.076	0.000	0.000	6.000
221	3211	894.400	1058.000	1.400	.721	.145	3.300	2.350
222	3211	894.300	1073.000	1.400	.226	.130	0.000	3.150
223	3211	892.300	1079.000	1.400	.076	0.000	0.000	6.100
224	3611	498.180	1014.000	1.400	.621	.130	3.240	2.350
225	3611	497.400	951.000	1.400	.226	.130	0.000	3.200
226	3611	499.400	967.000	1.400	.076	0.000	0.000	6.100
227	3611	578.500	987.000	1.400	.806	.250	4.000	2.500
228	3611	0.000	0.000					
229	3642	297.500	939.000	1.400	0.000	0.000	0.000	0.000
230	3642	289.100	935.000	1.400	0.000	0.000	0.000	0.000
231	3641	129.500	1006.000	1.400	.626	.245	4.000	2.700
232	3641	129.200	1011.000	1.400	.176	.140	4.850	3.700
233	3641	129.900	1005.000	1.400	0.000	0.000	0.000	0.000
234	3621	128.200	980.000	1.400	.665	.145	4.400	2.750
235	3621	129.000	991.000	1.400	.175	0.000	0.000	3.200
236	3621	128.000	988.000	1.400	0.000	0.000	0.000	0.000
237	3611	0.000	0.000					
238	3611	0.000	0.000					
239	3611	0.000	0.000					
240	3611	0.000	0.000					
241	3611	297.600	899.000	1.400	.501	.120	1.600	1.400
242	3611	297.600	912.000	1.400	.276	.120	2.150	1.650
243	3611	297.300	936.000	1.400	.166	.080	3.350	2.750
244	3611	297.200	943.000	1.400	.856	0.000	0.000	4.400
245	3611	148.700	917.000	1.400	.406	.060	1.400	1.200
246	3611	149.000	910.000	1.400	.176	.090	2.000	1.650
247	3611	0.000	0.000					

CONFIDENTIAL

CONFIDE

APPENDIX II (Continued)

Run	Conf Code	P _{0j}	P _{0j}	T _j	d ₁ /L	d ₂ /L	P _{FLAT} P _m	P _{SEP} P _m
248	7611	0.000	0.000					
249	7611	175.400	865.000	1.400	.276	.129	2.250	1.700
250	7611	175.900	874.000	1.400	.556	.115	2.500	1.400
251	7611	47.140	847.000	1.400	.471	.129	1.600	1.300
252	7611	0.000	0.000					
253	7611	0.000	0.000					
254	7611	298.200	833.000	1.400	.466	.125	1.600	1.250
255	7611	298.700	968.000	1.400	.076	.120	0.000	2.900
256	7611	614.300	1021.000	1.400	.526	.117	1.700	1.400
257	7611	617.600	1014.300	1.400	.326	.130	2.300	1.700
258	7611	616.600	1041.900	1.400	.211	.120	3.650	2.900
259	7611	1068.000	1060.000	1.400	.496	.090	1.700	1.400
260	7611	1070.000	1018.000	1.400	.176	.115	3.600	2.900
261	7611	1072.000	956.300	1.400	.486	.110	1.800	1.350
262	7611	1072.000	994.000	1.400	.076	0.000	0.000	2.700
263	7611	1072.000	872.000	1.400	.546	.125	1.850	1.500
264	7611	1071.000	905.000	1.400	.196	.120	3.700	2.900
265	7611	1352.000	895.000	1.400	.676	.155	2.000	1.400
266	7611	1354.000	869.000	1.400	.496	.160	2.900	2.300
267	7611	1354.000	864.000	1.400	.306	.150	3.850	2.950
268	7611	1352.000	864.000	1.400	.136	0.000	0.000	4.600
269	7611	84.410	788.000	1.400	.306	.130	1.400	1.000
270	7611	84.710	781.000	1.400	.066	.040	1.800	1.600
271	7641	297.100	799.000	1.400	.406	.135	1.450	1.100
272	7641	296.900	812.000	1.400	.056	0.000	0.000	1.700
273	7641	297.300	851.000	1.400	0.000	0.000	0.000	0.000
274	7642	0.000	0.000					
275	7642	0.000	0.000					
276	7642	296.500	876.000	1.400	.366	0.000	1.500	1.100
277	7642	296.700	905.000	1.400	.076	0.000	1.400	1.000
278	7621	297.200	911.000	1.400	.495	.090	1.600	1.200
279	7621	296.300	935.000	1.400	0.000	0.000	0.000	0.000
280	7631	296.500	932.000	1.400	.511	.110	1.600	1.200
281	7631	296.400	948.000	1.400	.031	0.000	0.000	0.000
282	7611	335.100	946.000	1.400	.476	.100	1.550	1.300
283	7611	673.700	1006.000	1.400	.536	.125	1.850	1.500
284	7611	296.900	926.000	1.400	.426	.090	1.550	1.300
285	7611	297.400	931.000	1.400	.226	.100	2.050	1.650
286	7611	297.500	928.000	1.400	.071	0.000	0.000	2.750
287	7611	637.200	895.000	1.290	.466	.170	2.100	1.900
288	7611	722.800	908.000	1.290	.466	.090	2.100	1.780
289	7611	158.400	878.000	1.290	.156	0.000	2.600	2.300
290	7611	361.200	772.000	1.668	.276	.060	0.000	1.400
291	7611	140.100	840.000	1.668	.206	0.000	0.000	1.200
292	7611	1354.000	940.000	1.400	.066	0.000	0.000	1.000
293	7611	0.000	0.000					
294	7611	0.000	0.000					
295	7611	0.000	0.000					
296	7611	0.000	0.980					
297	7611	0.000	0.000					
298	7611	174.100	825.000	1.400	.506	.160	2.350	1.900
299	7611	174.500	851.000	1.400	.276	.135	2.900	2.300
300	7611	174.400	876.000	1.400	.156	.085	0.000	4.000
301	7611	175.100	896.000	1.400	.046	0.000	0.000	7.000
302	7611	87.650	846.000	1.400	.426	.110	2.000	1.500
303	7611	87.460	880.000	1.400	.166	0.000	0.000	2.200
304	7611	87.440	879.000	1.400	.046	0.000	0.000	4.000
305	7611	87.400	842.000	1.400	0.000	0.800	0.000	0.000
306	7611	21.800	855.000	1.400	.196	.110	1.600	1.100
307	7611	349.100	925.000	1.400	.706	.215	2.700	1.900
308	7611	607.500	1012.000	1.400	.706	.240	2.700	1.900
309	7611	607.000	1042.000	1.400	.176	.095	0.000	4.200

CONFIDENTIAL

CONFIDENTIAL

OF DATA 11 (CONTINUED)

Run	Conf Code	P _{0j}	T _{0j}	γ_j	Q _{1/L}	Q _{2/L}	$\frac{P_{PLAN}}{P_m}$	$\frac{P_{SEP}}{P_m}$
310	7411	604.200	1071.000	1.400	.806	.260	2.700	1.900
311	7411	604.000	1070.000	1.400	.066	0.000	0.000	4.100
312	7511	605.100	1032.000	1.400	.906	.280	3.200	1.900
313	7511	606.400	1050.000	1.400	.196	.145	0.000	4.150
314	7111	173.900	903.000	1.400	.486	.150	2.150	1.700
315	7111	174.000	914.000	1.400	.161	0.000	0.000	2.200
316	7611	0.000	0.000					
317	7611	0.000	0.000					
318	7611	173.900	908.000	1.400	.586	.100	0.000	1.400
319	7611	173.600	910.000	1.400	0.000	0.000	0.000	0.000
320	7641	174.400	891.000	1.400	.426	0.000	2.200	1.500
321	7641	174.300	898.000	1.400	.186	0.000	0.000	2.200
322	7641	174.300	904.000	1.400	.106	0.000	0.000	4.000
323	7642	0.000	0.000					
324	7642	0.000	0.000					
325	7642	173.900	879.000	1.400	.426	.110	2.100	1.700
326	7642	174.000	896.000	1.400	.036	0.000	0.000	1.700
327	7621	174.200	888.000	1.400	.506	.135	2.400	1.400
328	7621	174.000	900.000	1.400	0.000	0.000	0.000	0.000
329	7631	173.600	890.000	1.400	.576	.140	2.350	1.900
330	7611	174.000	900.000	1.400	.031	0.000	0.000	0.000
331	7111	734.000	898.000	1.200	.736	.190	2.900	1.900
332	7111	167.800	891.000	1.200	.506	.190	2.500	1.900
333	7111	168.800	890.000	1.200	.356	.130	2.600	1.900
334	7111	168.600	890.000	1.200	.146	.130	0.000	2.400
335	7111	732.000	896.000	1.200	.316	.155	3.400	2.600
336	7111	149.300	863.000	1.666	.356	.152	2.000	1.400
337	7111	148.800	859.000	1.666	.206	0.000	0.000	1.700
338	7111	0.000	0.000					
339	7111	348.000	891.000	1.400	.586	.125	2.400	1.700
340	7611	0.000	0.000					
341	7611	0.000	0.000					
342	7611	79.510	798.000	1.400	.556	.130	2.900	2.000
343	7611	79.520	821.000	1.400	.276	.155	3.000	2.300
344	7611	40.310	806.000	1.400	.476	.135	0.000	2.100
345	7611	40.110	796.000	1.400	.166	.120	2.900	2.200
346	7611	700.600	962.000	1.400	.846	.190	3.100	1.900
347	7611	699.700	998.000	1.400	.426	.150	3.550	2.700
348	7611	699.400	913.000	1.400	.246	0.000	5.900	2.150
349	7611	701.300	865.000	1.400	.146	0.000	0.000	7.200
350	7611	347.300	859.000	1.400	.726	.220	2.700	1.900
351	7611	750.600	854.000	1.400	.176	0.000	0.000	4.100
352	7611	154.900	842.000	1.400	.506	.140	2.350	1.900
353	7611	155.600	849.000	1.400	.126	0.000	0.000	4.100
354	7611	0.000	0.000					
355	7611	0.000	0.000					
356	7611	839.200	972.000	1.400	.276	0.000	0.000	1.100
357	7611	839.300	971.000	1.400	0.000	0.000	0.000	0.000
358	7611	418.000	999.000	1.400	.176	0.000	0.000	1.150
359	7611	417.800	999.000	1.400	.076	0.000	0.000	2.100
360	7611	418.700	1005.000	1.400	0.000	0.000	0.000	0.000

CONFIDENTIAL

CONFIDENTIAL

APPENDIX III

UPPER SURFACE DATA

The data presented in this table is similar to that of Appendix B with the exception that this table presents delta configuration data measured along the 45° off-top centerline ray, and the interaction point measured from the nose is presented rather than interaction length.

<u>Run</u>	<u>α - Deg</u>	<u>Interaction Point (X/L)</u>	<u>P_{PLAT}/P_∞</u>	<u>P_{SEP}/P_∞</u>
104	0	.645	8.0	6.8
105	0	.7	4	3.4
106	5	.635	4	3.45
107	10	.60	2.85	2.4
108	15	.575	2.0	1.5
109	20	.63	1.6	1.2
111	0	.63	5.9	4.3
112	5	.395	5.7	3.0
113	10	.20	3.8	2.4
114	15	.17	2.9	1.7
115	20	.08	3.0	2.45
116	0	.63	6.65	4.65
117	5	.29	6.0	3.0
118	10	.16	4.2	2.85
119	15	.07	3.5	2.8
120	20	.03	5.4	5.3
121	0	.695	2.8	1.9
122	2.5	.7	2.9	2.2
123	5	.7	2.8	2.4
124	10	.635	2.15	1.45
127	2.5	.70	2.3	1.8
131	0	.69	3.3	2.2
132	2.5	.70	2.3	1.8
133	5.0	.635	3.3	2.5
134	10	.635	2.45	1.85
135	15	.60	1.8	1.4
145	0	.7	4.45	4.1
148	0	.7	3.8	3.3
151	0	.7	5.1	4.7
156	0	.7	4.0	.4
159	0	.71	4.3	3.1
163	0	.69	2.6	2.2
165	2.5	.7	3.3	2.9
166	0	.69	3.4	1.95
167	2.5	.76	---	2.2
172	0	.63	5.2	4.3
178	0	.7	4.4	3.9

CONFIDENTIAL

APPENDIX III (continued)

<u>Run</u>	<u>α ~ Deg</u>	<u>Interaction Point (X/L)</u>	<u>P_{Plat}/P_o</u>	<u>P_{SEP}/P_o</u>
179	0	.71	3.0	2.2
241	0	.71	1.9	1.7
242	5	.645	1.7	1.45
243	10	.635	1.35	1.1
244	15	.595	1.15	1.0
245	0	.71	1.65	1.3
246	5	.645	1.5	1.35
250	0	.70	2.0	1.8
256	0	.63	2.0	2.0
257	5	.645	1.9	1.7
258	10	.635	1.5	1.3
265	0	.63	2.5	2.0
266	5	.60	2.2	2.0
267	10	.635	1.7	1.5
268	15	.50	1.4	1.0
269	0	.71	1.45	1.1
298	0	.72	2.4	2.0
299	5	.65	2.4	2.0
300	10	.66	1.8	1.6
301	15	.67	1.4	1.2
302	0	.72	2.2	1.6
303	5	.65	2.3	2.1
304	10	.66	1.6	1.3
305	15	.67	1.25	1.0
307	0	.64	3.0	2.8
342	0	.70	2.8	2.5
346	0	.64	3.4	2.8
347	5	.46	3.35	1.6
348	10	.20	2.4	1.65
349	15	.24	1.9	1.2
350	0	.645	3.0	2.8
351	10	.66	2.0	1.8
352	0	.67	2.4	2.1
356	0	.84	---	1.6
358	0	.84	---	1.2

UNCLASSIFIED

APPENDIX IV

PLUME DATA

This appendix presents part of the data measured from the Schlieren photographs of the plume and separated region. The Reattachment point measurements are measured from an origin at the trailing edge of the lower surface elevon (X = 21.69 inches, Y = 0 inches) as shown in the text in Figure 164.

Run	Initial Radius ~ Inches	Initial Turning Angle ~ Deg.	Flow Separation Angle	Reattachment Point		Separation Length Inches
				X Inches	Y Inches	
13	3.64	76	-	.44	.44	-
14	3.64	78	-	.36	.44	-
22	6.0	82	-	.37	.75	-
28	5.0	80	-	.48	.62	-
34	5.0	77	-	.55	.59	-
43	4.55	80	-	.44	.53	-
44	4.09	87	-	.44	1.07	-
45	7.45	87	-	.53	1.6	-
46	4.55	90	-	.53	1.78	-
47	2.5	85	-	.36	.53	-
49	5.0	86	-	.36	.73	-
51	2.5	86	-	.50	.80	-
54	4.55	86	-	.53	.98	-
55	4.55	87	-	.53	1.25	-
57	4.09	70	-	.50	.57	-
60	3.18	75	-	.39	.53	-
61	2.95	80	-	.53	.71	-
64	2.73	82	-	.62	.89	-
67	3.64	87	-	.44	.80	-
69	3.64	86	-	.44	.71	-
72	6.00	86	-	.36	.89	-
73	4.55	83	-	1.07	.98	-
75	3.64	83	-	1.42	.62	-
77	6.0	82	-	1.33	.98	-
81	7.45	85	-	.41	1.33	-
82	2.05	83.5	-	.53	.80	-

UNCLASSIFIED

TABLE 1 (Continued)

Run	Initial Radius ~ Inches	Initial Turning Angle ~ Deg.	Flow Separation Angle	Reattachment Point		Separation Length Inches
				X Inches	Y Inches	
83	3.15	90	-	.53	1.15	-
85	3.18	66.5	-	.98	.71	-
105	4.55	77	5.91	.76	1.45	7.99
111	6.00	86	7.60	1.09	2.73	14.5
116	7.45	83	8.69	1.27	3.27	17.45
121	3.18	85	6.27	1.27	1.09	7.27
126	4.09	81	6.13	.73	.73	12.
131	4.55	80	6.84	1.05	1.45	8.4
145	4.09	79	6.06	.91	1.82	11.27
151	5.00	82	6.66	.91	2.0	15.4
153	4.55	79	7.40	1.45	1.09	-
156	7.45	77	7.87	1.63	1.82	15.3
161	4.54	81	7.13	1.33	1.87	-
163	5.0	71	-	-	-	-
166	7.45	60	-	-	-	-
168	10.36	62	-	-	-	-
169	4.09	82	6.28	1.07	1.51	14.3
172	6.0	80	7.37	1.07	2.49	15.1
178	4.54	82	6.37	1.09	1.82	15.6
179	4.09	78.5	6.34	1.42	1.57	12.6
195	4.09	83	6.68	1.45	2.0	14.5
199	5.0	83	7.61	1.08	1.91	15.6
204	6.0	75	7.44	1.42	1.91	15.3
211	4.09	88	6.55	2.42	1.91	17.8
218	4.54	83	5.02	1.65	1.25	-
221	4.09	82	6.26	1.31	1.74	14.4
224	4.09	77	6.55	1.13	1.57	-
227	4.55	85	7.19	1.09	2.18	12.4
231	5.0	81	-	-	-	-
234	6.0	76	9.2	2.52	2.44	-
241	4.54	82	7.74	.98	1.51	13.2
245	3.41	80	7.24	.89	1.16	15.3
250	4.09	81	7.9	1.33	1.74	16.4
251	3.41	81	7.57	1.15	1.42	13.5
256	4.09	86	8.36	.89	1.69	12.6
259	3.41	78	8.08	1.25	1.6	13.
261	3.18	77	8.04	1.51	1.60	10.1
263	5.0	85	8.79	1.09	1.87	11.4
265	4.55	85	7.65	.98	1.96	12.3
269	2.73	76	8.42	.98	1.07	6.9

UNCLASSIFIED

UNCLASSIFIED

UNCLASSIFIED

Run	Initial Radius ~ Inches	Initial Turning Angle ~ Deg.	First Separation Angle	Reattachment Point		Separation Length Inches
				X Inches	Y Inches	
271	4.55	82	5.21	1.51	.89	9.9
276	4.09	85	5.72	1.42	.89	10.5
278	4.09	82	7.96	1.78	1.51	10.3
280	3.18	86	7.35	2.47	1.60	11.2
282	2.73	83	7.62	.98	1.42	12.1
283	4.09	88	7.78	.89	1.60	12.5
284	3.64	82	7.97	1.16	1.37	16.5
287	5.0	38	10.24	.98	1.87	12.3
288	4.09	86	4.0	.71	.71	13.3
290	4.09	74	9.46	.73	.73	13.6
291	2.95	68	5.76	.98	.53	-
292	3.64	81	-	.14	.36	9.2
298	3.18	79	7.94	1.25	1.6	15.5
302	4.09	76	8.63	1.34	1.51	14.6
306	3.64	65	10.94	1.51	1.07	-
307	4.09	82	6.89	1.25	1.87	15.1
308	4.09	82	7.06	1.60	1.96	15.0
310	6.00	76	6.69	1.96	2.13	16.35
312	4.09	79	6.31	1.87	2.4	17.24
314	3.64	83	7.76	1.24	1.51	16.09
320	7.45	84	9.51	2.58	1.87	13.15
325	6.0	79	8.8	2.31	1.69	14.24
327	4.55	76	8.16	2.04	1.87	16.51
329	4.09	80	8.60	2.76	1.96	16.5
331	5.0	75	7.64	1.07	2.13	14.22
336	4.09	70	8.15	1.42	1.24	17.06
339	4.09	80	7.76	1.24	1.78	15.47
342	5.00	82	-	1.87	2.31	14.57
344	6.0	72	-	1.78	1.78	15.64
346	7.45	85	7.53	1.16	2.4	15.47
350	5.0	86	7.66	1.24	2.13	15.5
352	4.55	80	8.27	1.27	1.67	15.4
356	2.95	76	-	1.09	1.35	5.82

DOCUMENT CONTROL DATA - RAD		
1. REPORT TITLE		2. REPORT SEC. 5 TO 5.1 CLASSIFICATION
Air Force Flight Dynamics Laboratory Wright-Patterson AFB, Ohio		Confidential Group 4
3. REPORT TITLE Air Experimental Study of Plume Effects on Lifting Re-entry Vehicles (U).		
4. DESCRIPTIVE NOTES (Type of report and inclusive dates) Final Technical Report Sept. 1969 to March 1971		
5. AUTHOR(S) (Last name, first name, initial) Ramsch, John, R.		
6. REPORT DATE March 1971	7a. TOTAL NO. OF PAGES 309	7b. NO. OF REFS 15
8a. CONTRACT OR GRANT NO. F33615-70-C-1048	9a. ORIGINATOR'S REPORT NUMBER(S) GDCA-DCD71-001	
b. PROJECT NO. 1366	9b. OTHER REPORT NO(S) (Any other numbers that may be assigned this report) AFFDL-TR-71-34	
c. Task No. 3298		
10. AVAILABILITY/LIMITATION NOTICES This document is subject to special export controls and each transmittal to foreign nationals may be made only with prior approval of the Air Force Flight Dynamics Laboratory (FDMG).		
11. SUPPLEMENTARY NOTES None	12. SPONSORING MILITARY ACTIVITY Air Force Flight Dynamics Laboratory (FDMG) Wright-Patterson AFB, Ohio 45433	
13. ABSTRACT Tests were conducted at Mach numbers of 6, 8, and 10 on a representative lifting body entry vehicle and a Mach number of 10 on a flat plate using heated air and other gases to simulate rocket exhaust plumes. Extensive flow separation resulting from the plumes was observed on both configurations during the test program and the most powerful parameters which affected plume induced separation included: <ol style="list-style-type: none"> 1. Model shape 2. angle of attack 3. Reynolds number 4. nozzle expansion ratio 5. nozzle total pressure 6. nozzle gas temperature and specific heat. <p>The flat plate model showed much less flow separation than the delta planform at similar test conditions, however, serious problems in control effectiveness were indicated on both models for the aft mounted elevon. The data did not correlate well with existing semi-empirical correlations developed for control surface induced separation and plume shape. New semi-empirical correlations were developed for predicting plume shape in a region of plume induced separation and for predicting the pressure in and the extent of the separated region.</p> <p style="text-align: center;">UNCLASSIFIED ABSTRACT</p>		

DD FORM 1473

See Form of Standard Form
Approved: 1-1-58

INSTRUCTIONS

1. **ORIGINATING ACTIVITY:** Enter the name and address of the contractor, subcontractor, grantee, Department of Defense activity or other organization (corporate author) issuing the report.
- 2a. **REPORT SECURITY CLASSIFICATION:** Enter the overall security classification of the report. Indicate whether "Restricted Data" is included. Marking is to be in accordance with appropriate security regulations.
- 2b. **GROUP:** Automatic downgrading is specified in DoD Directive 5200.10 and Armed Forces Industrial Manual. Enter the group number. Also, when applicable, show that optional markings have been used for Group 3 and Group 4 as authorized.
3. **REPORT TITLE:** Enter the complete report title in all capital letters. Titles in all cases should be unclassified. If a meaningful title cannot be selected without classification, show title classification in all capitals in parenthesis immediately following the title.
4. **DESCRIPTIVE NOTES:** If appropriate, enter the type of report, e.g., interim, progress, summary, annual, or final. Give the inclusive dates when a specific reporting period is covered.
5. **AUTHOR(S):** Enter the name(s) of author(s) as shown on or in the report. Enter last name, first name, middle initial. If military, show rank and branch of service. The name of the principal author is an absolute minimum requirement.
6. **REPORT DATE:** Enter the date of the report as day, month, year; or month, year. If more than one date appears on the report, use date of publication.
- 7a. **TOTAL NUMBER OF PAGES:** The total page count should follow normal pagination procedures, i.e., enter the number of pages containing information.
- 7b. **NUMBER OF REFERENCES:** Enter the total number of references cited in the report.
- 8a. **CONTRACT OR GRANT NUMBER:** If appropriate, enter the applicable number of the contract or grant under which the report was written.
- 8b, 8c, & 8d. **PROJECT NUMBER:** Enter the appropriate military department identification, such as project number, subproject number, system numbers, task number, etc.
- 9a. **ORIGINATOR'S REPORT NUMBER(S):** Enter the official report number by which the document will be identified and controlled by the originating activity. This number must be unique to this report.
- 9b. **OTHER REPORT NUMBER(S):** If the report has been assigned any other report numbers (either by the originator or by the sponsor), also enter this number(s).
10. **AVAILABILITY/LIMITATION NOTICES:** Enter any limitations on further dissemination of the report, other than those

imposed by security classification, using standard statements such as:

- (1) "Qualified requesters may obtain copies of this report from DDC."
- (2) "Foreign announcement and dissemination of this report by DDC is not authorized."
- (3) "U. S. Government agencies may obtain copies of this report directly from DDC. Other qualified DDC users shall request through _____."
- (4) "U. S. military agencies may obtain copies of this report directly from DDC. Other qualified users shall request through _____."
- (5) "All distribution of this report is controlled. Qualified DDC users shall request through _____."

If the report has been furnished to the Office of Technical Services, Department of Commerce, for sale to the public, indicate this fact and enter the price, if known.

11. **SUPPLEMENTARY NOTES:** Use for additional explanatory notes.

12. **SPONSORING MILITARY ACTIVITY:** Enter the name of the departmental project office or laboratory sponsoring (paying for) the research and development. Include address.

13. **ABSTRACT:** Enter an abstract giving a brief and factual summary of the document indicative of the report, even though it may also appear elsewhere in the body of the technical report. If additional space is required, a continuation sheet shall be attached.

It is highly desirable that the abstract of classified reports be unclassified. Each paragraph of the abstract shall end with an indication of the military security classification of the information in the paragraph, represented as (TS), (S), (C), or (U).

There is no limitation on the length of the abstract. However, the suggested length is from 150 to 225 words.

14. **KEY WORDS:** Key words are technically meaningful terms or short phrases that characterize a report and may be used as index entries for cataloging the report. Key words must be selected so that no security classification is required. Identifiers, such as equipment model designation, trade name, military project code name, geographic location, may be used as key words but will be followed by an indication of technical context. The assignment of links, rules, and weights is optional.